

Functionalized Cucurbit[7]urils for Molecular Recognition: Electrochemiluminescence- and Fluorescent-based Sensing Strategies

Zur Erlangung des akademischen Grades eines

DOKTORS DER NATURWISSENSCHAFTEN

(Dr. rer. nat.)

von der KIT-Fakultät für Chemie und Biowissenschaften
des Karlsruher Instituts für Technologie (KIT)

genehmigte

DISSERTATION

von

M.Sc. Patrick Gruhs

1. Referent: Priv. Doz. Dr. Frank Biedermann
2. Referent: Prof. Dr. Stefan Bräse

Tag der mündlichen Prüfung: 16.12.2025

Erklärung zur Dissertation

Hiermit erkläre ich, Patrick Gruhs, dass ich die vorliegende Arbeit mit dem Titel „*Functionalized Cucurbit[7]urils for Molecular Recognition: Electrochemiluminescence- and Fluorescent-based Sensing Strategies*“ selbstständig verfasst und keine anderen als die angegebenen Quellen und Hilfsmittel verwendet habe, sowie die wörtlich und inhaltlich übernommenen Stellen als solche kenntlich gemacht habe. Weiterhin erkläre ich, dass ich die Satzung des Karlsruher Instituts für Technologie (KIT) zu Sicherung der guten wissenschaftlichen Praxis in der gültigen Fassung beachtet habe. Die Dissertation wurde bisher an keiner anderen Hochschule oder Universität eingereicht.

Patrick Gruhs

Ort, Datum

Table of Contents

1. Abstract.....	1
2. Kurzzusammenfassung.....	2
3. General Introduction.....	3
3.1. Principles of Supramolecular Chemistry	3
3.2. Approaches to Characterizing Binding Constants	6
3.3. Tools for Monitoring Binding Events.....	6
3.4. Synthetic Macrocycles as Platforms for Chemosensor Design.....	9
3.4.1. Crown Ethers: A Historic Milestone in Host-Guest Chemistry.....	9
3.4.2. Cryptands and Lariat Ethers: Extending the Concept.....	10
3.4.3. Calixarenes: Phenolic Macrocycles with Tunable Recognition Properties	11
3.4.4. Cyclodextrins: Biocompatible Cavities for Molecular Recognition.....	13
3.4.5. The Reintroduction of Cucurbiturils and Their Rise in Supramolecular Sensing	16
3.4.5.1. Origins and Revival of the Cucurbit[<i>n</i>]uril Family	16
3.4.5.2. Unlocking the Full Potential of Cucurbit[<i>n</i>]urils: The Discovery of Higher Homologues	19
3.4.5.3. Synthesis of Cucurbiturils and Factors Influencing Homologue Distribution	20
3.4.5.4. Mechanism of Cucurbituril Formation.....	23
3.4.5.5. Architectural Features Driving Host-Guest Recognition in CB _{<i>n</i>} Macrocycles.....	26
3.4.5.6. The Hydrophobic Effect as a Key Element in Cucurbituril Binding Mechanisms	31
3.4.6. Cucurbituril Functionalization as a Gateway to Molecular Tools	33
3.4.6.1. The Building Block Approach: Precursor-Driven Functionalization of Cucurbiturils	34
3.4.6.2. Direct Functionalization of Cucurbiturils: Unlocking the Post-Synthetic Modification	35
3.4.6.3. From Hydroxyl to Handle: Installing Allyl and Propargyl Groups on Cucurbiturils for Downstream Derivatization	36
3.4.7. Cucurbiturils in Biomedical Applications: Toward Smart Molecular Tools.....	37
3.4.7.1. Synthetic Ion Transport with CB _{<i>n</i>}	37
3.4.7.2. Encapsulation of Drugs by CB _{<i>n</i>} -Based Systems.....	38

3.4.7.3.	Targeted Drug Delivery from Cucurbituril-Based Systems	39
3.4.7.4.	Cucurbiturils for Bioimaging and Real-Time Bioprocess Analysis	40
3.4.7.5.	Alleviating and Modulating Side Effects of Drug Administration with Cucurbiturils	43
3.4.7.6.	Biosensors Based on Cucurbiturils	44
4.	Aim of this Thesis.....	48
5.	Design and Development of a CB7-RuBiPy Conjugate as an Electrochemiluminescent Chemosensor for Biorelevant Analyte Detection.....	50
5.1.	Fundamentals of Electrochemiluminescence	50
5.1.1.	The Central Role of Tris(2,2'-bipyridyl)ruthenium(II) in Modern Sensing Applications	50
5.1.2.	Instrumentation Essentials for Electrochemiluminescence-Based Sensing	50
5.1.3.	Photophysical characteristics of Tris(2,2'-bipyridyl)ruthenium(II).....	52
5.1.4.	Mechanistic Pathways of Electrochemiluminescence: From Electron Transfer to Light Emission	53
5.1.4.1.	Ion Annihilation Pathway	53
5.1.4.2.	Co-reactant Pathway.....	54
5.1.5.	Established Analytical Applications of Ruthenium-Based Electrochemiluminescence ...	56
5.1.5.1.	ECL-Based Immunoassays: Principles, Platforms, and Performance	56
5.1.5.2.	Illuminating the Genome: ECL-Based Strategies for DNA Sensing.....	58
5.1.5.3.	Integrating Aptamer and DNAzyme Technologies in ECL Biosensing	60
5.2.	Design and Synthesis of CB7-Ru.....	61
5.3.	Structural Characterization of CB7-Ru.....	66
5.4.	Photophysical Properties and Sensing Capabilities of CB7-Ru.....	70
5.5.	Electrochemical Properties and ECL-Sensing Capabilities of CB7-Ru.....	84
5.6.	Photodynamic Therapy: Mechanisms and Biomedical Applications	88
5.6.1.	Bioanalytical Evaluation of CB7-Ru for Light-Activated Anticancer Applications	89
5.7.	Conclusions.....	90
5.8.	Experimental Part.....	91
5.8.1.	Material and Methods	91
5.8.1.1.	Material	91
5.8.1.2.	Nuclear Magnetic Resonance (NMR) Spectroscopy	92

5.8.1.3.	High-Performance Liquid Chromatography (HPLC).....	92
5.8.1.4.	Electrospray Ionization Mass Spectrometry (ESI-MS).....	92
5.8.1.5.	Absorbance Spectra.....	92
5.8.1.6.	Fluorescence Spectra.....	93
5.8.1.7.	Excited State Lifetime Measurement.....	93
5.8.1.8.	High-Performance Liquid Chromatography-mass spectrometry (HPLC-MS).....	93
5.8.1.9.	Electrochemiluminescence (ECL) Instrumentation.....	94
5.8.1.10.	Cell culture.....	94
5.8.1.11.	(Photo)toxicity.....	94
5.8.1.12.	Subcellular Localization by Confocal Microscopy.....	95
5.8.2.	Synthesis and Characterization.....	95
5.8.2.1.	Glycoluril.....	95
5.8.2.2.	Cucurbit[7]uril (CB7).....	96
5.8.2.3.	Monohydroxylated CB7 (CB7-OH).....	97
5.8.2.4.	Monopropargyloxylated CB7 (CB7-OPr).....	99
5.8.2.5.	2,5-dioxopyrrolidin-1-yl 4-(4'-methyl-[2,2'-bipyridin]-4-yl)butanoate (BiPy-NHS)	100
5.8.2.6.	Ru-NHS.....	101
5.8.2.7.	Ru-N ₃	103
5.8.2.8.	CB7-Ru.....	105
5.8.2.9.	Ada-Ru.....	107
5.9.	Supporting Information.....	108
6.	Distinguishing Biorelevant Analytes by a CB7-Coumarin Sensor Library.....	125
6.1.	Fundamentals of Coumarins: Chemistry and Natural Origins.....	125
6.2.	Synthetic Strategies for Coumarin Derivatives.....	126
6.3.	Functional Roles and Practical Applications of Coumarin Derivatives.....	130
6.4.	Host-Guest Binding of CB7 with Coumarin Dyes.....	133
6.5.	Design and Synthesis of a CB7-Coumarin Sensor Library.....	137
6.6.	Structural Characterization of CB7-Coumarins.....	141

6.7. pH-Responsive Photophysical Behavior and Sensing Capabilities of CB7-Coumarin Conjugates.....	149
6.8. Comparative Discussion of Photophysical Behavior across the CB7-Coumarin Conjugates.....	159
6.9. Microplate-Based Two-Dimensional Analysis for Analyte Discrimination Using CB7-Coumarin Chemosensors.....	161
6.10. Conclusions.....	173
6.11. Experimental Part.....	176
6.11.1. Material and Methods.....	176
6.11.1.1. Material.....	176
6.11.1.2. Nuclear Magnetic Resonance Spectroscopy (NMR).....	176
6.11.1.3. High Performance Liquid Chromatography (HPLC).....	176
6.11.1.4. Electrospray Ionization Mass Spectrometry (ESI-MS).....	177
6.11.1.5. Absorbance Spectra.....	177
6.11.1.6. Fluorescence Spectra.....	178
6.11.1.7. High Performance Liquid Chromatography Mass Spectrometry (HPLC-MS).....	178
6.11.2. Synthesis and Characterization.....	178
6.11.2.1. Ethyl 7-(diethylamino)-2-oxo-2H-chromene-3-carboxylate.....	178
6.11.2.2. 7-(diethylamino)-2-oxo-2H-chromene-3-carboxylic acid.....	180
6.11.2.3. <i>N</i> -(2-(2-(2-(2-azidoethoxy)ethoxy)ethoxy)ethyl)-7-(diethylamino)-2-oxo-2H-chromene-3-carboxamide (DEC-N ₃).....	182
6.11.2.4. CB7-diethylcoumarin (CB7-DEC).....	184
6.11.2.5. 2-(7-amino-4-methyl-2-oxo-2H-chromen-3-yl)- <i>N</i> -(2-(2-(2-(2-azidoethoxy)ethoxy)ethoxy)ethyl)acetamide (AMCA-N ₃).....	186
6.11.2.6. CB7-AMCA.....	188
6.11.2.7. <i>N</i> -(2-(2-(2-(2-azidoethoxy)ethoxy)ethoxy)ethyl)-6,8-difluoro-7-hydroxy-2-oxo-2H-chromene-3-carboxamide (Pacific Blue-N ₃).....	190
6.11.2.8. CB7-Pacific Blue.....	192
6.11.2.9. Ethyl 7-(dimethylamino)-2-oxo-2H-chromene-3-carboxylate.....	194
6.11.2.10. 7-(dimethylamino)-2-oxo-2H-chromene-3-carboxylic acid.....	196
6.11.2.11. <i>N</i> -(2-(2-(2-(2-azidoethoxy)ethoxy)ethoxy)ethyl)-7-(dimethylamino)-2-oxo-2H-chromene-3-carboxamide (DMC-N ₃).....	198

6.11.2.12.	CB7-dimethylcoumarin (CB7-DMC).....	200
6.11.2.13.	3-(dipropylamino)phenol.....	202
6.11.2.14.	4-(dipropylamino)-2-hydroxybenzaldehyde.....	204
6.11.2.15.	Ethyl 7-(dipropylamino)-2-oxo-2 <i>H</i> -chromene-3-carboxylate.....	206
6.11.2.16.	7-(dipropylamino)-2-oxo-2 <i>H</i> -chromene-3-carboxylic acid.....	207
6.11.2.17.	<i>N</i> -(2-(2-(2-(2-azidoethoxy)ethoxy)ethoxy)ethyl)-7-(dipropylamino)-2-oxo-2 <i>H</i> -chromene-3-carboxamide (DPC-N ₃)	209
6.11.2.18.	CB7-dipropylcoumarin (CB7-DPC).....	211
6.11.2.19.	3-(dibutylamino)phenol.....	213
6.11.2.20.	4-(dibutylamino)-2-hydroxybenzaldehyde.....	215
6.11.2.21.	Ethyl 7-(dibutylamino)-2-oxo-2 <i>H</i> -chromene-3-carboxylate.....	217
6.11.2.22.	7-(dibutylamino)-2-oxo-2 <i>H</i> -chromene-3-carboxylic acid.....	219
6.11.2.23.	<i>N</i> -(2-(2-(2-(2-azidoethoxy)ethoxy)ethoxy)ethyl)-7-(dibutylamino)-2-oxo-2 <i>H</i> -chromene-3-carboxamide (DBC-N ₃).....	221
6.11.2.24.	CB7-dibutylcoumarin (CB7-DBC).....	223
6.11.2.25.	<i>N</i> -(2-(2-(2-(2-azidoethoxy)ethoxy)ethoxy)ethyl)-11-oxo-2,3,6,7-tetrahydro-1 <i>H</i> ,5 <i>H</i> ,11 <i>H</i> -pyrano[2,3- <i>f</i>]pyrido[3,2- <i>l</i> - <i>ij</i>]quinoline-10-carboxamide (DCC-N ₃).....	225
6.11.2.26.	CB7-dicyclohexylcoumarin (CB7-DCC)	227
7.	References	230
8.	List of Abbreviations	256
9.	Appendices	259
9.1.	Curriculum Vitae	259
9.2.	Acknowledgements.....	261
9.3.	Artificial Intelligence (AI) Disclaimer.....	262

1. Abstract

Over recent years, supramolecular chemistry has gained tremendous popularity and has significantly contributed to advances across various scientific disciplines, ranging from drug delivery to molecular machinery. Supramolecular chemists rely on dynamic, non-covalent intermolecular interactions – such as π - π stacking, hydrophobic effects, electrostatic interactions, hydrogen bonding, and solvent effects – to design molecular assemblies with unique physicochemical properties. While early research centered around naturally occurring cyclodextrins, the synthetic macrocyclic family of cucurbit[*n*]urils (CB*n*) has since taken center stage. Among them, cucurbit[7]uril (CB7) has gained particular prominence due to its good water solubility, rigid hydrophobic cavity, and high binding affinities for a wide range of biorelevant analytes. With a cavity size that is especially well-matched to small drug-like molecules and biological metabolites, CB7 has become a preferred platform for designing host-guest systems in aqueous and physiological environments. CB7 has been widely applied in fluorescence-based chemosensing, particularly through indicator displacement assays (IDAs) using non-covalent bound dyes. While effective, these systems often suffer from limited stability in high-salt conditions, which can lead to dissociation of the host-dye complex. To address this issue, covalent conjugation of the dye directly to the CB7 framework offers a robust alternative, enhancing both stability and sensing performance. Furthermore, covalent modifications enable additional functionalization for improved selectivity, opening the door to more targeted analyte recognition.

In this thesis, unimolecular CB7-dye conjugates were successfully synthesized and evaluated for their potential in biomedical sensing. The first project focused on a CB7-ruthenium(II) tris(bipyridine) conjugate, which was investigated for both photoluminescent and electrochemiluminescent (ECL) applications. In both detection modes, supramolecular proximity effects near the CB7 portals played a central role in modulating the signal. Notably, the system enabled the sensitive ECL-based detection of spermidine, a cancer-associated biogenic amine, with a limit of detection (LOD) of 76 nM, providing an alternative to standard ELISA methods.

In a second project, a library of seven CB7-coumarin conjugates was synthesized to explore analytes discrimination in complex conditions. The sensing behavior was strongly influenced by pH, salt type, and ionic strength, which were used as orthogonal parameters to tune selectivity. By combining multiple sensor conditions, the system was capable of distinguishing between structurally similar analytes, including closely related steroid hormones. Together, these findings underscore the power of CB7 as a versatile host in aqueous chemosensing, especially when integrated into covalently linked, unimolecular sensor designs.

2. Kurzzusammenfassung

In den letzten Jahren hat sich die supramolekulare Chemie als äußerst vielversprechendes Werkzeug für die Entwicklung funktioneller Systeme in Bereichen wie Wirkstofffreisetzung, Diagnostik und molekularer Sensorik etabliert. Im Mittelpunkt dieser Disziplin steht der gezielte Einsatz dynamischer, nicht-kovalenter Wechselwirkungen – darunter π - π -Wechselwirkungen, Wasserstoffbrückenbindungen, elektrostatische Kräfte, und hydrophobe Effekte – zur Konstruktion maßgeschneiderter molekularer Architekturen. Unter den verschiedenen makrozyklischen Wirtsmolekülen hat sich Cucurbit[7]uril (CB7) als besonders attraktiv erwiesen. Es zeichnet sich durch eine gute Wasserlöslichkeit, eine starre hydrophobe Kavität und hohe Bindungsaffinitäten gegenüber einer Vielzahl biorelevanter Analyten aus. Aufgrund seiner idealen Kavitätsgröße für kleine, biologisch relevante Moleküle ist CB7 ein bevorzugtes Wirtsmolekül für Anwendungen in physiologischen Medien und wässriger Chemosensorik. CB7 wird häufig in fluoreszenzbasierten Sensorsystemen eingesetzt, insbesondere im Rahmen von Indicator-Displacement-Assays (IDA) mit nicht-kovalent gebundenen Farbstoffen. Diese Systeme zeigen jedoch in Medien mit hoher Salzkonzentration oftmals eine eingeschränkte Stabilität durch Dissoziation der Wirts-Gast-Komplexe. Eine vielversprechende Lösung bietet die kovalente Verknüpfung des Farbstoffs mit dem CB7-Gerüst, wodurch die Stabilität und Leistungsfähigkeit des Sensors deutlich verbessert werden können. Darüber hinaus erlaubt diese Strategie eine gezielte Funktionalisierung zur Erhöhung der Selektivität gegenüber bestimmten Analyten.

Im Rahmen dieser Arbeit wurden verschiedene unimolekulare CB7-Farbstoff-Konjugate synthetisiert und im biomedizinischen Kontext untersucht. Im ersten Projekt wurde ein CB7-Ruthenium(II)-tris(bipyridin)-Konjugat entwickelt und sowohl auf photolumineszente als auch elektrochemilumineszente (ECL) Eigenschaften hin untersucht. In beiden Detektionsmodi spielten supramolekulare Näheeffekte an den CB7-Portalen eine zentrale Rolle für die Signalmodulation. Besonders hervorzuheben ist die sensitive ECL-Detektion von Spermidin, einem biogenen Amin mit Relevanz in der Krebsdiagnostik, mit einer Nachweisgrenze von 76 nM. Dies stellt eine Alternative zur klassischen ELISA-Methode dar.

In einem zweiten Projekt wurde eine Bibliothek von sieben CB7-Cumarinkonjugaten synthetisiert, um die Diskriminierungsfähigkeit gegenüber ähnlichen Analyten zu untersuchen. Die Sensorantwort hing stark von Parametern wie pH-Wert, Salztyp und Ionenkonzentration ab, die als zusätzliche analytische Dimensionen genutzt wurden. Durch gezielte Kombination dieser Bedingungen war es möglich, auch strukturell ähnliche Analyte wie Steroidhormone voneinander zu unterscheiden. Diese Ergebnisse unterstreichen das Potenzial von CB7 als vielseitiges Wirtsmolekül in der wässrigen Chemosensorik – insbesondere in Form kovalent stabilisierter unimolekularer Sensoren mit hoher Analytenaffinität und -selektivität.

3. General Introduction

3.1. Principles of Supramolecular Chemistry

Although the conceptual foundation of supramolecular chemistry was laid as early as 1873 with Johannes Diderik van der Waals' hypothesis of the existence of intermolecular forces, the discipline has only in recent decades emerged as a major field for understanding how molecules interact with each other.¹ It is generally defined as 'chemistry beyond the molecule'^{2,3}, a term established by one of the key pioneers of the concept of supramolecular and host-guest chemistry, Jean-Marie Lehn.⁴ For his outstanding contributions to the field he got acknowledged with the Nobel prize in 1987.⁵ It was awarded jointly with Donald J. Cram and Charles J. Pedersen "*for their development and use of molecules with structure-specific interactions of high selectivity*".^{6,7} This milestone emphasized the fundamental importance of supramolecular chemistry and established it as a distinct and influential discipline within the chemical sciences. However, the significance of the area got further recognized by another Nobel prize in 2016. It was awarded jointly to Jean-Pierre Sauvage, Sir J. Fraser Stoddart and Bernard L. Feringa "*for the design and synthesis of molecular machines*".⁸⁻¹⁰

Generally, classical molecular or synthetic chemistry typically focuses on the specific manipulation of individual atoms or covalent bonds within a molecule. A notable example is the Diels-Alder-Reaction, which describes the cycloaddition of a conjugated diene and a substituted alkene resulting the simultaneous formation of two covalent carbon-carbon bonds. In contrast, supramolecular chemistry is fundamentally concerned with non-covalent interactions. Intramolecular non-covalent forces surely play a role, but particularly those operating between molecules (intermolecular) are of high importance. Nature has always inspired the research since basically all biological functions could not happen without supramolecular assemblies. Just to name a few examples, drugs bind to substrate receptors that possess well-defined binding cavity, and enzymes interact with DNA in order to promote the replication of genetic information.² Overall, supramolecular chemistry is highly interdisciplinary and bridges concepts from organic, biological and physical chemistry. Organic chemistry provides adaptable strategies for synthetic receptor construction, biological systems offer models for substrate-enzyme interactions, and physical chemistry with both experimental and theoretical investigations of non-covalent forces.² Probably the most important concept of supramolecular chemistry is molecular recognition, which is controlled by specific non-covalent interactions.¹¹

It is particularly interesting to note that, even though in our macroscopic world humans perceive the environment through vision, touch and hearing, the actual underlying mechanisms of these sensory processes happen on molecular scale and are based on molecular recognition. In contrast to humans, molecules lack sensory organs. Their 'communication' entirely relies on non-covalent forces, which not only enable recognition but also allow for processing and storage of information.³

Another essential feature of supramolecular species is their reactivity. The integration of molecular recognition with reactive functions leads to a catalyst, which promotes the transformation of reactants

into products. This concept closely mimics biological systems, most notably enzymes. They rely on providing a well-defined cavity for precise molecular recognition in order to achieve exceptional efficiency and selectivity. In contrast to enzymes, supramolecular systems are abiotic reagents, still they may be able to perform the exact same reactions while using similar or even completely different mechanistic pathways. Regardless of their artificial origin, they may still be able to achieve the same chemical transformations as natural enzymes, and in some cases even surpass them in terms of performance and stability. In addition, it is also possible to rationally design synthetic receptors in order to catalyze transformations that are beyond the scope of biological systems. This represents a highly interesting area for further development and research. Today, many chemical species are already produced through genetically modified organisms (GMOs), which often are superior over conventional synthesis.¹² However, significant work remains to be done, but with continued advances in our understanding of chemical reactivity supramolecular catalysis could become widely applied in industrial processes.¹²⁻¹⁶

Appropriately modified synthetic receptors may also replicate another vital function they commonly share with their biological counterparts.^{17, 18} When integrated into artificial or biological membranes, they can act as carriers enabling the selective transport of substrates.¹⁹ Both molecular recognition and membrane transport are crucial for maintaining biological function – disruption of such delicate systems can result in severe physiological consequences.²⁰ One well-known example is cystic fibrosis (CF), a genetic disorder caused by mutations in the CFTR (Cystic Fibrosis Transmembrane Conductance Regulator) gene, which encodes a membrane-bound molecular carrier protein for chloride ions in epithelial cells. Mutations in CFTR, especially those that cause protein misfolding and loss of structure lead to impaired chloride and water transport across cell membranes. The symptoms include chronic respiratory infections amongst other severe issues which significantly reduces quality of life for patients.²¹ Supramolecular chemistry may offer some promising approaches for CF therapy. Most notably, studies have identified small molecules capable of promoting anion transport in cells and membranes with a similar efficiency to CFTR protein.²² These anionophores may restore and compensate the loss of CFTR function in affected cells. Common therapeutic options for CF primarily rely on modulation of CFTR protein using potentiators and correctors, which regulate conductivity in the membrane, aiming to restore chloride transport by enhancing the function or stability of mutant CFTR proteins.^{19, 20} Nevertheless the outcome and success of these treatments dramatically depend on the exact type of mutation carried by the patient, meaning not all benefit equally. Therefore, the development and integration of anionophores as mutation-independent alternatives represent an important direction for future research and drug development. If successful, such systems could offer broader therapeutic applicability and potentially help restoring damaged CFTR channels.^{19, 23}

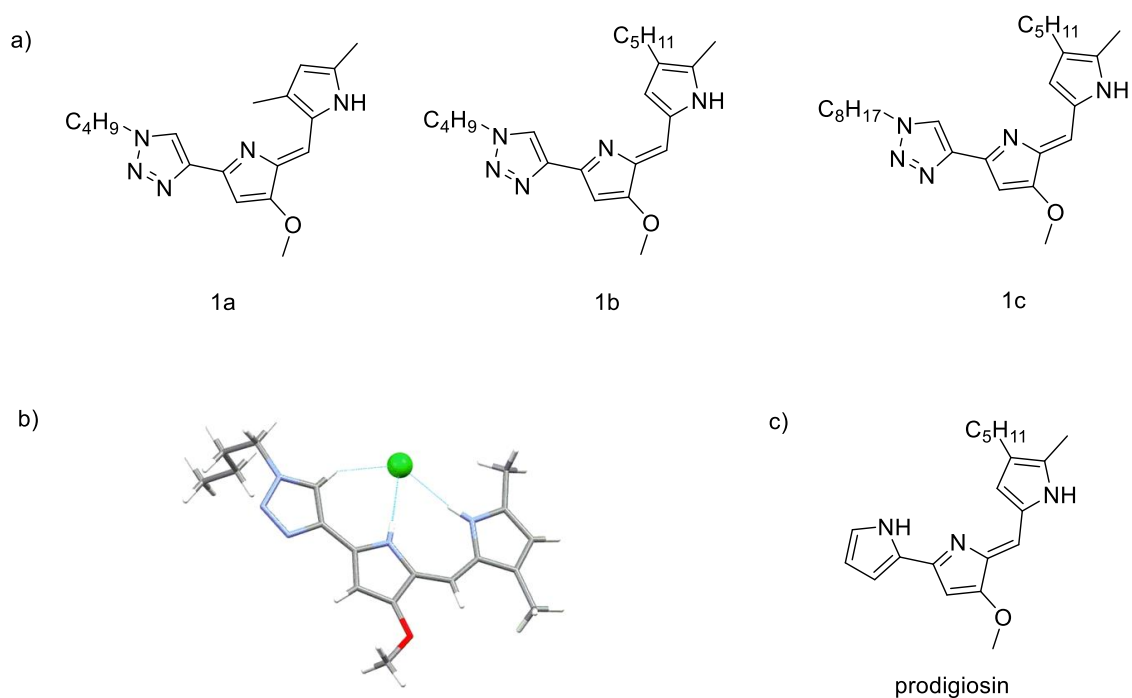


Fig. 3.1: Structures of anionophores. a) Chemical structures of synthetic anionophores. Upon protonation, chloride can bind to the respective transporter molecule. b) X-ray structure of HCl salt of compound 1a. c) Structure of the natural product prodigiosin, which also serves as an anionophore. Adapted with permission from ref ²³. © Nature Research

Supramolecular entities are characterized by the presence of a wide range of non-covalent interactions existing. Depending on the specific structure, ion pairing, hydrogen bonding, electrostatic contributions, halogen bonding, π - π -stacking, dispersive forces, cation- π and anion- π interactions may occur, as well as contributions from the hydrophobic effect.^{3, 24} It is surely no coincidence that these interactions build the foundation of all biological systems, since they collectively contribute to highly specific binding events. The energetics of non-covalent interactions are often highly sensitive to slight changes in structure and electronic properties of the respective interaction partners, also solvent effects play a significant role and must be carefully considered.^{25, 26}

Several strategies exist in order to quantify these non-covalent interaction energies, while the synthetic complexes offer more flexibility compared to biological systems in terms of their chemical and physical environment.²⁷

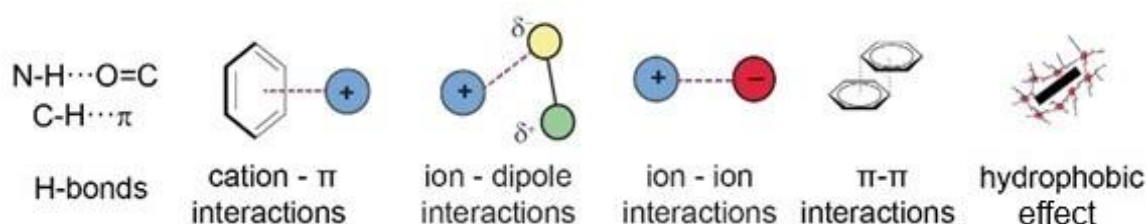


Fig. 3.2: Possible non-covalent interactions.

3.2. Approaches to Characterizing Binding Constants

A thorough understanding of binding affinity and the resulting complex stability is critically important for the rational design of supramolecular systems, particularly when targeting real-world applications. For the detection of small biomolecules, high selectivity and strong binding affinity are crucial to ensure accurate and reliable sensor performance. The stability of a host•guest complex is generally defined by the binding constant K_a , also called the association constant.²⁴ As the most common approach to measure K_a the supramolecular titration method has become a standard analytical approach for determination. The method involves the gradual addition of the guest molecule to a fixed concentration of the host, during which changes in measurable physical properties are monitored, such as chemical shifts in nuclear magnetic resonance (NMR), variations in UV-vis absorption or fluorescence emission bands, or generated heat in isothermal titration calorimetry (ITC).²⁸ The resulting experimental data must then be fitted to appropriate binding models in order to extract K_a . Despite the seemingly easy execution, a number of factors may influence the quality of the data gained from supramolecular titrations. These include the purity of the compounds and the accuracy of the measurement instruments. Still, planning of the experiment or subsequent data analysis are equally important. The selection of appropriate concentration ranges, binding models and fitting algorithms all play a role in the reliability of the outcome. Especially to assess variability and reduce uncertainty, the replication of experiments is essential. Depending on the size and structural features of the respective components involved, multiple binding modes are possible, and stoichiometries beyond simple 1:1 host•guest complexes may arise. K_a is typically expressed in M^{-1} , as it is calculated based on the equilibrium concentrations of the interacting species. While the most rigorous definition uses activities, in practice, especially in dilute solutions, concentrations are used as an acceptable approximation. A high K_a value indicates strong binding affinity between host and guest molecules.²⁷

To experimentally evaluate such binding interactions and determine association constants practically, various sensing assay formats have been developed – each fitted to specific system requirements. Of particular relevance to this thesis are binding assays based on emission (fluorescence and phosphorescence), which serve as essential tools for analyzing molecular recognition events. These can generally be categorized into three principal types, each offering distinct advantages and mechanisms.

3.3. Tools for Monitoring Binding Events

The direct binding assay (DBA) represents the most straightforward sensing assay and is among the simplest and most intuitive methods for sensing molecular recognition events – provided the system of interest is suitable for such an approach.²⁹ The system of investigation only involves two components: the host (receptor) and the guest (analyte). Upon the binding event happening, the associative interaction between host and guest ideally results in a directly measurable and easily quantifiable signal change, which manifests as the emergence, shift, enhancement or quenching of an absorption or emission

band.^{29, 30} In the ideal case, these photophysical changes are direct, significant, and readily quantifiable, allowing for straightforward analysis of binding strength and selectivity.

Direct Binding Assay (DBA)

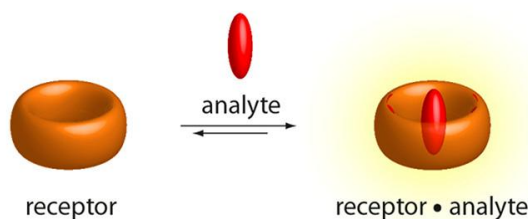


Fig. 3.3: Schematic representation of a direct binding assay (DBA). Reprinted with permission from ref ³¹. © American Chemical Society

In some cases, the DBA approach is impractical, because both analyte and host are spectroscopically silent and therefore do not produce an optical response.³⁰ An effective alternative is the indicator displacement assay (IDA), a competitive binding assay (CBA) in which a chromophoric or fluorogenic dye first forms a host•indicator complex.^{32, 33} Upon addition of a competing guest, the indicator dye is displaced from the host cavity, which can be followed by a measurable change in the spectroscopic properties of the indicator dye.^{29, 31, 34} Since the signal originates from the freed indicator, IDAs enable sensitive and real-time monitoring of host-guest interactions.

Indicator Displacement Assay (IDA)

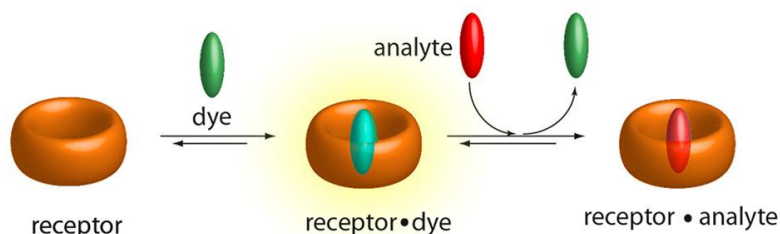


Fig. 3.4: Schematic representation of an indicator displacement assay (IDA). Reprinted with permission from ref ³¹ © American Chemical Society

In contrast to the simplicity of a DBA, the effective design of an IDA demands prior knowledge of the host to identify the appropriate size, charge and hydrophobicity of a complementary indicator. The assay relies on a fundamental requirement: the analyte (guest) must have a similar or stronger binding affinity than the indicator dye at the working concentrations, ensuring an efficient displacement.^{34, 35} The exact choice of indicator is therefore dependent on a specific application. Preferably, the host•indicator complex should display a “turn-on”-response.³⁶⁻³⁹ That is, fluorescence (or absorbance) is fully quenched while the indicator is bound and is restored upon displacement by the analyte of interest, what improves sensitivity and simplifies data interpretation.³⁷ In a biological context, colorimetric indicators can be problematic since biological media often absorb or scatter visible light. To overcome this, near-infrared (NIR) emitting fluorophores ($\lambda_{em} \approx 650-900$ nm) can be used as they allow deeper penetration of live tissue

and a higher sensitivity with less background autofluorescence and photodamage.⁴⁰⁻⁴² Unfortunately to this date, only a limited number of NIR dyes currently are complementary in terms of size, geometry and solubility to most common synthetic hosts, making development of NIR-based IDAs challenging. IDA performance is extraordinarily environment-dependent. Elevated ionic strength, competitive salts, or pH fluctuations can weaken or entirely dissociate the preformed host•indicator complex before the analyte is introduced, what is especially problematic for real samples. Additionally, IDA is limited to soluble guests. Furthermore, since displacement of the indicator solely depends relative binding affinities, any unintended species that is present and binds the host with comparable affinity will also displace the indicator and generate a false-positive response. Some strategies to mitigate this drawback include engineering hosts with multi-point recognition sites for enhanced selectivity, or integrating IDAs into sensor arrays.^{29, 34}

A closely related variant of the IDA is the guest displacement assay (GDA). While an IDA begins with a pre-formed host•indicator complex, GDA starts with a pre-equilibrated host•guest complex that is disassembled by an added competitively binding indicator dye. The dye must bind more strongly in order to eject the guest from the cavity. Because of the nature of GDA, it is especially valuable for weakly binding analytes. An IDA might fail in this case since the analyte may be unable to outcompete the indicator, leading to a decreased signal. By reversing the roles – high-affinity dye displaces a weaker bound analyte – sensitivity is restored. A source of complication, as with IDAs, may be salt, pH, and competing species that can disassemble the host•guest complex prior to dye addition.^{43, 44}

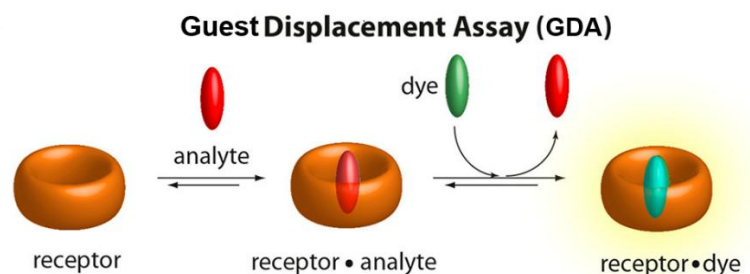


Fig. 3.5: Schematic representation of a guest displacement assay (GDA). Reprinted with permission from ref ³¹ © American Chemical Society

The third common binding assay is the associative binding assay (ABA). Unlike IDA or GDA, ABA relies on the simultaneous co-encapsulation of two guest molecules within a single host cavity. Consequently, an ABA can only be implemented with receptors that possess a sufficiently large cavity.^{30, 45, 46} For optical sensing with a spectroscopically silent host, the receptor is first equilibrated with an indicator dye, similar to the IDA protocol. Nevertheless, addition of the guest does not displace the dye. Instead, the analyte binds in close proximity to the dye in the host cavity, enabling electronic coupling between the two co-bound molecules.³⁰ Depending on the photophysical properties of the pair of interest, the coupling may manifest as different electronic effects, such as charge-transfer (CT) interactions.⁴⁷ Since the optical response arises from an analyte-specific interaction with the indicator, the resulting spectra often display distinct “fingerprints” that even allow differentiation of structurally closely related

analytes. This offers a powerful route to pattern-based sensing, despite the dye itself is unchanged. The ABA concept is especially advantageous when guest and dye cooperatively form a stabilized ternary complex and their structural complementarity promotes strong electronic communication.^{48, 49}

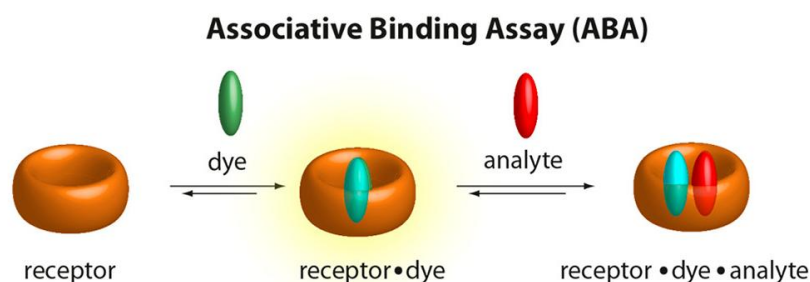


Fig. 3.6: Schematic representation of a associative binding assay (ABA). Reprinted with permission from ref ³¹ © American Chemical Society

3.4. Synthetic Macrocycles as Platforms for Chemosensor Design

To recognize and selectively bind specific molecules, ions or atoms as guests, synthetic macrocycles must exhibit a set of various well-defined structural features. A key necessity is the presence of a hydrophobic cavity that can accommodate guest species of various sizes and geometries. To ensure good water-solubility and biocompatibility at the same time, synthetic hosts should possess a hydrophilic outer surface. In addition to these structural requirements, ideal macrocyclic hosts should be easily synthetically accessible preferably in an industrial scale, also chemically stable and readily accessible to post-synthetic functionalization. Through modifications, binding affinity, selectivity, and solubility should be tunable, or the introduction of reporter groups for sensing applications may be achieved. As a result of the dynamic nature of non-covalent interactions, their binding behavior and optical response can be modulated by external stimuli, while guest binding is the primary trigger for host response. Other factors may be changes in pH, ionic strength, temperature or redox potential, among others.⁵⁰⁻⁵³ This stimulus-responsive nature makes synthetic macrocyclic hosts ideal platforms for chemosensor design and controlled release systems, what is an important treatment strategy for the emerging field of theranostics.⁵⁴ Over the past several decades, a wide variety of synthetic macrocyclic receptors have been developed, each offering specific cavity geometries, binding motifs and functional capabilities. In the following some of the most important scaffolds are discussed.

3.4.1. Crown Ethers: A Historic Milestone in Host-Guest Chemistry

The first synthetic macrocyclic hosts introduced to the scientific community were the crown ethers (CE), discovered in the mid-1960s by Charles Pedersen.^{7, 55} In their simplest form, they represent cyclic oligomers of ethylene glycol units, forming a flexible ring rich in electron-donating oxygen atoms. Pedersen originally intended to synthesize a compound by linking two catechol molecules via an ethyleneoxy bridge and anticipated it to interact with metal cations through ionization of hydroxyl groups. To his surprise a macrocyclic byproduct was isolated capable of complexing of potassium

cations, despite lacking any ionizable hydroxyl group.⁵⁶ This highlighted the first appearance of a purely neutral synthetic host molecule forming a stable complex with a metal cation, based on ion-dipole interactions. Because of their similarity of the molecular shape, the molecules were named crown ethers.

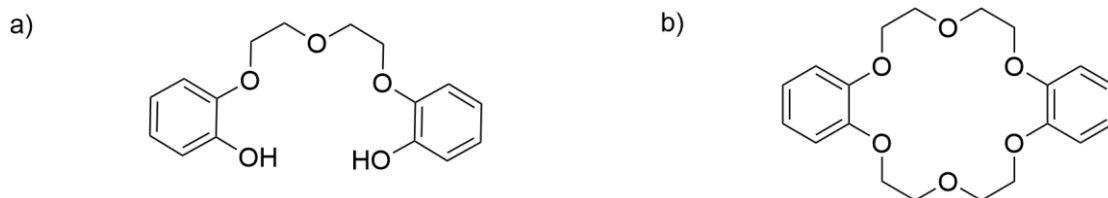


Fig. 3.7: a) Pedersons' originally intended complexing agent with two free hydroxyl groups. b) Isolated side product, dibenzo-18-crown-6.

Mainly in organic solvents and to some extent in the gas phase, CEs exhibit high flexibility, allowing them to adjust to the size and coordination preferences of various alkali and alkaline earth metal ions.⁵⁷⁻⁵⁹ The electron-rich cavity, formed by lone electron pairs on the oxygens, provides a concentrated region negative electrostatic potential, what is ideal for accommodating positively charged ions.^{7, 55, 59} The size match between cation and ring diameter is the key parameter for the high affinity.^{7, 56} This discovery had great implications for biological chemistry, as it offered the first synthetic model systems capable of mimicking ion selectivity channels and enzymes.⁶⁰ By binding Na^+ , K^+ , Mg^{2+} , Ca^{2+} and NH_4^+ , crown ethers provided important insights into transport, storage and regulation of these biologically essential metal ions. They enabled systematic study of cation size, charge density and their influence on binding – all critical parameters for understanding processes such as nerve signaling, muscle contraction or enzyme activity.^{60, 61}

3.4.2. Cryptands and Lariat Ethers: Extending the Concept

Shortly after Pedersen's pioneering work, Howard E. Simmons and Jean-Marie Lehn both independently recognized the potential of macrocycles capable of binding atoms and expanded the concept and synthesized the family of Cryptands.^{62, 63} Instead of using the planar catechol as the anchor, two nitrogen atoms served as pivot atoms, but still with ethyleneoxy units as connecting strands. In this way the macrocyclic framework was extended into three dimensions. The newly emerged compounds do have multiple binding sites arranged in a cage-like geometry, providing higher preorganization and greater affinity for a wide range of cations.⁶⁴ Cryptands introduced an important concept for supramolecular chemistry: encapsulation, which means fully trapping of a guest within a defined molecular cavity.

Building on both the crown ether and the cryptand structure, another subclass known as lariat ethers (LE) emerged. Here the three-dimensionality of cryptands and the faster complexation dynamics of crown ethers are combined. An LE has one or more sidearms attached to a core macroring.⁶⁵

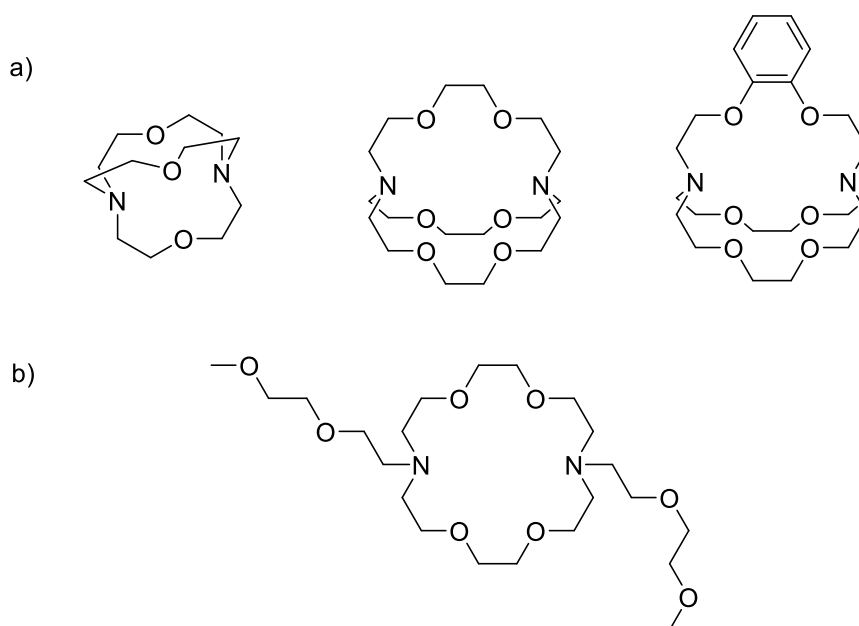


Fig. 3.8: a) Structures of representative cryptands. b) Structure of a lariat ether.

3.4.3. Calixarenes: Phenolic Macrocycles with Tunable Recognition Properties

Calix[*n*]arenes ($n=4, 5, 6, 8$) are a prominent class of phenol-based macrocyclic hosts, whose name derives from the Greek *calix*, meaning “chalice”, inspired by their bowl-shaped molecular architecture. Although calixarenes were first reported in the 1940s, they also date back to the investigations of the condensation of phenol and formaldehyde by Adolf von Baeyer in 1872. Nevertheless their significance in host-guest chemistry was only realized in the 1980s, when C. David Gutsche systematically synthesized and investigated various derivatives.⁶⁶ Calixarenes are readily synthesized in one-pot reactions via the condensation of phenols with paraformaldehyde or aqueous formaldehyde under basic conditions, resulting in methylene-bridged cyclic oligomers.⁶⁷ Different homomeric ring sizes can be selectively obtained by variation of reaction conditions.

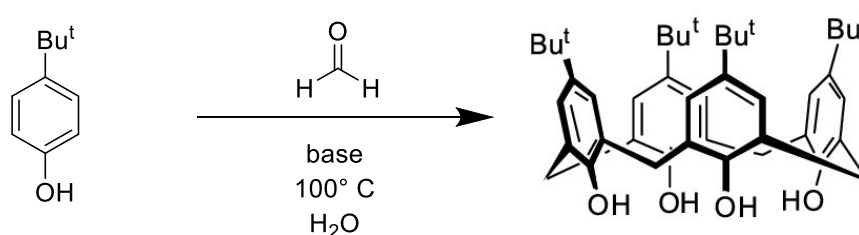


Fig. 3.9: Synthesis of Calix[4]arene.

Among the known synthetic macrocycles, the calixarenes are in the group of the most widely investigated scaffolds in supramolecular chemistry, especially due to their ease of preparation and their highly tunable chemical and physical properties, which derive from a unique combination of features. Calixarenes possess preorganized nonpolar cavities which allow for excellent size- and shape-selective guest recognition, mainly driven by the hydrophobic effect.⁶⁸ Additionally, the phenolic rings represent

π -electron-rich interiors enabling cation- π interactions.⁶⁹ The defined upper and lower rims permit orthogonal functionalization, while particularly functionalization with hydrogen-bond donor and acceptor groups on the upper rim support analyte discrimination.^{53, 66, 69-73} These combined features make calixarenes ideal candidates for selective binding of both ions and neutral molecules in both organic and aqueous systems. Noteworthy, most derivatization strategies applicable to simple phenols can similarly be used for calixarenes, nevertheless some geometric constraints may arise due to their macrocyclic nature. Conformational flexibility of calixarenes derives from the free rotation around the methylene bridges, particular in calix[4]arenes, allowing the macrocycle to adopt four distinct diastereomeric conformations: cone, partial cone, 1,2-alternate, and 1,3-alternate. Higher homologues, such as calix[6]arene, exhibit even more conformational diversity. These well-defined conformations are strongly influenced by substituent patterns, solvent effects and guest binding.^{53, 69}

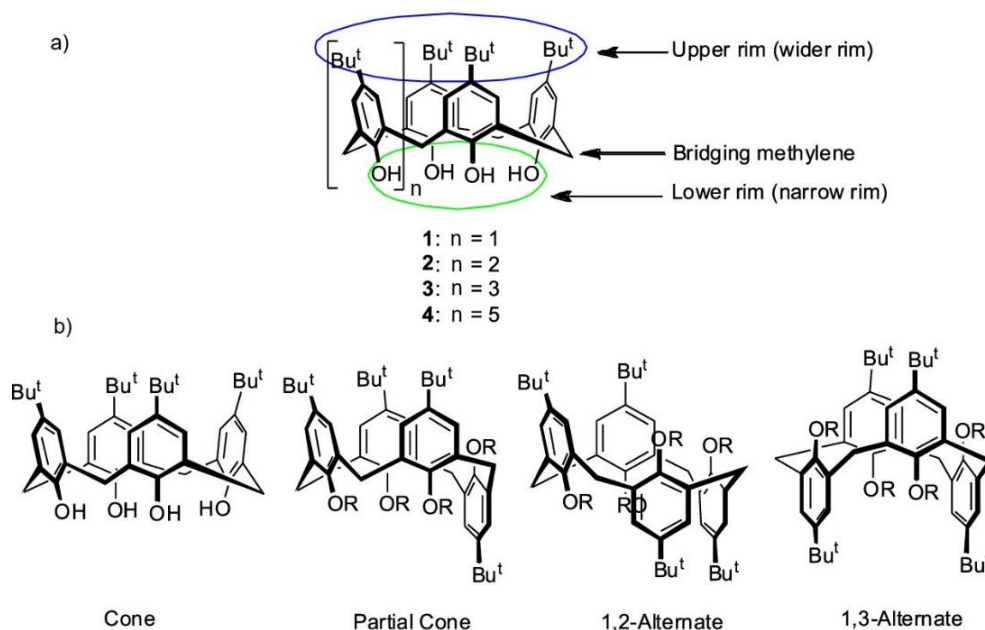


Fig. 3.10: a) Structure of the Calix[n]arenes with the wider upper rim, bridging methylene groups and the easily derivatizable narrow lower rim. b) Different conformations of the Calix[4]arene. Adapted with permission from ref ⁶⁹. © American Chemical Society

Importantly, chemical modifications can be used to lock calixarenes into specific conformations, enhancing selectivity for a particular guest within a family of structurally close molecules.^{74, 75} In this way, a single calixarene scaffold can represent multiple host architectures, with the exact number depending on ring size and conformational control. Alternatively, switchable hosts can be designed to undergo conformational rearrangement upon guest binding, offering dynamic recognition behavior. Among the possible conformers for Calix[4]arene, the cone and 1,3-alternate conformations are the most investigated and functionally relevant.^{72, 73} The cone conformation offers the best possibilities for selective modification and precise cavity design, enabling tailored binding properties. On the other hand, the 1,3-alternate conformation, featuring two opposing binding sites, represents a π -basic tunnel what is

very promising for synthetic ion channels. This effect is further enhanced by introducing selective ion-binding functionalities at the lower rim, such as carboxylate or crown ether-type groups.⁷¹⁻⁷³

The majority of calixarene-based sensing systems rely on fluorescent derivatives.⁷⁰ Absorbance- and emission-based techniques are both rapid, non-invasive and well-suited to multicomponent analysis, while the latter is generally superior in terms of sensitivity and detection limits. While absorbance-based techniques can detect analytes in concentrations down to ~ 10 - $100 \mu\text{M}$, fluorescence-based techniques can measure analytes at concentrations in the range of $\sim 100 \text{ nM}$, making the technique ideal for observing and monitoring events at the molecular level.⁷⁶⁻⁷⁸

3.4.4. Cyclodextrins: Biocompatible Cavities for Molecular Recognition

Cyclodextrins (CDs) are a family of cyclic oligosaccharides and can be obtained from the enzymatic degradation of one of the most abundant and essential polysaccharides, starch. Structurally, CDs are cyclic oligomers composed of 1,4-linked α -D-glucose subunits, forming a cone-shaped macrocycle, similar to the calixarenes, with a hydrophobic inner cavity and a hydrophilic outer surface area.⁷⁹ This amphiphilic architecture is the key to their widespread use in many applications in host-guest chemistry and molecular encapsulation. The three naturally occurring cyclodextrins are α -cyclodextrin (six glucopyranose units), β -cyclodextrin (seven units), and γ -cyclodextrin (eight units). Larger homologues, such as δ - and ϵ -cyclodextrin, containing nine and ten glucopyranose units respectively, can also be formed by certain enzymatic processes, though they occur much less frequently in nature.^{50, 80-82} Each variant has a distinct size, offering different inclusion selectivity for guest molecules of varying dimensions. CDs are generally considered as non-toxic, edible and biodegradable, highlighting the attractiveness for biomedical and pharmaceutical applications. CDs were formally discovered as early as 1891 by Antoine Villers, as he studied enzymatic degradation of potato starch in bacteria.⁸¹ In the 1950s CDs were actually mistakenly classified as toxic compounds, after an incorrect performed experiment, what actually delayed research and application for several decades.⁸³

CDs exhibit outstanding stability in aqueous media and in certain organic solvents, making them ideal candidates in a broad range of applications.⁷⁹ They are particularly stable under alkaline conditions, whereas, at acidic conditions, they undergo acid-catalyzed hydrolysis, resulting in ring-opening reactions and the formation of linear oligosaccharides and individual glucose units.⁸⁴ Each D-glucose subunit adopts a chair conformation, what contributes the overall structural flexibility of CDs.⁸⁵ This shapes the macrocycle into a truncated cone, rather than a cylinder, also comparable to the calixarenes. The depth of the hydrophobic hollow cavity is consistent across all five native cyclodextrins, while their internal diameters vary according to the number of glucose subunits. Due to the cone-like geometry, the free hydroxyl groups are all oriented to the outward of the molecule, allowing the external surface to form hydrogen bonds with water molecules, resulting in good water solubility. However, regardless of their structural similarity, the solubility of CDs varies greatly: α -CD 149 mM, β -CD 16.2 mM, γ -CD 179 mM.⁸⁶ The reason for the anomalous solubility of the β -CD is probably due to its more stable crystal structure.

In addition, some of the hydroxyl groups are able to form intramolecular hydrogen bonds, resulting in a belt-like structure, what limits the ability of β -CD to form intermolecular hydrogen bonds with the surrounding water molecules. In contrast, the hydroxyl groups in α - and γ -CD are more available for hydrogen bonding with surrounding solvent.^{87, 88} Despite the seemingly rigid chair conformation of the glucose units, analytical studies, especially NMR techniques, revealed considerable conformational flexibility.^{89, 90} Even upon inclusion of a guest molecule within the cavity, the overall confirmation is maintained, thereby retaining the truncated cone shape and contributing to the stability of the inclusion complex.

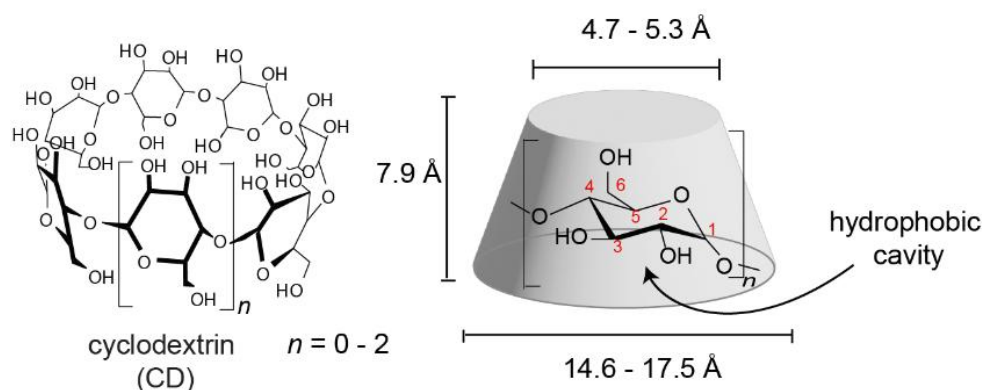


Fig. 3.11: Chemical structure and schematic representation of cyclodextrins.

One of the main limitations for the widespread industrial and pharmaceutical use of CDs is the relatively low water solubility. To conquer this, extensive research has focused since decades on chemical modifications of the hydroxyl groups, what enhances solubility and expands functional utility of CDs in various applications.⁹¹⁻⁹⁴ For example, a well-known and industrial applied example is 2-hydroxypropyl- β -CD (HP- β CD), which exhibits a more than 80-fold increase aqueous solubility compared to native β -CD.⁷⁹ The derivative has found pharmaceutical relevance, particularly in the solubilization and delivery of poorly water-soluble drugs. A notable example is its use in the complexation of two imidazole-based antiparasitic drugs, albendazole and fenbendazole.⁹⁵ They are both used to treat alveolar echinococcosis caused by *Echinococcus multilocularis*, formerly known as tapeworms.⁹⁶

Besides pharmaceuticals, native CD and derivatives have found broad application across various fields. The versatility of modification by easy substitution reactions of the hydroxyl groups has enabled their incorporation into materials, sensing platforms and analytical tools.^{50, 86, 88, 91, 92, 94, 95} One particularly interesting use is in gas chromatography.⁹⁷ Stationary phases of columns equipped with CDs are routinely used for chiral separation of analytes.

CD Used	Albendazole Aqueous Solubility ($\mu\text{g/mL}$)	Fenbendazole Aqueous Solubility ($\mu\text{g/mL}$)
-	0.4188	0.1054
β -CD	93.47	45.56
HP- β CD	443.06	159.39

Table 3.1: Comparison of aqueous solubility of Albendazole and Fenbendazole non-complexed and complexed with β -CD and HP- β CD. Data taken from ref ⁹⁵

Cyclodextrins are capable of forming inclusion complexes with a wide array of guest molecules, ranging from branched and cyclic alkyl groups in polymer chains to aromatic compounds, small drug molecules, and even biomacromolecules such as proteins.⁹⁸⁻¹⁰⁰ This versatility is based on their hydrophobic cavity, which represents a unique environment for molecular encapsulation, leading to the formation of stable-host-guest complexes with a wide range of structural characteristics. The most common complexation stoichiometry observed is 1:1, where a single guest molecule is encapsulated within one CD host.⁷⁹ However, depending on the size, shape and interaction geometry of both partners, even more complex stoichiometries like 1:2, 2:1, 2:2 etc. complexes have been reported.⁸⁶

Several key factors influence the CD complexation formation. Obviously, shape and size of the cavity are important factors to consider. According to the different characteristic internal diameters of the three native CDs, they are suitable for guests of specific size ranges. Optimal binding is usually achieved when the guest molecule matches the dimensions of the cavity, a well-documented correlation.^{101, 102} Self-assembly and aggregation behavior of CDs may also impact complexation.¹⁰³ At higher concentrations, CDs are prone to aggregation, which may hinder guest accessibility or even alter apparent binding constants. Generally, increasing the CD concentration promotes the formation of aggregates, resulting in a reduced number of free CD molecules available for guest inclusion. However, certain guest molecules have been shown to interfere with or reduce CD aggregation, what effectively lowers the critical aggregation concentration.¹⁰⁴

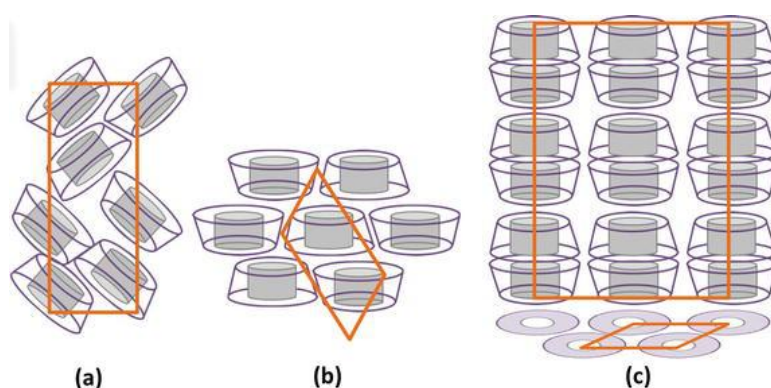


Fig. 3.12: Schematic representation of possible arrangements in CD aggregates. a) cage-type; b) layer-type; c) head-to-tail channel-type. Adapted with permission from ref ¹⁰⁵ © InTech

Due to the hydrophobic nature of the CD cavity and its slightly positive electrostatic potential, the most stable and strongest complexes are typically formed with guest molecules that are non-polar,

negatively charged, and structurally compatible with the cavity's inner diameter.¹⁰⁶ These guests primarily interact *via* van der Waals forces, hydrophobic interactions, and displacement of high-energy water molecules from the cavity.⁶⁸ In summary, successful complexation with CDs depends on a careful balance between host structure, guest properties and experimental conditions.⁹³ For further optimization of applications, understanding and controlling these variables is a key factor for research.

3.4.5. The Reintroduction of Cucurbiturils and Their Rise in Supramolecular Sensing

Among the macrocyclic hosts discussed so far, the cucurbit[*n*]uril (CBn) family has emerged as one of the most promising and rapidly developing classes within the supramolecular chemistry. Since their reintroduction to the scientific community in the late 20th century, cucurbiturils have gained significant attention for their exceptional molecular recognition properties, extraordinarily high binding affinities and distinct structural features.

Structurally different from other macrocycles, cucurbiturils offer a more rigid, symmetrical and preorganized cavities, formed by methylene-bridged glycoluril units, which form a hydrophobic internal cavity flanked by polar carbonyl portals. They offer a strong tendency for encapsulating a wide variety of guest species, particularly with cationic and hydrophobic properties. Their ability to form ultra-stable host-guest complexes, reaching exceptionally high binding constants of up to 10^{19} M⁻¹, placing them among the strongest non-covalent interactions known to date.¹⁰⁷ These unique properties have positioned them as powerful tools over a broad spectrum of applications, including the development of chemosensors, drug delivery systems, and supramolecular catalysis. Of particular relevance to this thesis is their use in emission-based chemosensing, where their binding-induced modulation enables highly sensitive and selective analyte detection.³⁰ In the following sections, the structural characteristics, complexation behavior and functional versatility of CBs will be explored in detail. Especially highlighted will be their central role in the design of chemosensors, spotlighting their tunable cavity sizes, water solubility profiles, and selective binding mechanisms making them extraordinarily suited for constructing responsive supramolecular systems.

3.4.5.1. Origins and Revival of the Cucurbit[*n*]uril Family

The cucurbit[*n*]uril family, today recognized as a key class of supramolecular chemistry, had a surprisingly early but overlooked origin. As early as 1905, the German chemist Robert Behrend reported the preparation of two substances with some unusual properties during the acid-catalyzed condensation of glycoluril and formaldehyde, of which he suggested contains “at least three molecules of glycoluril”, based on elemental analysis. Although he intended to synthesize a different compound, Behrend observed the formation of insoluble, powdery materials. He described that these reaction products showed high water uptake while retaining their dry, powdery appearance, an uncommon property that suggested a unique structure.^{108, 109} Additionally, the materials showed a remarkably high affinity for a wide range of salts, as well as a high capacity to remove organic dyes from solutions, already indicating their potential

for host-guest interactions well before such a concept was formally established. Despite these fascinating findings, Behrend was unable to determine the exact molecular structure of the compounds, since the available analytical techniques at the time did not allow the investigation of insoluble materials.^{108, 110} However, he proposed a hypothesis, that proved to be true later: that the condensation involved the elimination of water, formed by reaction of formaldehyde oxygen atoms with glycoluril hydrogens. This mechanism was actually confirmed by modern analytical techniques.¹¹¹

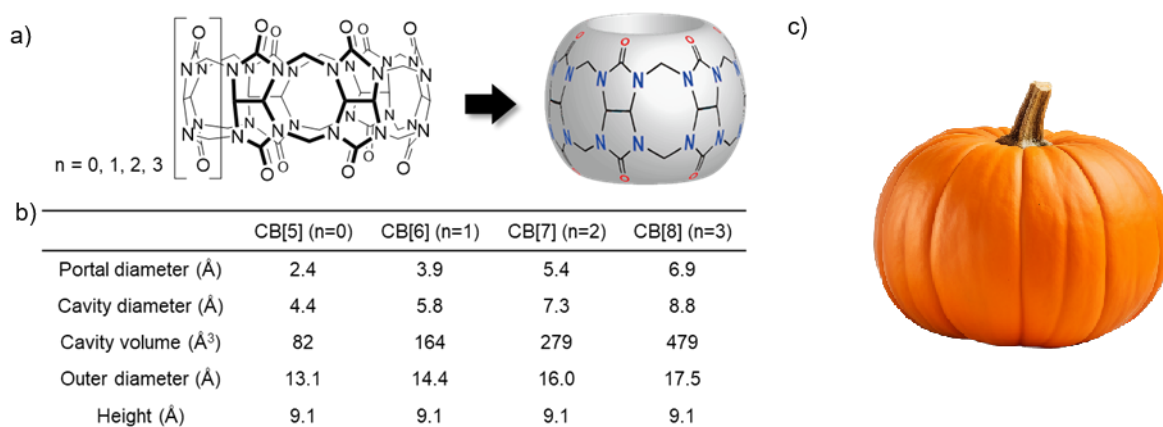


Fig. 3.13: a) Chemical structure and illustration of the cage-like structure of CB. b) Structural parameters of CB5-8. c) Illustration of a pumpkin. The name cucurbituril was adapted from the botanical name for the family of *Cucurbitaceae*.

Only eighty years after Behrend's initial report, the mysterious condensation product re-entered the scientific spotlight. In 1981, William J. Mock and colleagues revisited Behrend's forgotten work, buried in the literature of the late 19th and early 20th centuries. Intrigued by the special properties previously described, they reproduced the synthesis and had little difficulty in isolating a product consistent with Behrend's original observations.¹¹² The obtained substance showed an infrared absorption (IR) band at 1720 cm⁻¹ together with a remarkably simple proton NMR spectrum, showing three signals of equal intensity, indicating a highly symmetric structure. These findings, in combination with X-ray crystallographic analysis of crystals of a calcium bisulfate complex with cucurbituril, enabled the first structural clarification of the compound. The structure was revealed to be a highly symmetric macrocyclic hexamer, composed of six glycoluril units linked by methylene bridges. The molecule featured a rigid, barrel-shaped geometry, with carbonyl portals forming hydrophilic rims on both faces and a hydrophobic central cavity. Because of its close structural resemblance to a pumpkin, a member of the *Cucurbitaceae* family, Mock coined the term "cucurbituril" for the compound, in order to avoid the highly complex IUPAC name. At the time, the hexameric form was reported as the only product.^{109, 112} However, it turned out not much later the cucurbituril was part of a family, which consists of macrocycles with varying numbers of *n* glycoluril units.¹¹¹ This marked the beginning of a new era in supramolecular chemistry, as researchers began to realize the unique features of cucurbituril.

Beyond clarification of the structure of cucurbituril, Mock also made significant contributions to the understanding of its host-guest chemistry, particularly that of CB6. Through detailed NMR spectroscopy studies, Mock systematically investigated the selective and high affinity complexation of numerous alkyl(di)-ammonium species, together with the factors contributing to binding selectivity.¹¹³⁻¹¹⁵ These early studies showed, CB6 forms strong 1:1 inclusion complexes in aqueous formic acid solutions, demonstrating a preference for cationic guests with suitable size. Compared to other synthetic hosts such as crown ethers, CB6 exhibited high binding affinity and specificity, with binding constants reported as high as 7.8×10^8 M for spermidine.¹¹⁴ The exceptional selectivity and tight binding were attributed to the hydrophobic cavity and the polar carbonyl portals, which both facilitate and constrain guest entry. A fascinating aspect of CB6 molecular recognition is its kinetic profile. Studies revealed slow association rates and even slower dissociation rates, what is attributed to the many carbonyl groups that form portals at both entrances of the macrocycle. These act as energetic barriers, effectively “locking” the guest one complexed.¹¹⁴

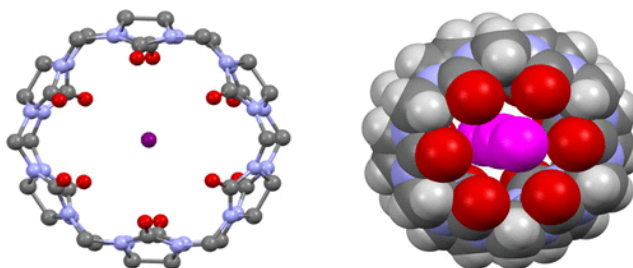


Fig. 3.14: Two views of CB6 crystals reported by Freeman and Mock. On the right side, the space filling view with three entrapped molecules of water is illustrated. Reprinted with permission from ref ¹⁰⁹. © American Chemical Society

Another interesting feature Mock discovered, is the catalytic potential of CB6. The molecule is able to accelerate the Huisgen 1,3-dipolar cycloaddition reaction between alkynes and azides.¹¹⁶ By confining the reactants within its cavity, CB6 acted in an enzyme-like fashion, promoting the reaction rate through proximity and orientation effects. However, the system also revealed a major limitation: the triazole product formed during the reaction remained tightly bound within the cavity, making product release difficult, what is obviously undesirable for catalytic turnover.

Despite these interesting findings, practical applications of cucurbituril were initially limited. By the late 1990s, other macrocyclic hosts such as CDs and calixarenes were already established in host-guest chemistry, particularly due to their water solubility, and ease of synthesis and modification.^{69, 70, 79, 81, 86, 93, 98} In contrast, CB6 is virtually insoluble in water, meaning a significant challenge for its widespread use and slowing development of practical applications. Nevertheless, the pioneering work of Mock laid the foundational understanding of cucurbituril chemistry and uncovered the extraordinary potential as high-affinity and highly selective hosts. This promise was only fully realized after advances in solubilization, derivatization, and most importantly, synthetic access to larger CB n homologues discovered shortly after.

3.4.5.2. Unlocking the Full Potential of Cucurbit[*n*]urils: The Discovery of Higher Homologues

Inspired by the homologue diversity observed in other macrocycles such as calixarenes, Kim and co-workers made a significant breakthrough by successfully synthesizing and isolating higher homologues of cucurbituril.¹¹⁷ By modification of the reaction parameters originally reported by Behrend, they were able to obtain CB5, CB7 and CB8, in addition to the previously known CB6. Since the reaction always yielded a mixture of the homologues in varying amounts, they also developed an effective fractional crystallization strategy to separate and purify the individual macrocycles. Though the NMR spectral patterns of the homologues were similar to CB6, distinct changes in chemical shifts reflected subtle differences in the electronic environments and cavity dimension.¹¹⁷

The discovery of larger cavity sizes in CB7 and CB8 opened promising new avenues for host-guest chemistry, enabling the inclusion of larger and more complex guests and even supporting alternative binding stoichiometries. For example, molecular modeling studies suggested a naphthalene-type guest, which is too bulky to fit inside CB6, would form a 1:1 complex with CB7, and even a 2:1 complex with CB8. The predictions were experimentally confirmed using NMR spectroscopy, mass spectrometry and X-ray crystallography, which revealed the existence of multiple guest orientations within the CB8 cavity, stabilized by π - π stacking interactions.¹¹⁷

In addition to its increased cavity size, CB7 exhibits significantly enhanced water solubility compared to CB6, dramatically improving its suitability for biological and analytical applications. The cavity of CB7 is especially well-suited for the encapsulation of ferrocene and methyl viologen, enabling the development of redox-responsive sensing systems.¹¹⁸⁻¹²⁰ The synthesis of these higher homologues not only expanded the structural diversity of the cucurbituril family, but also dramatically increased their functional versatility, laying the groundwork for a wide range of practical applications in chemosensing, catalysis and biomedical applications.

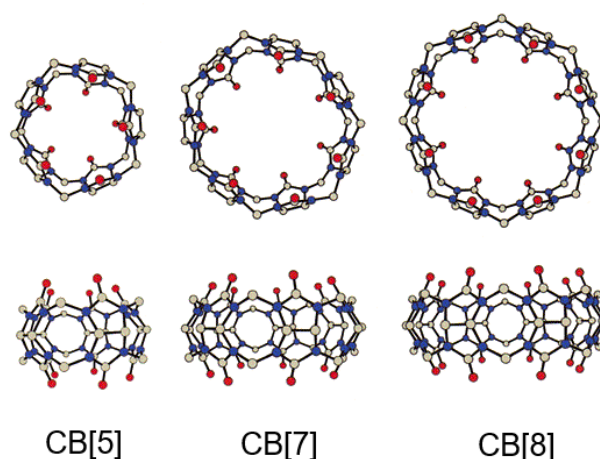


Fig. 3.15: X-ray crystal structures of the larger homologues CB5, CB7 and CB8. Reprinted with permission from ref ¹¹⁷. © American Chemical Society

3.4.5.3. Synthesis of Cucurbiturils and Factors Influencing Homologue Distribution

Prior to the year 2000, nearly all cucurbituril-related research focused exclusively on CB6, with the sole exception being the synthesis of a decamethylated CB5 analogue reported by the Stoddart group in 1992.¹²¹ Following the revolutionary introduction of different sized cucurbiturils by Kim, the Day group systematically investigated the factors that govern cucurbituril synthesis, ultimately identifying optimized conditions to increase the relative yield of individual CB n homologues.¹²² Although Kim's modified conditions successfully produced CB5, CB7 and CB8, they still did not really address a central question: Why does the reaction intrinsically favor the formation of the hexameric CB6? Their answer may be found in the subtle interplay of the reaction conditions and especially the thermodynamics and kinetics of the system.

The originally reported procedure by Behrend involves a two-step acid condensation reaction between glycoluril and an excess of formaldehyde. This process yielded an amorphous insoluble intermediate, which is subsequently dissolved in hot sulfuric acid and precipitated by dilution with water, ultimately yielding pure CB6, as later confirmed by Mock.^{108, 109, 112} In contrast, Kim's method makes use of a one-pot condensation of glycoluril and formaldehyde, but at lower reaction temperatures (75-90°C) compared to the ~110°C used in Behrend's synthesis.¹¹⁷ These milder conditions allow for the isolation of kinetically controlled products, expanding the product distribution to include other CB n homologues. The exact contents varied from batch to batch, still the mixture typically contained ~60% of CB6, ~10% of CB5, ~20% of CB7 together with ~10% of other higher CB n homologues.¹¹⁷

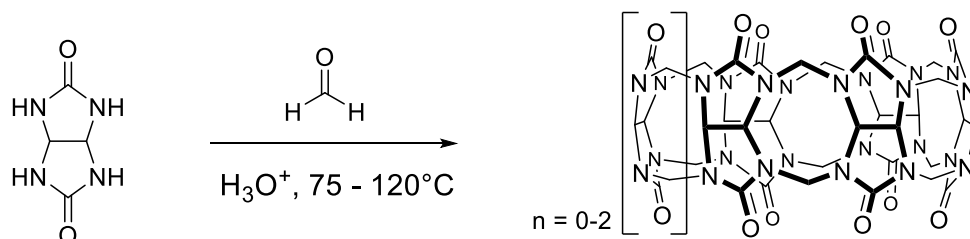


Fig. 3.16: Synthesis of the acid-catalyzed synthesis of the various cucurbituril homologues.

Building on this work, the Day group uncovered a number of additional variables that significantly influence product distribution during the macrocycle formation.¹²² Basically, any strong acid is capable of catalyzing the cyclization into cucurbituril rings, offering flexibility in synthetic design. Additionally, the traditional Behrend method involves an oligomerization step, followed by an isolation of the resulting intermediate. Day could demonstrate, that this transformation can proceed efficiently as a single-step process under strong acidic conditions. The variation of the acid concentration, while keeping glycoluril constant, leads to considerable changes in the relative yields of the CB n homologues, indicating a relationship between acid strength and quantity and ring size preference. As already showed by Kim, Day confirmed the importance of the control of the reaction temperature as well as the influence of glycoluril monomer concentration.^{117, 122} Another interesting concept established by Day got later successfully used by the Isaacs group.¹²³ It was shown, that template ions can direct product formation. For example, the

addition of potassium chloride to the reaction mixture significantly enhanced the relative yield of CB5, probably by stabilizing its intermediate during cyclization. Template variation leads to preference of other homologues.¹²¹⁻¹²⁴ These findings highlight the multifactorial nature of the cucurbituril synthesis. By carefully tuning the reaction parameters, it is now possible to lead the synthesis toward specific CB n , nevertheless the reaction always leads to mixtures of different CB n species which must be carefully separated.¹²⁵

In addition to the commonly studied main family members CB5 to CB8, the acid-catalyzed condensation between glycoluril and formaldehyde can also result in the formation of higher homologues and structural variants, such as inverted or twisted cucurbiturils, each possessing distinct molecular architectures and unique binding properties.^{121, 126-128} A practical and widely used technique for identifying individual CB n is NMR, particularly interpretation of the ¹³C NMR spectrum. As the ring size increases, the methylene and methine carbon signals shift progressively downfield, allowing a reliable identification of CB n species even in crude reaction mixtures prior to purification.^{122, 127, 129}

To isolate individual cucurbiturils from reaction mixtures, fractional crystallization proved to be an easy yet very effective method.¹²⁵ Kim's group demonstrated that carefully controlling the solvent system results in the stepwise separation of CB n homologues.¹¹⁷ Depending on the exact reaction conditions, crystalline CB8 often precipitates spontaneously from the mixture when it is allowed to stand overnight, sometimes in combination with a minor fraction of CB6. The subsequent isolation of the major fraction of CB6 from the resulting mixture is straightforward. The simple addition of water selectively induces the crystallization of pure CB6, caused by its poor aqueous solubility. In the remaining aqueous portion, isolation and separation of CB5 and CB7 can be achieved using acetone-water and methanol-water mixtures, respectively.^{125, 130} Effective purification of the individual CBs is crucial for accurate determination of binding affinities, since the behavior of host-guest systems can significantly be affected by even trace amounts of impurities. Generally, the better water-soluble CB n (CB5 and CB7) are more challenging to purify and face greater contamination problems. In particular, residual acids from the synthesis process can become trapped within the CB cavity, altering both solubility and guest-binding features. In contrast, acid-free CB6 can be obtained by conducting the condensation in hydrochloric acid, followed by evaporation of the residual acid in a vacuum oven, yielding a highly pure product.¹³¹

An alternative approach was developed by the Scherman group.¹³² To improve the separation of CB5 and CB7, which are notoriously difficult to purify due to their similar solubility properties, an environmentally friendly complexation-based purification strategy was demonstrated. The method utilizes a tailored alkyl-imidazolium based guest molecule that selectively forms a complex with CB7, enabling careful separation from CB5. In addition, other methods include silica gel column chromatography under harsh acidic conditions, and ion exchange chromatography.^{133, 134} The strong and selective guest-binding properties can complicate both preparation and purification, as unintended guest inclusion may occur at various stages. So far, development of efficient and scalable strategies for selective synthesis of cucurbiturils remains a major challenge for the practical application, but Aqdot is the first

company to already commercialize mixtures of CB n for odor and volatile organic compounds elimination.¹³⁵

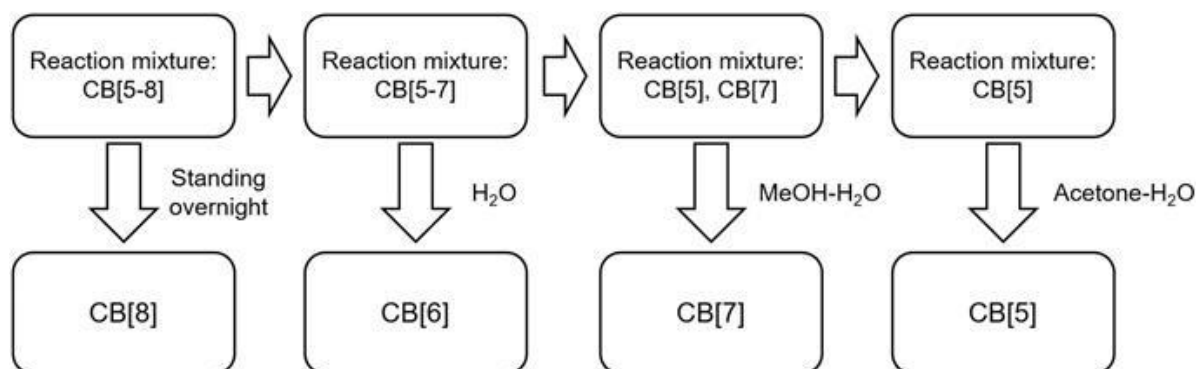


Fig. 3.17: Schematic illustration of the isolation protocol for the native cucurbit[n]uril family members. Reprinted with permission from ref ¹³⁶. © The Royal Society of Chemistry

In addition to identifying key parameters for the synthesis of cucurbiturils, Day also provided interesting interpretations as to why CB6 is consistently the favored product in the acid-catalyzed condensation of glycoluril and formaldehyde, despite variation of the reaction parameters such as temperature and acid type.^{122, 137, 138} These insights were later further explored by the Isaacs group, which deeply investigated the oligomerization.^{123, 139, 140} The findings point to a combination of factors involving the thermodynamic stability of individual CB n homologues, the reactivity and conformational preferences of glycoluril-based oligomeric precursors, as well as the kinetic accessibility and templating effects. During the condensation process, linear glycoluril oligomers are formed prior to macrocyclization, what can be observed by ¹³C NMR as complex mixtures. The complexity mainly arises from the conformational orientation of the methylene bridges linking the two five-membered rings in the glycoluril unit. Each methylene bridge is able to adopt one of the two possible orientations depending on the face of the glycoluril involved. In the *endo* conformation, both concave faces are aligned on the same site, whereas in the *exo* conformation, both concave faces are aligned on opposite sites. Only the all-*endo* conformation enables successful macrocyclization into CB n , while all mixed *endo-exo* arrangements are energetically less favored. As a result, oligomers with *exo*-oriented segments will eventually undergo reversible disconnection and reformation of methylene bridges to reach the all-*endo* state necessary for the cyclization.^{122, 138} This was experimentally supported by the acid-catalyzed contraction of CB8. If a purified sample of CB8 gets heated in concentrated hydrochloric acid at 100°C, it would degrade to smaller homologues. This demonstrated that CB formation is a reversible process, and ring contraction occurs *via* partial cleavage and rearrangement of methylene linkers in order to reach an energetically more favored structure. When the same thermal stability studies are performed with CB5, CB6 and CB7, they shown a higher stability and remain intact in concentrated hydrochloric acid at 100°C for at least 24h. This suggests that CB6 represents a thermodynamic minimum and the energetically most favored structure under typical reaction conditions.¹²²

Day could show in high-dilution experiments that the rate of oligomerization is limited to a duration of five or six units before the cyclization happens. In this fashion, smaller CBs are favored.¹²² In contrast, at higher concentrations of glycoluril and formaldehyde, the reaction equilibrium shifts to favor the formation of longer oligomers, increasing the probability of generating larger CB_n homologues like CB7 and CB8. This is likely determined by the combination of the extended residence time of reactive oligomers, which allows for further chain elongation before ring closure, and a reduced rate of oligomer breakdown, what stabilizes longer chains and promotes formation of higher homologues.^{111, 122, 137} Both reaction temperature and acid concentration act as critical regulators of both oligomer growth and ring closure kinetics. While elevated temperatures may facilitate chain mobility and rearrangement, acid strength heavily influences both condensation and methylene bridge exchange. The understanding of the mechanism of cucurbituril formation not only explains the natural dominance of CB6 in standard reaction conditions, but also provides a framework for directing the synthesis and product distribution toward desired homologues, what is an essential step for cucurbituril-based applications in chemosensing, molecular recognition and functional materials. In the following section the exact mechanism of cucurbituril formation and the role of glycoluril oligomers will be further explored.

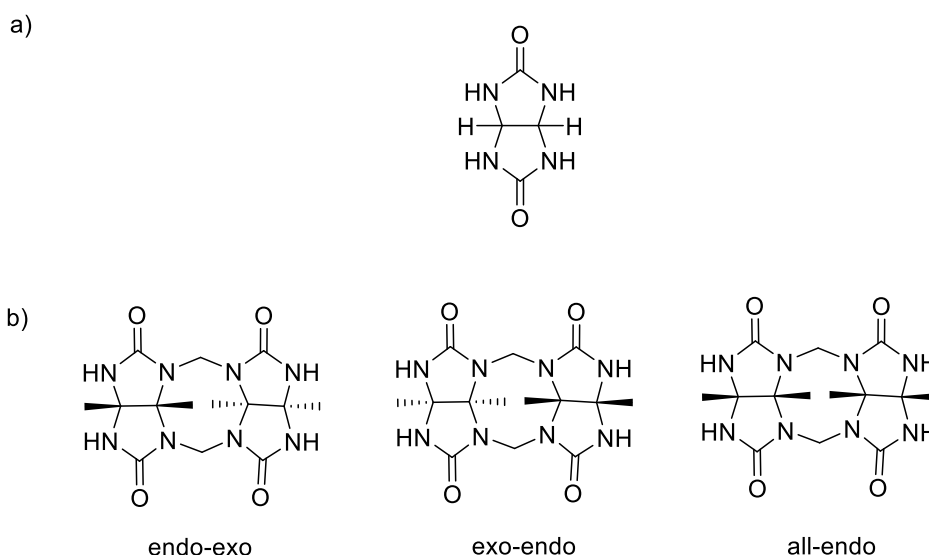


Fig. 3.18: a) Structure of the glycoluril monomer with one possible conformation of the methine hydrogen atoms. b) Possible conformations of the methine hydrogen atoms in glycoluril dimers.

3.4.5.4. Mechanism of Cucurbituril Formation

The formation of CBs begins with a rapid acid-catalyzed condensation reaction between glycoluril and formaldehyde, resulting in the generation of methylene-bridged glycoluril dimers. These dimers serve as the fundamental building block in the construction of the macrocyclic framework. A key factor in understanding the formation mechanism was the recognition that CB_n synthesis shows close resemblances to a classical step-growth polymerization reaction.¹³³ Specifically, the stoichiometric ratio plays an important role in determining the extent of oligomerization, what guides the size and distribution

of macrocycles. Maintaining the appropriate between the two monomers glycoluril and formaldehyde is essential to favor macrocycle formation in form of discrete, well-defined CB homologues.

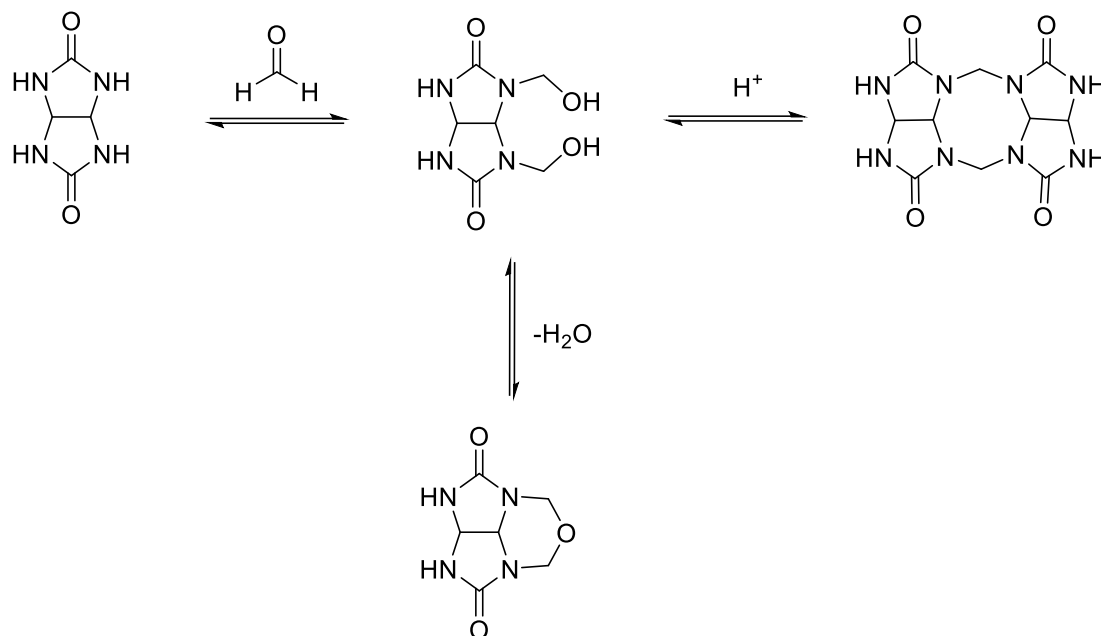


Fig. 3.19: Synthesis of the methylene-bridged glycoluril dimer.

A key step in the mechanism of CB formation is the initial condensation between glycoluril and formaldehyde, yielding methylene-bridged glycoluril dimers, serving as essential intermediates in macrocycle assembly. To gain mechanistic insight into this early stage, the Isaacs group designed a constrained glycoluril monomer capped on one site with a *o*-xylylene unit, effectively limiting the reaction to the dimerization step (**Fig. 3.19**).^{138, 141} To improve solubility in organic media, the compound was additionally functionalized with CO₂Et groups on its convex face.^{139, 140} Under acidic conditions, the condensation with formaldehyde yielded to distinct diastereomers. They found a C-shaped dimer, in which all four CO₂Et groups are oriented on the same face of the molecule, as well as a S-shaped dimer with the substituent groups oriented on opposite sites. Interestingly, the S-shaped geometry was identified as the kinetic product, forming more rapidly under the reaction conditions. However, upon further heating in the presence of formaldehyde, the S-shaped diastereomer gradually converted into the C-shaped diastereomer, indicating that this conformation is the thermodynamically more stable product. This preference is also structurally significant, since the C-shaped form already provides the necessary curvature to facilitate macrocyclization into the CB_n architecture.¹⁴¹

Following the initial formation of methylene-bridged glycoluril dimers, the subsequent steps in cucurbituril synthesis closely resemble the mechanism of a classical step-growth polymerization reaction, particularly a co-polymerization between two multifunctional monomers. In this analogy, glycoluril bearing four reactive NH groups, functions as a tetrafunctional monomer, whereas formaldehyde, capable of reacting with two NH groups, represents a bifunctional monomer. Therefore, the ideal stoichiometric ratio for efficient chain elongation is 1:2 (glycoluril to formaldehyde). As the reaction proceeds, the

growing oligomers may adopt conformations stabilized by intramolecular hydrogen bonding and van-der-Waals interactions, which both contribute to the preorganization necessary for ring closure. Interestingly, under certain conditions, these chain growth mechanisms may be altered, resulting in structurally distinct species such as chiral *nor-seco* cucurbiturils, representing twisted analogues.^{126, 138} Isaacs further explored the oligomerization pathway by controlling the formaldehyde concentration, which enabled to isolate and characterize acyclic oligomeric intermediates, thereby confirming the stepwise chain elongation process.¹²³ These oligomeric intermediates can serve as molecular clips, exhibiting a whole new range of binding properties.¹⁴¹⁻¹⁴³

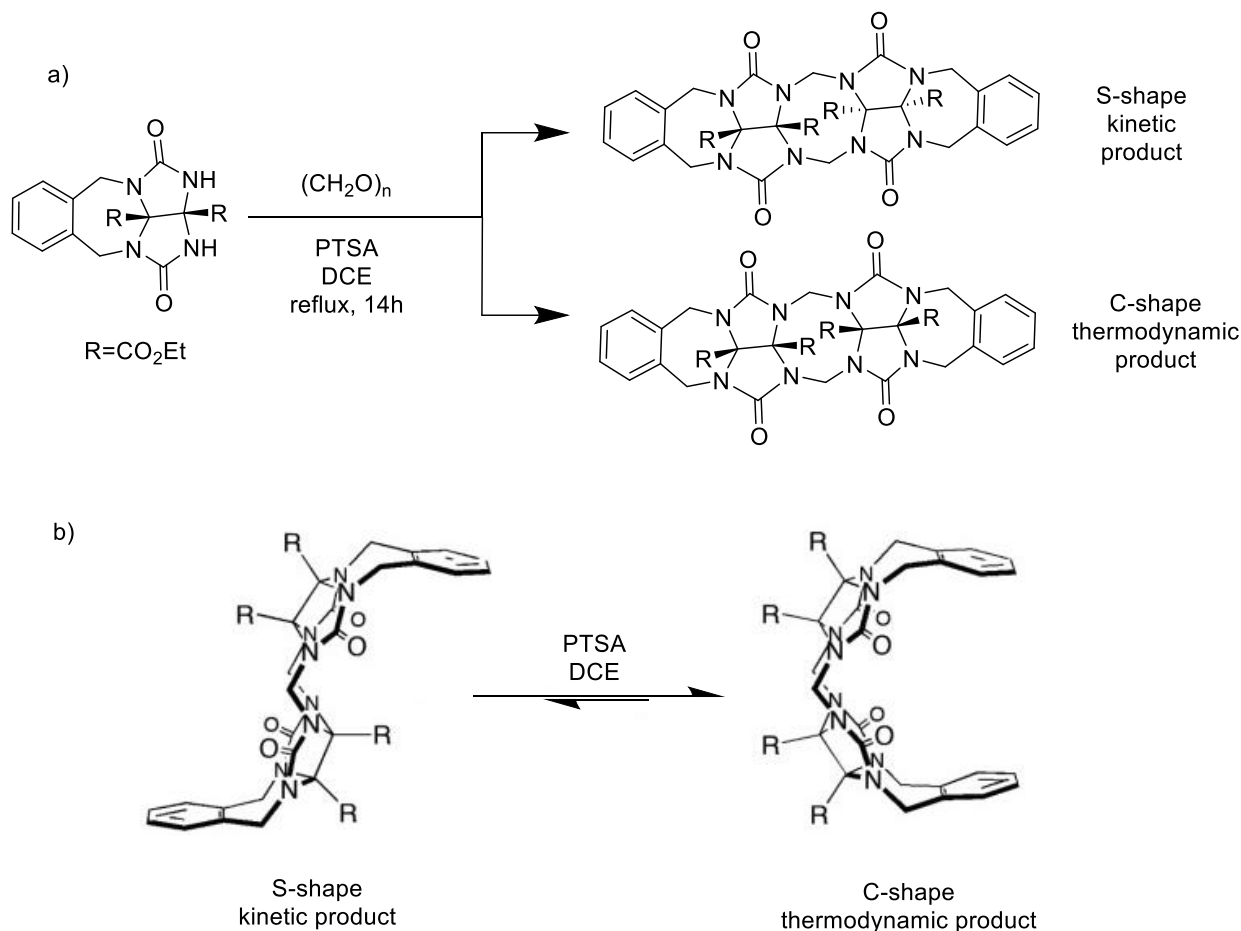


Fig. 3.20: a) Synthesis of the *o*-xylylene capped glycoluril dimer. b) Equilibration between the diastereomers with the thermodynamically preferred C-shape. Adapted with permission from ref ¹³⁸. © The Royal Society of Chemistry.

Once a linear oligomer reaches a sufficient length, which is five to seven glycoluril units, it becomes capable of macrocyclization. This final ring-closing event is initiated by the addition of one equivalent of formaldehyde, resulting in a hydroxymethylated intermediate. At this stage, side reactions may lead to the formation of twisted, inverted, or *nor-seco* CB analogues, depending on the spatial arrangement and reactivity of the distinct intermediate. These analogues are isolatable; however, they represent kinetic intermediates and undergo rearrangement to ultimately yield the thermodynamically favored CB5, CB6 and CB7 by the addition of another equivalent of formaldehyde.¹²⁶⁻¹²⁸

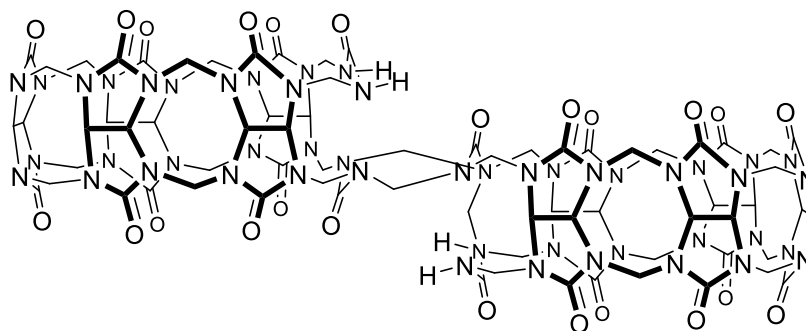


Fig. 3.21: Structure of bis-*nor seco*-CB10, an example of a double cavity CB host with interesting binding properties.¹²⁶

3.4.5.5. Architectural Features Driving Host-Guest Recognition in CB n Macrocycles

The defining feature of the cucurbit[n]uril family lies in their highly symmetrical, barrel-shaped architecture. Each macrocycle consists of n glycoluril units linked by methylene bridges, forming a rigid structure with two identical portals consisting of negatively polarized carbonyl groups. These carbonyl-rich rims enclose a central, nonpolar cavity, exhibiting hydrophobic properties. This unique combination of rigid symmetry, polar portals and hydrophobic interior is critical in understanding the host-guest properties of CB n , since both the portal size and cavity volume increase with the number of glycoluril units.

Electrostatic potential maps provide interesting insight into the binding behavior of CB n (**Fig. 3.22**). The negatively polarized carbonyl-lined portals exhibit significant electron density, creating strong dipoles that especially favor the complexation of positively charged species. These ion-dipole interactions enable CB n to function as highly effective cation receptors (see **Table 3.2**).¹⁴⁴ Actually, the first reports of CB n binding involved metal cations acting as “lids” bound to the portals of CB.^{113, 145} In addition to metal ions, CB n readily bind to a broad range of organic cations, such as ammonium and imidazolium species.¹⁴⁵⁻¹⁴⁹ Notably, for the less water-soluble members of the family, especially CB6 and CB8, complexation with cationic guests often improves solubility.

While the portals of CB n are characterized by their highly polar electronegative carbonyl groups, the hydrophobic inner cavity presents a stark contrast. Consisting of the fused glycoluril subunits, the cavity lacks polar functional groups or accessible lone electron pairs. However, the cavity of the macrocycle made from the fused rings of glycoluril subunits do have no functional groups electron pairs accessible to the inner cavity, only C-H bonds are oriented inward. This results in a remarkably hydrophobic interior, with a strong preference for encapsulating neutral, nonpolar guest molecules.^{117, 118, 122, 125} Upon guest encapsulation and the binding event happening, notable changes in the photophysical properties of the guest are typically observed. This may be noticeable by shifts in absorption, fluorescence, and NMR spectra, what is collectively described as complexation-induced spectral changes. Such effects result from alterations in the electronic and magnetic environments surrounding the guest molecule.

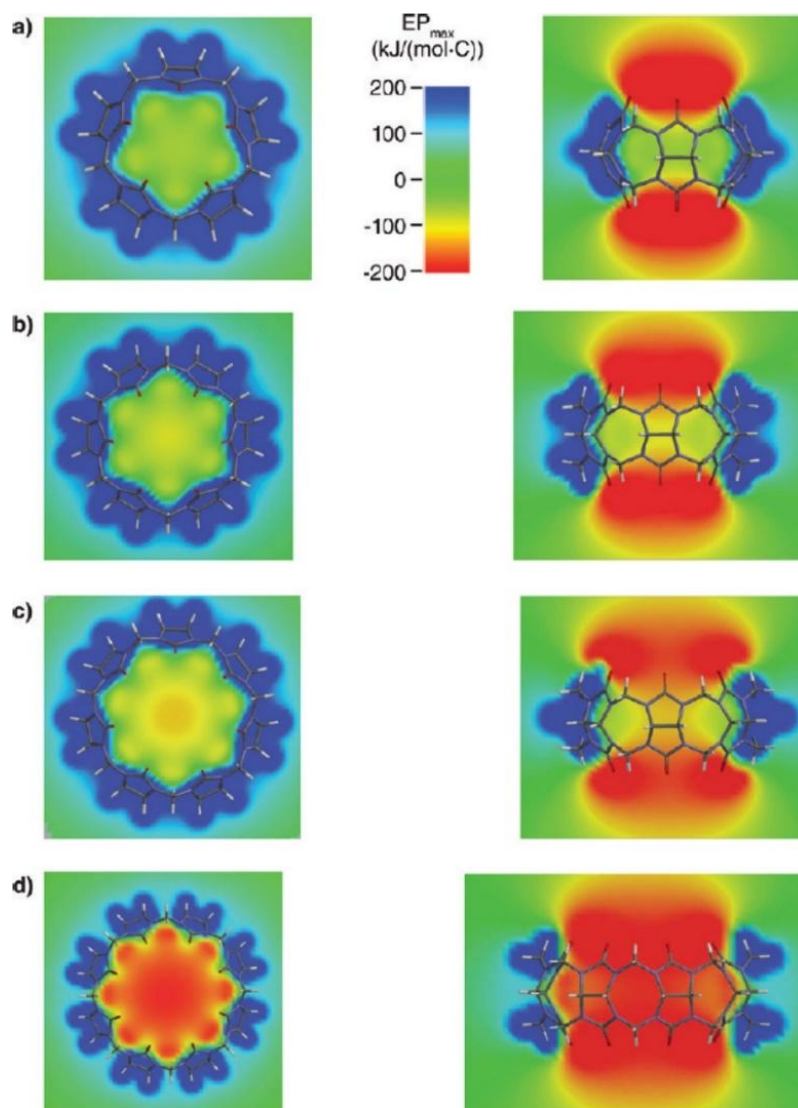


Fig 3.22: Calculated electrostatic potential, represented for a) CB5, b) CB6, c) CB7, and d) CB8. Adapted with permission from ref ¹⁵⁰. © American Chemical Society

To investigate the nature of the CB_n cavity, several studies have employed solvatochromic dyes, which are fluorescent or chromogenic molecules known to exhibit spectral shifts in response to changing solvent polarity.^{151, 152} These dyes provide valuable insight, as their well-characterized optical responses serve as indirect reporters of the local environment.¹⁵³ Encapsulation of such solvatochromic dyes by CB7, for instance, often results in a bathochromic shift in both absorption and fluorescence spectra, consistent with immersion into a less-polar environment. Additionally, the observation of pronounced Stokes shifts in certain dye-CB7 complexes further supports the presence of a hydrophobic, nonpolar interior.¹⁵¹ Nevertheless, the interpretation of these results is not always straightforward. Because of the confined geometry of the cavity, along with specific binding interactions, the correlation between spectral shifts and polarity is complicated. Additionally, many known solvatochromic dyes are relatively large and cannot be fully encapsulated within the CB cavity.¹⁵⁴ As a result, their optical responses need to be treated with caution, since they may actually represent a mixed environment, caused by being partially

inside the nonpolar host and partially exposed to the polar aqueous phase. This can introduce uncertainty into polarity assessments.

Cations	r (Å)	$-\Delta G_{\text{hyd}}$ (kJ mol ⁻¹)	CB5	CB6	CB7	CB8
H ₃ O ⁺	1.12	-	≤0.5	1.06	2.22	-
NH ₄ ⁺	1.48	285	2.59	3.79	2.82	-
Li ⁺	0.69	475	2.02	2.41	2.34	1.69
Na ⁺	1.02	365	3.94	3.89	3.41	2.49
K ⁺	1.38	295	4.73	3.81	3.46	2.66
Rb ⁺	1.49	275	3.22	4.30	3.43	2.64
Cs ⁺	1.70	250	2.61	5.31	3.50	2.55
Ag ⁺	1.15	430	-	3.87	3.54	2.32
Mg ²⁺	0.72	1830	2.50	2.57	3.24	2.72
Ca ²⁺	1.00	1505	2.64	4.22	4.25	3.31
Sr ²⁺	1.13	1380	5.16	4.91	4.79	3.63
Ba ²⁺	1.36	1250	6.44	5.29	5.28	3.95
Ni ²⁺	0.69	1980	2.73	2.59	3.50	2.73
Cu ²⁺	0.73	2010	-	2.88	3.75	2.86
Zn ²⁺	0.75	1955	-	2.45	3.40	2.67
Al ³⁺	0.53	4525	-	3.81	2.90	2.90
Fe ³⁺	0.65	4265	3.66	5.71	4.18	3.0
Yb ³⁺	0.87	3570	3.71	3.50	4.42	3.44
La ³⁺	1.05	3145	4.17	1.10	5.28	3.76

Table 3.2: Binding constants (given as log K_a values) of various cations with CB n ($n=5-8$). Data taken from ref ¹⁴⁴

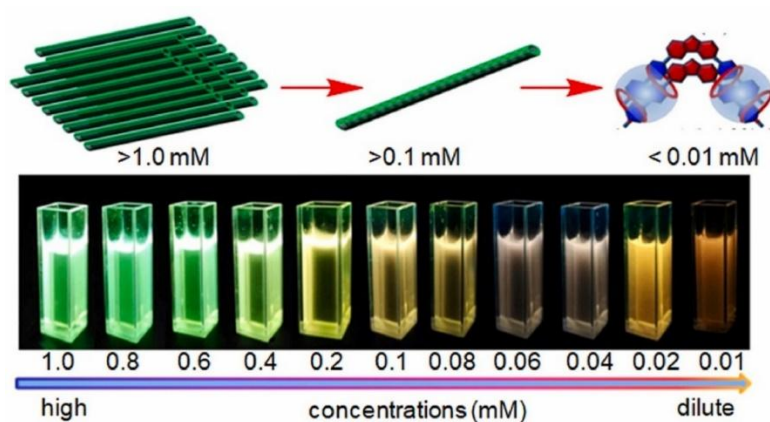


Fig 3.23: Concentration-dependent fluorescence enhancement of a supramolecular polymer associated with cucurbit[8]uril. With increasing concentration of the polymer, and therefore bound CB8, the fluorescence increases. Adapted with permission from ref ¹⁵⁵ © Elsevier

The extraordinarily low polarizability of the cucurbituril cavity has been further clarified through a series of elegant studies by Nau and co-workers, who investigated the photophysical behavior of 2,3-diazabicyclo[2.2.2]oct-2-ene (DBO), a neutral azoalkane with an exceptionally long-lived fluorescence lifetime of up to 1 μs .¹⁵⁶ DBO is a particularly insightful probe for CB7 due to its small, nearly spherical shape and its ability to be completely encapsulated within the cavity, perfectly reflecting the microenvironment. Nau's findings revealed that the absorption spectrum of DBO is highly sensitive to its local environment. Upon encapsulation with CB7, DBO exhibited spectroscopic behavior more closely related to that in the gas phase. This provided powerful experimental support for Cram's longstanding hypothesis that the interior of molecular containers, such as CBs, constitutes a distinct supramolecular phase, and is fundamentally different from traditional condensed phases such as liquids or solids.^{6, 157} The remarkable low polarizability of the CB7 cavity can be readily attributed to its unique molecular structure. With its electron-deficient cavity that has no lone electron pairs and polarizable bonds, together with rigid and highly symmetric interior provides minimal dielectric response to an encapsulated guest. Consequently, any molecule bound in the cavity is subject to an environment far more similar to the gas phase than a polar solvent.¹⁵⁸

This unique property directly has significant implications for molecular recognition and sensing. Interestingly, many fluorophores exhibit their longest recorded fluorescence lifetimes when encapsulated in CB cavities. This phenomenon is attributed to a reduction in the radiative decay rate, which is determined by the ratio of fluorescence quantum yield to fluorescence lifetime.^{151, 157} Remarkably, this cavity-induced lifetime extension is observable even for some dyes that are too spacious to be fully encapsulated within the CB_n structure. Partial encapsulation therefore is already sufficient to influence the photophysical behavior of the guest, further highlighting the profound and far-reaching impact of the CB environment on molecular properties. Some noteworthy examples are Rhodamine 6G and Fluorescein, both widely used as laser dyes, whose photostability and emission properties can be significantly enhanced through stabilization by cucurbiturils.¹⁵¹

Another fundamental determinant of guest binding within the CB cavity is the principle of size complementarity between host and guest, what is closely aligned with the classical key-and-lock model. This concept allows for predictive insights into the binding behavior of various CBs, based on their internal cavity dimensions. For example, the relatively small cavity of CB5 makes it almost exclusively suitable for encapsulating gases, while CB6 is already able to accommodate small organic molecules. The even larger internal volume of CB7 is capable of binding small aromatic molecules, and CB8 possesses sufficient space to simultaneously host two guest molecules.¹⁵⁰ To assess the spatial availability for hydrophobic interactions within CB_n cavities, the volume of the cavity is often estimated or calculated, what tends to converge for the larger CBs. Although computational models provide a good estimate for cavity volumes, these often slightly exaggerate the true accessible volume due to the omission of portal-bound water molecules or metal cations present in the medium, which may partially obstruct guest entry. It is important to note that while theoretical cavity volume can indicate potential guest capacity, it does

not necessarily equate to actual usable space within the host structure. The extent to which a guest can occupy the cavity is directed by both spatial and entropic considerations.¹⁵⁹

To quantitatively describe the steric compatibility of host-guest complexes, Mecozzi and Rebek introduced the concept of the packing coefficient (PC), which is defined as the ratio of the volume of the guest to that of the host cavity.¹⁶⁰ This metric provides a useful predictive parameter for assessing the likelihood and strength of complex formation. Studies have shown that the optimal PC for stable inclusion complexes lies around 55%, depending on the exact host cavity, with an acceptable range between 45% and 65%. Guest with PCs significantly above this range (e.g., >75%) are typically too large to enter the cavity without incurring substantial entropic penalties, unless additional stabilizing interactions such as ion-dipole or π - π interactions are present, also a strong hydrophobic effect, for example steroid binding to CB7, can lead to stable complexes despite high PCs.¹⁶¹ On the other hand, guest with PCs below ~30% often fail to form stable complexes due to insufficient van der Waals contact and reduced desolvation gain.¹⁵⁸

This principle has proven to be a valuable tool in predicting complexation behavior of various CBs with structurally appropriate guest molecules.¹⁵⁹ The remaining unoccupied space within the host-guest complex (typically around 45%) is generally attributed to the retention of vibrational and, in some cases, translational degrees of freedom of the guest. These degrees of freedom would otherwise be restricted in an overly compressed complex. Importantly, while the ideal packing coefficient generally provides a reference point for optimal fit, guests with slightly smaller or larger PCs may still yield viable complexes, however, typically with reduced binding affinities. Noteworthy, this situation significantly differs in the solid state. Here, PCs are often larger than 68%, which helps to explain why certain guests offer only weak binding in solution, still they can be isolated in the crystalline state as stable host-guest complexes, as seen with the cucurbit[6]uril•diethyl ether complex.¹⁵⁹

The packing coefficient concept provides useful insight into observed trends in CB host-guest chemistry. For example, CB5 hosts display PCs ranging from approximately 28% to 69%, indicating a significant volume of void space for smaller guests.¹⁶² CB5 is especially effective to bind gases, as its cavity is too small to accommodate larger organic molecules.^{121, 147, 149} In the case of CB6, optimal binding is observed for C4-C5 residues, such as alkylammonium, diammoniumalkyl and cycloalkylammonium salts. These guests yield PCs very close to the ideal 55%, correlating with maximum binding affinities.¹¹³ For CB7, a broader variety of guests is known to be encapsulated, but smaller guest molecules often leave enough space in the cavity for residual water molecules to co-occupy the interior.^{163, 164} Peak binding affinities are typically observed at PCs of around 60%, corresponding well to guests like ferrocene and adamantane, which are known to be very strong binders to CB7.¹⁵⁹ For higher homologues like CB8, the error of the PC increases with the size of the host and the decreasing rigidity. These observations illustrate that analyzing the PC of a given CB n not only aids in rational guest design but also allows for prediction of binding constants and qualitative assessment of whether encapsulation is reasonable. Ultimately these results underscore the major role of the inner cavity volume in host-guest interactions.^{115, 137, 159}

Another important structural feature of cucurbiturils is the presence of highly polarized dipole regions at the carbonyl-lined portals. These regions result from the alignment of the dipoles associated with the ureido carbonyl groups and represent areas of concentrated electron density. They play a crucial role in host-guest recognition, particularly in the binding of cationic substituents of organic guest molecules through strong ion-dipole interactions.¹⁶⁵ The spatial extent of these dipolar regions is size-dependent and varies significantly among the CB homologues. For CB5, the dipole region on each portal is relatively compact, with approximately 15 \AA^3 , providing a tight fit only suitable for small guests like gases. This limited volume allows for the fixed positioning of atomic-scale guests at the portals but efficiently restricts the threading of larger substituents through the cavity. In contrast, CB6 features substantially larger dipole regions of around 35 \AA^3 per portal, which already accommodate the threading of small alkyl chains such as isobutyl groups.¹⁶⁶ This spatial feature makes CB6 particularly attractive for the synthesis of higher supramolecular architectures like rotaxanes, where a linear guest is threaded through the macrocycle and stabilized by electrostatic interactions at the portals.¹⁶⁷ With the even larger homologues such as CB7 and CB8, the portal regions expand significantly, providing dipole regions of $>100 \text{ \AA}^3$. This allows for the stable positioning of larger molecular fragments, including charged aromatic rings and bulky side chains, within the dipolar binding sites. This increased capacity facilitates multivalent interactions and further opens the door for more elaborate supramolecular assemblies, including molecular switches, shuttles, and responsive materials.^{168, 169}

3.4.5.6. The Hydrophobic Effect as a Key Element in Cucurbituril Binding Mechanisms

Among the various forces that drive supramolecular interactions, the hydrophobic effect is often considered the most significant, particularly in host-guest complexation mechanisms.^{68, 159} The partial or complete encapsulation of guest molecules within macrocyclic hosts is largely driven by the displacement of energetically unfavorable, or high-energy, water molecules from the host cavity. All cavities larger than a critical size contain water molecules, for entropic reasons, even if the breaking of hydrogen bonds is necessary.¹⁵⁰ Traditionally explained by the Frank-Evans model, this effect is attributed to an entropic gain upon release of these structured water molecules into the bulk solvent. Other models emphasize enthalpic contributions, suggesting that the expelled water gains energy by forming stronger hydrogen bonds with other water molecules in the bulk medium, what is also referred as the “nonclassical” hydrophobic effect.^{68, 159} This principle has been supported by extensive studies on cucurbiturils, where displacement of high-energy water molecules has been shown to contribute considerably to binding. Calorimetric and molecular dynamics studies have revealed extraordinarily high binding constants as high as $K_a = 7 \times 10^{17} \text{ M}^{-1}$, even outshining those of the tightest biological complexes.¹⁷⁰ These unusually strong affinities correlate with both the number and energetic frustration of confined water molecules inside the CB cavity.

Importantly, hydrophobic interactions in CBs differ from those in other host systems like calixarenes and cyclodextrins. Crucially, hydrophobic and dispersion interactions are often mistakenly grouped

together, as both are believed to peak for nonpolar guests in aqueous environments. However, the underlying situation for those interactions is different for CBs. The cavity of CBs is actually less polarizable than water, meaning that dispersion interactions of hydrophobic guests, typically enhanced in less polar environments, actually favor solvation in water rather than in the CB cavity.^{68, 159} As a result, the encapsulation of neutral guests or nonpolar residues within CBs is primarily driven by true hydrophobic interactions, provided that electrostatic contributions from the carbonyl portals are negligible or properly accounted for.

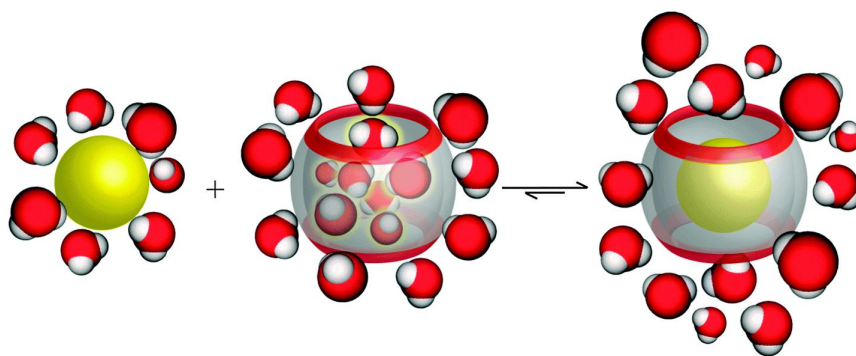


Fig 3.24: Schematic representation of the release of high-energy water molecules from the CB7 cavity upon binding of a hydrophobic guest. Adapted with permission from ref ¹⁵⁸ © American Chemical Society

The hydrophobic effect in cucurbituril host-guest chemistry is governed by both entropic and enthalpic factors.^{68, 159} A major entropic contribution arises from the displacement of water molecules confined within the hydrophobic interior of CBs. Depending on the exact ring size, CB n cavities are able to accommodate between 2 (CB5) and 22 (CB10) water molecules. These numbers have been estimated using various methods, including molecular dynamics simulations and packing coefficient calculations, which show all good agreement. Still, the PC-based estimates are especially useful, as they allow direct comparison between guest volumes and the number of displaced water molecules. In contrast, water molecules located at the polar carbonyl-lined portals are more difficult to quantify due to their specific hydrogen bond and dipole-dipole interactions. These contribute less predictably to the thermodynamics of complexation and become more dominant.

In the case of CB7, guests like adamantane and ferrocene are spacious enough to fully displace all internal water molecules, triggering strong enthalpic gains due to the expulsion of so called very-high-energetic water.⁶⁸ These water molecules are highly energetically frustrated, since they are unable to form full hydrogen-bond network inside the confined cavity and thus contribute significantly to the binding energy when released into bulk media. Consequently, differences in binding affinities among similar guests often reflect differences in the degree of desolvation, particularly of the guest's hydrophobic residues. Interestingly, for guest molecules such as linear alcohols and carboxylic acids that bind CB6 with a consistent orientation and depth, binding constants remain relatively uniform due to similar desolvation profile.¹⁷¹ This underscores the importance of desolvation symmetry for stable host-guest binding. Energetically, while individual water molecules in smaller CBs (e.g., CB5 and CB6) are actually more energetically frustrated due to limited hydrogen bonding with other water molecules, CB7 provides

the most favorable net enthalpic contribution upon guest binding. This is because it balances a relatively high individual water molecule energy with a larger total number of displaced water molecules. In contrast, the cavity of CB8 is already spacious enough to allow internal water to form a stable hydrogen-bond network similar to those in bulk water, effectively reducing the energetic gain from their release.^{68,}

159

CB <i>n</i>	Number of water molecules in inner cavity		
	X-ray	MD simulations	PC analysis
CB5	1-2	2	2
CB6	3-4	4 [3]	4
CB7	...	7	8
CB8	11-12	10	12
CB9	...	14	16
CB10	...	20	22

Table 3.3: Occupancy of the inner cavities of CBs with water molecules. Data taken from ref ¹⁵⁹

Kim and co-workers also highlighted an additional influence of the solvent on the binding mechanism.¹⁷² In gas-phase studies of CB complexes, ion-dipole interactions between host and guest dominate. However, in aqueous environments, the hydrophobic effect, driven by the release of high-energy water, becomes the dominant driving force for complexation.

3.4.6. Cucurbituril Functionalization as a Gateway to Molecular Tools

Although the discovery of CB homologues significantly expanded the scope of CB chemistry, early practical applications remained limited, primarily due to their poor solubility in common organic solvents and water and the challenge of introducing functional groups. In contrast, other macrocyclic hosts such as cyclodextrins, calixarenes, or pillararenes offer convenient possibilities for modification by introduction of functional groups, what further opens the door for countless applications in all kinds of fields.^{69, 70, 79, 80, 173-175} However, CBs are notoriously resistant to modification. Their exceptional chemical stability, while advantageous for many applications, presents a major obstacle for chemical derivatization and widespread use. Functionalization is essential to unlock the full potential of CBs, enabling enhanced solubility and guest affinity, covalent attachment to surfaces, and integration of reporter groups for sensing and diagnostics. To overcome these challenges, researchers have developed four general strategies for introducing substituents to cucurbiturils.¹³⁶ First, the use of substituted glycoluril monomers, second, the use of substituted glycoluril oligomers, third, use of other aldehydes than formaldehyde, and fourth, the direct post-synthetic functionalization of preformed CBs. Especially in the early stages, the first three approaches, collectively representing the building-block strategy, were the primary routes explored for cucurbituril derivatization.^{139, 140}

3.4.6.1. The Building Block Approach: Precursor-Driven Functionalization of Cucurbiturils

The foundational strategy for CB functionalization is rooted in modifying its primary building block, glycoluril. This compound is readily synthesized in high yield by the acid-catalyzed condensation of two equivalents of urea with one equivalent of glyoxal. Importantly, the aldehyde component can also be replaced with other carbonyl containing species like ketones, such as 2,3-butanedione or 1,2-cyclohexanedione, leading to substituted glycolurils in which the methine positions bear alkyl or other functional groups instead of hydrogen (**Fig. 3.25**).¹³⁶ This method enabled the synthesis of decamethyl-CB5, the first example of substituted CBs.^{121, 149} Notably, this derivative was discovered before the unsubstituted parent CB5.^{121, 149} Later, Day and co-workers significantly expanded this concept, improving the yield of decamethyl-CB5 and introducing a strategy to obtain partially methylated CB n homologues.¹⁷⁶ A key intermediate for their synthetic process was the tetracyclic diether of dimethylglycoluril, which was reacted with glycoluril in a 1:1 ratio in the presence of LiCl as templating agent. This generated a mixture of symmetrical and asymmetrical methylated CB species, favoring symmetrical hexamethyl-CB6.¹⁷⁶

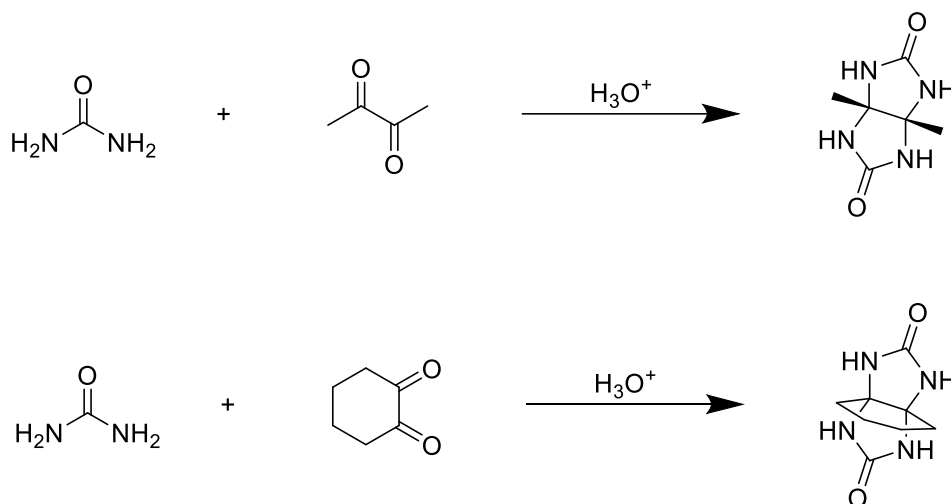


Fig. 3.25: Synthesis of substituted glycolurils from urea and different ketones.

The Isaacs group further advanced this approach by systematically employing substituted glycoluril monomers and oligomers.^{139, 177} Collaborating with the Day group they developed monomers bearing electron-withdrawing substituents designed to selectively heterooligomerize with unmodified glycoluril units.¹⁷⁷ This gave rise to CBs with specific substitution patterns and enhanced solubility and functionality.^{176, 177} Isaacs also reported a series of structurally and optically distinctive CB analogues derived from substitution of the carbonyl species with bis(phthalhydrazide) (**Fig.3.26**). These yielded macrocycles incorporating carboxylic acids, amides, or imides, with altered sizes, unusual shapes, and optical properties. Particularly striking was the introduction of fluorescent CB derivatives, attributed to the introduced aromatic system. Guest binding led to measurable changes in their emission spectra, opening avenues for their application as responsive probes.¹⁷⁸

In addition to multifunctional derivatives, Isaacs demonstrated the synthesis of selectively monofunctionalized CBs.¹⁷⁹ A monofunctionalized CB7 derivative was obtained by reacting a glycoluril hexamer with a monoalkyl chloride-substituted cyclic diether of glycoluril, using potassium iodide as a template. This led to the first “clickable” CB7 derivative, following substitution of the chloride for an azide group.¹⁷⁹

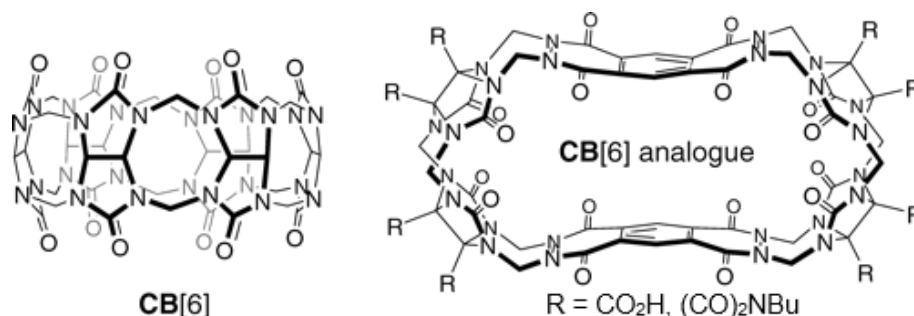


Fig. 3.26: Structure of the parent CB6 and the self-fluorescent CB6-phthalhydrazide analogue. Reprinted with permission from ref ¹⁷⁸ © American Chemical Society

3.4.6.2. Direct Functionalization of Cucurbiturils: Unlocking the Post-Synthetic Modification

Despite the success of early approaches to functionalize cucurbiturils via modified building blocks, these methods were often synthetically complex, poorly controlled, and yielded only low amounts of the desired product. Additionally, while alkyl substituents helped to lessen the problem of solubility in water, they did not resolve the key challenge of selective or monofunctional modification. This prompted efforts to develop more practical strategies, leading to the exploration of direct post-synthetic functionalization approaches of preformed cucurbiturils. One major obstacle for such approaches lies in the poor solubility in common organic solvents and water and their remarkable thermal and chemical stability, indicating harsh reaction conditions would be necessary.

In 2003, the Kim group reported a breakthrough method for direct oxidation of CBs.¹⁸⁰ Each CB n homologue was separately subjected to oxidation by more than $2n$ equivalents of potassium peroxodisulfate ($\text{K}_2\text{S}_2\text{O}_8$) in water at elevated temperatures, yielding perhydroxy-CB n . These hydroxyl groups were selectively introduced at the equatorial region, without affecting the overall structure of the macrocycle. The method proved to be most effective for perhydroxylation of CB5 and CB6, while yields for CB7 and CB8 remained low. This was attributed to the reduced chemical stability of the hydroxylated products, which was already demonstrated by the contraction of CB8 to smaller homologues upon heating in acid.¹²² Although the exact mechanism is still under investigation, it is assumed that hydroxylation proceeds *via* a radical mechanism, where hydroxyl radicals generated from persulfate attack the equatorial methine positions. The introduction of hydroxy groups represented an important milestone in CB chemistry, as it significantly improved solubility in organic solvents and finally enabled reactions in DMSO or DMF, opening the door for further derivatization.¹⁸⁰ However, the availability of multiple

reactive hydroxy groups leads to formation of a mixture of fully or partially derivatized CBs in subsequent reactions, complicating purification of the desired product.¹⁸¹

To address this, researchers optimized conditions to obtain monofunctionalized derivatives. Scherman demonstrated that increasing initial solubility of the macrocycle improves control over the number of hydroxylations. By pre-complexing CB6 with a bis-imidazolium guest in a 1:1 ratio, solubility in water was greatly enhanced, and the following treatment with 1 equivalent of ammonium persulfate ($(\text{NH}_4)_2\text{S}_2\text{O}_8$) yielded monohydroxylated CB6-OH.¹⁶⁶ Kim later applied a similar strategy to CB7, using submolar amounts of $\text{K}_2\text{S}_2\text{O}_8$ and six equivalents of K_2SO_4 as a solubilizing additive.¹⁸² Nevertheless, both methods faced delicate limitations: Scherman's strategy left a tightly bound guest in the cavity, while Kim's approach still led to mixtures of products which were hard to separate. A more refined method was introduced by Kaifer, who optimized the conditions for monohydroxylation of CB7 by controlling the reagent ratio CB7: $(\text{NH}_4)_2\text{S}_2\text{O}_8$ at 1:1.5, lowering the reaction temperature, and extending the reaction time.¹⁸³ Additionally, sodium bisulfite (NaHSO_3) was used as a mediator, and the purification process employed a polymer column, enabling recovery of both the monohydroxylated product and unreacted CB7, which could then be used again in a subsequent reaction.

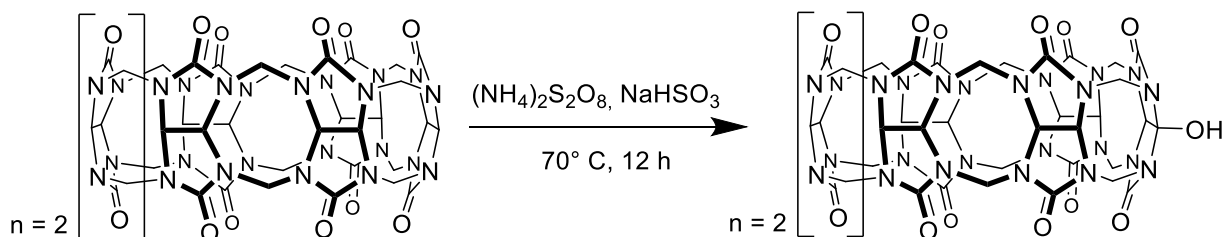


Fig. 3.27: Process of CB7 monohydroxylation developed by Kaifer.¹⁸³

3.4.6.3. From Hydroxyl to Handle: Installing Allyl and Propargyl Groups on Cucurbiturils for Downstream Derivatization

Taking advantage of their enhanced solubility in water and organic solvents such as DMSO, hydroxylated CB n can be further functionalized to introduce a variety of groups, to either improve solubility in organic media or to install reactive substituents for further derivatization. Among these, allyl and propargyl moieties have proven to be especially valuable, as they enable efficient covalent conjugation with thiol- or azide-functionalized species *via* thiol-ene and azide-alkyne click reactions.

In their initial report on the direct hydroxylation of cucurbiturils, Kim also demonstrated subsequent conversion into perallyloxy and peracetyloxy derivatives.¹⁸⁰ Following deprotonation of the hydroxyl groups in anhydrous DMSO using a base like sodium hydride, the reaction with allyl bromide or propionic anhydride proceeded smoothly. Moreover, the perallylated CB6 derivative successfully underwent a thiol-ene photoclick reaction with an alkylthiol compound.¹⁸⁰ The group of Ritter later introduced a perpropargyloxy-CB6 derivative and demonstrated its successful microwave-assisted click reaction with an azide-functionalized cyclodextrin.¹⁸⁴ This functionalization strategy was further extended to monohydroxylated CBs, affording monoallyloxy and monopropargyloxy derivatives.^{166, 182, 185} These

mono-functional CB_n opened the door to a wide range of applications, providing versatile handles for site-specific conjugation, material immobilization, and development of chemosensors.

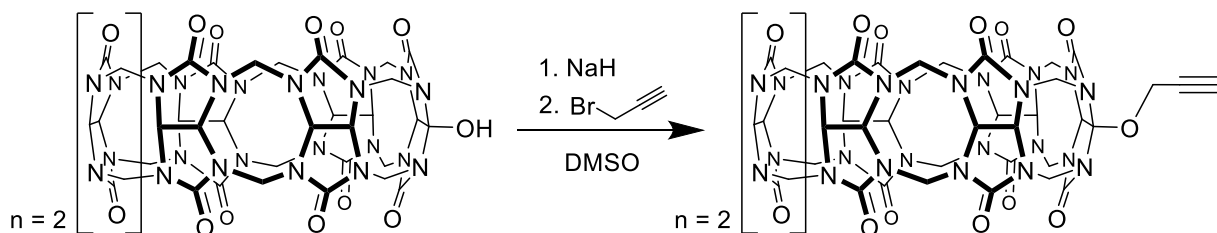


Fig 3.28: Process of monopropargylation of CB7-OH.

3.4.7. Cucurbiturils in Biomedical Applications: Toward Smart Molecular Tools

In the following section, a selection of important applications of unmodified and functionalized cucurbiturils will be presented, with a particular focus on CB7. Emphasis will be placed on how chemical modification of the CB framework enables tailored molecular recognition, targeted drug delivery, sensing of biorelevant analytes, and therapeutic potential in complex biological environments.

3.4.7.1. Synthetic Ion Transport with CB_n

An essential feature of all living cells is the presence of ion channels, which are specialized membrane proteins that facilitate the controlled and selective transport of ions across biological membranes.¹⁸⁶ These channels basically serve as molecular filters, distinguishing between ions based on size, charge and coordination chemistry. For example, potassium ion channels exhibit remarkable selectivity, effectively distinguishing K^+ from Na^+ ions despite their similar properties. This discrimination arises from the finely tuned dimensions of the channel pore, which precisely accommodate the larger K^+ ion while excluding the smaller Na^+ ion due to suboptimal coordination.¹⁸⁶

While numerous synthetic ion channels based on synthetic receptor molecules have been reported over the years, most fail to replicate the elegant selectivity found in nature. However, CB-based systems have shown promise in this area. Kim introduced a pioneering example using perallyloxy-CB6 integrated with mercaptooctanethiol into lipid vesicles composed of egg yolk L- α -phosphatidylcholine (EYPC). Encapsulation of a pH-sensitive fluorescent dye enabled monitoring of proton transport, revealing that the CB6 based construct could indeed facilitate proton transport upon addition of acetylcholine. Moreover, ion selectivity studies demonstrated a preference for Li^+ over other alkali metals, what could be attributed to the size of the CB6 carbonyl portals.¹⁸⁷

Further advancements for CB-based synthetic ion channels came from Yang and co-workers, who engineered a hybrid synthetic ion channel by combining acyclic CBs with pillar[5]arenes.¹⁸⁸ This construct successfully integrated into lipid bilayers forming artificial channels capable of selectively transporting cations. Remarkably, these channels exhibited high selectivity for K^+ over Na^+ , what is a key characteristic of biological potassium channels.¹⁸⁶ This selectivity could even be modulated by altering the linker length between the CB and pillararene units, offering a tunable platform for biomimetic ion

channel design. Such systems not only provide insights into ion recognition mechanism but also represent promising candidates for therapeutic applications.¹⁸⁸

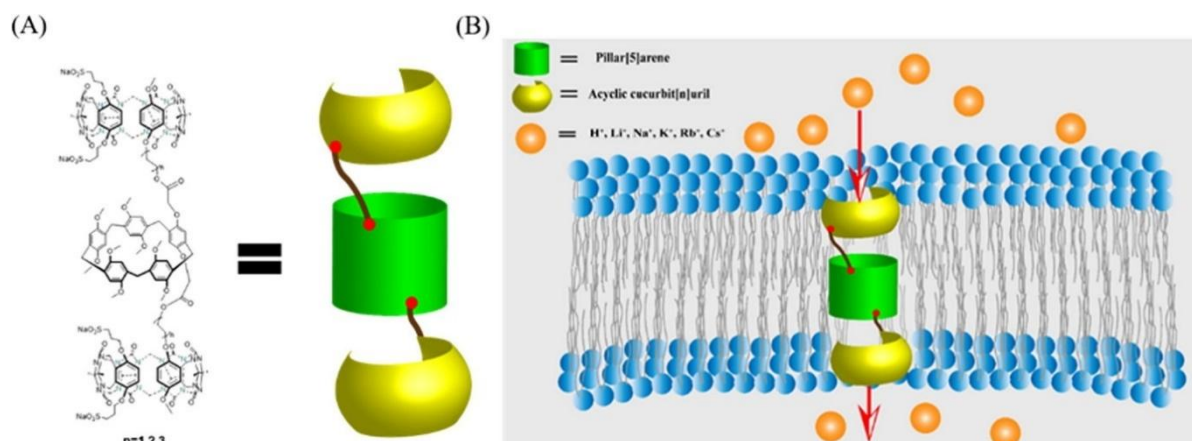


Fig. 3.29: a) Structure of the newly synthesized synthetic transmembrane channel molecules. b) Schematic representation of the ion transport through a bilayer membrane. Adapted from with permission from ref ¹⁸⁸ © Elsevier

3.4.7.2. Encapsulation of Drugs by CB n -Based Systems

Cucurbiturils have been extensively explored as supramolecular hosts for the encapsulation of a wide array of drug molecules, including antibiotics, antivirals, enzyme inhibitors, hormones, neurotransmitters and vitamins.^{189, 190} Their ability to form stable high-affinity host-guest complexes enables modulation of the solubility, stability and biological activity of pharmaceutical agents, addressing some of the key challenges in drug formulation.^{125, 191-194}

Benzimidazole derivatives represent an important scaffold in medicinal chemistry and an important class of therapeutics, serving as anthelmintics (e.g., thiabendazole, albendazole) and proton pump inhibitors (e.g., pantoprazole). Due to their poor solubility in neutral form, their bioavailability is often limited.^{191, 195} Several studies have systematically investigated the supramolecular complexation of these benzimidazoles with cucurbiturils, particularly CB7.¹⁹⁶ Upon protonation, their binding affinity to CB7 dramatically increases, shifting from millimolar to micromolar dissociation constants. Remarkably, the encapsulation of albendazole resulted in a 2000-fold enhanced water solubility.¹⁹⁷

Beyond solubility enhancement, cucurbiturils can mediate or modulate the interaction of drugs with biological targets. For instance, the Nau group demonstrated that the binding of the triphenylmethane (TPM) dye Brilliant Green (BG) to bovine serum albumin (BSA) is significantly enhanced in the presence of CB7.¹⁹⁸ TPM dyes are promising drugs for photodynamic therapy and as antimicrobial agents. Although the dye is not fully encapsulated within the cavity, partial complexation involving the protonated amine groups influence both the photophysical properties and binding affinity of BG to BSA. The residual exposed aryl groups remain available for protein interaction, resulting in a synergistic enhancement of biological activity. Such studies highlight the therapeutic potential of CBs to act as supramolecular mediators in drug delivery and therapeutic enhancement strategies.¹⁹⁸

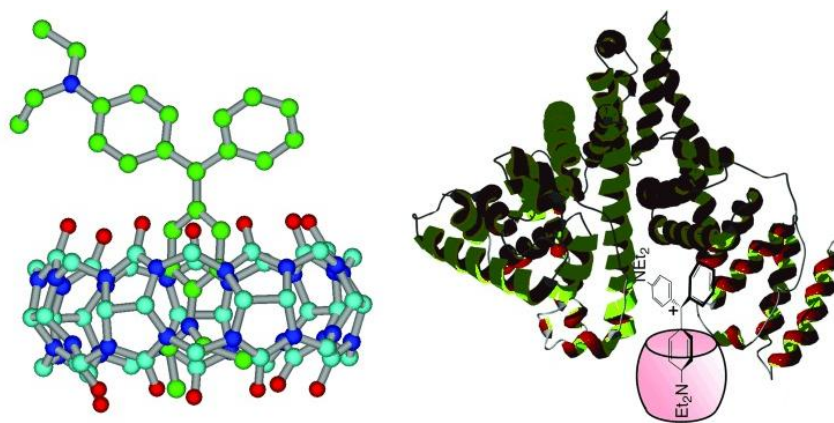


Fig. 3.30: Structure of the CB[7]•BG complex, and how the complex interacts with the BSA protein. Adapted with permission from ref ¹⁹⁸ © Wiley-VCH

In a similar fashion to the enhancement observed with TPM dyes, the antibacterial efficacy of fluoroquinolone antibiotics has also been shown to improve upon complexation with CBs. The groups of El-Sheshtawy and Feng demonstrated that the antibacterial activity of danofloxacin, norfloxacin and ofloxacin is significantly enhanced through 1:1 host-guest complex formation with CB7.¹⁹⁹ The supramolecular encapsulation likely stabilizes the protonated forms of these drugs, improving their aqueous solubility, and modulating their interaction with bacterial targets.¹⁹⁹

3.4.7.3. Targeted Drug Delivery from Cucurbituril-Based Systems

Controlled release and site-specific delivery of therapeutic agents remain central goals in drug delivery research.²⁰⁰ Cucurbituril offers a versatile platform for encapsulating drug, with spontaneous release often driven by dilution, competitive displacement, or changes in pH within specific cellular components.²⁰¹⁻²⁰⁵ However, due to their non-specific nature, CBs require functionalization to selectively recognize and bind to target tissues or certain cellular markers, since the parent CB cannot distinguish very specifically. To address this limitation, the Isaacs group developed two CB7-biotin conjugates for the targeted delivery of oxaliplatin to cancer cells.²⁰⁶ Biotin, a known ligand for overexpressed biotin receptors on cancer cells, enabled the site-specific targeting what significantly enhanced the therapeutic efficacy of oxaliplatin.

A complementary strategy was introduced by Agasti and co-workers, who synthesized CB7-conjugated antibodies (CB7-Ab) directed against microtubules in fixed mouse embryonic fibroblast (MEF) cells.²⁰⁷ Making use of the high-affinity host-guest complexation between CB7 and adamantane, they achieved robust and specific fluorescent labeling using an adamantane-functionalized dye. The resulting fluorescent signal proved to be highly stable as it showed resistance against multiple washing steps, and the strategy was further adapted for super-resolution imaging of the microtubules network by using a combination of an adamantane-functionalized DNA strand for hybridization with another strand functionalized with a fluorescent dye.²⁰⁷

Expanding into receptor-mediated uptake, Bardelang and co-workers developed a peptide-functionalized CB7 conjugate, CB7-VH4127, that targets the Low Density Lipoprotein Receptor

(LDLR).²⁰⁸ They could demonstrate a new kind of drug delivery system, since the VH4127 maintained its binding affinity to the LDLR. The uptake potential was evaluated with another conjugate combining adamantylamine as high-affinity group for CB7 with the fluorescent tracker Alexa680 (A680). This system enabled specific endocytosis in LDLR-expressing cells. The resulting A680-Ada•CB7-VH4127 maintained high binding affinity for LDLR and showed enhanced intracellular accumulation via receptor-mediated endocytosis, pointing to promising applications in LDLR-targeting drug delivery.

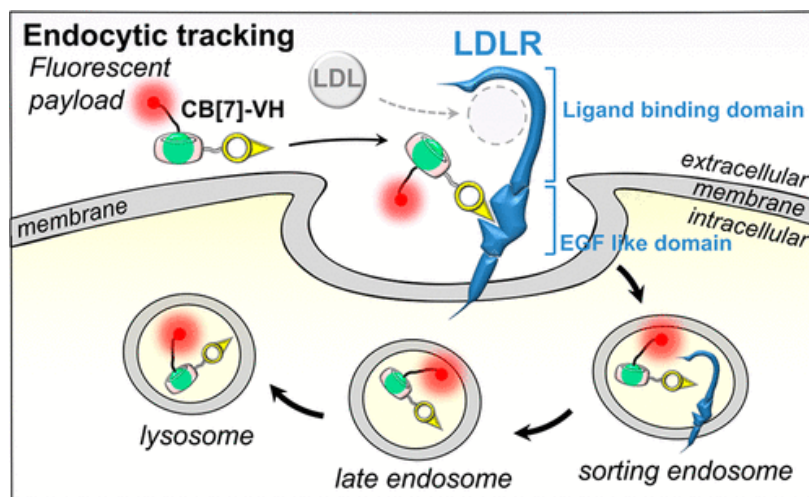


Fig 3.31: CB[7]-VH4127 conjugate targeting LDLR for efficient intracellular delivery in LDLR expressing cells, tissues or tumors. Reprinted with permission from ref ²⁰⁸ © American Chemical Society

Park and co-workers demonstrated a CB6-based nanoparticle system for hydrophobic drug delivery.²⁰⁹ The dye Nile Red (NR) was encapsulated in CB6 nanoparticles, which were further modified with a folate-spermidine conjugate *via* CB6•spermidine host-guest interaction. This system enabled folate-receptor-mediated uptake into HeLa cells, followed by intracellular release of NR, what was confirmed by confocal microscopy. Based on these results, CB6 nanoparticles were also used for targeting delivery of an anticancer drug to folate receptor-overexpressing cells.

In another work, Jung and co-workers developed a CB6-hyaluronate (CB6-HA) conjugates for targeting formyl peptide receptor (FPRL1)-expressing cancer cells.²¹⁰ A spermidine-peptide conjugate served as a model FPRL1 ligand, while fluorescein-labeled spermidine provided imaging capability. *In vitro* studies with B16F1 melanoma cell showed HA receptor-mediated uptake, and functional delivery to FPRL1-expressing breast cancer cells was verified by increased intracellular Ca^{2+} concentrations, accompanied by strong fluorescence signal changes.

3.4.7.4. Cucurbiturils for Bioimaging and Real-Time Bioprocess Analysis

Conjugation of CBs with fluorescent dyes has enabled a wide range of bioimaging and biomonitoring applications.^{158, 211-214} Since native CB7 lacks intrinsic fluorescence, the attachment of a fluorophore is essential for real-time tracking and signal-generation.

A pioneering example comes from the Urbach group, which developed a CB7-tetramethylrhodamine conjugate (Q7R) capable of cellular uptake (**Fig. 3.32**).²¹⁵ Upon guest binding, Q7R undergoes

fluorescence quenching, while retaining K_d values comparable to unmodified CB7. This makes Q7R a versatile unimolecular host-indicator system, capable of directly reporting binding events in real-time. Confocal fluorescence microscopy of live and fixed HT22 neurons revealed Q7R uptake and punctate cytoplasmic localization, demonstrating its potential as a cell-permeable sensor for dynamic intracellular processes.

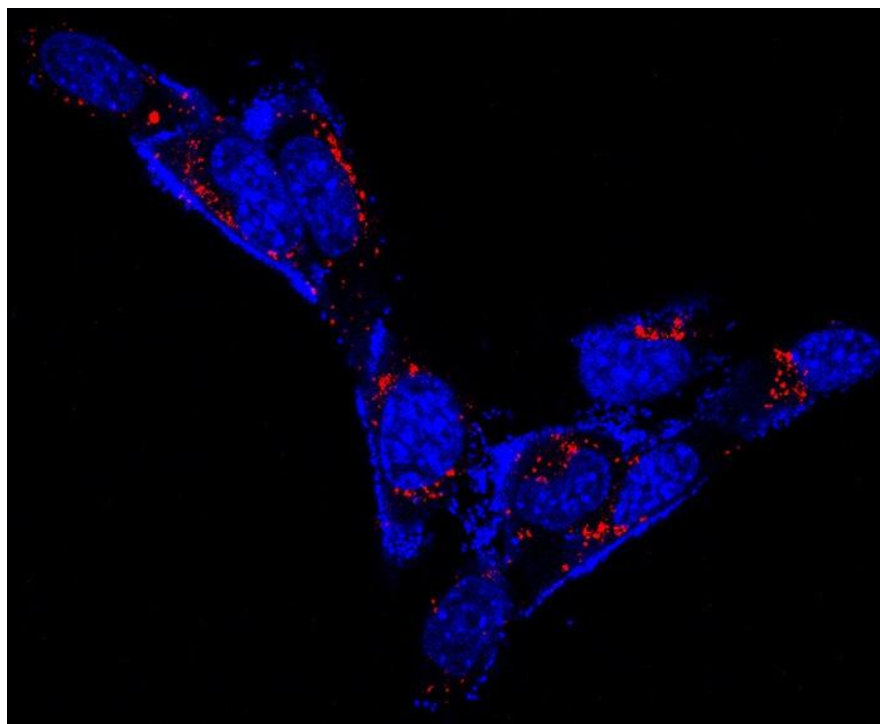


Fig 3.32: False color confocal fluorescence micrograph of live HT22 cells treated with both Q7R (red) and Hoechst 33342 (blue). Reprinted with permission from ref ²¹⁵ © American Chemical Society

An alternative approach was presented by the Fürstenberg group.²¹⁶ They utilized unmodified CB7 to boost the performance of red-emitting oxazine fluorophores (ATTO655, ATTO680, ATTO700). Encapsulation by CB7 significantly increased their fluorescence brightness and prevented water-induced quenching, thus dramatically enhancing imaging precision in super resolution.

Kim and co-workers developed a supramolecular protein labelling system using the high-affinity interactions of CB7 with with adamantyl- and ferrocenyl-ammonium groups (**Fig. 3.31**).²¹³ Proteins in (or on) the cells were tagged with these moieties and subsequently visualized using a cyanine conjugated CB7, enabling precise imaging in living cells and in *C. elegans* with minimal interference from endogenous biomolecules.

The sequence selectivity of CB7 has also found use in monitoring enzymatic activity. Thermolysin-catalyzed cleavage of peptides at phenylalanine residues results in fragments with N-terminal Phe, which are selectively recognized by CB7, opening the door for assays for protease substrate profiling and inhibitor screening (**Fig 3.32**).²¹⁷ Scherman extended this concept to peptide separation by immobilizing CB8 on surfaces to selectively bind N-terminal tryptophan peptides, while Sankaran showed that larger

biological structures, such as cells, can be adsorbed and released *via* surface-bound CB8 ternary complexes.^{218, 219}

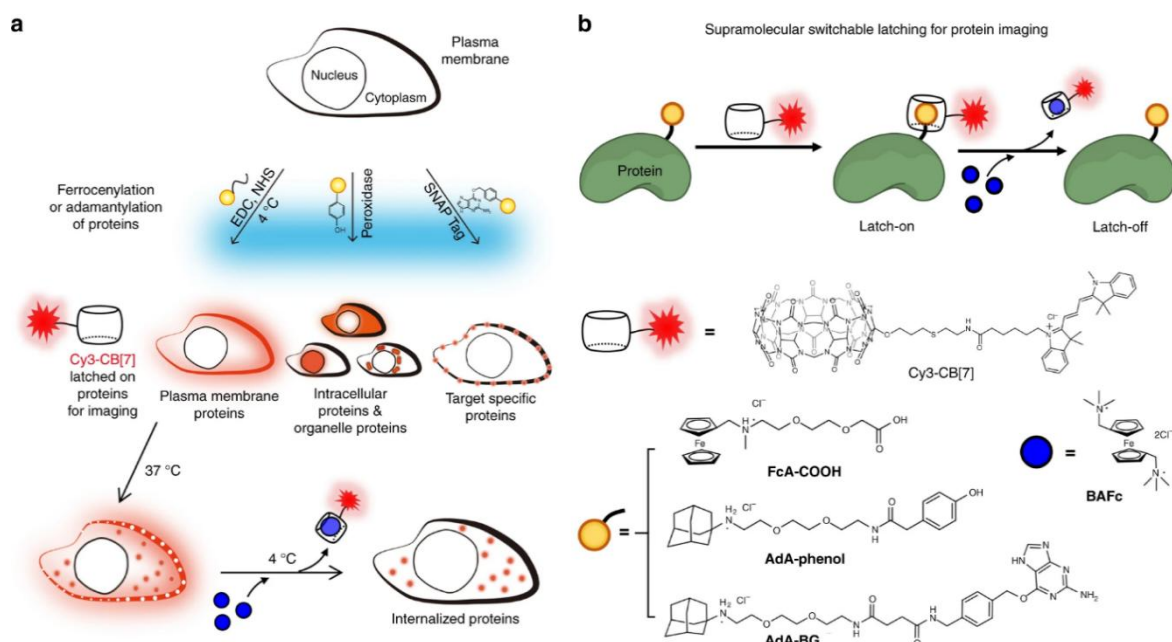


Fig. 3.33: a) Universal and selective imaging of cellular proteins using a switchable supramolecular latching system based on the ultrastable host-guest interactions between the CB-dye conjugate Cy3-CB7 and adamantane or ferrocene. b) CB7-based ultrastable binding pairs used in the study of Kim. Adapted with permission from ref²¹³ © Nature Publishing Group

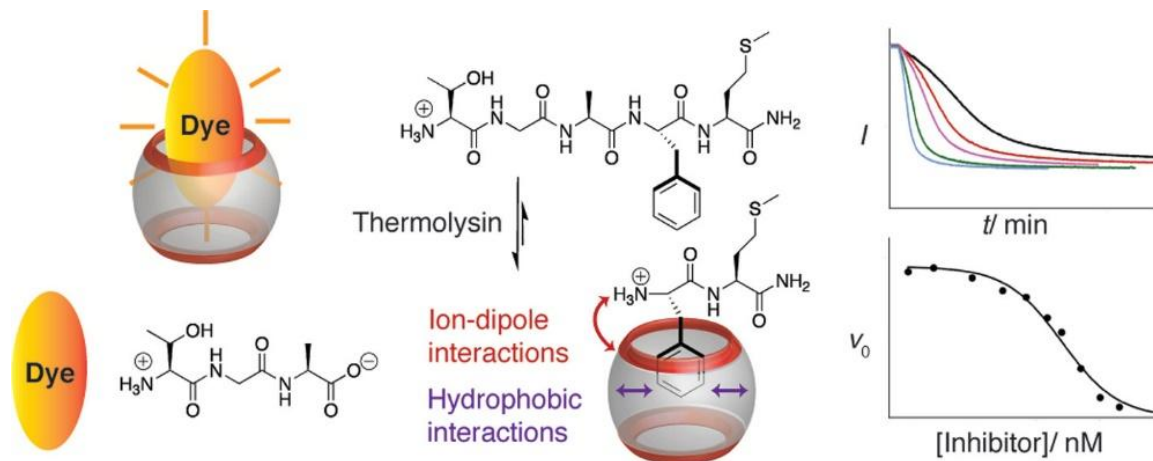


Fig 3.34: Schematic representation of the protease substrate profiling with thermolysin. Adapted with permission from ref²¹⁷ © American Chemical Society

For deep-tissue inflammation imaging, Wang and co-workers designed supramolecular luminol-AIEgen nanoparticles (SLA NPs) using CB[7]-adamantane host-guest interactions (**Fig. 3.35**).²²⁰ The particles exhibited bioluminescence resonance energy transfer (BRET) from luminol to AIEgens, and demonstrated high stability and biocompatibility *in vitro* and *in vivo*, outperforming commercial luminol in imaging inflamed tissue.

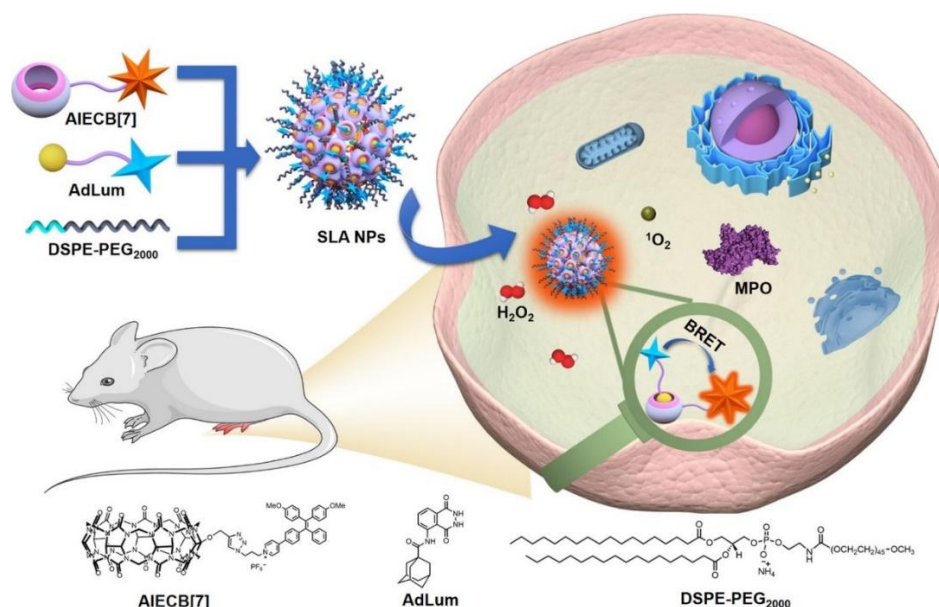


Fig 3.35: Scheme of the designed SLA NPs and their activation mechanism during *in vitro* and *in vivo* inflammation imaging, as demonstrated by Wang. Adapted from ²²⁰ © American Chemical Society

3.4.7.5. Alleviating and Modulating Side Effects of Drug Administration with Cucurbiturils

Beyond their roles in drug delivery and imaging, cucurbiturils, especially CB7 and CB8 and their derivatives, offer remarkable potential for modulating drug activity and mitigating adverse side effects through encapsulation of active pharmaceutical ingredients.²²¹⁻²²³

One powerful example comes from the Isaacs group, who investigated CB8 and its tetramethylated analogue Me₄CB8 for their ability to bind a range of drugs of abuse (**Fig. 3.36**).²²⁴ Using a combination of ¹H NMR spectroscopy and isothermal titration calorimetry (ITC) in phosphate-buffered water, they demonstrated nanomolar binding affinities to structural motifs present in compounds such as phencyclidine (PCP), ketamine and morphine. In particular, both CB8 and Me₄CB8 were shown to encapsulate the 1-amino-1-aryl-cyclohexane ring (found in anesthetics like ketamine and PCP) and the morphinan scaffold (present in opioids like morphine) with high affinity. *In vivo* experiments in mice revealed that Me₄CB8 could successfully reverse hyperlocomotion induced by PCP, whether administered before or after drug exposure, and exhibited good tolerability, highlighting its therapeutic promise in drug overdose interventions.

A further notable application involves the reversal of neuromuscular blocking agents (NMBAs), essential drugs in surgical anesthesia. Conventional NMBA reversal agents used to speed up the patient's recovery after the surgical process may carry cardiovascular risks, spurring the search for safer alternatives. Isaacs and co-workers showed that acyclic CB_n-type molecular containers exhibit exceptionally high binding affinities toward widely used NMBAs like vecuronium and pancuronium.²²⁵ In preclinical studies using NMBA-dosed rats, CB-based agents effectively reversed muscle paralysis without the cardiovascular complications associated with traditional treatments. These findings position cucurbiturils as viable supramolecular reversal agents, potentially rivaling commercial supramolecular

options such as the cyclodextrin derivative sugammadex, and paving the way for safer anesthetic protocols.

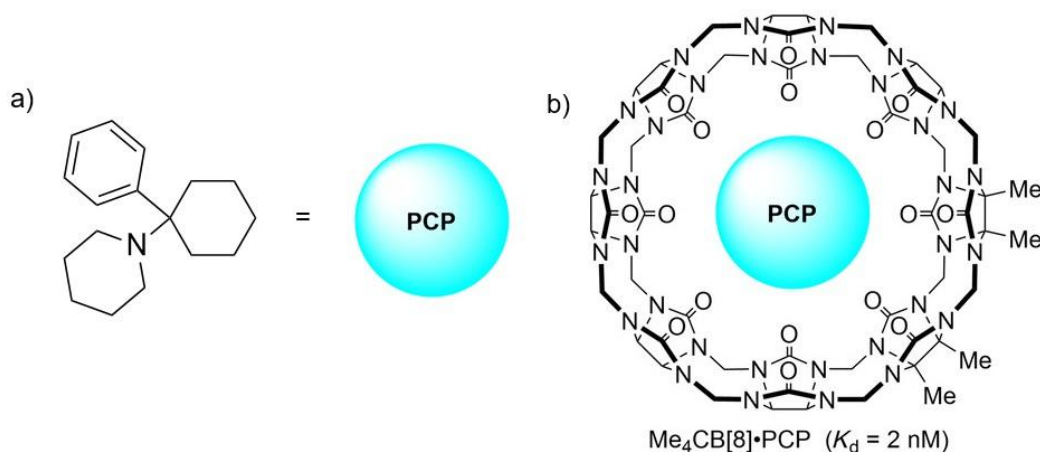


Fig. 3.36: a) Molecular structure of phencyclidine (PCP). b) Structure of the Me₄CB[8]•PCP complex reported by Isaacs. Reprinted with permission from ref ²²⁴ © Wiley VCH

3.4.7.6. Biosensors Based on Cucurbiturils

At the heart of this thesis lies the development and application of cucurbit[*n*]uril-based biosensors, a field that leverages the exceptional host-guest recognition properties of these macrocycles to monitor biological and chemical processes with high precision. The unique features of CB*n*, including ultrahigh binding affinities, rapid complexation kinetics, and excellent biocompatibility, make them ideal candidates for developing biosensors in complex biological environments.^{30, 31} CB*n*-based chemosensors offer a number of important advantages over conventional analytical methods. The continuous monitoring of biophysical or enzymatic processes enables the collection of real-time kinetic data, while their low-cost assay design only requires small sample volumes and readily accessible host and dye molecules.^{30, 136, 137, 158, 226} CB-based assays are compatible with standard laboratory instrumentation such as fluorimeters and UV-VIS spectrometers. In the following, some interesting sensitive and selective examples of CB*n*-based biosensors will be presented.

Unmodified CB7 has regularly been used for biosensing, most notably through IDAs, where a fluorescent reporter dye is non-covalently encapsulated within the CB cavity and displaced by the analyte of interest.^{29, 34, 43, 45, 158} This convenient, label-free method has been applied to real-time enzymatic activity monitoring, such as in supramolecular tandem assays combining CBs and calixarenes to follow amino acid decarboxylase reactions.²¹¹ This approach offers an alternative to conventional methods involving antibodies, radioactive tracers, or covalently labeled substrates.^{227, 228}

To expand the utility of CB7 in fluorescence-based biosensing, several research groups have developed covalently modified CB7 conjugates with integrated fluorophores.²¹⁵ For instance, the Nau group engineered a carboxyfluorescein-functionalized CB7 capable of forming a FRET pair with DAPI, a DNA-binding dye (**Fig 3.37**).²²⁹ The resulting host-guest FRET system enabled dual-emission

fluorescence sensing for DNA quantification, offering excellent linearity and sensitivity, potentially rivaling established real-time PCR techniques.²³⁰

A key challenge in supramolecular sensing is maintaining supramolecular sensor integrity in biological or saline environments, where non-covalent CB•dye assemblies often disassemble.^{30, 31} To address this, Hu developed covalent CB7-berberine conjugates using ethylene glycol linkers to ensure solubility in water and allowing for the self-encapsulation of the indicator dye in the host cavity.²³¹ These conjugates displayed superior stability in buffer and high salt concentrations, retaining strong fluorescence changes even in physiologically relevant media. The platform enabled selective sensing of amantadine, a drug commonly used in Parkinson's and Alzheimer's treatment, and clearly outperformed its non-covalent counterpart.

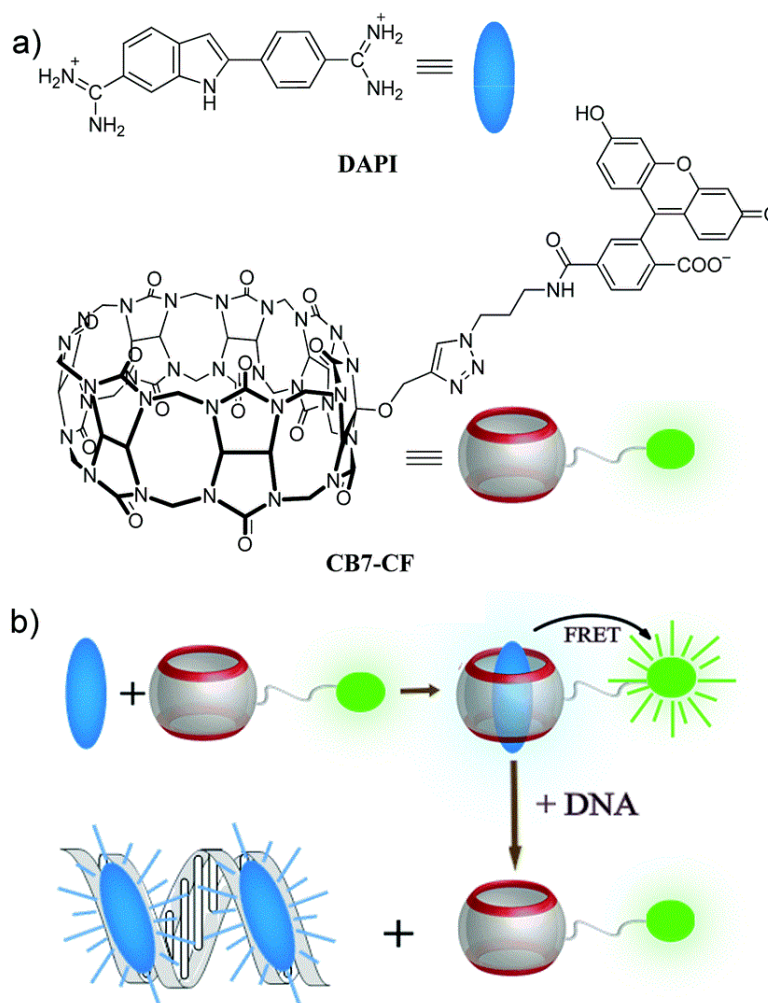


Fig. 3.37: a) Molecular structures of DAPI, the guest and donor of the FRET pair with carboxyfluorescein-labelled CB7 (CB7-CF). b) Schematic illustration of a DNA chemosensing ensemble based on FRET between DAPI and CB7-CF. Reprinted with permission from ref ²²⁹ © American Chemical Society

Building on this concept, our group also introduced an salt-adaptive CB7-nitrobenzoxadiazole (CB7-NBD) conjugate capable of analyte discrimination *via* salt induced fluorescence modulation (**Fig. 3.36**).²³² This system could be used to differentiate among 14 biorelevant analytes through stepwise

salt additions, highlighting a strategy for differential sensing with minimal synthetic effort. Moreover, structural analysis revealed an unusual ternary complex geometry, similar to CB8 complexes, further expanding the mechanistic understanding of CB sensing.

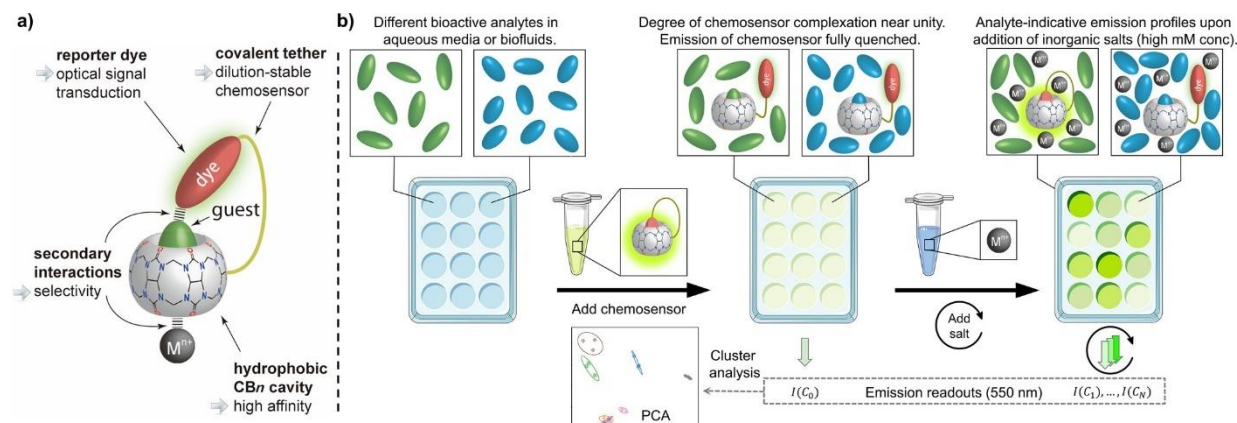


Fig. 3.38: a) Schematic representation of CB7-NBD salt-induced adaptive binding mechanism. b) Principle of the salt-addition workflow enabling the distinction of biorelevant analytes using the CB7-NBD salt adaptive assay. Reprinted with permission from ref ²³² © American Chemical Society

Beyond fluorescence, CBs have also been incorporated into surface-enhanced Raman spectroscopy (SERS) platforms. The Lee group reported SERS biosensors based on CB-mediated hierarchical nanoparticle assemblies, with potential applications in biosensing, environmental analysis, and the emerging field of wastewater-based epidemiology, particularly for detecting pollutants, pharmaceuticals, and pathogens.²³³

To diversify CB sensing platforms even further, Kumar introduced a chemiluminescence-based detection system.²³⁴ Chemiluminescence-based methods are valued for their high signal-to-noise ratios and compatibility with commercial immunoassay reagents and are widely used for chemosensors.²³⁵⁻²³⁸ The use of CB8 with a phenoxy 1,2-dioxetane dye enabled the low-micromolar detection of drugs in human urine and human serum samples. The simple addition of an equimolar amount of CB8 to commercially available dioxetane used in standard enzymatic chemiluminescent immunoassays resulted in a 15-fold signal enhancement. The assay was successfully applied for the detection of paraquat, a toxic herbicide.²³⁹

As another alternative from optical methods, our group demonstrated a CB7-based electrochemical biosensor capable of detecting pancuronium bromide, a NMBA, in buffer and human urine (**Fig. 3.39**).²⁴⁰ This competitive binding assay employed an electrochemically active Pt(II) complex as a displacement reporter and required no surface modification of the electrode.^{241, 242} The sensor was fully compatible with commercially available screen-printed electrodes, supporting its use in portable and point-of-care diagnostics.

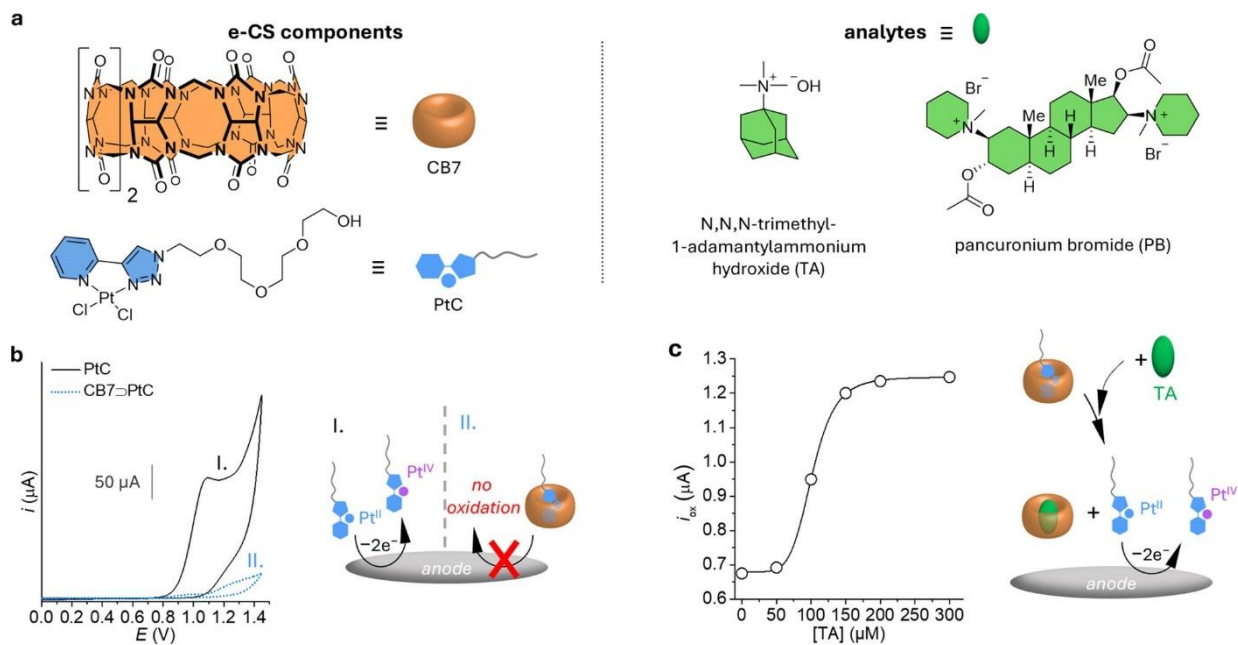


Fig. 3.39: a) Chemical structures of the host (CB7), the indicator (guest, Pt(II) compound) and the analytes. b) CV studies of PtC and CB7•PtC in water. c) TA-dependent I obtained from CV experiments in water. Reprinted with permission from ref²⁴⁰ © American Chemical Society

4. Aim of this Thesis

Molecular diagnostics is a rapidly evolving field that demands sensitive, selective, and robust analytical tools capable of detecting small molecules, metabolites, and disease-related biomarkers in complex biological environments. These tools should ideally function under physiologically relevant conditions and be able to distinguish specific analytes even in the presence of high salt concentrations and structurally similar interferents. While antibody-based detection systems remain a standard in many assays, they are limited by high production costs, stability issues, and long development timelines. In contrast, artificial chemosensors based on supramolecular host-guest recognition offer attractive advantages in terms of stability, versatility, modularity, and easy of production.

Among the most promising scaffolds for such chemosensors are cucurbit[*n*]urils (CB*n*), a class of macrocyclic hosts known for their high binding affinities, selectivity for cationic guests, and tunable chemical functionality. CB7, in particular, has gained significant attention due to its good water solubility and compatibility with physiological environments. However, the broad guest scope of CB7 can also pose a challenge to selectivity. Covalent conjugation of CB7 to optical or electrochemical reporter units presents an effective strategy to improve assay stability and enables tailored sensing properties through structural modifications. This thesis focuses on the design, synthesis, and analytical evaluation of two new CB7-based chemosensor platforms, each targeting different challenges in supramolecular sensing.

The first project centers on the development of a unimolecular chemosensor based on CB7 covalently linked to the well-established electrochemiluminescent dye [Ru(bpy)₃]²⁺. The goal was to create a system that not only maintains the optical and electrochemical properties of the Ru center but also takes advantage of the unique supramolecular interactions at the CB7 portals. The anticipated benefits included enhanced ECL signal output through co-reactant preorganization, dual-mode responsiveness (photoluminescence and ECL), and potential for analyte detection in aqueous and bioanalytical contexts. The CB7 unit provides an opportunity for bio-targeting *via* known high-affinity binders such as adamantane-derivatives, which may also allow selective delivery of the photosensitizer to biological targets.

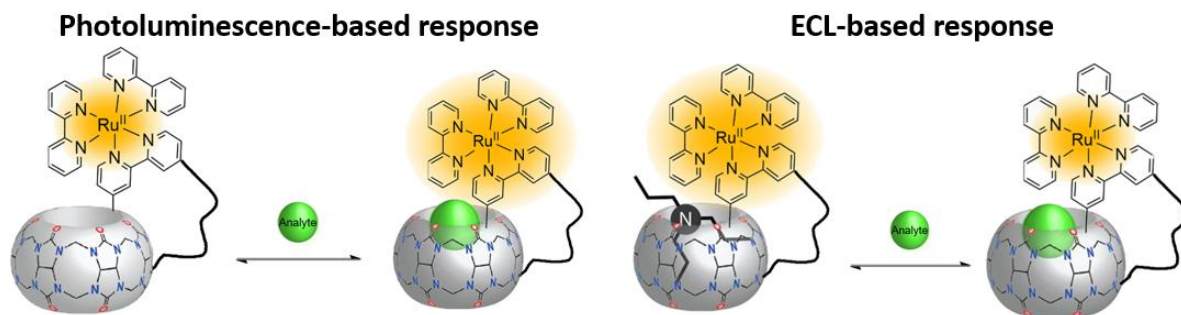


Fig. 4.1: Mechanistic hypothesis of CB7-Ru in a photoluminescent- and ECL-based assay upon analyte binding.

The second project expands the sensing dimension by exploring a family of CB7-coumarin conjugates designed for multivariate discrimination of structurally related small-molecule analytes. Coumarins are well-suited for this purpose due to their tunable photophysical properties and environmental sensitivity, particularly to pH changes. Building on earlier work in the group, the aim was to systematically investigate the influence of pH and ionic strength on a panel of structurally diverse CB7-coumarin conjugates. Structural tuning was achieved through variation in linker length, introduction of additional binding motifs (*e.g.*, hydroxy groups), and substitution patterns on the coumarin moiety.

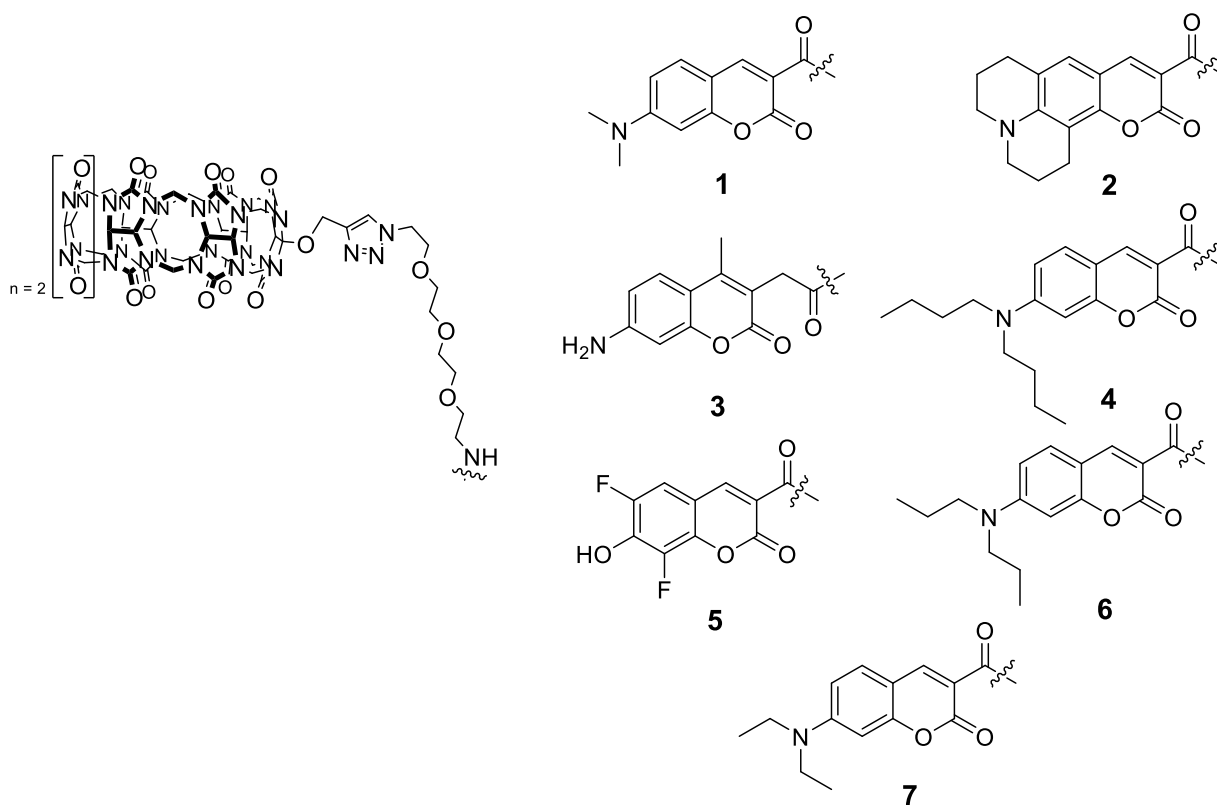


Fig. 4.2: Overview of the planned CB7-coumarin chemosensors.

In summary, the overarching aim of this thesis is to explore the potential of CB7-dye conjugates as versatile chemosensors for biomedical applications. By integrating covalent design strategies, photophysical and electrochemical readouts, and multivariate sensing logic, this work contributes to the development of next-generation supramolecular sensors.

5. Design and Development of a CB7-RuBiPy Conjugate as an Electrochemiluminescent Chemosensor for Biorelevant Analyte Detection

5.1. Fundamentals of Electrochemiluminescence

5.1.1. The Central Role of Tris(2,2'-bipyridyl)ruthenium(II) in Modern Sensing Applications

Electrochemiluminescence (ECL) has emerged as a cornerstone technique in analytical chemistry and biomedical diagnostics, offering exceptional sensitivity, tunable emission control and minimal background interference.²⁴³ Defined as the generation of light through electron transfer reactions occurring at the electrode-electrolyte interface, ECL distinguishes itself from other luminescence phenomena such as photoluminescence, what is driven by photon absorption. In contrast, chemiluminescence is purely arising from chemical reactions and electroluminescence, resulting from direct electrical excitation.²⁴⁴⁻²⁴⁶ The spatial and temporal precision offered by ECL, combined with its compatibility with small sample volumes and readily available instrumentation, has pushed it to one of the leading biosensing technologies.

At the heart of ECL systems is the luminophore. Among all reported ECL luminophores, ranging from organic molecules, metal complexes and nanomaterials, Tris(2,2'-bipyridyl)ruthenium(II), or Ru(bpy)₃²⁺, remains the gold-standard in both fundamental research and practical applications.²⁴⁷ Its remarkable photophysical properties, including high photostability and reversible redox behavior, all contributed to its central position. In particular, the discovery of the Ru(bpy)₃²⁺/tri-*n*-propylamine (TPrA) co-reactant system in the 1990s revolutionized ECL, allowing for efficient and robust signal generation under physiological conditions in aqueous media. This progress significantly broadened the utility of ECL in bioanalytical chemistry, especially in immunoassays and nucleic acid detection.²⁴⁴⁻²⁴⁶

Ru(bpy)₃²⁺-based systems are typically employed in two main formats: homogeneous, where the luminophore is freely diffusing in solution, and heterogeneous, where it is immobilized on a solid substrate such as electrodes, nanoparticles, or within polymer matrices. Homogenous systems offer valuable insights into mechanistic aspects and are commonly used for screening new co-reactants or luminophore derivatives. In contrast, heterogeneous systems are more suited for applied sensing and imaging applications due to their reusability, stability, and ease of integration into diagnostic platforms.²⁴⁴⁻²⁴⁶ Moreover, Ru(bpy)₃²⁺ offers chemical versatility. The bipyridine ligands can readily be functionalized with reactive groups (e.g., NHS-esters) to enable covalent conjugation to biomolecules such as DNA, proteins or antibodies.²⁴⁸ These functionalized complexes have become indispensable in modern bioassays, serving as stable luminescent labels with high signal-to-noise ratios.²⁴⁹

5.1.2. Instrumentation Essentials for Electrochemiluminescence-Based Sensing

Although commercial electrochemiluminescence (ECL) instruments, ranging from benchtop to portable formats, have been available for quite some time, a significant amount of ECL experiments reported in the literature are still carried out using custom-built setups. This is largely due to the simplicity and

flexibility of ECL instrumentation.^{250, 251} A schematic illustration of a basic ECL instrument is shown below (**Fig 5.1**). At its core, a typical ECL instrument comprises only two main components. On the one hand, an electrochemical setup, responsible for delivering electrical stimulation to the electrochemical cell. On the other hand, an optical detection system, necessary to measure the light emitted during the ECL process, usually a photomultiplier tube (PMT). Additionally, alternative detectors such as charge-coupled devices (CCDs) or photodiodes can also be employed. Notably, CCD cameras offer several advantages over conventional PMTs, allowing real-time imaging, higher spatial resolution, and the capability for multichannel detection, making them extraordinarily useful for ECL imaging applications.^{252, 253} The general instrumentation setup typically involves a potentiostat, together with a light detector connected to the data acquisition system. These components are located in a light-tight enclosure containing a transparent electrochemical cell, often made out of glass. To record ECL spectra, two main approaches are used. Either by the integration of a monochromator between the detector and the light source, or by coupling the potentiostat with a fluorescence spectrometer, combining a three-electrode setup within the measurement cuvette.²⁵⁴ In standard ECL experiments, both the light emission and the corresponding current are recorded simultaneously. Common working electrodes include glassy carbon, graphite carbon paste, and noble metals such as gold and platinum. Accurate positioning of the light detector relative to the working electrode is essential for signal optimization and depends on the geometry parameters and size of the electrode.

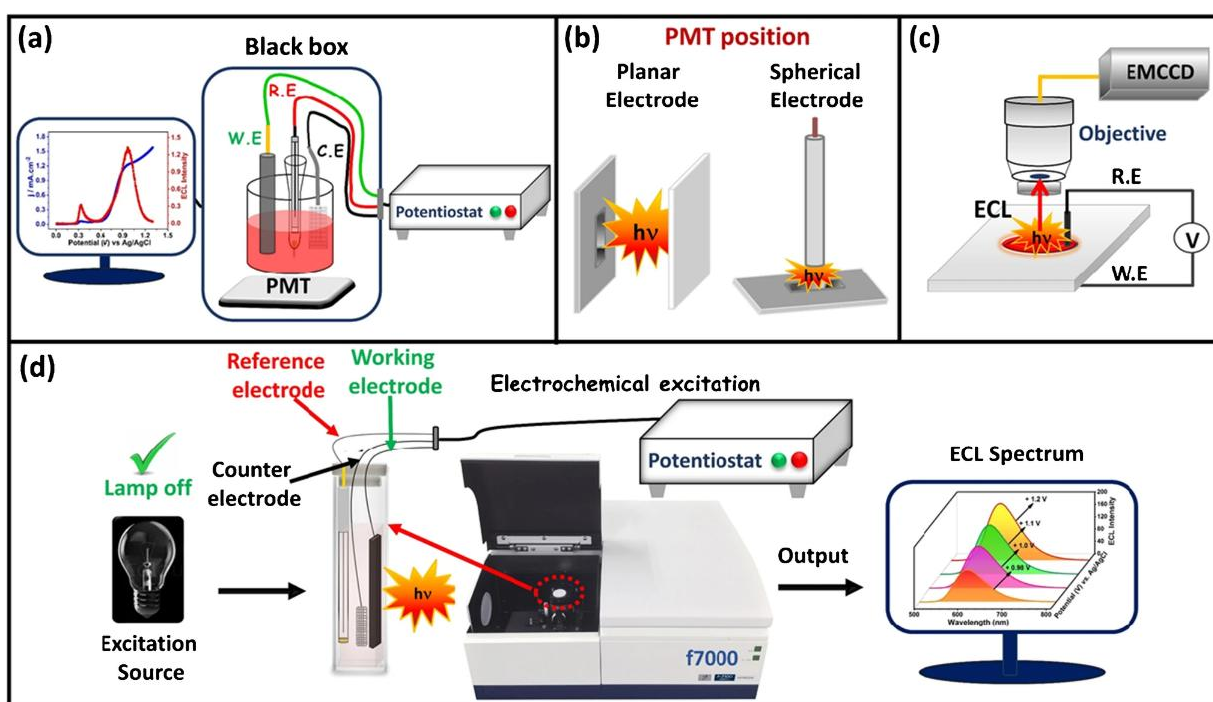


Fig. 5.1: a) Basic ECL setup with a data acquisition system and a three-electrode setup, b) positioning of the PMT for different shaped electrodes, c) experimental setup with a CCD camera for ECL imaging, and d) *in situ* ECL spectra measurement setup. Reprinted with permission from ref ²⁵⁵ © Springer Nature

5.1.3. Photophysical characteristics of Tris(2,2'-bipyridyl)ruthenium(II)

The photophysical behavior of $[\text{Ru}(\text{bpy})_3]^{2+}$ has been extensively studied due to its exceptional luminescent properties, making it a benchmark luminophore in ECL research. Below the UV-visible absorption and the fluorescence emission spectra of $[\text{Ru}(\text{bpy})_3]^{2+} \cdot \text{Cl}_2 \times 6 \text{ H}_2\text{O}$ in aqueous solution is shown. The $[\text{Ru}(\text{bpy})_3]^{2+}$ is a classical octahedral d^6 transition metal complex, with Ru^{2+} adopting a $[\text{Kr}]4d^6$ electron configuration. Within this complex, the six 4d electrons occupy the low-energy, nonbonding t_{2g} orbitals, while the ligand system contributes 12 σ - and 36 π -electrons. These electrons populate the $t_{2g}(\pi)$ molecular orbitals, establishing the ground-state configuration. The absorption spectrum of $[\text{Ru}(\text{bpy})_3]^{2+}$ shows distinct bands corresponding to different electronic transitions. A strong ultraviolet band at 285 nm is attributed to the spin-allowed intraligand (IL) $\pi_L \rightarrow \pi_L^*$ transitions localized on the bipyridine ligands. An intense visible band at 450 nm arises from a spin-allowed metal-ligand charge transfer (MLCT) $d_M \rightarrow \pi_L^*$ transition, specifically a $d_M(\text{Ru}) \rightarrow \pi^*(\text{bpy})$ transition. This MLCT process is central to the compounds ECL and photoluminescence properties. Upon excitation of the MLCT band, $[\text{Ru}(\text{bpy})_3]^{2+}$ undergoes photoluminescence, emitting light with a maximum at around $\lambda_{\text{max}} = 610 \text{ nm}$, corresponding to a transition energy of approximately 2.03 eV. The photophysical relaxation pathway proceeds from the initially excited singlet MLCT ($^1\text{MLCT}$) state, which rapidly undergoes intersystem crossing to a vibronically excited triplet MLCT ($^3\text{MLCT}$) state at 3.1 eV. This excited state then relaxes to a thermally equilibrated $^3\text{MLCT}$ at $\sim 2.21 \text{ eV}$ via vibrational relaxation. These favorable photophysical characteristics, including strong MLCT absorption and long-lived excited states, are the reason for the attractiveness of $[\text{Ru}(\text{bpy})_3]^{2+}$ for use in ECL-based sensing systems.^{256, 257}

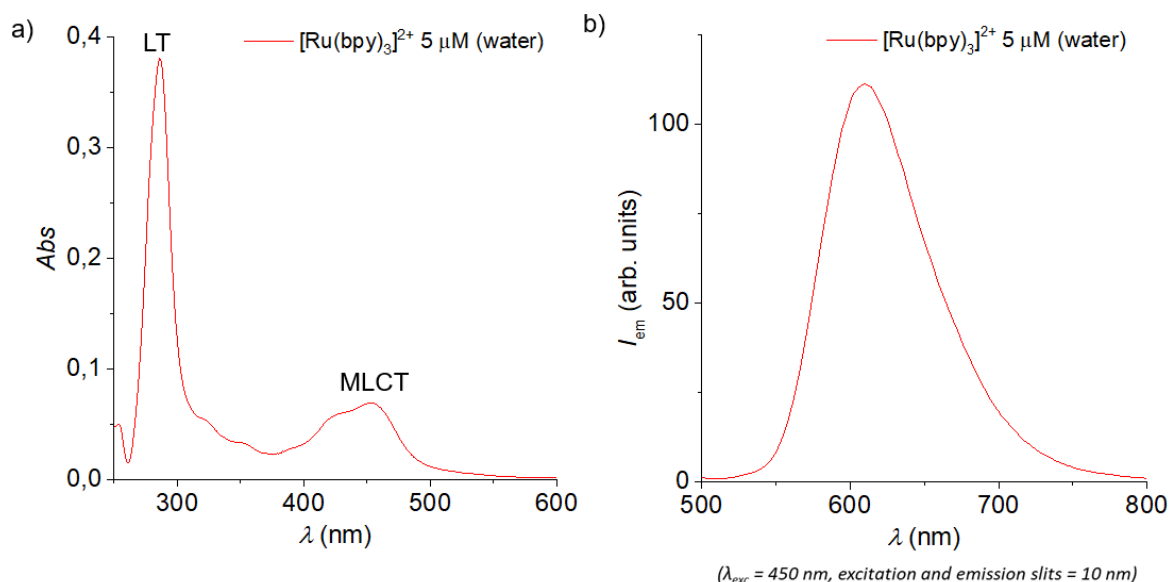


Fig. 5.2: a) UV-Vis spectrum of $[\text{Ru}(\text{bpy})_3]^{2+} \cdot \text{Cl}_2 \times 6$ with the ligand transition (LT) and the metal-ligand charge transfer (MLCT) band highlighted. b) shows the fluorescence spectrum of $[\text{Ru}(\text{bpy})_3]^{2+} \cdot \text{Cl}_2 \times 6 \text{ H}_2\text{O}$ at $\lambda_{\text{exc}} = 450 \text{ nm}$. Both spectra were recorded at a concentration of $5 \mu\text{M}$ in water.

5.1.4. Mechanistic Pathways of Electrochemiluminescence: From Electron Transfer to Light Emission

5.1.4.1. Ion Annihilation Pathway

In the classical annihilation pathway of ECL, both oxidized and reduced species of the luminophore are generated electrochemically at the electrode surface through a potential step or sweep. These reactive intermediates subsequently undergo electron transfer reactions in solution, leading to the formation of both the ground state and electronically excited species. The excited species then relaxes to the ground state by emission of a photon, giving rise to the observed luminescence. This process is generally described by the following sequence of reactions, in which the excited singlet $^1A^*$ and triplet $^3A^*$ correspond to the previously discussed 1MLCT and 3MLCT in systems such as $[Ru(bpy)_3]^{2+}$.²⁵⁵



or

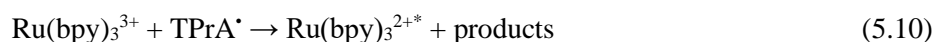


In systems where the energy available from the annihilation reaction is sufficiently high, the excited singlet state can be generated directly, as shown in eq. 5.1-5.3. This mechanistic route is often referred to as the singlet route, also called the “S-route”, and is characteristic of many aromatic luminophores.²⁵⁸ In contrast, in systems where the annihilation energy is insufficient to access the singlet excited state directly, the excited triplet state $^3A^*$ will first be produced. This triplet state can subsequently undergo a bimolecular annihilation reaction (triplet-triplet-annihilation), to form the higher-energy singlet state, from which emission occurs. This pathway is referred to as the triplet pathway, or “T-route”, as shown in eq. 5.4-5.6. A typical example of this mechanism is the well-studied DPA/TMPD system (DPA=9,10-diphenylanthracene and TMPD=*N,N,N',N'*-tetramethyl-*p*-phenylenediamine), which undergo triplet-triplet annihilation to yield intense luminescence.^{259, 260} Although the annihilation mechanism played a foundational role in early ECL research, its practical application is limited due to several stringent experimental requirements. These include the need for larger potential windows to

generate both stable anionic and cationic radical species, strictly deoxygenated environments to prevent quenching of radical species, and often the use of organic solvents or electrolytes to ensure the stability of the intermediates. These limitations have spurred interest in finding alternative pathways, most notably the co-reactant ECL mechanism, which offers milder operational conditions and greater compatibility with aqueous and biological systems. This approach has become dominant in contemporary ECL-based sensing and diagnostic applications.²⁶¹

5.1.4.2. Co-reactant Pathway

Beyond the classical ion annihilation mechanism, ECL can also be generated *via* co-reactant pathways, which have become the dominant strategy for practical applications, especially in aqueous media and biological systems.^{244, 245, 261, 262} In these systems, ECL is typically induced by unidirectional potential scanning in the presence of both the luminophore (Ru(bpy)₃²⁺) and a suitable co-reactant. The co-reactant undergoes electrochemical activation to generate a reactive intermediate that participates in electron-transfer reactions, ultimately leading to an excited-state luminophore and light emission. Historically, the first reported co-reactant was the oxalate ion (C₂O₄²⁻).²⁶³ Notably, the oxidation of oxalate leads to the generation of a strong reductant CO₂^{•-}, instead of an oxidant, what is the reason for the name “oxidation-reduction” ECL. A widely studied and commercially implemented example is the Ru(bpy)₃²⁺/TPrA (tri-*n*-propylamine) system, which is the basis of many modern ECL immunoassays and DNA diagnostics.^{264, 265} Over time, four mechanistic routes have been proposed to explain the ECL behavior in this system.²⁶⁶ In the first, referred to as dual oxidation pathway, both Ru(bpy)₃²⁺ and TPrA are oxidized at the electrode surface. The oxidized luminophore Ru(bpy)₃³⁺ is then reduced by the TPrA[•] radical to yield the excited state.



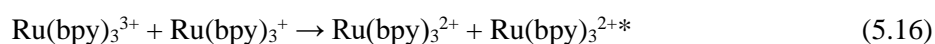
In the second possible mechanism, called the disproportionation route, Ru(bpy)₃²⁺ is reduced by TPrA[•], and the resulting Ru(bpy)₃⁺ reacts directly with Ru(bpy)₃³⁺ to form the excited state and then emit light.²⁶⁰ The third mechanism involves only Ru(bpy)₃³⁺ being generated at the electrode surface, while TPrA is only oxidized chemically in solution by the generated Ru(bpy)₃³⁺.²⁶⁰ This pathway only becomes

relevant at higher luminophore concentrations. The fourth process occurs with the direct oxidation of TPrA at the electrode surface to form $\text{TPrA}^{\bullet+}$ and TPrA^{\bullet} .²⁶⁰ The subsequent reaction between TPrA^{\bullet} and $\text{Ru}(\text{bpy})_3^{2+}$ generates $\text{Ru}(\text{bpy})_3^+$, which then reacts with $\text{TPrA}^{\bullet+}$ to form the excited state $\text{Ru}(\text{bpy})_3^{2+*}$, following by light emission. Among these, the fourth route is particularly advantageous, as it requires only a modest oxidation potential sufficient to oxidize TPrA, leaving $\text{Ru}(\text{bpy})_3^{2+}$ unchanged until secondary chemical steps occur.

The efficiency of the $\text{Ru}(\text{bpy})_3^{2+}/\text{TPrA}$ system is highly pH-dependent, with maximum ECL intensity typically observed near physiological pH (~7.5), making the system very attractive for biological applications.²⁴⁵ Several other strategies have been utilized to further enhance ECL intensity. Addition of surfactants can lead to significant enhancement in ECL efficiency.^{267, 268} For example, up to 8-fold increase in ECL efficiency can be observed in nonionic surfactant media, what probably attributed to the increased hydrophobicity of the electrode surface caused by adsorption of surfactant on the electrode surface, what facilitates the direct oxidation of TPrA. The same findings can also be done by the addition of nonionic fluorosurfactants and ionic surfactants, while the observed ECL intensity is even increased by 50-fold and 30-fold, respectively.^{269, 270} Surfactant addition can also help to reduce the oxidation potential, offering milder conditions for sensitive systems. Notably, in order to effectively act as promoters of the ECL reaction, the concentration of these surfactants must be carefully controlled, in order to avoid micelle-formation and association with metal complexes. Another common approach to dramatically increase ECL efficiency is to increase the polarity of the solvent. Hydroxylic solvents, especially fluorinated alcohols, have a profound effect on the system.²⁷¹ Hydrogen bonding and dipole forces dramatically affect the ground- and excited state properties in $\text{Ru}(\text{bpy})_3^{2+}$, resulting in greater electrochemical potential separation ($\Delta E_{1/2}$), and shifts in UV-Vis absorption, photoluminescence, and ECL bands. With decreasing polarity of the solvent, the $\Delta E_{1/2}$ and the ECL emission increases. Outstanding increases in ECL efficiency of up to 270-fold were observed in mixed alcohol/water solutions compared to water, representing the most effective way to enhance $\text{Ru}(\text{bpy})_3^{2+}$ ECL.²⁶¹

Despite its success, the $\text{Ru}(\text{bpy})_3^{2+}/\text{TPrA}$ system has several limitations. TPrA is volatile, toxic, and typically used at high concentrations (usually up to 100 mM) to obtain good sensitivity, which may pose issues for environmentally sensitive or biological applications. As a more environmentally-friendly co-reactant, 2-(dibutylamino)ethanol (DBAE) was recently introduced.²⁷² The $\text{Ru}(\text{bpy})_3^{2+}/\text{DBAE}$ system seems very promising, since it produces stronger ECL signals than TPrA at significantly lower concentrations (~20 mM), offers greater aqueous solubility, and is less toxic and volatile. The presence of the hydroxyl group appears to promote catalytic oxidation at the electrode surface, showing that electron-withdrawing substituents on co-reactants can enhance ECL efficiencies. Further investigations with co-reactants showed that two hydroxy groups enhance the efficiency even more, but surprisingly, two amino groups significantly decreased the efficiency. The diminished performance of diamines is attributed to their increased tendency to side reactions and reduced redox stability.²⁷³

In addition to oxidative-reductive pathways, a second category of co-reactant systems, the reductive-oxidative pathway, has also been established. A classic example is the $\text{Ru}(\text{bpy})_3^{2+}/\text{S}_2\text{O}_8^{2-}$ system, where a strong oxidizing agent ($\text{S}_2\text{O}_8^{2-}$) is reduced at the electrode to generate $\text{SO}_4^{\cdot-}$, which in turn oxidizes $\text{Ru}(\text{bpy})_3^+$ to its excited state.



However, such systems often require very negative potentials, which can lead to hydrogen evolution and electrode instability in aqueous solutions. To ease this, carbon paste or bismuth electrodes are sometimes used.^{274, 275} Together, co-reactant ECL offers a versatile and tunable platform for analytical applications, especially when combined with the robust photophysical properties of $\text{Ru}(\text{bpy})_3^{2+}$.

5.1.5. Established Analytical Applications of Ruthenium-Based Electrochemiluminescence

5.1.5.1. ECL-Based Immunoassays: Principles, Platforms, and Performance

Electrochemiluminescence immunoassays represent one of the most important applications of the $\text{Ru}(\text{bpy})_3^{2+}/\text{TPrA}$ system in clinical diagnostics.^{244, 245, 261, 262, 276} In this context, $\text{Ru}(\text{bpy})_3^{2+}$ derivatives serve as highly effective luminescent labels, offering a wide range of advantages compared to other conventional detection systems. This ECL detection system has many distinct advantages over other diagnostic detection systems. ECL-based detection enables high sensitivity, with reliable quantification at subpicomolar concentrations and a dynamic range spanning more than six orders of magnitude. Due to their low molecular weight and good water solubility, $\text{Ru}(\text{bpy})_3^{2+}$ labels can be conjugated to biomacromolecules such as proteins or oligonucleotides without affecting immunoreactivity, solubility or hybridization capacity. Additionally, ECL immunoassays are compatible with both heterogeneous (separation-based) and homogeneous (non-separation) assay formats, as selective electrode accessibility can be exploited to distinguish between bound and unbound labeled species. The method is adaptable to a broad spectrum of analytes, ranging from small molecules to large biomacromolecules, with minimal sample preparation and straightforward disposal.^{250, 277} Measurements are usually very rapid and

reproducible, and the ECL labels exhibit superior chemical stability compared to conventional chemiluminescent systems – remaining viable for over a year at room temperature, even longer under refrigerated conditions. The overall simplicity of the instrumentation, combined with the method's high throughput capacity, has brought ECL immunoassays to widespread adaption in commercial diagnostic platforms. Today, over 150 ECL-based immunoassays are commercially available, generating substantial global revenues and underscoring the technology's central role in modern bioanalytical science.

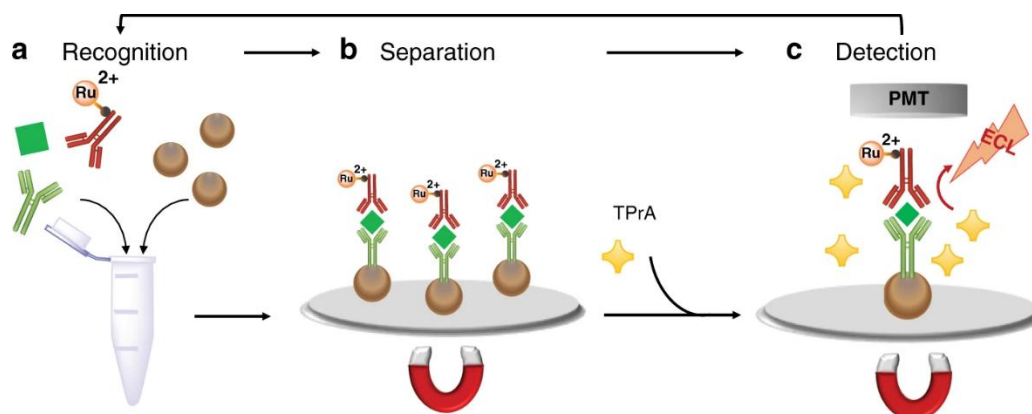


Fig. 5.3: Schematic representation of the commercial ECL sandwich immunoassay. For the recognition **a**, a specific antigen (green square) is mixed together with an antigen-specific biotinylated monoclonal antibody (green) and an antigen-specific monoclonal antibody labelled with $\text{Ru}(\text{bpy})_3^{2+}$ to form a sandwich complex to bind together to streptavidin-coated magnetic microparticles (brown). For the separation **b**, the microparticles are magnetically captured onto the surface of the electrode and unspecific substances are washed away. Then follows the detection **c**, in which a voltage is applied to the electrode resulting in ECL emission, which is measured by a photomultiplier tube. Reprinted with permission from ref ²⁷⁸ © Nature Research

As a subcategory of disease biomarkers, protein biomarkers, have become increasingly central targets in ECL immunoassays.²⁷⁷ These proteins, secreted during the onset or progression of disease, reflect physiological or pathological changes in the body and serve as important and reliable dynamic indicators for clinical diagnosis.²⁷⁹ Protein biomarkers are commonly classified into three categories: enzymes, hormones, and other disease-associated proteins. Among these, clinically relevant examples include carcinoembryonic antigen (CEA), carbohydrate antigens (CA), and prostate-specific antigen (PSA), all of which are widely used in diagnostics of different forms of cancer. Additional proteins such as C-reactive protein (CRP) and lactoferrin serve as biomarkers for inflammatory or infectious diseases.²⁷⁷

Carbohydrate antigens, originally identified via monoclonal antibody technologies from tumor cell lines, exhibit high diagnostic specificity for certain malignancies. Of these CA125 is a primary biomarker for epithelial ovarian and endometrial cancers. Other CAs are employed in the diagnosis of breast and pancreatic cancers.²⁷⁹⁻²⁸¹ Numerous ECL immunosensors have been developed for the sensitive detection of CA antigens. For instance, a sandwich-type ECL immunosensor has been reported for CA125 detection using a nanoporous gold-modified glassy carbon electrode (GCE). In this design, $\text{Ru}(\text{bpy})_3^{2+}$ -gold nanoparticles (Ru-AuNP) were assembled with poly(diallyldimethylammonium chloride) (PDDA)-

functionalized graphene nanosheets and served as the ECL label. The resulting system achieved a wide linear response range with a detection limit of 0.005 U/mL.²⁸⁰

With the global rise in aging-related diseases such as cardiovascular disorders and neurodegenerative conditions, there is an increasing demand for highly sensitive and specific ECL platforms tailored for the detection of diverse biomarkers. To this end, different strategies have been employed to improve ECL assay sensitivity and extend application of ECL-based immunoassays. For example, a highly sensitive sandwich-type immunoassay for CRP was developed by entrapping of a hydrophobic ruthenium derivative on polystyrene beads, enabling single-antibody labelling. Remarkably, the Ru(bpy)₃²⁺ loading capacity reached up to 10⁹ per bead, providing substantial signal amplification and achieving a detection limit as low as 0.01 µg/mL, surpassing most conventional high-sensitivity CRP assays.²⁸² Generally, holding multiple labels in a larger container is a common approach to increase sensitivity. The Bard group demonstrated that Ru(bpy)₃²⁺ can be effectively incorporated into liposomal carriers and released upon the addition of 0.1 M TPrA in buffered solution containing NaCl and Triton X-100.²⁸³ This concept has also been successfully extended to the detection of hemagglutinin, a surface glycoprotein essential for influenza virus infectivity.²⁸⁴

Beyond soluble biomarkers, ECL has also found application in the detection of cell surface proteins on live suspension cells.²⁸⁵ In this format, carbon-based electrodes integrated into the base of microwell plates enable immobilization of cells without centrifugation, allowing for direct washing and detection. Compared to conventional approaches such as flow cytometry or ELISA, ECL-based assays offer superior ease of handling, enhanced signal-to-noise ratios, and simplified workflows, highlighting their potential as powerful tools for high-throughput cellular diagnostics.

5.1.5.2. Illuminating the Genome: ECL-Based Strategies for DNA Sensing

DNA probe-based assays have become indispensable tools across a broad spectrum of disciplines, including clinical diagnostics, forensic science, environmental analysis, pharmaceutical development, and the detection of biological warfare agents.^{276, 286} ECL has emerged as a particularly powerful technique in this domain, owing to its exceptional sensitivity, wide dynamic range and compatibility with aqueous media. Analogous to ECL immunoassays, ECL-based DNA detection platforms frequently employ Ru(bpy)₃²⁺ as the luminophore and TPrA as the co-reactant. Numerous strategies have been developed to further enhance the sensitivity and specificity of ECL DNA sensing. These include the use of high-efficiency labels, multilabelling strategies, and signal amplification approaches. Importantly, the molecular recognition in ECL genosensors is mediated by highly specific Watson-Crick base pairing, enabling the precise detection of DNA, RNA and microRNA targets. This inherent specificity makes ECL genosensors well-suited for applications in clinical diagnostics, environmental surveillance, food safety monitoring, and biomedical research.^{244, 245, 253, 261}

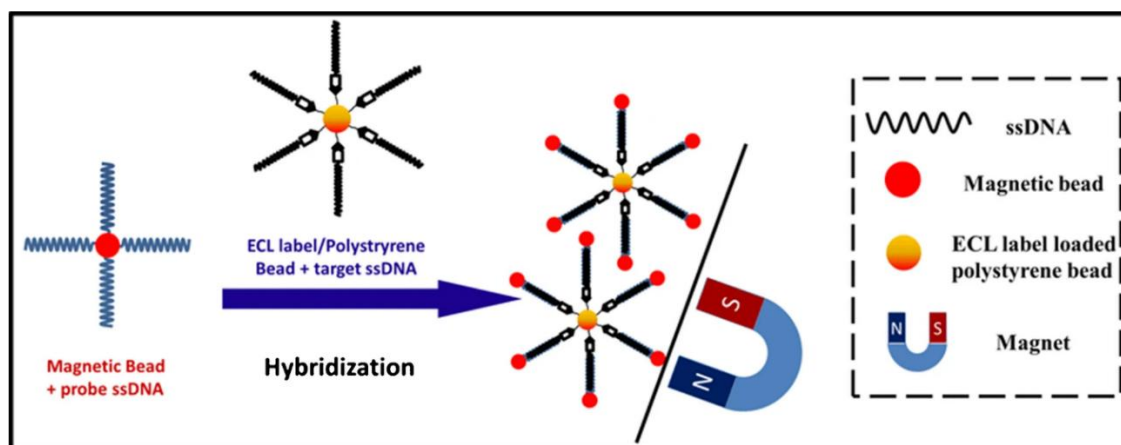


Fig. 5.4: Schematic representation of DNA hybridization on a polystyrene bead as the ECL label carrier and a magnetic bead for the separation of ECL label/polystyrene beads after hybridization with the analyte. Reprinted with permission from ²⁵⁵ © Nature Research

One noteworthy example involves an ultrasensitive ECL method utilizing polystyrene microbeads loaded with hydrophobic ECL labels of $\text{Ru}(\text{bpy})_3[\text{B}(\text{C}_6\text{F}_5)_4]$.²⁸⁶ These microbeads serve to amplify the ECL signal upon DNA hybridization. Another elegant system was introduced by the Zhang group and employs a highly selective hairpin-structured DNA probe labelled with ruthenium bis(2,2'-bipyridine)(2,2'-bipyridine-4,4'-dicarboxylic acid)-*N*-hydroxysuccinimide ester ($[\text{Ru}(\text{bpy})_2(\text{dcbpy})\text{NHS}]$) as the ECL active species.²⁸⁷ In the absence of target ssDNA, the folded hairpin configuration brings the luminophore close to the electrode, generating a strong ECL signal. Hybridization with target ssDNA unfolds the hairpin structure into a linear duplex, displacing the Ru-tag from the electrode surface, resulting in a measurable decrease in ECL intensity. Sensitivity and selectivity can be tuned by modifying the loop length of the probe, even allowing for the discrimination of single-nucleotide mismatches.

Recently, ECL-inducible DNA intercalators such as doxorubicin, daunorubicin and 2-phenylindole have been integrated into hybridization assays.²⁷⁶ These molecules selectively intercalate into dsDNA, enabling ECL emission in the presence of $\text{Ru}(\text{bpy})_3^{2+}$, whereas ssDNA remains inactive. This approach has enabled the sensitive detection of genetic mutations, including single nucleotide polymorphisms associated with hepatitis viruses. Another innovative concept is based on ECL quenching by ferrocene-labelled DNA probes.²⁸⁸ In one approach, a complementary DNA strand functionalized with a ferrocene moiety hybridizes with the target sequence and quenches $\text{Ru}(\text{bpy})_3^{2+}$ emission upon proximity. This method has been further developed into a solid-state platform, using a molecular beacon (MB) strategy.²⁸⁹ Here, $\text{Ru}(\text{bpy})_3^{2+}$ modified gold nanoparticles are immobilized on a cysteamine-functionalized gold electrode, and a ferrocene-labeled DNA MB is self-assembled *via* Au-S chemistry. Hybridization with target DNA or temperature-induced conformational changes alters the MB stem-loop structure, modulating the distance between ferrocene and $\text{Ru}(\text{bpy})_3^{2+}$ and thus the ECL intensity. Such platforms offer promising potential for reagentless DNA sensing and real-time monitoring of hybridization thermodynamics.

Collectively, these examples illustrate the power and versatility of ECL in nucleic acid sensing, offering robust, sensitive, and adaptable strategies for future biosensing technologies.

5.1.5.3. Integrating Aptamer and DNAzyme Technologies in ECL Biosensing

Aptamers are short, single-stranded DNA or RNA oligonucleotides that fold into well-defined three-dimensional structures capable of binding specific targets with high affinity and selectivity.²⁹⁰⁻²⁹³ These targets range from small molecules and proteins to entire cells. Compared to conventional molecular recognition elements such as antibodies, aptamers offer a broad range of advantages, including ease of chemical synthesis, straightforward functionalization, high chemical and thermal stability, and low immunogenicity. Owing to these features, aptamers have found broad application as recognition elements in various analytical platforms, including chromatography, capillary electrophoresis (CE), MS, and a wide range of biosensors such as colorimetric, fluorescent, electrochemical, and ECL-based formats.²⁶¹ The first reports of ECL-based aptamer biosensors appeared in 1999, demonstrating the detection of biological threats such as anthrax spores, cholera toxin, and staphylococcal enterotoxin B.²⁹⁰ Since then, numerous aptamer-based ECL sensing strategies have been developed, primarily using Ru(bpy)₃²⁺ and its derivatives as ECL luminophores, along with TPrA as a co-reactant.

A prominent example is the ECL aptasensor for thrombin detection in a sandwich-type format using AuNPs for signal amplification.²⁹² In this approach, capture aptamers were immobilized on a thiol-silanized indium tin oxide (ITO) electrode *via* Au-S bonds. Upon target binding, Ru(bpy)₃²⁺-labelled signal aptamers were introduced, enabling ECL detection with TPrA as co-reactant. This method achieved a detection limit of 10 nM and demonstrates compatibility with microfabrication, offering high potential for array-based miniaturized platforms.

Another approach utilized a displacement strategy, where a aptamer immobilized on a gold electrode was hybridized with a complementary DNA (cDNA) stand labelled with Ru(bpy)₃²⁺-doped silica nanoparticles (**Fig. 5.5**).²⁹⁴ Binding of thrombin led to displacement of the labelled cDNA, resulting in a decrease in ECL intensity. This method achieved femtomolar detection limits and demonstrated high specificity, with negligible interference from non-target proteins.

Aptamer-based ECL platforms have also proven effective for the detection of small molecules. Zhang and co-workers developed an ECL biosensor for cocaine based on aptamer recognition.²⁹¹ The system utilized a Ru(bpy)₃²⁺-tagged probe immobilized on an Au electrode. Target binding induced a structural rearrangement of the aptamer to a three-way junction, positioning the luminophore closer to the electrode surface and enhancing the ECL response. The method showed a linear response in the nanomolar range, with a detection limit of 1.0×10^{-9} M, demonstrating the potential for small-molecule drug analysis.

Beyond target detection, aptamer-ECL systems have also enabled the analysis of enzymatic processes. A notable example is the application of aptamer-based ECL biosensing to study RNA editing reactions.²⁹³ RNA editing describes the molecular processes in which the information content in an RNA molecule is altered through a chemical change in the base make-up.²⁹⁵ In this assay, a streptavidin-binding aptamer

was activated by conformational change upon RNA editing. The reporter RNA, labelled with a Ru-complex, generated ECL when immobilized at the base of streptavidin-coated microtiter plates with integrated carbon electrodes. This platform allowed sensitive detection of RNA editing products at low femtomole levels and is well-suited for high-throughput screening of RNA-modifying enzymes or drug candidates.

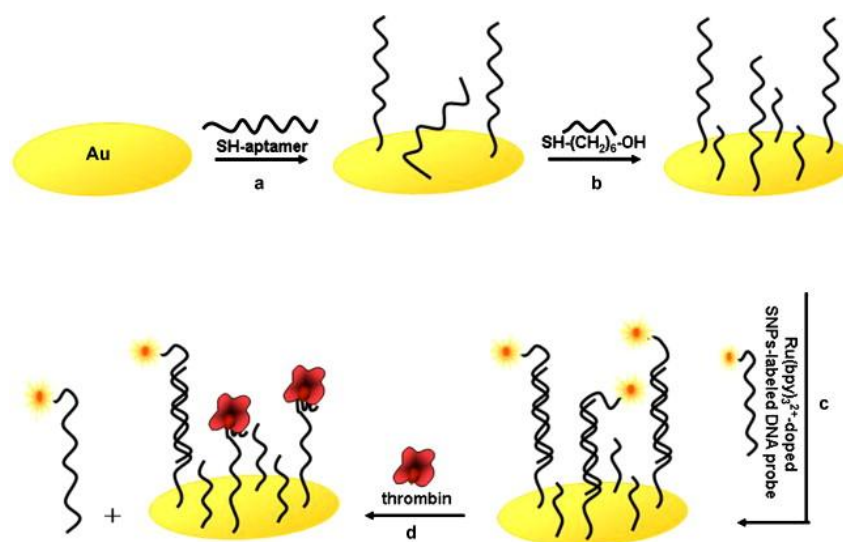


Fig. 5.5: Schematic diagram for the principle of the developed aptasensor for detecting thrombin reported by Fang.²⁹⁴ a) and b) shows the formation of self-assembled monolayers of aptamers on Au electrodes *via* Au-S interactions. c) shows the hybridization of the aptamer with the Ru-labelled sDNA probe, yielding the dsDNA modified electrode. d) shows the target-induced (thrombin) strand displacement, following by ECL detection of the displaced Ru-labelled DNA. Reprinted with permission from ref ²⁹⁴ © Elsevier

5.2. Design and Synthesis of CB7-Ru

Infectious diseases continue to challenge public health systems worldwide, as demonstrated with unprecedented clarity during the COVID-19 pandemic. Despite remarkable progress in diagnostics and therapeutics, the urgent need persists for analytical tools that not only highly sensitive and selective, but also accessible, affordable, and suitable for decentralized or point-of-care testing. In this context, ECL has emerged as a particularly promising technique. Its unique combination of low background noise, excellent sensitivity, wide dynamic range, and simple instrumentation has already led to successful commercialization in high-throughput clinical assays and has positioned ECL as a versatile platform for biosensing applications, as already demonstrated in previous sections.^{244, 245, 253, 261} Traditionally, the Ru(bpy)₃²⁺/TPrA system has been the gold standard in ECL-based diagnostics. The favorable redox properties, high quantum yield, and stability of Ru(bpy)₃²⁺ in aqueous environments make it particularly well-suited for bioanalytical applications. However, current research in the ECL field has increasingly focused on developing alternative luminophores, including inorganic complexes, organometallic species, and new organic molecules with enhanced photophysical features.^{253, 262} These new systems are often integrated into nanostructures, such as silica nanoparticles or cyclodextrins, that offer multifunctionality, improved signal amplification, and specific molecular recognition properties.²⁹⁶⁻³⁰⁰ Despite these

advances, the development of innovative ECL-active constructs remains a critical research priority, especially to overcome the diffusion-limited behavior of conventional solution-phase luminophores.²⁹⁶ Numerous amplification strategies have been investigated, including resonance energy transfer, catalytic cycles, aggregation-induced ECL, and surface immobilization.³⁰¹⁻³⁰³ However, immobilizing hydrophilic ECL luminophores like Ru(bpy)₃²⁺ on electrode surfaces remains technically challenging, often suffering from limited robustness and reproducibility. Consequently, the identification of suitable nanocarriers for stable immobilization is still an unresolved issue. This context motivates the exploration of molecular architectures that combine ECL activity with supramolecular recognition elements to generate next-generation dynamic biosensors.

Concurrently, there is growing interest in the development of sensing systems for small molecules such as cellular metabolites and steroid hormones, analytes that are difficult to detect using traditional antibody-based assays. These approaches are typically expensive, chemically fragile, and limited in scalability.^{304, 305} Therefore, ECL sensors based on reversible, non-covalent interactions offer an attractive alternative for designing label-free or displacement-based detection schemes.^{245, 277, 300}

To address these challenges, it was aimed to develop a novel unimolecular ECL construct by covalently linking a ruthenium (II) complex (Ru(bpy)₃²⁺) to cucurbit[7]uril. The design employs a flexible tetraethylene glycol (TEG) spacer to connect the Ru(bpy)₃²⁺ unit with CB7, resulting in a well-defined conjugate that retains both photophysical activity and guest-binding functionality. Unlike earlier approaches where CB7 was employed non-covalently to enhance ECL signals by bringing luminophores close to the electrode surface, this design enables intramolecular host-guest interactions between CB7 and the appended ruthenium complex.^{306, 307} Importantly, this configuration allows competitive binding of external guests to modulate the luminescence properties dynamically. The steric bulk of the bipyridine ligands in Ru(bpy)₃²⁺ prevents full encapsulation within the CB7 cavity, still the negatively polarized carbonyl portals were expected to interact with the positively charged ruthenium. This ensures that guest binding can occur at the macrocyclic site as the luminophore does not sequester it. This design provides a modular platform for competitive binding-based sensing, enabling real-time signal modulation in response to biorelevant analytes. Thus, the CB7-Ru conjugate introduces a novel class of supramolecular ECL labels with potential applications in biological sensing and small-molecule diagnostics.

As previously established, copper(I)-catalyzed azide-alkyne cycloaddition (CuAAC) has proven to be a reliable and chemoselective method for the covalent functionalization of CBs.^{220, 229, 231, 232} Nonetheless, an alternative synthetic route was initially explored based on direct amide-bond formation as the key coupling step, still the click reaction was part of the synthetic pathway. The strategy aimed to couple an NHS-activated ruthenium complex with an amine-functionalized CB7 derivative (CB7-NH₂) under mild peptide coupling conditions.

As the ruthenium component, bis(2,2'-bipyridine)-[4-(4'-methyl-2,2'-bipyridin-4-yl)butanoic acid]ruthenium (II) (Ru-COOH) was chosen due to its commercial availability and established use in bioconjugation. The corresponding activated ester (Ru-NHS) was generated *in situ* using standard

NHS/TSTU coupling chemistry. The synthesis of the CB7-NH₂ intermediate was envisioned *via* CuAAC reaction between mono-propargyloxylated CB7 (CB7-OPr) and a bifunctional azido-amino linker. While the click step proceeded successfully, purification of the resulting CB7-NH₂ posed significant difficulties due to the lack of UV-absorbing chromophores, making preparative HPLC monitoring and purification unreliable with our Abs/Fluorimetry-based HPLC. To address this issue, the amine functionality of the linker was temporarily protected with a UV-active Fmoc group, enabling effective purification by preparative HPLC. Subsequent Fmoc deprotection using standard peptide cleavage conditions (20% piperidine in DMF) yielded the free amine-derivative. Although the labelled intermediate was successfully purified in good yields, removal of the Fmoc group proved inefficient and resulted in significant material loss, with the final CB7-NH₂ obtained only in poor overall yield. Compounding the challenge, the NHS-activated ruthenium complex displayed considerable instability toward hydrolysis, particularly under ambient moisture conditions, limiting its handling and scalability. Despite confirming the formation of CB7-NH₂ by ESI-MS, attempts to couple it with Ru-NHS in solution failed to afford the desired conjugate under various tested conditions. Due to the synthetic and purification limitations encountered in this approach, the amide coupling route was ultimately abandoned. A schematic overview of this initial synthetic route is provided in **Fig. 5.6**.

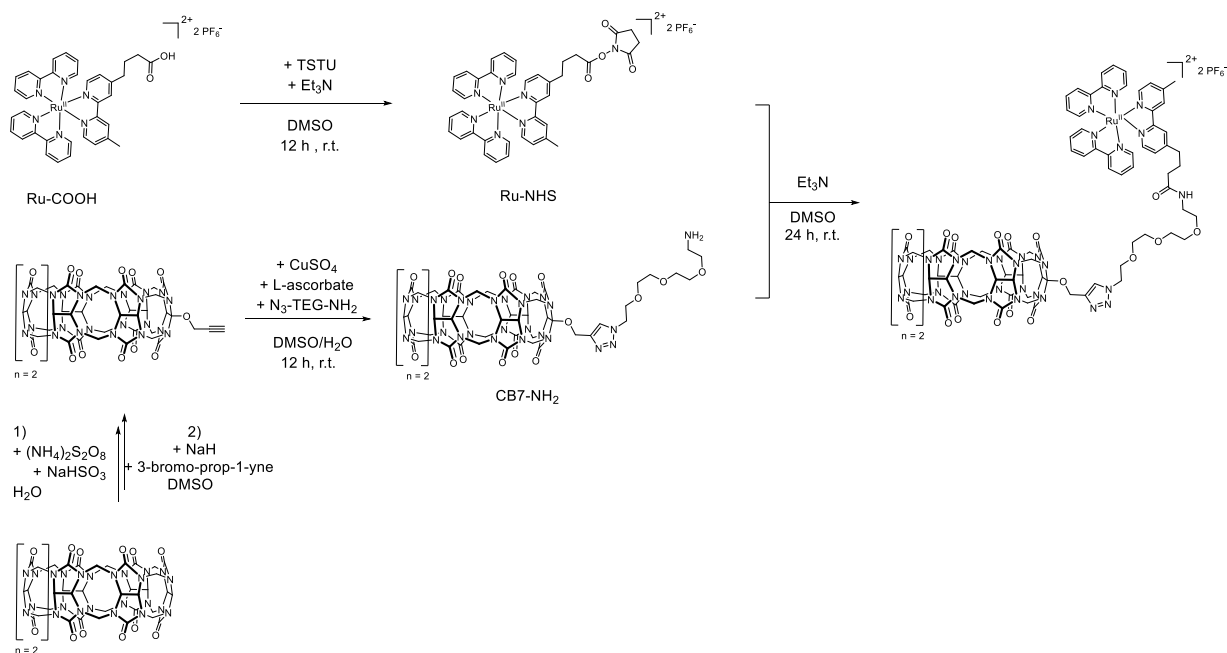


Fig 5.6: Failed synthesis of CB7-Ru *via* amide coupling as key step.

In an alternative synthetic approach, a strategy was pursued based on the well-established ligand exchange reaction using the commercially available ruthenium precursor *cis*-Bis(2,2'-bipyridine)dichlororuthenium(II). This method offers a versatile platform for the preparation of Ru(bpy)₃²⁺-type derivatives by substitution of the two chlorine atoms with a suitably functionalized bipyridine ligand. The aim of this route was to first prepare a CB7-bipyridine conjugate (CB7-BiPy)

through a CuAAC reaction and subsequently employ this ligand in a coordination reaction with the ruthenium precursor. The CuAAC reaction proceeded as expected, yielding the desired CB7-BiPy product. However, severe purification challenges were encountered. Preparative HPLC, typically reliable for CB7 conjugates bearing chromophoric moieties, failed to isolate the target compound. This failure is attributed to the protonation of the bipyridine nitrogen atoms under the acidic conditions necessary for dissolution, particularly upon the addition of trifluoroacetic acid (TFA) to the crude reaction mixture. Protonation likely induces strong intramolecular host-guest binding of the bipyridinium unit within the CB7 cavity, thereby altering the compound's retention behavior.

Interestingly, the presence of the desired conjugate could be confirmed by ESI-MS prior to TFA addition, yet no trace of the product was detectable afterwards. Despite the purification setback, the crude CB7-BiPy product was carried forward to the ligand exchange step with the ruthenium precursor under standard conditions. However, this reaction failed to yield the expected CB7-Ru conjugate. No product formation could be observed by ESI-MS or UV-Vis spectroscopy, likely due to either insufficient ligand availability or steric hindrance arising from the bulky CB7 scaffold. Given the irreproducibility and low efficiency of this route, as well as the incompatibility of the acidic purification conditions with the CB7-BiPy conjugate, this strategy was ultimately abandoned. A schematic representation of the attempted synthetic sequence is shown in **Fig. 5.7**.

Following this series of unsuccessful synthetic attempts, efforts were redirected toward a streamlined and more reliable approach as the main coupling step: the copper-catalyzed azide-alkyne cycloaddition (CuAAC) between mono-propargyloxy-functionalized CB7-OPr and an azide-functionalized ruthenium(II) complex (Ru-N₃). This strategy offers clear advantages in terms of reaction selectivity and functional group compatibility.

Initially, the Ru-N₃ precursor was obtained *via* functionalization of the commercially available carboxy-substituted ruthenium complex Ru-COOH through activation to the NHS ester (Ru-NHS) followed by amidation with a bifunctional azido-amino linker. While this approach gave satisfactory results at small scale, its scalability was hampered by the high cost of the Ru-COOH precursor and the hydrolytic sensitivity of the intermediate Ru-NHS ester under the reaction conditions employed. To overcome these limitations, the synthesis was adapted to a more cost-effective and scalable route starting from the previously mentioned *cis*-Bis(2,2'-bipyridine)dichlororuthenium(II), a widely available and affordable ruthenium precursor. In this optimized protocol, the precursor was first subjected to a ligand exchange reaction with an NHS-derivatized bipyridine ligand followed by isolation of this intermediate. Subsequent amidation with the bifunctional azido-amino linker yielded the desired Ru-N₃ in good overall yield. The compound was isolated by column chromatography on neutral aluminum oxide using acetone/water (7:1) as the eluent.

Design and Development of a CB7-RuBiPy Conjugate

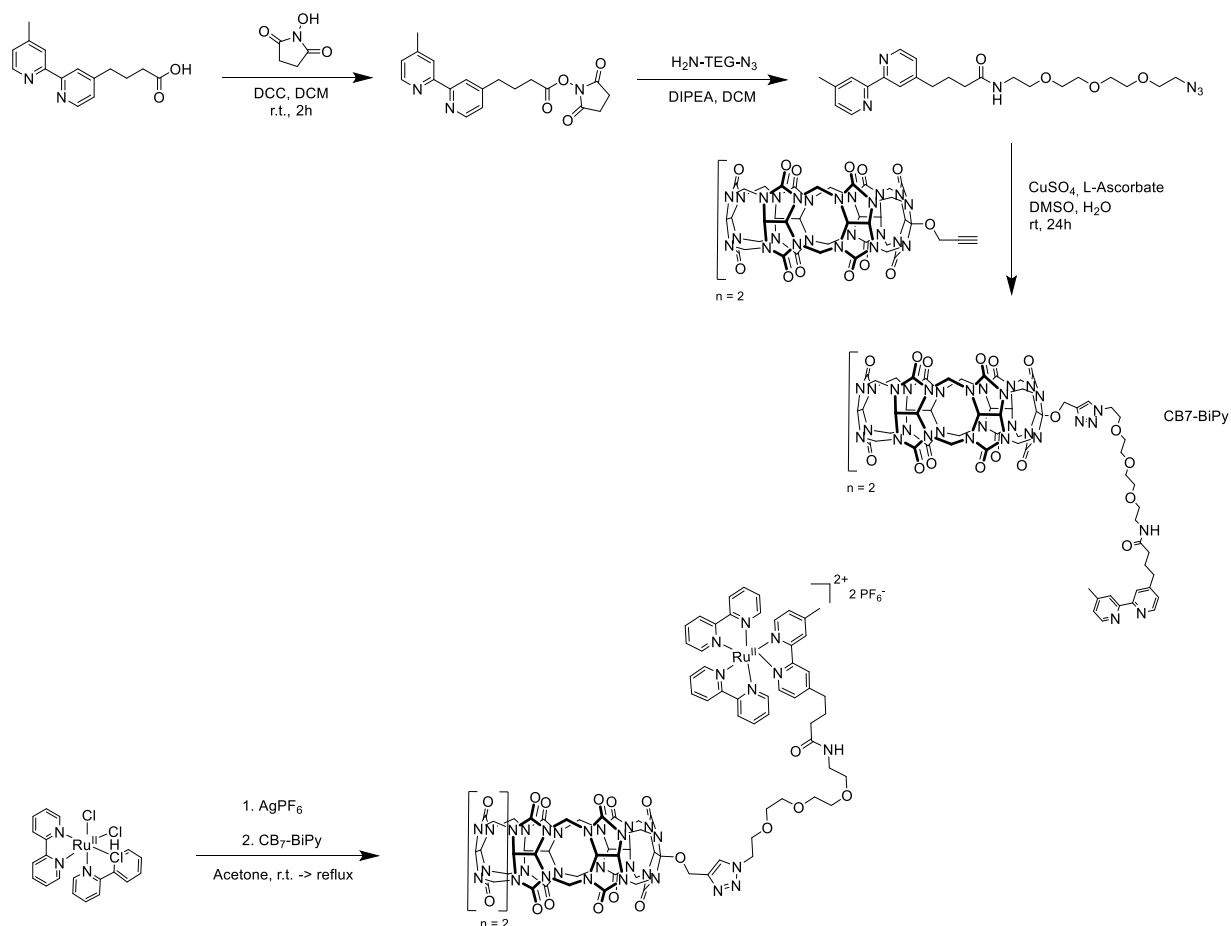


Fig. 5.7: Failed synthesis of CB7-Ru *via* ligand exchange reaction.

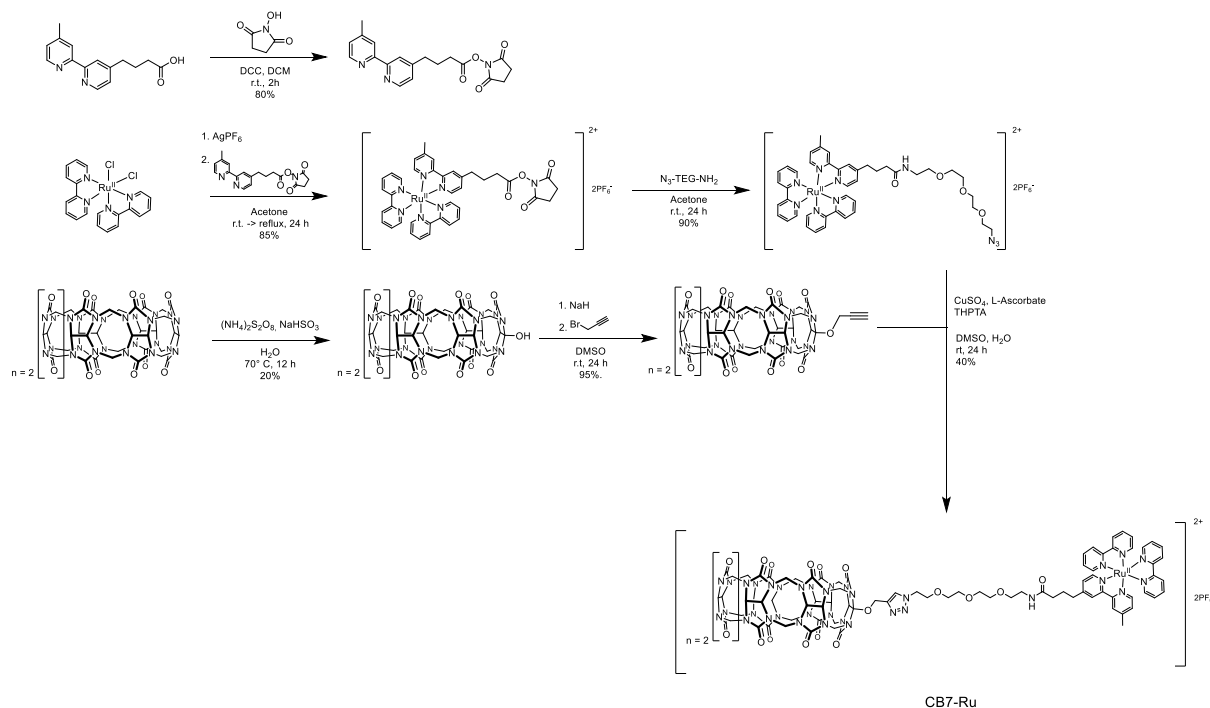


Fig. 5.8: Synthetic pathway of CB7-Ru *via* click reaction.

The key CuAAC reaction between CB7-OPr and Ru-N₃ was carried out under standard conditions using Cu(I) catalysis. Notably, the addition of tris(3-hydroxypropyltriazolylmethyl)amine (THPTA) as a stabilizing ligand for Cu⁺ ions significantly improved the efficiency of the cycloaddition, increasing the yield of the final coupling step from 20% to 40%. THPTA is known to enhance click reaction rates and suppress side reactions by stabilizing the copper(I) species in aqueous media.³⁰⁸ The resulting CB7-Ru conjugate was purified by size-exclusion chromatography (SEC) using a water/acetonitrile gradient (0-25%), taking advantage of the large molecular size and hydrophilicity of the product. The overall synthetic sequence, which is summarized in **Fig. 5.8**, provides a reproducible and efficient route to a novel unimolecular CB7-Ru ECL-active chemosensor with a well-defined architecture.

5.3. Structural Characterization of CB7-Ru

Ion mobility experiments and DFT calculations in this section were conducted by Dr. Papri Chakraborty, Emily Janz, and Dr. Marco Neumaier.

The CB7-Ru conjugate was characterized using a combination of techniques. The structural integrity and intramolecular interactions of the CB7-Ru conjugate were investigated by ¹H NMR spectroscopy in D₂O. The spectrum confirmed the successful formation of the triazole linkage resulting from the CuAAC reaction, as evidenced by the appearance of a characteristic singlet at 8.12 ppm, corresponding to the triazole proton.

Comparison with the ¹H NMR spectrum of the azide-functionalized precursor Ru-N₃ revealed a uniform upfield shift of all aromatic resonances in the conjugate, indicative of a change in the electronic environment upon conjugation to CB7. A particularly diagnostic feature was the singlet at 2.87 ppm on Ru-N₃, which integrated for three protons and corresponds to the methyl group on the bipyridine ligand. In the CB7-Ru conjugate, this resonance was observed at 2.49 ppm, representing a downfield shift of approximately 0.4 ppm. This chemical shift perturbation suggests an altered local environment of the methyl group, likely due to proximity of the CB7 portals or partial inclusion in the macrocyclic cavity.

To probe the possibility of self-inclusion of the methyl-bearing bipyridine into the CB7 cavity, excess amantadine – a well-established high-affinity guest for CB7 – was added to the sample (**Fig. 5.9**).^{231, 232} In cases of self-inclusion, displacement of the intramolecularly bound group by a stronger external guest typically results in significant chemical shift changes or signal broadening due to the transition between bound and unbound states.^{231, 232} However, for CB7-Ru, the spectral response to the amantadine addition was subtle. Only minor shifts (~0.01 ppm) were observed in the aromatic region, and the CB7-associated singlets in the low-field region – initially observed as two singlets at 5.82 and 5.86 ppm – underwent a transformation into two doublets at 5.83 and 5.87 ppm, respectively. This splitting likely arises from a slight perturbation in the symmetry or chemical environment of the CB7 methylene bridges upon guest binding. Importantly, no significant shift of the methyl resonance at 2.49 ppm was observed after amantadine addition, suggesting that this group is not deeply sequestered within the cavity under the conditions studied. However, the clear difference in chemical shifts compared to the Ru-N₃ precursor

indicates a strong intramolecular interaction between the ruthenium complex and the CB7 host. This interaction is likely responsible for the observed perturbation in the NMR spectrum, even though it does not involve full encapsulation of the bipyridine methyl group or other bipyridine moieties. Nevertheless, binding of amantadine was confirmed *via* NMR, as indicated by strong peak shifting.

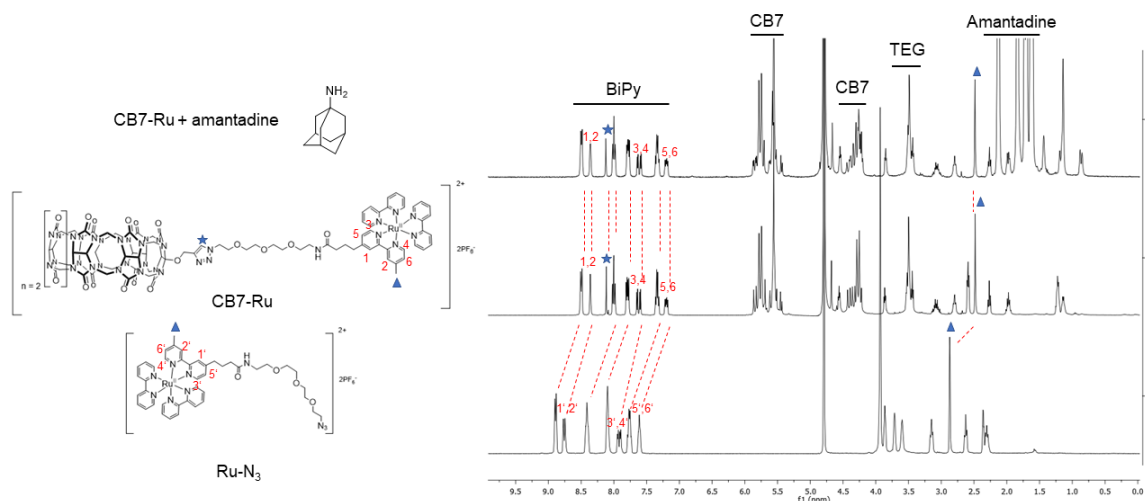


Fig. 5.9: Overlay of ^1H NMR (400 MHz, D_2O) spectra of Ru-N_3 (bottom), CB7-Ru (middle) and CB7-Ru with excess amantadine (top).

Further insights into the binding behavior were obtained from a comparative ^1H NMR experiment involving the non-conjugated precursor Ru-COOH and one equivalent of CB7 in D_2O (**Fig 5.10**). Upon addition of CB7 , the signals corresponding to the aliphatic chain of the carboxylic acid moiety shifted and broaden, suggesting that this segment is involved in inclusion within the CB7 cavity. Such binding would place the $\text{Ru}(\text{bpy})_3^{2+}$ core in close proximity to the CB7 portals, thereby altering the local environment of the coordinated bipyridine ligands. This is reflected in the observed shifts of the aromatic resonances, which differ slightly from those seen in the spectrum of Ru-COOH alone. Notably, the aromatic proton signals of Ru-COOH do not correspond to those found in the spectrum of the Ru-N_3 precursor. These findings provide additional evidence for the ability of CB7 to modulate the spatial orientation and local environment of the Ru complex *via* non-covalent interactions, which likely contributes to the distinct photophysical properties observed in CB7-Ru . Altogether, the ^1H NMR data indicate, that the ruthenium core stays near the CB7 portals even when amantadine is bound, suggesting a unique interaction mode that differs fundamentally from known binary or unimolecular CB7 complexes.

High-resolution electrospray ionization mass spectrometry (HR-ESI-MS) performed in the presence of $\text{C}_8\text{mim}_2^{2+}$ as reporter guest gave a diagnostic ion at $m/z=590.7196$. The observed isotopic distribution pattern was in excellent agreement with that expected for a $[\text{CB7-Ru} + \text{C}_8\text{mim}_2]^{4+}$ adduct. To further elucidate the conformational landscape and binding modes of the CB7-Ru conjugate, ion mobility spectrometry (IMS) was combined with semi-empirical DFT calculations (GFN2-xTB) and conformer ensemble sampling via CREST.^{309, 310} Structural analysis of the CREST-derived ensemble revealed five distinct conformational motifs (P1–P5), defined by the binding of different bipyridine ligands into the CB7 cavity. Specifically, the unlinked bipyridine ligands can individually bind via one of their pyridine

rings (P1–P4), while the linker-bearing bipyridine can insert its methylated pyridine moiety into the cavity (P5).

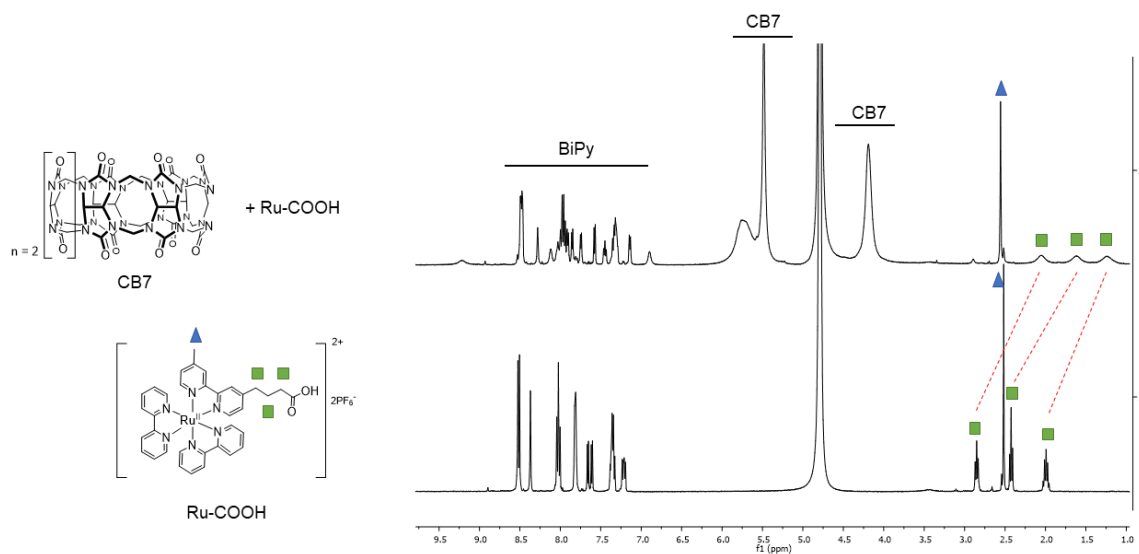


Fig. 5.10: Overlay of ^1H NMR (400 MHz, D_2O) spectra of Ru-COOH (bottom) and Ru-COOH in the presence of one equivalent of CB7.

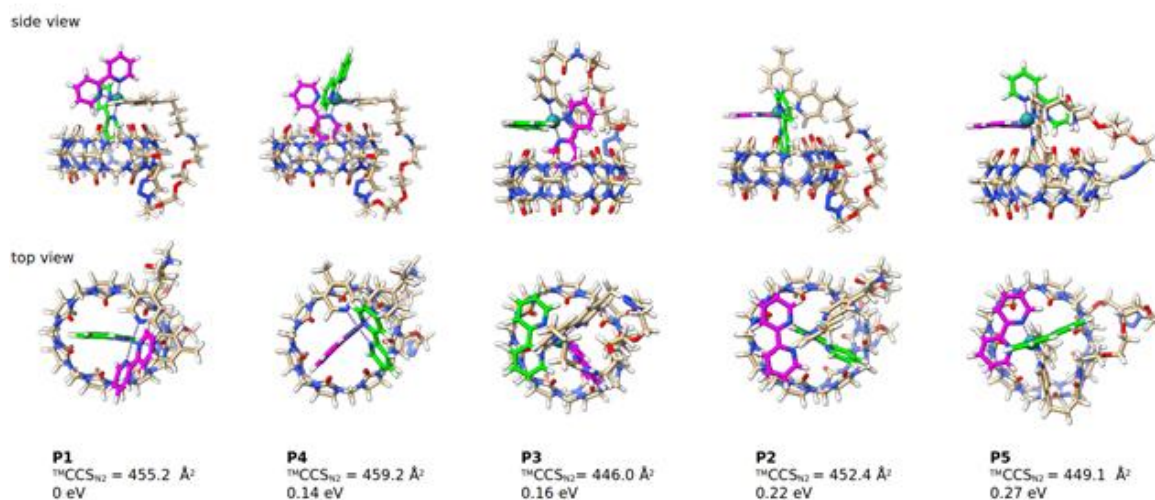


Fig. 5.11: Results of the DFT calculations with a 0.25 eV energy window. The structures were scaled with a factor of 0.9715.

Conformer P5, featuring partial inclusion of the methyl-substituted bipyridine into the CB7 cavity, aligns well with the upfield shift observed for this methyl group in the ^1H NMR spectrum of CB7-Ru. Importantly, none of the lowest-energy structures displayed either a fully extended or fully self-included geometry, consistent with NMR data that suggests a dynamic equilibrium between folded and partially folded states in solution.

IMS experiments revealed three distinct conformers in the gas phase, with tmsCCS_{n2} values of 446.0 \AA^2 , 449.2 \AA^2 , and 452.2 \AA^2 . These values fall within the same range as the calculated theoretical CCS_{n2} (TMCCS_{n2}) values obtained using the trajectory method (IMoS) for the P1–P5 structures.³¹¹ To match the experimental CCS_{n2} values more closely, the theoretical data were scaled by a factor of 0.9715.

These results support the existence of multiple coexisting conformers that differ in the identity and orientation of the ligand bound to the CB7 cavity.

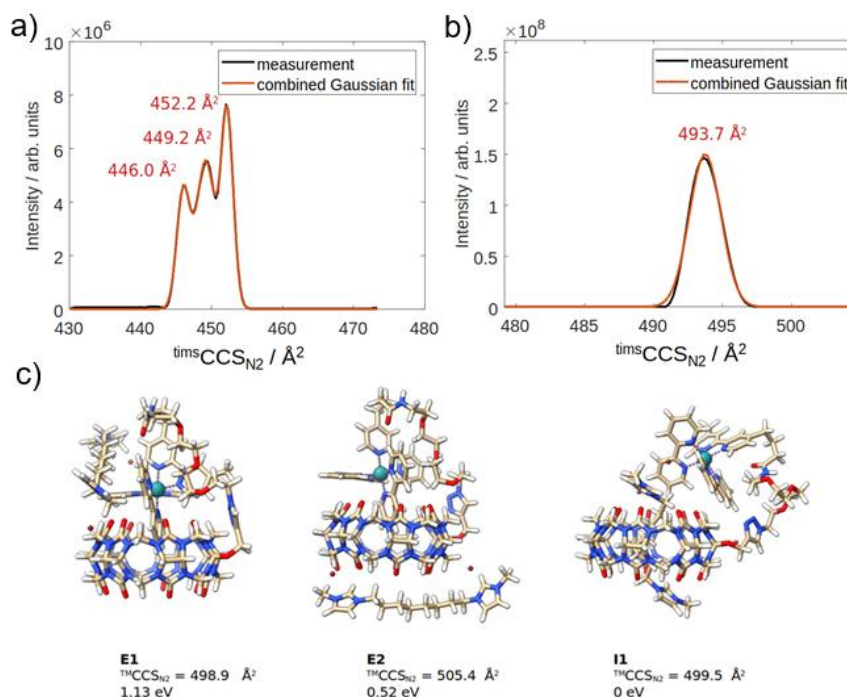


Fig. 5.12: Results from the IMS experiments. a) CB7-Ru without guest. b) CB7-Ru as $[\text{CB7-Ru} + \text{C}_8\text{mim}_2\text{Br}_2]^{2+}$. c) Results of the DFT calculation with a 0.25 eV energy window for $[\text{CB7-Ru} + \text{C}_8\text{mim}_2\text{Br}_2]^{2+}$

Further IMS experiments were carried out to study complex formation with external guest molecules. Among the guests tested, only $\text{C}_8\text{mim}_2\text{Br}_2$ produced a sufficiently intense signal when bound to CB7-Ru. Unlike the multiple conformers observed for unbound CB7-Ru, the guest-bound complex displayed only a single conformer in the gas phase. To investigate this, the conformational landscape of the $[\text{CB7-Ru} + \text{C}_8\text{mim}_2\text{Br}_2]^{2+}$ complex was explored using CREST and automated docking via aISS, employing GFN2-xTB.³¹² Both inclusion (I1) and exclusion (E1) complex models were generated. The calculated TMCCSN_2 values for these structures were nearly identical, making them indistinguishable by IMS alone. However, the inclusion complex I1 was found to be significantly more stable at the GFN2-xTB level. Higher-level calculations using r2SCAN-3c are currently ongoing to further validate this energetic preference.³¹³ The presence of only a single IMS peak for the guest-bound complex can be explained by a disruption of intramolecular binding between the Ru ligands and the CB7 cavity. Binding of the dicationic guest likely displaces the ruthenium ligands from the cavity, thereby increasing the conformational flexibility of the Ru moiety. This enhanced mobility facilitates interconversion between conformers on the IMS timescale (~ 500 ms), leading to the appearance of a single, time-averaged signal in the gas phase.

However, it is crucial to note that IMS is conducted in the gas phase and may not fully reflect solution-phase behavior. Supporting ^1H NMR experiments demonstrated guest-induced conformational changes in solution: upon C_8mim_2 addition, pronounced chemical shift changes were observed in the

CB7-Ru spectrum (see Supporting Information), consistent with an equilibrium between open and folded conformations. These findings highlight the dynamic nature of CB7-Ru, both in solution and in the gas phase, and emphasize the importance of using complementary techniques for structural elucidation.

5.4. Photophysical Properties and Sensing Capabilities of CB7-Ru

Photophysical measurements and determination of binding affinities of salts and analytes were done in cooperation with Vahideh Mahram. Quantum yields and lifetime decays were determined by Maria Vittoria Balli.

A comprehensive photophysical investigation was conducted to evaluate the optical properties of the CB7-Ru conjugates and its responsiveness to high-affinity guests and bioanalytically relevant analytes. To establish a comparative baseline, the spectral characteristics of CB7-Ru were analyzed alongside those of the reference compound $[\text{Ru}(\text{bpy})_3]\text{Cl}_2 \times 6 \text{H}_2\text{O}$ in aqueous solution. The UV-visible absorption spectrum of CB7-Ru exhibited a strong ligand-centered (LC) transition in the ultraviolet region, centered around 290 nm, and a series of moderately intense, broad absorption bands between 420 and 480 nm, characteristic of the metal-to ligand charge transfer (MLCT) transitions typically observed in Ru(II)-polypyridine complexes. Notably, the MLCT band appeared to be slightly broader in CB7-Ru compared to the parent $[\text{Ru}(\text{bpy})_3]^{2+}$ complex, which may be attributed to the influence of the covalently attached CB7 host. Photoluminescence measurements revealed that CB7-Ru maintains the emissive properties typical of Ru(II)-bipyridine systems, while also displaying distinct differences. In aerated aqueous solution, the conjugate exhibited a biexponential emission decay with lifetimes $\tau_1 = 92 \text{ ns}$ (12.1%) and $\tau_2 = 275 \text{ ns}$ (87.9%), and an overall quantum yield (Φ) of 0.012. This biexponential behavior stands in contrast to the monoexponential decay commonly reported for free $[\text{Ru}(\text{bpy})_3]^{2+}$ under the same conditions, which displays a single lifetime of $\tau = 365 \text{ ns}$ and a higher quantum yield of $\Phi = 0.028$. The observed biexponential decay suggests the presence of two emissive environments or excited-state conformers in CB7-Ru, possibly resulting from partial interactions of the Ru moiety with the CB7 cavity.

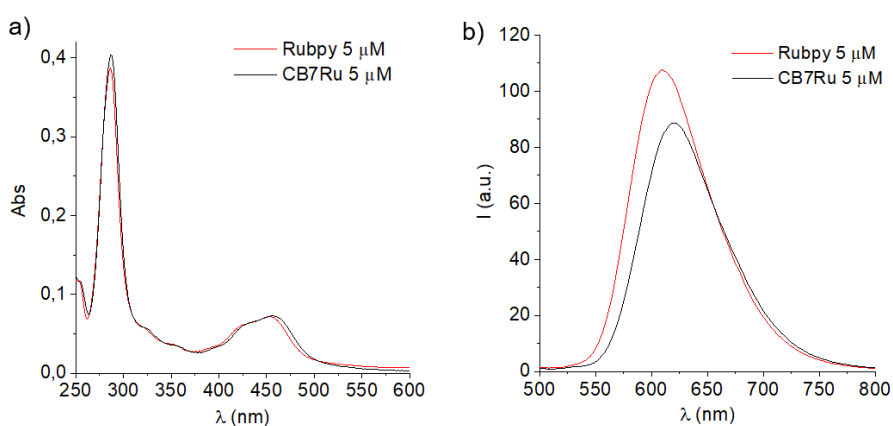


Fig. 5.13: a) Absorption spectra of $[\text{Ru}(\text{bpy})_3]^{2+}$ and CB7-Ru in water, both measured at a concentration of 5 μM . b) Emission spectra of $[\text{Ru}(\text{bpy})_3]^{2+}$ and CB7-Ru in water, both measured at a concentration of 5 μM ($\lambda_{\text{exc}} = 452 \text{ nm}$)

Additionally, the emission maximum of CB7-Ru was found to be slightly red-shifted ($\lambda_{em} = 626$ nm) compared to $[\text{Ru}(\text{bpy})_3]^{2+}$ ($\lambda_{em} = 609$ nm). This shift, together with the altered decay dynamics, provides further evidence that the proximity of the macrocyclic host affects the photophysical behavior of the attached Ru(II) complex, even in the absence of complete cavity inclusion.

Interestingly, the excited-state lifetime behavior of CB7-Ru was found to be highly dependent on the solvent environment. While the conjugate exhibited a biexponential decay profile in pure water, substitution of the solvent with buffered media led to a transition to a monoexponential decay, along with an overall increase in the emission lifetime. In PBS (pH = 7.4, 0.01 M), the lifetime increased to $\tau = 304$ ns, and in PB (pH = 6.8, 0.3 M), it further extended to $\tau = 327$ ns. These values approach the typical monoexponential lifetime observed for the parent $[\text{Ru}(\text{bpy})_3]^{2+}$ under similar conditions. This transition in decay suggests that the microenvironment around the Ru center is influenced by the ionic strength and composition of the buffer. It is likely that ionic interactions or competition with buffer constituents for the CB7 cavity or portals modulate the conformational flexibility of the conjugate, thereby reducing heterogeneity in the excited state population. The extended lifetimes in buffered solutions also indicate a suppression of non-radiative decay pathways, which may be linked to decreased quenching from dissolved oxygen or stabilization of a more rigid conformer.

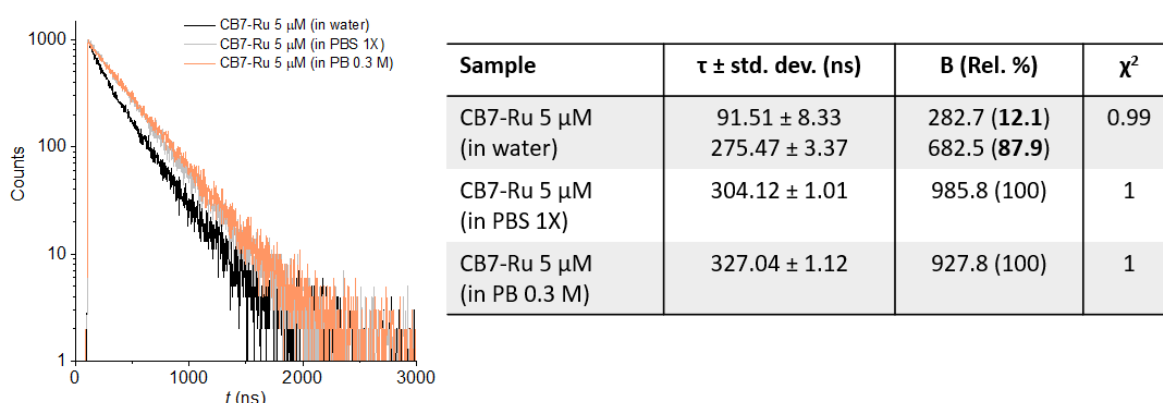


Fig. 5.14: Fluorescence lifetime decays of CB7-Ru in different solvents at 5 μM .

The fluorescence emission properties of CB7-Ru were found to be highly sensitive to the chemical composition of the surrounding medium. When measurements were performed in various buffered aqueous environments – including PBS, PB and HEPES, each with pH = 7.4 and a concentration of 0.01 M – a significant enhancement in emission intensity was observed relative to the spectrum recorded in pure water (**Fig. 5.15**). This increase in luminescence was accompanied by a moderate blue shift in the emission maximum, indicating changes in the local polarity or the conformational dynamics of the conjugate.

Among the tested buffers, PBS and HEPES induced the most pronounced increase in emission intensity, suggesting that ionic strength and buffer composition play key roles in modulating the photophysical behaviour of the CB7-Ru conjugate. The increase may result from stabilization of the excited state, reduced non-radiative decay, or a decreased likelihood of dynamic quenching interactions

in the buffered media. Additionally, specific interactions between buffer ions and the CB7 cavity – such as competitive guest binding or shielding of the electrostatic environment – may further influence the luminescence output. For comparison, the emission spectra of the parent $[\text{Ru}(\text{bpy})_3]^{2+}$ complex were also recorded under identical buffer conditions, both in absence and presence of up to five equivalents of free CB7. In contrast to the covalent CB7-Ru, no significant difference in emission intensity or shift in spectral properties was observed in the presence and absence of CB7. This highlights the importance of covalent tethering in creating a well-defined microenvironment around the luminophore, which in turn enables a more pronounced and tuneable photophysical response to external stimuli.

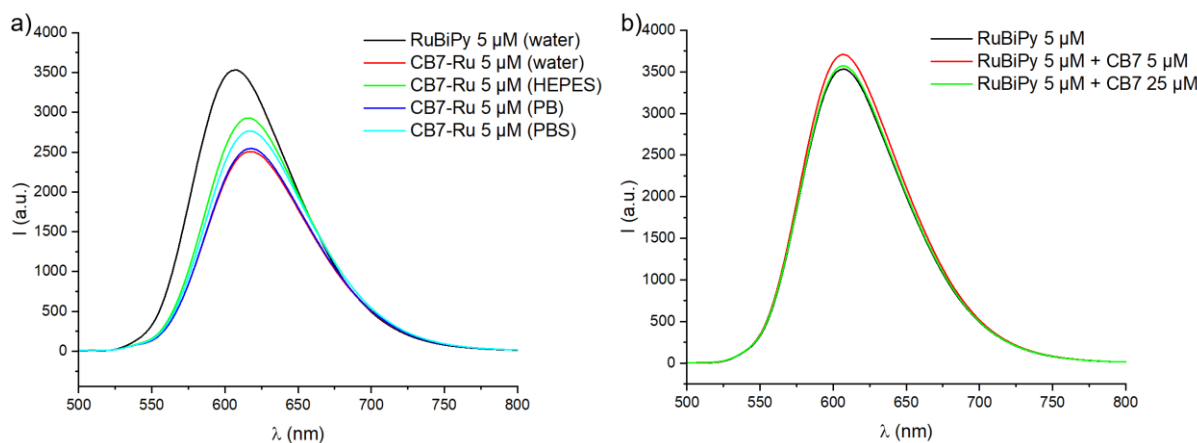


Fig. 5.15: a) Comparison of the fluorescence response ($\lambda_{\text{exc}} = 452 \text{ nm}$) of $[\text{Ru}(\text{bpy})_3]\text{Cl}_2 \times 6 \text{ H}_2\text{O}$ in water (5 μM) and CB7-Ru in water (5 μM) and various buffers (5 μM), each at 0.01M concentration and pH=7.4. b) Fluorescence response of $[\text{Ru}(\text{bpy})_3]\text{Cl}_2 \times 6 \text{ H}_2\text{O}$ (5 μM) with 0, 1 or 5 equivalents of CB7 added in water.

Prompted by the notable solvent dependent photophysical behaviour of CB7-Ru, a model compound was designed and synthesized to further investigate the role of proximity-driven supramolecular effects exerted by CB7 on the ruthenium luminophore. In this construct, a high-affinity guest moiety – adamantane – was covalently tethered to a $[\text{Ru}(\text{bpy})_3]^{2+}$ core, yielding a molecule hereafter referred to as Ada-Ru. Adamantane was selected for its exceptional binding affinity toward CB7, which ensures complete and stable occupation of the host cavity. Crucially, this configuration brings the Ru(II) center into close spatial proximity to the carbonyl-lined portals of CB7 without enabling the encapsulation.

Upon titration of CB7 into an aqueous solution of Ada-Ru, substantial changes were observed in the emission profile. Specifically, the emission maximum exhibited a red shift and a marked decrease in intensity, pointing toward a distinct alteration of the photophysical environment of the ruthenium center. These effects were not attributed to encapsulation of the $\text{Ru}(\text{bpy})_3$ unit, but rather to proximity-induced changes in the microenvironment caused by the interaction of the metal complex with the portal region of CB7.

When compared directly with CB7-Ru under identical aqueous conditions, the emission behaviour of Ada-Ru with CB7 added closely mirrored that of the conjugate (**Fig. 5.17 b**). This strongly supports the notion that even partial or peripheral interactions with CB7 – specifically at the rim of the cavity – are

sufficient to modulate the photophysical properties of the adjacent ruthenium complex. Such proximity effect is particularly notable given that it does not rely on the classical inclusion mechanism typically associated with cucurbituril host-guest chemistry, but arises from more subtle microenvironmental interactions such as hydrogen bonding, electrostatic interactions, or modulation of solvent dynamics at the host portals. These findings align with recent literature highlighting the capability of cucurbiturils to influence excited-state properties of nearby chromophores.³¹⁴ In this context, the Ada-Ru model system provides valuable insight into the non-encapsulating, yet functionally significant, interactions that can occur between CB7 and appended luminophores.

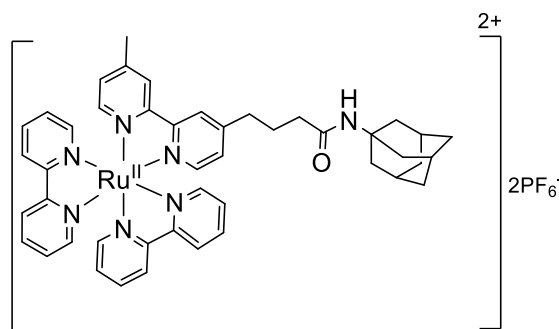


Fig. 5.16: Structure of Ada-Ru.

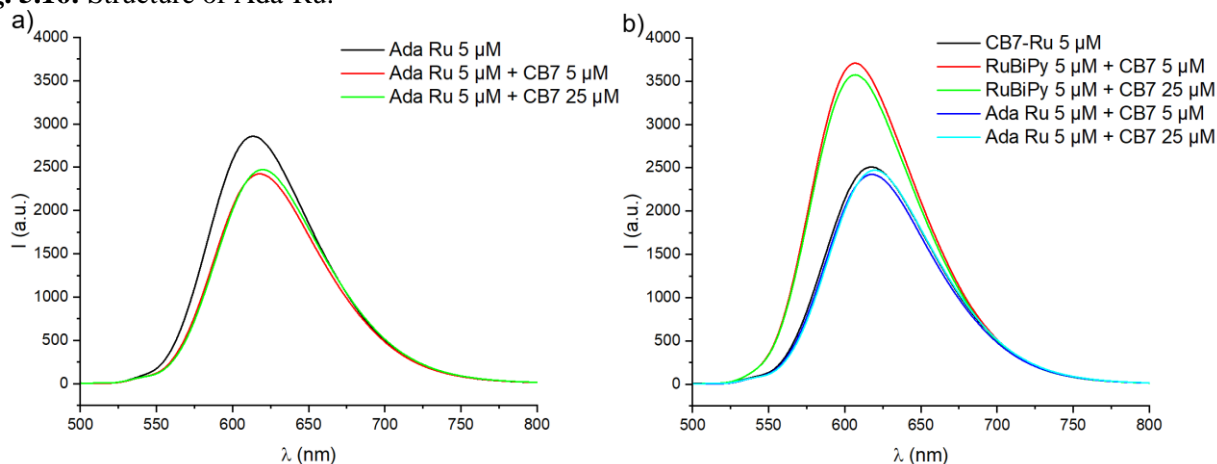


Fig. 5.17: a) Fluorescence response ($\lambda_{exc} = 452$ nm) of Ada-Ru (5 μ M) with 0, 1 and 5 equivalents of CB7 in water. b) Comparison of the fluorescence response of CB7-Ru (5 μ M), [Ru(bpy)₃]²⁺ (5 μ M) and Ada-Ru (5 μ M) with each 1 and 5 equivalents of CB7 in water.

To further investigate the role and necessity of covalent conjugation between the ruthenium complex and CB7, additional titration experiments were conducted using amantadine as the model guest. These control studies included the adamantane-functionalized ruthenium complex (Ada-Ru) and the unmodified [Ru(bpy)₃]Cl₂ × 6 H₂O, tested both as isolated dyes and in the presence of 1 or 5 equivalents of CB7 to form non-covalent assemblies. As expected, the dyes, whether in isolation or with excess CB7, did not exhibit any measurable changes in their absorption or fluorescence emission profiles upon addition of amantadine. This lack of response highlights the essential role of covalent linkage in the CB7-Ru construct, which enables a defined spatial arrangement and proximity-driven modulation of photophysical behaviour. These results clearly underscore that non-covalent mixtures of Ru(bpy)₃-based dyes CB7 are

insufficient to produce the analyte-dependent optical changes observed in the CB7-Ru conjugate. The fixed, unimolecular architecture is thus critical for achieving effective signal modulation in response to guest binding. Detailed spectroscopic data from these control experiments are provided in the Supplementary Information.

As anticipated, the non-covalent assemblies of CB7 with either free $[\text{Ru}(\text{bpy})_3]^{2+}$ or Ada-Ru – as amantadine cannot displace it – displayed negligible changes in fluorescence upon amantadine addition, independent of the solvent system. This contrasts starkly with the behaviour of the covalently linked CB7-Ru conjugate, which exhibited a clearly discernible fluorescence response to amantadine titration, particularly under aqueous conditions. These findings confirm that the unimolecular architecture of CB7-Ru is essential for eliciting a defined sensing output.

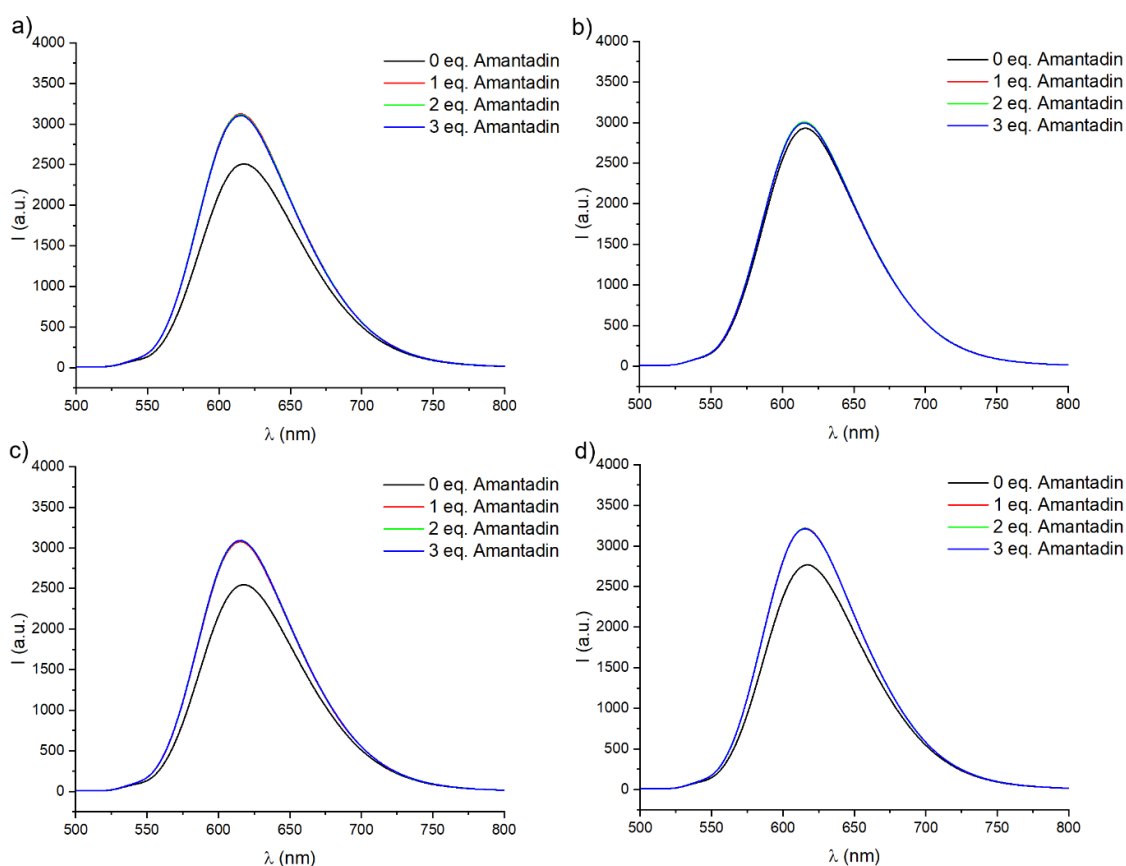


Fig. 5.18: Fluorescence response ($\lambda_{\text{exc}} = 452 \text{ nm}$) of CB7-Ru ($5 \mu\text{M}$) upon addition of increasing equivalents of amantadine. a) water, b) HEPES, c) PB, and d) PBS (buffer concentration 0.01M and pH 7.4 each)

Notably, the fluorescence response of CB7-Ru to amantadine was highly dependent on the buffer environment. In pure water, the system exhibited its most robust and interpretable response, characterized by an increase in emission intensity upon guest addition. In contrast, the use of PBS and HEPES buffer (both at $\text{pH} = 7.4$, 0.01 M) resulted in a diminished sensitivity and pronounced baseline shifts, likely due to pre-existing buffer interactions with CB7. In particular, the organic nature of HEPES appeared to interfere strongly with the emission properties of the conjugate, rendering HEPES unsuitable for sensitive fluorescence-based sensing. PBS, which contains added NaCl, showed a similar reduced responsiveness,

while standard PB induced only minor perturbations, suggesting it to be the most suitable buffering system among those tested.

These observations are consistent with the known affinity of cucurbiturils for alkali and organic cations at the carbonyl-lined portals.¹⁴⁴ In this context, it is likely that buffer cations engage in competitive interactions with the CB7 moiety, partially displacing the appended ruthenium complex and altering the emission characteristics. A qualitative trend could be observed in which the size and charge density of the buffer ions appeared to correlate with the extent of interferences: smaller inorganic cations such as Na⁺ and K⁺ induced modest effects, whereas the bulkier HEPES molecule induced significant emission alterations.

Taken together, these results reinforce the importance of carefully selecting the buffer environment in supramolecular sensing assays based on CB7-luminophore conjugates. While CB7-Ru demonstrates promising guest-responsive emission behaviour in water, its performance is comprised in buffers that compete for binding at the CB7 portals or are bound to the CB7 cavity (*e.g.*, HEPES). These findings highlight the sensitive interplay between supramolecular structure, guest binding affinity, and medium composition, which must be carefully balanced in the design of robust sensing platforms.

Encouraged by the observed sensitivity of CB7-Ru to its chemical environment, next the influence of various biologically relevant metal cations on its fluorescence emission properties was evaluated (see Supporting Information). Specifically, a series of mono-, di-, and trivalent cations – Li⁺, Na⁺, K⁺, Mg²⁺, Eu³⁺, and Gd³⁺ – were systematically introduced to aqueous solutions of CB7-Ru (1 μM), in concentrations ranging up to 10 mM. A general trend emerged in which increasing cationic charge and/or ionic radius was associated with a progressive enhancement in emission intensity. This behaviour is consistent with a model where electrostatic repulsion between the dicationic ruthenium (II) center and other positively charged species modulates the local environment of the luminophore. The addition of multivalent cations such as Mg²⁺, Eu³⁺, Gd³⁺ likely stabilizes the spatial arrangement of the CB7-Ru conjugate by interacting with the carbonyl-lined portals, thereby indirectly influencing the electronic properties of the nearby ruthenium center what causes the enhanced emission. Interestingly, the behavior of Na⁺ and K⁺ diverged from this monotonic trend and exhibited a biphasic response. At lower concentrations (≤ 1 mM), both ions induced a moderate quenching of the emission signal. However, upon further addition (≥ 1 mM), fluorescence intensity increased, eventually surpassing the baseline observed in the absence of cations. This non-linear response suggests a more complex binding equilibrium or competitive interaction at the CB7 cavity.

A reasonable interpretation for the observed behavior is that, at low concentrations, Na⁺ and K⁺ preferentially associate with the carbonyl portals of CB7 on the side opposite to the ruthenium center. This partial occupancy likely induces a unfavorable geometry or alters the local solvation structure at the portals, leading to ion-induced quenching effects or changes in microenvironmental polarity that reduce emission intensity. At higher ion concentrations, however, Na⁺ and K⁺ may competitively displace the Ru(II) unit from partial engagement with the CB7 portals altogether (**Fig. 5.20 b**). This displacement

could relieve quenching effects or promote a more favorable, emissive conformation, thereby restoring or even enhancing fluorescence intensity. Supporting evidence for this mechanism was obtained from NMR experiments, where the addition of excess potassium (as chloride salt) resulted in chemical shifts of the biipyridine ligand protons approaching those of the parent Ru-N₃ precursor (**Fig. 5.19**). This suggests a conformational unfolding of the CB7-Ru complex under high ion concentrations, consistent with the proposed displacement mechanism.

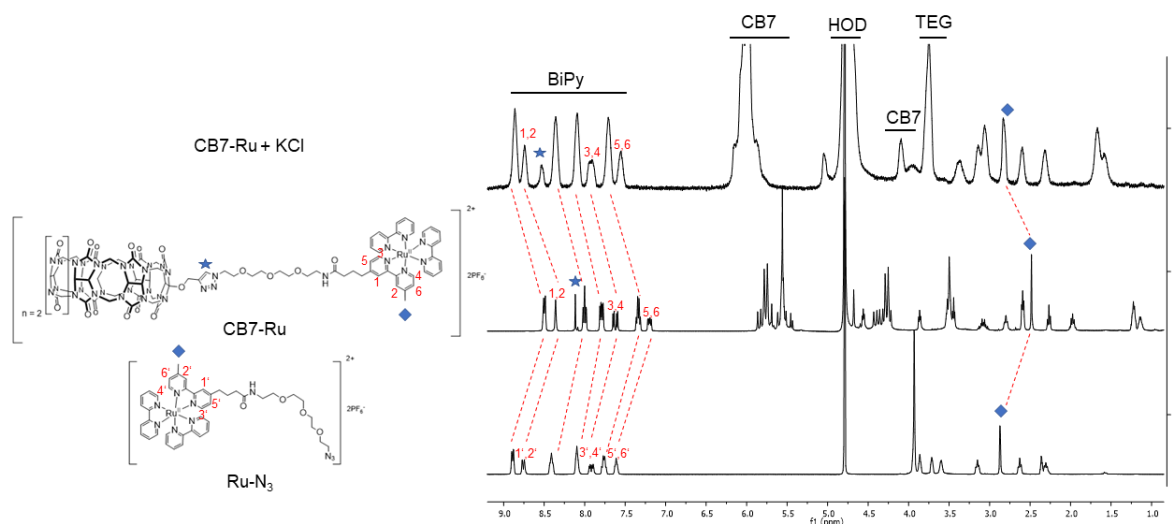


Fig. 5.19. Overlay of ¹H NMR (400 MHz, D₂O) spectra of Ru-N₃ (bottom), CB7-Ru (middle) and CB7-Ru with excess KCl (top).

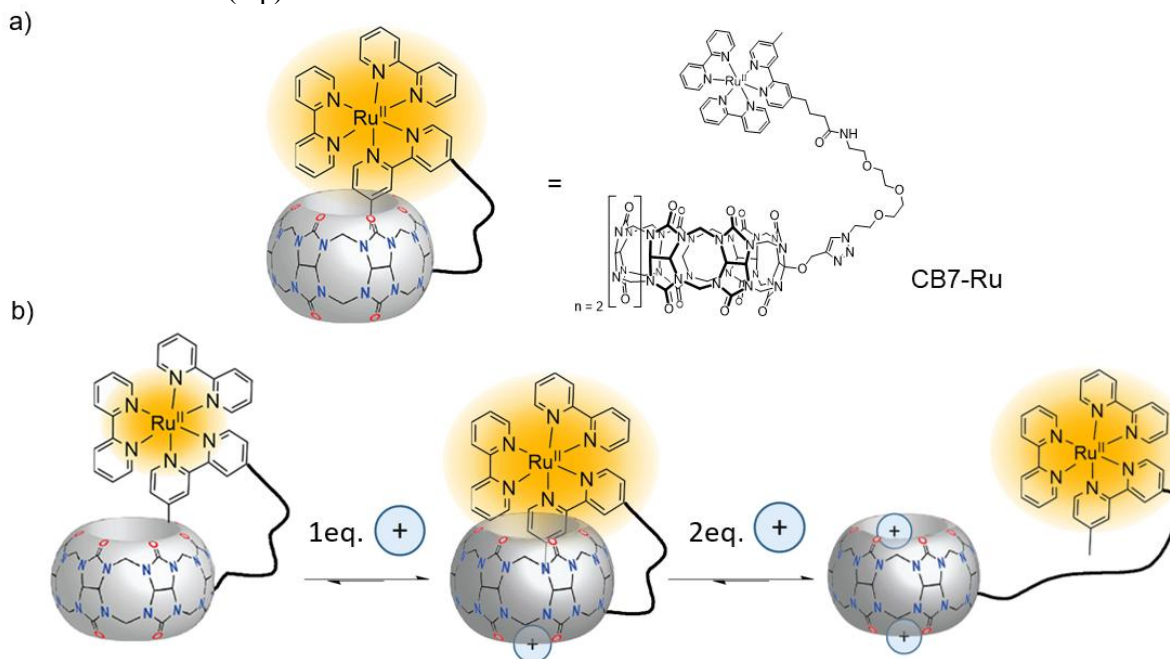


Fig. 5.20: a) Structure of CB7-Ru. b) Proposed two-step mechanism of salt binding.

Lithium, in contrast, demonstrated a purely quenching effect across the tested concentration range, suggesting a interaction with the CB7 portals that does not permit recovery or enhancement of the emissive state across the tested concentration range (up to 10 mM). This purely quenching effect may be

attributed to the small ionic radius and high charge density of Li^+ , which could lead to stronger electrostatic interactions at the portal, thereby perturbing the emissive state of Ru(II) without promoting favourable displacement dynamics. The distinct response profiles observed for different cations highlight the capacity of CB7-Ru to act as a sensitive probe for local ionic composition and may lead to future development of ion discriminating fluorescence sensors based on this architecture.

For selected metal ions that produced sufficiently well-defined and reproducible changes in the fluorescence emission of CB7-Ru, it was possible to extract quantitative binding information by fitting the titration data to appropriate binding models. Specifically, titration experiments were performed by stepwise addition of the cation to an aqueous solution of CB7-Ru ($1 \mu\text{M}$), and the corresponding emission intensities were recorded at the maximum emission wavelength ($\lambda_{\text{exc}} = 452 \text{ nm}$, $\lambda_{\text{em}} = 610 \text{ nm}$). In cases where the fluorescence response exhibited a clear saturation behaviour, the data were fitted using a 1:1 host-guest binding model, allowing for the estimation of the association constant (K_a). For the trivalent ions Eu^{3+} and Gd^{3+} , the fluorescence changes followed a clear saturation profile, allowing for reliable determination of K_a . For the CB7-Ru conjugate, the K_a for Eu^{3+} was determined to be 641 M^{-1} , and for Gd^{3+} 394 M^{-1} . These values are notably lower than those measured for free CB7, where K_a values of $2000 \text{ M}^{-1}\text{cm}^{-1}$ (Eu^{3+}) and $850 \text{ M}^{-1}\text{cm}^{-1}$ (Gd^{3+}) were determined.³¹⁵ The reduction in binding affinity upon covalent attachment of $\text{Ru}(\text{bpy})_3^{2+}$ to the CB7 framework suggests that steric or electronic interactions with the ruthenium complex may partially hinder access to the CB7 portals or alter the overall electrostatic potential of the cavity. Nevertheless, the observed affinities remain in a moderate range and are sufficient to induce measurable photophysical changes.

Cations	$r \text{ (\AA)}^{144}$	$K_a, \text{CB7-Ru (M}^{-1}\text{)}$	$K_a, \text{CB7 (M}^{-1}\text{)}$
Li^+	0.69	n.a.	2.34×10^0 ¹⁴⁴
Na^+	1.02	3.51×10^0	3.41×10^3 ¹⁴⁴
K^+	1.38	n.a.	3.46×10^0 ¹⁴⁴
Mg^{2+}	0.72	n.a.	3.24×10^0 ¹⁴⁴
Eu^{3+}	1.09	6.41×10^2	2.00×10^3 ³¹⁵
Gd^{3+}	1.19	3.94×10^2	8.50×10^2 ³¹⁵

Table 5.1: Ionic radius of the cations used in this study with the respective K_a with CB7-Ru and CB7 measured in MilliQ water. Data were fitted according to a 1:1 binding model.

To further explore the sensing capabilities of the CB7-Ru conjugate, attention was next directed toward determining the K_a of various biorelevant analytes (**Fig. 5.21**). The selected compounds span a diverse range of structural classes and functional roles in both biomedical and environmental contexts. Amantadine (Ama) was included due to its clinical relevance in the treatment of neurological disorders such as Parkinson's disease and its known high binding affinity for CB7. Methyl viologen (M_2V) was selected as a representative redox-active analyte, particularly relevant in agricultural and environmental toxicology.²³⁹ Biogenic polyamines – cadaverine (Cad), spermidine (Spd) and spermine (Spm) – were investigated owing to their established association with disease states, especially their elevated

concentrations in cancer and inflammatory pathologies. These polyamines are frequently studied as urinary and plasma biomarkers in clinical diagnostics. To assess the potential for interactions with amino acid-derived motifs, phenylalanine (Phe) and its dipeptide derivative (PheGly) were included. Their presence in protein structures makes them relevant probes for evaluating the CB7-Ru system's potential for protein or peptide sensing. Finally, *N*-tripropylamine (TPrA) was analysed due to its pivotal role as a co-reactant in ECL. Understanding the binding behaviour of TPrA is crucial, given that its interaction with CB7-Ru could modulate ECL signal generation and serve as a handle for signal amplification or modulation. An overview of the analytes is presented below.

To evaluate the binding behaviour of the selected analytes, fluorescence titration experiments were conducted by stepwise addition of analyte solutions to a 1 μ M aqueous solution of the CB7-Ru conjugate. The experiments were performed under different solvent conditions to assess the influence of buffer composition on sensing performance. Specifically, PB and HEPES buffer (both at pH = 7.4, 0.01 M) were tested in parallel with pure water. Emission intensities were monitored at the maximum emission wavelength ($\lambda_{\text{exc}} = 452$ nm, $\lambda_{\text{em}} = 610$ nm). In cases where a clear saturation of the emission response was observed upon analyte addition, the data were fitted using a standard 1:1 host-guest binding model to extract the apparent association constant (**Table 5.2**). As anticipated from previous experiments, the use of HEPES buffer significantly interfered with the fluorescence response of CB7-Ru, precluding reliable data fitting due to pronounced background effects. In contrast, PB allowed for meaningful titration curves, albeit with reduced sensitivity compared to pure water.

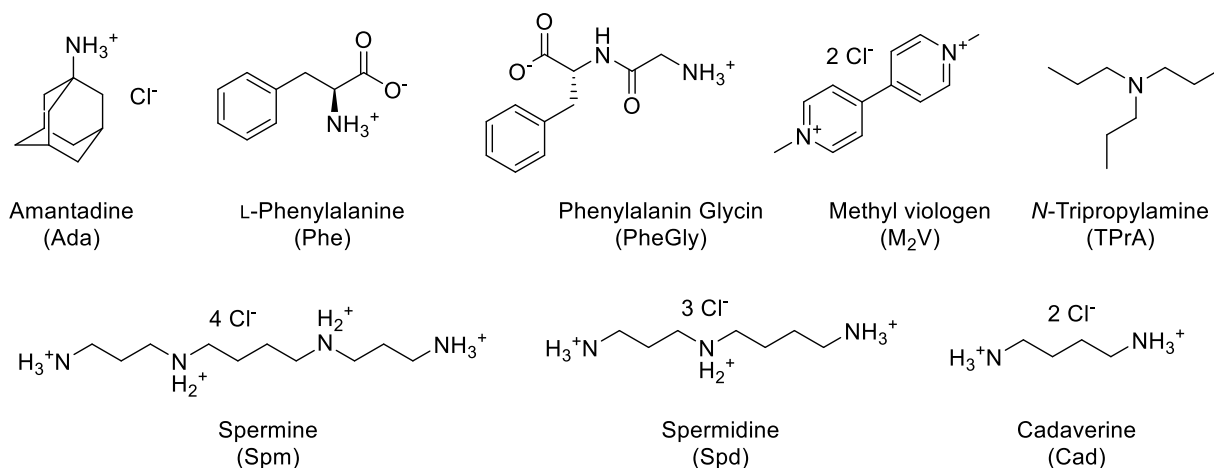


Fig. 5.21: Structures of the biorelevant analytes used for the fluorescence study of CB7-Ru.

From the fitted titration data, two key trends in the host-guest binding behaviour of the CB7-Ru conjugate emerged. As anticipated, the K_a for free CB7 in water were generally higher than those observed for CB7-Ru, either in water or PB. This trend is most likely due to the reduced steric accessibility of the CB7 cavity in the conjugate, where the covalently attached ruthenium complex may partially hinder guest entry. However, an interesting exception to this trend was observed for PheGly. In this case, the binding affinity was slightly higher for CB7-Ru ($5.10 \times 10^7 \text{ M}^{-1}$) compared to free CB7 ($3.00 \times 10^7 \text{ M}^{-1}$) in water. This suggests that the bipyridine moiety of the ruthenium complex may

contribute additional stabilizing interactions, possibly through π - π stacking or electrostatic effects, enhancing the binding of aromatic or peptide-like analytes such as PheGly.

Analytes	K_a , CB7-Ru(M^{-1})		K_a , CB7(M^{-1})	
	Water	PB	Water	PB
Ada	n.a.	n.a.	4.2×10^{12} ³¹⁶	n.a.
Phe	3.25×10^5	1.21×10^5	1.03×10^6 ³¹⁷	n.a.
PheGly	5.10×10^7	3.97×10^7	3.00×10^7 ³¹⁸	n.a.
M ₂ V	2.05×10^6	3.84×10^6	6.03×10^8 ²⁹	n.a.
TPrA	2.05×10^4	1.70×10^4	n.a.	n.a.
Spm	1.27×10^6	6.35×10^5	2.60×10^7 ³¹⁶	n.a.
Spd	1.94×10^5	1.40×10^5	n.a.	n.a.
Cad	8.33×10^5	2.23×10^5	1.40×10^7 ³¹⁶	n.a.

Table 5.2: Fitted K_a values for the analytes in water and PB buffer (0.01M, pH =7.4) for CB7-Ru and CB7.

A second trend was observed when comparing the binding affinities of CB7-Ru in water versus PB. In nearly all cases, higher K_a values were obtained in pure water, with the exception of M₂V. For M₂V, the K_a in PB ($3.84 \times 10^6 M^{-1}$) exceeded that in water ($2.05 \times 10^6 M^{-1}$). This anomalous behaviour is likely a result of photoinduced electron or energy transfer between the M₂V and the Ru(II) chromophore, leading to quenching of the ruthenium emission. This quenching phenomenon is also reflected in the inverse shape of the titration curve for M₂V: while the addition of other analytes typically resulted in an enhancement of emission intensity, M₂V uniquely caused a decrease in fluorescence intensity upon binding. This contrast further supports a photoinduced quenching mechanism, likely facilitated by close proximity and favourable orbital alignment between M₂V and the excited Ru(II) center. Together, these findings demonstrate that both the chemical nature of the analyte and the solution environment significantly influence the host-guest interaction strength and the associated photophysical response, highlighting the complex interplay between supramolecular structure and function in this CB7-Ru system.

Although the photophysical data for CB7-Ru clearly indicate a distinct sensing behavior – particularly in response to high-affinity guests like amantadine – the corresponding NMR spectra do not exhibit major chemical shift changes that would typically signal strong host-guest interactions. Interestingly, a similar fluorescence response is also observed for the non-covalent CB7 complex of the model compound Ada-Ru, suggesting that the proximity of the Ru(bpy)₃²⁺ core to the CB7 portals, rather than full inclusion, is sufficient to modulate the emission properties. This seemingly paradoxical behavior raises questions about the underlying mechanism, especially given that traditional NMR indicators of host-guest complexation are largely absent for amantadine. Additional ¹H NMR experiments reveal that significant unfolding of CB7-Ru can indeed occur under specific conditions. Upon addition of KCl pronounced peak shifts are observed, especially for signals associated with the bipyridine ligands, indicating a transition toward a more unfolded structure. In contrast, addition of the dicationic guest C₈mim₂²⁺ also causes

chemical shift changes, but to a lesser extent than KCl (see Supporting Information). This suggests that while $C_8mim_2^{2+}$ interacts strongly with the CB7 cavity or portals, it only induces partial displacement of the Ru moiety. Notably, the magnitude of the spectral shifts after $C_8mim_2^{2+}$ addition appears to lie between that observed for amantadine and KCl.

These findings also align with previous studies on CB host-guest interactions. For example, Scherman and co-workers demonstrated that the chemical shifts of guest protons within CB6 depend strongly on their spatial positioning relative to the cavity.³¹⁹ Protons deeply included within the hydrophobic cavity experience shielding (upfield shifts), whereas those near the carbonyl-rich portals are deshielded due to local π -electron density. In the case of CB7-Ru, the Ru(II) chromophore is likely located adjacent to, but not deeply within the cavity – close enough to experience environmental changes yet not sufficiently bound to trigger the classic NMR signatures of full inclusion. This interpretation is consistent with the lack of substantial shifts upon neutral guest binding (amantadine), but the observable changes upon addition of cationic species such as K^+ and $C_8mim_2^{2+}$ suggest that electrostatic repulsion plays a key role in modulating the conformational equilibrium of the conjugate.

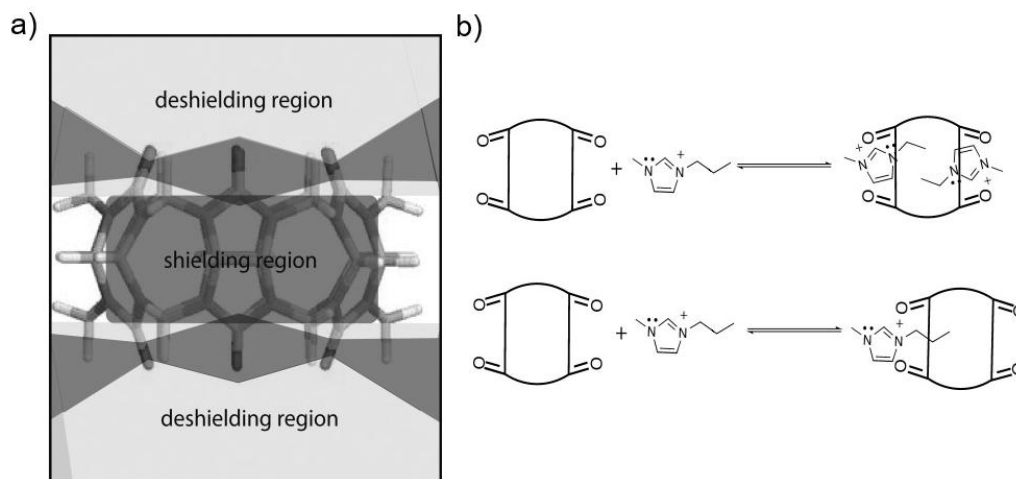


Fig. 5.22: a) Shielding and deshielding regions of CB6. b) Proposed two binding models as verified by NMR measurements. Slightly modified from ref ³¹⁹ © Wiley VCH

It was reported that imidazolium guests bind *via* their cationic nitrogen centers to the carbonyl portals of CB6, leading to preferential insertion of the alkyl chains into the cavity.³¹⁹ As chain length increases, portions of the guest molecule may extend beyond the cavity, leading to both shielding and deshielding effects within the same molecule. This study established a clear correlation between chemical shifts and spatial localization relative to the CB cavity and portals. Applying these insights to CB7-Ru, the lack of substantial chemical shift changes in the 1H NMR – especially in the aromatic region of the bipyridine ligands – suggests that the Ru(bpy)₃ core is not encapsulated. However, the strong photophysical response upon guest addition points to significant supramolecular interactions at the portals. One might assume that the distance between the Ru(II) core and the cavity is too large for any direct effect, but the consistent behavior across both CB7-Ru and Ada-Ru•CB7 complexes challenges this notion.

One hypothesis to explain this phenomenon is the quenching effect of dissolved molecular oxygen. It is well-established that O_2 is an efficient quencher of MLCT excited states in Ru(II) complexes.³²⁰ It could be hypothesized that CB7 binds molecular oxygen, and that guest binding to CB7-Ru reduces the accessibility of O_2 to the ruthenium center, thereby enhancing the emission. However, control experiments performed under degassed conditions showed that CB7-Ru retains its sensing behavior upon amantadine addition, but with overall higher emission intensity, as expected in the absence of O_2 . (**Fig. 5.23**) Therefore, while oxygen quenching plays a role in absolute emission intensity, it does not account for the guest-induced modulation, confirming that the sensing mechanism is not driven by oxygen displacement.

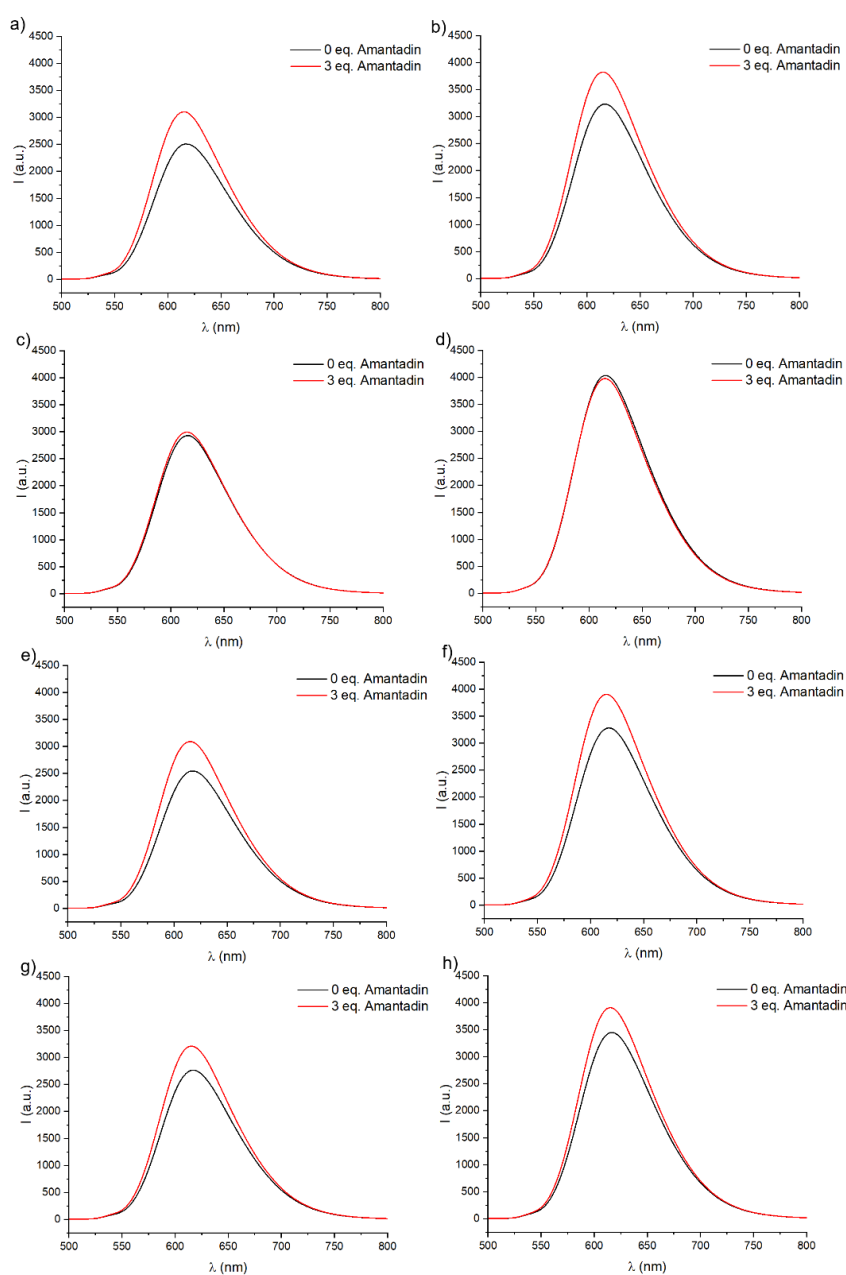


Fig. 5.23: Comparison of the emission spectra ($\lambda_{exc} = 452$ nm) of CB7-Ru upon addition of 3 equivalents amantadine under aerated and degassed conditions. a) Aerated, water. b) Degassed, water. c) Aerated, HEPES. d) Degassed, HEPES. e) Aerated, PB. f) Degassed, PB. g) Aerated, PBS. h) Degassed, PBS.

In parallel, the known solvatochromism for Ru complexes offers additional insight.³²¹ Ru(bpy)₃²⁺ is known to emit more intensely in less polar solvents, such as acetonitrile, than in water.³²² It also displays slight positive solvatochromism, with the emission maximum shifting from 611 nm in MeCN to 626 nm in H₂O.³²² When comparing RuBiPy in water (λ_{em} = 608 nm at 5 μ M) with the covalently tethered CB7-Ru (λ_{em} = 617 nm at 5 μ M), again a clear red shift and decreased emission intensity can be observed (**Fig. 5.13 a**). This is consistent with an increase in local polarity at the Ru center, induced by its proximity to the CB7 portals.

A more comprehensive explanation lies in the unique hydration structure and electrostatic environment at the CB7 portals. Recent studies have shown that formation of CBn inclusion complexes in water affects different molecular regions asymmetrically: encapsulated subunits experience reduced polarity, while subunits adjacent to the cavity experience an increase in local polarity. This cannot be explained by traditional electronic effects alone. Kaifer and others have proposed that the carbonyl portals act as ‘structure-makers’, organizing surrounding water molecules into tightly bound hydration shells.³¹⁴ This concept is supported by crystallographic evidence, including the observation of organized water clusters such as H₁₄O₆²⁺.^{323, 324} These highly polar, organized hydration layers may exert a strong influence on adjacent chromophores. In this context, the guest-induced displacement or disruption of these structured water molecules by amantadine and other guests likely reduces the local polarity experienced by the Ru(bpy)₃ core, resulting in the observed blue shift (λ_{em} = 617 nm to λ_{em} = 614 nm) and emission enhancement (**Fig 5.17, Fig. 5.18, Fig. 5.24**). This hypothesis is further supported by the similarity of the photophysical behavior between CB7-Ru and the Ada-Ru•CB7 non-covalent system (**Fig. 5.17 b**): proximity to the CB7 portal – not inclusion in the cavity – is sufficient to modulate emission.

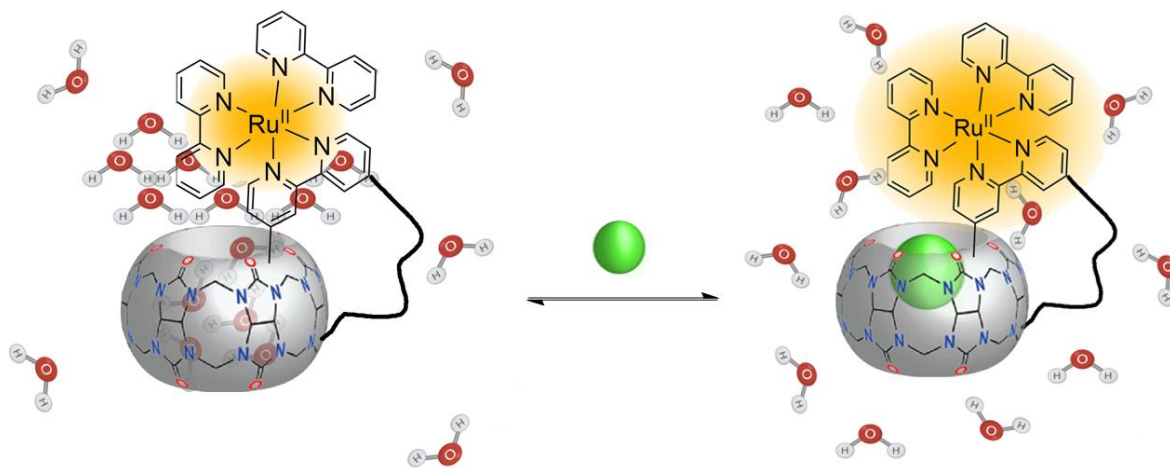


Fig. 5.24: Proposed mechanism of fluorescence response upon amantadine addition. The microenvironment of the portals is of higher polarity, causing a diminished fluorescent response. Upon guest addition, cavity-bound water is displaced and the network gets disrupted, causing the microenvironment to get less polar and an increase in fluorescence.

To further probe the origin of the observed shifts in fluorescence intensity and emission maxima, a comparative analysis of the emission behavior of Ada-Ru, RuBiPy, and CB7-Ru (λ_{exc} = 452 nm) was conducted (see Supplementary Information). These experiments aimed to evaluate whether the linker or

the covalent modification itself could account for the photophysical changes, or if they are more plausibly attributed to modifications in the hydration shell surrounding the CB7 portals.

Interestingly, all three compounds exhibited distinct emission spectra under identical conditions, indicating that structural differences – particularly the substitution of one bipyridine ligand – do influence the photophysical behavior. However, one would also expect different photophysical behavior of different compounds. To better understand the impact of (solvent) polarity on emission properties, additional control experiments were performed using RuBiPy (see Supplementary Information) and Ru-COOH in water, acetonitrile and methanol (**Fig. 5.25**). While a consistent trend in emission intensity across the solvents could not be established – likely due to differences in excitation efficiency at a fixed wavelength ($\lambda_{\text{exc}} = 452 \text{ nm}$) – a clear trend was evident in the emission maxima. As solvent polarity decreased from water to acetonitrile to methanol, a corresponding blue shift in the emission maximum was observed. This finding lends further support to the hypothesis that changes in the local solvation environment – particularly a reduction near the ruthenium center upon guest binding – play a key role in modulating fluorescence. Although ligand substitution may contribute to the observed photophysical changes, the solvatochromic behavior observed across the complexes, including those with substituted bipyridine ligands, underscores the generality of this polarity-dependent phenomenon.

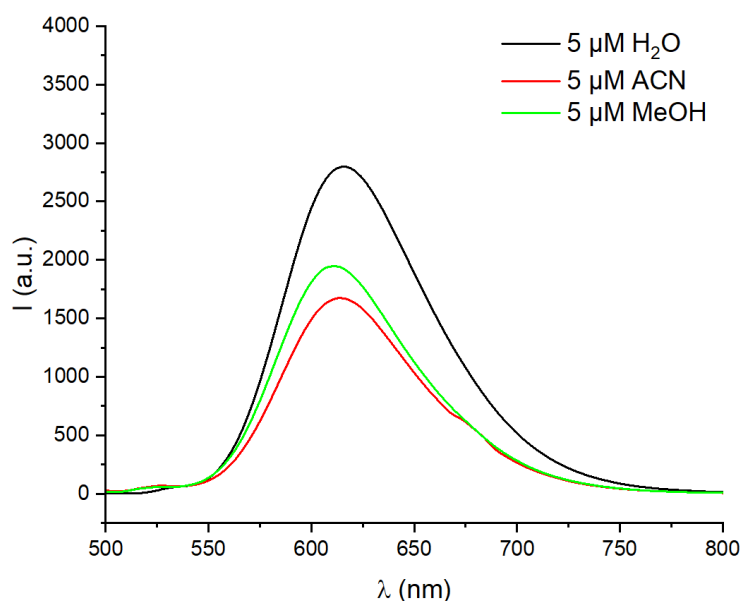


Fig. 5.25. Comparison of the fluorescence response ($\lambda_{\text{exc}} = 452 \text{ nm}$) of Ru-COOH in various solvents.

In summary, the emission changes in CB7-Ru are best understood as a result of dynamic reorganization of the local supramolecular microenvironment around the Ru(II) chromophore. This environment is shaped by electrostatic interactions, water structuring effects at the carbonyl portals, and guest-induced perturbations – rather than classical encapsulation or direct host-guest interactions detectable by NMR. These portal effects represent a previously rather underappreciated mechanism of emission modulation in supramolecular sensing systems and open new possibilities for the design of proximity-based fluorescent sensors.

5.5. Electrochemical Properties and ECL-Sensing Capabilities of CB7-Ru

Electrochemical measurements were partly done in cooperation with Maria Vittoria Balli, University of Bologna.

Having established the distinctive and interesting photophysical behavior of the CB7-Ru conjugate, attention was next directed towards its electrochemiluminescent properties. ECL, which involves the generation of excited states through electrochemical reactions, offers significant advantages for sensing applications due to its high sensitivity, low background noise, and spatially controlled excitation. In particular, the classical $[\text{Ru}(\text{bpy})_3]^{2+}/\text{TPrA}$ system has served as a benchmark in ECL-based assays, owing to its excellent redox and emissive properties under physiological conditions. However, as previously discussed, efficient ECL generation is governed not only by the intrinsic properties of the luminophore, but also by the spatial and dynamic proximity of the co-reactant. The covalent attachment of CB7 to the $\text{Ru}(\text{bpy})_3$ scaffold introduces a novel supramolecular dimension to this system. Specifically, the cavity of CB7 can host co-reactants such as TPrA, potentially altering the efficiency of radical cation formation, facilitating energy transfer to the Ru(II) and to create a supramolecular system for ECL signal amplification. This section investigates the ECL behavior of CB7-Ru, with particular attention to how host-guest interactions and the so called ‘portal effect’ impact ECL signal intensity, especially in the presence of competing guest analytes.

To complement the photophysical titration studies – which showed a characteristic fluorescence enhancement upon guest addition – ^1H NMR experiments were conducted to probe the binding behavior of TPrA (**Fig. 5.26**). As expected for small aliphatic amines, clear evidence of inclusion was observed. Upon addition of TPrA to CB7-Ru, the methylene group adjacent to the nitrogen (TPrA a) shifted from 2.36 ppm to 2.98 ppm, while the neighboring methylene (TPrA b) shifted from 1.47 ppm to 1.65 ppm. In contrast, the terminal methyl group exhibited only a minor shift (0.93 to 0.95 ppm), consistent with partial encapsulation of the TPrA alkyl chains.

Interestingly, comparison of the ^1H NMR spectra of CB7-Ru before and after TPrA addition (see Supplementary Information) revealed only subtle changes in the resonances associated with the chemosensor. This observation is consistent with the notion that small and non-cationic guest molecules such as TPrA do not induce a complete conformational rearrangement or unfolding of the CB7-Ru conjugate. Nevertheless, TPrA binding resulted in a clear enhancement of the fluorescence intensity, further supporting the hypothesis that guest inclusion displaces cavity-bound water and perturbs the structured solvation shell around the CB7 portals, thereby reducing the local microenvironmental polarity. These results provide a valuable mechanistic insight into how supramolecular interactions at the CB7 portals modulate the photophysical and electrochemical behavior of the appended ruthenium luminophore through proximity-driven effects.

For the initial evaluation of the ECL properties of CB7-Ru, a concentration of 10 μM was used (**Fig. 5.27**). ECL emission was generated *via* cyclic voltammetry (CV) in phosphate buffer (0.3 M, pH 6.8) in the presence of TPrA (120 mM). The results confirmed that the electrochemical activity of the

Ru(II) center is retained upon covalent conjugation to CB7. Comparative measurements were performed with $[\text{Ru}(\text{bpy})_3]^{2+}$, the model compound Ada-Ru, and its non-covalent complex with CB7 (Ada-Ru•CB7) under identical conditions. Interestingly, CB7-Ru produced a notably stronger ECL signal than $[\text{Ru}(\text{bpy})_3]^{2+}$ at the same concentration, indicating that the supramolecular architecture of the conjugate may enhance ECL performance – likely through proximity effects with the co-reactant. As expected, RuBiPy and Ada-Ru showed nearly identical ECL responses. Notably, the addition of 1 equivalent of CB7 to Ada-Ru did not lead to any signal enhancement. This suggests that the adamantane unit effectively blocks the CB7 cavity, thus preventing efficient co-reactant binding and access to the ruthenium center. After this successful proof-of-concept, further ECL investigations were carried out in Bologna using a more sensitive instrument to explore the system in greater detail.

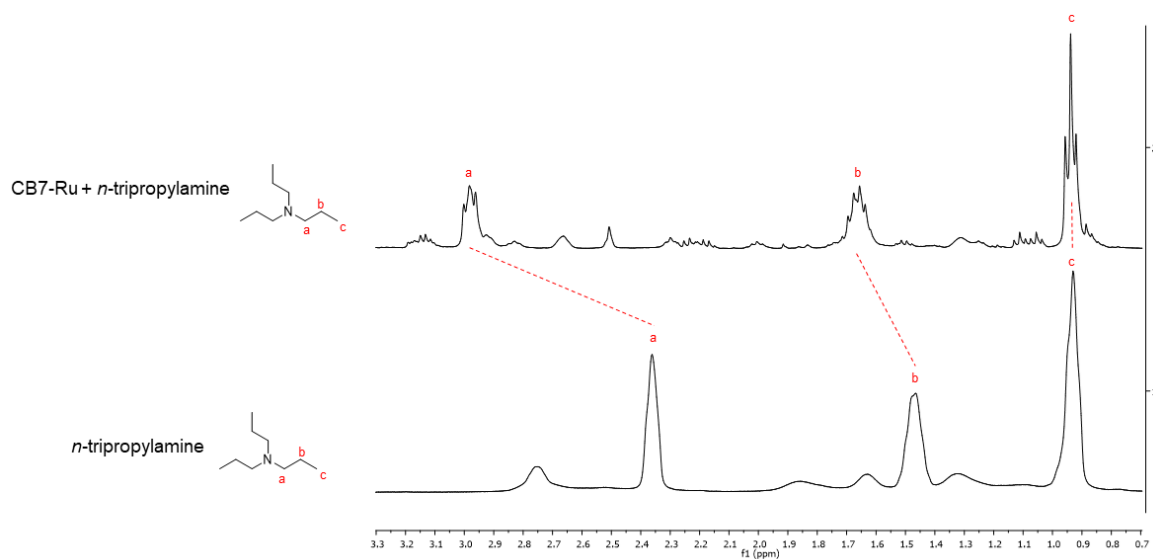


Fig. 5.26: Overlay of ^1H NMR (400 MHz, D_2O) spectra of tri-*N*-propylamine (bottom) and tri-*N*-propylamine in the presence of CB7-Ru (top).

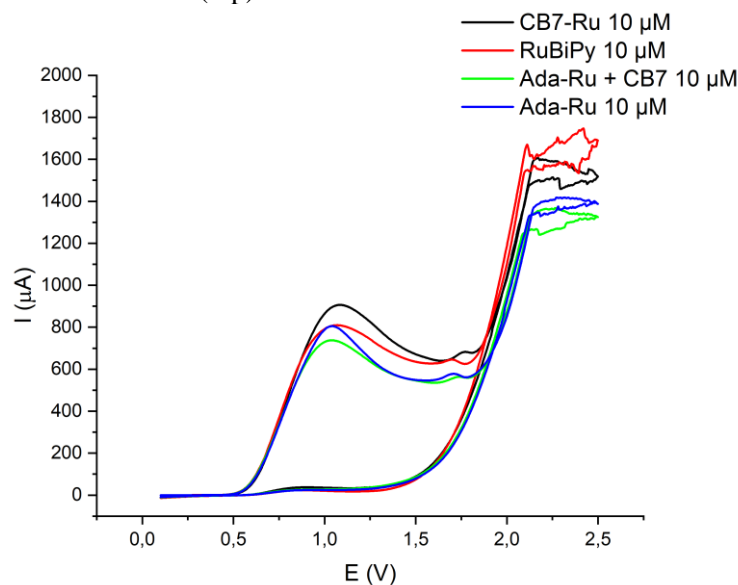


Fig. 5.27: CV plots of CB7-Ru, RuBiPy, Ada-Ru, and Ada-Ru•CB7, each at a concentration of 10 μM . Measurements were performed in PB 0.3 M, pH 6.8, TPrA 120 mM.

To optimize ECL performance and minimize potential aggregation effects, lower concentrations of CB7-Ru were explored. ECL emission could be effectively triggered at 0.5 μM in phosphate buffer (PB, 0.3 M, pH 6.8), yielding a 163% signal enhancement compared to $[\text{Ru}(\text{bpy})_3]^{2+}$ (RuBiPy) under identical conditions. This significant increase in ECL output further supports the signal amplification mechanism introduced by covalent CB7 conjugation.

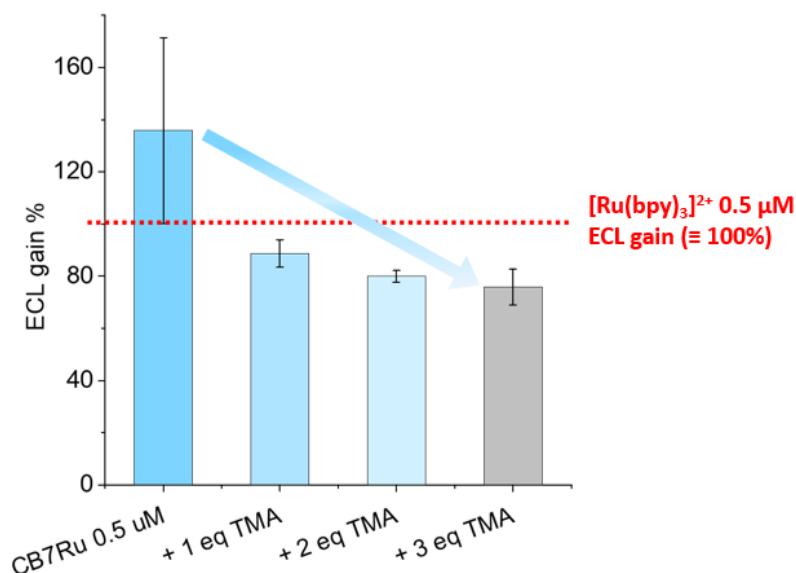


Fig. 5.28: ECL signal reported from CB7-Ru (0.5 μM) in PB (0.3 M, pH 6.8) with 180 mM TPrA. The signal was standardized on the ECL signal for $[\text{Ru}(\text{bpy})_3]^{2+}$ measured under the same conditions.

To identify the optimal TPrA concentration, CB7-Ru solutions were tested with increasing co-reactant levels (20 mM, 80 mM, 180 mM). The most consistent and highest signal enhancement was observed at 180 mM TPrA, which corresponds to the plateau concentration determined from the TPrA binding isotherm with CB7-Ru. This condition was adopted for all subsequent ECL measurements.

Due to the potentially interfering nature of amines in ECL assays, *N,N,N*-trimethyladamantaneammonium hydroxide (TMA) was employed instead of amantadine as a high-affinity CB7 guest. Notably, TMA addition resulted in ECL signal quenching, which contrasts sharply with the fluorescence enhancement seen under photoluminescence conditions. (**Fig. 5.28**) This opposing behavior can be rationalized by the competitive displacement of TPrA from the CB7 cavity by TMA. Two primary mechanisms are proposed for the ECL enhancement: on the one hand, pre-association of TPrA with CB7-Ru (**Fig. 5.29 a**), which facilitates interaction between the co-reactant and the Ru center because of close proximity, or, on the other hand, stabilization of the TPrA radical cation ($\text{TPrA}^{+\cdot}$) occurs, which supports the oxidation cycle of the ECL process. Indeed, cucurbiturils are known to bind and stabilize radical cations in aqueous media, which likely contributes to a shift in the ECL equilibrium toward $\text{TPrA}^{+\cdot}$ formation.^{325, 326} This supramolecular confinement of the co-reactant and/or its reactive intermediate reduces diffusional distances and improves ECL efficiency. Control experiments confirmed that this effect is not observed in non-covalent mixtures of CB7 and RuBiPy (1:1 or 1:10 ratios),

highlighting the critical importance of unimolecular integration in the CB7-Ru system (see Supporting Information).

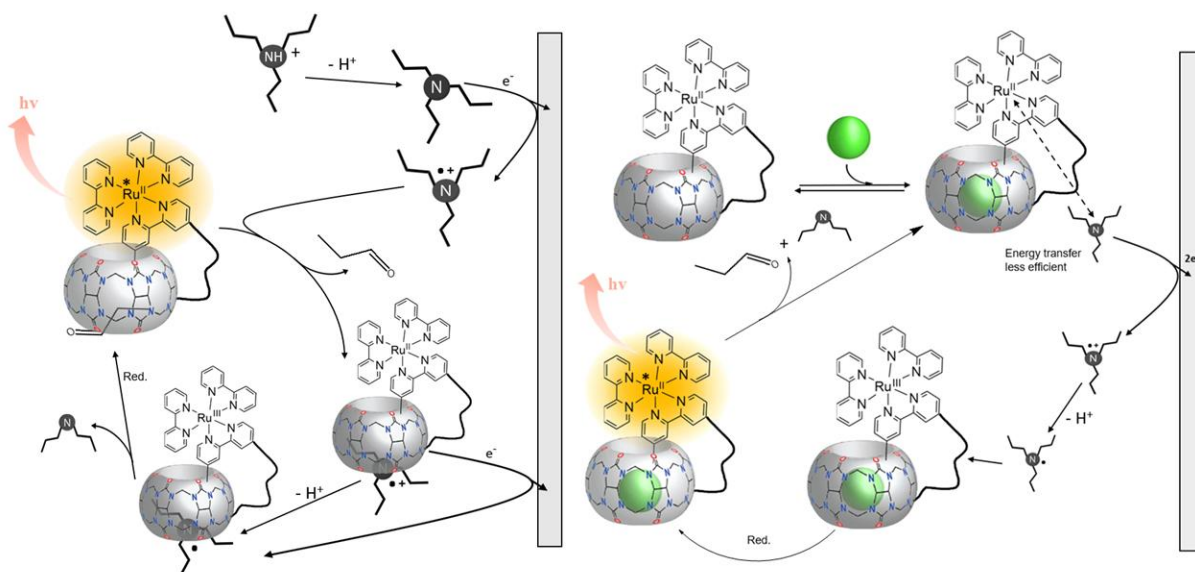


Fig. 5.29: The proposed ECL reaction mechanism is schematized in the following pictures, where: a) the ECL enhancement is due to the elimination of the coreactant diffusion contribution to the generation of the analytical signal, through the interaction of TPrA with the carbonyl portals of the CB7; b) the radical cation form of TPrA is stabilized upon its interaction with the CB7 carbonyl portals, shifting the equilibrium toward the formation of TPrA^{•+}.

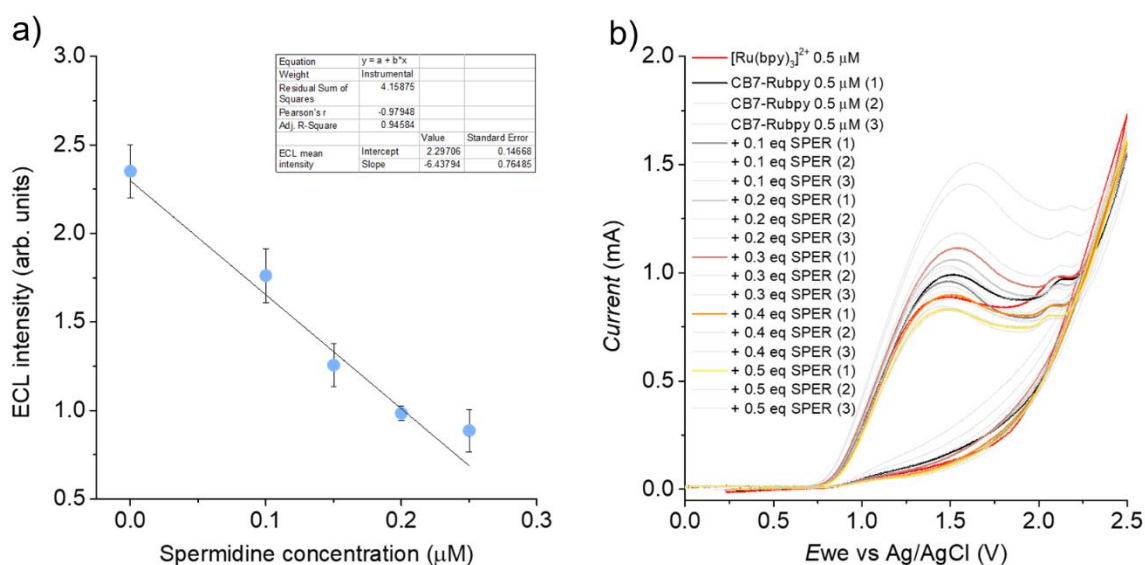


Fig. 5.30: CV-ECL measurements performed in a 0.3 M PB solution at pH 6.8, with TPrA 180 mM. The working electrode potential was scanned at 100 mV/s, and emission acquired every 100 ms (PMT bias 750 mV, positioned on the short side of the cell). Amplification level at 00.0 μA . a) Calibration curve for LoD determination, reporting ECL maximum intensities for CB7-Ru 0.5 μM vs the added spermidine trihydrochloride concentration (0.1-0.5 eq. SPER added, SD calculated for $n \geq 3$). b) Corresponding CV plots.

Building upon this promising behavior, the system was next evaluated for small-molecule detection, a domain typically challenging in ECL due to the limited size and epitope accessibility of such analytes.

Here, the universal binding capabilities of CB7 offer a major advantage over conventional antibody-based systems. As model analytes, nandrolone and spermidine – both of biomedical relevance – were tested (see Supporting Information). In both cases, ECL intensity decreased upon analyte addition, consistent with competitive displacement of TPrA or interference with its proximity to the Ru center. Importantly, the limit of detection (LOD) for spermidine was determined to be 76 nM, a value comparable to that reported for conventional enzyme-linked immunosorbent assays (ELISA), which typically reach LODs in the ~0.1 μ M range.

5.6. Photodynamic Therapy: Mechanisms and Biomedical Applications

Photodynamic therapy (PDT) is a non-invasive and highly selective therapeutic approach used in the treatment of various cancers and non-malignant diseases, including skin condition, bacterial infections, and chronic inflammatory disorders.^{327, 328} The fundamental mechanism of PDT involves the administration – either locally or systemically – of a photosensitizer, a molecule that preferentially accumulates in diseased tissues and becomes activated upon exposure to light of a certain wavelength.^{329, 330} Upon excitation, the photosensitizer transfers energy or electrons to surrounding biomolecules or molecular oxygen, initiating a cascade that generates reactive oxygen species (ROS).³³¹ These ROS, such as singlet oxygen or free radicals, subsequently lead to cellular damage and apoptosis, offering a minimally invasive and spatially controlled therapeutic effect.

The core photophysical processes in PDT closely mirror those found in photoredox catalysis. Upon light absorption, the photosensitizer enters an excited singlet state, which may undergo intersystem crossing (ISC) to form a longer-lived triplet state.^{332, 333} This triplet state can then engage in either type I (electron/hydrogen transfer) or type II (energy transfer) mechanisms to generate ROS. The efficiency of ISC, and therefore ROS generation, is critical for therapeutic efficacy. Polypyridyl ruthenium(II) complexes are of particular interest in this context due to their high photostability, efficient ISC, and tunable photophysical properties, enabling both fluorescence-based tracking and ROS production *via* electron transfer mechanisms.^{334, 335} Modern strategies aim to further improve PDT efficacy and specificity by combining photosensitizers with nanocarriers or supramolecular scaffolds.³³⁶ These systems can enhance tumor selectivity, improve water solubility, and reduce off-target toxicity. Moreover, integrating PDT with other therapeutic modalities, such as chemotherapy or immunotherapy, offers a promising route to synergistic treatment regimens.^{337, 338} Key criteria for an ideal photosensitizer include strong absorption in the visible or near-infrared region for better tissue penetration, low dark toxicity, and selective accumulation in diseased tissue. Addressing the latter is a central challenge in PDT. One promising approach is the supramolecular functionalization of photosensitizers with host molecules such as cucurbiturils, which are known to bind a variety of biologically relevant targets in aqueous environments with high affinity and selectivity.

In this context, the CB7-Ru conjugate developed in this work presents a novel unimolecular platform that integrates the luminescent and photosensitizing capabilities of $\text{Ru}(\text{bpy})_3^{2+}$ with the molecular

recognition properties of CB7. For instance, the inclusion of amantadine could serve as a disease-targeting moiety, allowing for functionalization with ligands or biomolecular vectors that direct the system to specific pathological environments. Furthermore, by leveraging CB7's capacity to dynamically bind and displace small molecules, this system could also allow on-demand activation or enhancement of PDT efficacy in the presence of specific biomarkers. This design enables responsive modulation of ROS generation, enhancing both the selectivity and safety profile of PDT agents. In the following section, the CB7-Ru conjugate is evaluated in a biological context and its photodynamic behavior under light activation is explored, aiming to assess the potential as a supramolecularly modulated photosensitizer for cancer therapy.

5.6.1. Bioanalytical Evaluation of CB7-Ru for Light-Activated Anticancer Applications

The biological evaluation of CB7-Ru was performed by Dr. Giulia Salluce at the Chimie ParisTech.

To investigate the potential of CB7-Ru as a photosensitizer for photodynamic therapy, a fluorometric viability assay was conducted across four different cell lines: glioblastoma (U87), lung adenocarcinoma (A549), colorectal adenocarcinoma (HT29), and non-cancerous retinal pigment epithelial cells (RPE-1). Cells were incubated with increasing concentrations of CB7-Ru (up to 100 μM) in culture medium for four hours. Following incubation, the medium was replaced with fresh culture medium prior to irradiation. Protoporphyrin IX (PpIX), a well-established photosensitizer, was used as a positive control. Cells were then either exposed or not exposed to 450 nm light, a wavelength corresponding to the $^3\text{MLCT}$ absorption band of CB7-Ru, for 2 minutes. Across all cell lines, CB7-Ru exhibited no significant cytotoxicity under dark conditions or upon irradiation. The observed cell viability post-illumination was comparable to that of the light only control, indicating that under these experimental conditions, CB7-Ru does not induce phototoxic effects.

Compound	Cell line	IC ₅₀ dark (μM)	IC ₅₀ light (μM)
CB7-Ru	U87	> 100	n.d.
	A549	> 100	n.d.
	HT29	> 100	n.d.
	RPE-1	> 100	n.d.
PpIX	U87	> 100	n.d.
	A549	> 100	0.55 \pm 0.16
	HT29	> 100	0.25 \pm 0.19
	RPE-1	> 100	0.05 \pm 0.01

Table 5.3. IC₅₀ values in the dark and upon light irradiation at 450 nm for 2 minutes on glioblastoma cells (U87), adenocarcinomic human alveolar basal epithelial cells (A549), adenocarcinomic human colorectal epithelial cells (HT29), and non-cancerous retinal pigmentary epithelial cells (RPE-1). Average of three independent measurements; n.d. = not determinable.

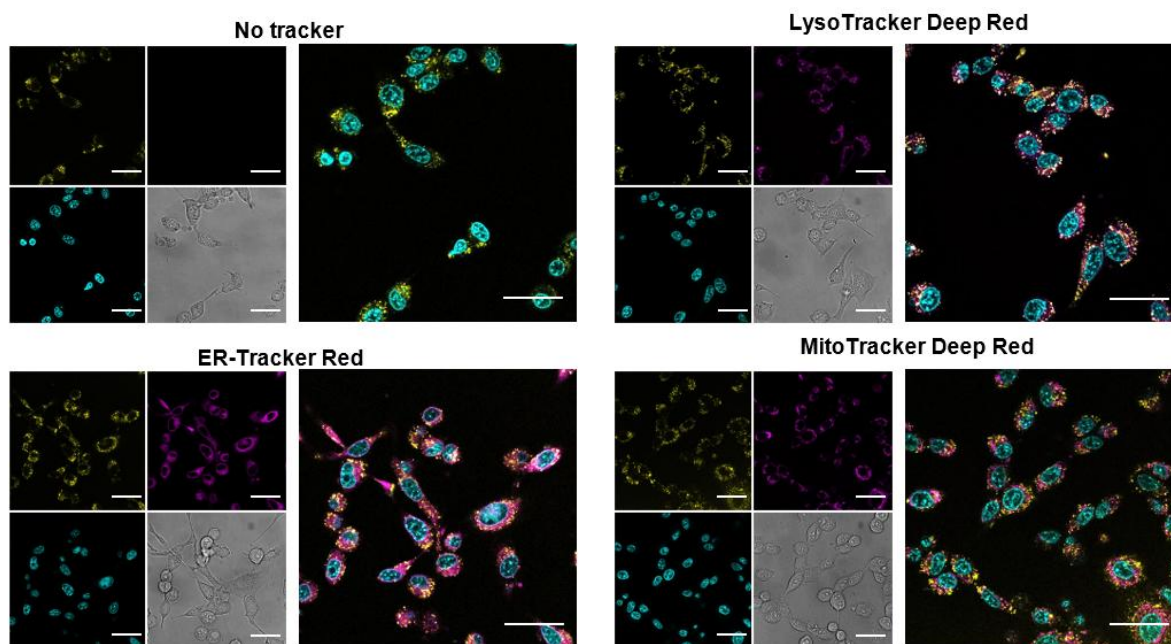


Fig 5.31: Subcellular localization of CB7-Ru in U87 cells by confocal fluorescence microscopy, following incubation with 20 μM CB7-Ru (yellow) for 4 h and then with Hoechst 33342 (cyan) to stain the nuclei and ER-Tracker RedTM, or LysoTracker Deep RedTM, or MitoTracker Deep RedTM to stain the endoplasmic reticulum, the lysosomes, or the mitochondria, respectively (magenta). Scale bars are 40 μm .

To evaluate the cellular uptake and intracellular distribution of CB7-Ru, confocal fluorescence microscopy was performed on U87 glioblastoma cells. Cells were incubated with 20 μM CB7-Ru in standard culture medium for 4 hours, followed by imaging. The resulting fluorescence images revealed a punctate distribution pattern throughout the cytoplasm, indicative of compartmentalized accumulation within discrete intracellular vesicles rather than homogeneous cytosolic or nuclear localization. This spatial confinement suggests that CB7-Ru is internalized *via* endocytic pathways and subsequently sequestered within vesicular compartments, likely limiting its interaction with vital cellular targets.

5.7. Conclusions

In this chapter, the successful design and synthesis of a unimolecular cucurbit[7]uril-ruthenium(II) tris bipyridine (CB7-Ru) conjugate has been presented. The system exhibits distinct and previously underappreciated photophysical behaviors, driven by proximity-induced effects at the CB7 portals, rather than by traditional host-guest encapsulation. Detailed spectroscopic investigations in aqueous media and buffered environments revealed that the variations in fluorescence intensity and emission maximum are primarily governed by the disruption of the structured hydration shell at the CB7 portals, rather than conformational unfolding of the conjugate. This so-called “portal effect” emerges as a key factor in modulating the photophysical and electrochemical properties of CB7-Ru. Notably, the system enables a dual readout *via* both photoluminescence and electrochemiluminescence, without requiring any surface modification of the electrode. Binding studies using ¹H NMR and photoluminescence further confirmed

that guest molecules can modulate the emission properties of the Ru center without compromising the unimolecular integrity of the sensor.

Interestingly, the system exhibits opposing signal trends in fluorescence versus ECL readouts, each governed by distinct mechanisms. In photoluminescence, the emission is primarily influenced by the local polarity at the CB7 portals. In absence of a guest, a highly structured water network forms around the portals, resulting in a more polar microenvironment and lower emission intensity. Guest binding disrupts this network, reducing local polarity and enhancing the emission – behavior reminiscent of solvatochromism in Ru(II) complexes. In electrochemiluminescence, the signal enhancement arises from favorable binding of the co-reactant TPrA to the CB7 cavity. This binding shortens the effective distance between TPrA (or its radical cation) and the Ru center, improving the efficiency of the electron-transfer process. Upon guest addition, TPrA is displaced from the cavity, increasing the spatial separation and consequently reducing the ECL signal.

The modular nature of the system allows for potential replacement of the ruthenium(II) bipyridine complex with alternative ECL-active units, such as more advanced ligands on ruthenium, either increasing water-solubility or affinity for certain motifs, or even the variation for other cyclometalated complexes such as iridium, which could broaden the spectral window or improve emission efficiencies depending on the desired application.

Looking forward, these results open intriguing perspectives for biological sensing applications. For example, the system could be adapted for the detection of adamantane-labelled biomolecules such as modified proteins or peptides. Furthermore, since the CB7-Ru conjugate exhibits measurable affinity for residues like phenylalanine and phenylalanine glycine – common motifs in proteins such as insulin – it may be possible to achieve direct detection of native proteins without chemical labelling.

5.8. Experimental Part

5.8.1. Material and Methods

5.8.1.1. Material

All purchased chemicals and solvents were used as received from suppliers without any further purification. PBS buffer (pH = 7.4, 0.01 M) was prepared by dissolving 8 g NaCl, 0.2 g KCl, 1.44 g Na₂HPO₄ and 0.245 g KH₂PO₄ in 1 L MilliQ water and adjust the solution with NaOH or HCl solution. PB buffer (pH = 7.4, 0.01 M) was prepared by dissolving 2.021 g Na₂HPO₄ and 0.339 g NaH₂PO₄ in 1 L MilliQ water and adjust the solution with NaOH or HCl solution. HEPES buffer (pH = 7.4, 0.01 M) was prepared by dissolving 2.38 g HEPES in 1 L MilliQ water and adjust the pH with NaOH solution. 1,1'-(octane-1,8-diyl)bis(3-methyl-1H-imidazol-3-ium) bromide (C₈mimBr₂)³³⁹ and 2,7-dimethyldiazapyrenium diiodide (MDAP)⁴⁹ were synthesized according to established literature methods. Solutions of [Ru(bpy)₃]Cl₂ × 6 H₂O, Ada-Ru and CB7-Ru were determined by UV-vis at 452 nm. CB7 solution was determined using a pre-determined solution of berberine chloride (22500 M⁻¹cm⁻¹ at 344 nm) and a pre-determined solution of amantadine. The concentration of metal

nitrate in solution was accurately determined using the molar absorption coefficient ($9500 \text{ M}^{-1}\text{cm}^{-1}$ at 201 nm). L-phenylalanine (Phe), L-phenylalanyl glycine (PheGly), methyl viologen (M_2V), and nortestosterone (nandrolone) were determined by using their molar absorption coefficients (L-phenylalanine: $200 \text{ M}^{-1}\text{cm}^{-1}$ at 257 nm, L-phenylalanyl glycine: $195 \text{ M}^{-1}\text{cm}^{-1}$ at 257.6 nm, methyl viologen: $20700 \text{ M}^{-1}\text{cm}^{-1}$ at 257 nm, and 19-nortestosterone: $15320 \text{ M}^{-1}\text{cm}^{-1}$ at 248 nm) by UV-Vis absorption titration measurements in MilliQ water. Concentration of the other analyte stock solutions was determined by weight. Fluorescence titration experiments with the Ru-species were conducted with $\lambda_{\text{exc}} = 452 \text{ nm}$ and $\lambda_{\text{em}} = 610 \text{ nm}$. For extraction of K_a , the data were fitted using a standard 1:1 host-guest binding model with the fitting app of Ahmad Omira. (<https://github.com/ahmadomira/fitting-tool>)

5.8.1.2. Nuclear Magnetic Resonance (NMR) Spectroscopy

^1H and ^{13}C NMR spectra were recorded either in deuterium oxide (D_2O), Chloroform- d_3 , DMSO- d_6 , Acetonitrile- d_3 or Methanol- d_4 on a Bruker Avance 400 spectrometer or a Bruker Avance 500 spectrometer at 25°C . The ^1H and ^{13}C NMR chemical shifts (δ) are given in ppm and refer to residual protons on the corresponding deuterated solvent.

5.8.1.3. High-Performance Liquid Chromatography (HPLC)

Analytical HPLC experiments were performed on an LC-2000Plus HPLC system equipped with a UV-2075 UV-Vis detector and a Kromasil 100 C18 5 μM LC column ($250 \times 4.6 \text{ mm}$, Agela) at a flow rate of 0.8 mL/min .

For the analytical HPLC the following parameters were used:

Anal. method 1: Isocratic elution $\text{H}_2\text{O}(+0.1\% \text{ TFA})/\text{ACN}$ 40:60; UV detection at $\lambda=450 \text{ nm}$; FL detection in single mode at $\lambda_{1,\text{abs}}=450 \text{ nm}$ and $\lambda_{1,\text{ems}}=628 \text{ nm}$.

5.8.1.4. Electrospray Ionization Mass Spectrometry (ESI-MS)

Spectra were recorded on a Orbitrap Exploris 240 (MM10525C) mass spectrometer (Thermo Fisher Scientific) equipped with a HESI II probe. The instrument was calibrated in the m/z range 200-2000 for positive mode using premixed calibration solutions (FlexMix-Thermo Scientific). Spray voltage, sheath gas and auxiliary gas pressure were used in the range of 1.75 V, for positive mode. Spray voltage, sheath gas and auxiliary gas pressure was set to 1.9 V. The ion transfer tube temperature was set to 320°C . MeOH: H_2O (1:1) solvents was used as eluent. Injection of the samples was carried out with the aid of a Hamilton® syringe 725RN 500 μL at a flow rate of $25 \mu\text{L/min}$ using a single syringe pump.

5.8.1.5. Absorbance Spectra

Absorbance spectra were measured in Milli-Q water on a Jasco V-730 double-beam UV-Vis spectrophotometer at 25°C . PMMA cuvettes with a light path of 10 mm and dimensions of $10 \times 10 \text{ mm}$ from Brand with a spectroscopic cut-off at 220 nm were utilized for UV-Vis absorption experiments. The

samples were equilibrated using a water thermostatic cell holder STR-812, while the cuvettes were equipped with a stirrer allowing rapid mixing.

5.8.1.6. Fluorescence Spectra

Steady-state emission spectra and time-resolved emission profiles were recorded on a Jasco FP-8300 fluorescence spectrometer equipped with a 450 W Xenon arc lamp, double-grating excitation and emission monochromators. Standard correction curves corrected the emission spectra for source intensity (lamp and grating) and the emission spectral response (detector and grating). All titration and kinetic experiments were carried out at 25°C using a water thermostatic cell holder STR-812, while the cuvettes were equipped with a stirrer allowing rapid mixing. PMMA cuvettes with a light path of 10 mm and dimensions of 10 × 10 mm from Brand with a spectroscopic cut-off at 300 nm were utilized for fluorescence-based titration experiments.

5.8.1.7. Excited State Lifetime Measurement

Lifetime decays were recorded with an Edinburgh FLS1000 equipped with an EPL – Picosecond Pulsed Diode Laser ($\lambda_{exc} = 475$ nm, pulses duration < 100 ps, repetition rates up to 20 MHz) and a standard detector photomultiplier tube (PMT) –980 in cooled housing (wavelength coverage of 185 nm to 900 nm, dark count rate of < 50 cps – cooled to -20°C). The instrument is also equipped with a time-correlated single photon counting (TCSPC) device (the detector is operated in single photon counting mode throughout all time ranges, with a detector response width of ~600 ps). The TCSPC is based on the probability that a single photon emitted by a luminescent sample is collected by a proper high sensitivity detector: this probability is statistically correlated with the variation of the concentration of the excited states in solution.

5.8.1.8. High-Performance Liquid Chromatography-mass spectrometry (HPLC-MS)

LC-MS measurements were performed on an Agilent 1260 Infinity II system consisting of a quaternary pump (GB7111B), autosampler (G7129A, 100 μ L sample loop), a temperature-controlled column oven (G7114A) and a variable UV-Vis detector (G7114A, VWD, flow cell G7114A 018, d = 10 mm, V = 14 μ L). Separation was performed on a C18 HPLC column (Agilent Poroshell 120 EC-C18 4.6x100 mm, 2.7 μ m) operating at 40 °C. A gradient of acetonitrile:H₂O 45:55 – 100:0 (v/v) (additive 10 mmol L⁻¹ ammonium formate) at a flow rate of 1 mL min⁻¹ during 9 min was used as the eluting solvent. The flow was directed into an Agilent MSD (G613BA, AP-ESI ion source). The instrument was calibrated in the m/z range 118-2121 in positive mode and 113-2233 in the negative mode, using a premixed calibration solution (Agilent). The following parameters were used: spray chamber flow: 12 L min⁻¹, drying temperature: 350 K, Capillary Voltage: 3000 V, Fragmentor Voltage: 100 V.

5.8.1.9. Electrochemiluminescence (ECL) Instrumentation

Measurements done in Karlsruhe:

For each measurement, a new screen-printed carbon electrode (Metrohm, SPE, DRP-110-U75) was used. Main features of SPEs: working electrode material = carbon (diameter 0.40 cm, position in the middle of the strip); auxiliary electrode material = carbon, reference electrode material = silver, contacts material = silver, substrate material = ceramic. Substrate size: length = 3.38 cm, width = 1.02 cm, thickness = 0.05 cm.

ECL emission was triggered and recorded using a SpectroECL device (Metrohm).

Measurements done in Bologna:

For each sample measurement, a new screen-printed carbon electrode (SPE, C110) was used. Main features of SPEs: working electrode material = carbon (diameter 0.40 cm, position closer to the end of the strip – designed for work in solution applications); auxiliary electrode material = carbon; reference electrode material = silver; contacts material = silver; substrate material = ceramic. Substrate size: length = 3.38 cm, width = 1.02 cm, thickness = 0.05 cm.

To record the ECL intensity, a PTFE homemade electrochemical cell was built using a Starna glass cell (type 3/G/20, path length = 2 cm), comprising the SPE, an external Pt counter and Ag/AgCl (3 M KCl) reference electrode. ECL spectra were collected by a PMT, and the recorded emission amplified to either a 0.00 μ A or a 00.0 μ A level using a Keithley Model 6485 Picoammeter (Keithley Instruments Inc., Ohio, United States). The system was enclosed in a homemade dark box to avoid interferences from external light. The ECL emission was triggered by anodic potential sweep during cyclic voltammetry controlled by a SP-300 potentiostat.

5.8.1.10. Cell culture

U87 cells were cultured in DMEM, A549 were cultured in Ham's F-12K medium, HT29 in McCoy's 5A modified medium, and RPE-1 cells in DMEM/F-12. All the media were from Gibco (Life Technologies, USA) and were supplemented with 10 % fetal bovine serum and 1 % penicillin-streptomycin mixture, both from Gibco. All cell lines were maintained in a humidified atmosphere at 37 °C and 5 % of CO₂

5.8.1.11. (Photo)toxicity

U87, A549, HT29, and RPE-1 cells were seeded at a density of 8,000 cells/well in 96-well plates (100 μ L/well) and incubated at 37 °C, 5 % CO₂. The next day, the medium was replaced by CB7-Ru or PpIX dilutions up to 100 μ M in fresh medium (100 μ L/well) from 10 mM stock solutions in DMSO. After 4 h of incubation at 37 °C, 5 % CO₂, the solutions were replaced with 100 μ L of fresh medium. Plates were then illuminated at 450 nm for 2 min using a LUMOS-BIO photoreactor (Atlas Photonics); control "dark" plates were not subjected to light irradiation. Cells were incubated for an additional 44 h at 37 °C, 5 % CO₂. After that, the medium was replaced with 100 μ L of fresh medium containing 0.2 mg/mL resazurin

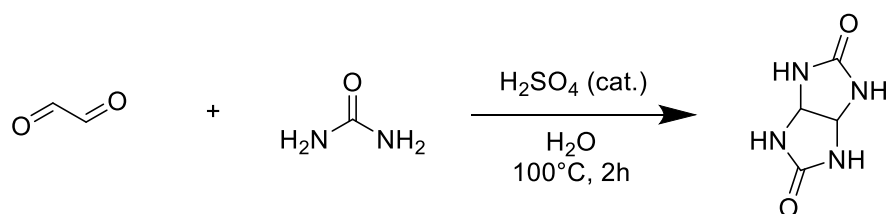
(Acros Organics). After 4 h of incubation at 37 °C, 5 % CO₂, the fluorescence signal of the resorufin product was read ($\lambda_{exc} = 540$ nm; $\lambda_{em} = 590$ nm) using a Cytation 5 Cell Imaging Multi-Mode Reader (Biotek - Agilent). Fluorescence data were normalized; data were fitted using GraphPad Prism Software, and IC50 was calculated by non-linear regression (Figure SX).

5.8.1.12. Subcellular Localization by Confocal Microscopy

U87 cells were seeded at a density of 60,000 cells/well in 8-well plates for confocal imaging and incubated overnight at 37 °C, 5 % CO₂. The next day, cells were incubated at 37 °C, 5 % CO₂ for 4 h with 20 μ M CB7-Ru diluted in culture medium. Then, the compound was replaced with staining solutions containing 1 μ g/mL Hoechst 33342 plus ER-Tracker Red (Invitrogen™), or LysoTracker Deep Red (Invitrogen™), or MitoTracker Deep Red (Invitrogen™), in times and concentrations according to manufacturer's protocol. Cells were then washed with PBS and imaged in phenol red-free DMEM on an SP8 confocal microscope (Leica Microsystems, Nanterre, France) equipped with an x63/1.40 plan apochromat oil objective. The excitation/emission wavelengths used to image the compounds were 405/420-460 nm (Hoechst), 488/605-640 nm (CB7-Ru), 522/590-640 nm (ER-Tracker Red), and 638/650-700 nm (LysoTracker Deep Red and MitoTracker Deep Red). Laser intensities were kept as low as possible to avoid any phototoxicity. Single-channel images were merged using the ImageJ software.

5.8.2. Synthesis and Characterization

5.8.2.1. Glycoluril



According to literature procedures³⁴⁰, 250 mL of H₂O, glyoxal (50 g, 0.861 mol, 1.00 equiv., 125 ml of a 40wt. % solution in H₂O), and urea (129.4 g, 2.154 mol, 2.50 equiv.) were added to a 1 L round-bottom flask and equipped with a stirrer. The reaction mixture was heated to 90°C and was stirred for 5 min. Concentrated H₂SO₄ (10 mL) was added dropwise over 5 min, and a white solid formed 10 minutes after addition of the acid. The reaction mixture was stirred for an additional 2 h. The reaction mixture was cooled to room temperature, and a 50% aqueous solution of NaOH was added until the pH of the reaction was adjusted to 14. The stirring was stopped, and the reaction mixture was cooled to 0°C. The suspension was isolated by vacuum filtration on a Büchner funnel, and the solid was washed with cold water (2 x 1000 mL). The solid was left to dry on the Büchner funnel under suction for 3 h, was transferred to a 700 mL beaker, and was dried for 16 h at 80°C to yield glycoluril (45.0 g, 304 mmol, 92% yield) as an off-white powder. ¹H NMR (500 MHz, DMSO) δ 7.16 (s, 4H), 5.24 (s, 2H).

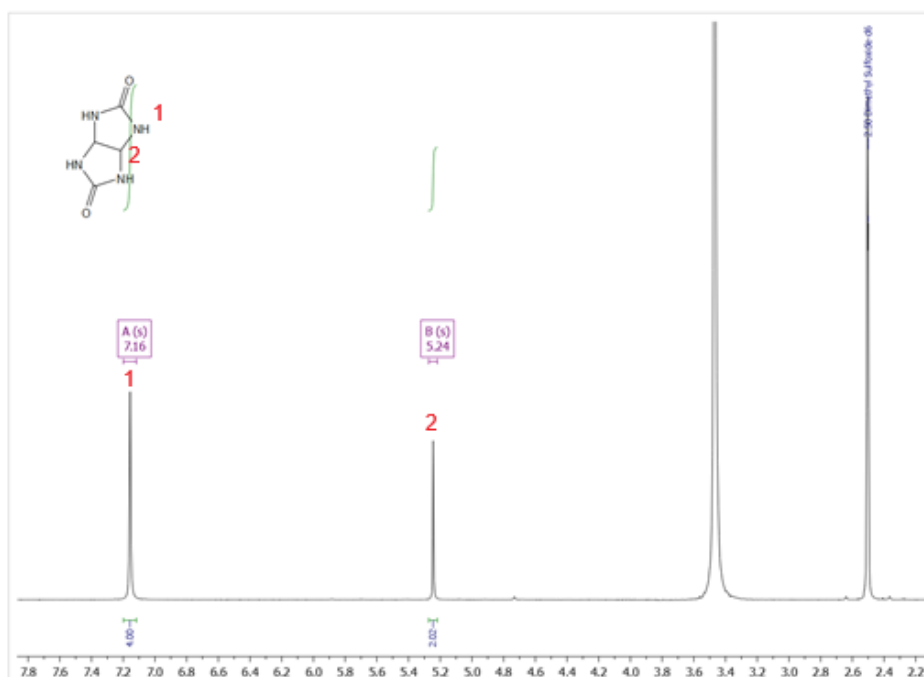
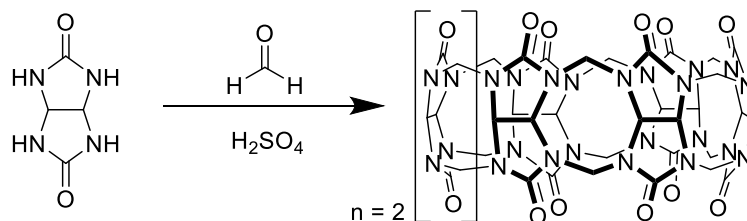


Fig. 5.32. ^1H NMR (DMSO- d_6) of Glycoluril

5.8.2.2. Cucurbit[7]uril (CB7)



According to literature procedures¹²⁵, formaldehyde (14 mL of a 37% aqueous solution, 182 mM) was mixed with sulfuric acid (60 mL of a 9 M aqueous solution), and the magnetically stirred mixture was cooled down to 5°C. Glycoluril (11.4 g, 80 mM, 1 equiv.) was added, which dissolved slowly to produce a thick transparent red gel. After 30 min, the gel became too viscous to allow further stirring, and at this point, the temperature was elevated to 100°C, resulting in the gel dissolving again. The reaction mixture was heated for 72 h and then poured into 200 mL of distilled water. Upon adding 800 mL of acetone, all CB n oligo- and polymers were precipitated from the solution. The solid mixture was filtered and subsequently washed with 1.5 L of cold acetone/water (v/v = 8:2) to remove the acid and produce a mixture of CB n as a white powder. 400 mL of distilled water was added, and all water-soluble CB n was dissolved except for CB6 and CB8. When the filtrate was treated with 300 mL of acetone, a new precipitate mainly containing CB7 appeared. This precipitate was dissolved into 100 mL of distilled water again, and 20 mL of acetone was added, which caused the precipitation of CB7 with other unidentified homologues. The further addition of acetone (100 mL) into filtrate led to the precipitation of the major fraction of CB7. The product was washed with acetone and methanol and subsequently dried under vacuum at 80°C for 24 h. ^1H NMR (400 MHz, D_2O) δ 5.78 (d, J = 15.4 Hz, 1H), 5.51 (s, 1H), 4.21 (d, J = 15.4 Hz, 1H). ESI-MS calcd. for $[\text{M}+\text{C}_8\text{mim}_2]^{2+}$ 719.2931; found 719.2934

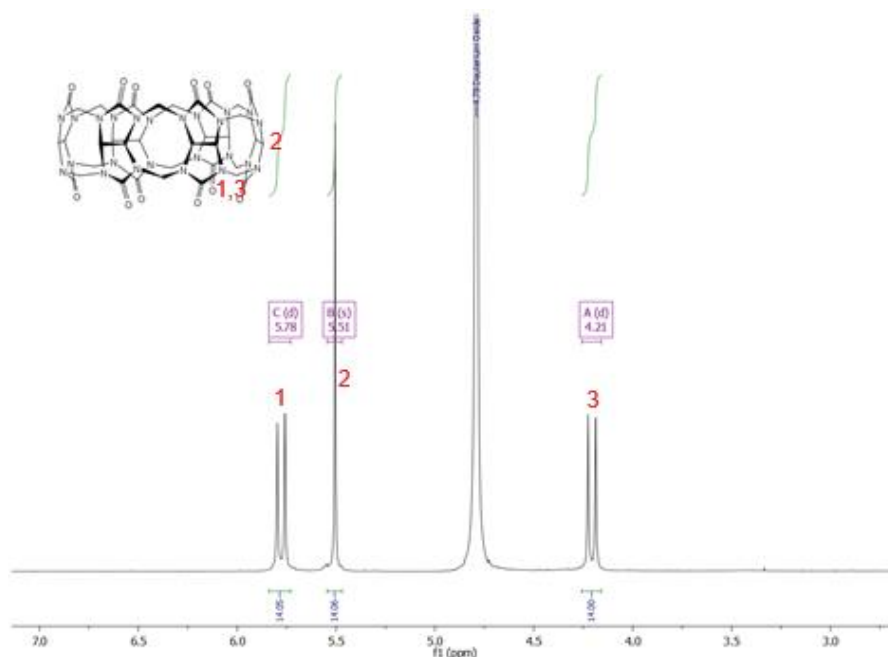
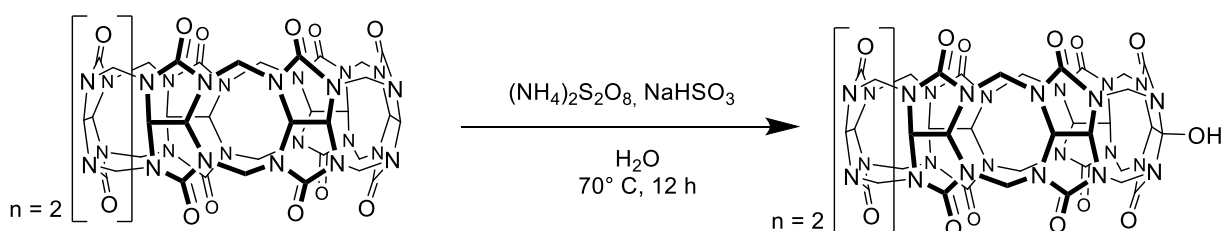


Fig. 5.33. ^1H NMR (D_2O) of CB7.

5.8.2.3. Monohydroxylated CB7 (CB7-OH)



According to literature procedures¹⁸³, CB7 (500 mg, 0.43 mmol, 1 equiv.), $(\text{NH}_4)_2\text{S}_2\text{O}_8$ (147.2 mg, 0.645 mmol, 1.25 equiv.) and NaHSO_3 (67.1 mg, 0.645 mmol, 1.25 equiv.) were placed into a 100 mL round-bottomed flask. Afterwards, 60 mL of purified water was added and kept at 65°C for 12 h. After finishing the reaction, the flask was connected to a rotary evaporator in a 70°C water bath to concentrate the reaction mixture further. When the volume of the reaction mixture was reduced to about 15 mL, the evaporation was stopped, and the resulting solution in the flask was cooled to about 30°C and ready for chromatography.

The concentrated solution was loaded onto the CHP20P resin column. The column was then eluted with purified water (15 mL per fraction). The fractions were monitored by ESI-MS, for which species was mixed with an excess of $\text{C}_8\text{mim}_2\text{Br}_2$. The CB7 peak is at m/z 719²⁺ ($\text{CB7}\cdot\text{C}_8\text{mim}$), CB7-OH is at m/z 727²⁺ ($\text{CB7-OH}\cdot\text{C}_8\text{mim}$) and CB7-(OH)_2 is at m/z 735²⁺ ($\text{CB7-(OH)}_2\cdot\text{C}_8\text{mim}$). The fractions in which CB7-OH was the dominant portion were collected. These fractions were concentrated to approximately 10 mL and the CB7-OH was precipitated by the addition of MeOH (100 mL). The mixture was centrifugated and washed with further MeOH. The resulting powder was dried *in vacuo*. The product was obtained as a white powder (89.7 mg, 0.076 mmol, 17.7%). ^1H NMR (500 MHz, D_2O) δ 5.84 (d, J =

15.3 Hz, 4H), 5.77 (d, J = 15.4 Hz, 20H), 5.55 – 5.45 (m, 27H), 5.24 (s, 2H), 4.49 (d, J = 15.5 Hz, 4H), 4.28 – 4.17 (m, 23H). ESI-MS calcd. for $[M+C_8mim_2]^{2+}$ 719.2844; found 719.2914

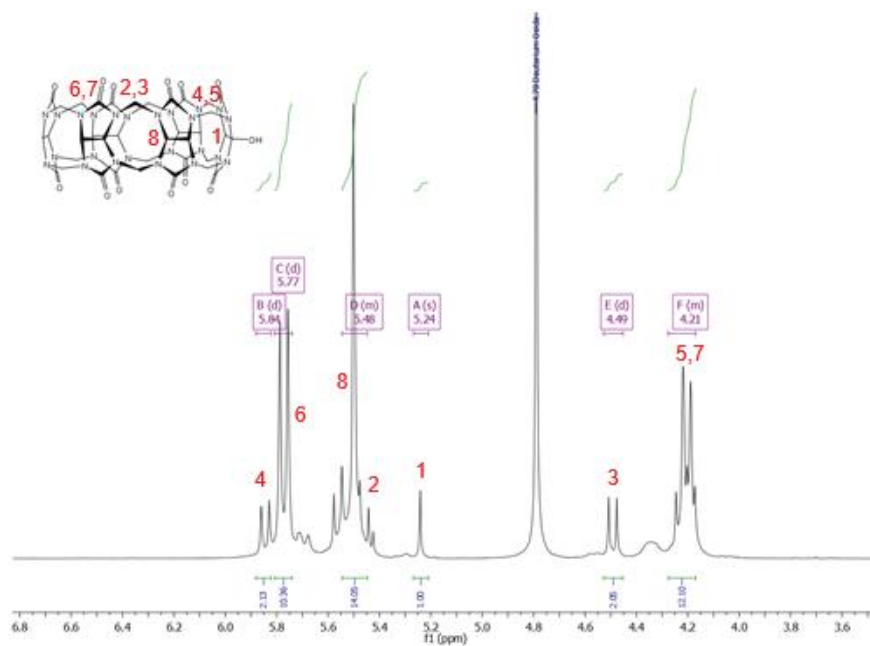


Fig. 5.34. 1H NMR (D_2O) of CB7-OH.

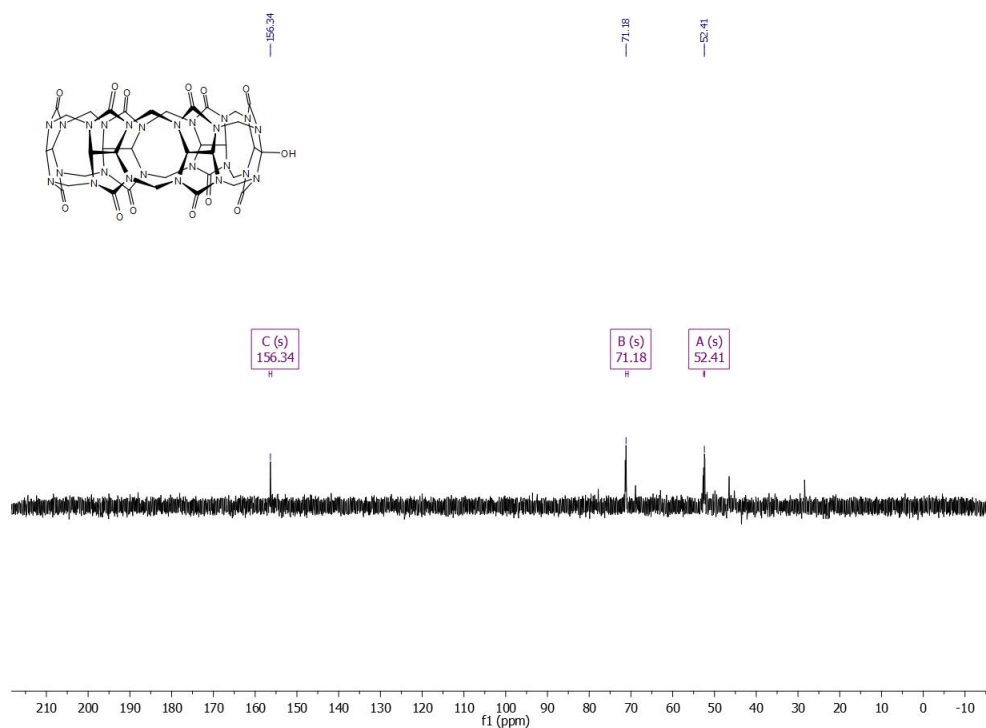


Fig. 5.35. ^{13}C NMR (D_2O) of CB7-OH.

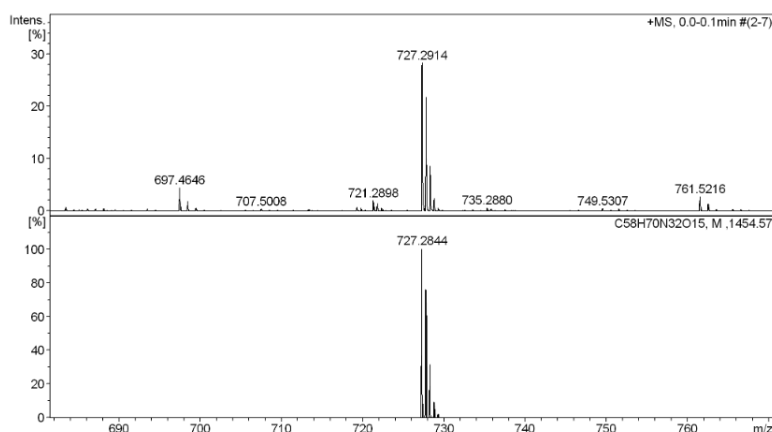
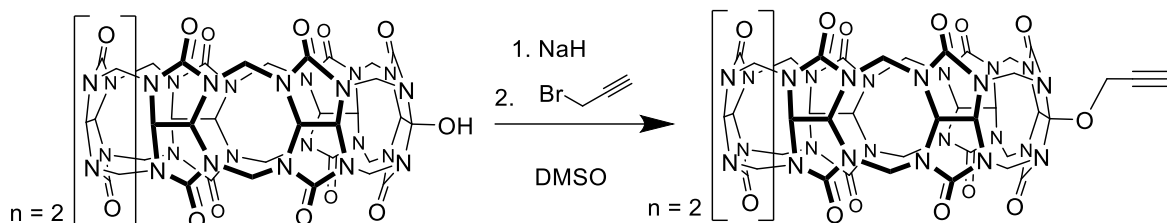


Fig. 5.36. ESI-MS of CB7-OH measured (top) and simulated (bottom), shown as the C_8mim_2 complex.

5.8.2.4. Monopropargyloxyated CB7 (CB7-OPr)



According to literature procedures³⁴¹, CB7-OH (149.2 mg, 0.126 mmol, 1 eq) was dissolved in 7 mL anhydrous DMSO and the suspension was first treated to ultrasound, then purged with N_2 . NaH (74.38 mg, 3.1 mmol, 24.5 eq, 60% purity as dispersion in mineral oil) was added under N_2 , and the mixture was stirred at room temperature under N_2 atmosphere for 3 h. Subsequently, the mixture was cooled to $0^\circ C$, propargyl bromide (450 μL , 3.1 mmol, 24.5 eq, 80 % in toluene) was added under N_2 , and the reaction mixture was stirred at room temperature for 24 h. 100 mL MeOH was added, and the resulting precipitate was isolated by centrifugation and washed three times with MeOH (3×50 mL) and dried in oven at $80^\circ C$ to yield CB7-OPr as a light brown powder. (132.3 mg, 0.108 mmol, 86%) ESI-MS calcd. for $[M+C_8mim_2]^{2+}$ 746.2922; found 746.2945

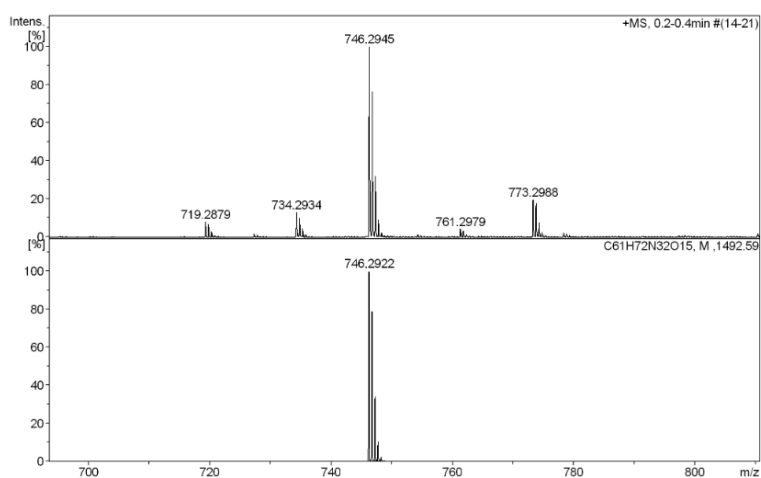
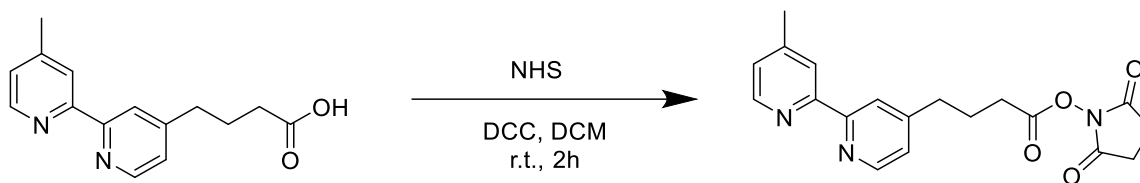


Fig 5.37. ESI-MS of CB7-OPr measured (top) and simulated (bottom), shown as the C_8mim_2 complex.

5.8.2.5. 2,5-dioxopyrrolidin-1-yl 4-(4'-methyl-[2,2'-bipyridin]-4-yl)butanoate (BiPy-NHS)



According to literature procedures³⁴², BiPy-COOH (150 mg, 0.6 mmol, 1 equiv.) was dissolved in a flame dried flask in dry DCM (5 mL) under N₂ atmosphere. DCC (132.8 mg, 0.6 mmol, 1.1 equiv.), and *N*-hydroxysuccinimide (74.1 mg, 0.6 mmol, 1.1 equiv.) were added and stirred at r.t. for 2h. The mixture was then filtered and washed with DCM. The solvent was evaporated in vacuo and the crude product was purified by column chromatography. (EtOAc/Hex 1:1 then EtOAc/MeOH 95:5). The product was obtained as a semi-solid. (203.3 mg, 0.57 mmol, 98%) ¹H NMR (400 MHz, CDCl₃) δ 8.65 – 8.51 (m, 2H), 8.26 (d, *J* = 11.5 Hz, 2H), 7.23 – 7.10 (m, 2H), 2.90 – 2.79 (m, 6H), 2.66 (t, *J* = 7.3 Hz, 2H), 2.45 (s, 3H), 2.23 – 2.12 (m, 2H). ¹³C NMR (101 MHz, CDCl₃) δ 169.06 (s), 149.24 (s), 124.85 (s), 124.12 (s), 122.24 (s), 121.35 (s), 34.08 (s), 30.26 (s), 25.60 (s), 25.19 (s), 21.25 (s). HPLC-MS 6.576 min, *m/z*=257.1

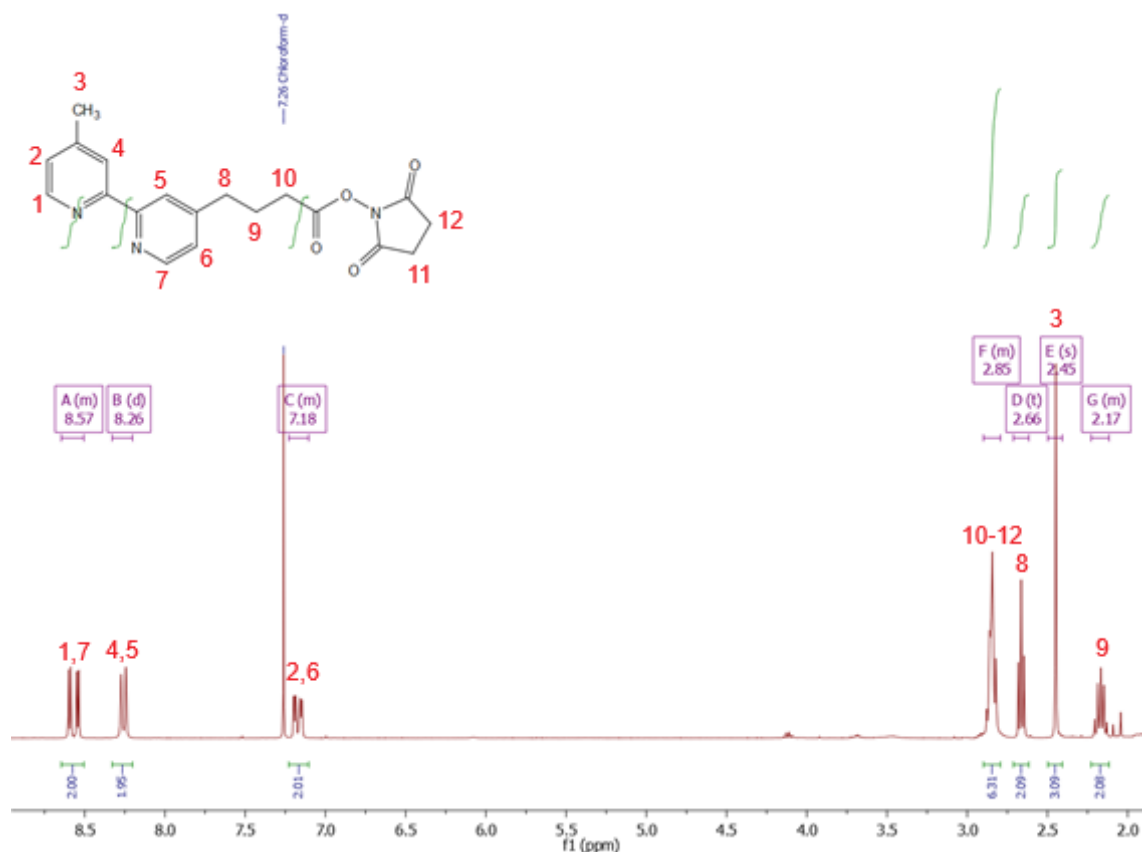


Fig. 5.38. ¹H NMR (CDCl₃) of BiPy-NHS.

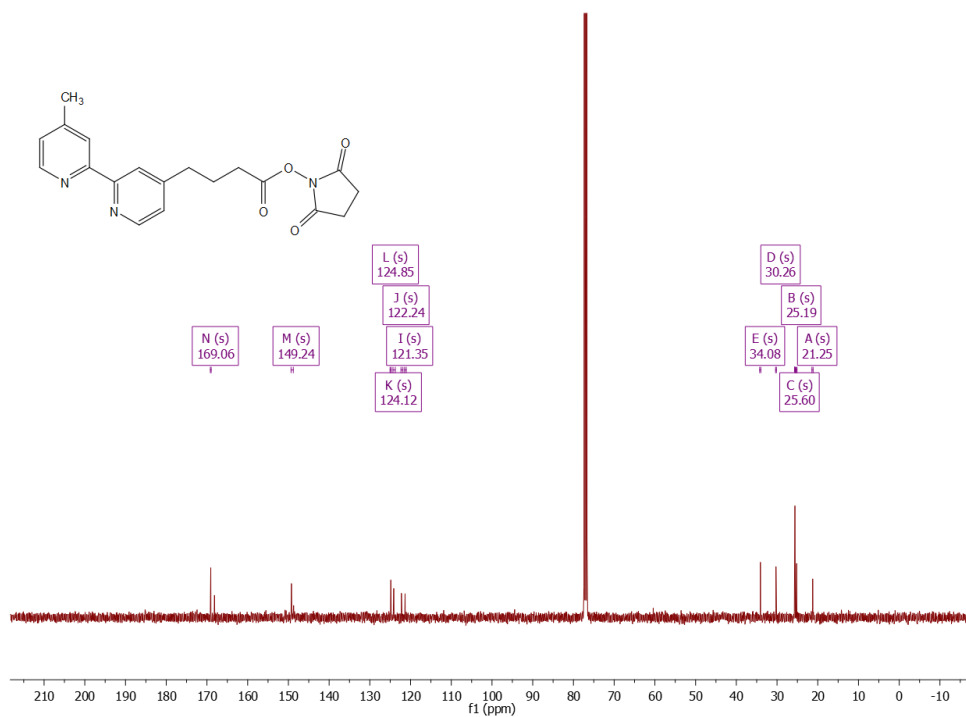


Fig. 5.39. ¹³C NMR (CDCl₃) of BiPy-NHS.

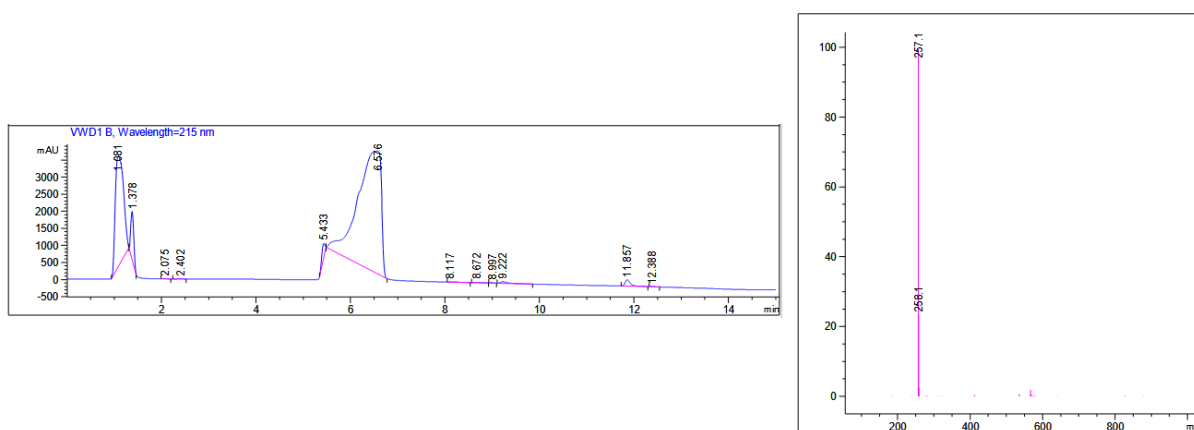
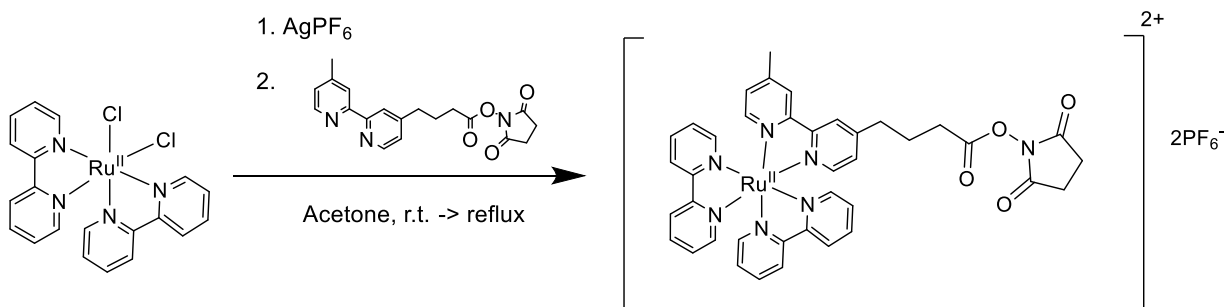


Fig. 5.40. HPLC-MS trace at $\lambda=215$ nm (left) and observed mass (right).

5.8.2.6. Ru-NHS



According to literature procedures³⁴³, cis-bis-(2,2'-bipyridine)-dichlororuthenium (II) (200 mg, 0.4 mmol, 1 equiv.) and AgPF₆ (208.8 mg, 0.45 mmol, 1.5 equiv.) were added to a flame dried schlenk flask and the

flask was evaporated and backfilled with N_2 . Dry acetone (40 mL) was then added and the solution was purged with N_2 . The reaction mixture was allowed to stir at room temperature under N_2 atmosphere for 8 h. To the mixture was added BiPy ligand (218.9 mg, 0.45 mmol, 1.5 equiv.) dissolved in dry acetone (2 mL) and stirred for 24 h at reflux under N_2 atmosphere. The solvent was filtered twice to remove all AgCl precipitate and the solvent was evaporated in vacuo. Et₂O (100 mL) was added, and the initially dark red sticky solid turned into a light red solid after some time. It was collected by centrifugation and then dried under a high vacuum. The product was obtained as a red solid. (406.6 mg, 0.38 mmol, 93%)
¹H NMR (400 MHz, CD₃CN) δ 8.50 – 8.44 (m, 2H), 8.41 – 8.33 (m, 1H), 8.26 (d, *J* = 6.8 Hz, 1H), 8.08 – 8.00 (m, 2H), 7.72 (dd, *J* = 8.9, 4.9 Hz, 2H), 7.60 – 7.49 (m, 1H), 7.43 – 7.34 (m, 2H), 7.25 (dt, *J* = 9.0, 2.8 Hz, 2H), 2.90 (t, *J* = 7.6 Hz, 1H), 2.86 – 2.80 (m, 1H), 2.77 (s, 1H), 2.69 (dt, *J* = 11.9, 7.3 Hz, 2H), 2.53 (s, 2H). Even after multiple attempts, it was not possible to measure the ¹³C spectrum of Ru-NHS. ESI-MS: Calcd. for [M]²⁺: 383.5897; found: 383.6044

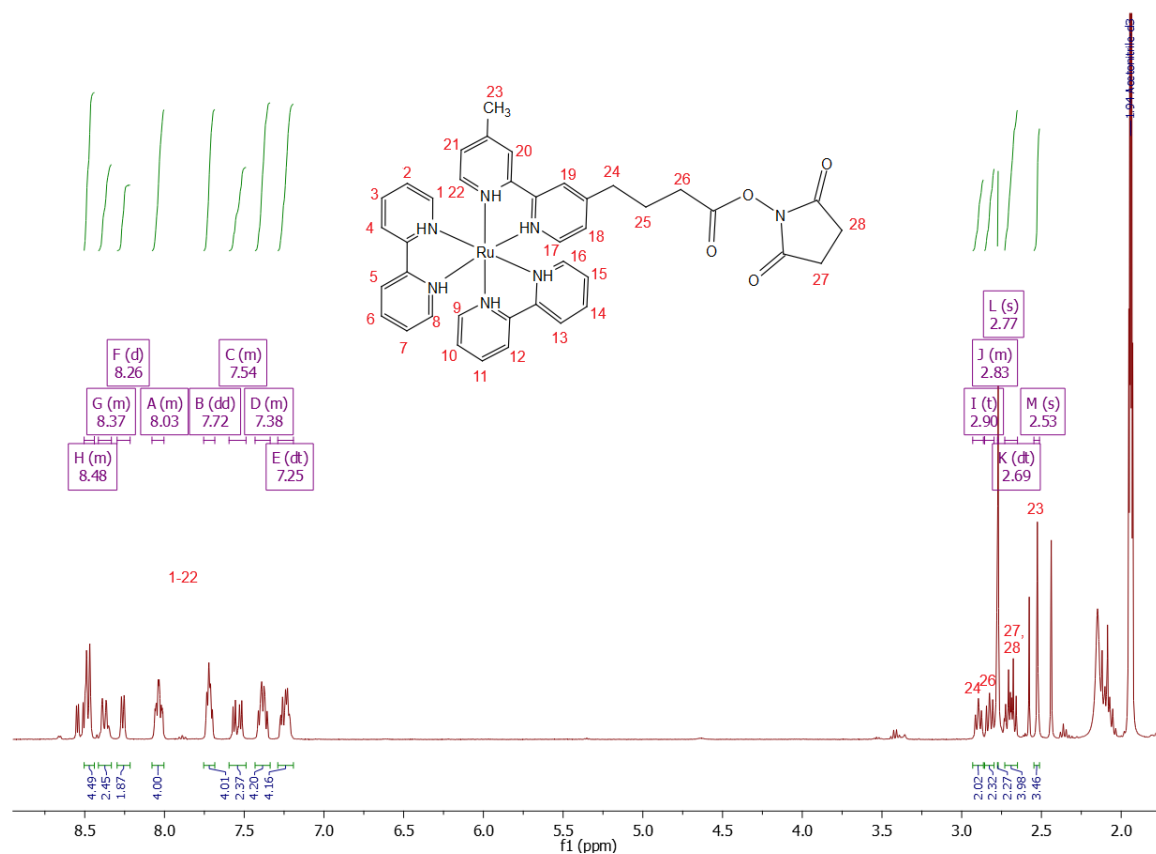


Fig. 5.41. ¹H-NMR (CD₃CN) of Ru-NHS.

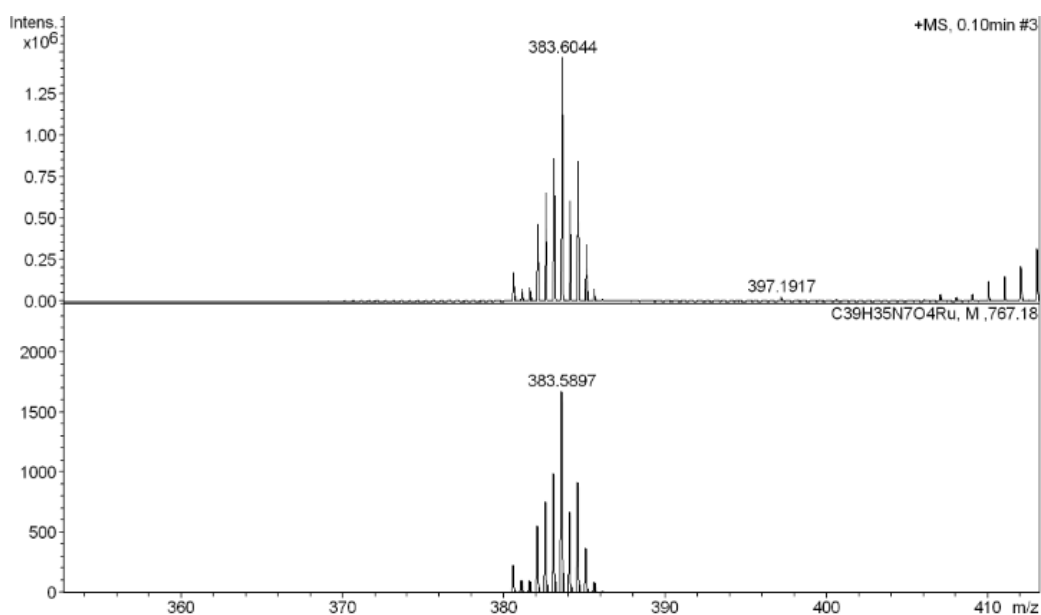
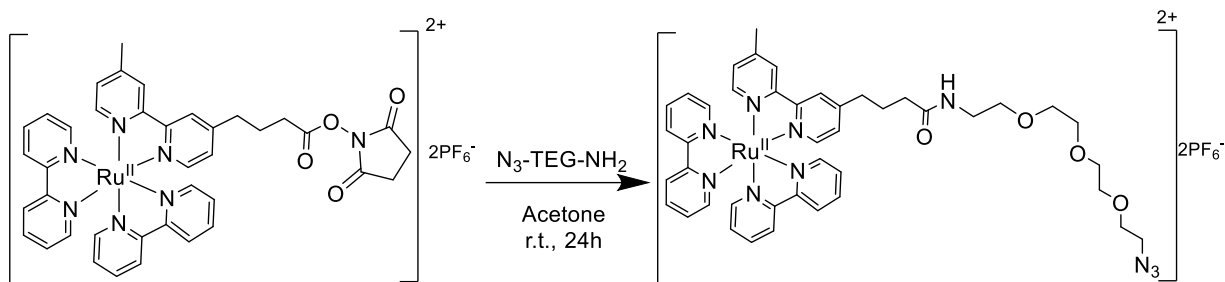


Fig. 5.42. ESI-MS of Ru-NHS measured (top) and simulated (bottom).

5.8.2.7. Ru-N₃



A 90 mM solution of 11-Azido-trioxaundecan-1-amine in dry acetone (35.6 μl in 2 mL) was prepared and Na_2SO_4 was added to this solution. 1600 μl (15.5 mg, 1.5 equiv.) of the linker solution was added to a solution of Ru-NHS (100 mg, 1 equiv.) in 2 mL dry acetone. The mixture was stirred overnight under an atmosphere of N_2 . Then, the product was precipitated by pouring in Et_2O (300 mL). This was left for 3h in the fridge. The crude product is obtained by centrifugation. It was then purified by neutral alumina column chromatography. (Acetone/ H_2O 7:1). The acetone was removed in vacuo and the product was obtained after freeze-dry as an orange solid. (98.6 mg, 0.085 mmol, 90%) ^1H NMR (400 MHz, CD_3CN) δ 8.46 (d, $J = 8.2$ Hz, 4H), 8.36 (d, $J = 14.5$ Hz, 2H), 8.07 – 7.98 (m, 4H), 7.70 (dd, $J = 9.8, 4.9$ Hz, 4H), 7.51 (t, $J = 5.5$ Hz, 2H), 7.38 (dddd, $J = 11.2, 7.3, 4.4, 1.2$ Hz, 4H), 7.26 – 7.17 (m, 2H), 6.41 (s, 1H), 3.60 – 3.48 (m, 10H), 3.43 (t, $J = 5.6$ Hz, 2H), 3.34 – 3.29 (m, 2H), 3.22 (dd, $J = 11.0, 5.2$ Hz, 2H), 2.83 – 2.74 (m, 2H), 2.51 (s, 3H), 2.19 (t, $J = 7.2$ Hz, 2H), 2.12 – 2.06 (m, 2H). Even after multiple attempts, it was not possible to measure the ^{13}C spectrum. ESI-MS: Calcd. for $[\text{M}]^{2+}$: 435.1452; found: 435.1568

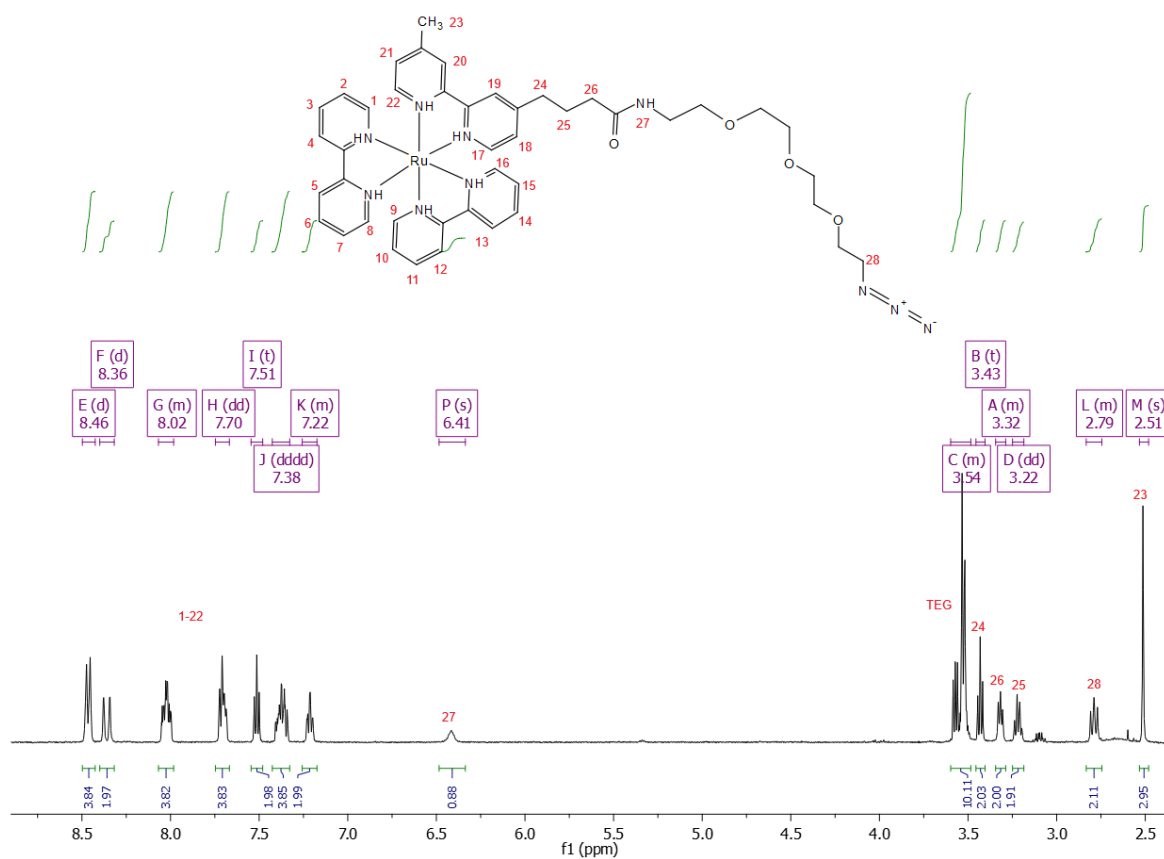


Fig. 5.43. $^1\text{H NMR}$ (CD₃CN) of Ru-NHS.

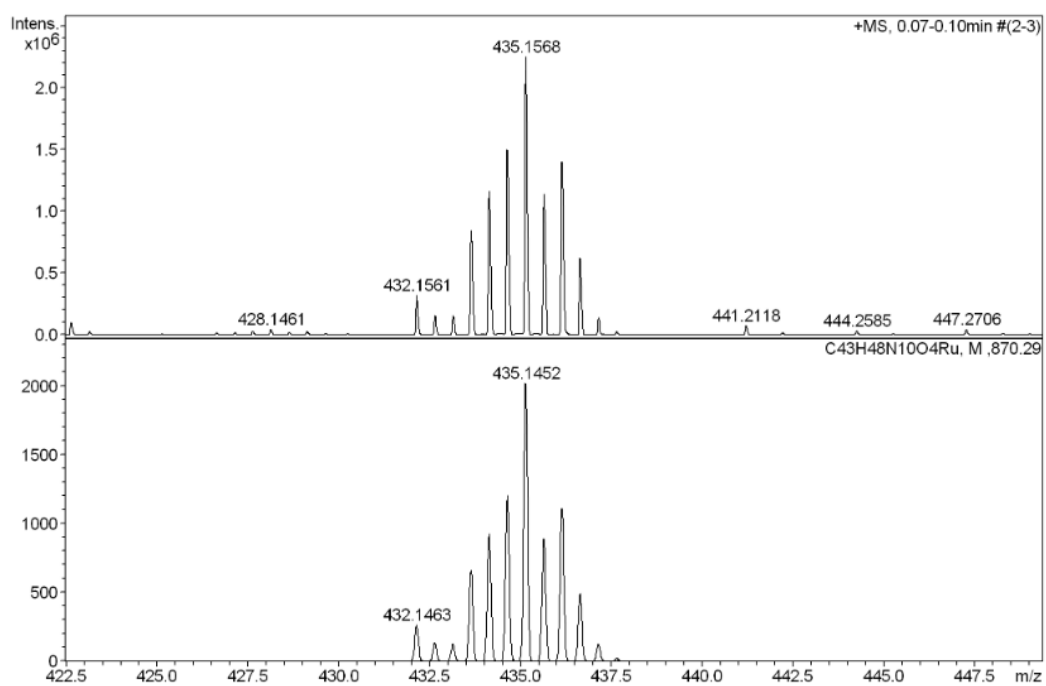
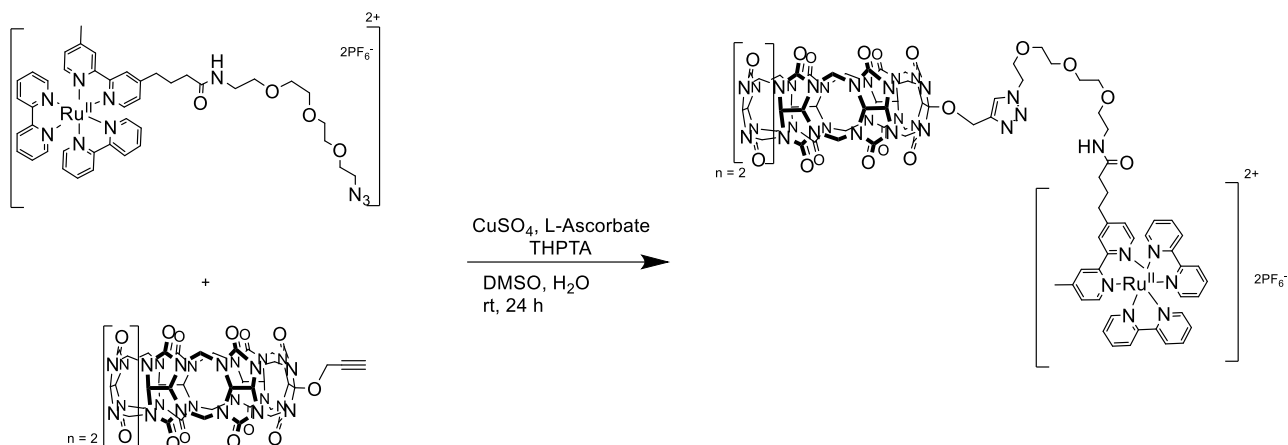


Fig. 5.44. ESI-MS of Ru-N₃ measured (top) and simulated (bottom).

5.8.2.8. CB7-Ru



In a vial Ru-TEG-N₃ (21.4 mg, 0.018 mmol, 1.5 equiv.), CB7-OPr (15 mg, 0.012 mmol, 1 equiv.) and THPTA (21.4 mg, 0.050 mmol, 4 equiv.) were suspended in DMSO (1 mL). In a second vial, sodium L-ascorbate (24.4 mg, 0.123 mmol, 10 equiv.) was added to 5 mL 55% DMSO aqueous solution containing CuSO₄ (11.8 mg, 0.074 mmol, 6 equiv.). The two solutions were mixed and stirred at room temperature for 24 h in the dark under an N₂ atmosphere. Afterwards, the product was precipitated by addition of the reaction solution in MeOH/THF 1:1. Washing with MeOH/THF 1:1 afforded the crude product, purification is done by size exclusion chromatography (SEC) using a H₂O/ACN gradient. (0% ACN → 25% ACN) The product is obtained as a light-orange solid after freeze dry. (11.4 mg, 0.0048 mmol, 40%) ¹H NMR (400 MHz, D₂O) δ 8.50 (d, J = 8.0 Hz, 4H), 8.36 (s, 2H), 8.10 (d, J = 11.2 Hz, 1H), 8.00 (t, J = 7.5 Hz, 4H), 7.79 (dd, J = 10.3, 5.4 Hz, 4H), 7.62 (dd, J = 18.1, 5.8 Hz, 2H), 7.34 (dd, J = 13.2, 7.1 Hz, 4H), 7.20 (dd, J = 10.5, 5.9 Hz, 2H), 5.99 – 5.33 (m, 26H), 4.47 – 4.14 (m, 14H), 3.91 – 3.82 (m, 2H), 3.48 (dq, J = 10.7, 5.5 Hz, 12H), 3.15 – 3.00 (m, 2H), 2.80 (t, J = 7.0 Hz, 2H), 2.64 – 2.55 (m, 4H), 2.48 (s, 3H), 2.27 (t, J = 7.0 Hz, 2H), 2.02 – 1.90 (m, 2H), 1.26 – 1.09 (m, 6H). Due to the complex structure, a precise assignment of all peaks was not possible. Even after multiple attempts, it was not possible to measure the ¹³C spectrum. However, the CB7-Ru was characterized by multiple other analytical techniques. ESI MS: Calc. for [M+C8mim2]⁴⁺: 590.7191; found: 590.7195. Analyt. HPLC: 4.98 min.

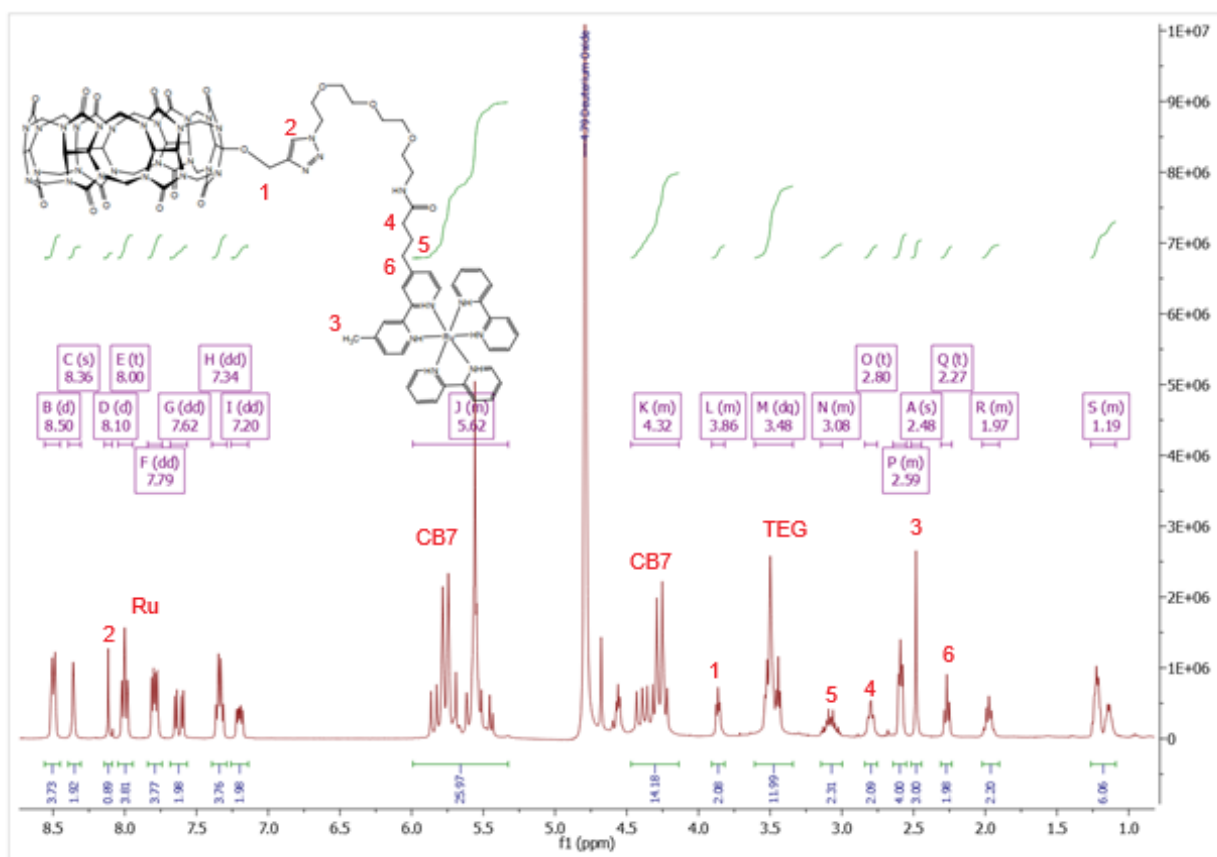


Fig. 5.45. ¹H NMR (D₂O) of CB7-Ru.

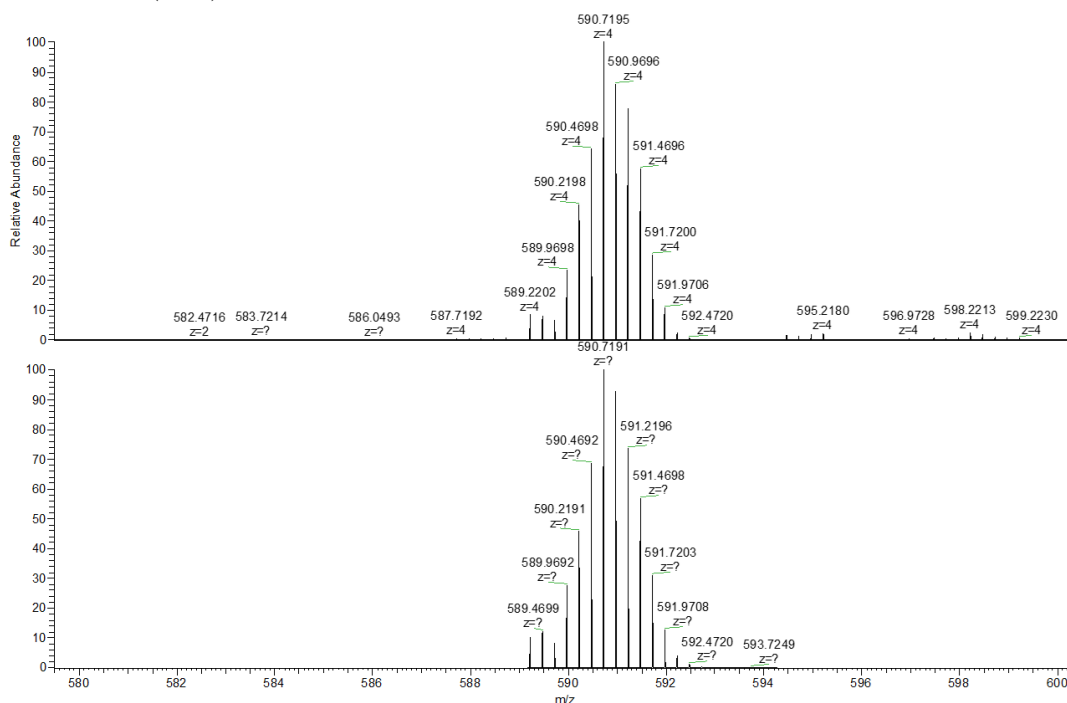


Fig. 5.46. ESI-MS of CB7-Ru measured (top) and simulated (bottom), shown as C₈mim₂ adducts.

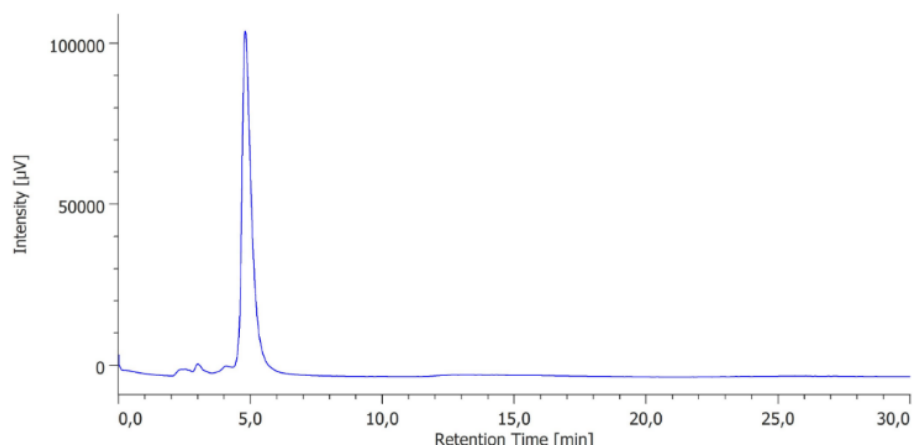
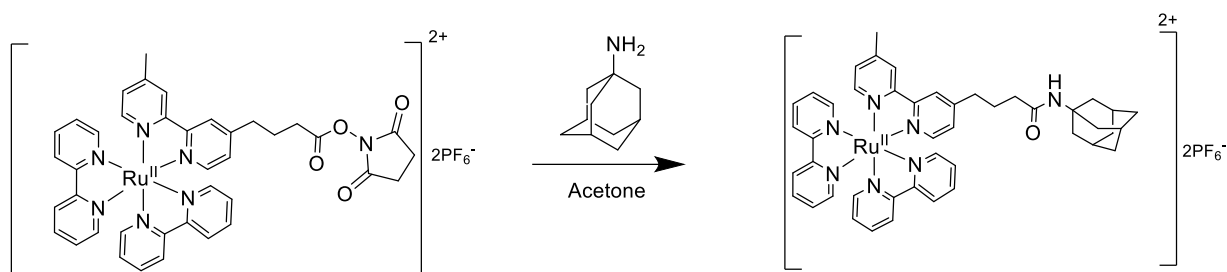


Fig. 5.47. Analytical trace of CB7-Ru.

5.8.2.9. Ada-Ru



1-adamantamine (28.6 mg, 2 equiv.) and 50 μL triethylamine were dissolved in dry acetone (1 mL). Ru-NHS (100 mg, 1 equiv.) was then added and the mixture was purged with N_2 . The mixture was stirred overnight under an atmosphere of N_2 . Then, the product was precipitated by pouring in Et_2O (200 mL). This was left for 3h in the fridge. The crude product is obtained by centrifugation. It was then purified by neutral alumina column chromatography. (Acetone/ H_2O 7:1) The product was obtained as a red-orange powder after freeze-dry. ^1H NMR (400 MHz, CD_3CN) δ 8.48 (d, $J = 8.1$ Hz, 4H), 8.41 – 8.31 (m, 2H), 8.09 – 7.98 (m, 4H), 7.72 (t, $J = 6.0$ Hz, 4H), 7.53 (dd, $J = 7.9, 5.8$ Hz, 2H), 7.44 – 7.33 (m, 4H), 7.23 (dd, $J = 5.5, 2.2$ Hz, 2H), 2.83 – 2.75 (m, 2H), 2.53 (s, 3H), 2.11 (dt, $J = 8.7, 5.0$ Hz, 4H), 2.00 (s, 3H), 1.92 – 1.87 (m, 2H), 1.72 – 1.60 (m, 7H), 1.18 (d, $J = 3.8$ Hz, 3H).

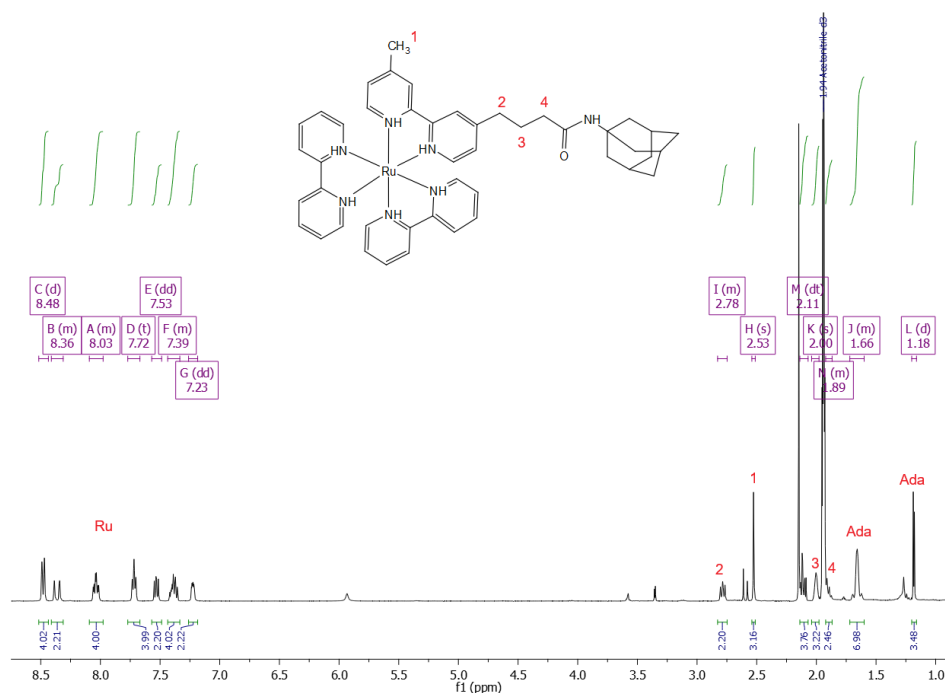


Fig. 5.48. ^1H NMR (CD_3CN) of Ada-Ru.

5.9. Supporting Information

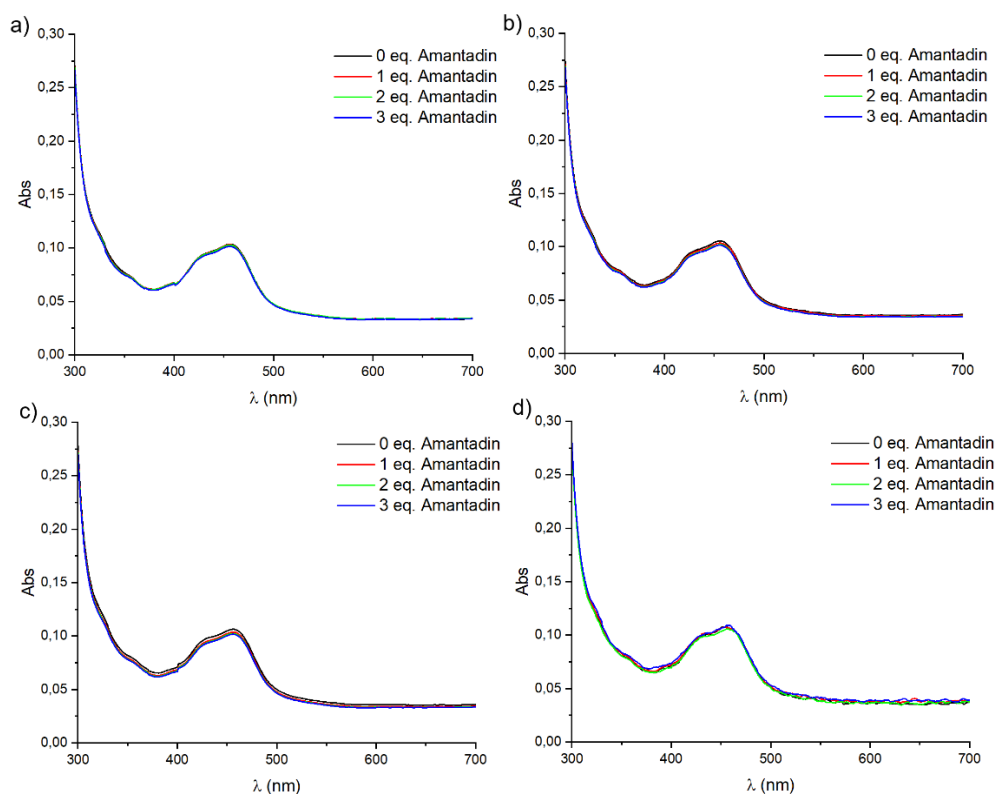


Fig. 5.49. UV-vis absorption spectrum of Ada-Ru ($5\ \mu\text{M}$) upon titration with amantadine in a) water, b) HEPES, c) PB, d) PBS.

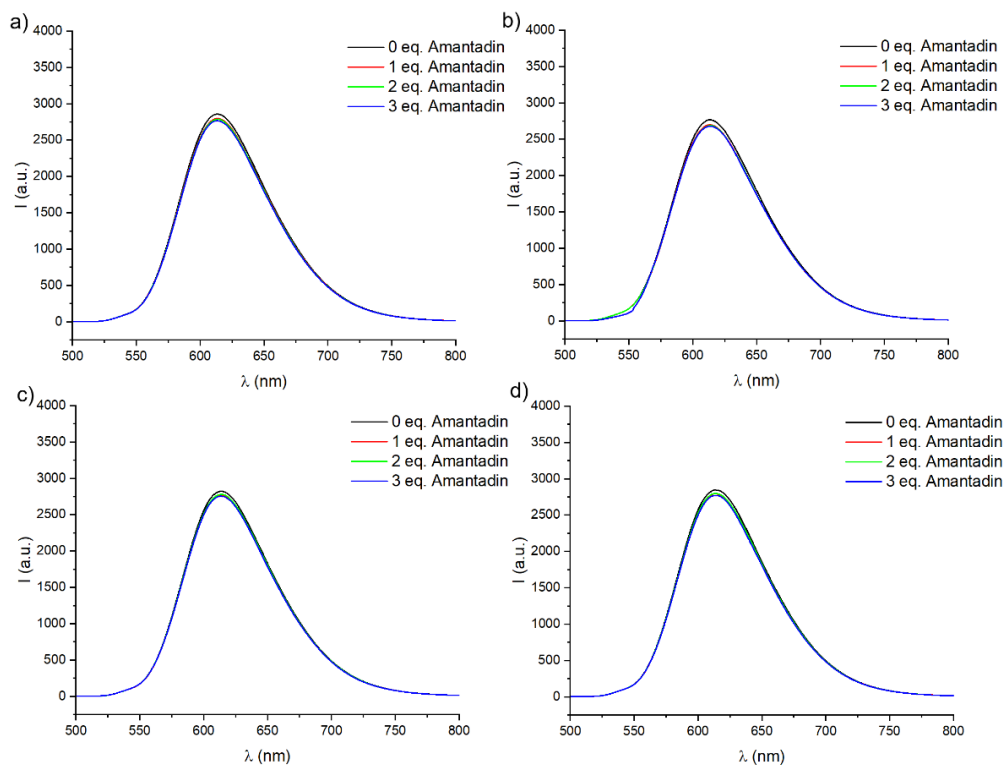


Fig. 5.50. Emission spectra ($\lambda_{\text{exc}} = 452 \text{ nm}$) of Ada-Ru ($5 \mu\text{M}$) upon titration with amantadine in a) water, b) HEPES, c) PB, d) PBS.

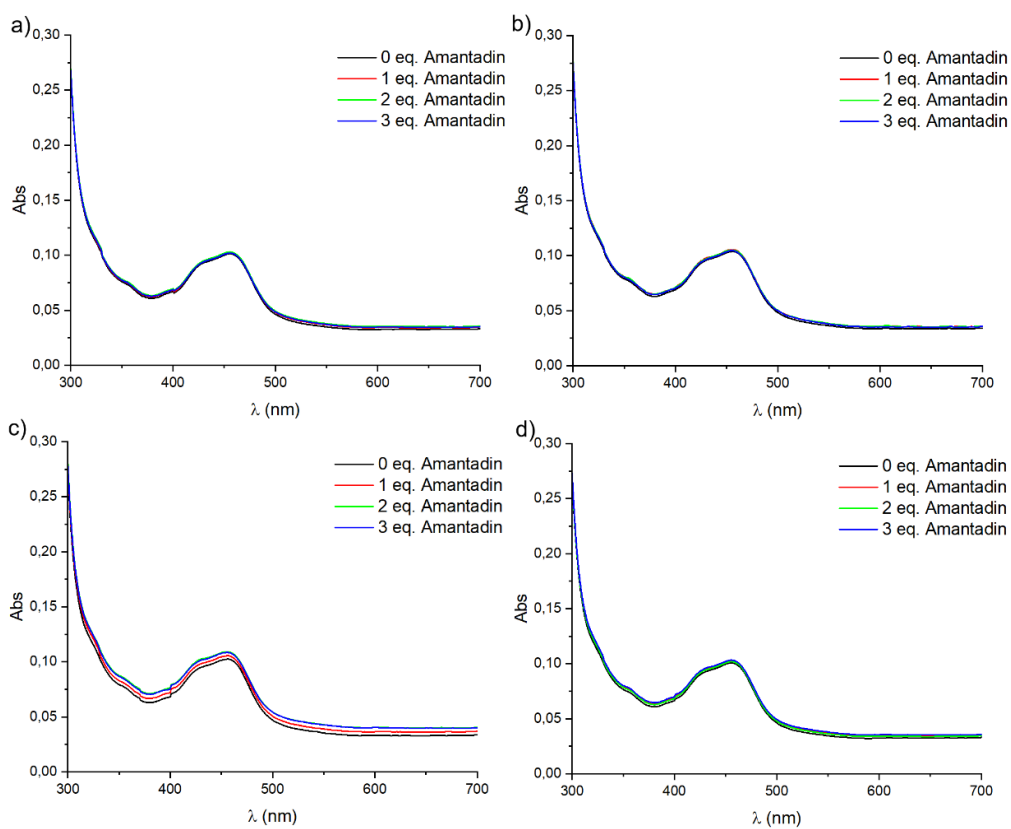


Fig. 5.51. UV-vis absorption spectra of Ada-Ru ($5 \mu\text{M}$) and CB7 ($5 \mu\text{M}$) upon titration with amantadine in a) water, b) HEPES, c) PB, d) PBS.

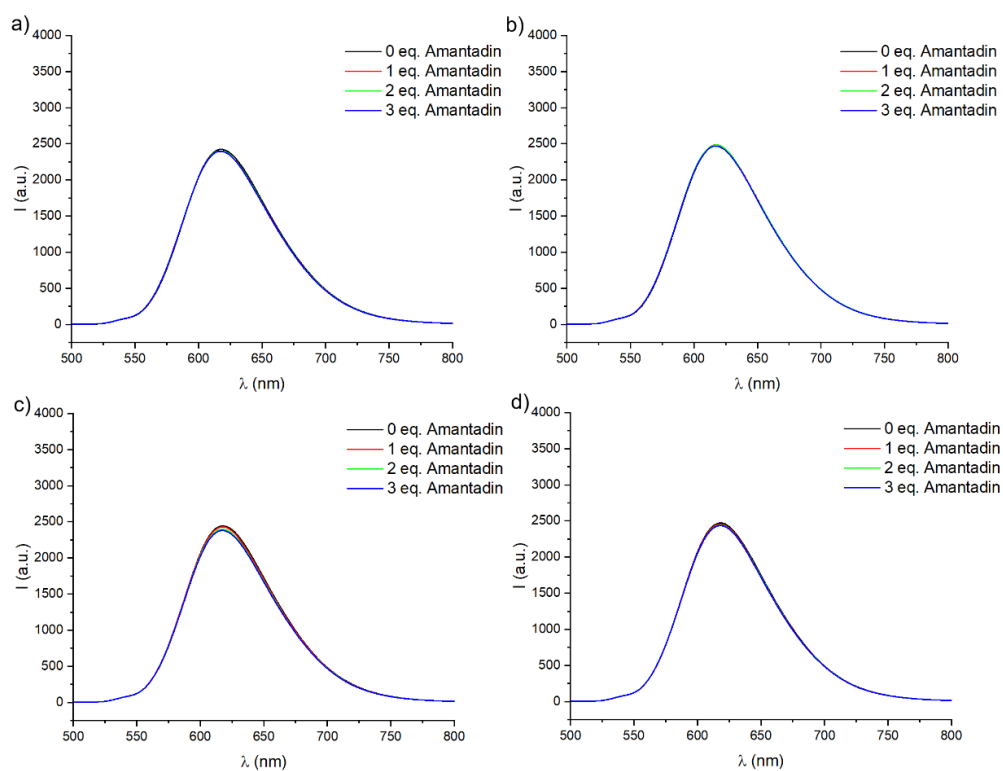


Fig. 5.52. Emission spectra ($\lambda_{\text{exc}} = 452 \text{ nm}$) of Ada-Ru (5 μM) and CB7 (5 μM) upon titration with amantadine in a) water, b) HEPES, c) PB, d) PBS.

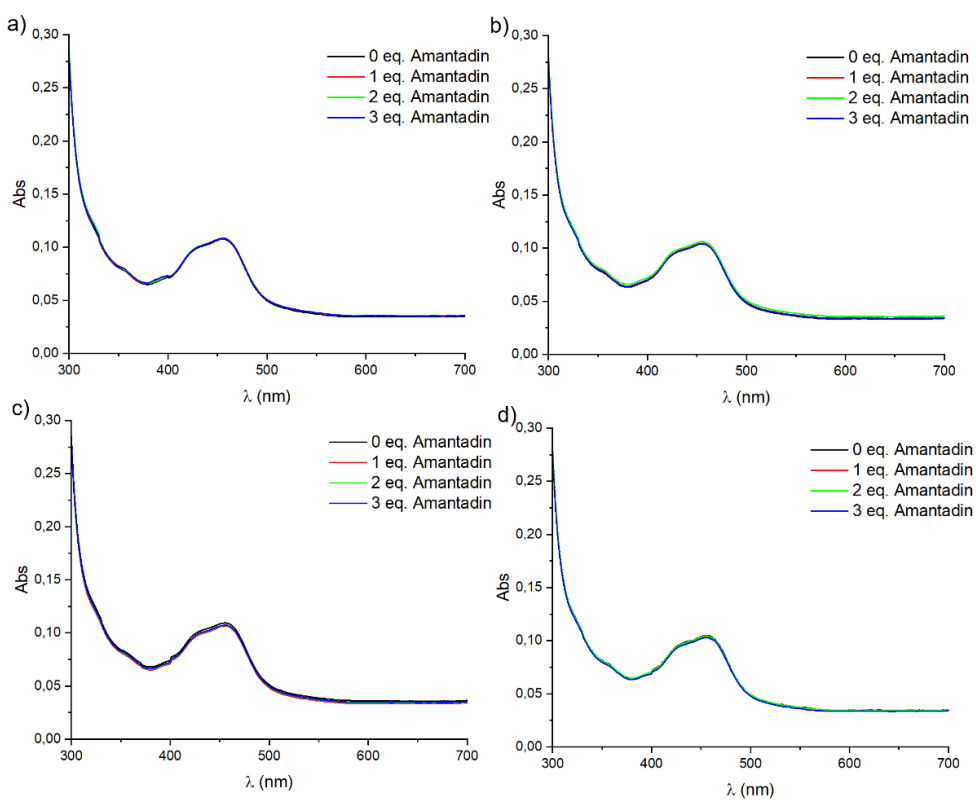


Fig. 5.53. UV-vis absorption spectra of Ada-Ru (5 μM) and CB7 (25 μM) upon titration with amantadine in a) water, b) HEPES, c) PB, d) PBS.

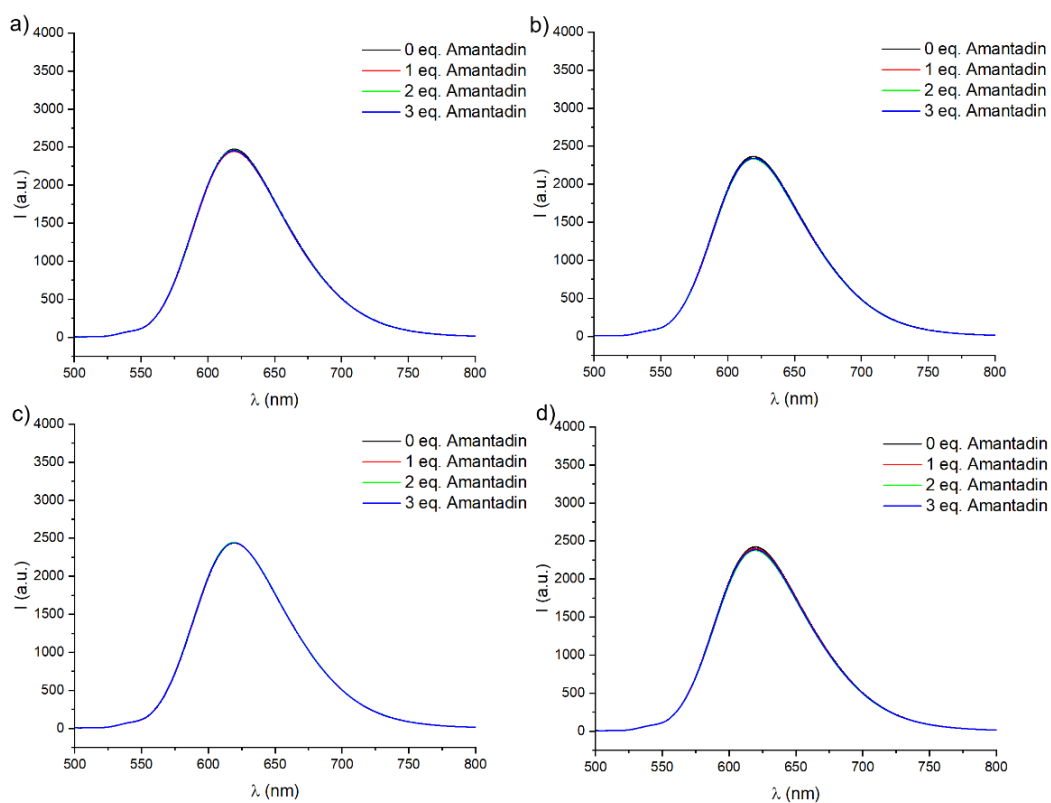


Fig. 5.54. Emission spectra ($\lambda_{\text{exc}} = 452$ nm) of Ada-Ru (5 μM) and CB7 (25 μM) upon titration with amantadine in a) water, b) HEPES, c) PB, d) PBS.

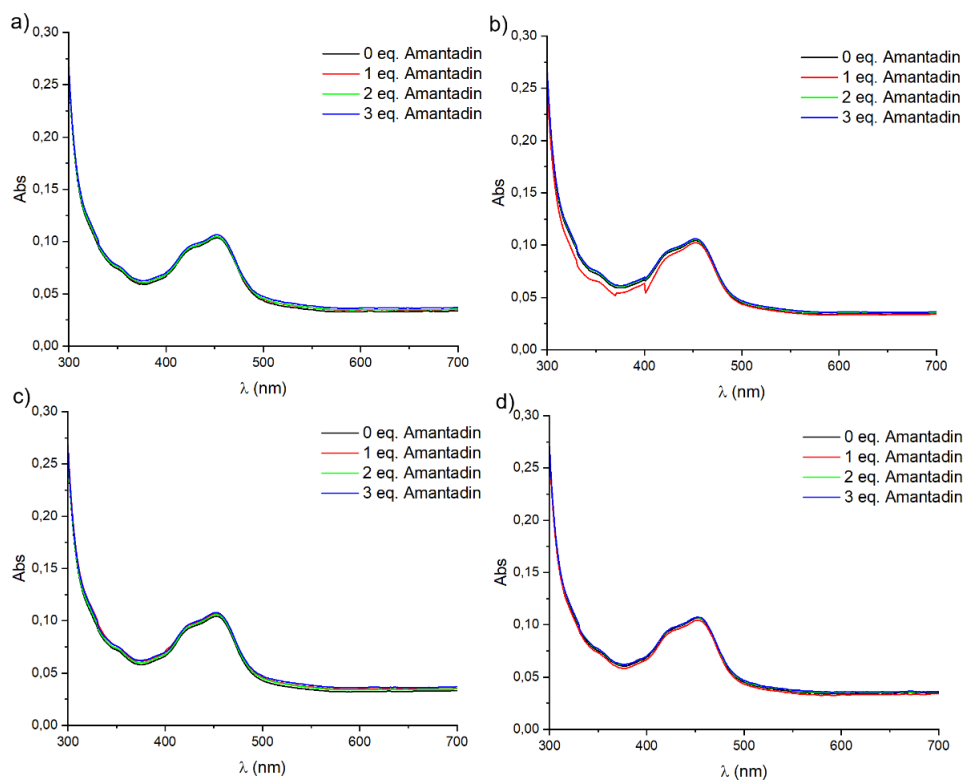


Fig. 5.55. UV-vis absorption spectra of $[\text{Ru}(\text{bpy})_3]\text{Cl}_2 \times 6 \text{H}_2\text{O}$ (5 μM) upon titration with amantadine in a) water, b) HEPES, c) PB, d) PBS.

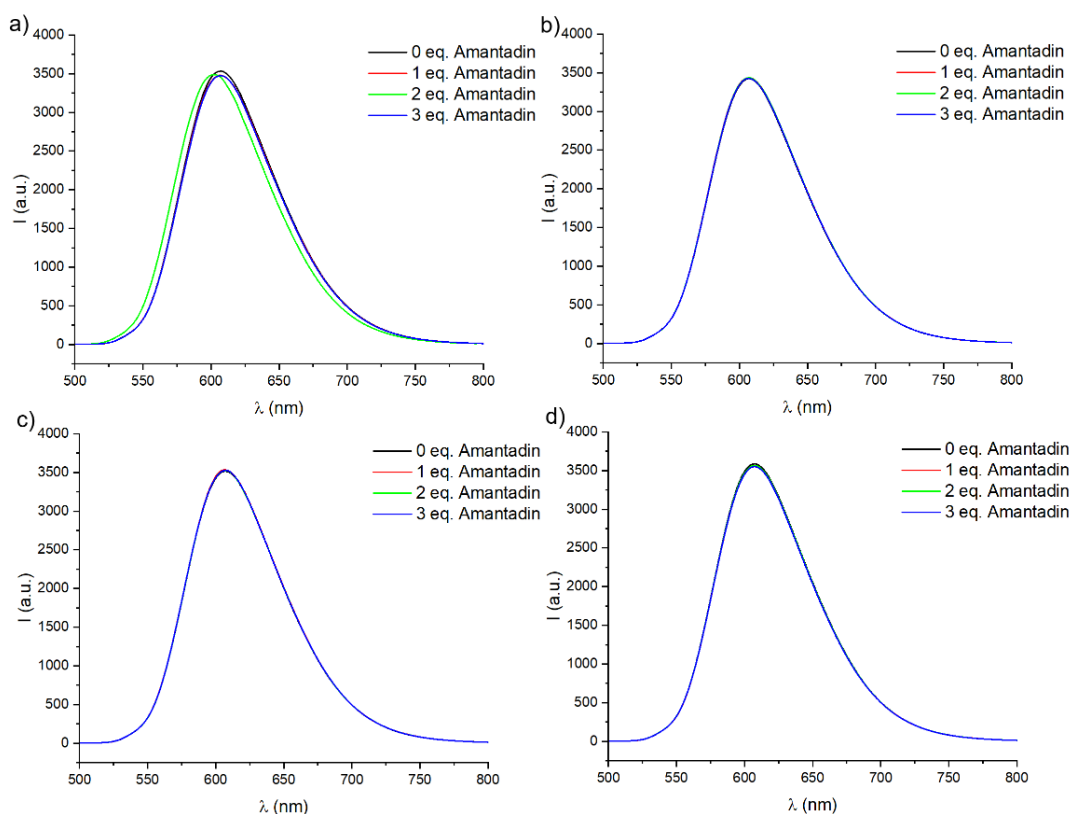


Fig. 5.56. Emission spectra ($\lambda_{\text{exc}} = 452 \text{ nm}$) of $[\text{Ru}(\text{bpy})_3]\text{Cl}_2 \times 6 \text{H}_2\text{O}$ (5 μM) upon titration with amantadine in a) water, b) HEPES, c) PB, d) PBS.

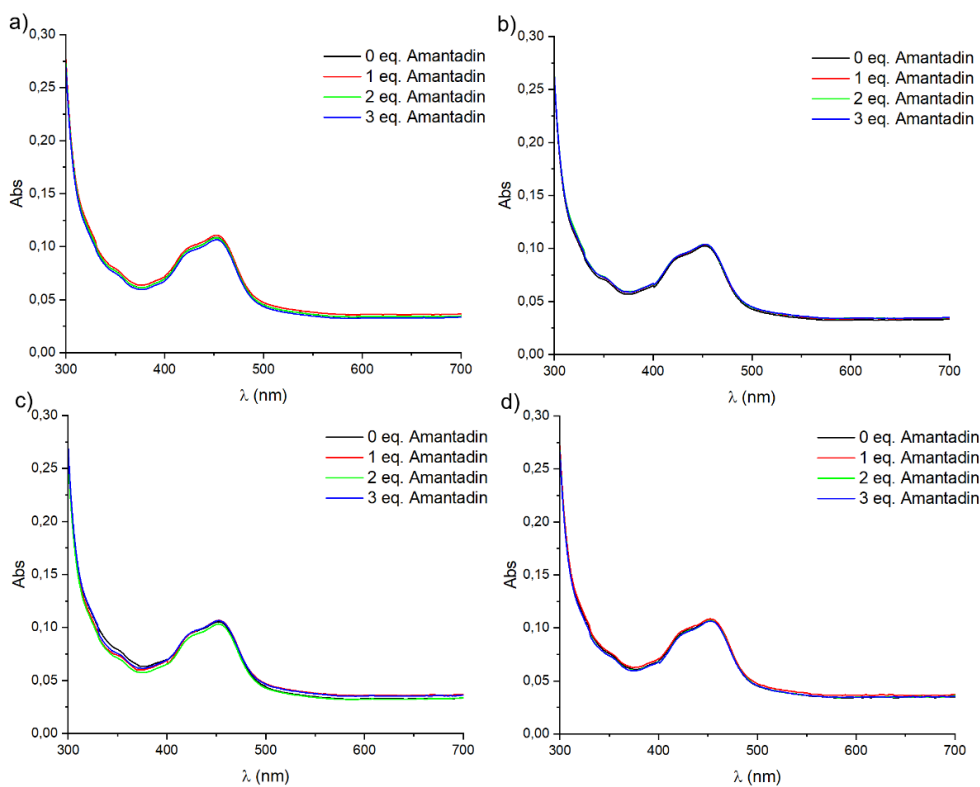


Fig. 5.57. UV-vis absorption spectra of $[\text{Ru}(\text{bpy})_3]\text{Cl}_2 \times 6 \text{H}_2\text{O}$ (5 μM) and CB7 (5 μM) upon titration with amantadine in a) water, b) HEPES, c) PB, d) PBS.

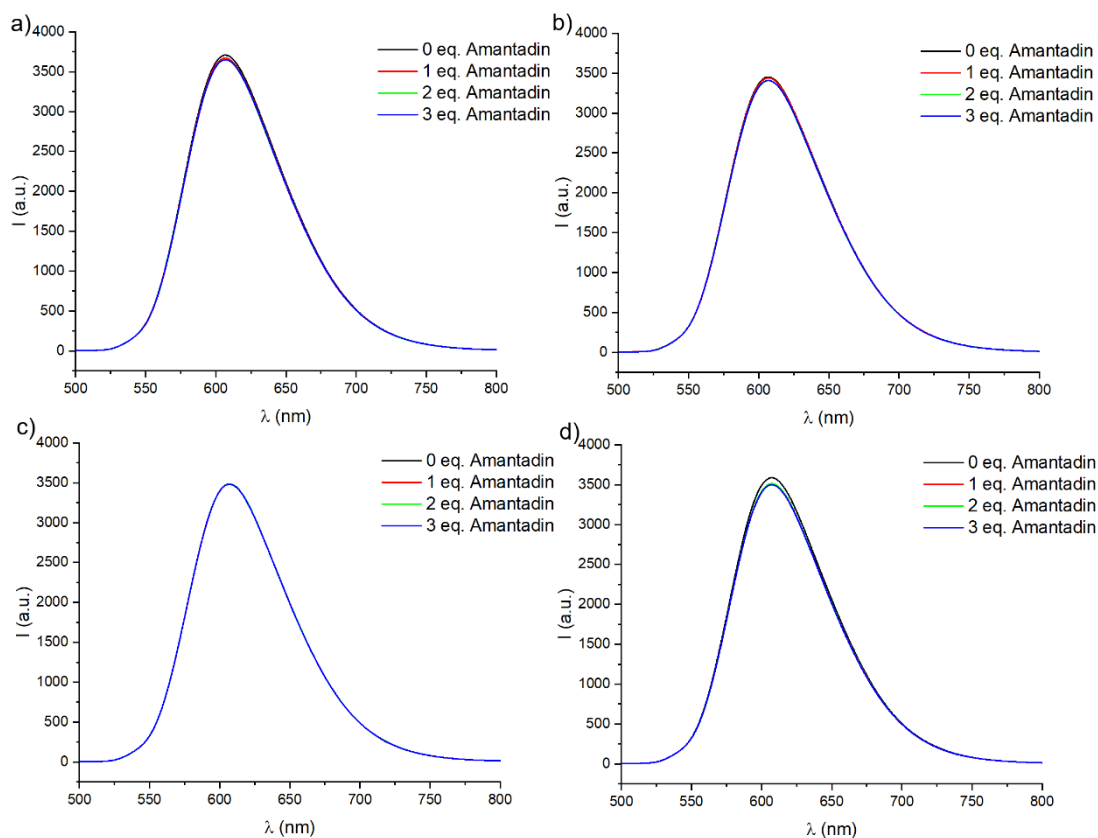


Fig. 5.58. Emission spectra ($\lambda_{exc} = 452$ nm) of $[\text{Ru}(\text{bpy})_3]\text{Cl}_2 \times 6 \text{H}_2\text{O}$ ($5 \mu\text{M}$) and CB7 ($5 \mu\text{M}$) upon titration with amantadine in a) water, b) HEPES, c) PB, d) PBS.

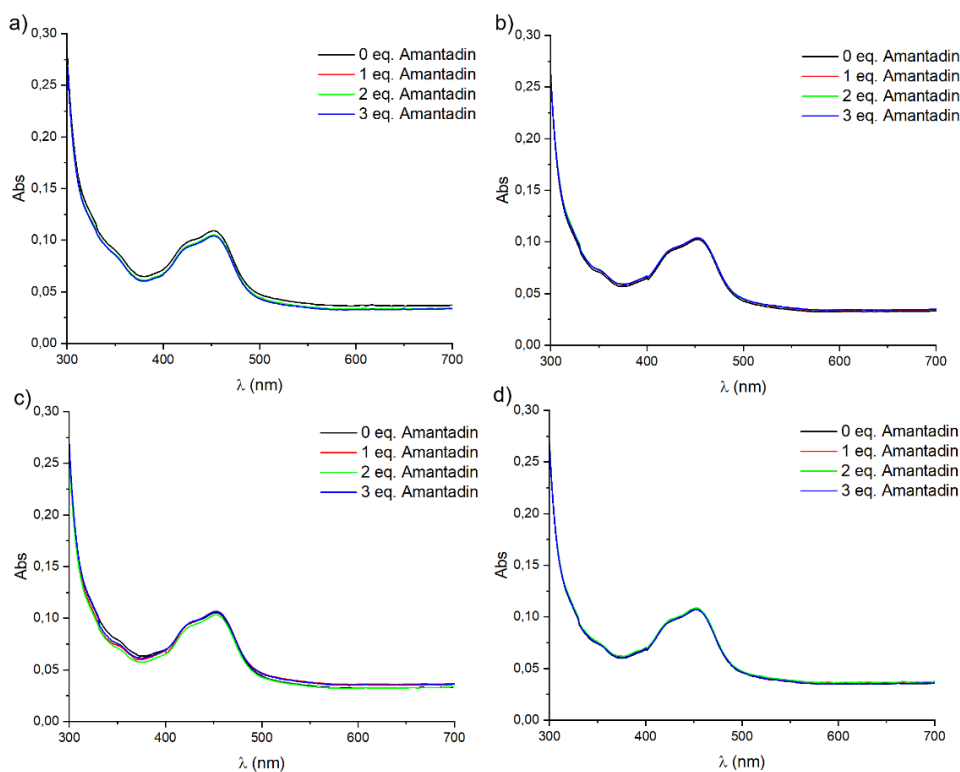


Fig. 5.59. UV-vis absorption spectra of $[\text{Ru}(\text{bpy})_3]\text{Cl}_2 \times 6 \text{H}_2\text{O}$ ($5 \mu\text{M}$) and CB7 ($25 \mu\text{M}$) upon titration with amantadine in a) water, b) HEPES, c) PB, d) PBS.

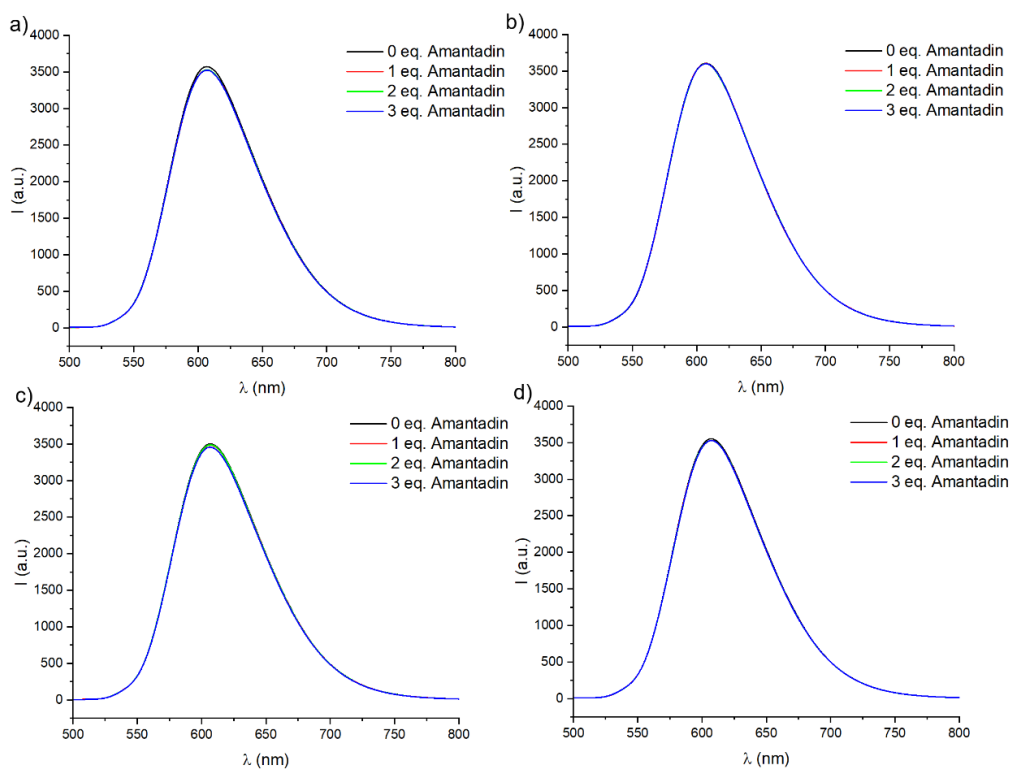


Fig. 5.60. Emission spectra ($\lambda_{\text{exc}} = 452 \text{ nm}$) of $[\text{Ru}(\text{bpy})_3]\text{Cl}_2 \times 6 \text{ H}_2\text{O}$ ($5 \mu\text{M}$) and CB7 ($25 \mu\text{M}$) upon titration with amantadine in a) water, b) HEPES, c) PB, d) PBS.

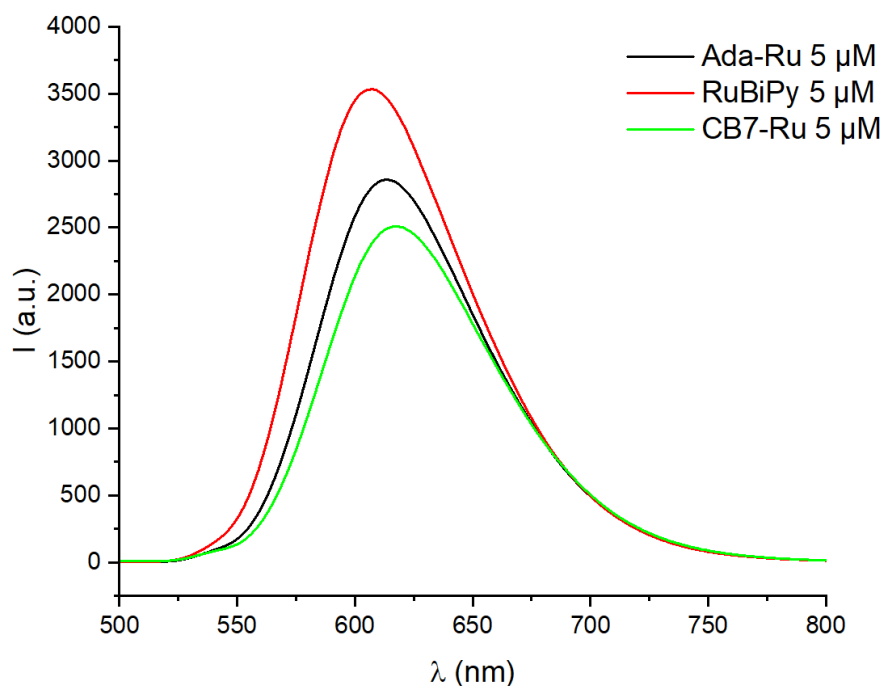


Fig. 5.61. Comparison of the emission spectra ($\lambda_{\text{exc}} = 452 \text{ nm}$) of Ada-Ru, RuBiPy and CB7-Ru each $5 \mu\text{M}$ in water.

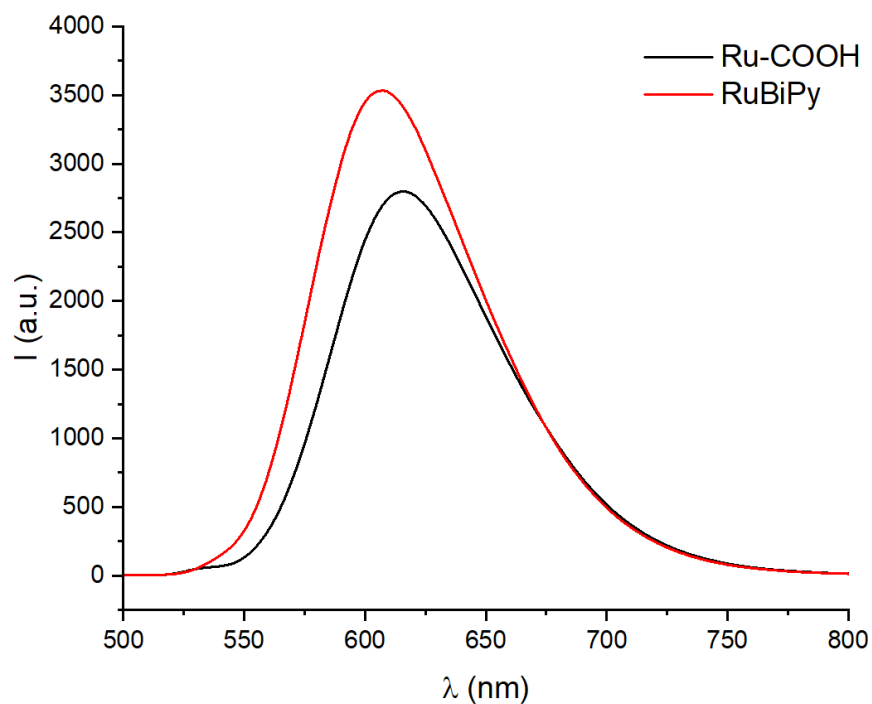


Fig. 5.62. Comparison of the emission spectra ($\lambda_{\text{exc}} = 452$ nm) of Ru-COOH and RuBiPy, each $5 \mu\text{M}$ in water.

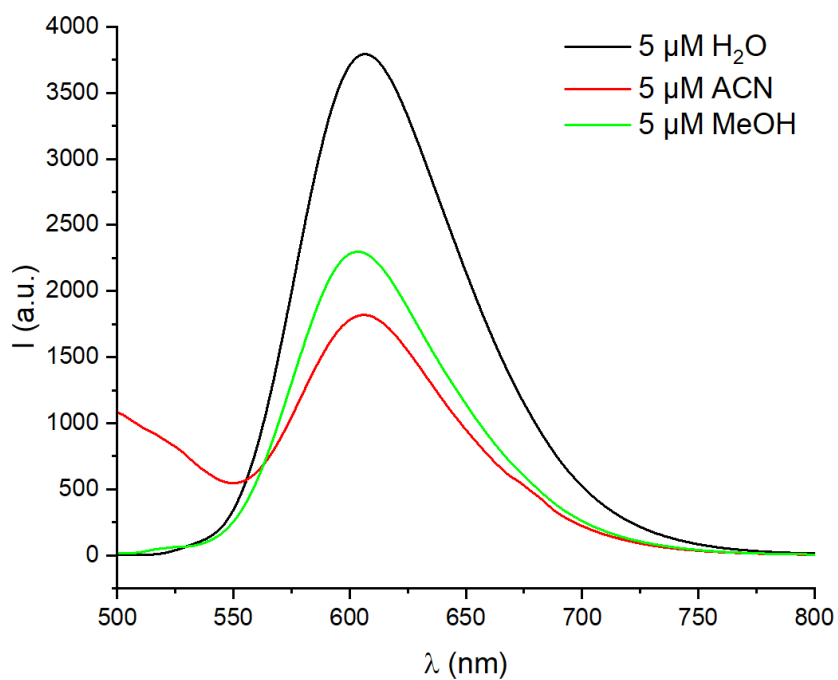


Fig. 5.63. Comparison of the emission spectra ($\lambda_{\text{exc}} = 452$ nm) of RuBiPy ($5 \mu\text{M}$) in various solvents.

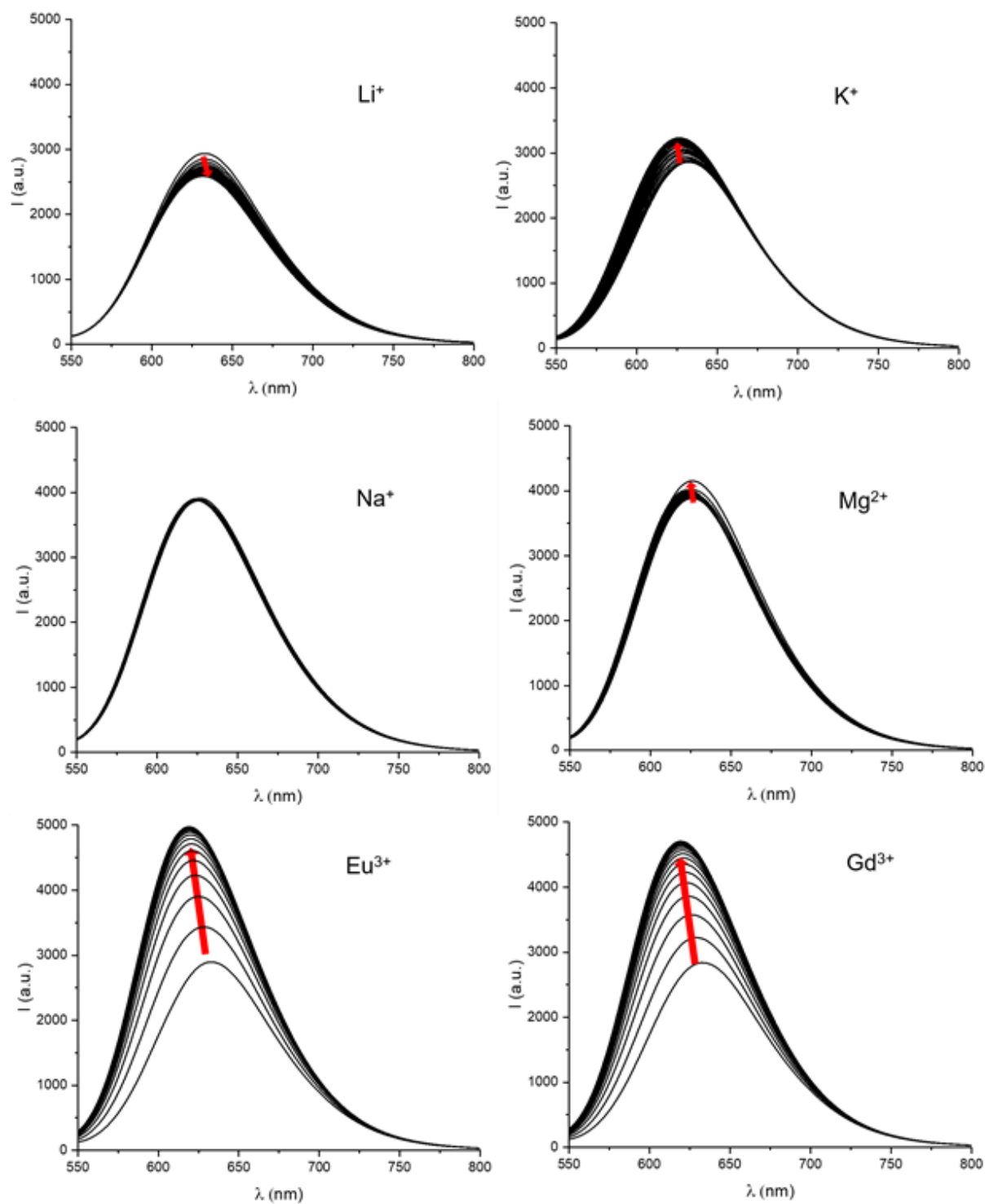


Fig. 5.64. Emission spectra ($\lambda_{\text{exc}} = 452$ nm) of CB7-Ru in water (5 μM) upon addition of various cations (up to 10 mM).

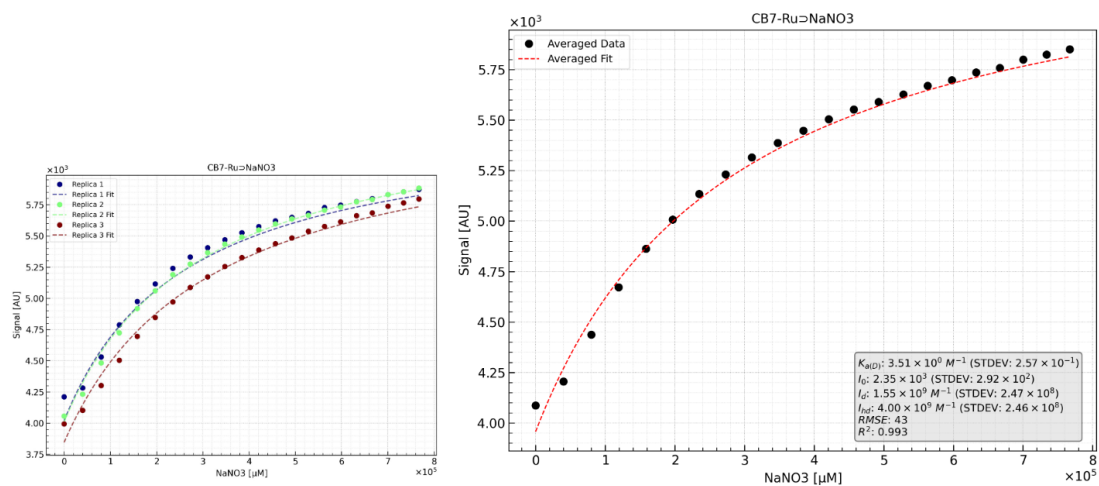


Fig. 5.65. Titration curve and fit (1:1 model) of NaNO_3 with CB7-Ru in water.

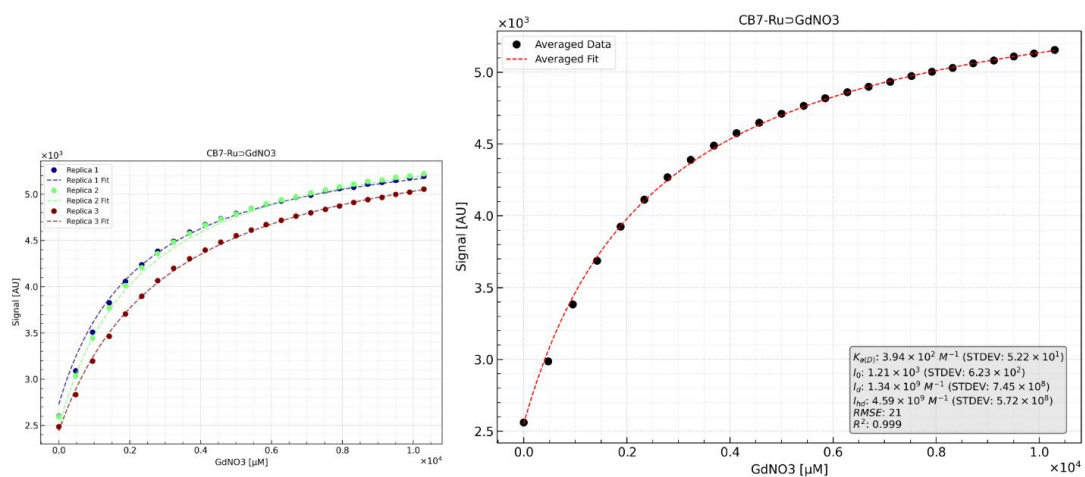


Fig. 5.66. Titration curve and fit (1:1) model of GdNO_3 with CB7-Ru in water.

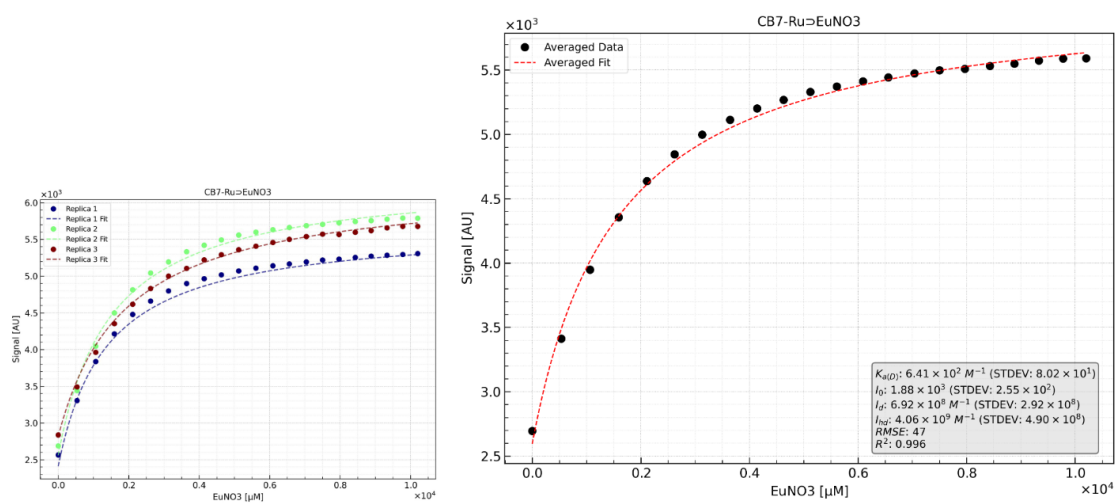


Fig 5.67. Titration curve and fit (1:1 model) of EuNO_3 with CB7-Ru in water.

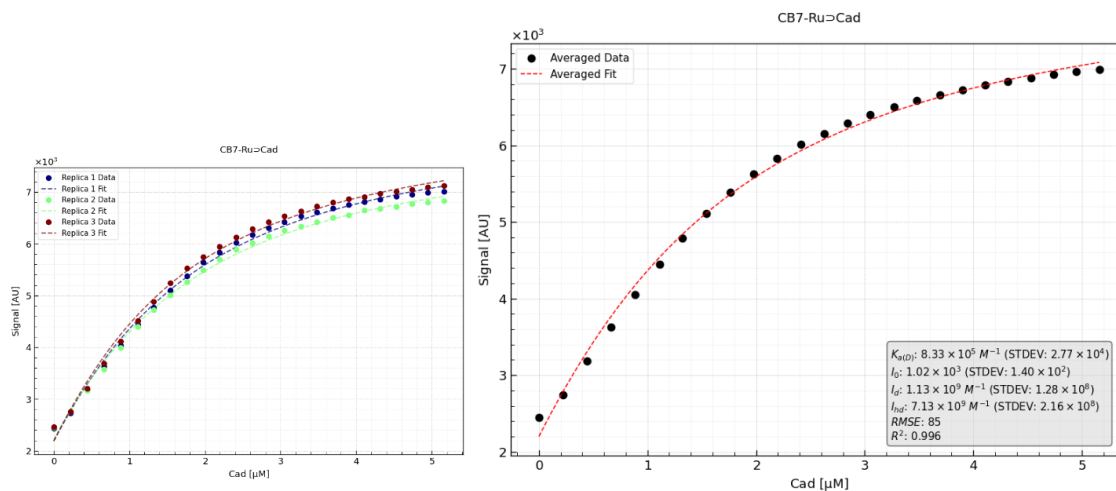


Fig. 5.68. Titration curve and fit (1:1 model) of cadaverine with CB7-Ru in water.

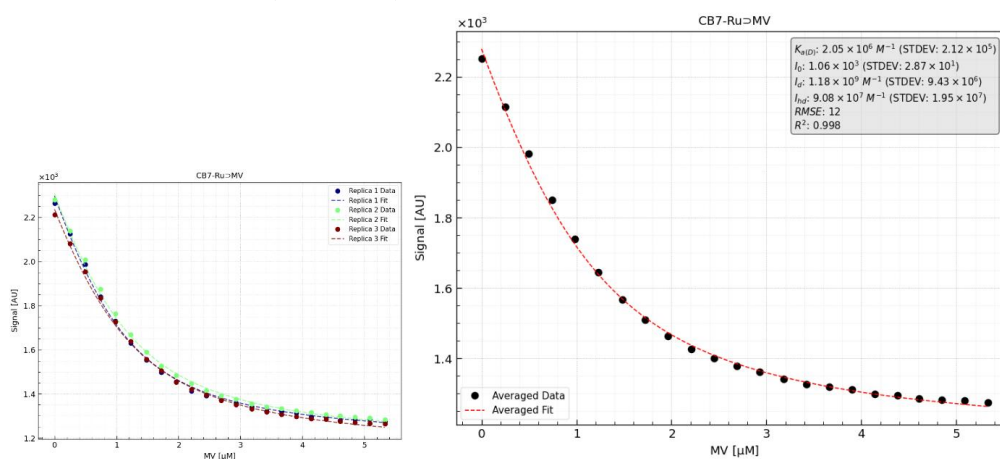


Fig. 5.69. Titration curve and fit (1:1 model) of methyl viologen with CB7-Ru in water.

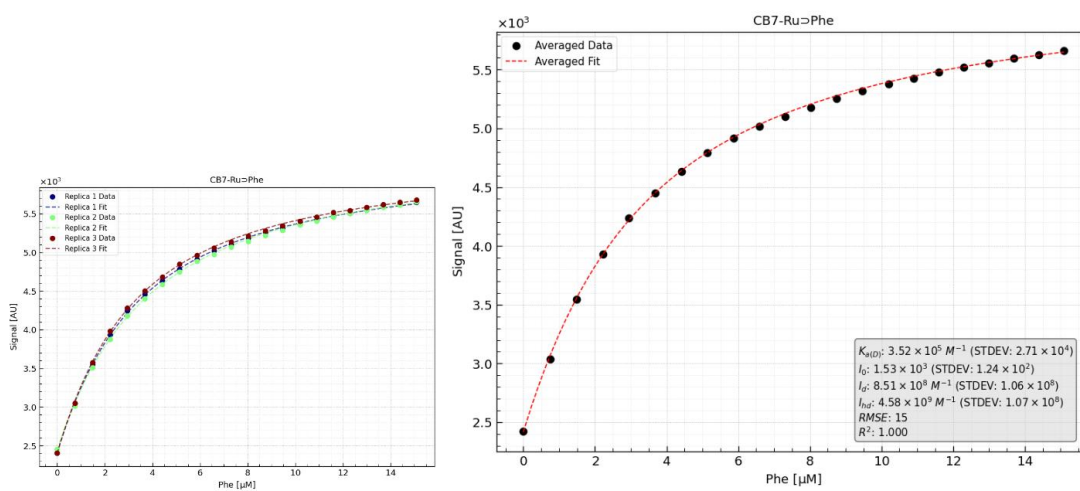


Fig. 5.70. Titration curve and fit (1:1 model) of phenylalanine with CB7-Ru in water.

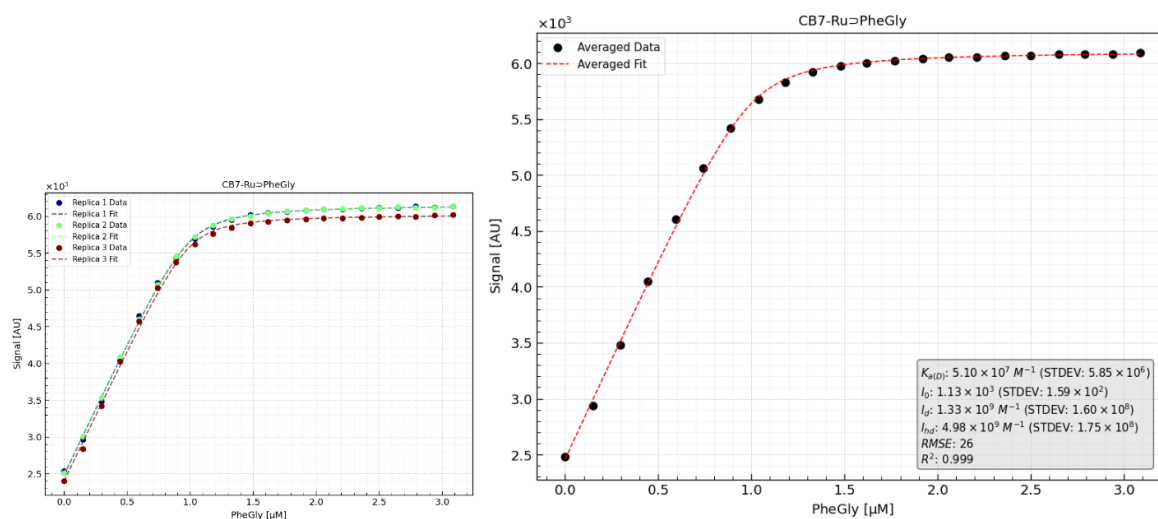


Fig. 5.71. Titration curve and fit (1:1 model) of phenylalanine glycine with CB7-Ru in water.

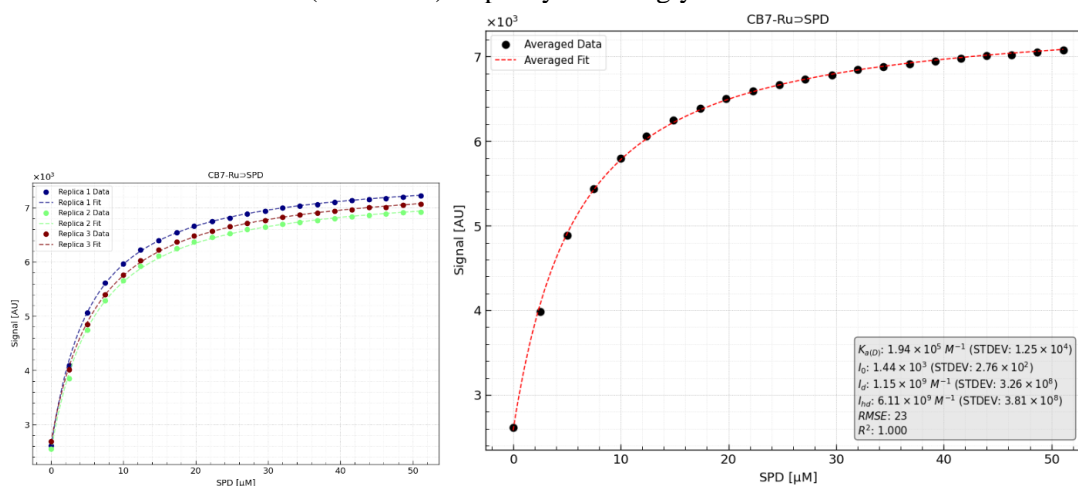


Fig. 5.72. Titration curve and fit (1:1 model) of spermidine with CB7-Ru in water.

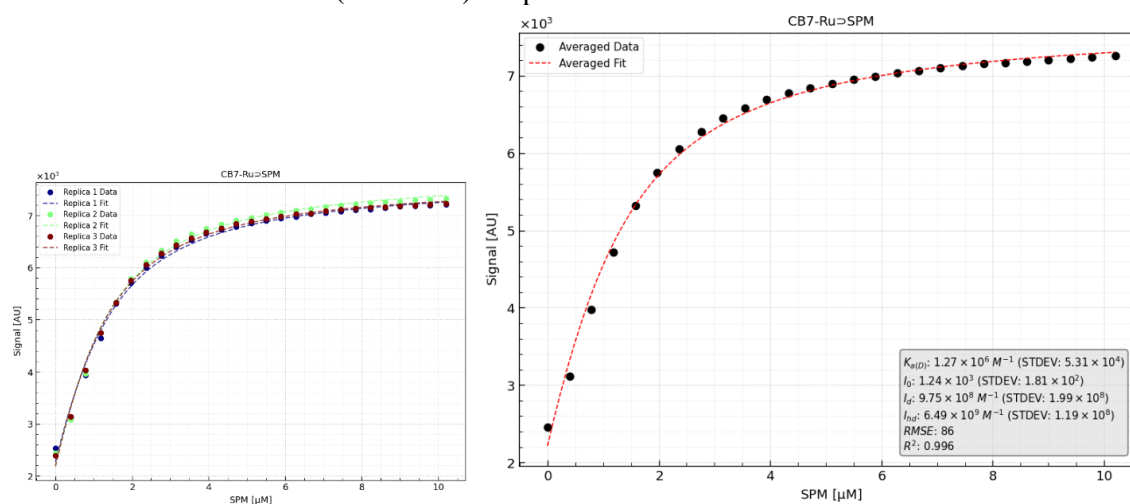


Fig. 5.73. Titration curve and fit (1:1 model) of spermine with CB7-Ru in water.

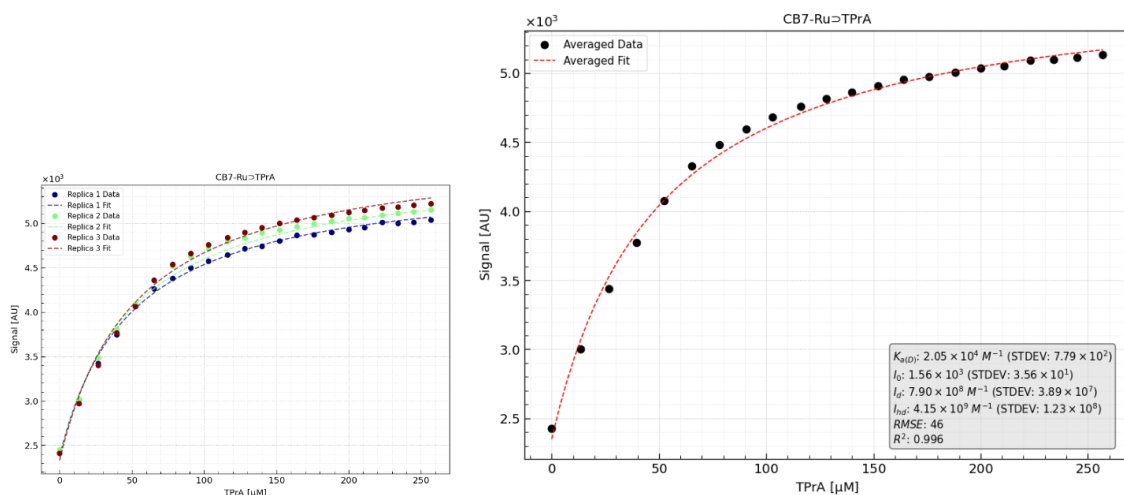


Fig. 5.74. Titration curve and fit (1:1 model) of tripropylamine with CB7-Ru in water.

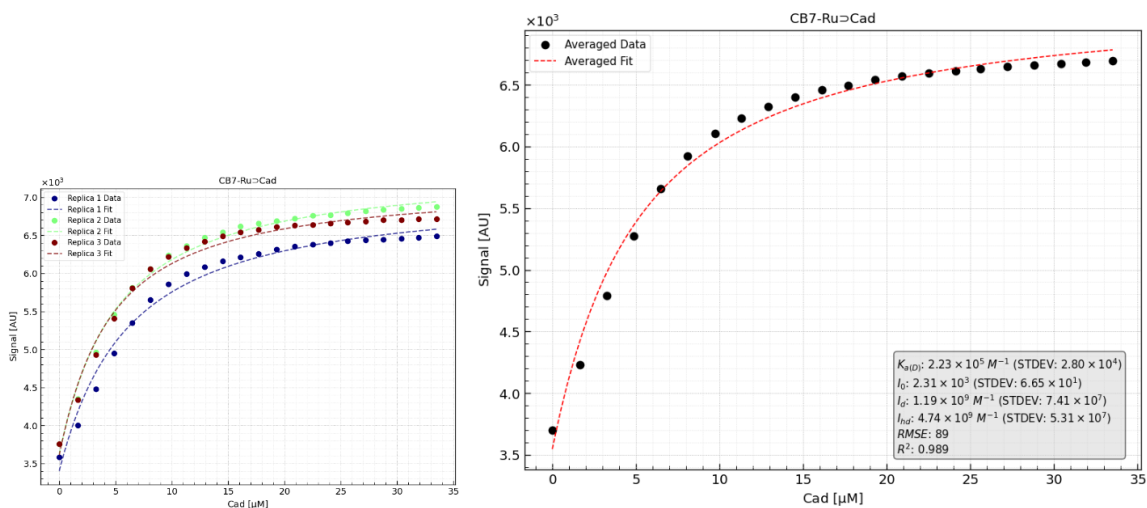


Fig. 5.75. Titration curve and fit (1:1 model) of cadaverine with CB7-Ru in PB (0.01 M, pH = 7.4).

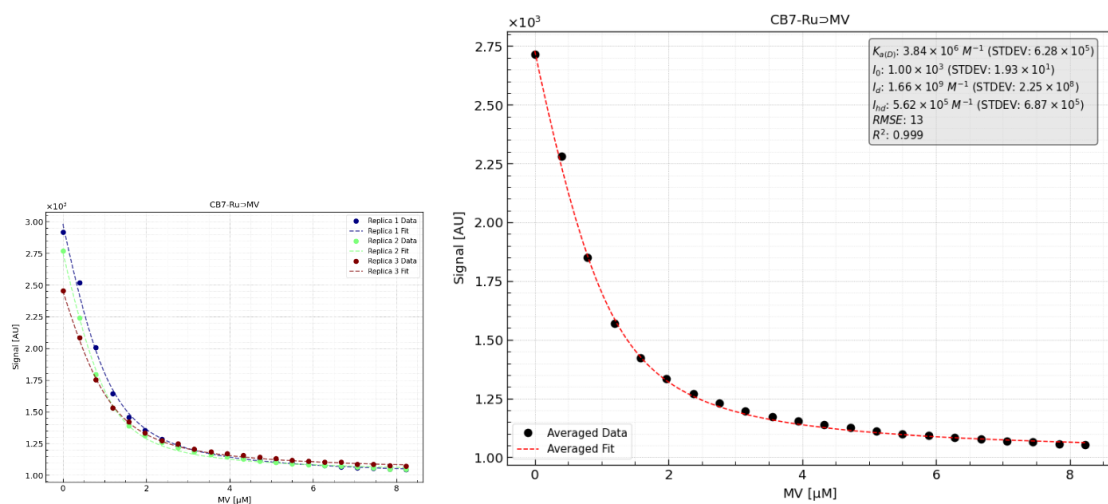


Fig. 5.76. Titration curve and fit (1:1 model) of methyl viologen with CB7-Ru in PB (0.01 M, pH = 7.4)

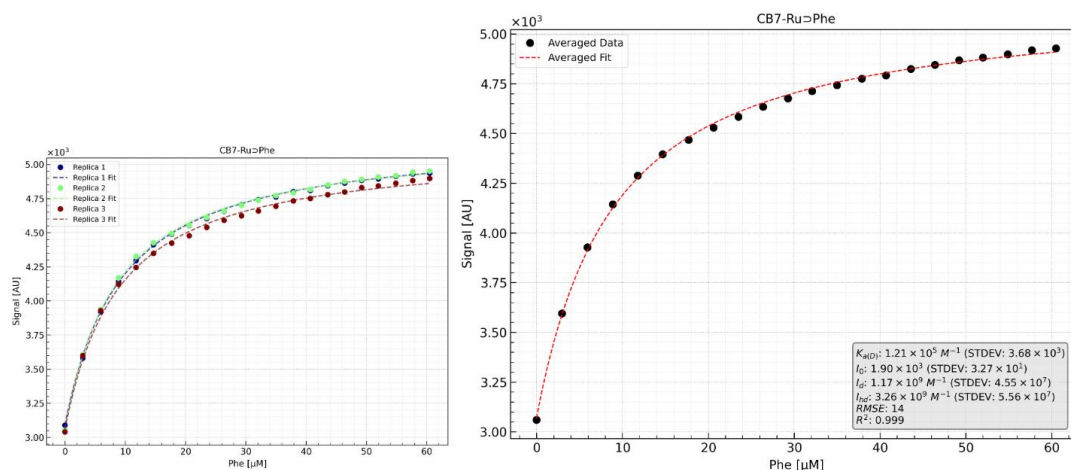


Fig. 5.77. Titration curve and fit (1:1 model) of phenylalanine with CB7-Ru in PB (0.01 M, pH = 7.4)

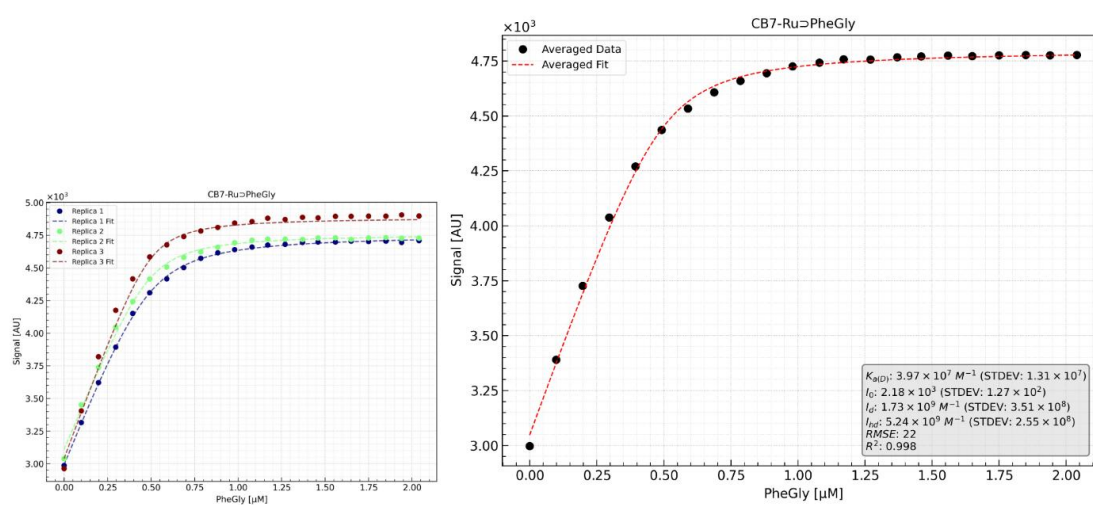


Fig. 5.78. Titration curve and fit (1:1 model) of phenylalanine glycine with CB7-Ru in PB (0.01 M, pH = 7.4)

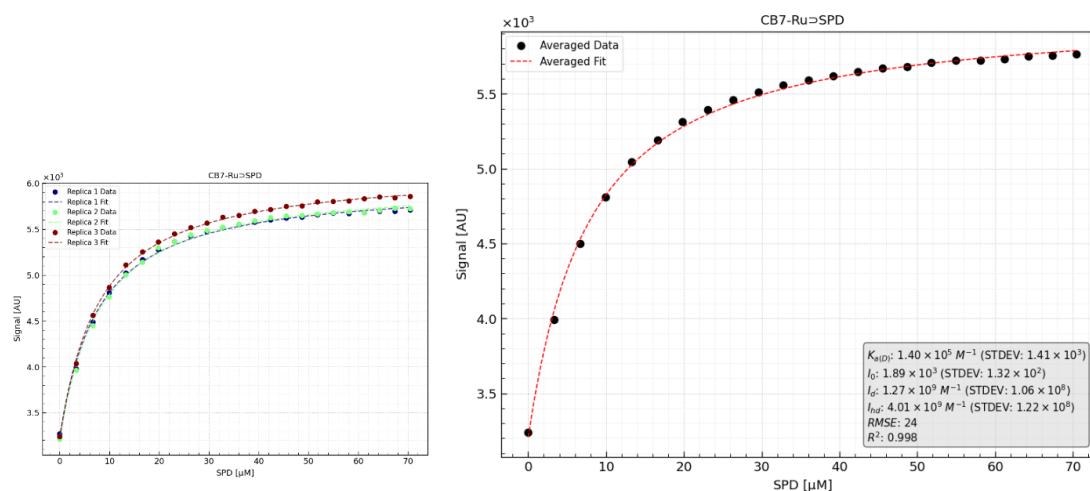


Fig. 5.79. Titration curve and fit (1:1 model) of spermidine with CB7-Ru in PB (0.01 M, pH = 7.4)

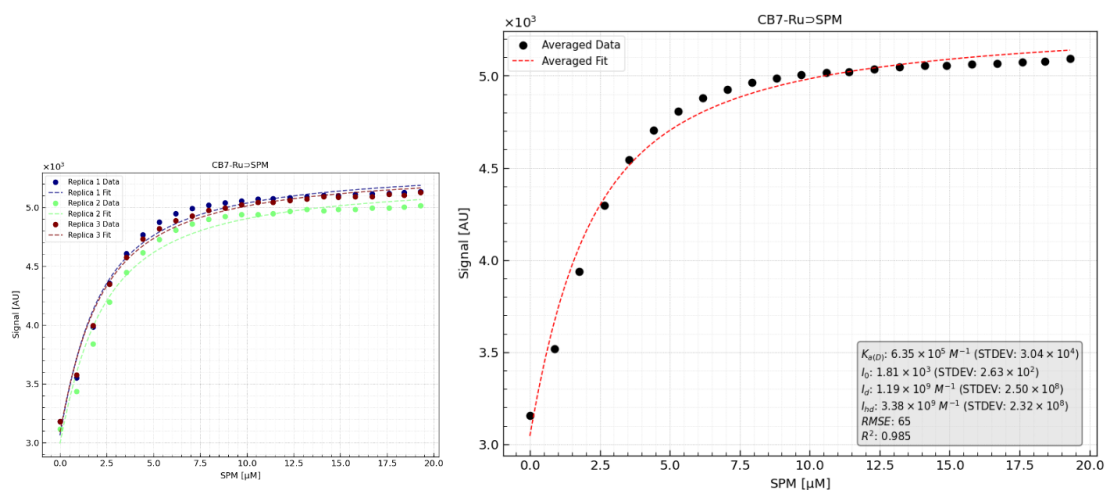


Fig. 5.80. Titration curve and fit (1:1 model) of spermine with CB7-Ru in PB (0.01 M, pH = 7.4)

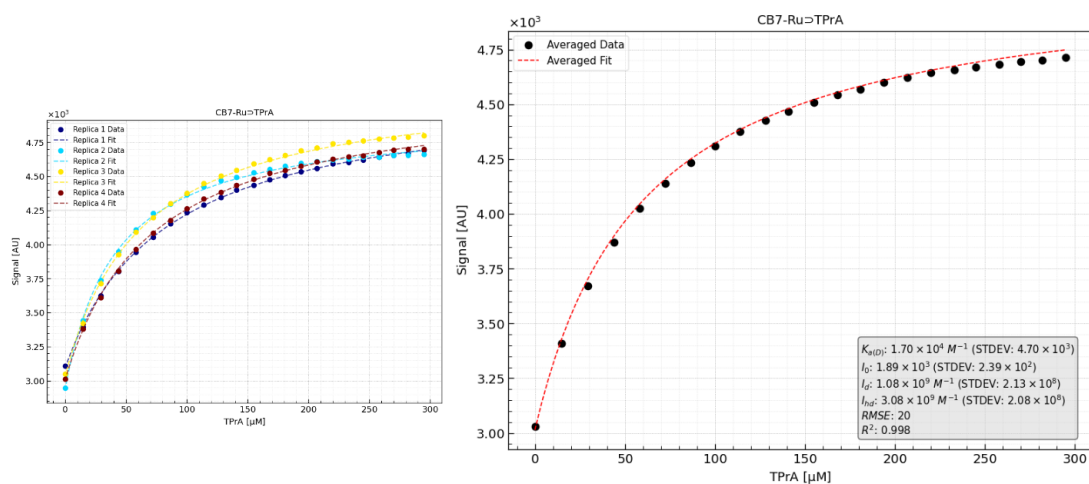


Fig. 5.81. Titration curve and fit (1:1 model) of tripropylamine with CB7-Ru in PB (0.01 M, pH = 7.4)

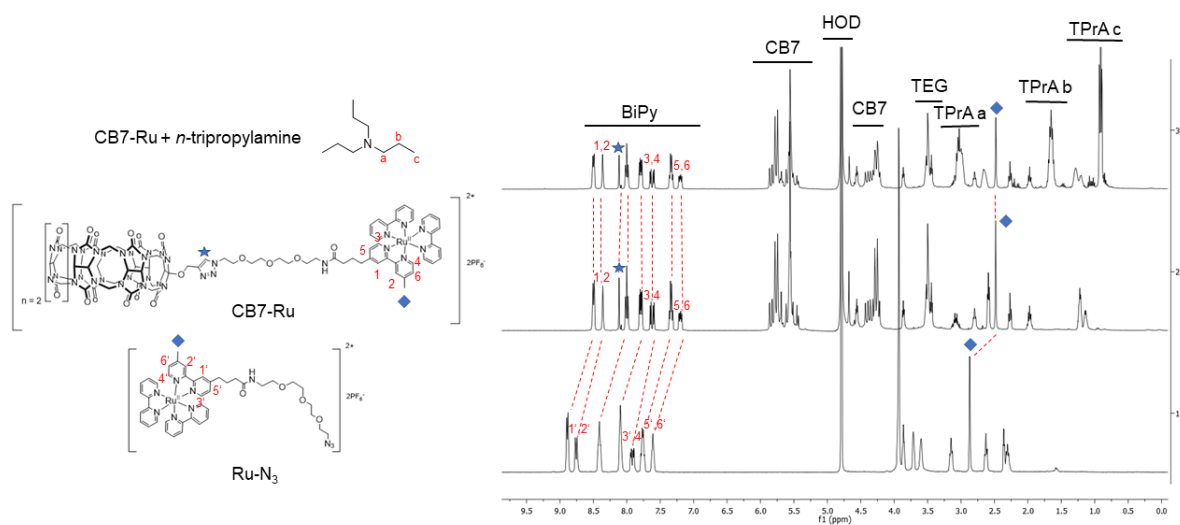


Fig. 5.82. Overlay of ^1H NMR (400 MHz, D_2O) spectra of Ru-N_3 (bottom), CB7-Ru (middle) and CB7-Ru with excess TPrA (top).

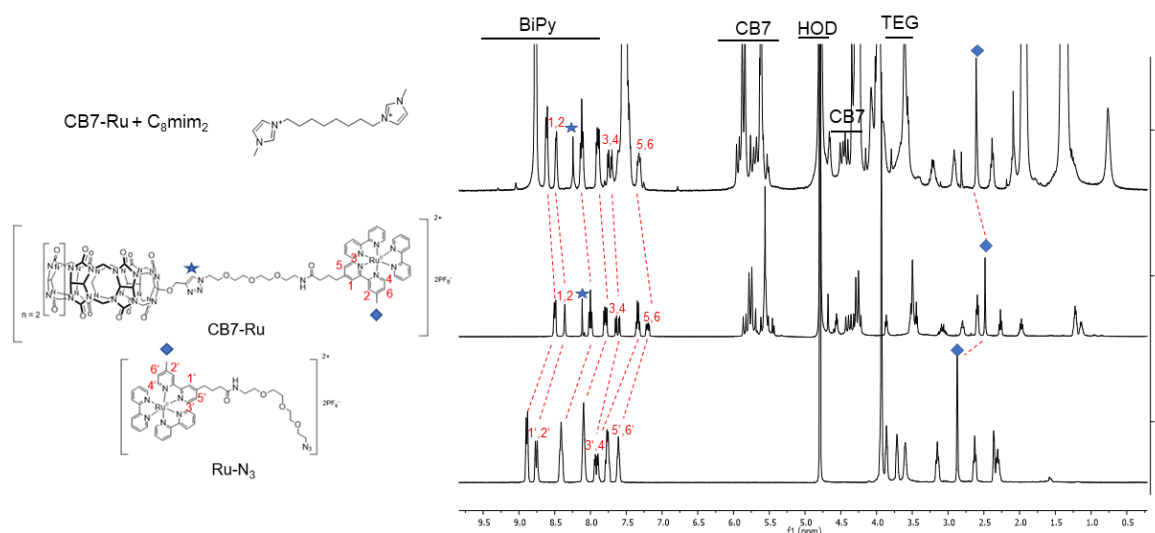


Fig. 5.83. Overlay of ^1H NMR (400 MHz, D_2O) spectra of Ru-N_3 (bottom), CB7-Ru (middle) and CB7-Ru with excess C_8mim_2 (top).

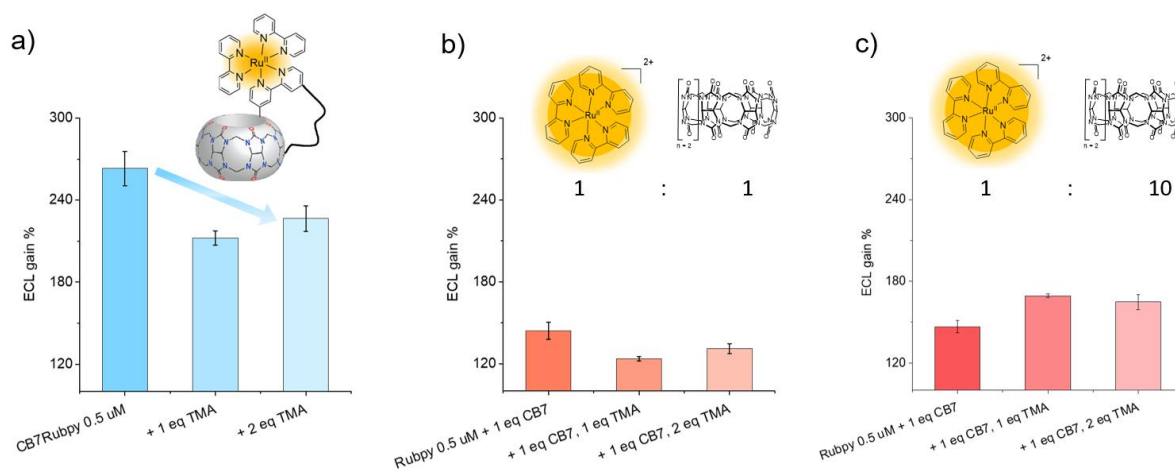


Fig. 5.84. CV-ECL measurements performed in a 0.3 M PB solution at pH 6.8, with TPrA 180 mM. The working electrode potential was scanned at 100 mV/s, and emission acquired every 100 ms (PMT bias 750 mV, positioned on the short side of the cell). Amplification level at 00.0 μA . The resulting ECL signal intensity is normalised on the $[\text{Ru}(\text{bpy})_3]^{2+}$ 0.5 μM ECL signal, and reported for a) CB7-Ru 0.5 μM , either alone or in the presence of 1-3 eq. of TMA; b) $[\text{Ru}(\text{bpy})_3]^{2+}$ 0.5 μM in the presence of 1 eq. of CB7 , upon addition of 1-3 eq. of TMA; c) $[\text{Ru}(\text{bpy})_3]^{2+}$ 0.5 μM in the presence of 10 eq. of CB7 , upon addition of 1-3 eq. of TMA (SD calculated for $n \geq 3$).

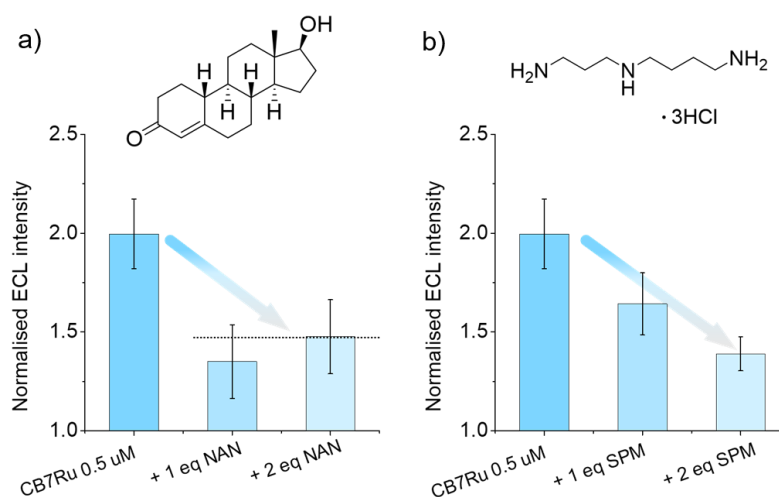


Fig. 5.85. CV-ECL measurements performed in a 0.3 M PB solution at pH 6.8, with TPrA 180 mM. The working electrode potential was scanned at 100 mV/s, and emission acquired every 100 ms (PMT bias 750 mV, positioned on the short side of the cell). Amplification level at 00.0 μA. The resulting ECL signal intensity is normalised on the $[\text{Ru}(\text{bpy})_3]^{2+}$ 0.5 μM ECL signal, and reported for a) CB7-Ru 0.5 μM, either alone or in the presence of 1–2 eq. of nandrolone; b) CB7-Ru 0.5 μM, either alone or in the presence of 1–2 eq. of spermidine trihydrochloride (SD calculated for $n \geq 3$).

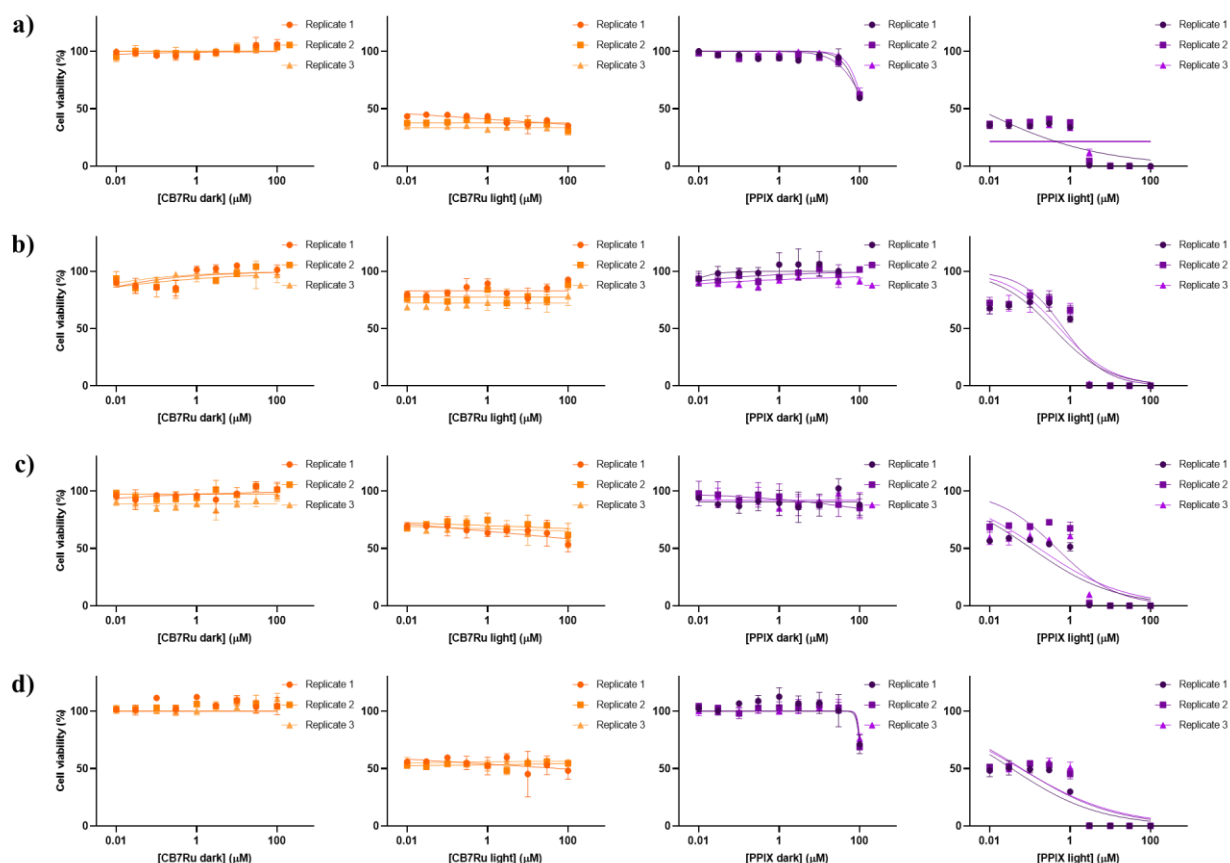


Fig. 5.86. Cell viability graphs after 4 h incubation with CB7-Ru or PpIX, \pm light irradiation (450 nm, 2 min), and 44 h rest in a) U87 cells, b) A549 cells, c) HT29 cells, and d) RPE-1 cells. The biological evaluation of CB7-Ru was performed by Dr. Giulia Salluce at the Chimie ParisTech.

6. Distinguishing Biorelevant Analytes by a CB7-Coumarin Sensor Library

6.1. Fundamentals of Coumarins: Chemistry and Natural Origins

Coumarins are a prominent class of plant-derived secondary metabolites originating from the phenylpropanoid biosynthetic pathway. They play crucial roles in plant growth, defense, and adaptation to environmental stimuli. To date, over 1300 coumarin compounds have been identified, primarily in green plants, and are distributed across nearly 30 plant families – including *Umbelliferae*, *Apiaceae*, *Asteraceae*, *Fabaceae*, *Moraceae* - but also fungi and microorganisms have been described as producers of coumarins^{344, 345, 346} The discovery of coumarins dates back to 1820, when the simplest member of the class, coumarin itself, was first isolated by Vogel from *Coumarouna odorata* (now *Dipteryx odorata*), a plant known for its fragrant seeds.³⁴⁷ Extensive phytochemical investigations have since revealed the structural diversity of coumarins across various plant tissues, including roots, leaves, fruits and flowers. Their broad spectrum of biological activities has led to wide-ranging applications in pharmaceuticals, cosmetics, perfumery, and sustainable agriculture.^{345, 348, 349} Based on their chemical complexity, natural coumarins are generally classified into several subclasses: simple coumarins, isocoumarins, furanocoumarins (both linear and angular), pyranocoumarins (both linear and angular), biscoumarins, and phenylcoumarins.

Structurally, coumarins are characterized by a fundamental α -benzopyranone (1,2-benzopyranone) skeleton, a fused system consisting of a benzene ring and a lactone moiety.³⁵⁰ Simple coumarins feature substitutions such as hydroxyl, methoxy, methylenedioxy or prenyl groups on the benzene ring and lack additional fused heterocycles. In contrast, composite coumarins contain additional cyclic systems formed via intramolecular condensation reactions. For instance, furanocoumarins arise from cyclization involving the C7 hydroxyl group and adjacent C6 or C8 carbons, forming fused furan rings, whereas pyranocoumarins form via interactions between hydroxyl or methoxy groups and neighboring carbon atoms to generate pyran-fused rings. These can adopt either linear or angular configurations depending on ring orientation.³⁵¹

Coumarins possess several desirable physicochemical and biological features: low molecular weight, structural simplicity, good solubility in most organic solvents, low toxicity, and high bioavailability.³⁵² These characteristics, coupled with their extensive pharmacological activities – including anticoagulant, antimicrobial, anti-inflammatory, antidiabetic, neuroprotective, and antiproliferative effects – make them valuable scaffolds for drug development.^{344, 349, 350, 352} Their relevance also extends to the food industry, where their antioxidant and antifungal activities are under investigation for food preservation and safety applications.³⁵³ Beyond their biological functions, coumarins are widely recognized for their luminescent properties, which stem from their electron-rich π -conjugated systems and charge-transfer capabilities. These photophysical characteristics have positioned coumarin derivatives as key molecular frameworks in fluorescent probes, optical sensors, and laser dyes, and form the foundation for their use in supramolecular chemosensing applications.³⁵⁴⁻³⁵⁶

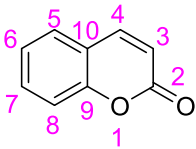
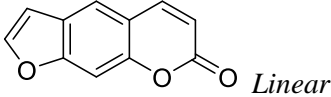
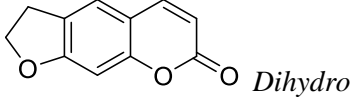
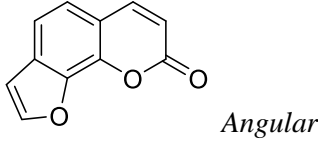
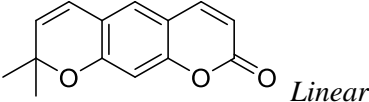
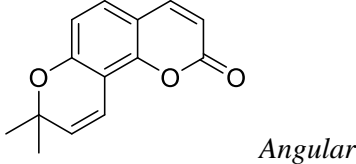
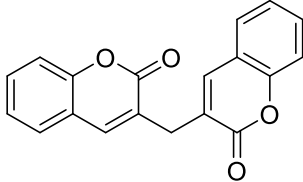
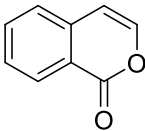
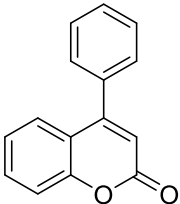
Class	General Structure	Examples
Simple coumarins		Osthole
Furanocoumarins	 <i>Linear</i>  <i>Dihydro</i>  <i>Angular</i>	Psoralen, Antoghenol, Columbianadin
Pyranocoumarins	 <i>Linear</i>  <i>Angular</i>	Grandivittin, Inophyllum A
Biscoumarins		Dicoumarol
Isocoumarins		Thunberginol
Phenylcoumarins		Isodispar B

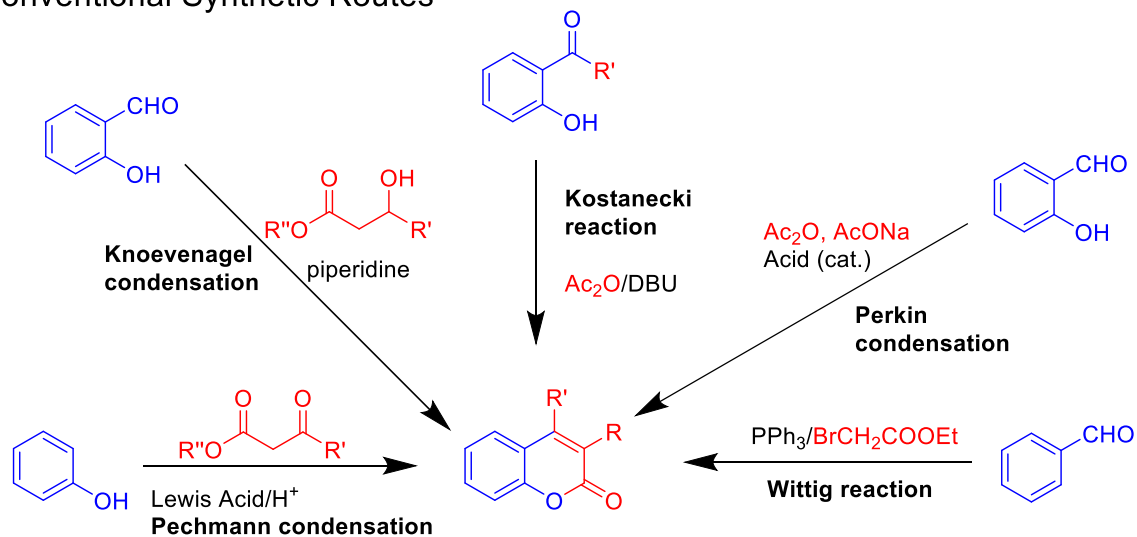
Table 6.1. Classes, basic structures and examples of naturally occurring coumarins.

6.2. Synthetic Strategies for Coumarin Derivatives

A wide variety of synthetic methods have been developed for the preparation of coumarins and their derivatives, with the choice of route largely depending on the desired substitution pattern and functional group compatibility. Classical condensation reactions remain the foundation of coumarin synthesis, while

modern adaptations have improved yields, selectivity, and reaction conditions. **Fig. 6.2** shows an overview of conventional and modern synthetic strategies. These routes offer flexibility for introducing diverse substituents at specific positions on the coumarin scaffold.

Conventional Synthetic Routes



Modern Synthetic Strategies

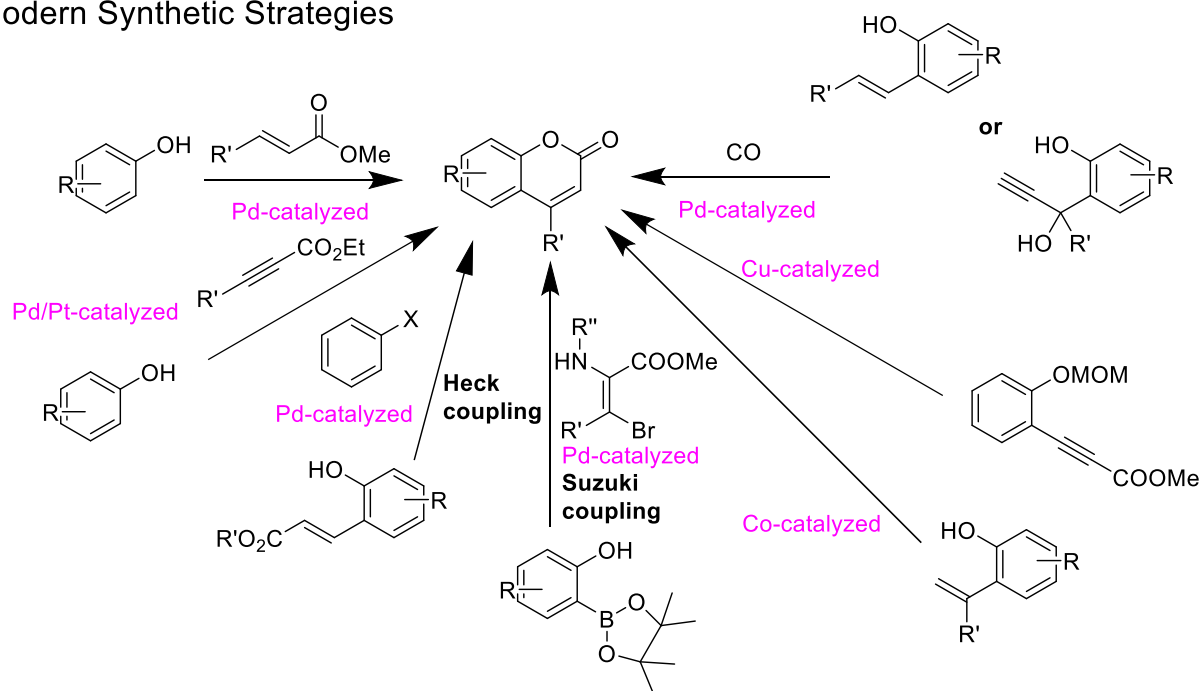


Fig. 6.1. Conventional and modern synthetic strategies to access the coumarin scaffold. Slightly modified from ref ³⁵⁴

The Pechmann condensation is one of the most widely used and efficient methods for synthesizing substituted coumarins, particularly those bearing electron-donating groups on the aromatic ring. This reaction involves the acid-catalyzed condensation of phenols (or phenolic derivatives) with β -ketoesters, typically in presence of a Lewis acid catalyst such as AlCl_3 . The reaction mechanism begins with

activation of the β -ketoester's carbonyl group by the Lewis acid, increasing its electrophilicity. The phenol, often deprotonated to a phenolate anion, performs a nucleophilic attack on the activated β -ketoester, forming a C-C bond. The intermediate then undergoes intramolecular electrophilic aromatic substitution, leading to cyclization and subsequent dehydration, which yields the coumarin core structure.³⁵⁴ The Pechmann reaction is particularly attractive due to its operational simplicity, broad substrate tolerance, and ability to furnish coumarins in good to excellent yields under mild conditions. It remains a foundational strategy in both academic and industrial synthesis of coumarin-based molecules, including fluorescent dyes, pharmaceuticals, and agrochemicals.

The Knoevenagel condensation is a well-established and versatile method for synthesizing 3-substituted coumarins, particularly those bearing aryl or alkyl groups at the 3-position. This reaction typically involves the condensation of *o*-hydroxybenzaldehyde (or related aromatic aldehydes) with malonic acid or malonic esters (as 1,3-dicarbonyl compounds), in the presence of a basic catalyst such as piperidine or piperazine. The reaction mechanism proceeds through base-catalyzed enolate formation, where deprotonation of the methylene group in malonic acid or its ester forms a stabilized enolate ion. This nucleophile then attacks the electrophilic carbonyl carbon of the aldehyde, yielding a β -hydroxy intermediate, which undergoes dehydration to form a α,β -unsaturated carbonyl compound. In the case of *o*-hydroxybenzaldehyde, the adjacent hydroxyl group facilitates intramolecular nucleophilic attack, promoting cyclization and lactonization to generate the coumarin ring system.³⁵⁷ The Knoevenagel reaction can be conducted under thermal or microwave-assisted conditions, and a variety of heterogeneous catalysts have been explored to improve sustainability and reaction efficiency. For example, using cellulosic sulfonic acid (CSA) as a solid catalyst enables the synthesis of 3-substituted coumarins under mild, eco-friendly conditions.^{358, 359} Due to its broad substrate scope and adaptability to green chemistry protocols, the Knoevenagel condensation remains a key strategy in the preparation of functionally diverse coumarins.

The Perkin reaction is a classical synthetic method for the preparation of 3-aryl- or heteroaryl-substituted coumarins, particularly useful for introducing extended conjugation into the coumarin scaffold. This reaction involves the base-catalyzed condensation of aromatic aldehydes with acetic anhydride (Ac_2O) in the presence of a basic salt, typically sodium acetate.³⁶⁰ Mechanistically, the reaction proceeds through the formation of a β -aryl acrylic acid intermediate (a substituted cinnamic acid), which arises from the aldol-type condensation between an aromatic aldehyde and Ac_2O . Upon heating, this intermediate undergoes intramolecular cyclization and decarboxylation, resulting in the formation of the coumarin ring system. The Perkin reaction offers a straightforward and cost-effective route to synthetically valuable 3-substituted coumarins, and remains relevant for both academic research and industrial applications. Variations of the original procedure, including microwave-assisted or solvent-free conditions, have also been developed to enhance reaction efficiency and sustainability.³⁵⁴

The Kostanecki reaction is a valuable method for the synthesis of 4-aryl coumarins, particularly under mild and efficient conditions. It involves the condensation of 2-hydroxybenzophenones with Ac_2O in the

presence of a strong organic base, such as 1,8-diazabicyclo[5.4.0]undec-7-ene (DBU). This reaction facilitates intramolecular cyclization through acetylation of the phenolic hydroxyl group, followed by lactonization, yielding 4-aryl coumarins in good yields.³⁵⁴ In addition to simple 4-aryl derivatives, 3,4-disubstituted coumarins can also be accessed *via* the Kostanecki reaction, using appropriately substituted 2-acyloxybenzophenones as starting materials. These intermediates are readily prepared and allow for structural variation at both the 3- and 4-positions of the coumarin ring, offering a flexible route to functionalized derivatives. Due to its compatibility with mild conditions and broad substrate tolerance, the Kostanecki reaction remains a useful strategy for the construction of highly substituted coumarin frameworks in synthetic and medicinal chemistry.

The Baylis-Hillman reaction offers a powerful C-C bond-forming strategy for the synthesis of functionalized coumarin derivatives, particularly at the 3-position. This reaction involves the coupling of an α,β -unsaturated carbonyl compound (such as an enone or acrylate) with an electron-deficient aldehyde or ketone, catalyzed by a Lewis base, typically 1,4-diazabicyclo[2.2.2]octane (DABCO).³⁵⁴ A representative example involves the reaction of 2-hydroxybenzaldehydes with methyl acrylate under DABCO catalysis, yielding chroman and coumarin derivatives through a tandem Baylis-Hillman condensation and cyclization. Subsequent treatment of the Baylis-Hillman adducts with concentrated HCl in refluxing AcOH produces 3-(chloromethyl)coumarins in excellent yields. Further transformations, such as reaction with HI in an Ac₂O/AcOH mixture, afford 3-methylcoumarins, which can be oxidized with SeO₂ to yield 3-formylcoumarins, valuable intermediates. In a related work, Rashamuse *et al.* synthesize phosphonated 3-(benzylaminomethyl)coumarins via this strategy, demonstrating its applicability to structurally diverse coumarin scaffolds.³⁶¹ These transformations showcase the modularity and efficiency of Baylis-Hillman based routes for constructing highly functionalized coumarins

While not explicitly discussed, the Wittig reaction also serves as a complementary method for forming 3-alkylidene coumarins *via* olefination of aldehydes with stabilized phosphonium ylides, enabling the introduction of various alkenyl substituents at the 3-position of the coumarin core.

Advancements in synthetic methodology have led to the development of modern, transition metal-catalyzed strategies for the efficient construction and functionalization of coumarin derivatives, particularly at the 3-position. These methods often rely on C-H activation or cross-coupling protocols, providing access to structurally diverse and highly functionalized coumarins under mild and selective conditions. Among these, the most widely used techniques include Suzuki-Miyaura, Heck, and Buchwald-Hartwig coupling reactions, which utilize Pd-, Pt-, Cu-, or Co-based catalysts to forge new C-C and C-N bonds. Other notable transformations involve alkenylation of phenols, carbonylation of vinyl phenols, and hydroarylation reactions all of which expand the synthetic utility of the coumarin scaffold.³⁶²⁻³⁶⁷

The Suzuki-Miyaura coupling is a powerful cross-coupling protocol for introducing aryl heteroaryl groups at the 3-position of the coumarin core. It involves the palladium-catalyzed coupling of an aryl (or

heteroaryl) halide with a boronic acid or boronate ester in the presence of a base. The catalytic cycle proceeds through three key steps. First, oxidative addition of the aryl halide to a Pd(0) species proceeds, forming a Pd(II) complex. Subsequently, transmetalation with the boronic acid (or ester), yielding a new aryl-Pd(II) intermediate. Lastly, reductive elimination producing the desired 3-arylcoumarin and regenerating the active Pd(0) catalyst. This method is highly versatile, tolerates a wide range of functional groups, while providing excellent regioselectivity, making it a preferred approach for accessing substituted coumarins with aryl or heteroaryl functionalities.

The Buchwald-Hartwig amination is another Pd-catalyzed method, widely used for the direct introduction of amino groups at the 3-position of coumarin derivatives. The reaction proceeds very similar to the Suzuki-Miyaura coupling and also involves three distinct catalytic steps. Again, oxidative addition of an aryl halide to Pd(0) occurs, forming a Pd(II) complex. Then, the process continues with coordination and deprotonation of an amine, followed by transmetalation to the Pd(II) center. As last step, reductive elimination proceeds, yielding the C-N coupled product, a 3-amino substituted coumarin.³⁶⁸ This reaction also offers broad functional group compatibility and can be used to introduce a variety of primary and secondary amines onto the coumarin framework.

The Heck reaction is another valuable Pd-catalyzed C-C coupling strategy, particularly effective for installing aryl or vinyl substituents at the 3-position of olefinic coumarin derivatives. It involves the reaction of an aryl halide with a coumarin bearing a C=C double bond, under basic conditions. The mechanism also includes oxidative addition as the starting point, and proceeds with migratory insertion of the olefin, β -hydride elimination, and reductive elimination. The Heck reaction enables the formation of extended π -systems and has been used to synthesize conjugated coumarins for applications in fluorescence and photophysics.³⁶⁹

The synthesis of coumarins has evolved from classical condensation reactions to modern metal-catalyzed coupling strategies, offering chemists a versatile toolkit for accessing structurally diverse derivatives. Traditional methods still remain foundational for constructing the coumarin core, particularly due to their simplicity, efficiency, and broad substrate scope. In contrast, transition metal-catalyzed reactions also enable late-stage functionalization and the introduction of complex aryl, heteroaryl, or amino substituents at specific positions on the coumarin scaffold. Together, these approaches provide a robust and adaptable synthetic framework that supports both target-oriented synthesis and structure-activity relationship (SAR) exploration in medicinal and materials chemistry.

6.3. Functional Roles and Practical Applications of Coumarin Derivatives

The remarkable structural diversity of coumarins underpins their wide range of biological activities, making them valuable scaffolds in drug discovery and development.³⁴⁵ Although not flavonoids in the strict biochemical sense, coumarins are often grouped with flavonoid-related natural products due to their biosynthetic origin and functional similarities. In plants flavonoid compounds fulfill key physiological roles, while in mammals, coumarins influence numerous cellular pathways and enzymatic functions. As

natural products, coumarins and their derivatives exhibit a broad spectrum of pharmacological activities, including antiviral (e.g., anti-HIV), antitumor, antioxidant, antimicrobial, anti-inflammatory, analgesic, and anticoagulant effects. Their chemical versatility and biological relevance have positioned them as promising candidates for the development of novel therapeutics.³⁷⁰⁻³⁷² In the following, a selection of the most important pharmacological applications will be described in more detail.

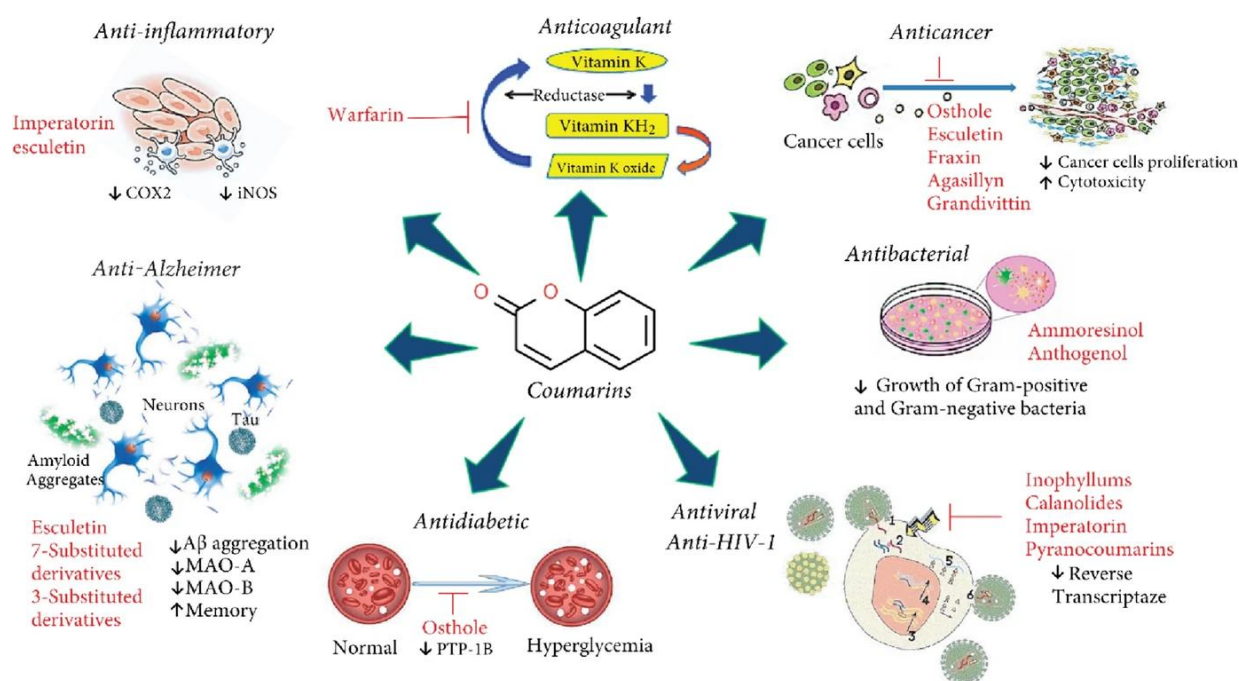


Fig. 6.2. Various molecular mechanisms and pharmacologically relevant applications of common coumarins and their derivatives. Reprinted with permission from ref³⁵⁴ © Springer

The fight against human immunodeficiency virus (HIV) took a major step forward in 1987 with the introduction of zidovudine, the first nucleoside reverse transcriptase inhibitor targeting HIV reverse transcriptase (RT).³⁷³ This was followed by the development of additional RT inhibitors such as didanosine and zalcitabine. However, the emergence of drug-resistant HIV strains spurred a search for alternative therapeutic agents, including those from natural sources. In 1992, Kashman *et al.* reported a groundbreaking discovery: an extract from the rainforest tree *Calophyllum lanigerum* exhibited strong anti-HIV activity along with low cytotoxicity to healthy human cells.³⁷⁴ Calanolide A became the first coumarin-derived natural product to enter clinical trials as an anti-HIV agent. Its promising profile prompted the synthesis of numerous structurally modified pyranocoumarin analogues with enhanced potency and pharmacokinetic properties.³⁷⁵ Beyond Calanolides, a broad array of naturally occurring and semi-synthetic coumarins have demonstrated potent anti-HIV activity. These compounds act primarily by inhibiting key viral enzymes, including HIV RT, HIV protease (PR), and HIV integrase (IN).³⁷⁶ Among them, the tetracyclic pyranocoumarin scaffold has emerged as a structural motif essential for HIV inhibition, offering a foundation for the design of new therapeutic agents. These findings position

coumarins as valuable lead structures in the ongoing development of novel anti-HIV therapeutics, particularly those capable of overcoming resistance to conventional drugs.^{354, 370}

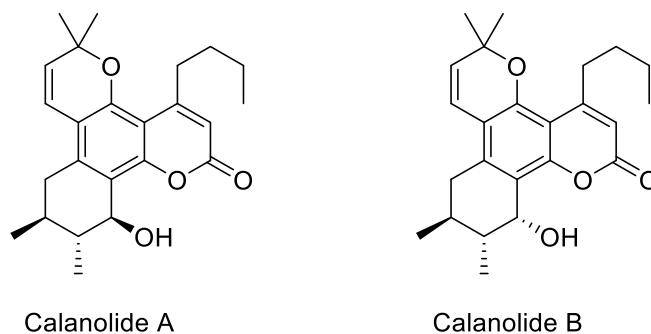


Fig. 6.3. Structures of Calanolide A and B, both tetracyclic pyranocoumarins found in the extract of *Clophyllum lanigerum*.

In recent years, an increasing number of naturally occurring coumarins with anticancer properties have been isolated and characterized from various plant sources.^{348, 350, 352} These compounds have gained significant attention due to their ability to interfere with multiple molecular targets and signaling pathways implicated in tumor progression, often with selective toxicity toward cancer cells. One particular promising target is heat shock protein 90 (Hsp90), a molecular chaperone involved in the stabilization and function of several oncogenic proteins. Unlike single-target therapies with limited efficacy across tumor types, Hsp90 inhibitors offer broader antitumor activity and can distinguish between normal and malignant cells. Studies have shown that coumarin-based antibiotics may serve as novel class of Hsp90 inhibitors, thereby expanding the repertoire of potential antineoplastic agents.³⁷⁷ A notable example is 4-methyl-7,8-dihydroxycoumarin (DHMC), which has demonstrated apoptosis-inducing effects in non-small cell lung carcinoma (NSCLC) cells. Its mechanism involves partial inhibition of ERK/MAPK signaling, independent of reactive oxygen species (ROS) production.³⁷⁸ DHMC has also shown potent cytotoxic activity against U-937 mononuclear leukemia cells and HL-60 myeloid leukemia cells, with evidence suggesting that the phenolic hydroxyl groups play a key role in mediating apoptosis.³⁷⁹ Further investigations revealed that the δ -lactone ring is essential for DHMC's biological activity, and that maintaining the structural integrity of the parent coumarin nucleus is critical for its antitumor efficacy.³⁸⁰ Additionally, some coumarins have been found to reduce the oxidative stress caused by conventional chemotherapeutic agents such as doxorubicin, thereby mitigating side effects without compromising antitumor potency in human breast cancer cells.³⁸¹ The structure-activity relationship (SAR) of coumarins reveals that antitumor potential is highly dependent on the substitution pattern and specific functional groups. Key structural features that contribute to cytotoxicity were found to include *ortho*-diphenol hydroxyl groups, alkyl groups at the C-6 position, phenyl or hydroxyl groups at the C-4 position, isopentyl or farnesyl side chains, khellactone-type scaffolds, and 2-phenylpyrimidine moieties. These functional groups exert antitumor effects through modulation of cell cycle progression, induction of apoptosis, and inhibition of key signaling pathways. Extensive *in vitro* studies using diverse

cancer cell lines have demonstrated that coumarin derivatives act *via* multiple mechanisms, underscoring their potential as multifunctional anticancer agents.³⁷⁰

The antibacterial potential has been recognized since 1945, when dicoumarol was first reported to inhibit the growth of several bacterial strains.³⁸² Since then, numerous natural and synthetic coumarin derivatives have demonstrated activity against a broad range of bacterial and fungal pathogens, making them attractive candidates for antimicrobial drug development. Coumarins act primarily as bacteriostatic agents, meaning they are capable of interfering with microbial processes such as spore germination, mycelial growth, and fruiting body formation.³⁷⁰ Their efficacy is strongly influenced by structural features, particularly the nature and position of substituent groups on the coumarin ring system.^{345, 349, 370, 382} Particularly, structure-activity relationship studies have revealed that the presence of free hydroxyl groups is a key determinant of antimicrobial potency, while a C-7 hydroxyl group on the parent coumarin nucleus is essential for antibacterial activity. Furthermore, a C-6 hydroxyl group seems to be critical for both antifungal and antibacterial properties. When a C-7 methoxy group is present, the addition of a free hydroxyl at C-6 or C-8 enhances broad-spectrum antimicrobial activity. The antimicrobial action of hydroxycoumarins may be linked to their phenolic structure, which enables free radical scavenging, thereby disrupting microbial metabolism. Interestingly, 4-hydroxycoumarin lacks antifungal activity, indicating that substitution at this position alone is insufficient for antifungal activity. In 6,7,8-trisubstituted coumarins, the polarity of the C-8 substituent significantly influences antifungal properties.³⁸³ The design of synthetic coumarins has further highlighted the importance of molecular properties in antimicrobial activity. For example, 3-ethylamino-substituted coumarins exhibit enhanced antibacterial activity when acyl chain length is extended. Lipophilicity is crucial – compounds with greater fat solubility can better penetrate bacterial membranes *via* passive diffusion. Structural features such as molecular planarity and the avoidance of long, bulky chains promote better interaction with and penetration through bacterial cell walls.³⁸⁴ Antibacterial and antifungal activities of coumarins are closely linked to specific hydroxylation patterns, lipophilicity, and structural geometry. These insights inform the rational design of coumarin-based antimicrobials with improved efficacy and selective pathogen targeting.

6.4. Host-Guest Binding of CB7 with Coumarin Dyes

CB7 is a rigid, hollow macrocycle well-known for its high-affinity binding to biorelevant molecules and cations in aqueous media. Due to its hydrophobic cavity and electronegative carbonyl-laced portals, CB7 forms stable inclusion complexes with a wide range of guest molecules through a combination of hydrophobic interactions, ion-dipole forces, and van der Waals forces. Coumarin dyes – which typically possess polarizable aromatic cores and basic amine substituents – form particularly effective 1:1 host-guest complexes with CB7.^{68, 122, 231, 232} The size and shape of the CB7 cavity are well-matched to accommodate coumarin derivatives, often encapsulating functional groups such as *N,N*-diethylamino substituents while leaving the remaining portions of the dye exposed to the medium. This binding mode

has been confirmed through various spectroscopic analyses, including NMR chemical shift perturbations, which indicate, for example, the inclusion of the 7-*N,N*-diethylamino “tail” of 7-*N,N*-diethylaminocoumarin carboxylic acid within the CB7 cavity. The resulting host-guest complexes typically exhibit 1:1 stoichiometry, with binding constants ranging from 10^4 to 10^6 M⁻¹ in water. Higher affinities can be observed when the coumarin dye carries multiple positive charges, owing to stronger electrostatic interactions with the CB7 portals. In contrast, bulky or sterically hindered coumarins may fail to bind effectively inside the cavity, leading to minimal photophysical changes upon CB7 addition.^{385, 386} Overall, the inclusion of coumarins within the CB7 cavity forms the basis for significant photophysical modulation, which is central to their use in fluorescence sensing, signal transduction, and molecular recognition systems.

The binding mode and thermodynamic profile of coumarin-CB7 complexes are strongly influenced by the protonation state of the guest dye. In general, CB7 exhibits significantly higher binding affinities toward protonated or cationic species of coumarin derivatives, driven by ion-dipole interactions between the guest’s positive charge and the carbonyl-rich portals of CB7.^{125, 154, 158, 165, 226} A representative example is the benzimidazole-piperazine-coumarin dye (**Table 6.2**, entry 4), which binds preferentially in its protonated form. Upon complexation, CB7 effectively stabilizes the charged form by raising the dye’s pK_a , by approximately 3 units, enhancing binding and shifting the protonation equilibrium.³⁸⁷ This phenomenon, widely observed across various systems, is referred to as a supramolecular pK_a shift, wherein CB7 encapsulates and favors the protonated species, often increasing pK_a values by 2-5 units.^{136, 159, 165, 386} From a thermodynamic perspective, CB7’s tight and selective binding arises from a combination of hydrophobic interactions, electrostatic stabilization at the portals, and the entropically favored release of high-energy water molecules from the cavity upon guest binding.^{68, 136, 150}

One of the most striking consequences of CB7 complexation is the modulation of the photophysical properties of coumarin dyes. Encapsulation within CB7 alters the dye’s local microenvironment and conformational dynamics, often leading to significant changes in absorption and emission behavior. A common and notable outcome is the enhancement of fluorescence intensity, observed in many coumarin derivatives upon inclusion. This fluorescence enhancement is highly structure-dependent, influenced by both the position and the nature of substituents on the coumarin core. For instance, the encapsulation of coumarin-1 (C1) and coumarin-481 (C481) (**Table 6.2**, entries 1 and 2) results in pronounced increase in fluorescence quantum yield and excited-state lifetime.³⁸⁵ This effect is attributed to CB7’s rigid, non-polar cavity, which suppresses non-radiative deactivation pathways such as twisted intramolecular charge transfer (TICT). In the case of C1 and C481, complexation with CB7 effectively restricts the rotational freedom of the flexible *N,N*-diethylamino substituent, thereby inhibiting TICT quenching and promoting radiative decay.³⁸⁵ Similarly, a stryrylcoumarin dye (**Table 6.2**, entry 6) exhibited a substantial enhancement in fluorescence quantum yield upon CB7 binding, resulting in significantly brighter emission in aqueous solution.³⁸⁸ This is especially valuable for applications in fluorescence imaging or sensing, where brightness and signal contrast are critical. In general, CB7 encapsulation places the dye in

a less polar, conformationally restricted environment – a molecular micro-solvent – which enhances radiative decay rates and reduces solvent- or conformation-induced quenching.

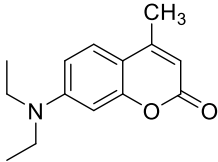
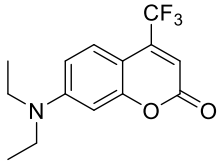
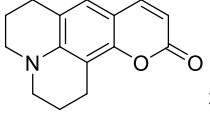
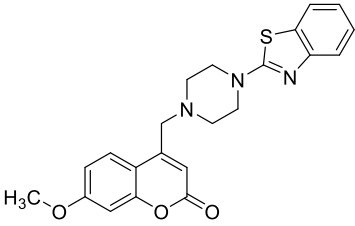
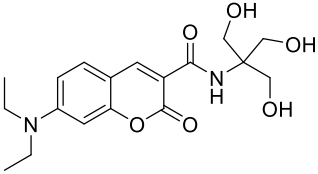
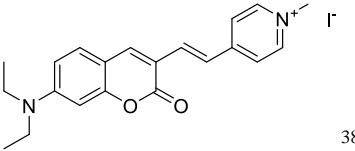
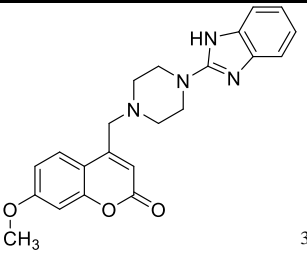
Coumarin dye	CBn host	Binding constant (K_a)	Fluorescence effect upon binding (aqueous solution)
 385	CB7	$1.8 \pm 0.1 \times 10^5 \text{ M}^{-1}$	Emission yield and lifetime greatly increased (3-fold)
 385	CB7	$6.0 \pm 0.4 \times 10^4 \text{ M}^{-1}$	Emission yield and lifetime greatly increased (3-fold)
 385	CB7	$1.5 \pm 0.1 \times 10^4 \text{ M}^{-1}$	Minimal spectral changes
 386	CB7	$2.8 \pm 0.05 \times 10^6 \text{ M}^{-1}$ (protonated)	Fluorescence turn-on by up to 45-fold at pH 3.5
 389	CB7	$\sim 10^5 \text{ M}^{-1}$ (estimated)	Bathochromic shift, fluorescence intensity highly increased (5-fold)
 388	CB7	$1.06 \pm 0.27 \times 10^6 \text{ M}^{-1}$ (1:1 stoichiometry) $1.45 \pm 0.17 \times 10^4 \text{ M}^{-1}$ (2:1 stoichiometry)	Significant bathochromic shift, fluorescence intensity highly increased (8-fold)
 387	CB7	$5.5 \pm 0.1 \times 10^6 \text{ M}^{-1}$ (deprotonated, 2:1 stoichiometry)	Fluorescence on-off switching: CB7-bound (protonated) dye is highly fluorescent, free dye (neutral) is quenched by intramolecular PET

Table 6.2. Selected coumarin-CB complexes and their respective binding constants (in aqueous solution) together with the observed fluorescence response upon complexation.

In addition to enhancing fluorescence intensity, CB7 complexation often induces spectral shifts in coumarin dyes, reflecting changes in their electronic environments. These shifts typically arise from perturbations in the electronic distribution upon binding. A common observation is a bathochromic (red) shift in the absorption maximum ($\lambda_{\text{max,abs}}$). For example, coumarin 1 (C1) exhibits a noticeable red shift in its absorption spectrum upon inclusion by CB7.³⁹⁰ This shift is attributed to stabilization of the dye's charge-transfer (CT) excited state through dipolar interactions with the carbonyl-lined portals of CB7. In another study, two red-emitting coumarin fluorophores demonstrated significant red-shifts in both absorption and, in some cases, emission maxima upon CB7 binding.³⁸⁸ These shifts suggest that the dyes localize at or near the portal regions of the host, where interactions with electronegative carbonyl groups influence the energy levels of the excited states. However, not all coumarins exhibit pronounced spectral changes. In some cases, only minor shifts or no detectable changes are observed, particularly when the binding does not significantly perturb the electronic structure of the chromophore.³⁸⁹ Such outcomes depend on factors including the position of substituents, guest orientation within the cavity, and the degree of conjugation within the dye.

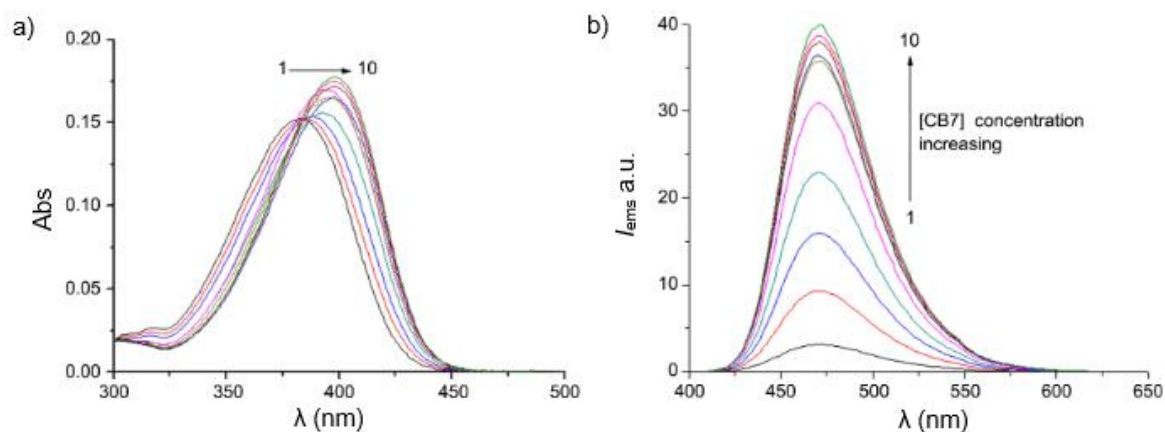


Fig. 6.4. a) UV-Vis absorption spectra of coumarin-1 (C1) with increasing concentrations of CB7; 1 no CB7, 10 54.7 mM CB7. A bathochromic shift can be observed. b) Fluorescence intensity increase of C1 with increasing addition of CB7; 1 no CB7, 10 54.7 mM CB7. Adapted from ref ³⁹⁰

While CB7 often enhances coumarin fluorescence, in some cases, fluorescence quenching or turn-off effects are observed upon complexation. Although CB7 is intrinsically non-fluorescent, it can indirectly facilitate non-radiative decay pathways depending on the binding orientation or presence of secondary components, such as metal cations. For instance, Aliaga *et al.* reported a coumarin-based dye that showed no fluorescence enhancement upon CB7 binding, likely due to an unfavorable binding geometry that did not restrict non-radiative decay.³⁸⁹ More notably, the addition of Hg^{2+} ions led to fluorescence quenching through the formation of a ternary dye-CB7- Hg^{2+} complex, demonstrating a turn-off mechanism for metal ion sensing. In general, pure CB7 rarely acts as a quencher, but quenching effects in CB7-coumarin systems are often intentional, designed through either analyte-induced displacement or binding, or photoinduced electron transfer (PET) mechanisms built into the dye structure.

Many coumarin derivatives are engineered as fluorogenic PET sensors, where fluorescence is suppressed by intramolecular electron transfer from a donor group (e.g., an amine) to the coumarin core. Upon CB7 binding, the macrocycle can encapsulate and protonate the donor group, thereby inhibiting PET and triggering a fluorescence turn-on response. A compelling example is the coumarin-benzothiazole-piperazine dye (**Table 6.2.**, entry 4), which is weakly fluorescent in its neutral form due to PET self-quenching. Upon complexation, CB7 preferentially binds and protonates the benzothiazole unit, thereby suppressing PET and resulting in a ~45-fold increase in fluorescence intensity.³⁸⁷ In this way, CB7 acts as a molecular switch, converting a non-emissive internal charge-transfer (ICT) state into a bright fluorophore by freezing out the non-radiative pathway. Similarly, CB7 can prevent twisted intramolecular charge transfer (TICT) states. Barooah *et al.* demonstrated that CB7 halted the ICT → TICT transition in coumarin-1 (C1), significantly increasing the fluorescence compared to the unbound dye.³⁸⁵ This structural restriction mechanism is key to the observed enhancement in quantum yield and lifetime.

In summary, CB7 can profoundly alter the photophysical behavior of coumarin dyes, often resulting in increased fluorescence intensity, wavelength shifts, and suppression or activation of PET or TICT pathways. These effects arise from the non-polar, conformationally restricted environment of the CB7 cavity and its ability to selectively stabilize charged or protonated species. Such interactions underpin the utility of CB7-coumarin complexes in chemosensing applications, where changes in fluorescence serve as sensitive indicators of analytes, environmental shifts, or molecular events.

6.5. Design and Synthesis of a CB7-Coumarin Sensor Library

As discussed in the previous sections, non-covalent chemosensors based on supramolecular complexes between various coumarin dyes and cucurbiturils have been widely applied in proof-of-concept sensing systems.^{385, 387-391} While effective in controlled aqueous environments, such bimolecular assemblies face major limitations in complex biological media due to instability under high salt conditions. Biofluids such as saline, urine, and blood serum represent chemically diverse and highly dynamic matrices, where ionic strength, pH value, and sample variability can significantly compromise binding performance. Although CB n -based chemosensors benefit from high binding affinities and rapid kinetics in deionized water, the non-covalent interactions between CB n and reporter molecules are highly sensitive to the surrounding chemical environment. In particular, competitive or cooperative binding of cations to the carbonyl-rich portals of CB7 can drastically affect guest binding, a phenomenon commonly referred to as the salt effect.^{31, 40, 232} Furthermore, like all bimolecular assemblies, CB n •dye complexes are prone to dissociation upon dilution, limiting their practical use especially in low-concentration or high-volume samples. As a result, many reported CB n -based sensing systems are only operational in water or minimal buffers and often fail in high-salt or variable ionic strength.

To overcome these limitations, an alternative strategy involves the covalent integration of the indicator and the receptor into a single, non-dissociable unimolecular chemosensor, eliminating dissociation

equilibria and reducing susceptibility to salt interference. For example, Urbach and co-workers synthesized a CB7-rhodamine conjugate that functioned as a cell-permeable fluorescence probe for bioimaging.²¹⁵ More recently, our group developed a CB7-berberine (CB7-BC) conjugate, in which the indicator dye is covalently linked to the macrocycle, allowing for selective and robust sensing of amantadine – a therapeutic agent for Parkinson’s and Alzheimer’s disease – in both $10 \times$ PBS buffer and high-salt media (up to 1.4 M NaCl).²³¹ Compared to its non-covalent CB7•berberine counterpart, the unimolecular conjugate showed superior sensitivity, faster response time, and better operational stability. Notably, the covalent system avoids the slow equilibrium and dilution effects that hamper non-covalent assemblies, as the indicator dye undergoes self-inclusion into the CB7 cavity in the absence of the analyte. In a follow-up study, we also demonstrated that the addition of different salts could enhance the discrimination capability of a CB7-nitrobenzoxadiazole (CB7-NBD) unimolecular chemosensor, likely due to fine-tuned competition and binding site modulation.²³²

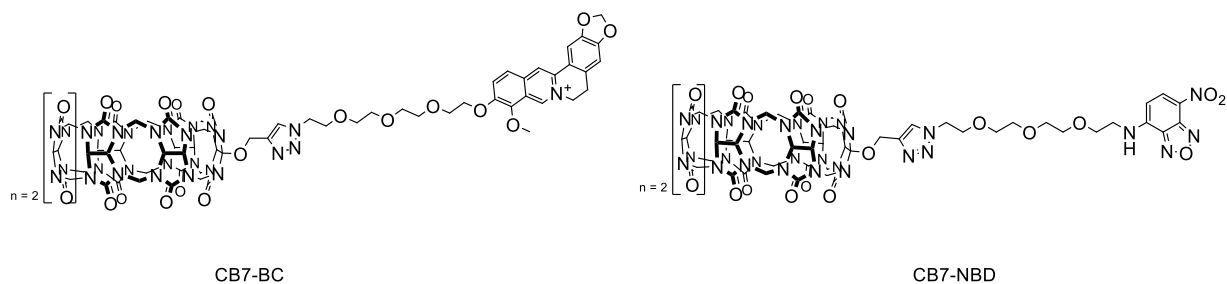


Fig. 6.5. Structures of the CB7-BC and CB7-NBD chemosensors.^{231, 232}

Thanks to advances in macrocyclic chemistry, it is now feasible to synthesize CB7 derivatives bearing chemically reactive handles suitable for covalent conjugation.^{180, 183} Among the most effective and versatile methods are thiol-ene and click-reactions, which offer high functional group tolerance, mild conditions, and broad structural flexibility. Early CB7 conjugates often employed short alkyl linkers, which prevented dye encapsulation, resulting in modest signal changes or necessitating the use of external indicator dyes.^{215, 220} More recent designs focus on linker optimization to enable self-encapsulation, maximizing signal contrast upon guest binding. In my approach, coumarin dyes were selected as reported units due to their ease of preparation, structural tunability, and desirable photophysical properties. The Knoevenagel condensation was identified as the key synthetic route for accessing a library of coumarin carboxylic acids. This reaction allows modular assembly of derivatives by simply varying the benzaldehyde precursor, enabling consistent reaction conditions while tuning the electronic and steric properties of the coumarin core to achieve different selectivity for analytes. Literature analysis revealed that amino-substituted salicylaldehydes are suitable starting materials to introduce alkylamino side chains of various lengths, which can modulate both binding affinity and photophysical behavior. In some cases, commercially available coumarin carboxylic acids were also employed to streamline synthesis. To render these coumarin derivatives compatible with click chemistry, the synthesized carboxylic acids were further modified with a bifunctional azido-amino linker through amide bond formation, introducing a

terminal azido group for CuAAC. This modular design allows for the rapid generation of CB7-coumarin conjugates with diverse structural features and optimized sensing performance for applications in aqueous and biological environments.

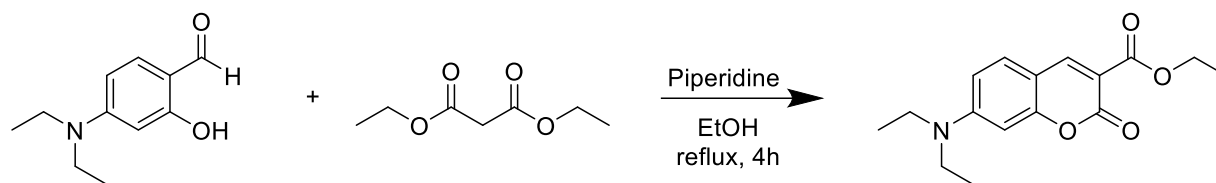


Fig. 6.6. Synthesis of the coumarin scaffold *via* a Knoevenagel approach.

To further enhance analyte discrimination, it was considered not only to use the influence of salt identity and concentration (as previously discussed), but also the role of pH as an additional orthogonal input parameter. Given that the coumarin derivatives contain alkylated amino groups, which vary in basicity, their pK_a values differ depending on the length of the alkyl chain. By designing a chemosensor set that varies only in this substituent while keeping the rest of the structure constant, it was aimed to explore pH-dependent modulation of sensor performance, thereby improving the selectivity and resolution in detecting both structurally distinct and closely related analytes. For the linker, a tetraethylene glycol (TEG) spacer was selected. This choice ensured sufficient flexibility and hydrophilicity, allowing for unhindered movement of the coumarin moiety into and out of the CB7 cavity. To maintain comparability among the conjugates, structural variation was limited to the length of the alkyl chain on the amino group, enabling a clear assessment of the influence of pK_a and hydrophobicity. Accordingly, a series of methyl-, ethyl-, propyl-, and butyl-substituted aminocoumarin carboxylic acids was synthesized. For the methyl and ethyl analogs, the respective amino-salicylaldehyde precursors were commercially available. For the propyl and butyl derivatives, a synthetic route starting from 3-aminophenol was employed. This involved a two-step sequence starting with the S_N2 alkylation of the phenolic hydroxyl group to introduce the desired alkyl chain, yielding 3-alkylaminophenols. Subsequently, a Vilsmeier-Haack formylation was performed to convert these intermediates into the corresponding alkylamino-salicylaldehydes. These aldehydes served as substrates for the Knoevenagel condensation with diethyl malonate, producing the alkylaminocoumarin ethyl esters. Following silica column chromatography, residual diethyl malonate was often observed due to similar polarity, but this did not interfere with the downstream processing. During subsequent ester cleavage, the desired coumarin carboxylic acids could be cleanly isolated by precipitation, while malonic acid remained soluble and was easily removed. To introduce a handle for click chemistry, the resulting coumarin carboxylic acids were coupled to a bifunctional azido-amino linker *via* an amide bond-forming reaction. Purification by silica chromatography yielded azide-functionalized coumarins, ready for CuAAC click conjugation with CB7.

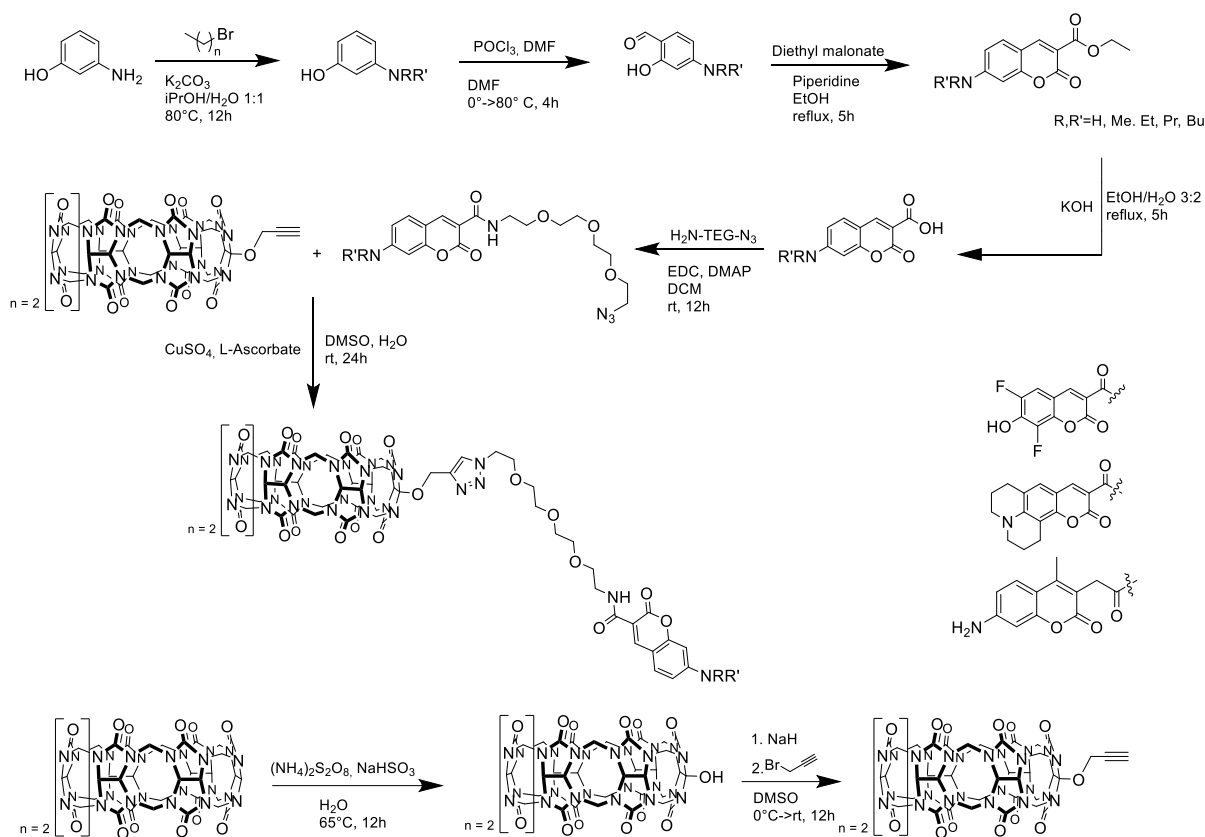


Fig. 6.7. Overview of the synthetic pathway to obtain different CB7-coumarin chemosensors.

In parallel, I sought to expand the substitution pattern and include both functional diversity and negative controls. For this purpose, three commercially available coumarin carboxylic acids were selected (**Fig. 6.8**). Coumarin 343, with a bulky dicyclohexylamino substituent, served as a negative control, as its size is expected to prevent cavity inclusion and result in minimal spectral response. 7-Amino-4-methyl-3-coumarinylacetic acid (AMCA) was included to assess the behavior of a free amino group, potentially enabling additional hydrogen bonding or protonation-controlled photophysical behavior. Lastly, 3-carboxy-6,8-difluoro-7-hydroxycoumarin (Pacific Blue) was selected to explore the effect of a hydroxy group instead of an amino substituent and to investigate fluorine-mediate interactions with potential analytes. These commercially available coumarin carboxylic acids were incorporated into the chemosensor library using the same synthetic strategy of adding the bifunctional linker *via* amidation. The structures are shown below.

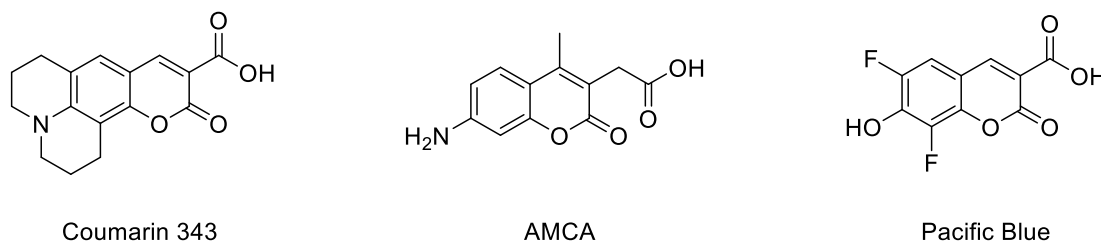


Fig. 6.8. Structures of the commercially available coumarin carboxylic acids used to prepare the corresponding CB7-coumarin chemosensors.

For the CB7 component, two different synthetic approaches were evaluated.^{125, 392} Among them, the method published by Nau *et al.* proved to be superior in terms of reproducibility and scalability. However, the reported 49% yield reported in the original publication could not be fully replicated under the experimental conditions. To introduce a functional handle for further derivatization, the CB7 core was subjected to radical hydroxylation. The method described by Kaifer was adopted, which cleverly employs ammonium persulfate as the radical initiator and sodium bisulfite as a mediator.¹⁸³ This combination allows for partial control over the otherwise challenging radical hydroxylation of CB7, which contains 14 equivalent methylene protons and is therefore prone to overfunctionalization. Kaifer's protocol biases the reaction toward formation of the monohydroxylated CB7 (CB7-OH) while minimizing the formation of multihydroxylated by-products. Nevertheless, purification by SEC remained necessary to isolate the desired mono-substituted derivative. The resulting CB7-OH was then activated for click chemistry *via* an alkylation with propargyl bromide in DMSO, using sodium hydride as the base. This reaction generated CB7-OPr, the alkyne-functionalized precursor required for CuAAC. To improve reaction efficiency and suppress Cu(I) oxidation, THPTA was added as a stabilizer for Cu⁺ ions, as already established during the synthesis of CB7-Ru. After conjugation with the azide-modified coumarin derivatives, the reaction was monitored and confirmed by ESI-MS. The crude products were precipitated by the addition of MeOH and collected by centrifugation. Sequential MeOH washes were used to remove unreacted coumarin. Using this strategy, a total of seven distinct CB7-coumarin derivatives were successfully synthesized. The structures of these conjugates are shown in **Fig. 6.9**.

The crude conjugates were further purified by preparative HPLC. Despite structural similarities among the conjugates, it was necessary to develop individual HPLC methods, highlighting the subtle but significant differences in polarity introduced by the various amino substituents. This observation foreshadowed the differential sensing behaviors observed later in the analyte screening experiments. For the purification step, the crude products – still containing residual CB7-OPr – were redissolved according to their polarity. For the more polar conjugates (**Fig. 6.9.**, entries 1, 3, 5, 7) a 3:2 (v/v) mixture of H₂O/ACN was used. For the more hydrophobic conjugates (**Fig. 6.9.**, entries 2, 4, 6), the inverse mixture (ACN/H₂O 3:2) was found to be more effective. To aid solubility, a few drops of TFA were added to each solution. The overall synthetic route is summarized in **Fig. 6.7.**, illustrating the modular design of the CB7-coumarin sensor platform from building blocks to final products.

6.6. Structural Characterization of CB7-Coumarins

The supramolecular behavior of the synthesized CB7-coumarin conjugates was characterized by mass spectrometry experiments and ¹H NMR to determine whether the conjugates adopt the expected self-bound, or folded, conformation. After chromatographic purification, HR-ESI-MS was performed in the presence of C₈mim₂²⁺ as a reporter ion. For all 7 CB7-coumarins, the diagnostic peak corresponding to the [CB7-coumarin + C₈mim₂]²⁺ ion was observed. In all cases, the measured spectra were in perfect agreement with the simulated spectra, confirming the expected molecular compositions. A typical method

to further verify the structural integrity of CB conjugates in solution is ^1H NMR spectroscopy, in which the conjugate is first measured alone and then in presence of a high-affinity guest such as amantadine. Upon guest addition, the dye is expected to be displaced from the CB7 cavity, leading to unfolding of the conjugate and corresponding chemical shift changes. These spectra are then compared to those of the free dye or dye plus linker. For example, in the case of CB7-BC, this experiment could be performed in pure D_2O , while for CB7-NBD, dissolution was facilitated by NaCl addition.^{231, 232} In contrast, the CB7-coumarin conjugates proved more challenging. Neither pure D_2O nor NaCl-assisted strategies yielded spectra of sufficient quality, even after repeated trials with higher salt concentrations and extended acquisition times. This difficulty is attributed to the hydrophobic character of the coumarin residues, which promoted aggregation and caused poor spectral resolution. To overcome this challenge, dissolution in a 3:2 (v/v) mixture of acetonitrile and water was found to be highly effective, similar to the conditions employed for dissolution prior to HPLC purification. This allowed for reliable acquisition of ^1H NMR spectra for all conjugates. Importantly, the formation of the triazole linkage resulting from the CuAAC reaction was confirmed in every case by the appearance of a characteristic singlet at ~ 8.1 ppm. Importantly, the free dye-linker intermediates also required this acetonitrile/water mixture for solubility, indicating that the limitation was intrinsic to the coumarin residues rather than the conjugated CB7.

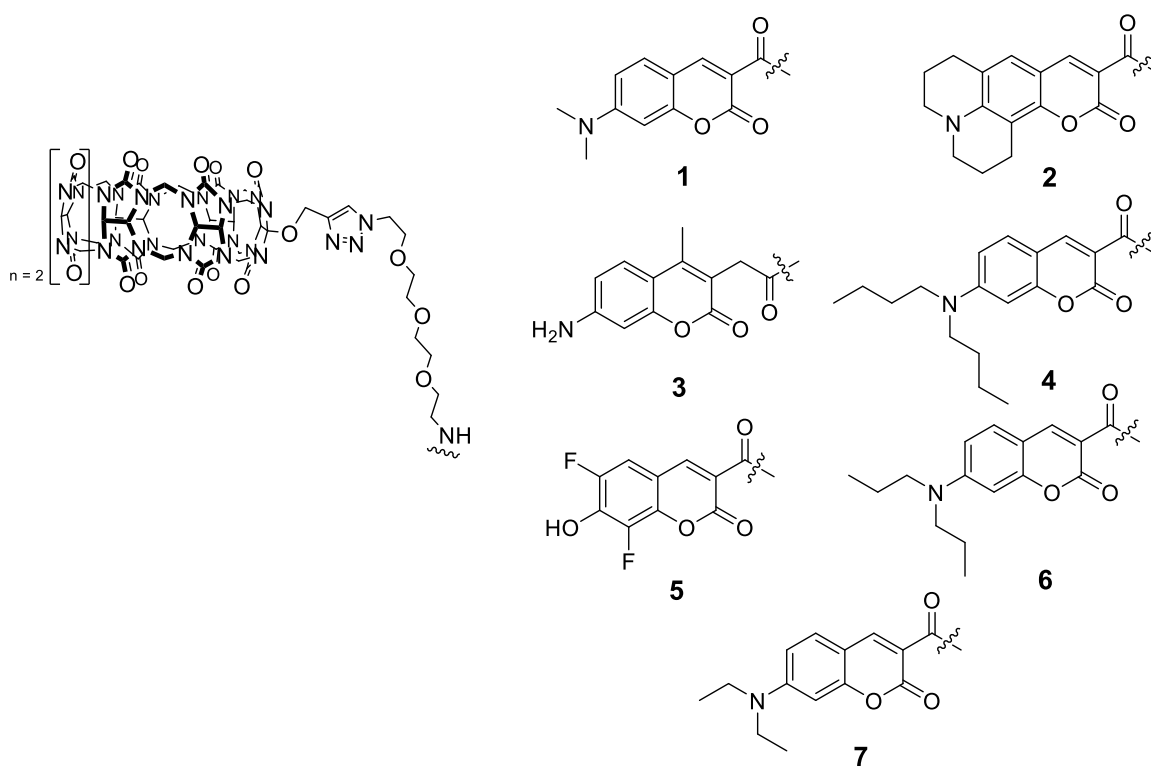


Fig. 6.9. Overview of the different synthesized CB7-coumarin chemosensors.

The reliance on acetonitrile, however, introduced new challenges. In aqueous solution, self-inclusion of aminoalkyl chains can normally be confirmed by adding excess amantadine.^{231, 232} In case of the coumarin conjugates, self-inclusion could not be reliably confirmed by ^1H NMR spectroscopy. The addition of amantadine did not consistently yield the expected changes. This limitation most likely stems

from the use of the acetonitrile/water mixture, required for solubility of both the free dye-linker species and the conjugates. While this solvent system enabled acquisition of the spectra, it also created a partially organic microenvironment around the dye. As a result, spectral differences between the free and the CB7-bound states were diminished, making it difficult to distinguish inclusion from exclusion based solely on chemical shift behavior.

Despite this drawback, meaningful structural insights were still obtained. Comparison of the free linker spectra with those of the conjugates clearly indicated the inclusion of the coumarin dye to the CB7 host, consistent with the expected folded architecture. These findings emphasize both strengths and limitations of ^1H NMR analysis for hydrophobic dye-CB7 systems: while solubility challenges necessitate organic co-solvents that obscure fine details of inclusion, careful comparative analysis can still confirm the essential supramolecular arrangement.

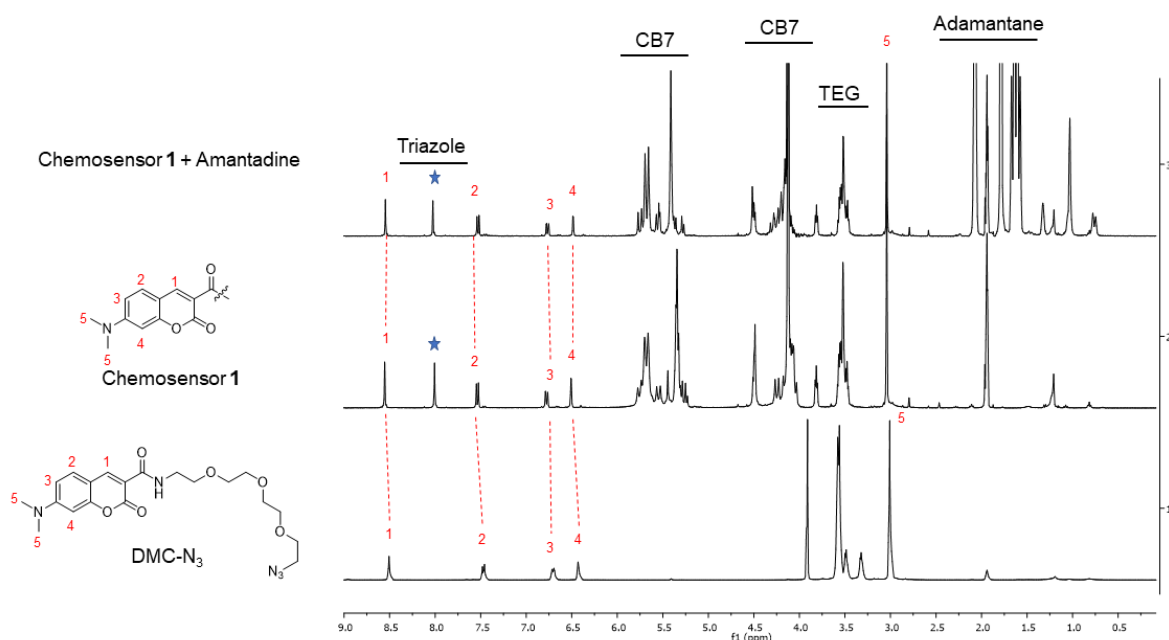


Fig. 6.10: Overlay of ^1H NMR (400 MHz, $\text{CD}_3\text{CN}/\text{D}_2\text{O}$ 3:2 (v/v)) spectra of DMC-N₃ (bottom), chemosensor **1** (middle), and chemosensor **1** with excess amantadine (top).

Comparison of the ^1H NMR spectra of chemosensor **1** (CB7-DMC) with and without amantadine does not provide unambiguous evidence for self-inclusion (**Fig. 6.10**). No clear, concerted shifts or line-shape changes are observed for protons that would be diagnostic of placement inside the CB7 cavity (*e.g.*, coumarin protons or protons of the aminoalkyl chain). Two plausible factors may account for this: the methyl-substituted aminoalkyl chain may be too small to drive stable self-inclusion against solvent competition; and/or steric encumbrance from the coumarin phenyl moiety could hinder a geometry that positions the alkyl segment deeply within the cavity.

The ^1H NMR spectra of Chemosensor **2** clearly indicate partial self-inclusion behavior, as evidenced by the broadening of the signals corresponding to the coumarin moiety (**Fig. 6.11**). This line broadening suggests that the dye experiences a less homogeneous magnetic environment due to dynamic exchange

between the free and encapsulated states within the CB7 cavity. Nevertheless, the absence of pronounced chemical shift changes or distinct splitting patterns implies that inclusion is not complete or deeply seated. It is likely that the bulky cyclohexaneaminoalkyl substituents restrict full penetration of the coumarin unit into the cavity, leading to a partially encapsulated equilibrium state with the dye positioned near the portal region. Similar to Chemosensors **1** and **7**, this behavior underscores that substituent geometry and steric demand critically govern self-inclusion, and that intermediate substituent size and hydrophobicity are optimal for stable and well-defined CB7 binding.

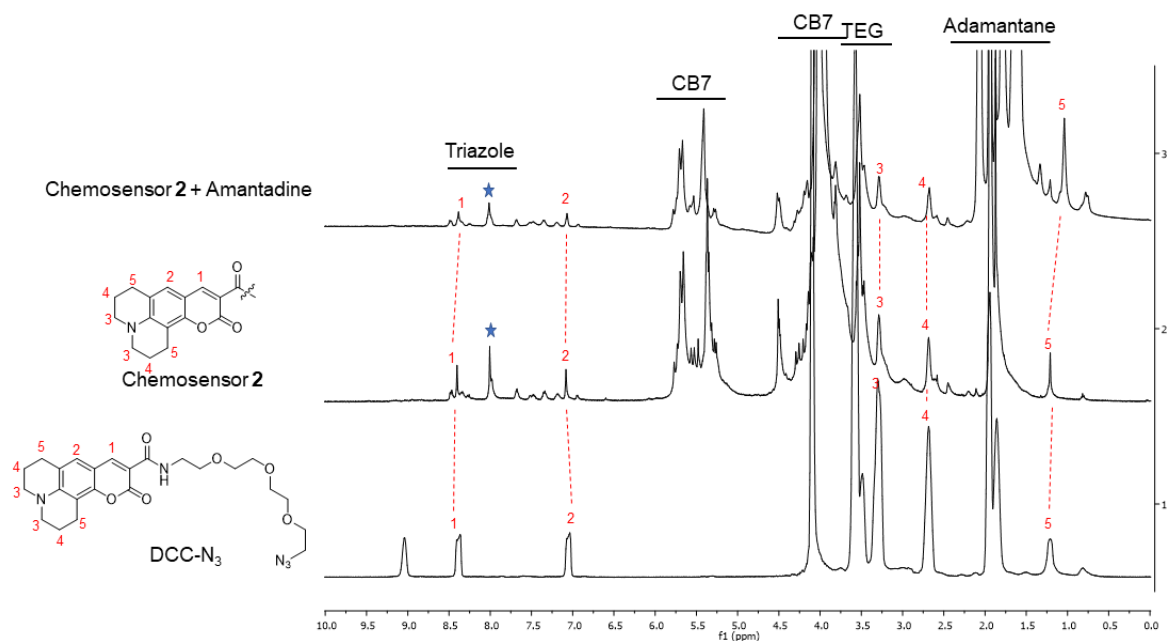


Fig. 6.11: Overlay of ^1H NMR (400 MHz, $\text{CD}_3\text{CN}/\text{D}_2\text{O}$ 3:2 (v/v)) spectra of DCC- N_3 (bottom), chemosensor **2** (middle), and chemosensor **2** with excess amantadine (top).

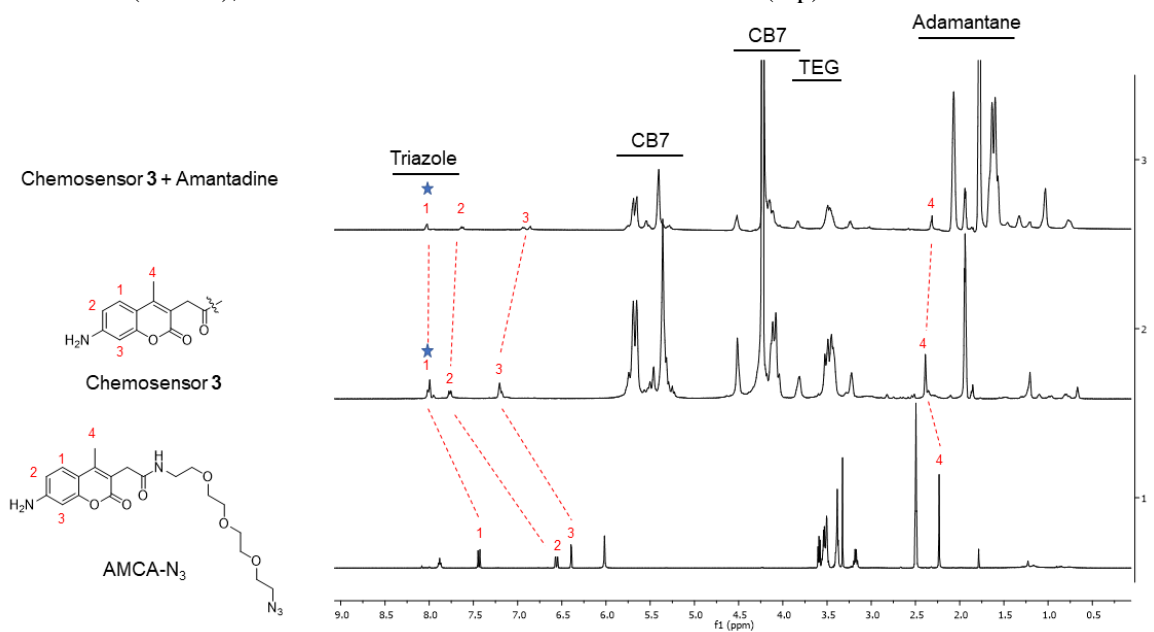


Fig. 6.12: Overlay of ^1H NMR (400 MHz, $\text{CD}_3\text{CN}/\text{D}_2\text{O}$ 3:2 (v/v)) spectra of AMCA- N_3 (bottom), chemosensor **3** (middle), and chemosensor **3** with excess amantadine (top).

For the chemosensor **3** (CB7-AMCA), the ^1H NMR spectra show clear evidence of inclusion (**Fig. 6.12**). Distinct chemical shift changes are observed for all aromatic protons, as well as for the methyl group adjacent to the coumarin core. These concerted shifts strongly indicate that the methyl-substituted phenyl ring is at least partially accommodated within the CB7 cavity. The pattern is consistent with the self-bound conformation, in which the aromatic moiety is deshielded by the host environment. This result contrasts with chemosensor **1**, where no such inclusion could be confirmed, and suggest that the steric and electronic balance in AMCA derivatives is well-matched to CB7's cavity size and portal interactions.

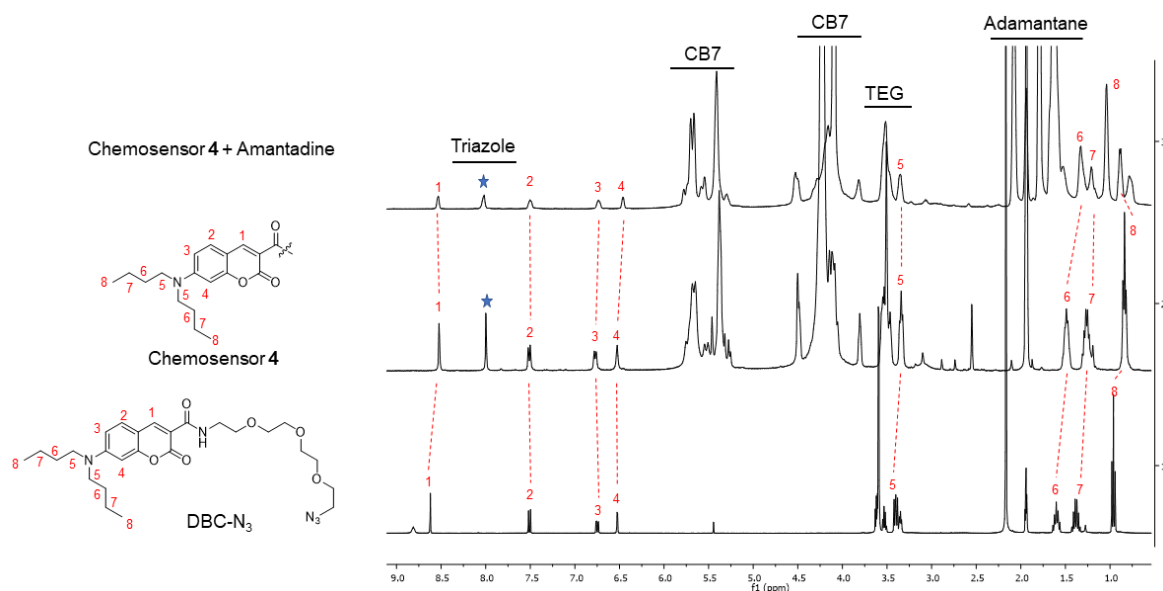


Fig. 6.13: Overlay of ^1H NMR (400 MHz, $\text{CD}_3\text{CN}/\text{D}_2\text{O}$ 3:2 (v/v)) spectra of DBC-N₃ (bottom), chemosensor **4** (middle), and chemosensor **4** with excess amantadine (top).

The spectra of chemosensor **4** (CB7-DBC) show clear evidence of self-inclusion (**Fig. 6.13**). Distinct chemical shift changes are observed for the butyl substituents, which represent the longest aminoalkyl chains among the synthesized CB7-coumarin conjugates. The most pronounced shifts are seen for the terminal methyl protons, suggesting that the butyl chains penetrate into the CB7 cavity. However, based on the available spectra it is not possible to determine whether only one or both butyl groups are included. Compared to chemosensor **3** (CB7-AMCA), where aromatic protons and a coumarin-adjacent methyl were implicated in cavity binding, chemosensor **4** highlights the role of long aliphatic chains as effective driving groups for self-inclusion. Together, these results illustrate that CB7 can either accommodate aromatic substituents or extended aliphatic chains, and can balance between size, flexibility, and orientation of substituents critically influences the binding mode.

For chemosensor **5** (CB7-Pacific Blue), the ^1H NMR spectra do not provide clear evidence of self-inclusion (**Fig. 6.14**). No concerted chemical shift changes diagnostic of cavity encapsulation is observed. A likely explanation is the presence of the phenolic ring, which may be too polar to be favorably accommodated within the largely hydrophobic CB7 cavity. While it is reasonable to assume that the coumarin moiety remains in close spatial proximity to the CB7 portals, this interaction is not directly evident from the spectral data. Unlike chemosensors **3** and **4**, which showed convincing signs of inclusion

(aromatic and alkyl, respectively), chemosensor **5** illustrates that increased polarity of substituents can hinder encapsulation, even when steric factors would otherwise permit binding. This emphasizes that hydrophobicity is a key driving force for CB7-coumarin self-inclusion, and overly polar groups reduce the likelihood of detectable cavity interactions.

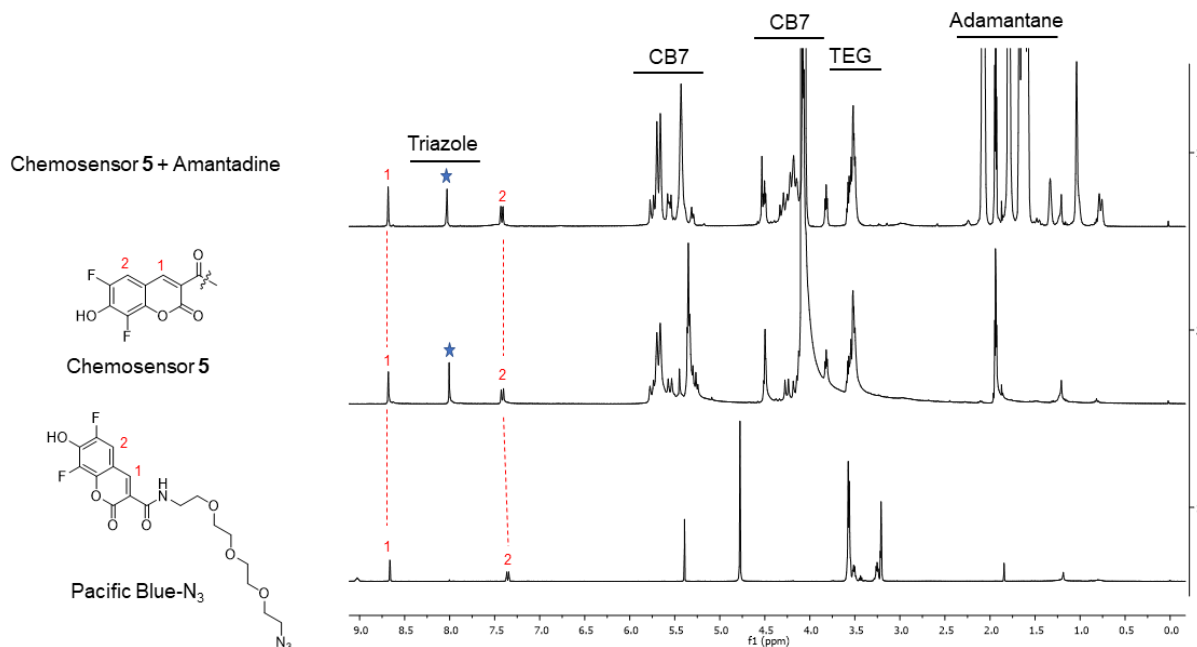


Fig. 6.14: Overlay of ¹H NMR (400 MHz, CD₃CN/D₂O 3:2 (v/v)) spectra of Pacific Blue-N₃ (bottom), chemosensor **5** (middle), and chemosensor **5** with excess amantadine (top).

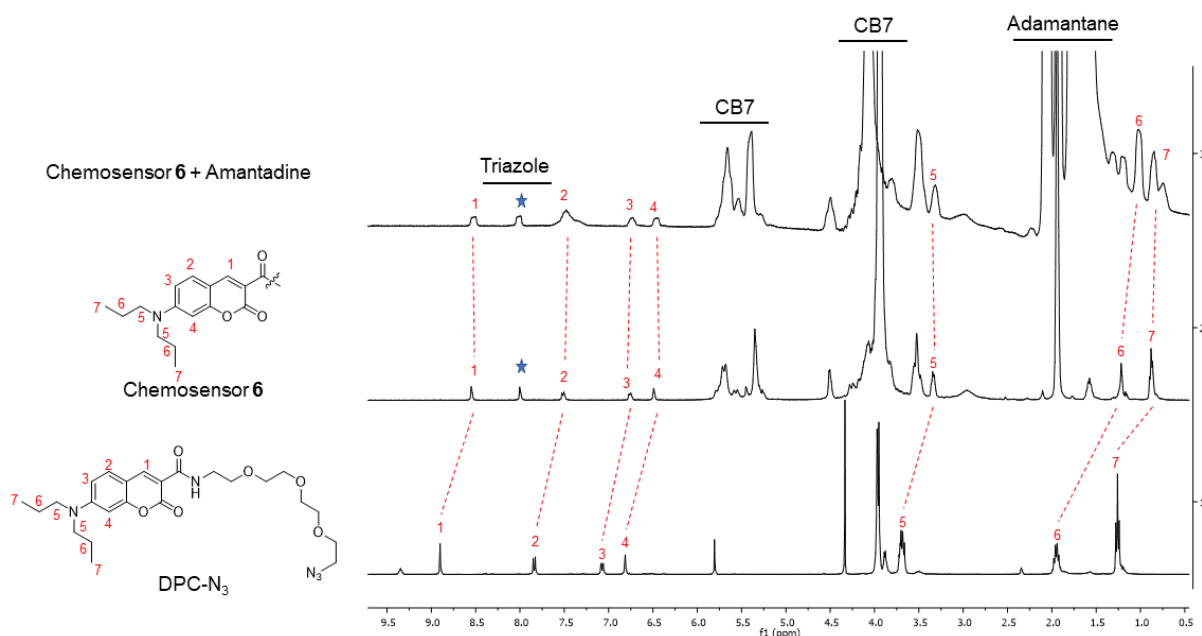


Fig. 6.15: Overlay of ¹H NMR (400 MHz, CD₃CN/D₂O 3:2 (v/v)) spectra of DPC-N₃ (bottom), chemosensor **6** (middle), and chemosensor **6** with excess amantadine (top).

The spectra of chemosensor **6** (CB7-DPC) provide clear evidence of self-inclusion (**Fig. 6.15**). As with chemosensor **4**, distinct chemical shift changes are observed for the aminoalkyl protons, indicating

that the propyl chains interact with the CB7 cavity. The strongest effects are again seen for the protons located toward the terminal regions of the chains. However, the spectra do not allow a definitive conclusion whether one or both propyl substituents are included at a given time. This behavior mirrors that of chemosensor **4** (butyl derivative), reinforcing the notion that longer alkyl chains are efficient driving elements for self-inclusion. Taken together, chemosensors **4** and **6** show that CB7 accommodates both butyl and propyl chains, suggesting a degree of flexibility in binding mode. These results underline that hydrophobic substituents – whether aromatic or aliphatic – are the most reliable for enabling self-inclusion in CB7-coumarin conjugates.

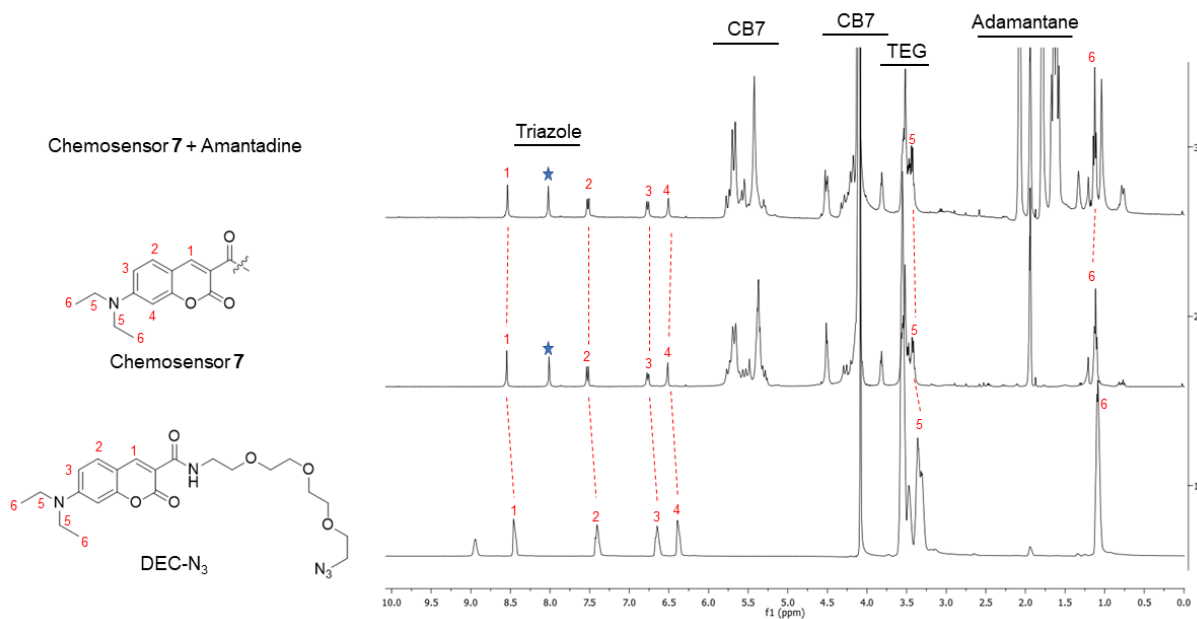


Fig. 6.16: Overlay of ^1H NMR (400 MHz, $\text{CD}_3\text{CN}/\text{D}_2\text{O}$ 3:2 (v/v)) spectra of DEC- N_3 (bottom), chemosensor **7** (middle), and chemosensor **7** with excess amantadine (top).

For chemosensor **7**, the ^1H NMR spectra do not show clear evidence of deep self-inclusion (**Fig. 6.16**). However, uniform deshielding of all coumarin proton signals is observed, which is indicative of portal binding rather than full cavity encapsulation. This suggests that the coumarin moiety interacts closely with the carbonyl portals of CB7, likely stabilized by weak ion–dipole and π – π interactions, while the chromophore itself remains largely outside the cavity. Similar to Chemosensor **1** (methyl derivative), the short ethylaminoalkyl substituents appear too small to provide sufficient hydrophobic driving force for stable self-inclusion. Together, Chemosensors **1** and **7** demonstrate that short-chain substituents favor peripheral, portal-associated binding modes, in contrast to Chemosensors **4** and **6**, where longer butyl and propyl chains promote cavity inclusion, and to Chemosensor **3**, where aromatic substitution enables strong host–guest stabilization. These findings further emphasize that chain length and substituent size are critical determinants governing the balance between portal association and full self-inclusion in CB7–coumarin conjugates.

Table 6.3 summarizes the results from the ^1H NMR experiments.

Chemosensor	Coumarin derivative (substituent)	Key NMR observations	Evidence for self-inclusion	Likely inclusion motif / interpretation
1	Dimethyl	No diagnostic shifts; no response to adamantane	X	Substituents too small; steric hindrance from coumarin core
2	Dicyclohexylamino	No diagnostic shifts; no response to adamantane; slight shielding and peak broadening	X	Substituents too bulky
3	AMCA	Clear shifts for phenyl protons and adjacent methyl group; strong deshielding	✓	Partial engulfment of methyl-substituted phenyl ring
4	Dibutyl	Clear shifts for butyl protons, esp. terminal methyl groups; slight shielding	✓	Butyl chains penetrate cavity (1 or both uncertain)
5	Pacific Blue	No diagnostic shifts; polar substituents disfavor encapsulation	X	Coumarin near portals, not inside cavity
6	Dipropyl	Clear shifts for propyl chain protons, esp. terminal regions; shielding	✓	Propyl chains accommodated in cavity (extent unclear)
7	Diethyl	No diagnostic shifts; similar to methyl derivative; uniform deshielding	X	Chains too short to promote inclusion; coumarin near portals

Table 6.3: Summary of the ^1H NMR experiments with the CB7-coumarin conjugates alone and upon excess adamantane addition.

6.7. pH-Responsive Photophysical Behavior and Sensing Capabilities of CB7-Coumarin Conjugates

A comprehensive photophysical investigation of the synthesized CB7-coumarin conjugates was carried out to assess their responsiveness to high-affinity guests under different pH conditions. Measurements were performed at three representative pH values: 3.8 (sodium citrate buffer), 7.45 (sodium phosphate monobasic buffer) and 10.8 (sodium phosphate dibasic buffer). The acidic and basic conditions were chosen to ensure complete protonation or deprotonation of the aminoalkyl substituents, thereby allowing evaluation of the influence of the charge state on the photophysical properties and sensing performance.

In principle, the spectra of the conjugates would be directly compared with those of the corresponding free coumarin dyes. However, this was not feasible, as the native coumarin dyes display extremely poor solubility in water, even under strongly acidic or basic conditions. Interestingly, this limitation is largely overcome in the CB7-coumarin conjugates, where binding to the CB7 moiety enhances solubility and allows reproducible photophysical measurements. The only exception was chemosensor **3** (AMCA derivative), which could not be reliably studied in aqueous media due to persistent solubility issues, preventing the acquisition of absorption and emission data under the chosen buffer conditions.

Thus, the covalent conjugation to CB7 not only enables sensing functionality but also provides a significant practical advantage in aqueous media. The following section presents the photophysical responses of each chemosensor across the selected pH values, highlighting how structural variation in the coumarin residues translates into distinct pH-dependent behavior and sensing performance.

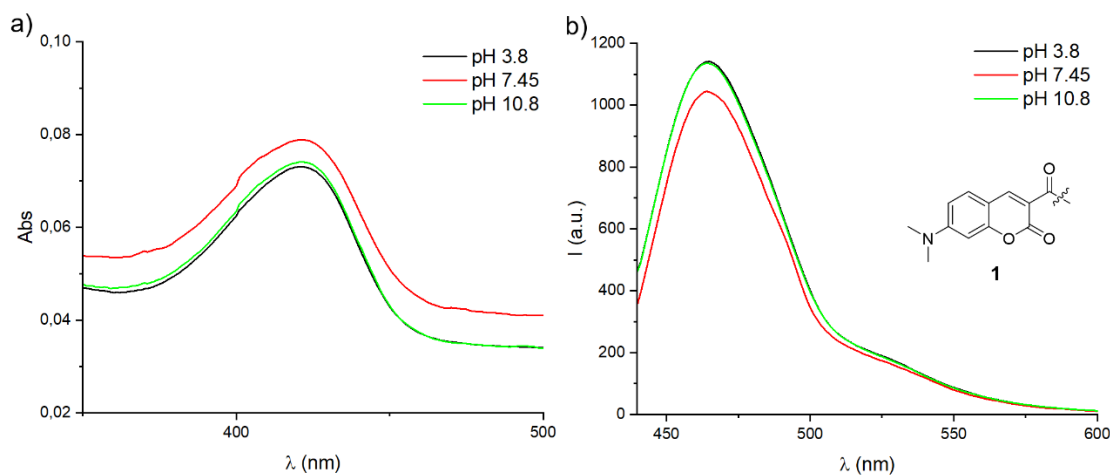


Fig. 6.17: a) Absorption spectra of chemosensor **1** (each 1 μ M) in different pH. b) Emission spectra ($\lambda_{\text{exc}} = 420$ nm) of chemosensor **1** (each 1 μ M) in different pH.

The absorption spectra of chemosensor **1** show an absorption maximum at 420 nm across all three buffer conditions (pH 3.8, 7.45, and 10.8), with no detectable intensity changes (**Fig. 6.17**). This indicates that the methyl substituents are not included in the CB7 cavity and exert minimal influence on the electronic properties of the coumarin core. The emission spectra likewise remain unaffected by pH, displaying a constant emission maximum at 465 nm at all pH values, again without great intensity variation. Interestingly, the spectra at pH 3.8 and 10.8 appear nearly identical, despite the aminoalkyl

groups being fully protonated under acidic conditions and fully deprotonated under basic conditions. This suggests that the short methyl substituents are too small to act as effective pH-responsive elements in this conjugate, resulting in negligible modulation of the photophysical properties.

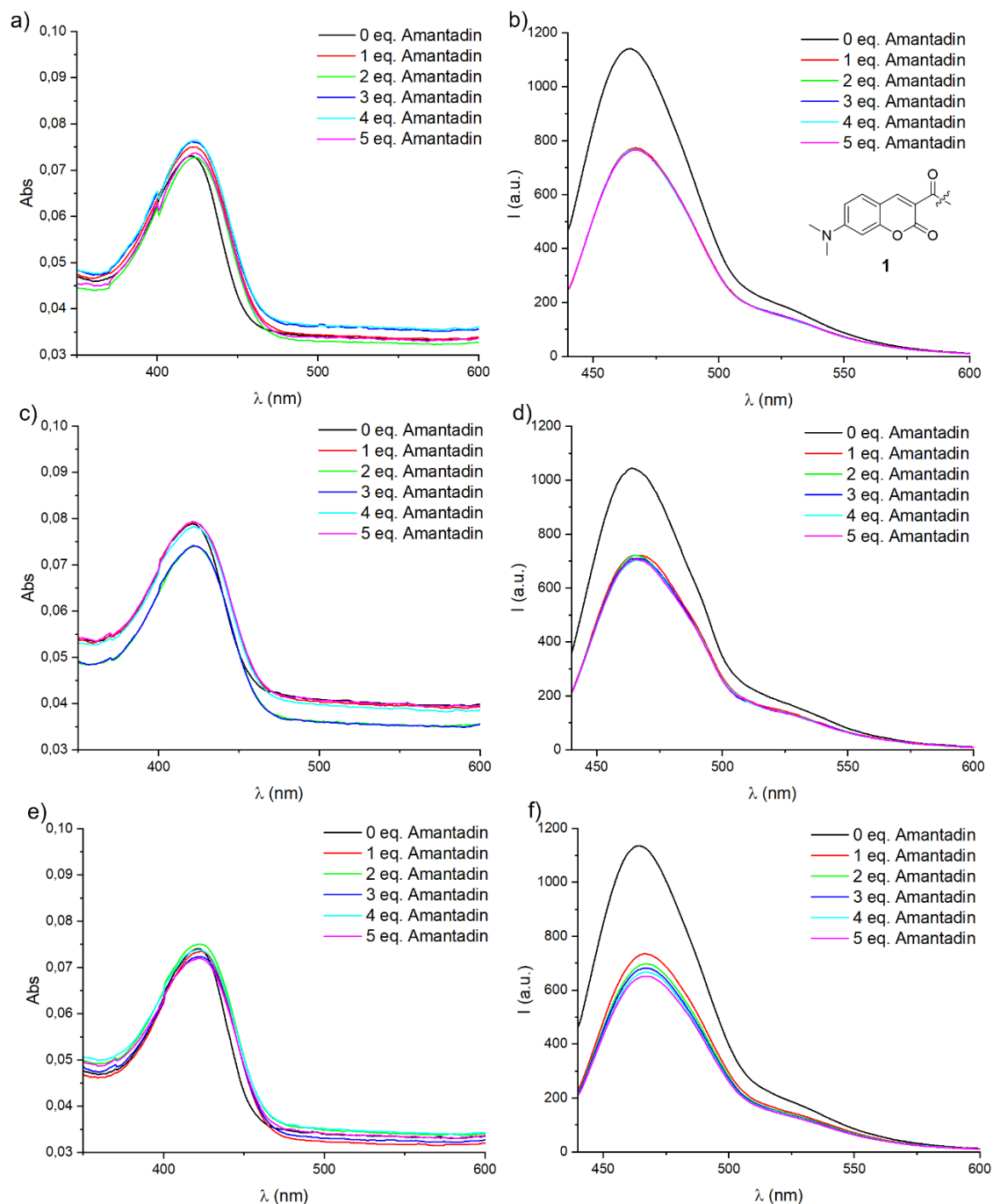


Fig. 6.18: Titration of amantadine to chemosensor **1** (each 1 μM) in different pH values. UV-vis absorption in a) pH 3.8, c) pH 7.45, e) pH 10.8 and emission spectra ($\lambda_{\text{exc}} = 420 \text{ nm}$) in b) pH 3.8, d) pH 7.4, f) pH 10.8.

Upon titration with amantadine, chemosensor **1** exhibited systematic fluorescence quenching across all pH values, accompanied with a slight red shift of the emission maximum from 464 nm to 467 nm (**Fig. 6.18**). The extent of quenching, however, was clearly pH-dependent. At pH 3.8 and 7.45, the addition of one equivalent of amantadine was already sufficient to achieve near-complete quenching,

whereas at pH 10.8, more than five equivalents are required for a comparable effect. This behavior suggests a reduced binding affinity of amantadine to the CB7 cavity under basic conditions, likely due to deprotonation, which diminishes favorable ion-dipole interactions with the CB7 portals.

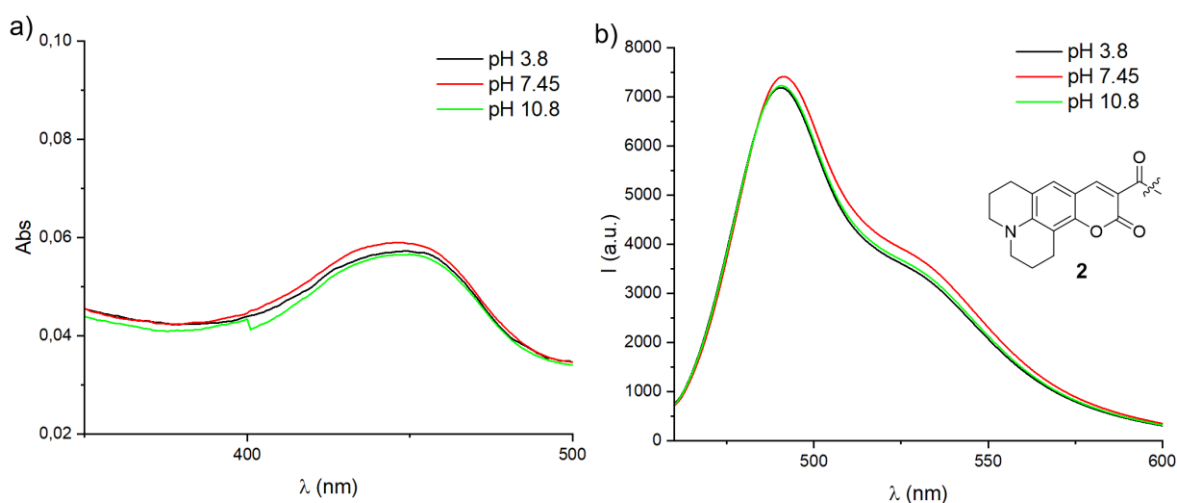


Fig. 6.19: a) Absorption spectra of chemosensor **2** (each 1 μM) in different pH. b) Emission spectra ($\lambda_{\text{exc}} = 449 \text{ nm}$) of chemosensor **2** (each 1 μM) in different pH.

The absorption spectra of chemosensor **2** show a consistent absorption maximum at 449 nm across all three buffer conditions, with only a minor variation at pH 7.45 (450 nm, **Fig. 6.19**). This stability is in line with the NMR results, which indicated that the bulky cyclohexylamino substituents are too large to be accommodated within the CB7 cavity, leaving the chromophore electronically unaffected by inclusion. The emission spectra display a constant maximum (491 nm) at pH 3.8 and pH 10.8, while a slight red shift (492 nm) is observed at pH 7.45. Across all pH values, chemosensor **2** is strongly emissive, but this property can be attributed primarily to the intrinsic photophysics of the coumarin 343 scaffold, rather than to CB7 conjugation. Thus, while the conjugate is spectrally well-defined, its behavior shows minimal modulation by pH or host-guest interactions.

Upon titration with amantadine, chemosensor **2** showed no significant photophysical response (**Fig. 6.20**). The absorption maximum remained constant at 449 nm, while the emission spectra displayed no meaningful changes in wavelength or intensity across all three pH values. This lack of responsiveness is consistent with the expectation that the bulky substituents prevent meaningful cavity interactions, thereby limiting both pH- and guest-dependent modulation.

Unlike the other conjugates, chemosensor **3** could not be reliably characterized by absorption or emission spectroscopy in aqueous media. Despite encapsulation by CB7, the conjugate still suffered from insufficient solubility under all tested buffer conditions. As a result, neither absorption spectra nor fluorescence emission data could be acquired. This limitation highlights that, while CB7 conjugation generally enhances the aqueous solubility of coumarin dyes, certain derivatives – particularly those with less favorable substituent patterns such as AMCA – may still fall outside the solubility range required for systematic photophysical studies.

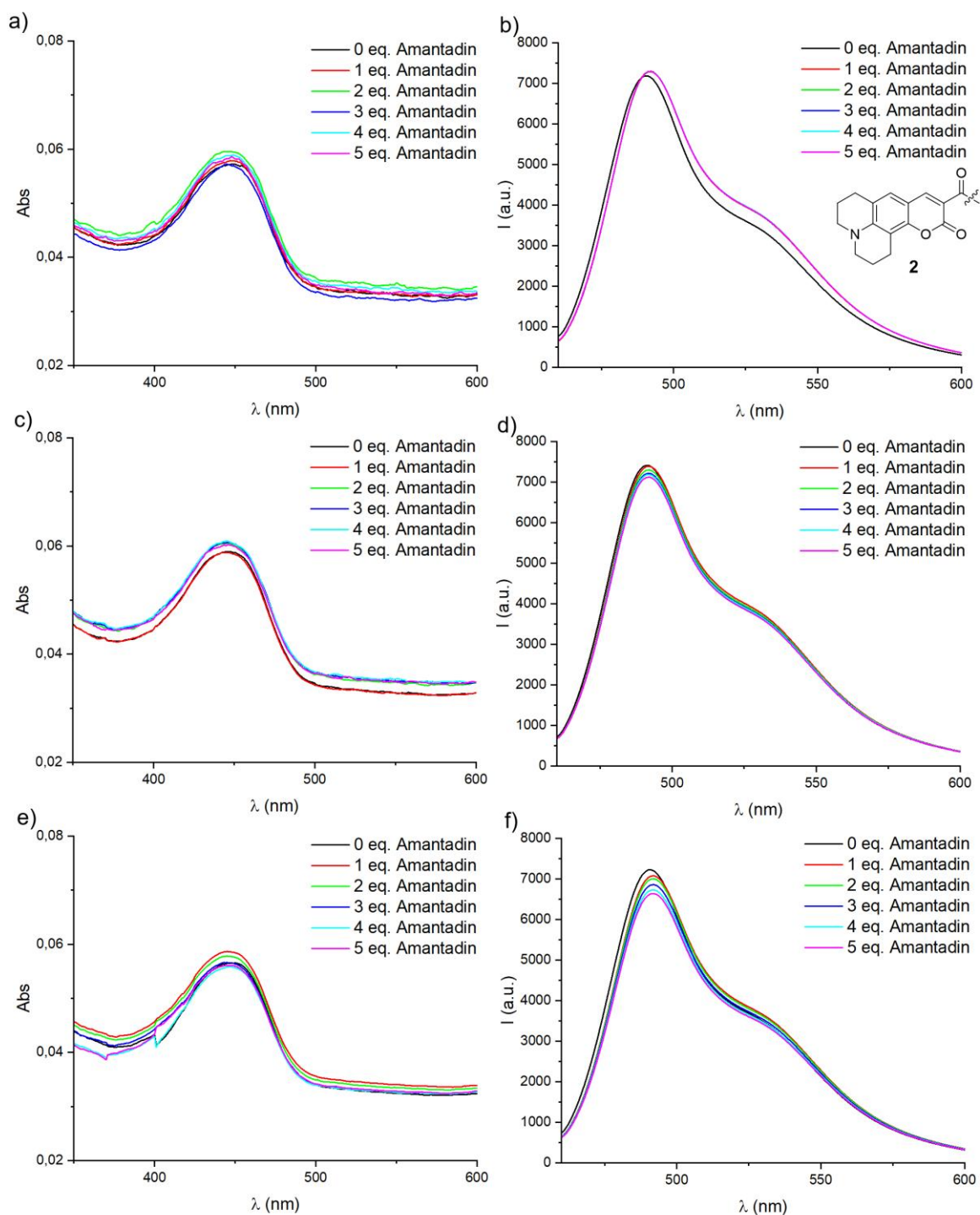


Fig. 6.20: Titration of amantadine to chemosensor **2** (each 1 μM) in different pH values. UV-vis absorption in a) pH 3.8, c) pH 7.45, e) pH 10.8 and emission spectra ($\lambda_{\text{exc}} = 449 \text{ nm}$) in b) pH 3.8, d) pH 7.4, f) pH 10.8.

The absorption spectra of chemosensor **4** reveal clear pH-dependent differences (**Fig. 6.21**). At pH 3.8, the absorption maximum is observed at 442 nm, shifting to 438 nm at pH 7.45 and then slightly to 440 nm at pH 10.8. Those modest but distinct shifts indicate that the protonation state of the butyl-substituted aminoalkyl chains influences the electronic environment of the coumarin chromophore. In contrast, the emission maximum remains constant at 483 nm across all pH values. However, the emission

intensity varies slightly, suggesting that the extent of protonation or deprotonation of the aminoalkyl groups modulates the efficiency of non-radiative decay pathways. Thus, while the emission wavelength itself is stable, the fluorescence output is clearly pH-sensitive. This is consistent with its long butyl chains, which drive self-inclusion and create a more responsive environment at the CB7 portals. These findings highlight the importance of substituent length and hydrophobicity for tuning pH-dependent photophysical properties.

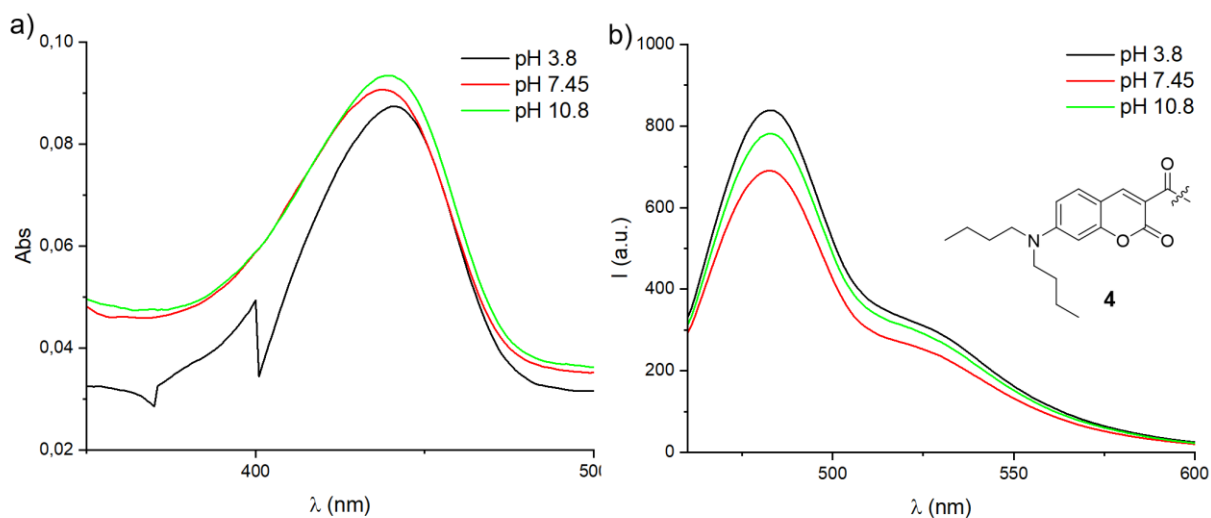


Fig. 6.21: a) Absorption spectra of chemosensor **4** (each 1 μ M) in different pH. b) Emission spectra ($\lambda_{\text{exc}} = 440$ nm) of chemosensor **4** (each 1 μ M) in different pH.

Upon titration with amantadine, chemosensor **4** exhibited blue shifts in both absorption and emission maxima (**Fig. 6.22**). The absorption maximum shifted from 440 to 431 nm, while the emission maximum shifted from 483 nm to 478 nm, independent of pH. In addition, the fluorescence signal was strongly quenched in all cases, with near-complete quenching achieved after the addition of one equivalent of amantadine. A slight pH dependency in the extent of quenching was observed, suggesting that while the overall response is robust, the binding efficiency is still subtly influenced by protonation state.

The absorption spectra of chemosensor **5** display a marked difference between acidic and neutral/basic conditions (**Fig. 6.23**). At pH 3.8, the absorption is drastically reduced, most likely due to protonation of the phenolic hydroxy group. Despite this drop in intensity, the absorption maximum remains constant at 403 nm across all conditions. This effect is mirrored in the emission spectra. While the emission maximum is stable at 453 nm, the fluorescence intensity at acidic pH is reduced by approximately a factor of three compared with the neutral (pH 7.45) and basic pH (10.8) conditions, which display nearly identical emission output. Thus, chemosensor **5** shows a pronounced pH-dependent intensity modulation, driven primarily by the acid-base state of the phenolic substituent, while maintaining absorption and emission maxima at the same wavelengths.

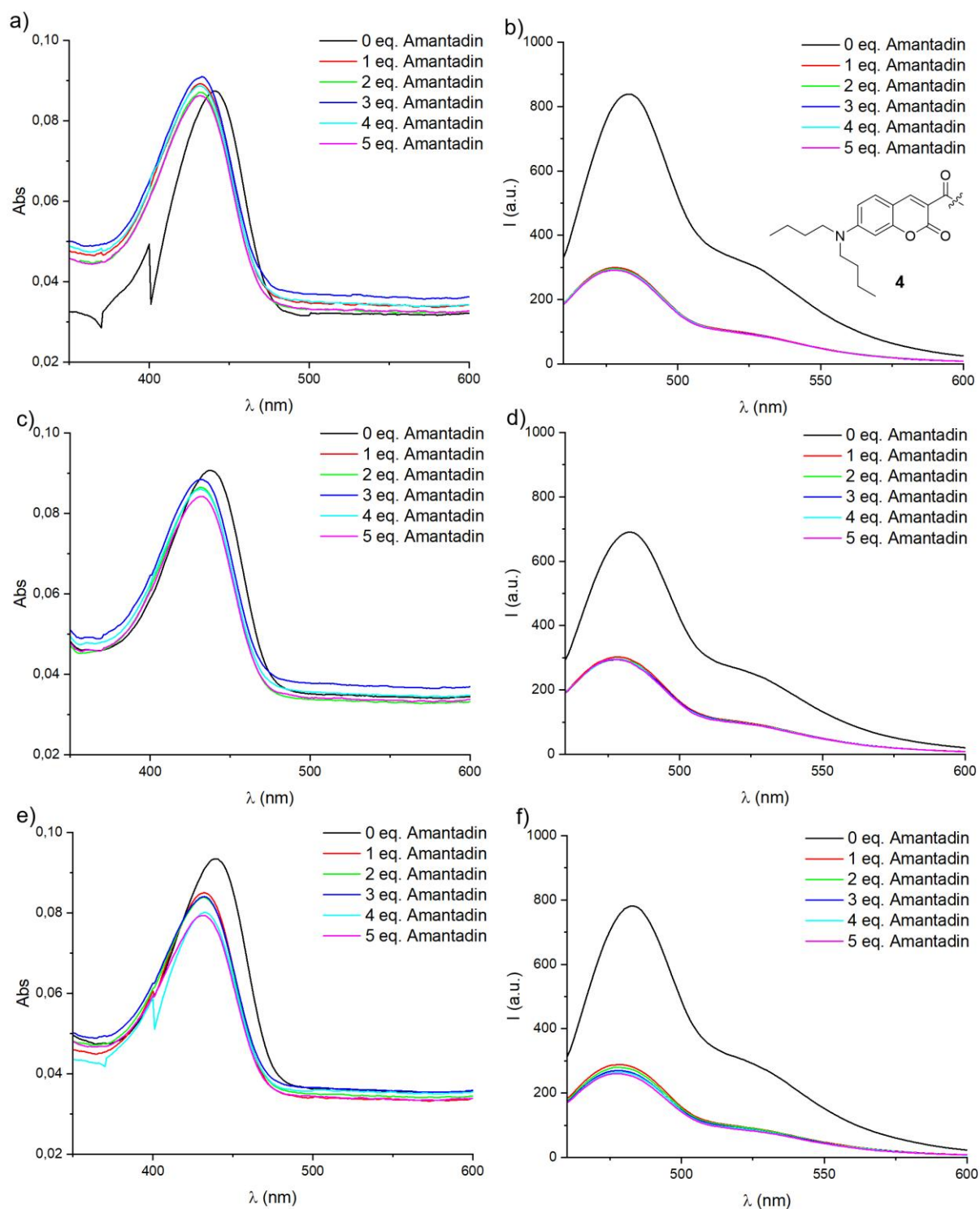


Fig. 6.22: Titration of amantadine to chemosensor **4** (each 1 μM) in different pH values. UV-vis absorption in a) pH 3.8, c) pH 7.45, e) pH 10.8 and emission spectra ($\lambda_{\text{exc}} = 439$ nm) in b) pH 3.8, d) pH 7.4, f) pH 10.8.

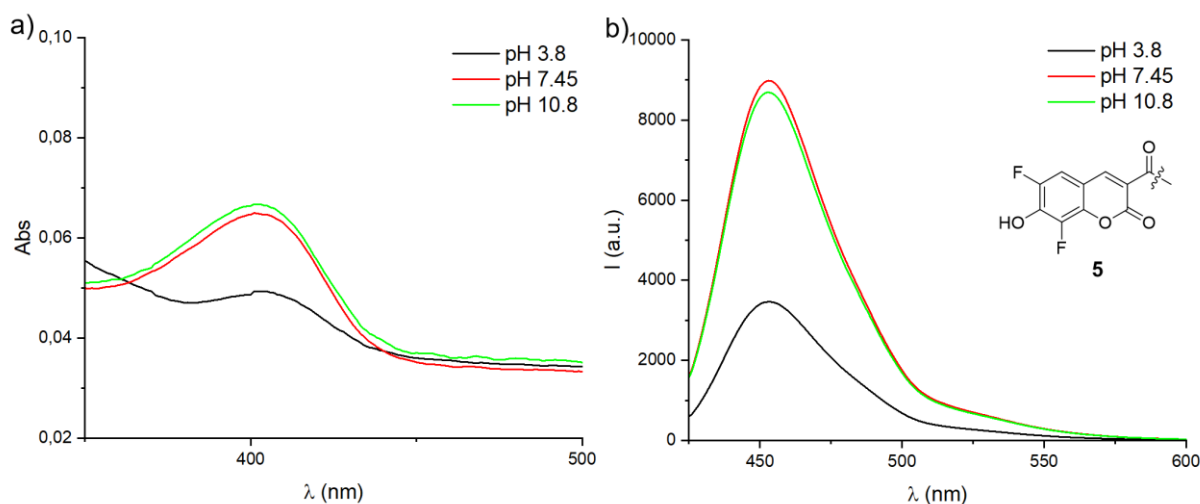


Fig. 6.23: a) Absorption spectra of chemosensor **5** (each 1 μ M) in different pH. b) Emission spectra ($\lambda_{\text{exc}} = 403$ nm) of chemosensor **5** (each 1 μ M) in different pH.

Despite the expected lack of responsiveness due to the absence of cavity inclusion, chemosensor **5** showed surprisingly distinct titration behaviors depending on pH (**Fig. 6.24**). At pH 3.8, amantadine addition resulted in a notable enhancement of emission intensity, in sharp contrast to the behavior of other conjugates. At pH 7.45, virtually no response was observed, while at pH 10.8, titration induced gradual fluorescence quenching. Complete quenching at basic pH required up to 10 equivalents of amantadine, far more than for other conjugates. These findings suggest that chemosensor **5**, while not engaging in strong inclusion-driven interactions, is nevertheless sensitive to external binding events at the CB7 portals, with the direction and magnitude of the response being highly pH-dependent.

Surprisingly, chemosensor **6** showed no detectable pH responsiveness, despite the clear signs of inclusion observed in the NMR studies (**Fig. 6.25**). The absorption maximum remained constant at 403 nm, and the emission maximum was stable at 471 nm across all three buffer conditions. No significant differences in intensity were observed in either absorption and emission. This lack of modulation indicates that, unlike chemosensor **4** (dibutyl derivative), the dipropyl substituents do not strongly influence the photophysical behavior of the coumarin chromophore under the tested conditions, even though structural inclusion is supported by NMR evidence. Only the longer butyl chains appear sufficient to translate inclusion into measurable pH-dependent optical effects.

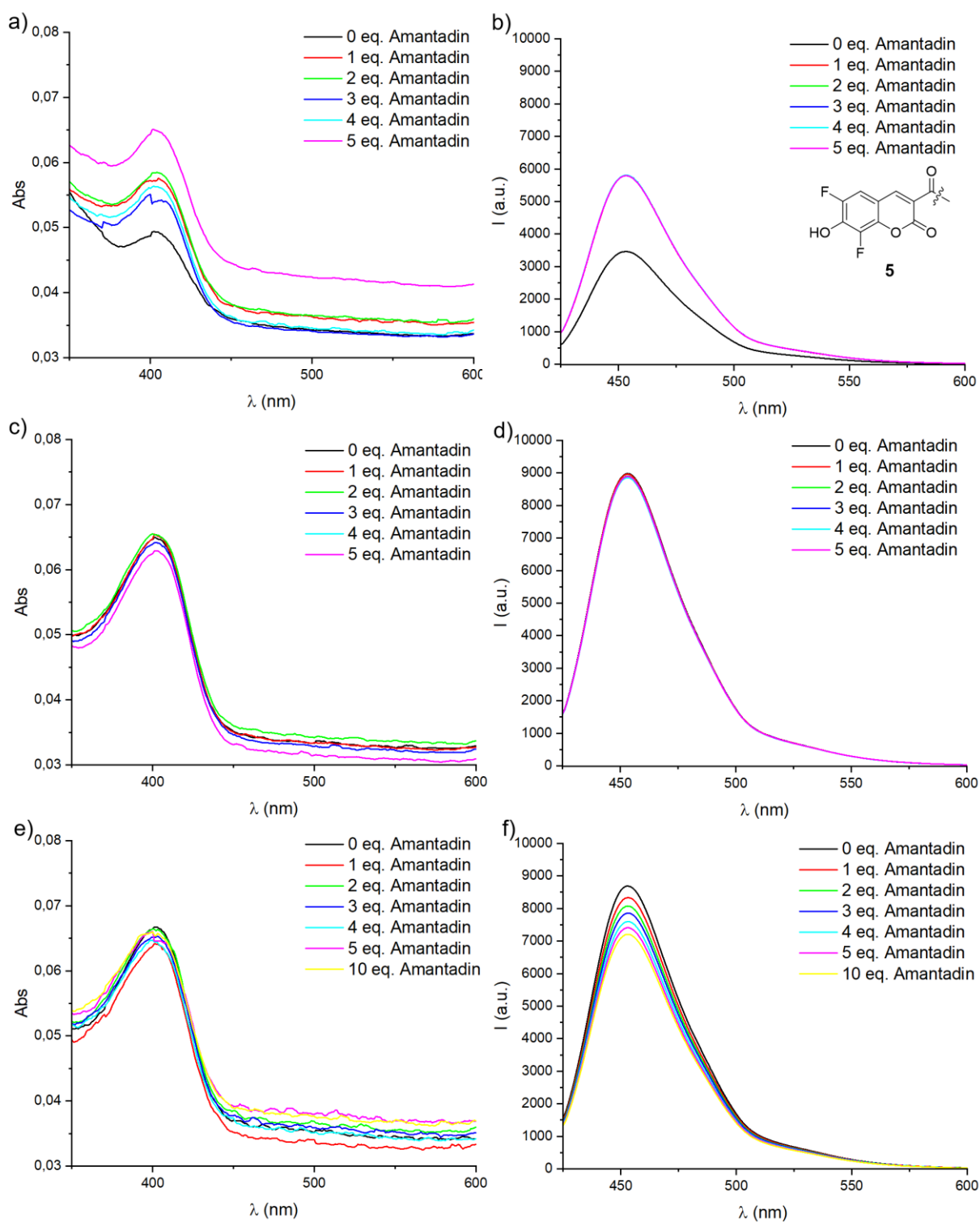


Fig. 6.24: Titration of amantadine to chemosensor **5** (each 1 μM) in different pH values. UV-vis absorption in a) pH 3.8, c) pH 7.45, e) pH 10.8 and emission spectra ($\lambda_{\text{exc}} = 403 \text{ nm}$) in b) pH 3.8, d) pH 7.4, f) pH 10.8.

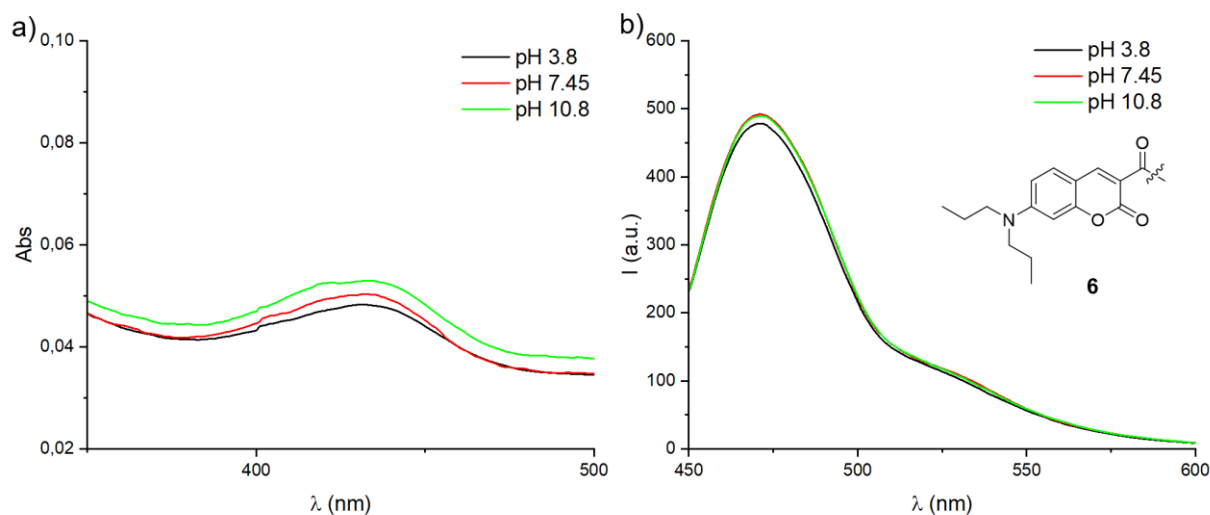


Fig. 6.25: a) Absorption spectra of chemosensor **6** (each 1 μ M) in different pH. b) Emission spectra ($\lambda_{\text{exc}} = 432$ nm) of chemosensor **6** (each 1 μ M) in different pH.

Upon titration with amantadine, chemosensor **6** exhibited clear signs of competitive inclusion, manifested as systematic fluorescence quenching across all pH values (**Fig. 6.26**). The emission maximum remained constant at 471 nm, but the quenching efficiency varied with pH. At lower pH values, on equivalent of amantadine was sufficient for near-complete quenching, whereas at higher pH, progressively larger equivalents were required. This trend indicates that increasing pH reduces the binding affinity of the amantadine for the CB7 cavity, consistent with deprotonation of the amino group weakening ion-dipole interactions at the portal. Compared with chemosensor **4**, chemosensor **6** shows that while both butyl and propyl promote inclusion, only the longer butyl chains yield intrinsic pH-dependent photophysical modulation, whereas propyl chains manifest their role primarily in guest-competition.

Chemosensor **7** shows modest pH responsiveness (**Fig. 6.27**). The absorption spectra remain essentially constant across all buffer conditions, with a stable absorption maximum at 438 nm. In contrast, the emission spectra, while also showing a constant emission maximum at 478 nm, display slight intensity variations. The fluorescence signal is highest at pH 7.45, with somewhat reduced emission under acidic and basic conditions. This indicates that the ethylaminoalkyl substituents are insufficient to promote strong cavity inclusion (as indicated by NMR), the protonation state still exerts a minor influence on the photophysical output giving rise to the small but noticeable pH-dependent intensity variation. This suggests that even short substituents can transit small protonation-dependent effects to the coumarin core, but without the stabilization of inclusion, such modulation remains minimal.

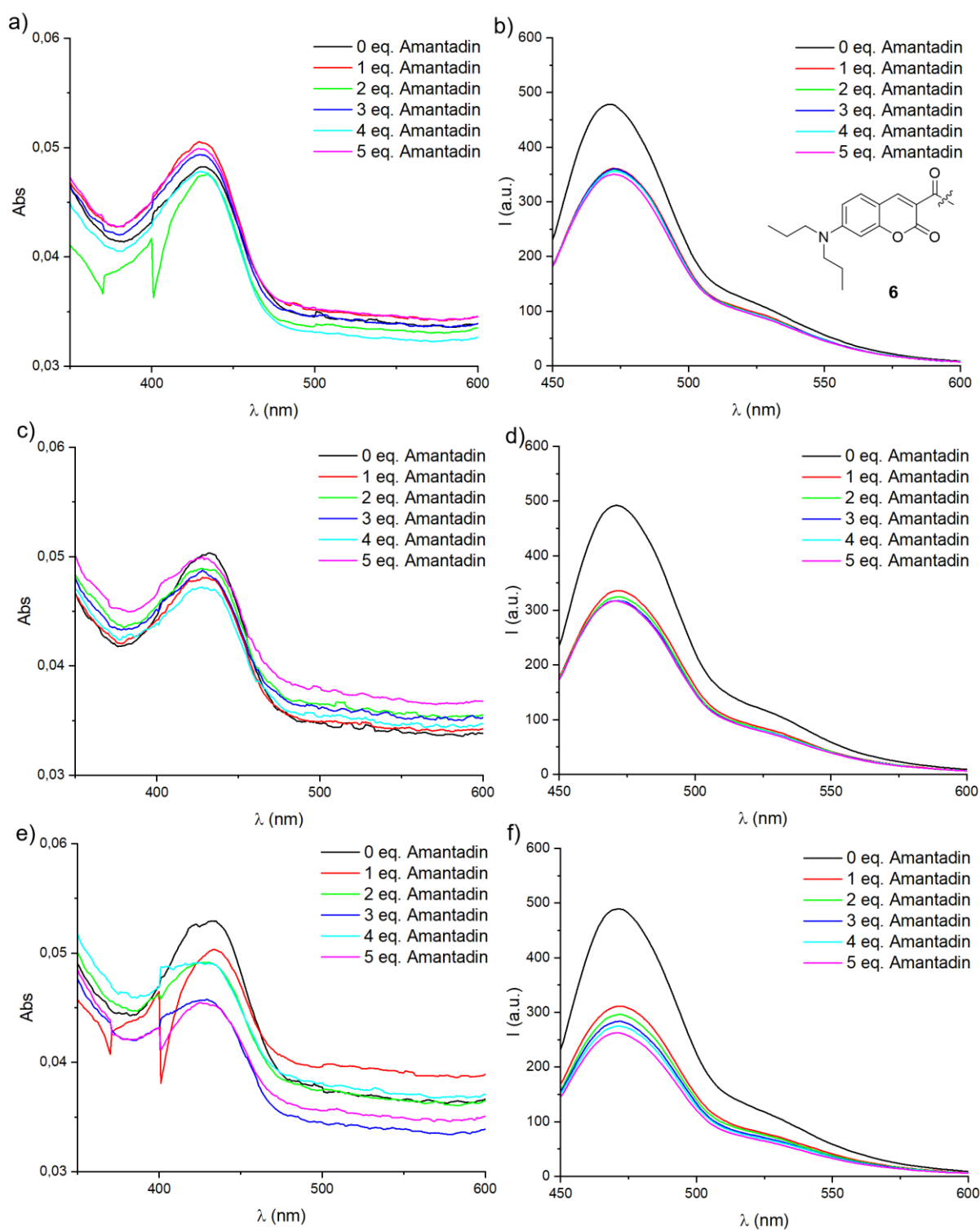


Fig. 6.26: Titration of amantadine to chemosensor **6** (each 1 μM) in different pH values. UV-vis absorption in a) pH 3.8, c) pH 7.45, e) pH 10.8 and emission spectra ($\lambda_{\text{exc}} = 433 \text{ nm}$) in b) pH 3.8, d) pH 7.4, f) pH 10.8.

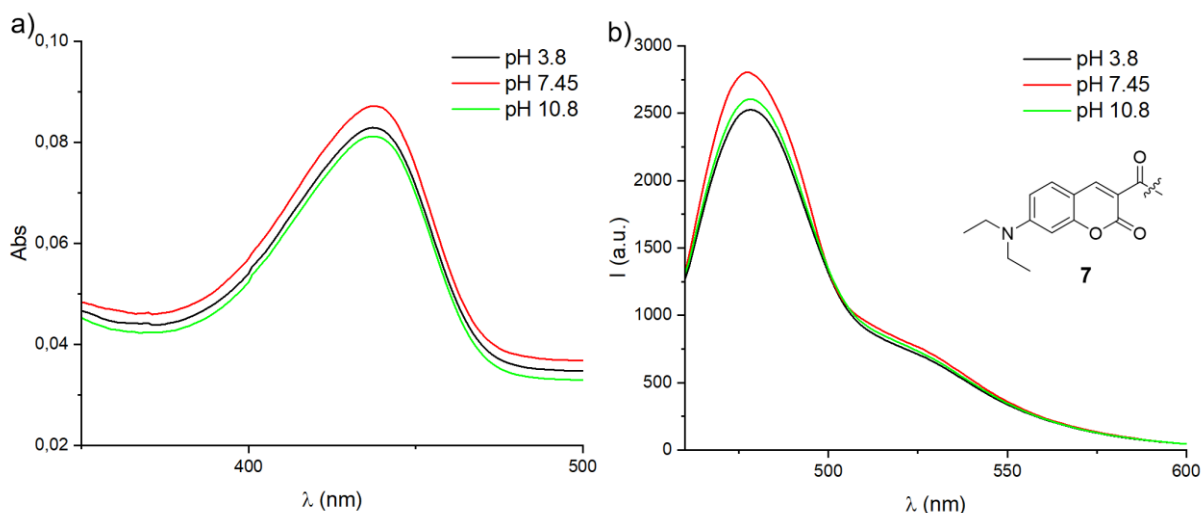


Fig. 6.27: a) Absorption spectra of chemosensor **6** (each 1 μM) in different pH. b) Emission spectra ($\lambda_{\text{exc}} = 438 \text{ nm}$) of chemosensor **7** (each 1 μM) in different pH.

Upon amantadine titration, chemosensor **7** exhibited clear and highly responsive inclusion behavior (**Fig. 6.28**). In the absorption spectra, the maximum underwent a blue shift from 438 nm to 430 nm across all pH conditions upon guest addition. The emission spectra showed the strongest quenching effect among all CB7-coumarin conjugates, with the fluorescence intensity reduced by nearly a factor of six. Despite this strong response, the emission maximum remained constant at 478 nm. These results demonstrate that, although the short substituents of chemosensor **7** limit intrinsic pH responsiveness, the conjugate is nevertheless highly sensitive to guest binding, translating cavity competition into a strong and reproducible photophysical signal. Chemosensor **7** stands out by combining weak intrinsic pH modulation with exceptionally strong quenching upon amantadine binding. This dual behavior reinforces the distinction between pH-dependent substituent effects and guest-induced competition effects, which can be pronounced even in conjugates lacking self-inclusion.

6.8. Comparative Discussion of Photophysical Behavior across the CB7-Coumarin Conjugates

Taken together, the photophysical investigations reveal clear structure-function relationships among the CB7-coumarin conjugates. Chemosensors with short substituents (**1**, dimethyl and **7**, diethyl) and bulky substituents (**2**, dicyclohexyl) exhibited minimal pH-dependent spectral changes, consistent with their lack of self-inclusion observed in NMR studies. Chemosensor **7**, however, stands out by showing exceptionally strong quenching upon amantadine titration, indicating that even short chains can yield robust guest-responsive signals through competitive binding.

Chemosensors with intermediate, hydrophobic substituents (**4** and **6**) displayed self-inclusion in NMR and clear responsiveness to amantadine titration, though their intrinsic pH modulation differed: chemosensor **4** (dibutyl) showed distinct absorption shifts and pH-sensitive emission intensities, while chemosensor **6** (dipropyl) remained spectrally stable across pH but respond strongly to amantadine

competition, with binding affinity decreasing at higher pH. These results highlight that substituent length defines whether inclusion translates into measurable pH-dependent optical effects or is only manifested under guest competition.

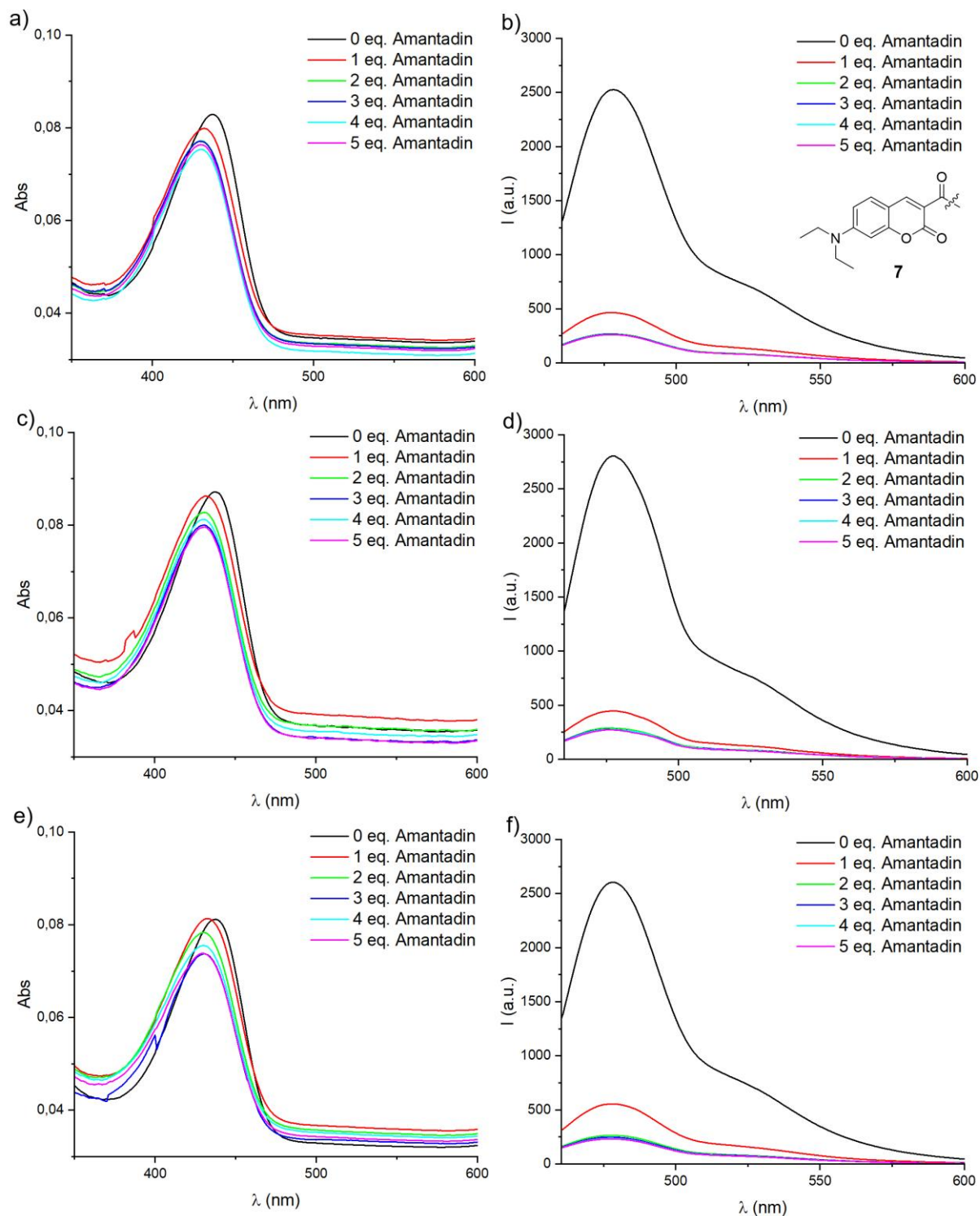


Fig. 6.28: Titration of amantadine to chemosensor **6** (each 1 μM) in different pH values. UV-vis absorption in a) pH 3.8, c) pH 7.45, e) pH 10.8 and emission spectra ($\lambda_{\text{exc}} = 438$ nm) in b) pH 3.8, d) pH 7.4, f) pH 10.8.

Chemosensor **5** (Pacific Blue) behaved differently, showing pronounced intensity modulation between acidic and neutral/basic conditions, driven by protonation of the phenolic substituent rather than cavity inclusion. Interestingly, it also displayed directional responses upon amantadine titration: fluorescence enhancement at acidic pH, no response at neutral pH, and quenching at basic pH, distinguishing it from the uniform quenching behavior of the other responsive conjugates.

Finally, chemosensor **3** (AMCA) could not be analyzed photophysically due to persistent solubility limitations, underscoring that not all coumarin scaffolds benefit equally from CB7 conjugation in terms of aqueous compatibility.

Overall, the combined data show that effective photophysical responsiveness in CB7-coumarin conjugates requires substituents of intermediate length and hydrophobicity, whereas very short, bulky, or polar groups suppress inclusion and reduce pH sensitivity. However, even such non-ideal scaffolds can exhibit guest-induced responses, demonstrating that the balance between intrinsic pH modulation and competitive binding effects is highly tunable across the series.

6.9. Microplate-Based Two-Dimensional Analysis for Analyte Discrimination Using CB7-Coumarin Chemosensors

Measurements from this section were partially performed by Hanna Hönle. Data analysis was performed by Dr. Thomas Jochmann.

For the final analyte discrimination experiments, a focused set of four CB7-coumarin conjugates was selected: chemosensor **1** (dimethyl), chemosensor **4** (dibutyl), chemosensor **6** (dipropyl) and chemosensor **7** (diethyl). This subset was chosen to balance structural diversity with comparability, as all four share the same coumarin scaffold but differ systematically in the length of their aminoalkyl substituents. Despite the considerable synthetic effort invested in preparing these conjugates, their use as a small but coherent sensor library offers substantial analytical advantages. With only four chemosensors, measured under three pH conditions (3.8, 7.45, 10.8) and in the presence of seven different salts in different concentrations (CaCl₂, CsCl, KCl, LiCl, MgCl₂, NaCl, NH₄Cl), the system provides a large combinatorial sensing space with high theoretical discrimination capacity.

The idea of incorporating salt as a second discriminating dimension builds on earlier success with the CB7-NBD system, where ion identity and concentration were shown to strongly modulate photophysical responses and thus improve analyte discrimination.²³² In the present work, this concept is extended to the CB7-coumarin conjugates, which are expected to behave differently from CB7-NBD due to their distinct binding properties. Notably, coumarins exhibit only moderate binding affinities toward CB7, a consequence of their neutral charge state and relatively small hydrophobic surfaces. This moderate affinity, however, is advantageous for sensing applications, as it leaves sufficient dynamic range for weaker binding analytes to compete for the CB7 cavity. Coumarins are also well-established binders to cucurbiturils, making them reliable and versatile reporter dyes in this context.

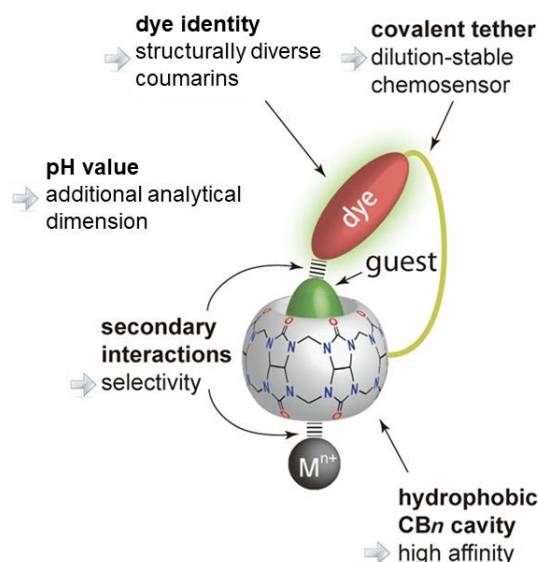


Fig. 6.29: Visualization of the working principle of the two-dimensional sensing. Adapted with permission from ref ²³² © American Chemical Society

In parallel, pH variation provides a complementary handle on sensor performance. Protonation of the aminoalkyl substituents at acidic pH enhances their affinity for the CB7 portals, whereas deprotonation at basic pH reduces these interactions. Thus, by combining pH modulation with salt titration, the sensing space becomes two-dimensional: one axis defined by the charge state of the dye substituents and analytes, the other by the competitive or cooperative binding effects of ions at the CB7 portals. The optical response of the coumarin dyes (changes in emission spectra) constitutes the output dimension, generating unique spectral patterns for each analyte under different conditions. When combined, this setup allows the construction of distinct optical fingerprints, enabling reliable analyte discrimination even among structurally related compounds.

It is noteworthy that while some CB7-based systems, such as CB7-Ru, have shown pronounced sensitivity to salt addition, the CB7-coumarin conjugates exhibit much greater robustness, maintaining their photophysical performance under varying ionic conditions. This stability, combined with their moderate affinity and tunable pH responsiveness, makes them especially well-suited for the development of a two-dimensional optical fingerprinting strategy. Together, these features enable the generation of distinct and reproducible spectral signatures for different analytes across a matrix of pH and salt conditions, providing a powerful platform for selective analyte identification.

The analyte distinction experiments were carried out using a fluorescence microplate reader, allowing parallel and high-throughput monitoring of the emission responses of the CB7-coumarin under systematic salt titration. This setup enabled efficient comparison of how different salts and their concentrations modulate the fluorescence behavior of the conjugates in the presence of various analytes. To guarantee reproducibility and precise liquid handling, all assays were performed with a titration robot, which automatically prepared the mixtures of buffer, chemosensor, and analyte under strictly standardized

conditions. A representative panel of 22 CB7-binding biorelevant guests was selected, encompassing a wide range of structural and physicochemical properties, including differences in size, charge, hydrophobicity, and binding affinity. This diverse analyte set was chosen to challenge the sensing system and to demonstrate the ability of the coumarin conjugates to produce distinct optical fingerprints across multiple chemical classes.

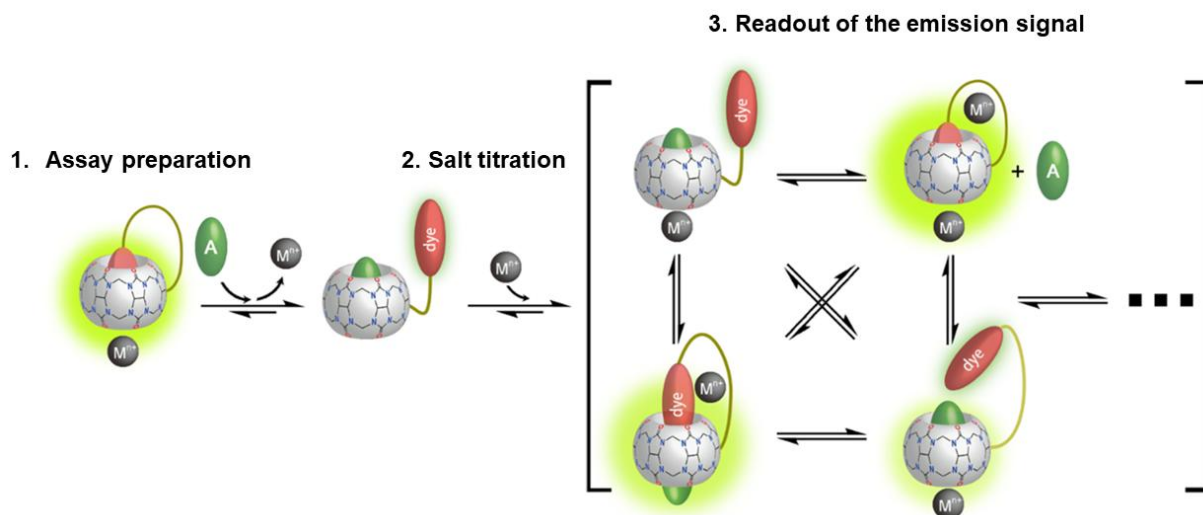


Fig. 6.30: Schematic representation of the two-dimensional sensing strategy using CB7-coumarin conjugates. The analyte discrimination concept integrates two orthogonal parameters: (1) pH variation, which modulates the protonation state of the aminoalkyl substituents and analytes and thereby alters their binding affinity toward the CB7 portals, and (2) salt titration, where the identity and concentration of different cations (Ca^{2+} , Cs^+ , K^+ , Li^+ , Mg^{2+} , Na^+ , NH_4^+) influence CB7–guest equilibria through competitive or cooperative interactions at the carbonyl-lined portals. The photophysical output of the coumarin dyes (absorption and emission spectra) serves as the readout dimension, producing unique response patterns for each analyte under the matrix of tested conditions. The combination of four chemosensors (dimethyl, diethyl, dipropyl, dibutyl derivatives), three pH values, and seven salts generates a large discriminatory sensing space, enabling analytes to be identified by their optical fingerprints. Adapted with permission from ref ²³² © American Chemical Society

For all experiments, the chemosensor concentration was fixed at $1\ \mu\text{M}$, while the analyte concentration was maintained at $15\ \mu\text{M}$ to ensure a high degree of binding displacement even for weaker affinity guests. Salt effects were examined by incremental titration in four steps of $250\ \text{mM}$, reaching a final concentration of $1000\ \text{mM}$ of salt.

For each experimental run, the fluorescence emission spectra of all chemosensor-analyte-salt combinations were recorded directly in the microplate format. Measurements were conducted under identical optical settings, except for the excitation wavelength, which was individually optimized for each chemosensor to achieve maximum signal intensity. The resulting data were compiled into response matrices, where each curve represents the relative fluorescence change at a defined pH, salt concentration, and analyte identity. Given the extensive dataset generated from the combination of four chemosensors, three pH values, and seven salts for each analyte-chemosensor combination, a complete description of every titration curve is impractical. Therefore, this section highlights the most representative and informative results, supported by principal component analysis (PCA) to visualize clustering and

discrimination trends. In addition, a general overview of the sensing behavior across conditions is provided to illustrate how variations in pH and ionic environment influence analyte recognition and overall system performance.

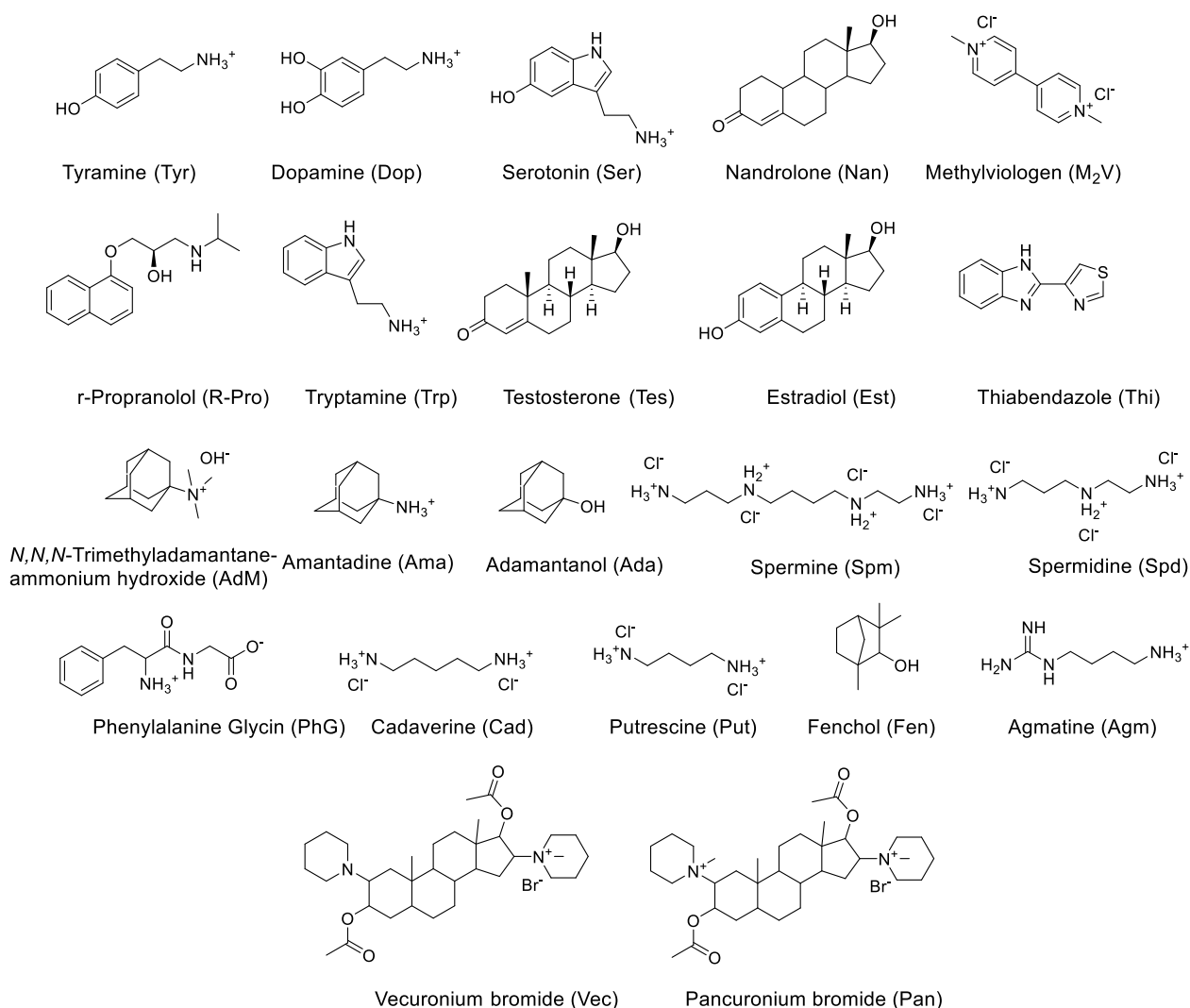


Fig. 6.31: Structures of the analytes used in the study with the CB7-coumarin conjugates, shown in their native charged states at pH=7.

Across the full dataset, the CB7-coumarin conjugates exhibited distinct and reproducible fluorescence response patterns upon exposure to different analytes, pH values, and salt environments. The emission intensity changes were generally analyte-dependent, reflecting variations in binding strength and interaction mode within the CB7 cavity. In most cases, addition of salts led to progressive quenching or enhancement of fluorescence, depending on the ionic strength and cation identity, indicating that the ionic environment plays a key modulatory role in host-guest equilibria.

Among the four CB7-coumarin conjugates studied, chemosensor **1** (dimethyl) exhibited the weakest overall sensing performance in terms of analyte discrimination (**Fig. 6.32**). This outcome is consistent with the NMR and photophysical characterization, which showed no clear evidence of self-inclusion or pronounced response to pH variation and amantadine addition. Despite its limited responsiveness, several

notable trends were observed, while several analytes displayed unique or counter-directional behaviors. Most prominently, dopamine at pH 10.8 produced a distinct and reproducible fluorescence quenching response that was largely independent of salt identity or concentration. Even in the absence of salt, and across all tested salts, dopamine caused near-complete fluorescence quenching, indicating a specific interaction mechanism that does not rely on ionic modulation. This pronounced effect at basic pH may arise because dopamine is predominantly deprotonated at pH 10.8, which alters its charge distribution and enhances its hydrophobic interactions with the CB7 cavity, thereby facilitating stronger binding and more efficient quenching of the coumarin emission. Methyl viologen (at both pH 3.8 and 10.8) and putrescine (at pH 7.45) exhibited increasing emission intensities upon salt addition, opposite to the quenching trends seen for the most other analytes. When NaCl was used as a representative salt for titration, the plots of emission intensity versus salt concentration revealed that, for nearly all analytes, the maximum fluorescence change occurred after the first addition step (*i.e.*, at 250 mM). Beyond this concentration, further salt addition led to diminishing discrimination capacity in most cases, as the response curves converged. Thus, for chemosensor **1**, the best analyte differentiation was obtained after the first salt-addition step, with resolution gradually decreasing at higher ionic strengths. For other salts, however, the discrimination capability deteriorated further – the corresponding titration curves were closely overlapping, making individual analytes difficult to resolve.

The principal component analysis (PCA) provided deeper insight into these patterns (**Fig. 6.33**). For NaCl, the basic condition again proved optimal for discrimination, where analytes such as methyl viologen, pancuronium bromide, putrescine, and agmatine were clearly separated from one another in the PCA plot. Across different salt, methyl viologen consistently emerged as one of the best-resolved analytes, particularly at acidic pH 3.8, where nearly all salts yielded distinct clustering. In contrast, neutral pH 7.45 produced extensive overlap among analyte clusters, confirming that chemosensor **1** performs best under strongly acidic or basic conditions. Overall, these results indicate that while chemosensor **1** limited general discrimination power, it retains specific sensitivity toward certain analytes, especially dopamine and methyl viologen, and that extreme pH conditions enhance its differentiation capability relative to neutral environments.

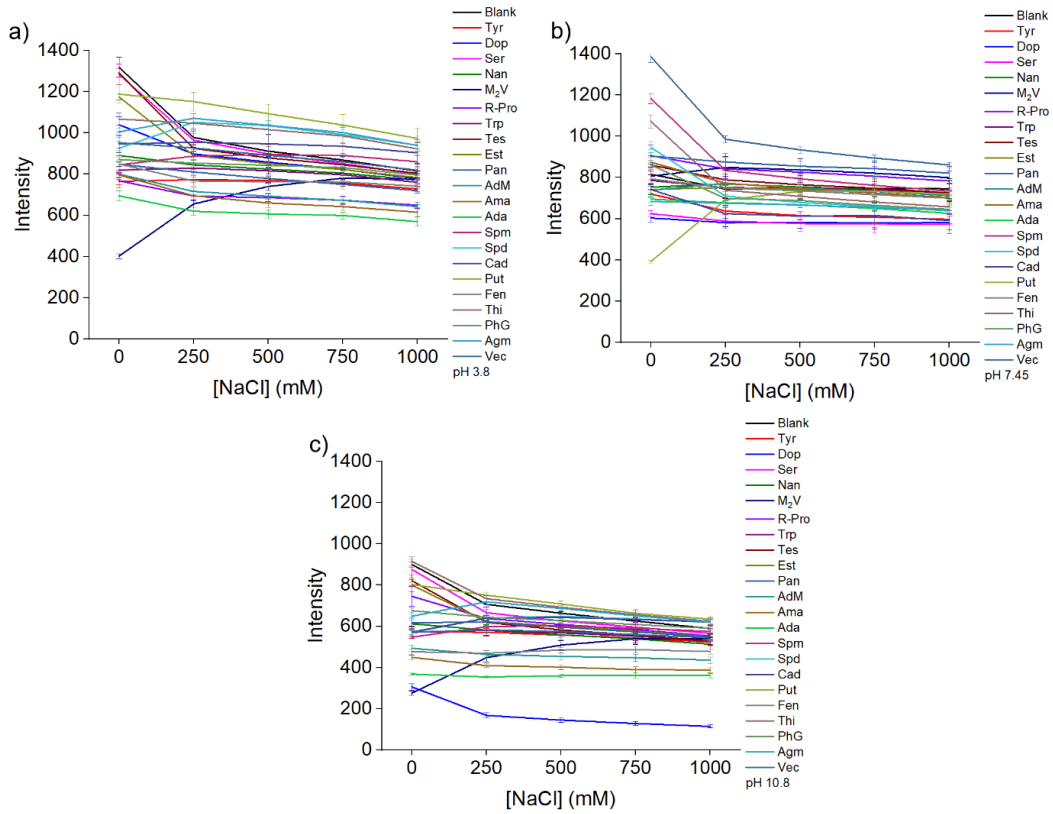


Fig. 6.32: Titration plots of the emission intensity at $\lambda_{exc} = 420$ nm of $1 \mu\text{M}$ chemosensor **1** in the presence of $15 \mu\text{M}$ analytes in 10 mM buffer. a) pH 3.8, b) pH 7.45, c) pH 10.8.

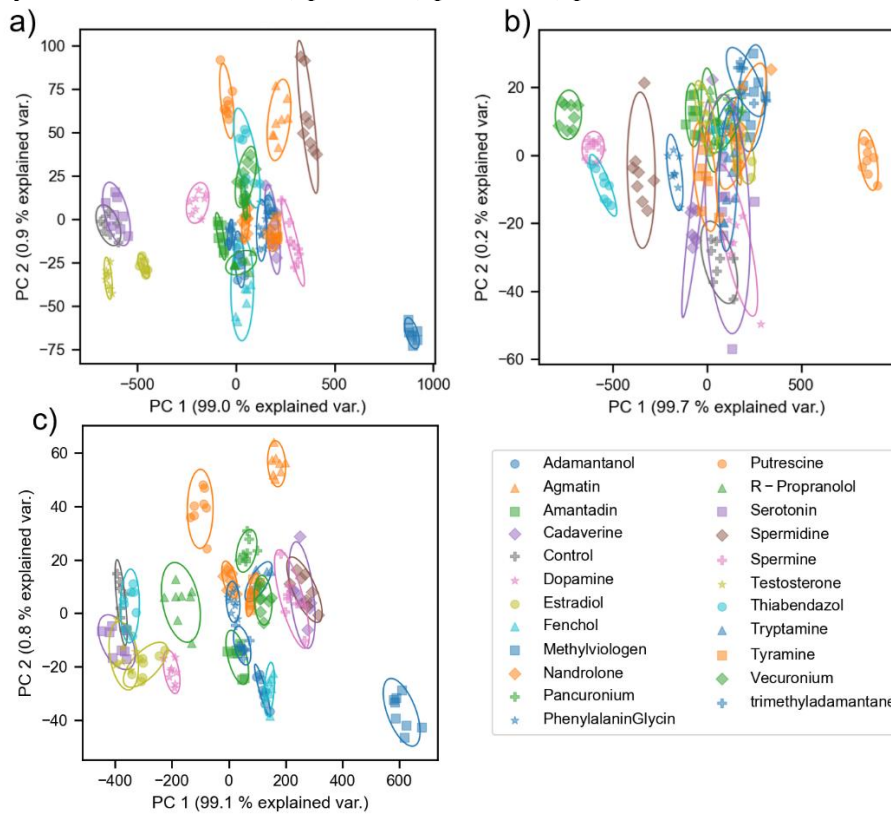


Fig. 6.33: PCA plots with 95% confidence ellipses resulting from the emission intensity at 465 nm ($\lambda_{exc} = 420$ nm) as a function of the concentration of NaCl with $1 \mu\text{M}$ chemosensor **1** at a) pH 3.8, b) pH 7.45, c) pH 10.8.

At first glance, the results obtained for chemosensor **4** (dibutyl) appeared somewhat unexpected, as the changes in fluorescence intensity were less pronounced than anticipated based on NMR and photophysical studies, which had indicated strong host-guest interactions and clear signs of self-inclusion (**Fig. 6.34**). Nonetheless, systematic analysis across all pH conditions revealed several meaningful patterns and analyte-dependent effects.

The overall extent of fluorescence quenching was generally smaller than that observed for chemosensor **1** under acidic and neutral conditions, but became considerably stronger at basic pH. At pH 3.8 and 7.45, the titration curves for most analytes showed substantial overlap, resulting in limited discrimination capacity. In contrast, at pH 10.8, the differences between analyte responses became more distinct, and several unique behaviors emerged.

As seen previously with chemosensor **1**, dopamine displayed a pronounced selectivity, producing almost complete fluorescence quenching in the presence of LiCl and KCl. Interestingly, for several analytes at both neutral and basic pH, a non-monotonic response was observed: an initial decrease in emission intensity the first salt addition (250 mM), followed by a gradual increase at higher salt concentrations. This dual-phase behavior contributed significantly to analyte differentiation and was particularly evident at pH 7.45 for testosterone and nandrolone, and at pH 10.8 for phenylalanine glycine, nandrolone, amantadine, adamantanol, and methyl viologen. Additional strong fluorescence responses were noted for thiabendazole, estradiol, and R-propranolol. As with chemosensor **1**, methyl viologen showed an increase in fluorescence intensity with salt addition, rather than quenching, emphasizing its consistent and distinctive spectral signature across the sensor array.

The PCA analysis further clarified these trends (**Fig. 6.35**). At acidic pH, the overall discrimination performance was poor for most salts, but cadaverine emerged as notably well-resolved analyte. At neutral pH, the overall resolution remained limited, but the selectivity shifted toward methyl viologen, consistent with its unusual salt-dependent fluorescence enhancement. The best analyte resolution was achieved at basic pH, where dopamine and methyl viologen were well-resolved from all other analytes, forming distinct and well-separated clusters in the PCA plots.

In summary, chemosensor **4** demonstrates moderate overall quenching sensitivity but high discrimination capacity at basic pH, particularly for dopamine, methyl viologen, and several hydrophobic or bulky analytes. The occurrence of dual-phase salt responses (initial quenching followed by intensity recovery) further enhances its ability to differentiate structurally diverse guests, highlighting the complex interplay between ionic environment, pH, and host-guest interactions in the CB7-coumarin systems.

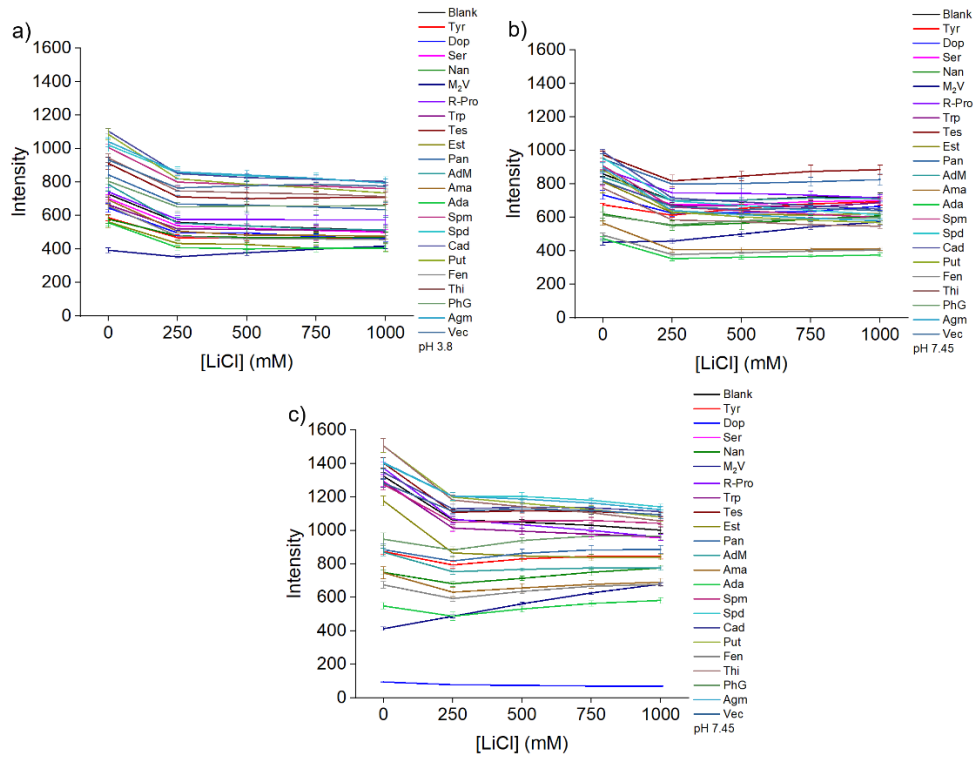


Fig. 6.34: Titration plots of the emission intensity at $\lambda_{exc} = 440$ nm of 1 μ M chemosensor **4** in the presence of 15 μ M analytes in 10 mM buffer. a) pH 3.8, b) pH 7.45, c) pH 10.8.

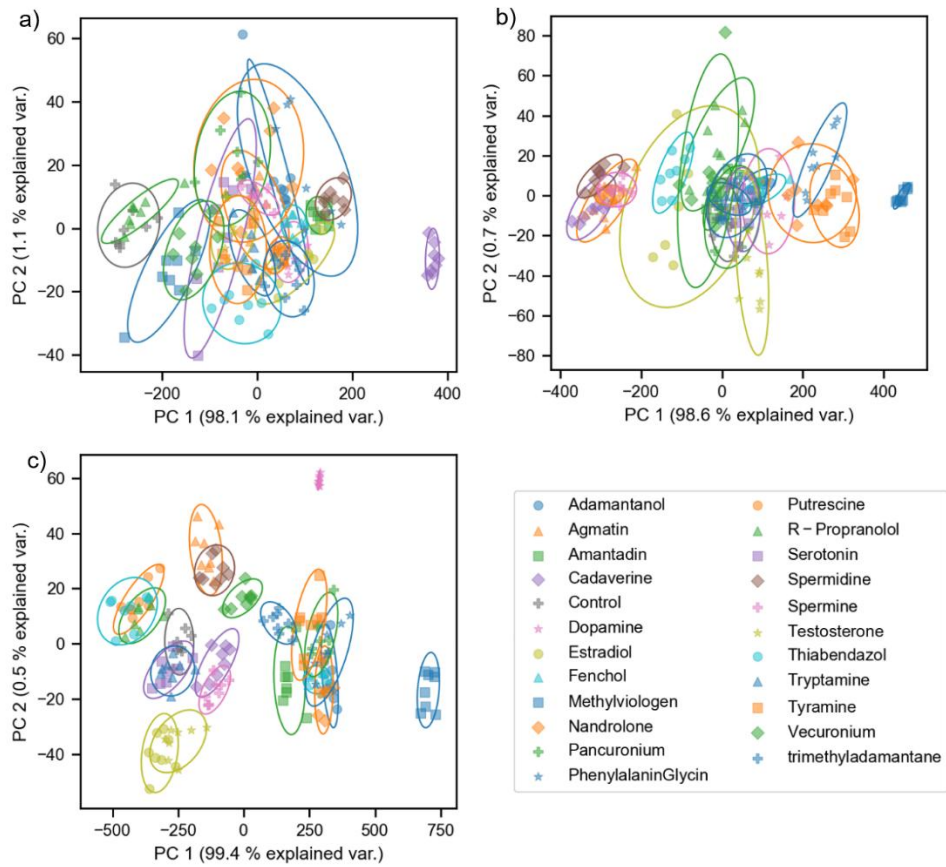


Fig. 6.35: PCA plots with 95% confidence ellipses resulting from the emission intensity at 483 nm ($\lambda_{exc} = 440$ nm) as a function of the concentration of NaCl with 1 μ M chemosensor **4** at a) pH 3.8, b) pH 7.45, c) pH 10.8.

Among all CB7-coumarin conjugates tested, chemosensor **6** (dipropyl) exhibited the strongest pH-dependent fluorescent response, despite earlier photophysical studies not revealing pronounced pH sensitivity (**Fig. 6.36**). Consistent with the NMR data indicating self-inclusion, this conjugate displayed a complex and highly analyte-dependent fluorescence behavior that proved particularly useful for discrimination.

Across all tested salts, KCl and NaCl produced the strongest fluorescence quenching effects, while the extent of quenching varied considerably between analytes. This variability enhanced the overall discrimination capacity of the chemosensor. The most striking behavior was observed at neutral pH, where the fluorescence responses were both strong and highly differentiated among analytes. As seen with other conjugates, the most substantial spectral changes generally occurred after the first salt addition step, with mostly little further change at higher salt concentrations. Unlike chemosensor **4**, no emission recovery after initial quenching was observed, except for methyl viologen, which again displayed its characteristic counter-directional increase in emission intensity.

At acidic pH, the strongest responses – particularly with KCl – were observed for dopamine, testosterone, and R-propranolol. At neutral pH, pronounced quenching or modulation was detected for dopamine, serotonin, R-propranolol, tryptamine, testosterone, estradiol, and thiabendazole, all showing distinctive titration profiles. At basic pH, the response pattern shifted: dopamine remained highly selective, while serotonin and amantadine showed particularly strong fluorescence changes. Across all pH values, KCl consistently provided the best enhancement of analyte discrimination, underlining the importance of specific cation-CB7 interactions in modulating fluorescence output.

The PCA analysis confirmed these observations and revealed sharp and well-separated clustering of analytes across all tested conditions (**Fig. 6.37**). Notably, estradiol emerged as one of the most distinguishable analytes, especially under acidic and basic conditions, where its response was clearly resolved from other guests. The best overall analyte resolution was achieved at basic pH, where multiple analytes formed distinct, non-overlapping clusters, underscoring the high discriminatory power of this chemosensor. In summary, chemosensor **6** demonstrates excellent analyte differentiation capability, driven by its strong pH dependence, reproducible quenching behavior, and consistent salt responsiveness. Its sensitivity across a broad range of analyte types – particularly at neutral and basic pH – highlights its potential as one of the most versatile and effective sensors in the CB7-coumarin series.

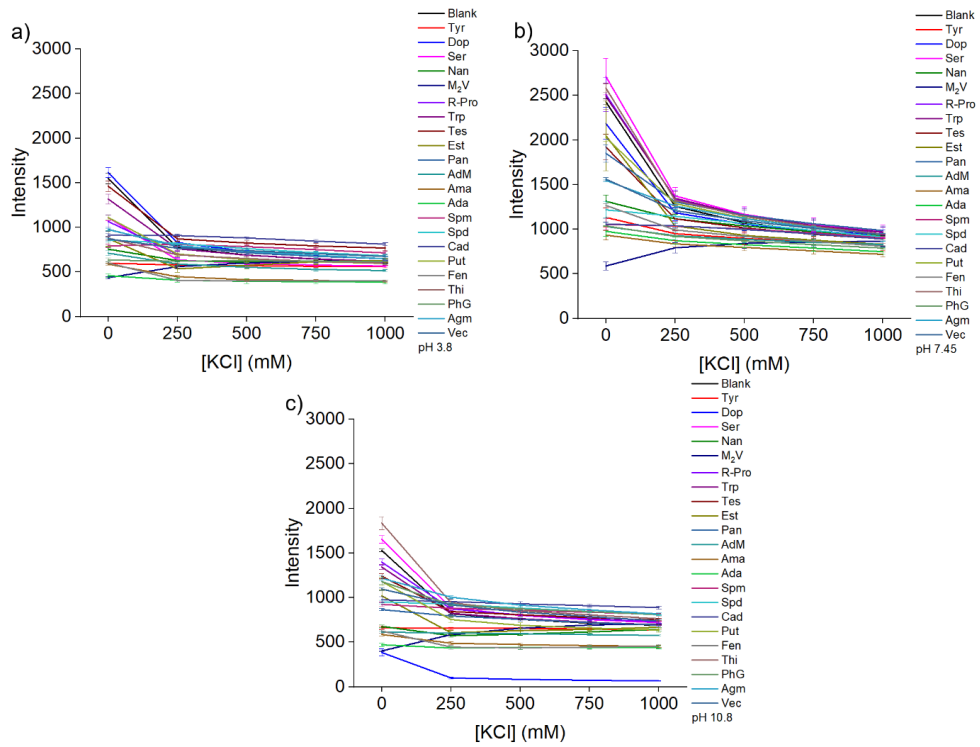


Fig. 6.36: Titration plots of the emission intensity at $\lambda_{exc} = 433$ nm of $1 \mu\text{M}$ chemosensor **6** in the presence of $15 \mu\text{M}$ analytes in 10 mM buffer. a) pH 3.8, b) pH 7.45, c) pH 10.8.

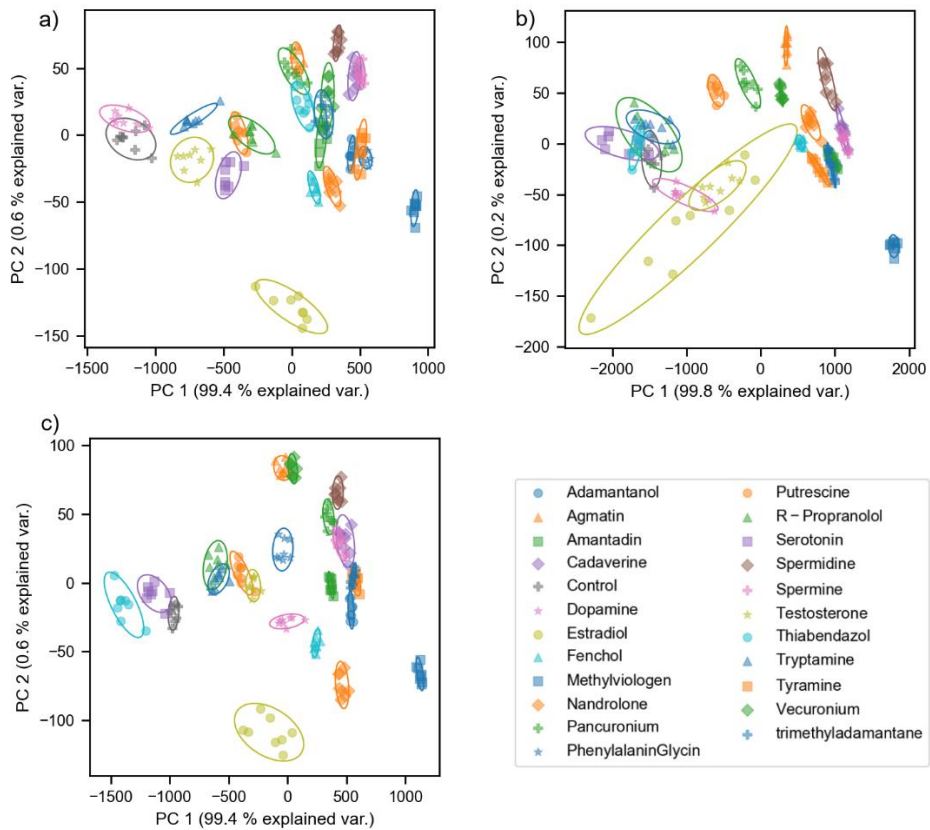


Fig. 6.37: PCA plots with 95% confidence ellipses resulting from the emission intensity at 471 nm ($\lambda_{exc} = 433$ nm) as a function of the concentration of NaCl with $1 \mu\text{M}$ chemosensor **6** at a) pH 3.8, b) pH 7.45, c) pH 10.8.

Although chemosensor **7** (diethyl) did not show definitive evidence of self-inclusion in the NMR studies, its strong photophysical responsiveness observed previously was confirmed in the analyte titration experiments (**Fig. 6.38**). Among the tested salts, CsCl had the most pronounced influence on modulating fluorescence behavior, producing the largest intensity variations across analytes. As observed for all other conjugates, the most significant spectral changes occurred after the first salt addition, with subsequent titration steps resulting in only subtle further modulation. The characteristic emission behavior of methyl viologen – fluorescence enhancement followed by quenching – was again evident, consistent with its distinctive interaction across the CB7-coumarin series.

Overall, chemosensor **7** displayed balanced and reproducible discrimination capacity across all pH values, without strong preference for acidic, neutral, or basic conditions. The strongest fluorescence responses were observed for amantadine and adamantanol, both high-affinity CB7 binders, although their signals were too similar to allow full differentiation from one another. At acidic pH, pronounced fluorescence changes were found for dopamine, serotonin, testosterone, estradiol, spermidine, spermine, putrescine, and agmatine, suggesting a broad responsiveness to both aromatic and polycationic guests. At neutral pH, a similar response pattern was maintained – particularly for dopamine, serotonin, testosterone, and estradiol – while the signal magnitude for other analytes decreased, largely independent of salt identity. At basic pH, a clear selectivity toward dopamine emerged, along with strong salt-dependent modulation of the fluorescence response for testosterone and estradiol, especially in the presence of CsCl, KCl and NaCl.

The PCA analysis supported these findings, revealing excellent discrimination capability for chemosensor **7** across the full dataset. In many cases, the analytes formed well-separated, non-overlapping clusters, confirming the high sensitivity and reproducibility of the fluorescence responses (**Fig. 6.39**). The neutral pH condition appeared particularly favorable for analyte resolution, yielding the sharpest clustering and minimal overlap among analyte groups.

In summary, chemosensor **7** combines broad responsiveness with high discrimination fidelity, maintaining consistent performance across pH and salt conditions. Its strong and tunable photophysical behavior – especially in combination with CsCl, KCl, and NaCl – demonstrates its potential as a robust and versatile optical sensor capable of resolving a wide range of analytes within the CB7-coumarin sensing framework.

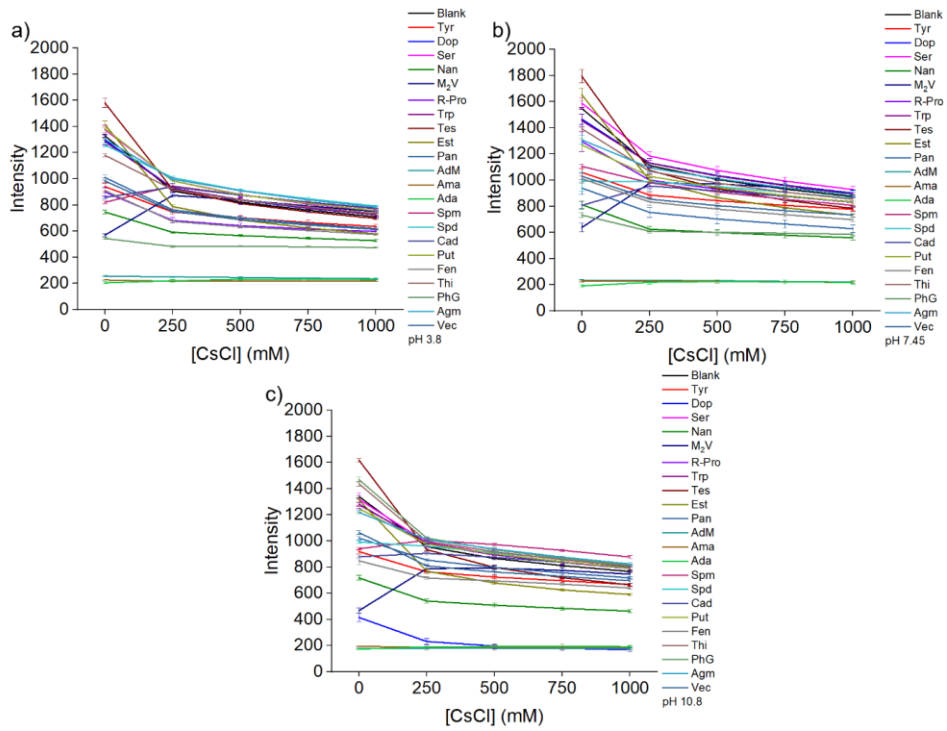


Fig. 6.38: Titration plots of the emission intensity at $\lambda_{exc} = 438$ nm of $1 \mu\text{M}$ chemosensor **7** in the presence of $15 \mu\text{M}$ analytes in 10 mM buffer. a) pH 3.8, b) pH 7.45, c) pH 10.8.

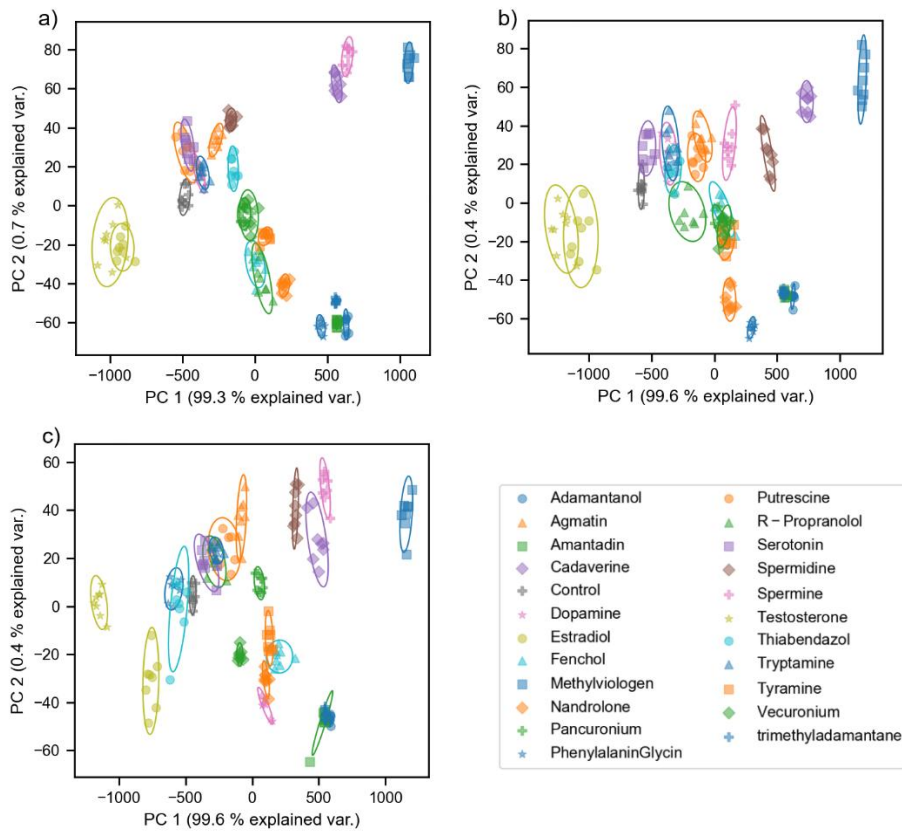


Fig. 6.39: PCA plots with 95% confidence ellipses resulting from the emission intensity at 478 nm ($\lambda_{exc} = 438 \text{ nm}$) as a function of the concentration of NaCl with $1 \mu\text{M}$ chemosensor **7** at a) pH 3.8, b) pH 7.45, c) pH 10.8.

6.10. Conclusions

In this chapter, a series of seven unimolecular CB7-coumarin conjugates were successfully synthesized and evaluated for their ability to differentiate structurally diverse analytes through their unique, salt-adaptive photophysical behaviors under varying pH conditions in buffered aqueous media. The chemosensors exhibited the expected pH-dependent spectral responses, confirming the critical role of dye protonation and host-guest equilibria in modulating sensing performance.

Given the large number of analytes examined (22 in total), the practical analytical challenge is not to discriminate all simultaneously but rather to differentiate within specific, chemically related groups. Based on structure and physicochemical characteristics, the analytes can be categorized into several meaningful groups, each requiring distinct sensing conditions for optimal separation.

The first group – adamantanol, amantadine, and *N,N,N*-trimethyladamantaneammonium hydroxide – comprises rigid, hydrophobic adamantane derivatives that are difficult to separate by conventional chromatographic methods due to their lack of UV responsiveness and similar structures. The combination of chemosensor **6** (dipropyl) at basic pH (10.8) with NaCl provided the best resolution for this group, as revealed by the PCA, which showed distinct clustering among these otherwise challenging analytes.

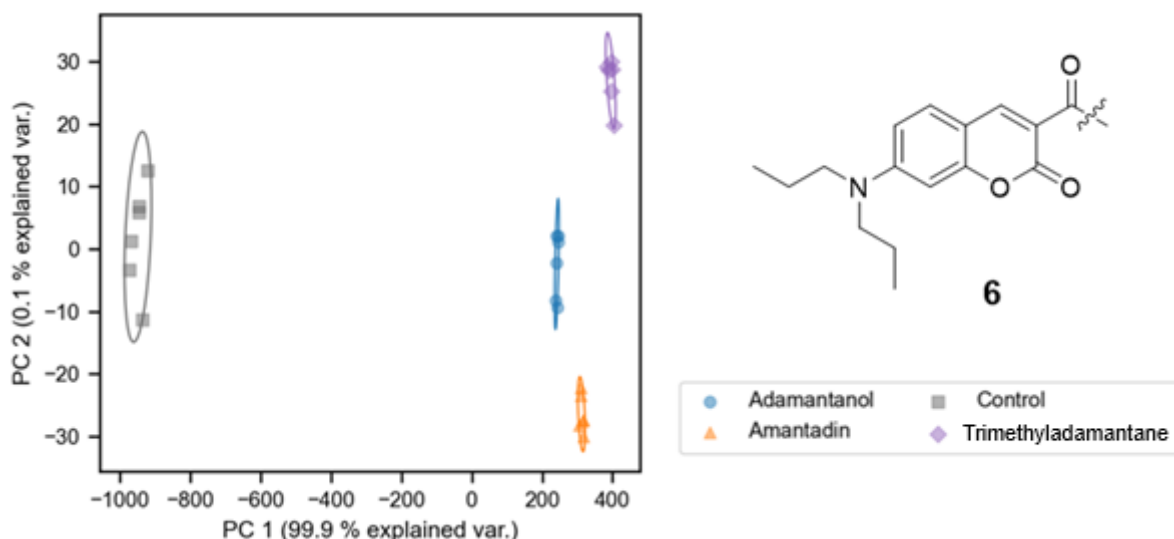


Fig. 6.40: PCA plot with 95% confidence ellipses resulting from the emission intensity at 471 nm ($\lambda_{\text{exc}} = 433$ nm) as a function of the concentration of NaCl with 1 μM chemosensor **6** at pH 10.8.

The second group includes the biogenic polyamines – cadaverine, putrescine, spermidine, and spermine – which are biologically important molecules involved in metabolic regulation and disease processes such as cancer. Because of their high structural similarity and flexible, cationic nature, they are typically difficult to distinguish. To broaden the analytical scope of this group, tryptamine and tyramine were also included, as they share the amine motif and may act as potential interfering species in polyamine analysis. The ability to discriminate not only between the biogenic amines themselves but also from structurally related aromatic amines is therefore highly advantageous. The best discrimination within this expanded group was achieved using chemosensor **6** (dipropyl) at neutral pH (7.45) in the presence of

NH₄Cl, where PCA analysis revealed clear separation among all amine-containing molecules, confirming the chemosensors strong capability for selective recognition within this important class of analytes.

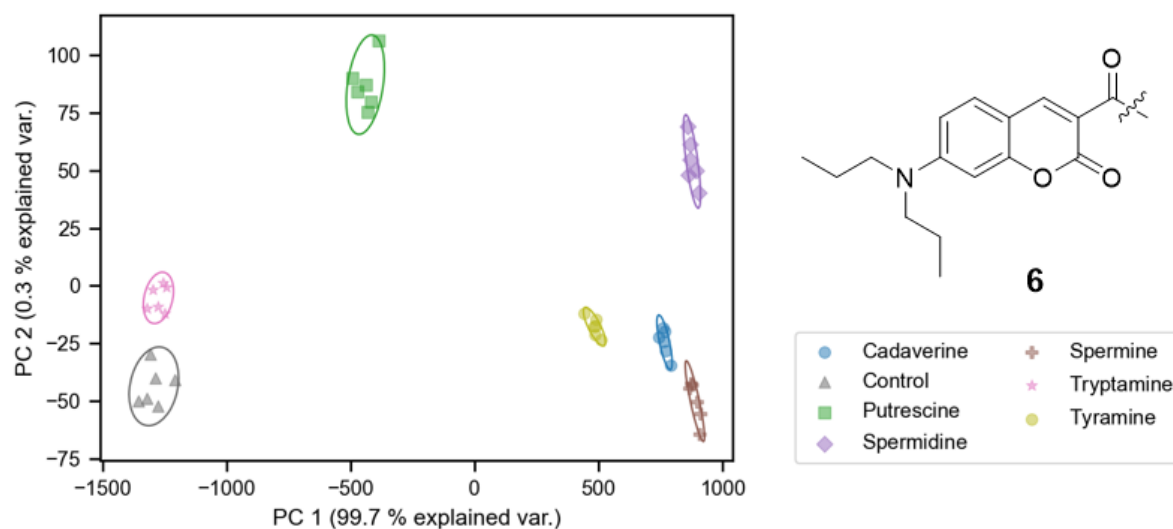


Fig. 6.41: PCA plot with 95% confidence ellipses resulting from the emission intensity at 478 nm ($\lambda_{\text{exc}} = 438$ nm) as a function of the concentration of NH₄Cl with 1 μ M chemosensor **6** at pH 7.45.

The third group consists of aromatic monoamines – tyramine, tryptamine, dopamine, serotonin, and agmatine – which are neurotransmitter-related analytes with comparable aromatic structures. Here, chemosensor **7** (diethyl) at neutral pH (7.45) with NH₄Cl addition provided the highest discrimination capacity, enabling distinct resolution of these compounds in the PCA space.

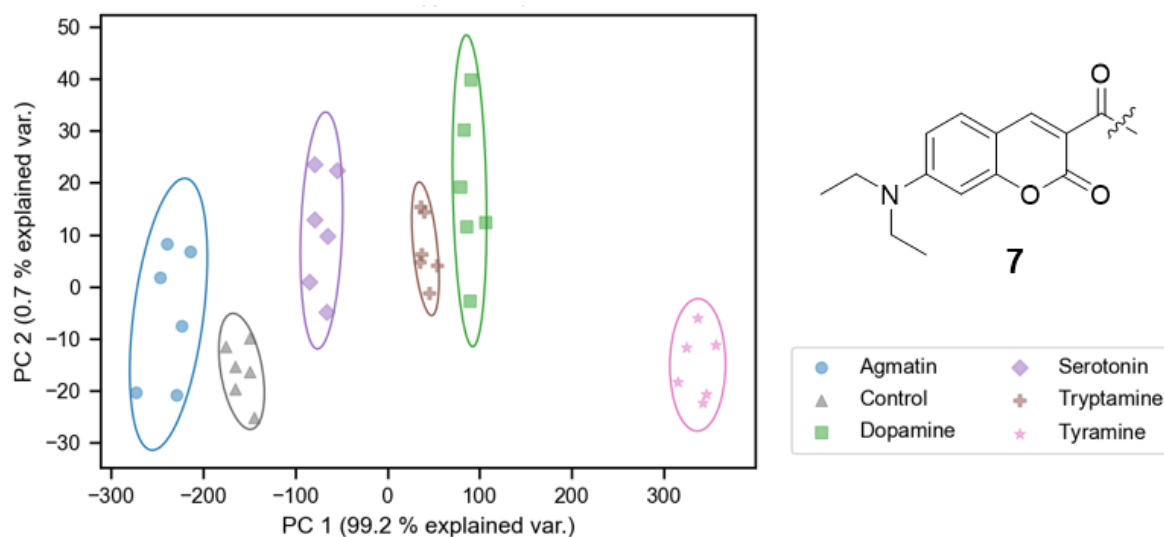


Fig. 6.42: PCA plot with 95% confidence ellipses resulting from the emission intensity at 471 nm ($\lambda_{\text{exc}} = 433$ nm) as a function of the concentration of NH₄Cl with 1 μ M chemosensor **7** at pH 7.45.

The final group includes the steroidal hormones – estradiol, testosterone, and nandrolone – which are notoriously difficult to distinguish due to their similar core skeletons and frequent cross-reactivity in immunoassays.³⁹³ Several sensing conditions enabled their resolution, but the most effective was

achieved with chemosensor **7** (diethyl) at neutral pH (7.45) in the presence of KCl, yielding good separation of all three steroid analytes.

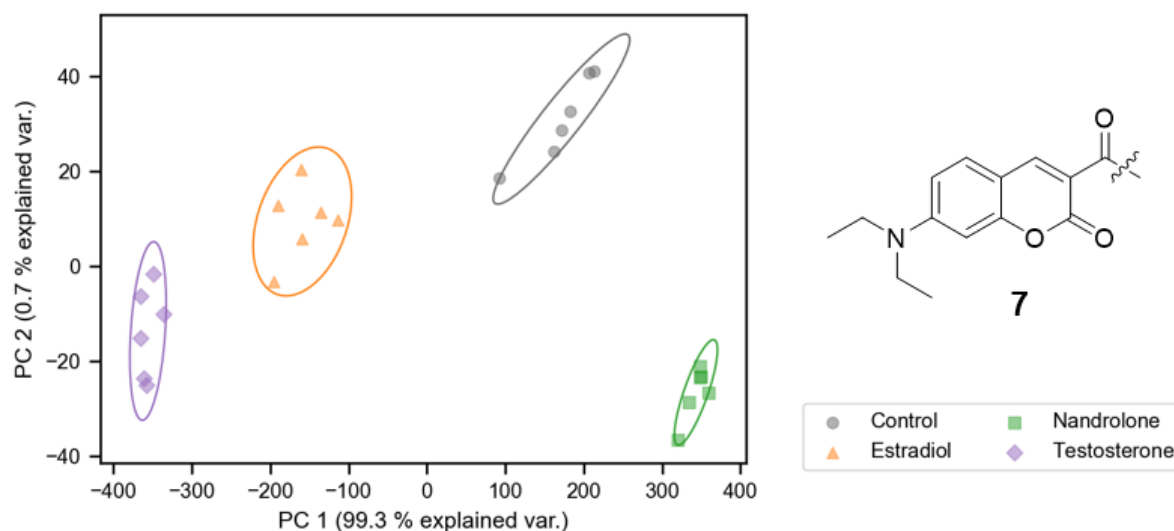


Fig. 6.43: PCA plots with 95% confidence ellipses resulting from the emission intensity at 471 nm ($\lambda_{\text{exc}} = 433$ nm) as a function of the concentration of KCl with 1 μM chemosensor **7** at pH 7.45.

During the course of the measurements, chemosensor **1** demonstrated a notable sensitivity toward sodium ions, as NaCl induced substantially greater fluorescence quenching than any other salt. This unique behavior suggests that this conjugate could serve as a promising template for selective sodium sensing in future studies. More broadly, the findings show that pH variation alone can provide a powerful means of enhancing analyte discrimination, as significant differences in fluorescence response were observed across the tested pH values for nearly all chemosensors.

Further optimization of the salt titration protocol could enhance both selectivity and sensitivity. Since the most significant spectral changes occurred after the first salt addition step (250 mM), future work may benefit from finer salt concentration increments to better capture subtle variations in the fluorescence response. Among the tested salts, CaCl_2 and MgCl_2 were generally less effective for analyte discrimination, whereas KCl, NaCl, and LiCl consistently improved spectral resolution and PCA separation. In summary, the results presented in this chapter demonstrate that the combination of pH modulation, salt identity, and tailored CB7-coumarin conjugate design creates a robust and versatile platform for multidimensional optical sensing. This approach enables reliable discrimination of chemically and structurally related analytes that are otherwise challenging by conventional analytical methods, highlighting the promise of unimolecular CB7-based chemosensors for advanced biosensing applications.

Future research should focus on translating these findings toward real-world sensing applications, particularly in complex biological environments such as serum or cellular media, where salt composition and pH vary dynamically. The demonstrated salt- and pH-adaptive behavior of the CB7-coumarin conjugates provides a strong foundation for developing intelligent supramolecular sensor arrays capable of real time, multiplexed analyte detection. Furthermore, integration of these chemosensors into

microfluidic or solid-state platforms could enable miniaturized, high-throughput diagnostic systems, expanding the applicability of CB7-based unimolecular sensors from proof-of-concept studies to practical analytical and biomedical use.

6.11. Experimental Part

6.11.1. Material and Methods

6.11.1.1. Material

All purchased chemicals and solvents were used as received from suppliers without any further purification. 1,1'-(octane-1,8-diyl)bis(3-methyl-1H-imidazol-3-ium) bromide (C_8mimBr_2)³³⁹ was synthesized according to established literature methods.

6.11.1.2. Nuclear Magnetic Resonance Spectroscopy (NMR)

1H and ^{13}C NMR spectra were recorded either in deuterium oxide (D_2O), Chloroform-*d*3, DMSO-*d*6, Acetonitrile-*d*3 or Methanol-*d*4 on a Bruker Avance 400 spectrometer or a Bruker Avance 500 spectrometer at 25°C. The 1H and ^{13}C NMR chemical shifts (δ) are given in ppm and refer to residual protons on the corresponding deuterated solvent.

6.11.1.3. High Performance Liquid Chromatography (HPLC)

Analytical HPLC experiments were performed on an LC-2000Plus HPLC system equipped with a UV-2075 UV-Vis detector and a Kromasil 100 C18 5 μ M LC column (250 \times 4.6 mm, Agela) at a flow rate of 0.8 mL/min. Preparatory HPLC was performed on the same system but equipped with a Kromasil 100 C18 5 μ M LC precolumn (50 \times 20 mm, Agela) and a Kromasil 100 C18 5 μ M LC preparative column (250 \times 50 mm, Agela) at a flow rate of 12 mL/min. For the more polar conjugates (**fig. 6.8.**, entries 1, 3, 5, 7) a 3:2 (v/v) mixture of H_2O/ACN was used. For the more hydrophobic conjugates, the inverse mixture (ACN/H_2O 3:2) was found to be more effective. To aid solubility, a few drops of TFA were added to each solution.

For the preparative HPLC, the following methods with their respective parameters were used:

Prep. method 1: Isocratic elution $H_2O(+0.1\%TFA)/ACN$ 60:40; UV detection at $\lambda=254$ nm; FL detection in dual mode at $\lambda_{1,abs}=366$ nm and $\lambda_{1,ems}=540$, $\lambda_{2,abs}=435$ and $\lambda_{2,ems}=480$

Prep. method 2: Isocratic elution $H_2O(+0.1\%TFA)/ACN$ 40:60; UV detection at $\lambda=254$ nm; FL detection in dual mode at $\lambda_{1,abs}=366$ nm and $\lambda_{1,ems}=540$, $\lambda_{2,abs}=435$ and $\lambda_{2,ems}=480$

Prep. method 3: Isocratic elution $H_2O(+0.1\%TFA)/ACN$ 50:50; UV detection at $\lambda=254$ nm; FL detection in dual mode at $\lambda_{1,abs}=366$ nm and $\lambda_{1,ems}=540$, $\lambda_{2,abs}=435$ and $\lambda_{2,ems}=480$

For the analytical HPLC, the following methods with their respective parameters were used:

Anal. method 1: Gradient elution

Time (min)	Water content (%)	Acetonitrile content (%)
0	100	0
5	50	50
7	50	50
8	30	70
10	30	70
20	30	70
25	0	100

UV detection at $\lambda=430$ nm; FL detection in dual mode at $\lambda_{1,abs}=366$ nm and $\lambda_{1,ems}=540$, $\lambda_{2,abs}=435$ and $\lambda_{2,ems}=480$

Anal. method 2: Gradient elution

Time (min)	Water content (%)	Acetonitrile content (%)
0	100	0
5	50	50
7	50	50
8	30	70
10	30	70
20	30	70
25	0	100

UV detection at $\lambda=345$ nm; FL detection in dual mode at $\lambda_{1,abs}=366$ nm and $\lambda_{1,ems}=540$, $\lambda_{2,abs}=435$ and $\lambda_{2,ems}=480$

6.11.1.4. Electrospray Ionization Mass Spectrometry (ESI-MS)

Spectra were recorded on a Orbitrap Exploris 240 (MM10525C) mass spectrometer (Thermo Fisher Scientific) equipped with a HESI II probe. The instrument was calibrated in the m/z range 200-2000 for positive mode using premixed calibration solutions (FlexMix-Thermo Scientific). Spray voltage, sheath gas and auxiliary gas pressure were used in the range of 1.75 V, for positive mode. Spray voltage, sheath gas and auxiliary gas pressure was set to 1.9 V. The ion transfer tube temperature was set to 320 °C. MeOH:H₂O (1:1) solvents was used as eluent. Injection of the samples was carried out with the aid of a Hamilton® syringe 725RN 500 μ L at a flow rate of 25 μ L/min using a single syringe pump.

6.11.1.5. Absorbance Spectra

Absorbance spectra were measured in Milli-Q water on a Jasco V-730 double-beam UV-Vis spectrophotometer at 25°C. PMMA cuvettes with a light path of 10 mm and dimensions of 10 \times 10 mm from Brand with a spectroscopic cut-off at 220 nm were utilized for UV-Vis absorption experiments. The samples were equilibrated using a water thermostatic cell holder STR-812, while the cuvettes were equipped with a stirrer allowing rapid mixing.

6.11.1.6. Fluorescence Spectra

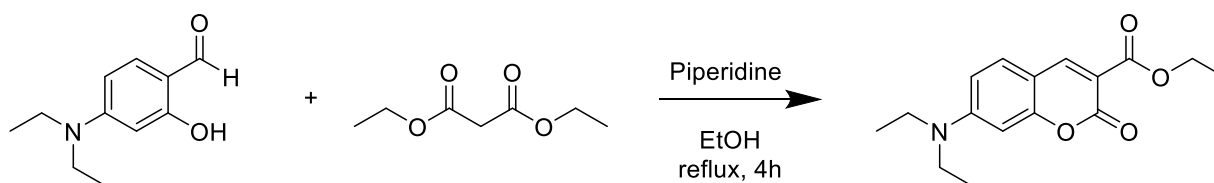
Steady-state emission spectra and time-resolved emission profiles were recorded on a Jasco FP-8300 fluorescence spectrometer equipped with a 450 W Xenon arc lamp, double-grating excitation and emission monochromators. Standard correction curves corrected the emission spectra for source intensity (lamp and grating) and the emission spectral response (detector and grating). All titration and kinetic experiments were carried out at 25°C using a water thermostatic cell holder STR-812, while the cuvettes were equipped with a stirrer allowing rapid mixing. PMMA cuvettes with a light path of 10 mm and dimensions of 10 × 10 mm from Brand with a spectroscopic cut-off at 300 nm were utilized for fluorescence-based titration experiments.

6.11.1.7. High Performance Liquid Chromatography Mass Spectrometry (HPLC-MS)

LC-MS measurements were performed on an Agilent 1260 Infinity II system consisting of a quaternary pump (GB7111B), autosampler (G7129A, 100 µL sample loop), a temperature-controlled column oven (G7114A) and a variable UV-Vis detector (G7114A, VWD, flow cell G7114A 018, d = 10 mm, V = 14 µL). Separation was performed on a C18 HPLC column (Agilent Poroshell 120 EC-C18 4.6x100 mm, 2.7 µm) operating at 40 °C. A gradient of acetonitrile:H₂O 45:55 – 100:0 (v/v) (additive 10 mmol L⁻¹ ammonium formate) at a flow rate of 1 mL min⁻¹ during 9 min was used as the eluting solvent. The flow was directed into an Agilent MSD (G613BA, AP-ESI ion source). The instrument was calibrated in the m/z range 118-2121 in positive mode and 113-2233 in the negative mode, using a premixed calibration solution (Agilent). The following parameters were used: spray chamber flow: 12 L min⁻¹, drying temperature: 350 K, Capillary Voltage: 3000 V, Fragmentor Voltage: 100 V.

6.11.2. Synthesis and Characterization

6.11.2.1. Ethyl 7-(diethylamino)-2-oxo-2H-chromene-3-carboxylate



According to literature procedures³⁹⁴, A flask was charged with 4-diethylaminosalicylaldehyde (800 mg, 4.1 mmol, 1 equiv.), diethyl malonate (1.326 g, 8.3 mmol, 2 equiv.), piperidine (500 µl) and EtOH (15 mL). The solution was heated to reflux for 3h. After cooling to room temperature the solvent was evaporated *in vacuo* and the crude product was purified by column chromatography (EtOAc/DCM 1:2). The product was isolated as a yellow oil. Note: the yield is always greater than 100% since residual diethyl malonate is very hard to remove. This can still be used for the next step. ¹H NMR (500 MHz, CDCl₃) δ 8.41 (s, 1H), 7.34 (d, J = 8.9 Hz, 1H), 6.59 (dd, J = 8.9, 2.1 Hz, 1H), 6.45 (d, J = 1.8 Hz, 1H), 4.36 (q, J = 7.1 Hz, 2H), 4.19 (q, J = 7.1 Hz, 4H), 3.43 (q, J = 7.1 Hz, 4H), 1.37 (t, J = 7.1 Hz, 3H), 1.26 (dd, J = 14.9, 7.8 Hz, 6H). ¹³C NMR (126 MHz, CDCl₃) δ 166.64 (s), 164.28 (s), 158.40 (d, J = 17.6 Hz), 152.86

(s), 149.22 (s), 131.03 (s), 109.50 (s), 108.96 (s), 107.68 (s), 96.71 (s), 61.50 (s), 61.15 (s), 45.10 (s), 41.68 (s), 14.39 (s), 14.06 (s), 12.42 (s), 0.19 (s), -0.01 (s). ESI-MS: Calcd. for $[M+Na]^+$: 312.1206; found: 312.1464

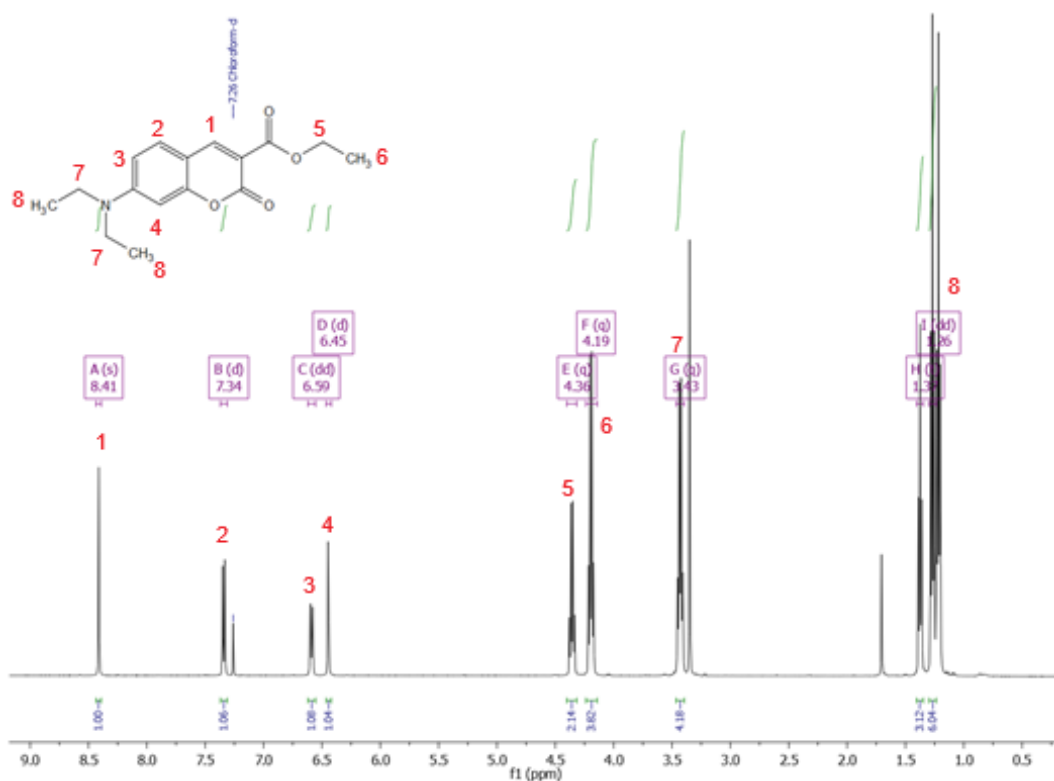


Fig. 6.44. ^1H NMR (CDCl₃) of Ethyl 7-(diethylamino)-2-oxo-2H-chromene-3-carboxylate.

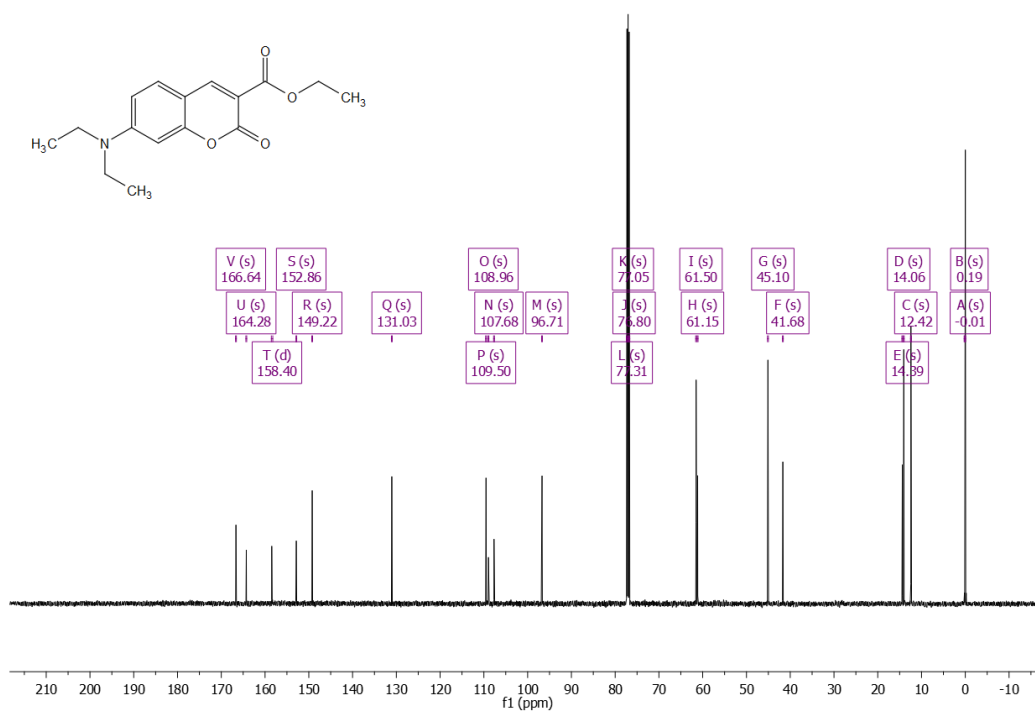


Fig. 6.45. ^{13}C NMR (CDCl₃) of Ethyl 7-(diethylamino)-2-oxo-2H-chromene-3-carboxylate.

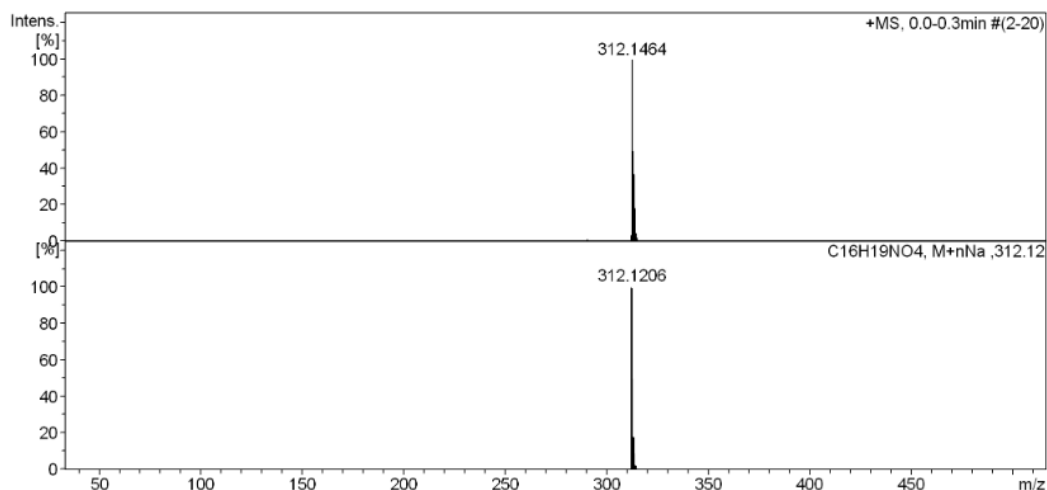
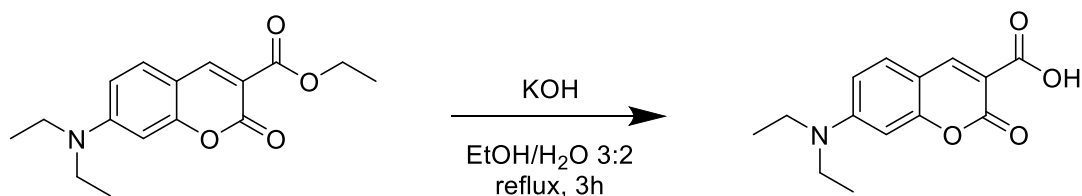


Fig. 6.46. ESI-MS of Ethyl 7-(diethylamino)-2-oxo-2H-chromene-3-carboxylate $[M+Na]^+$ measured (top) and simulated (bottom).

6.11.2.2. 7-(diethylamino)-2-oxo-2H-chromene-3-carboxylic acid



According to literature procedures³⁹⁵, a solution of 7-diethylaminocoumarin-3-carboxylic acid ethyl ester (450 mg, 1.6 mmol, 1 equiv.), KOH (140 mg, 2.5 mmol, 1.6 equiv.) in EtOH/H₂O 3:2 (10 mL) was heated to reflux for 3h. EtOH was evaporated in vacuo and the aqueous phase was first diluted with water, then acidified with 1.2 N HCl to pH=6. The precipitated solid was removed by filtration and washed with water and hexane. The product was obtained as a orange solid. (306.1 mg, 1.1 mmol, 59%) ¹H NMR (500 MHz, CDCl₃) δ 12.35 (s, 1H), 8.66 (s, 1H), 7.46 (d, J = 9.0 Hz, 1H), 6.71 (dd, J = 9.0, 2.5 Hz, 1H), 6.53 (d, J = 2.3 Hz, 1H), 3.49 (q, J = 7.2 Hz, 4H), 1.58 (s, 3H), 1.27 (t, J = 7.2 Hz, 7H). ¹³C NMR (126 MHz, CDCl₃) δ 165.69 (s), 164.63 (s), 153.89 (s), 150.48 (s), 132.11 (s), 111.03 (s), 108.74 (s), 97.01 (s), 45.49 (s), 12.54 (s). ESI-MS: Calc. for $[M+Na]^+$: 284.0893; found: 284.1173. Calc. for $[2M+Na]^+$: 545.1894; found: 545.2000. Note: the coumarin carboxylic acid was additionally found as dimerized species in the ESI-MS experiment.

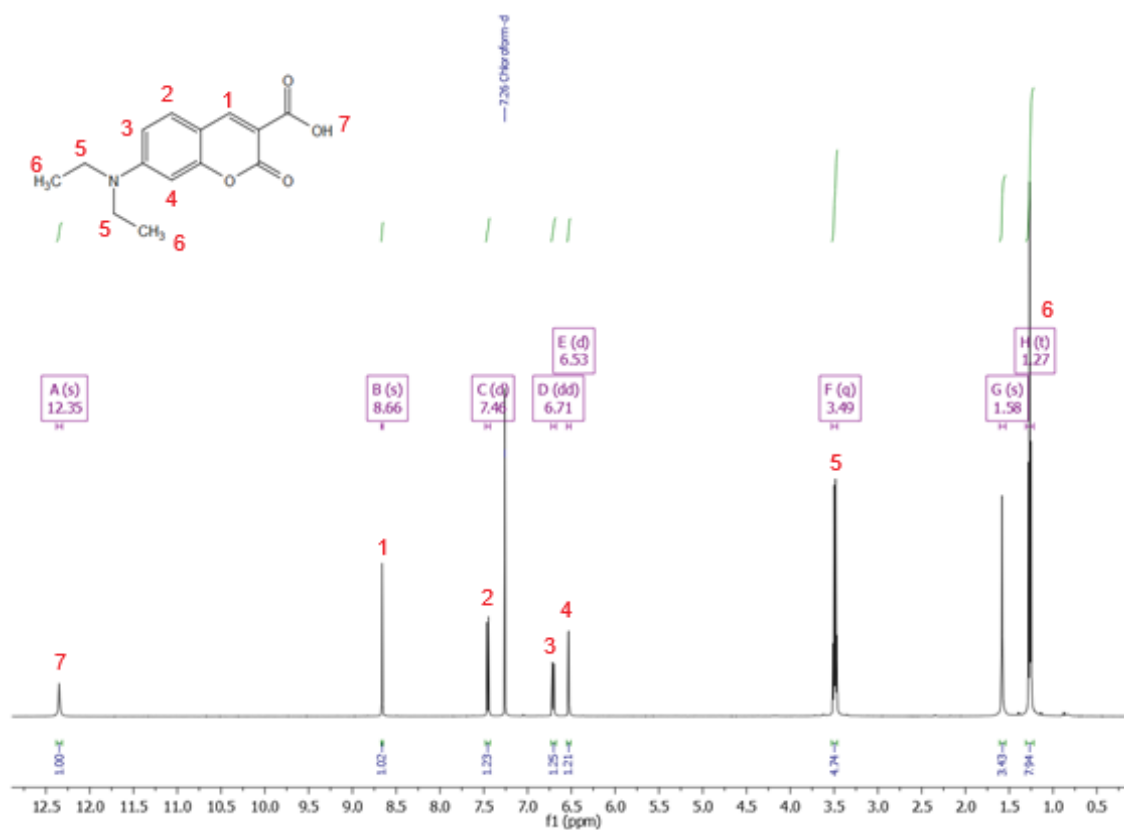


Fig. 6.47. ^1H NMR (CDCl₃) of 7-(diethylamino)-2-oxo-2H-chromene-3-carboxylic acid.

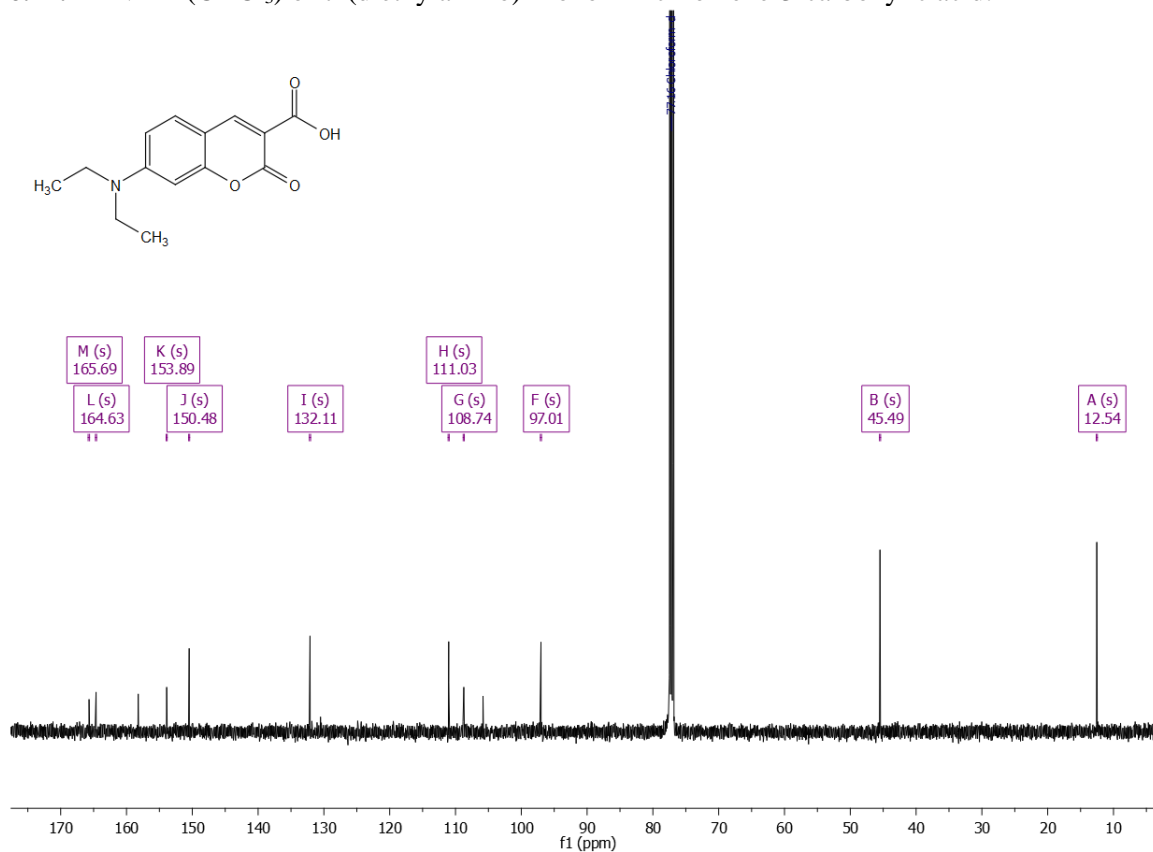


Fig. 6.48. ^{13}C NMR (CDCl₃) of 7-(diethylamino)-2-oxo-2H-chromene-3-carboxylic acid.

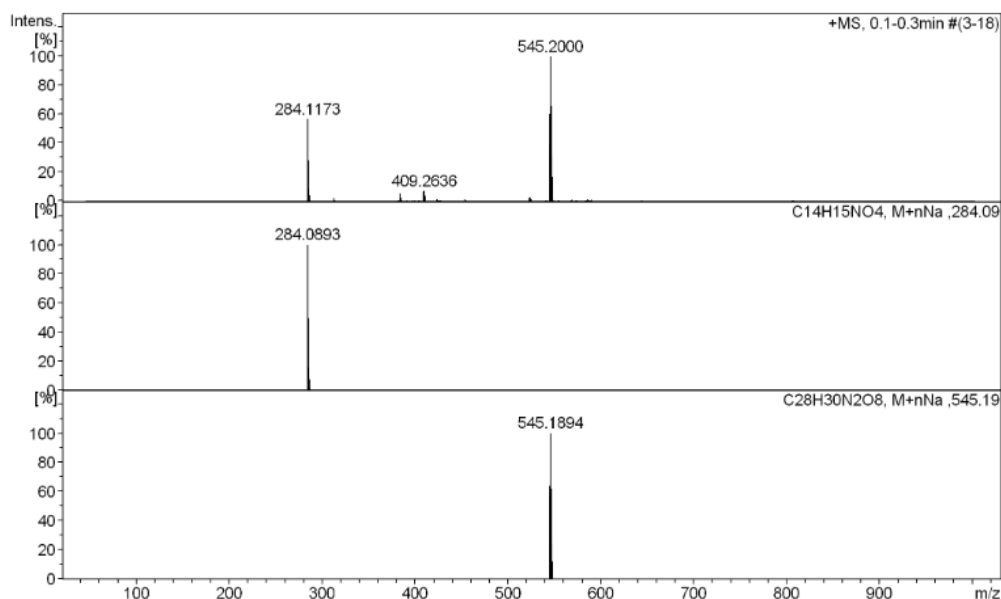
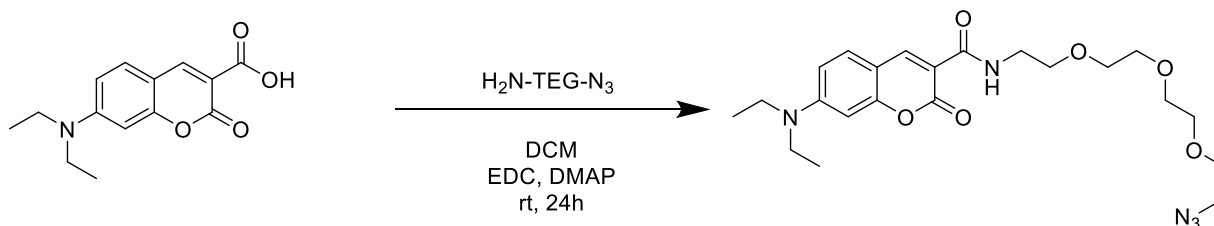


Fig. 6.49. ESI-MS of 7-(diethylamino)-2-oxo-2H-chromene-3-carboxylic acid $[M+Na]^+$ and $[2M+Na]^+$ measured (top), simulated $[M+Na]^+$ (middle), simulated $[2M+Na]^+$ (bottom).

6.11.2.3. *N*-(2-(2-(2-(2-azidoethoxy)ethoxy)ethoxy)ethyl)-7-(diethylamino)-2-oxo-2H-chromene-3-carboxamide (DEC-N₃)



According to literature procedures³⁹⁶, in a glass vial 7-diethylaminocoumarin-3-carboxylic acid (150 mg, 0.6 mmol, 1 equiv.) was dissolved in dry DCM (2 mL). To this solution was added 11-Azido-TEG-NH₂ (162.9 mg, 150 μ l, 0.7 mmol, 1.3 equiv.), 4-DMAP (84.2 mg, 0.7 mmol, 1.2 equiv.) and EDC HCl (121.1 mg, 0.6 mmol, 1.1 equiv.). The vial was closed and the mixture was stirred overnight under an N₂ atmosphere. The crude product was purified by silica gel column chromatography (CHCl₃/MeOH 20:1). The product was obtained as an intense yellow oil. (259.2 mg, 0.56 mmol, 93%) ¹H NMR (400 MHz, CDCl₃) δ 9.00 (s, 1H), 8.66 (s, 1H), 7.44 – 7.36 (m, 1H), 6.62 (dd, *J* = 9.0, 2.5 Hz, 1H), 6.47 (d, *J* = 2.3 Hz, 1H), 3.66 (ddd, *J* = 9.8, 4.6, 3.0 Hz, 11H), 3.43 (q, *J* = 7.1 Hz, 4H), 3.39 – 3.34 (m, 2H), 1.21 (t, *J* = 7.1 Hz, 6H). ¹³C NMR (101 MHz, CDCl₃) δ 163.35 (s), 162.64 (s), 157.74 (s), 152.60 (s), 148.10 (s), 131.19 (s), 110.43 (s), 109.98 (s), 108.43 (s), 96.65 (s), 70.75 (dd, *J* = 10.3, 6.3 Hz), 70.00 (d, *J* = 13.6 Hz), 50.78 (s), 45.15 (s), 39.57 (s), 12.50 (s), 0.08 (s). HPLC-MS: 9.956 min, *m* = 462.3⁺

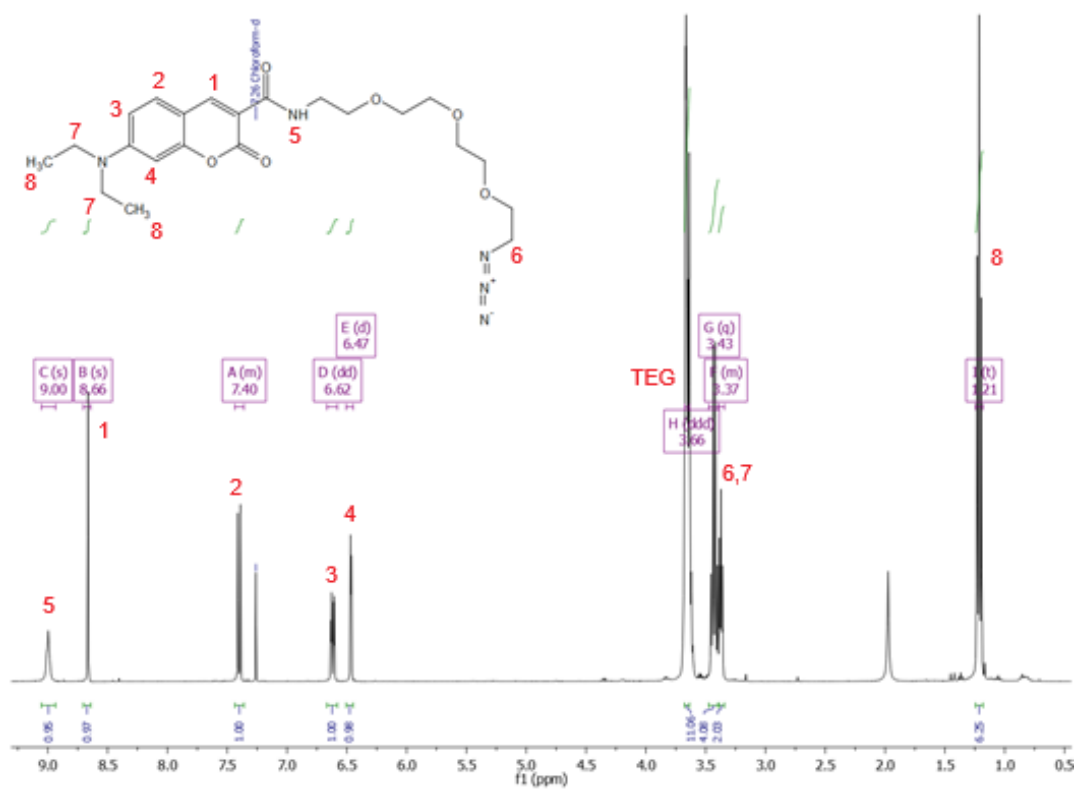


Fig. 6.50. ¹H NMR (CDCl₃) of DEC-N₃.

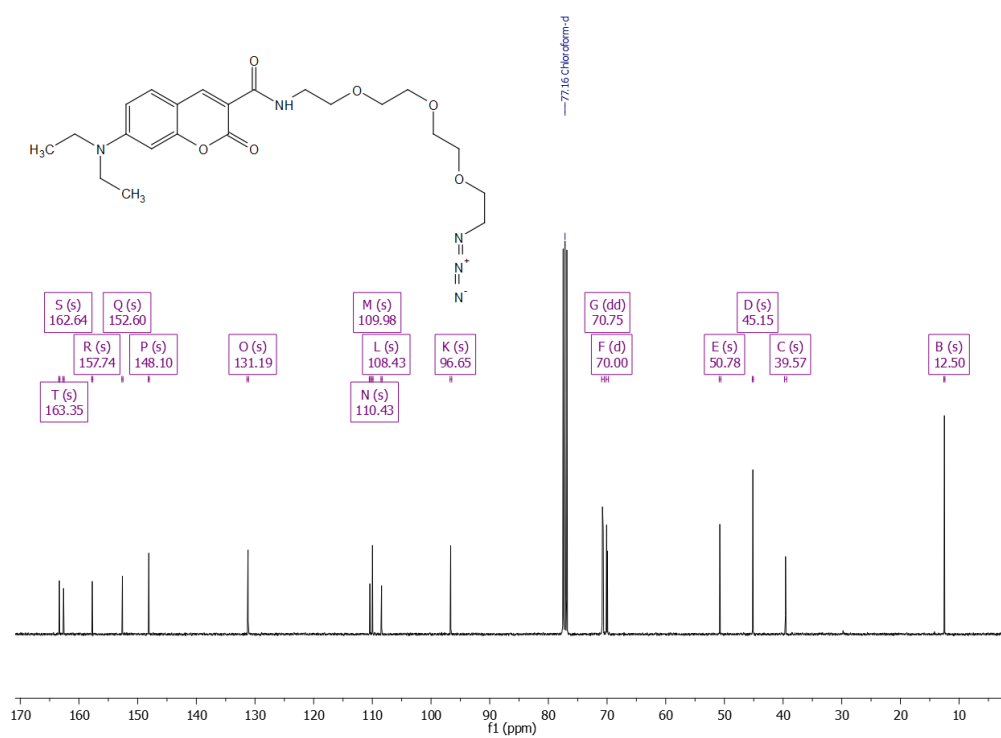


Fig. 6.51. ¹³C NMR (CDCl₃) of DEC-N₃.

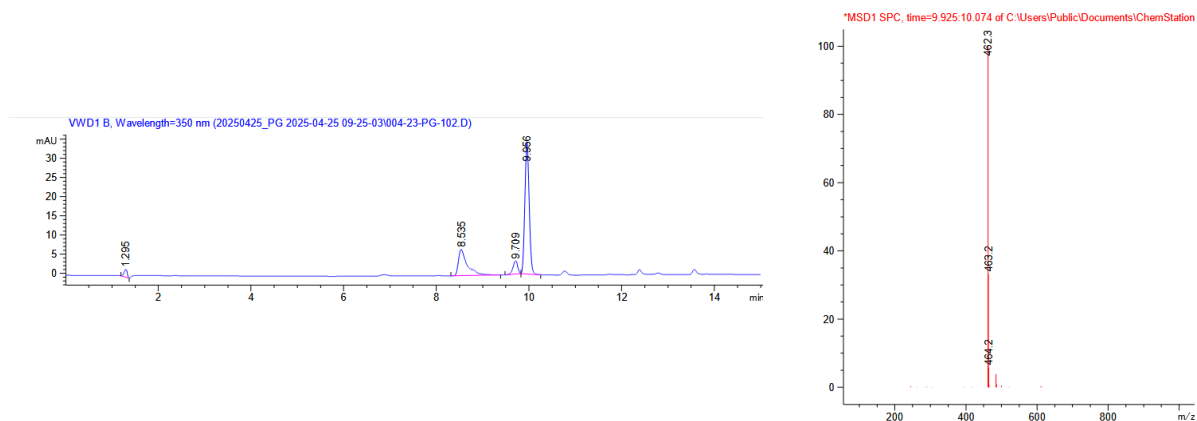
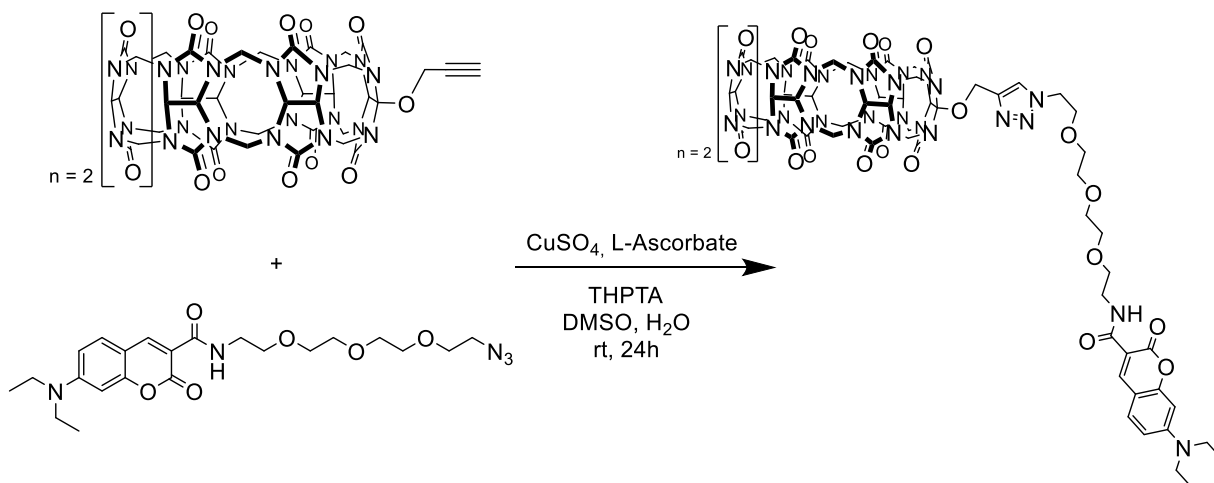


Fig. 6.52. Analytical trace at $\lambda=350$ nm (left) and observed mass at 9.9 min (right) in the positive mode.

6.11.2.4. CB7-diethylcoumarin (CB7-DEC)



CB7-(OPr) (17.4 mg, 14.4 μmol , 1 equiv.), DEC-N₃ (11.9 mg, 25.8 μmol , 1.8 equiv.), and THPTA (24.8 mg, 56 μmol , 4 equiv.) were placed in a vial and dissolved in 1400 μL DMSO. After closing of the vial, it was placed in ultrasound then purged with N₂. In a second vial, 5.6 mL 55% DMSO aqueous solution was also purged with N₂, then CuSO₄ (9.1 mg, 56.0 μmol , 4 equiv.) was added to the 55% DMSO followed by sodium L-ascorbate (19.8 mg, 100.0 μmol , 7 equiv.) while it was taken care for least oxygen exposure as possible. The click solution was placed in the ultrasound for approx. 1 min. while a color change to yellow (Cu⁺ forming) was observed. The two solutions were mixed and stirred at room temperature for 24 h under an N₂ atmosphere. Afterwards, the product was precipitated by dropwise addition of the reaction solution in 50 mL MeOH. The solid was then washed with MeOH (3 \times 25 mL). Purification is done by preparative HPLC. The product elutes at 22.0 min (prep. method 1). The product was obtained as a fluffy yellow solid after freeze-dry. (10.8 mg, 6.4 μmol , 45%) ¹H NMR (400 MHz, CD₃CN) δ 8.55 (s, 1H), 8.01 (s, 1H), 7.53 (d, J = 9.0 Hz, 1H), 6.76 (d, J = 8.9 Hz, 1H), 6.51 (s, 1H), 5.90 – 5.19 (m, 26H), 4.56 – 4.46 (m, 4H), 3.88 – 3.78 (m, 2H), 3.64 – 3.35 (m, 17H), 1.10 (dd, J = 17.2, 10.2 Hz, 6H). Due to complex structure, precise peak assignment was not possible. It was not

possible to measure ^{13}C NMR even after multiple attempts due to solubility issues. ESI MS: Calc. for $[\text{M}+\text{C}_8\text{mim}_2]^{2+}$: 977.4075; found: 977.4044. Analyt. HPLC: 9.50 min (anal. method 1)

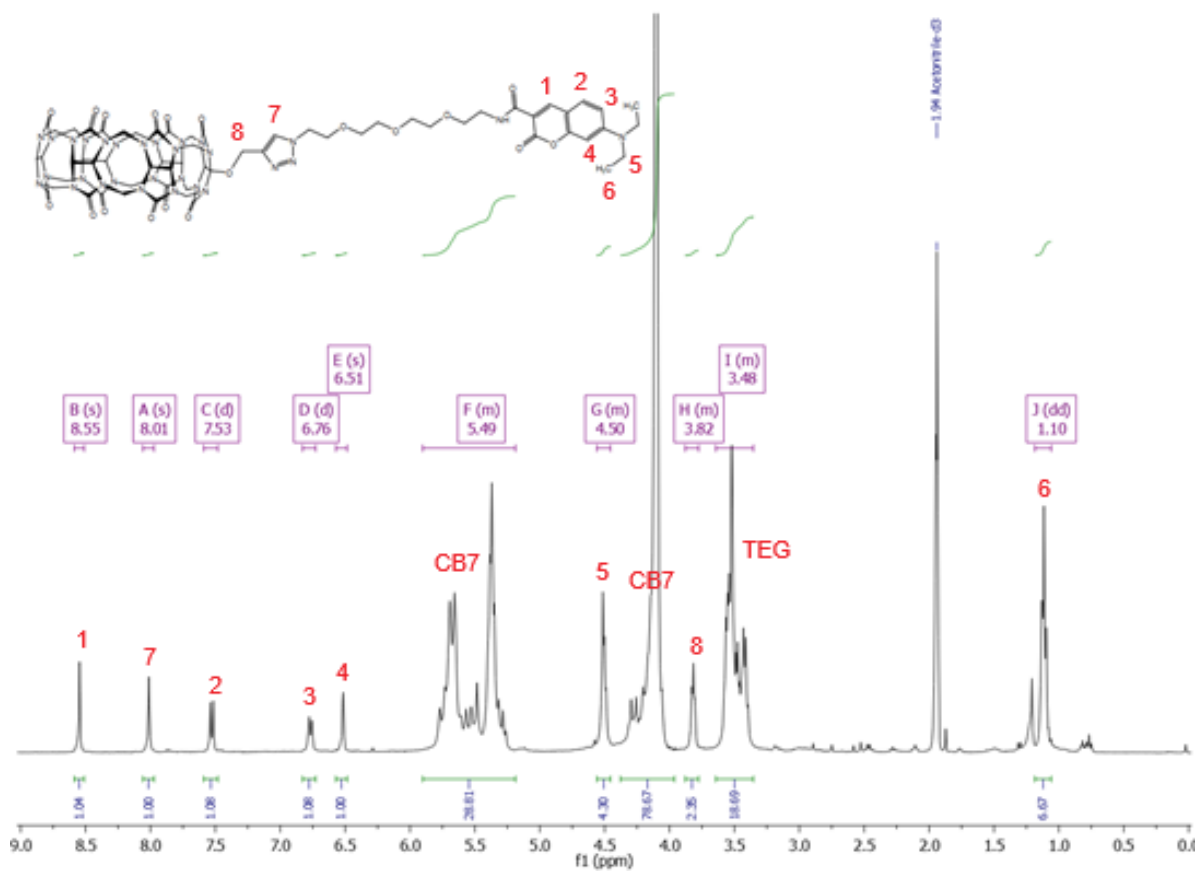


Fig. 6.53. ^1H NMR ($\text{CD}_3\text{CN}/\text{D}_2\text{O}$ 3:2) of CB7-diethylcoumarin

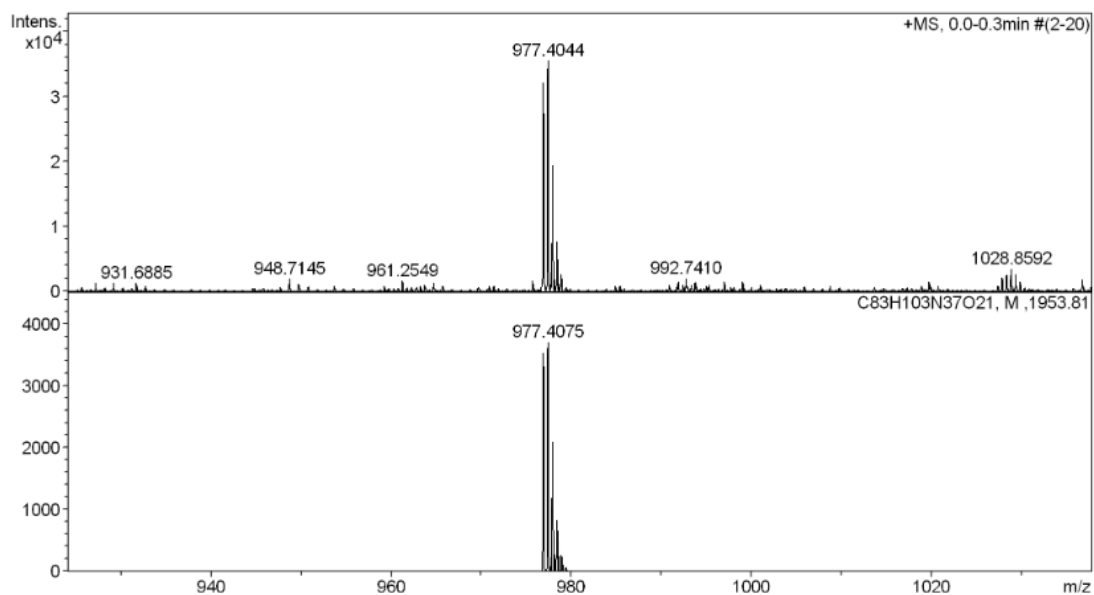


Fig. 6.54. ESI-MS of CB7-diethylcoumarin measured (top) and simulated (bottom), shown as C_8mim_2 adducts.

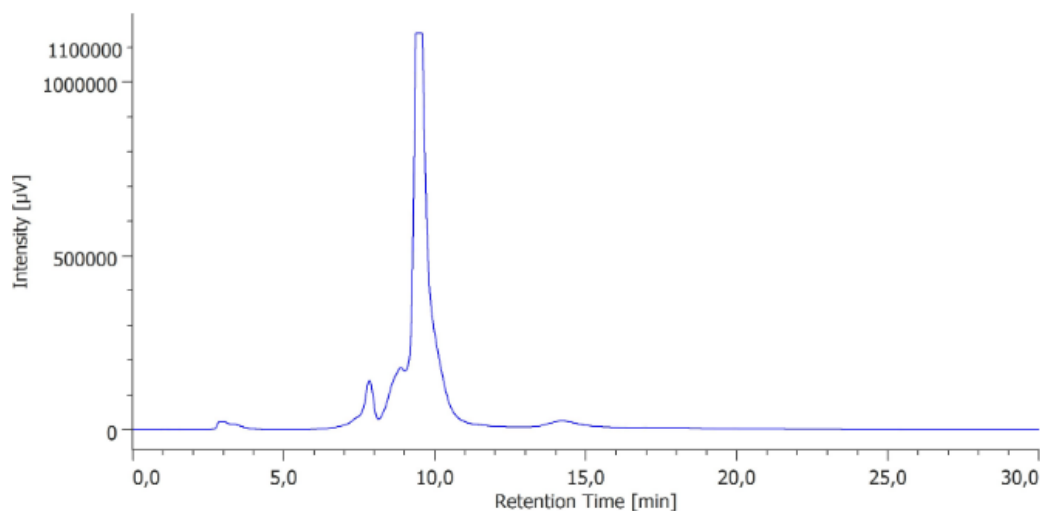
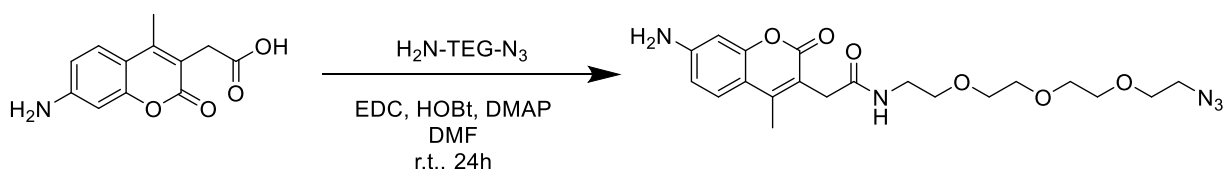


Fig. 6.55. Analytical trace of CB7-DEC (anal. method 1).

6.11.2.5. 2-(7-amino-4-methyl-2-oxo-2H-chromen-3-yl)-N-(2-(2-(2-(2-azidoethoxy)ethoxy)ethoxy)ethyl)acetamide (AMCA-N₃)



According to literature procedures³⁹⁷, in a glass vial AMCA (50 mg, 0.2 mmol, 1 equiv.), 11-azido-3,6,9-trioxaundecane-1-amine (93.6 mg, 85 µl, 0.2 mmol, 2 equiv.), HOBt (49.2 mg, 0.4 mmol, 1.7 equiv.) and DMAP (52.4 mg, 0.4 mmol, 2 equiv.) were dissolved in dry DMF (4 mL). The mixture was purged with N₂. Afterwards, EDC (61.6 mg, 0.4 mmol, 1.5 equiv.) was added and the vial was closed. The mixture was stirred overnight in the dark under an N₂ atmosphere. The crude product was then purified by silica column chromatography (CHCl₃/MeOH 9:1). The product was obtained as a colorless to yellowish oil. (173.1 mg, 0.12 mmol, 62%) ¹H NMR (400 MHz, DMSO) δ 7.89 (t, J = 5.6 Hz, 1H), 7.44 (d, J = 8.7 Hz, 1H), 6.57 (dd, J = 8.7, 2.2 Hz, 1H), 6.40 (d, J = 2.2 Hz, 1H), 6.02 (s, 2H), 3.59 (dd, J = 9.4, 4.2 Hz, 2H), 3.57 – 3.47 (m, 9H), 3.40 (d, J = 3.5 Hz, 2H), 3.18 (q, J = 5.6 Hz, 2H), 2.24 (s, 3H). ¹³C NMR (101 MHz, DMSO) δ 169.84 (s), 111.75 (s), 98.84 (s), 70.18 (dd, J = 15.6, 6.9 Hz), 69.72 (s), 50.46 (s). ESI MS: Calc. for [M+Na]⁺: 456.1854; found: 456.2077.

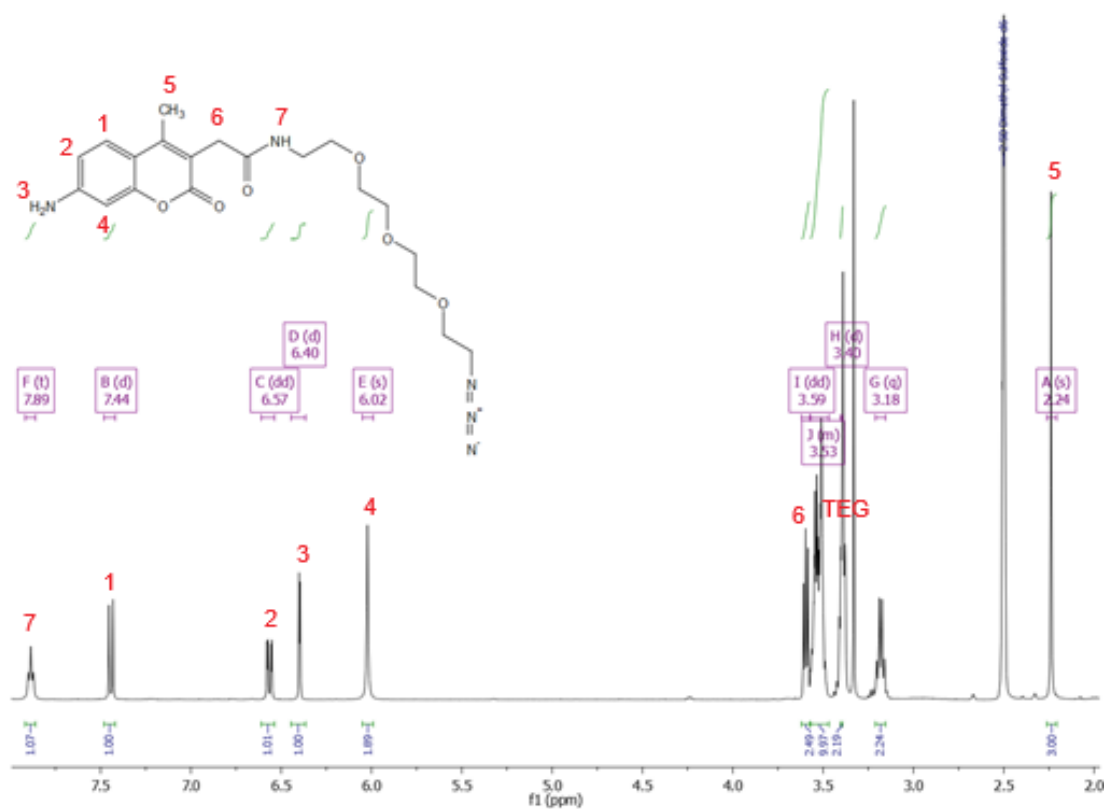


Fig. 6.56. ¹H NMR (DMSO-*d*₆) of AMCA-N₃.

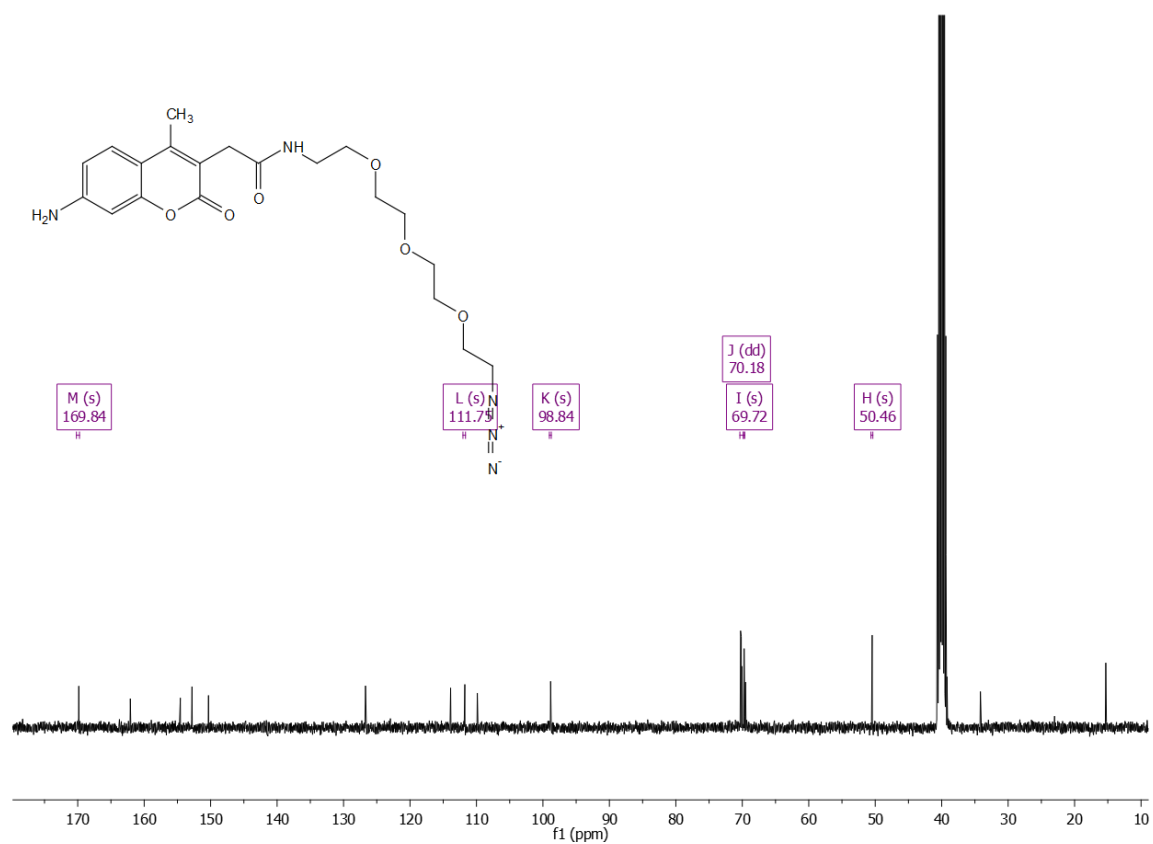


Fig. 6.57. ¹³C NMR (DMSO-*d*₆) of AMCA-N₃.

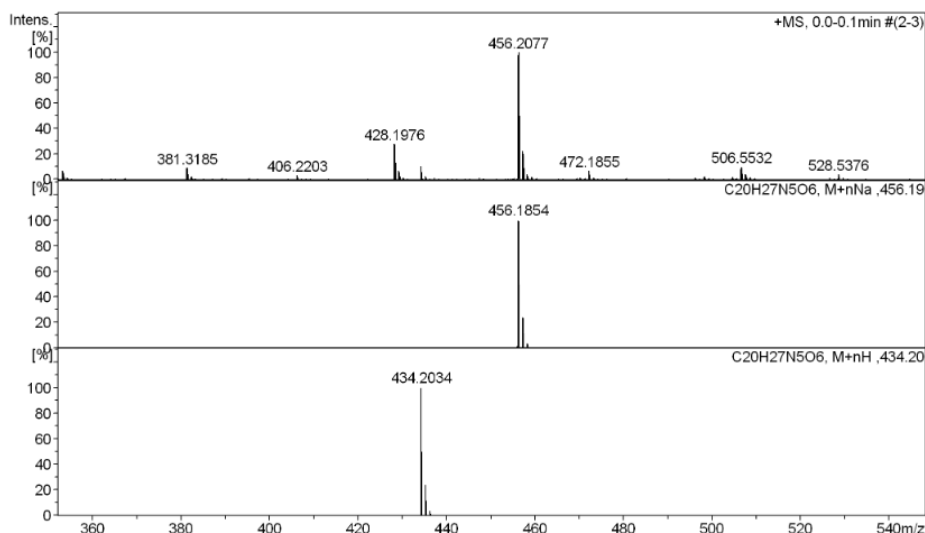
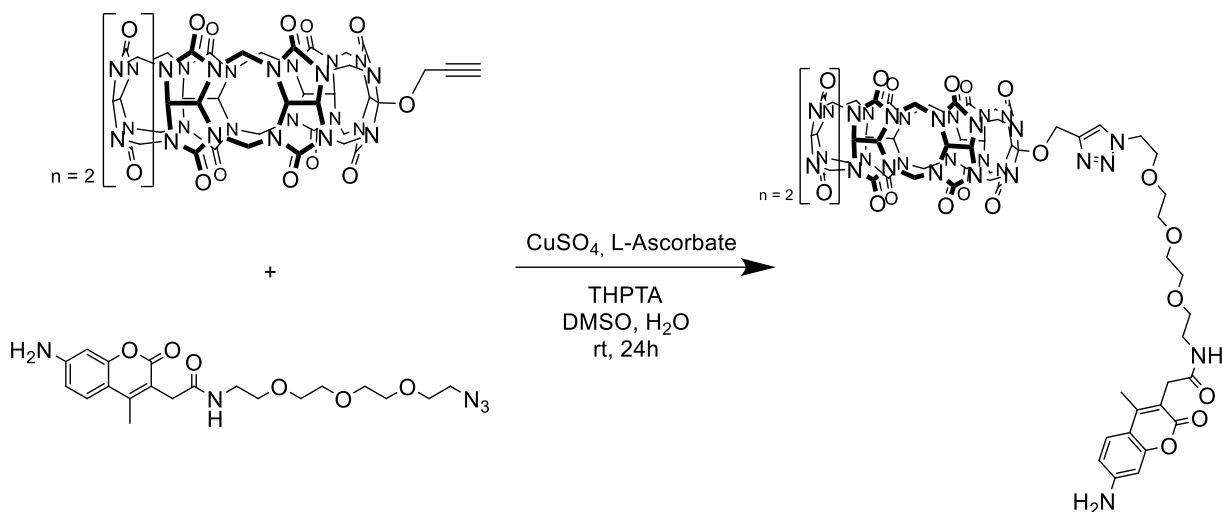


Fig. 6.58. ESI-MS of AMCA-N₃ [M+Na]⁺ (measured), simulated [M+Na]⁺ (middle), and simulated [M+H]⁺ (bottom).

6.11.2.6. CB7-AMCA



CB7-(OPr) (17.4 mg, 14.4 μmol , 1 equiv.), AMCA-N₃ (11.1 mg, 25.8 μmol , 1.8 equiv.), and THPTA (24.8 mg, 56 μmol , 4 equiv.) were placed in a vial and dissolved in 1400 μL DMSO. After closing of the vial, it was placed in ultrasound then purged with N₂. In a second vial, 5.6 mL 55% DMSO aqueous solution was also purged with N₂, then CuSO₄ (9.1 mg, 56.0 μmol , 4 equiv.) was added to the 55% DMSO followed by sodium L-ascorbate (19.8 mg, 100.0 μmol , 7 equiv.) while it was taken care for least oxygen exposure as possible. The click solution was placed in the ultrasound for approx. 1 min. while a color change to yellow (Cu⁺ forming) was observed. The two solutions were mixed and stirred at room temperature for 24 h under an N₂ atmosphere. Afterwards, the product was precipitated by dropwise addition of the reaction solution in 50 mL MeOH. The solid was then washed with MeOH (3 \times 25 mL). Purification is done by preparative HPLC. The product elutes at 12.65 min (prep. method 3) The product was obtained as a fluffy greyish solid after freeze-dry. ¹H NMR (400 MHz, CD₃CN) δ 7.99 (t, J = 13.5 Hz, 2H), 7.77 (d, J = 8.6 Hz, 1H), 7.19 (d, J = 10.6 Hz, 2H), 5.97 – 5.11 (m, 60H), 3.81 (s, 4H), 3.64

– 3.33 (m, 24H), 3.22 (s, 4H), 2.39 (s, 3H). Due to complex structure, precise peak assignment was not possible. It was not possible to measure ^{13}C NMR even after multiple attempts. ESI MS: Calc. for $[\text{M}+\text{C}_8\text{mim}_2]^{2+}$: 963.4012; found: 963.3933. Analyt. HPLC: 9.6 min (anal. method 1)

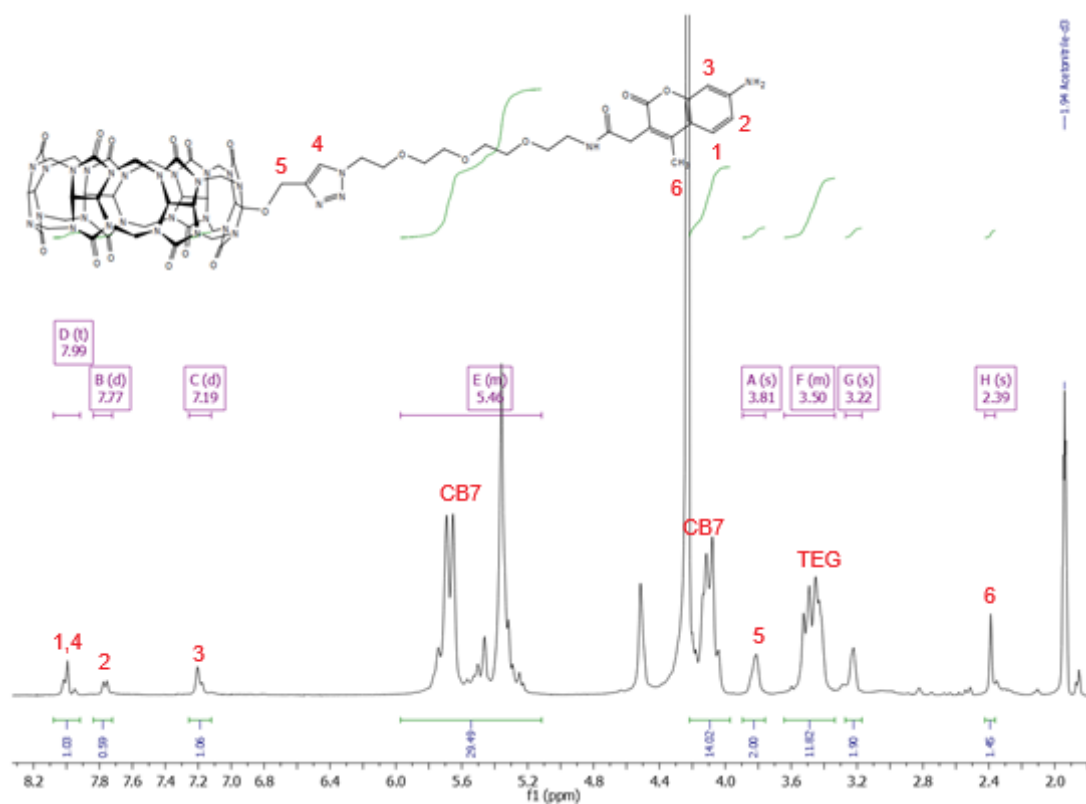


Fig. 6.59. ^1H NMR ($\text{CD}_3\text{CN}:\text{D}_2\text{O}$ 3:2) of CB7-AMCA

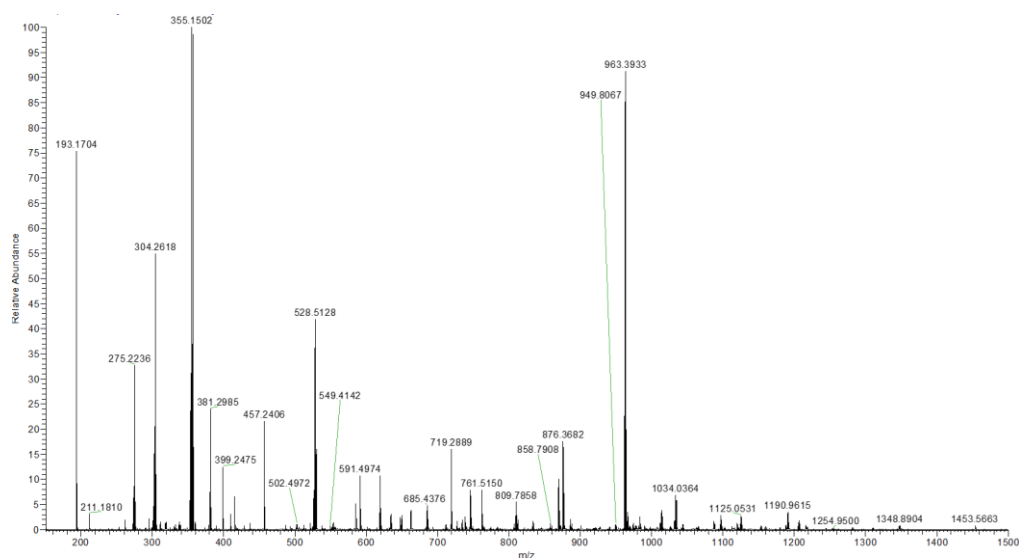


Fig. 6.60. ESI-MS of CB7-AMCA, measured as $[\text{M}+\text{C}_8\text{mim}_2]^{2+}$ adduct.

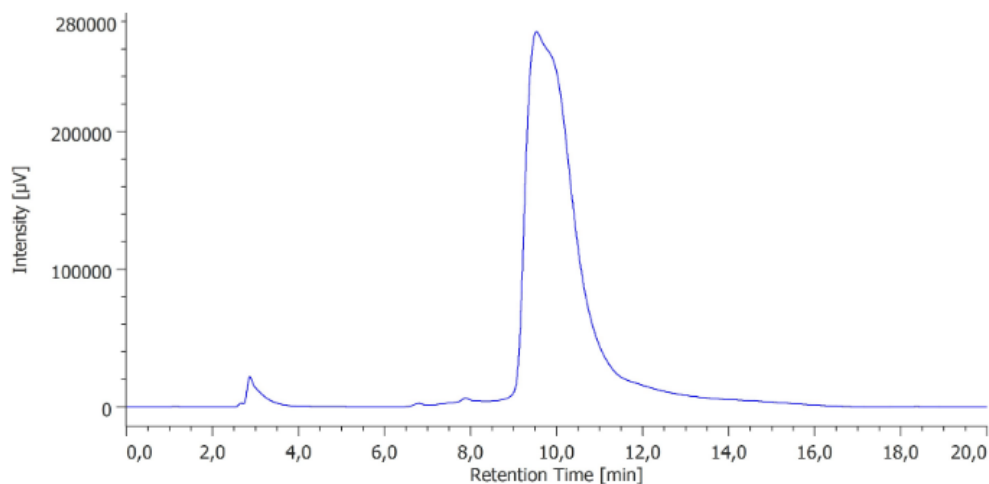
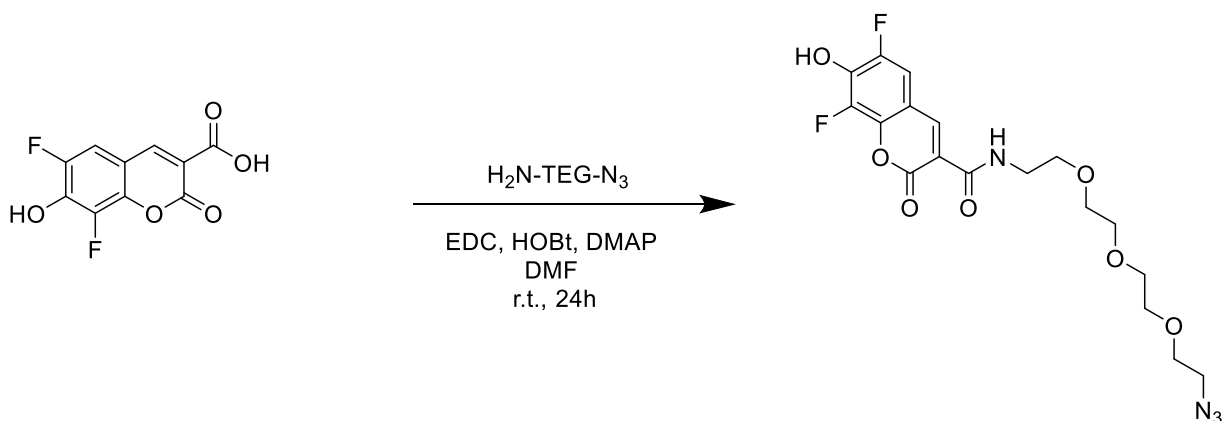


Fig. 6.61. Analytical trace of CB7-AMCA (anal. method 1).

6.11.2.7. *N*-(2-(2-(2-(2-azidoethoxy)ethoxy)ethoxy)ethyl)-6,8-difluoro-7-hydroxy-2-oxo-2H-chromene-3-carboxamide (Pacific Blue-N₃)



According to literature procedures³⁹⁷, in a glass vial Pacific Blue (50 mg, 0.2 mmol, 1 equiv.), 11-azido-3,6,9-trioxaundecane-1-amine (90.1 mg, 82 μ l, 0.4 mmol, 2 equiv.), HOBt (47.4 mg, 0.4 mmol, 1.7 equiv.) and DMAP (50.5 mg, 0.4 mmol, 2 equiv.) were dissolved in dry DCM (1 mL). The mixture was purged with N₂. Afterwards, EDC (59.4 mg, 0.3 mmol, 1.5 equiv.) was added and the vial was closed. The mixture was stirred overnight in the dark under an N₂ atmosphere. The crude product was then purified by silica column chromatography (CHCl₃/MeOH 9:1). The product was obtained as a greenish to yellowish semi-solid. (79.2 mg, 0.17 mmol, 86%) ¹H NMR (400 MHz, MeOD) δ 9.12 (s, 2H), 8.76 (d, J = 1.4 Hz, 3H), 7.45 (dd, J = 10.1, 2.1 Hz, 3H), 5.49 (s, 4H), 3.69 – 3.61 (m, 46H), 3.37 – 3.32 (m, 8H). ¹³C NMR (101 MHz, MeOD) δ 160.20 (s), 147.57 (s), 109.72 (s), 70.23 (dd, J = 15.7, 3.1 Hz), 69.73 (s), 68.97 (s), 53.40 (s), 50.36 (s), 39.34 (s). ESI MS: Calc. for [M-H]⁻: 441.1216; found: 441.1821

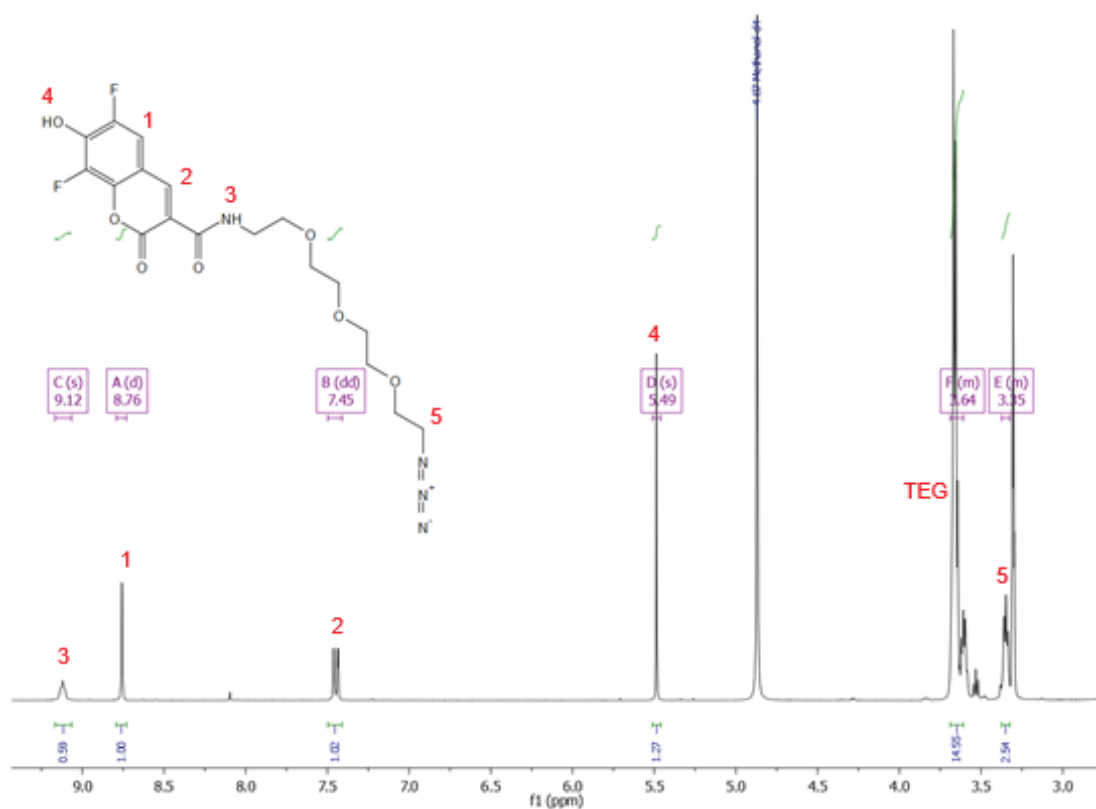


Fig. 6.62. ^1H NMR (MeOH- d_4) of Pacific Blue- N_3 .

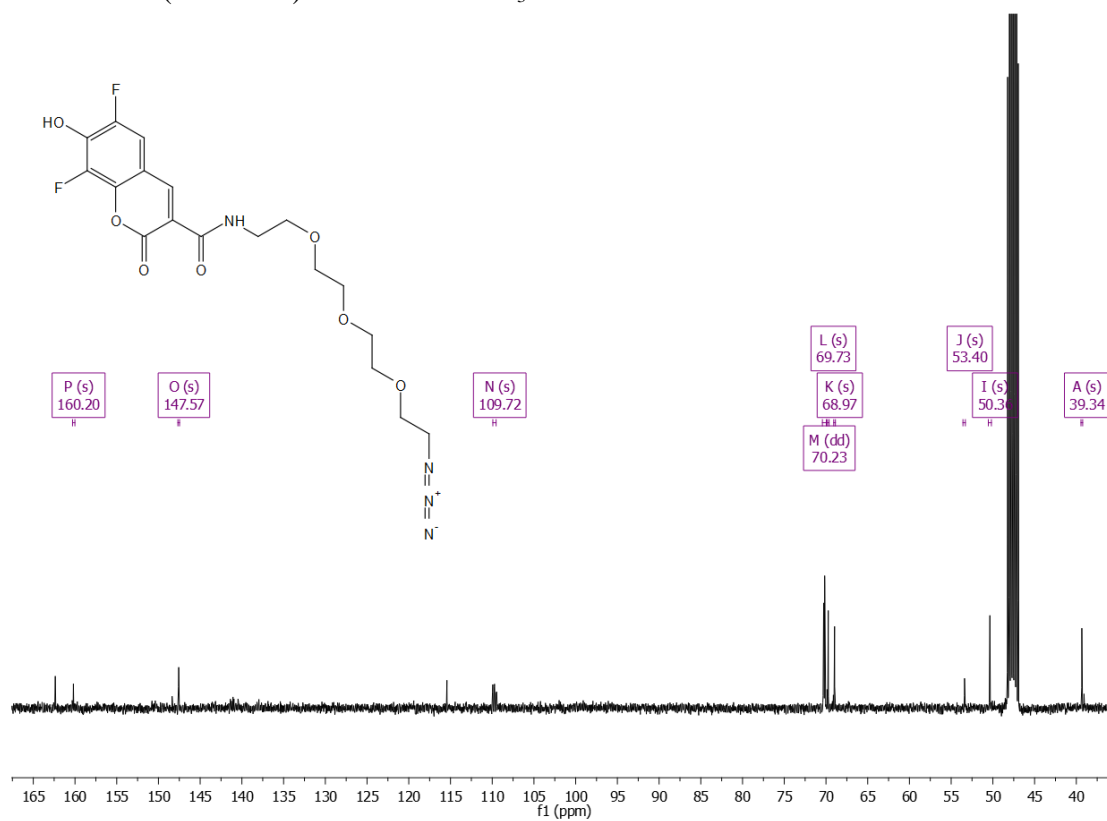


Fig. 6.63. ^{13}C NMR (MeOH- d_4) of Pacific Blue- N_3 .

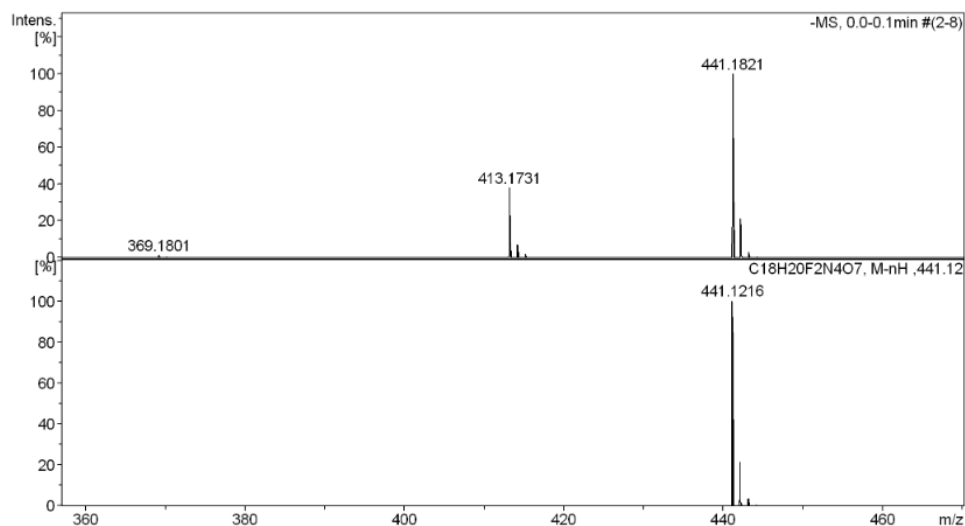
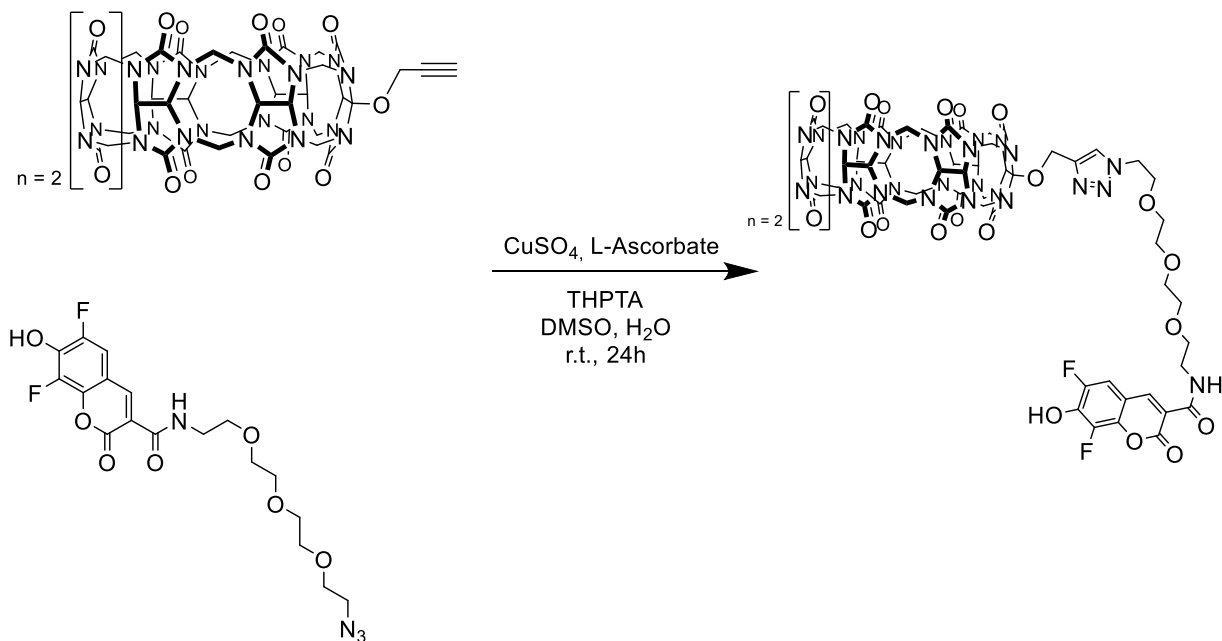


Fig. 6.64. ESI-MS of Pacific Blue- N_3 shown as $[M-H]^-$ measured (top), and simulated (bottom).

6.11.2.8. CB7-Pacific Blue



CB7-(OPr) (17.4 mg, 14.4 μmol , 1 equiv.), Pacific Blue- N_3 (11.4 mg, 25.8 μmol , 1.8 equiv.), and THPTA (24.8 mg, 56 μmol , 4 equiv.) were placed in a vial and dissolved in 1400 μL DMSO. After closing of the vial, it was placed in ultrasound then purged with N_2 . In a second vial, 5.6 mL 55% DMSO aqueous solution was also purged with N_2 , then CuSO_4 (9.1 mg, 56.0 μmol , 4 equiv.) was added to the 55% DMSO followed by sodium L-ascorbate (19.8 mg, 100.0 μmol , 7 equiv.) while it was taken care for least oxygen exposure as possible. The click solution was placed in the ultrasound for approx. 1 min. while a color change to yellow (Cu^+ forming) was observed. The two solutions were mixed and stirred at room temperature for 24 h under an N_2 atmosphere. Afterwards, the product was precipitated by dropwise addition of the reaction solution in 50 mL MeOH. The solid was then washed with MeOH (3×25 mL). Purification is done by preparative HPLC. The product elutes at 9.2 min (prep. method 3). The product was obtained as a fluffy light-yellow solid after freeze-dry. ^1H NMR (400 MHz, CD_3CN) δ 8.68 (s, 1H),

8.03 (s, 1H), 7.42 (dd, $J = 10.2, 2.0$ Hz, 1H), 5.84 – 5.25 (m, 28H), 4.53 (d, $J = 5.9$ Hz, 1H), 4.53 – 4.47 (m, 2H), 3.82 (t, $J = 5.0$ Hz, 2H), 3.62 – 3.42 (m, 14H). Note: To improve spectral resolution, 1-amandatine was added. Due to complex structure, precise peak assignment was not possible. It was not possible to measure ^{13}C NMR even after multiple attempts due to solubility issues. ESI MS: Calc. for $[\text{M}+\text{C}_8\text{mim}_2]^{2+}$: 967.3567; found: 967.3633. Analyt. HPLC: 7.23 min (anal. method 2)

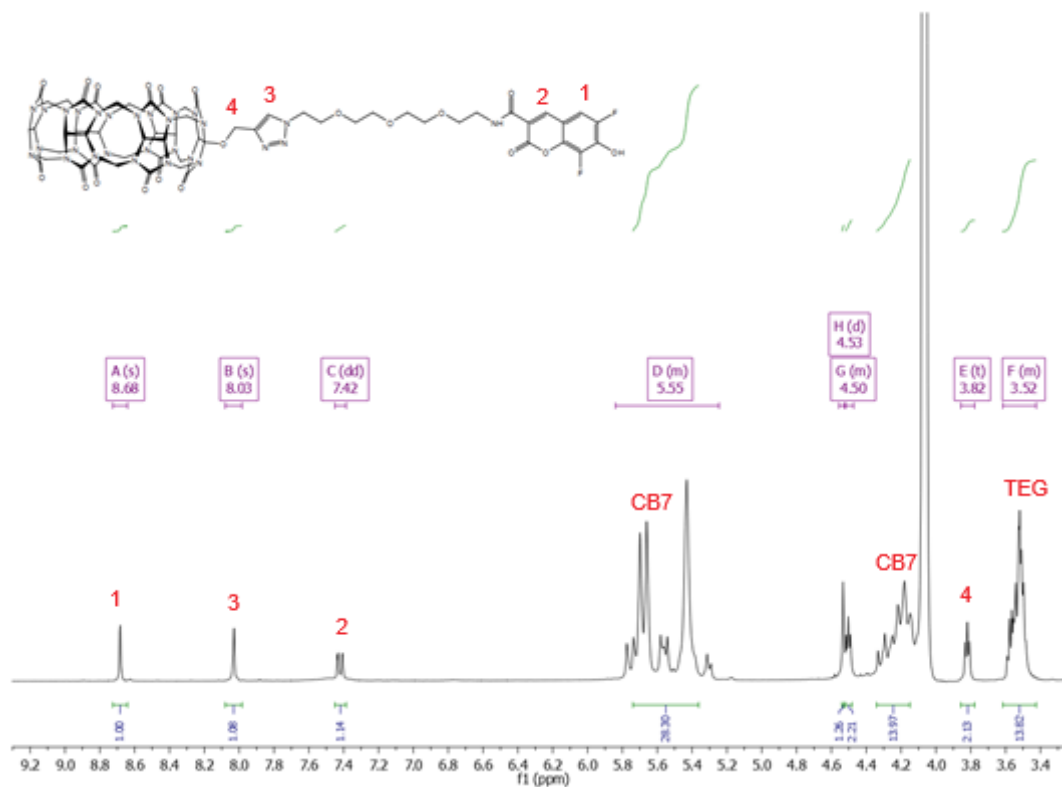


Fig. 6.65. ^1H NMR ($\text{CD}_3\text{CN}/\text{D}_2\text{O}$ 3:2) of CB7-Pacific Blue

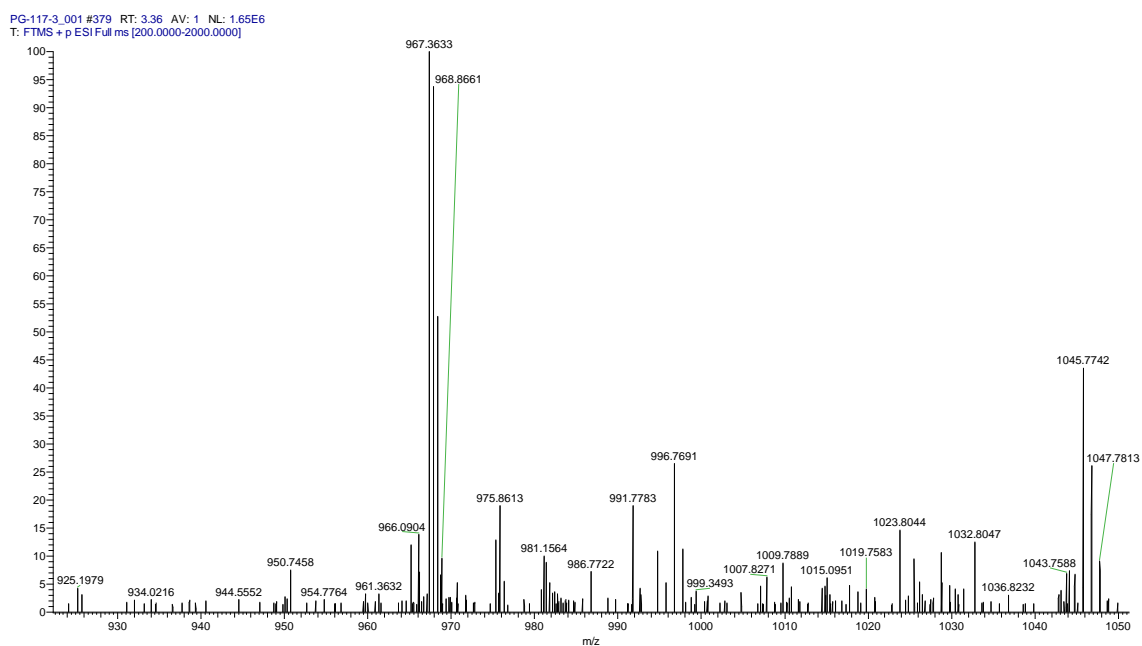


Fig. 6.66. ESI-MS of CB7-Pacific Blue, measured as $[\text{M}+\text{C}_8\text{mim}_2]^{2+}$ adduct.

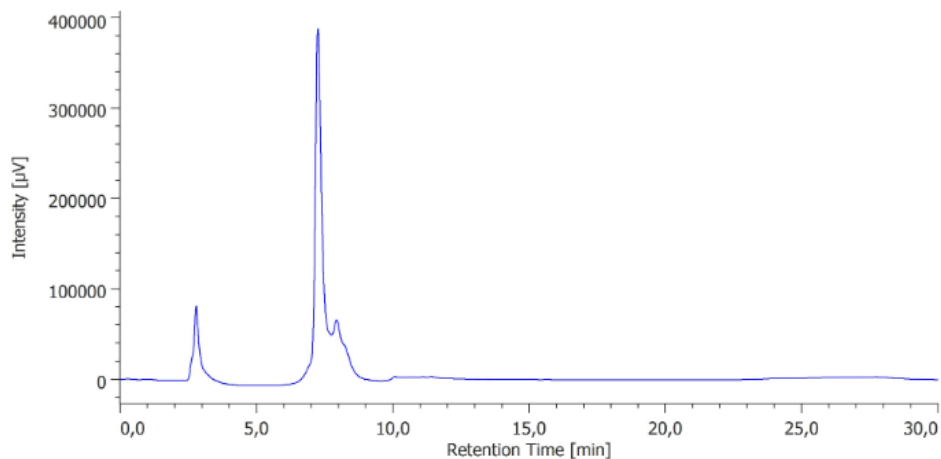
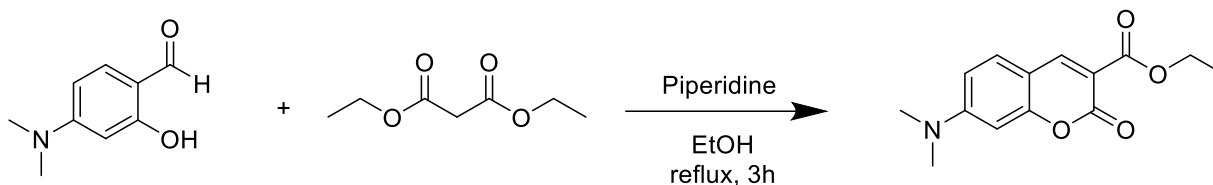


Fig. 6.67. Analytical trace of CB7-Pacific Blue (anal. method 2)

6.11.2.9. Ethyl 7-(dimethylamino)-2-oxo-2H-chromene-3-carboxylate



According to literature procedures³⁹⁴, a flask was charged with 4-dimethylaminosalicylaldehyde (700 mg, 4.2 mmol, 1 equiv.), diethyl malonate (1.35 g, 8.5 mmol, 2 equiv.), piperidine (200 μ l) and EtOH (15 mL). The solution was heated to reflux for 3h. After cooling to room temperature, the solvent was evaporated in vacuo and the crude product was purified by silica column chromatography (EtOAc/DCM 1:2). The product was obtained as intense yellow oil. (522.0 mg, 1.9 mmol, 94%) Note: the yield is always greter than 100% since redissual diethyl malonate is very hard to remove. This can still be used for the next step. ¹H NMR (500 MHz, CDCl₃) δ 8.42 (s, 1H), 7.36 (d, J = 8.9 Hz, 1H), 6.62 (dd, J = 8.9, 2.3 Hz, 1H), 6.45 (d, J = 1.9 Hz, 1H), 4.36 (q, J = 7.1 Hz, 2H), 3.10 (s, 6H), 1.38 (t, J = 7.1 Hz, 3H). ¹³C NMR (126 MHz, CDCl₃) δ 164.28 (s), 158.25 (d, J = 18.9 Hz), 154.91 (s), 149.44 (s), 130.87 (s), 109.79 (d, J = 9.4 Hz), 108.09 (s), 97.27 (s), 61.33 (s), 40.35 (s), 14.49 (s). ESI MS: Calc. for [M+Na]⁺: 284.0893; found: 284.1123. HPLC-MS: 8.498 min, m=262.0⁺

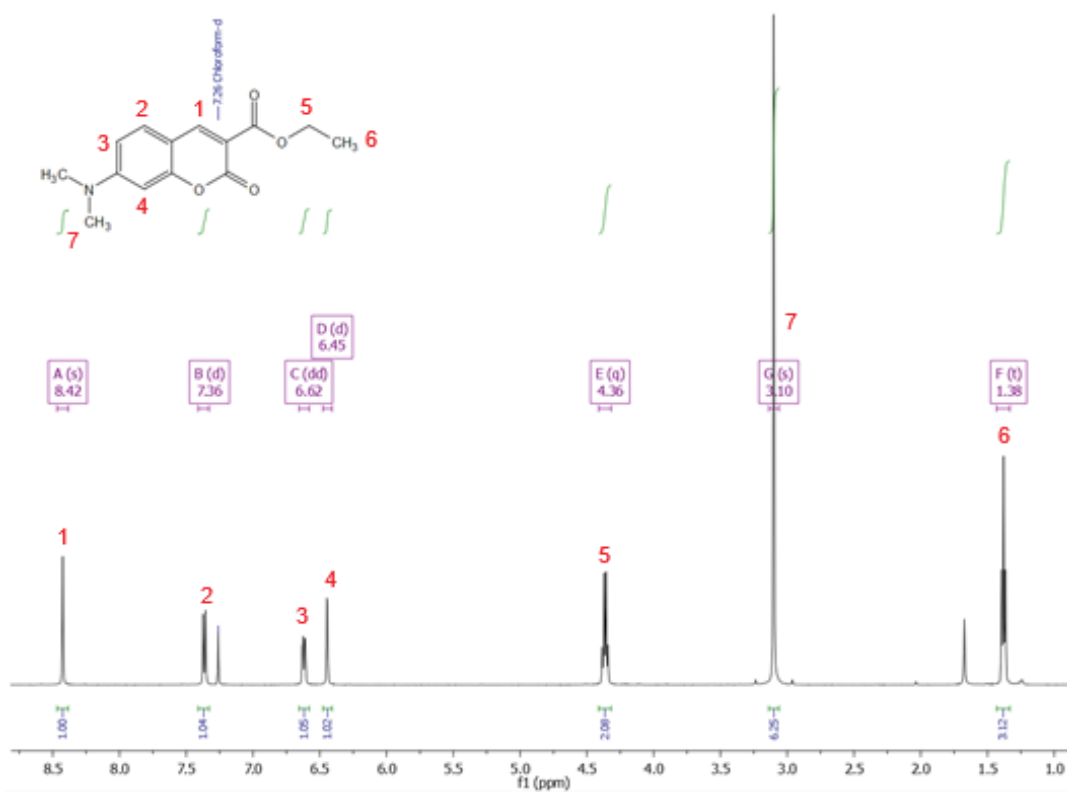


Fig. 6.68. ^1H NMR (CDCl_3) of Ethyl 7-(dimethylamino)-2-oxo-2H-chromene-3-carboxylate.

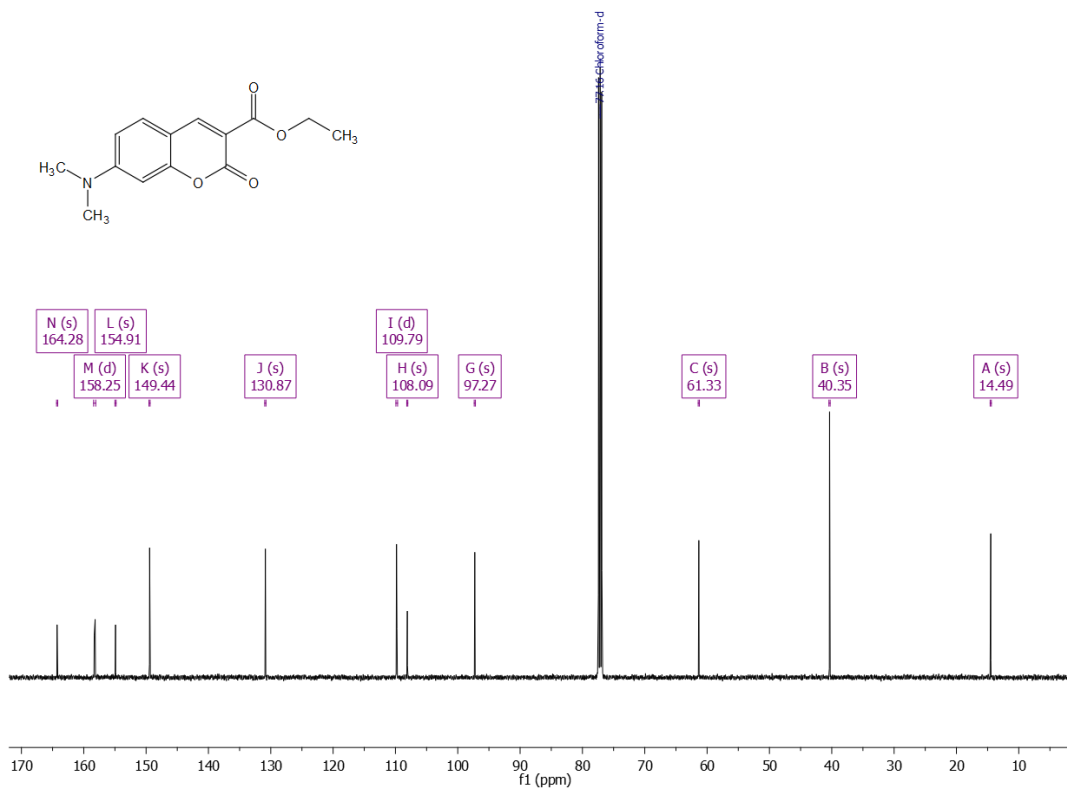


Fig. 6.69. ^{13}C NMR (CDCl_3) of Ethyl 7-(dimethylamino)-2-oxo-2H-chromene-3-carboxylate.

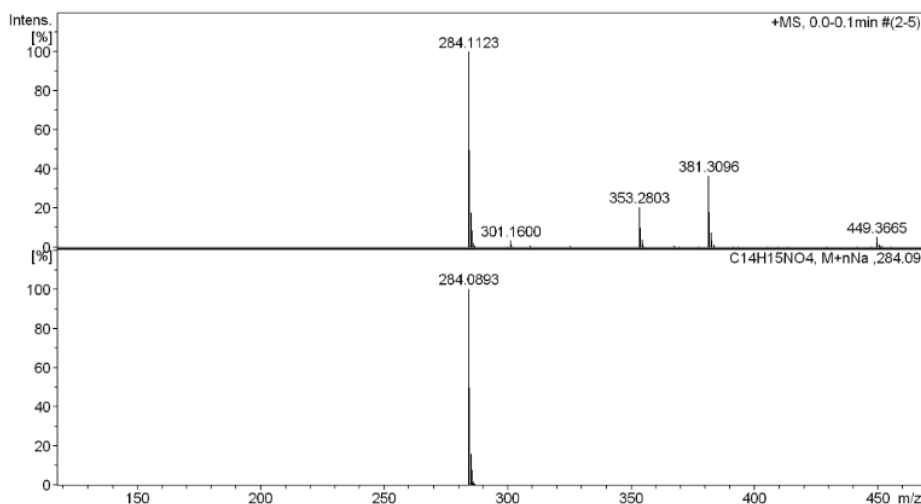


Fig. 6.70. ESI-MS of Ethyl 7-(dimethylamino)-2-oxo-2H-chromene-3-carboxylate shown as $[M+Na]^+$ measured (top), and simulated (bottom).

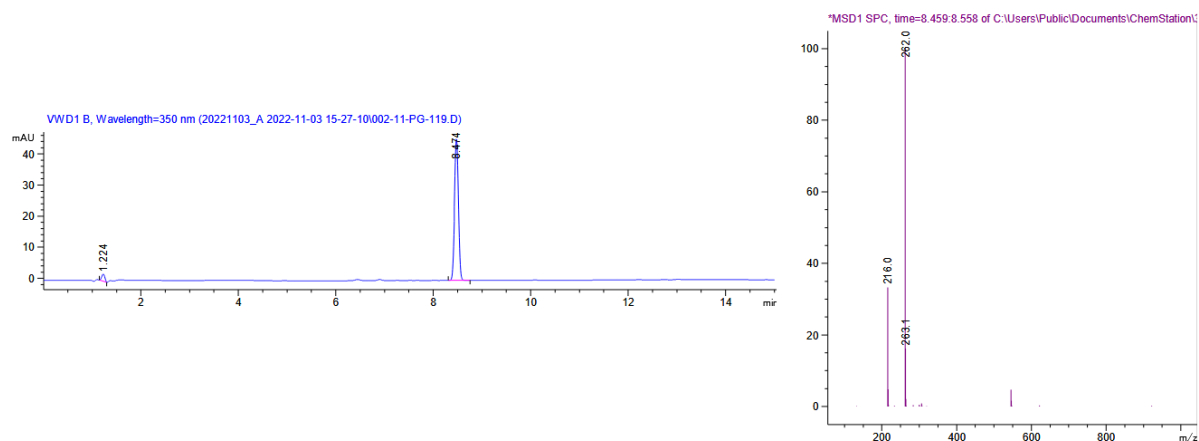
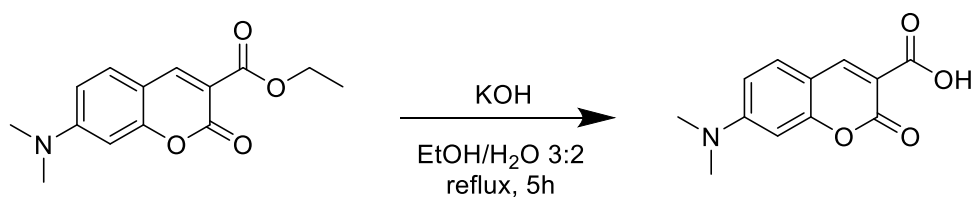


Fig. 6.71. Analytical trace (left) and observed mass (right).

6.11.2.10. 7-(dimethylamino)-2-oxo-2H-chromene-3-carboxylic acid



According to literature procedures³⁹⁵, a solution of 7-dimethylaminocoumarin-3-carboxylic acid ethyl ester (500 mg, 1.9 mmol, 1 equiv.) and KOH (171.8 mg, 3.1 mmol, 1.6 equiv.) in EtOH/H₂O 3:2 (10 mL) was heated to reflux for 5h. EtOH was evaporated in vacuo and the aqueous phase was acidified with dropwise addition of conc. HCl. The precipitated solid was removed by filtration and washed with water and hexane. The product was obtained as a yellow solid. (325.1 mg, 1.4 mmol, 73%) ¹H NMR (500 MHz, CDCl₃) δ 12.32 (s, 1H), 8.70 (s, 1H), 7.48 (d, J = 9.0 Hz, 1H), 6.74 (d, J = 7.5 Hz, 1H), 6.54 (s, 1H), 3.17

(s, 5H). ^{13}C NMR (126 MHz, CDCl_3) δ 150.76 (s), 131.85 (s), 111.17 (s), 97.41 (s), 40.55 (s). ESI MS: Calc. for $[\text{M}+\text{Na}]^+$: 256.0580; found: 256.0805

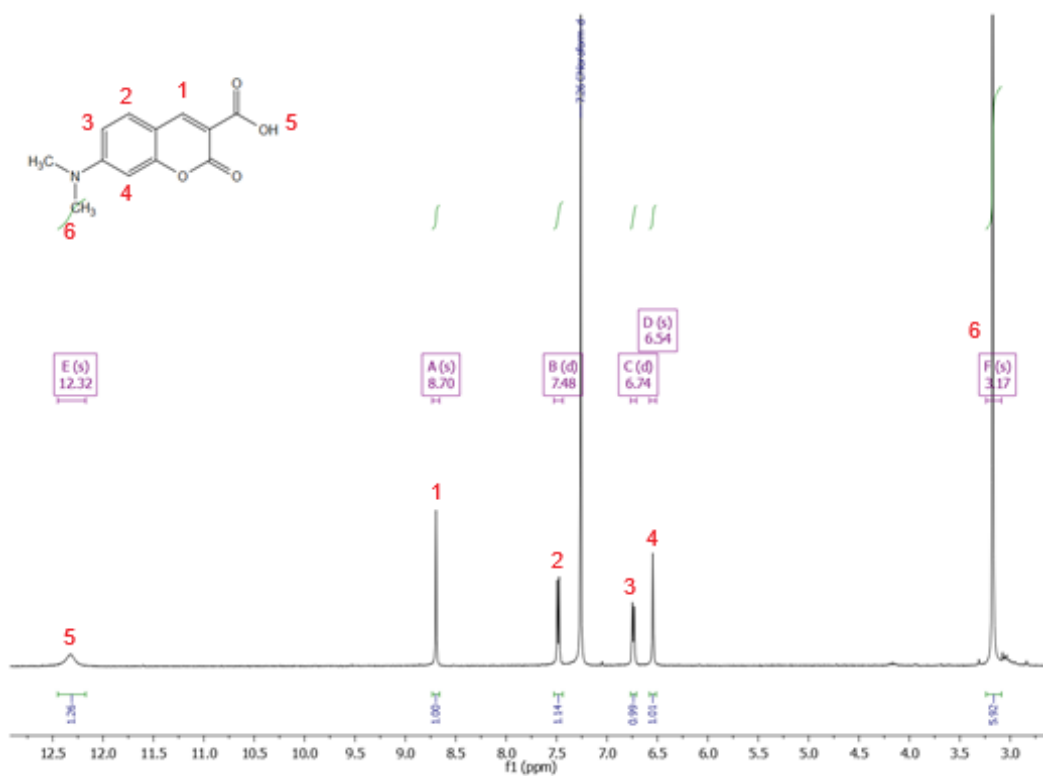


Fig. 6.72. ^1H NMR (CDCl_3) of 7-(dimethylamino)-2-oxo-2H-chromene-3-carboxylic acid.

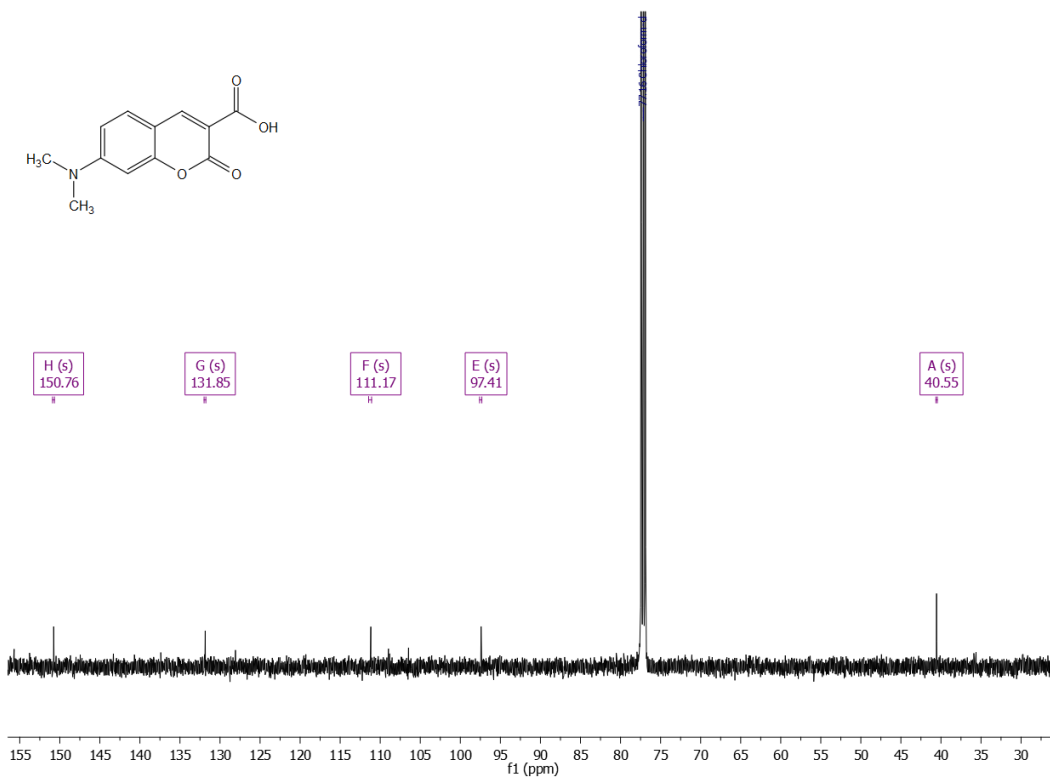


Fig. 6.73. ^{13}C NMR (CDCl_3) of 7-(dimethylamino)-2-oxo-2H-chromene-3-carboxylic acid.

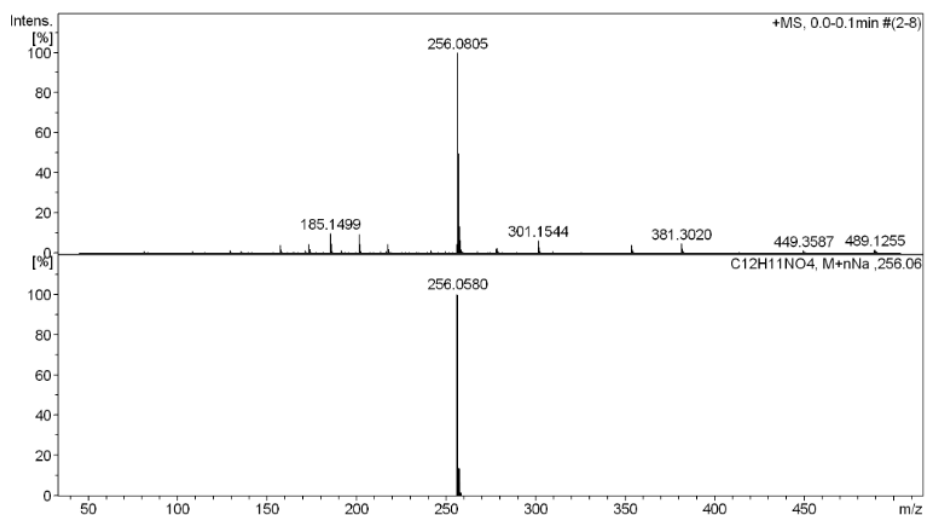
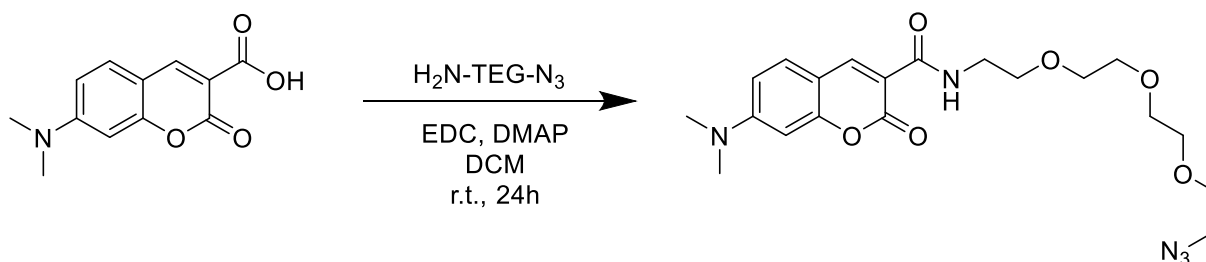


Fig. 6.74. ESI-MS of 7-(dimethylamino)-2-oxo-2H-chromene-3-carboxylic acid shown as $[M+Na]^+$ measured (top), and simulated (bottom).

6.11.2.11. *N*-(2-(2-(2-(2-azidoethoxy)ethoxy)ethoxy)ethyl)-7-(dimethylamino)-2-oxo-2H-chromene-3-carboxamide (DMC-N₃)



According to literature procedures³⁹⁶, in a glass vial 7-dimethylaminocoumarin-3-carboxylic acid (150 mg, 0.6 mmol, 1 equiv.) was dissolved in dry DCM (2 mL). To this solution was added 11-Azido-TEG-NH₂ (182.5 mg, 165.9 μ l, 0.8 mmol, 1.3 equiv.), 4-DMAP (94.3 mg, 0.8 mmol, 1.2 equiv.) and EDC HCl (135.6 mg, 0.7 mmol, 1.1 equiv.). The vial was closed and the mixture was stirred overnight in the dark under an N₂ atmosphere. The crude product was purified by silica gel column chromatography (CHCl₃/MeOH 20:1). The product was obtained as an intense yellow semi-solid. (262.2 mg, 0.6 mmol, 94%) ¹H NMR (500 MHz, CDCl₃) δ 9.00 (s, 1H), 7.46 – 7.41 (m, 1H), 6.65 (dt, *J* = 9.3, 4.6 Hz, 1H), 6.48 (d, *J* = 2.3 Hz, 1H), 3.74 – 3.59 (m, 16H), 3.38 (t, *J* = 5.1 Hz, 2H), 3.10 (d, *J* = 5.3 Hz, 6H). ¹³C NMR (126 MHz, CDCl₃) δ 163.47 (s), 162.83 (s), 157.61 (s), 154.82 (s), 148.53 (s), 131.20 (s), 111.32 (s), 110.46 (s), 109.03 (s), 97.39 (s), 71.04 (dd, *J* = 12.8, 7.9 Hz), 70.38 (d, *J* = 5.4 Hz), 70.20 (s), 51.05 (s), 40.61 (s), 39.86 (s). ESI-MS: Calc. for $[M+H]^+$: 434.2034; found: 434.2123. Calc. for $[M+Na]^+$: 456.1854, found: 456.1926.

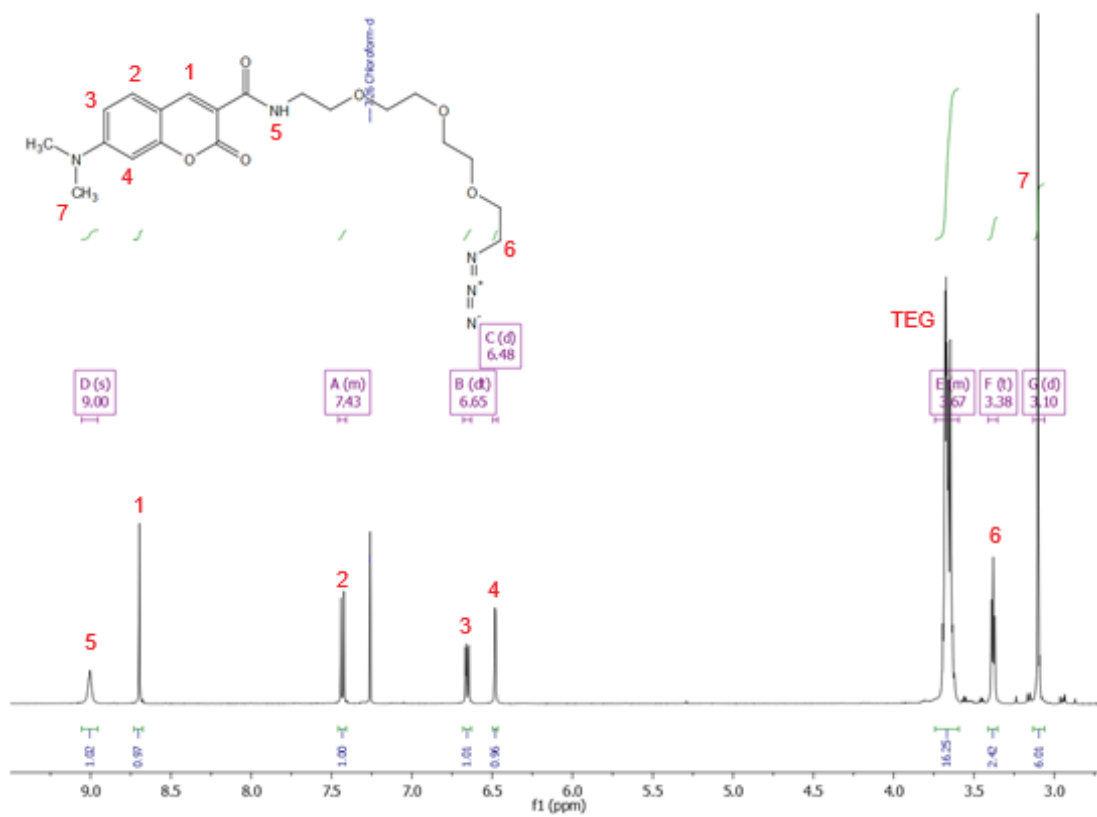


Fig. 6.75. ¹H NMR (CDCl₃) of DMC-N₃.

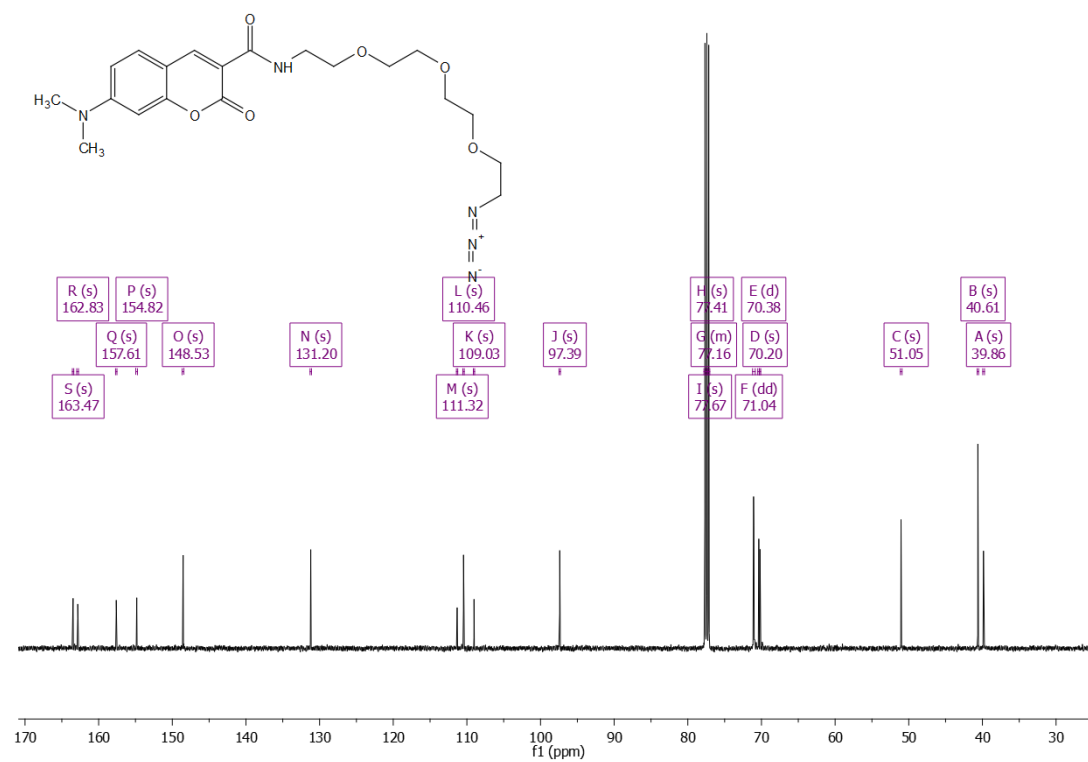


Fig. 6.76. ¹³C NMR (CDCl₃) of DMC-N₃.

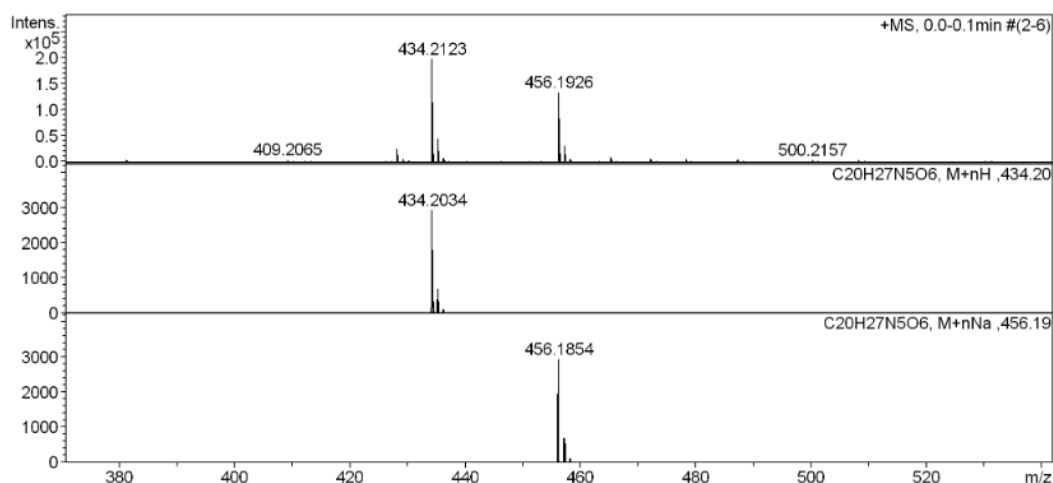
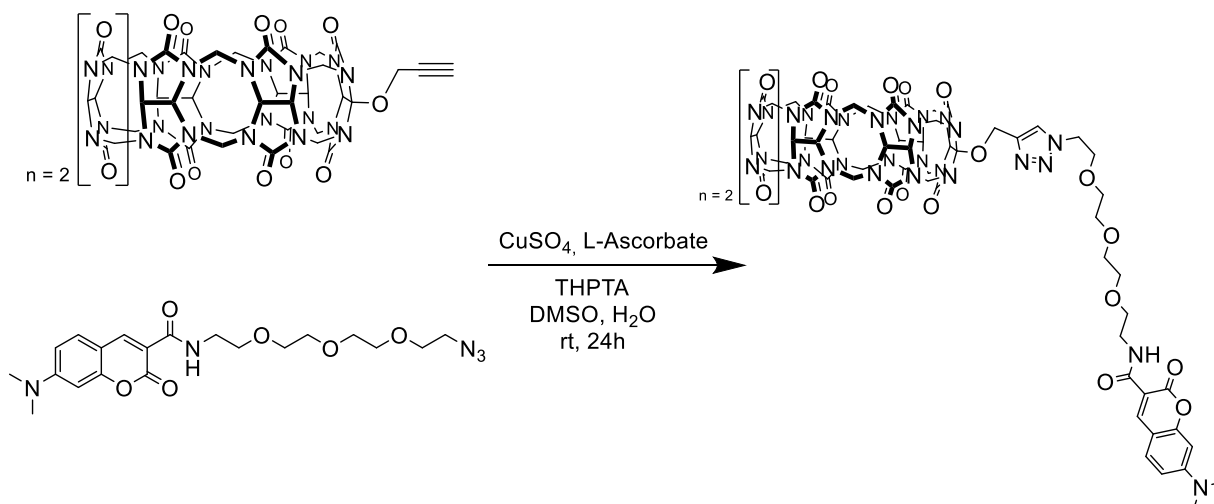


Fig. 6.77. ESI-MS of DMC- N_3 measured $[M+H]^+$ and $[M+Na]^+$ (top), simulated $[M+H]^+$ (middle), and simulated $[M+Na]^+$ (bottom).

6.11.2.12. CB7-dimethylcoumarin (CB7-DMC)



CB7-(OPr) (17.4 mg, 14.4 μmol , 1 equiv.), DMC- N_3 (11.4 mg, 25.8 μmol , 1.8 equiv.), and THPTA (24.8 mg, 56 μmol , 4 equiv.) were placed in a vial and dissolved in 1400 μL DMSO. After closing of the vial, it was placed in ultrasound then purged with N_2 . In a second vial, 5.6 mL 55% DMSO aqueous solution was also purged with N_2 , then $CuSO_4$ (9.1 mg, 56.0 μmol , 4 equiv.) was added to the 55% DMSO followed by sodium L-ascorbate (19.8 mg, 100.0 μmol , 7 equiv.) while it was taken care for least oxygen exposure as possible. The click solution was placed in the ultrasound for approx. 1 min. while a color change to yellow (Cu^+ forming) was observed. The two solutions were mixed and stirred at room temperature for 24 h under an N_2 atmosphere. Afterwards, the product was precipitated by dropwise addition of the reaction solution in 50 mL MeOH. The solid was then washed with MeOH (3×25 mL). Purification is done by preparative HPLC. The product elutes after 14.4 min (prep. method 1). The product was obtained as a fluffy yellow solid after freeze-dry. (9.4 mg, 5.7 μmol , 40%) 1H NMR (400 MHz, CD_3CN) δ 8.55 (d, $J = 6.7$ Hz, 1H), 8.01 (s, 1H), 7.54 (d, $J = 9.0$ Hz, 1H), 6.78 (d, $J = 8.9$ Hz, 1H), 6.51 (s, 1H), 5.97 – 5.18 (m, 28H), 4.54 – 4.43 (m, 4H), 4.12 (s, 14H), 3.81 (t, $J = 4.8$ Hz, 2H),

3.62 – 3.41 (m, 14H), 3.03 (d, $J = 12.7$ Hz, 6H). Due to complex structure, precise peak assignment was not possible. It was not possible to measure ^{13}C NMR even after multiple attempts. ESI MS: Calc. for $[\text{M}+\text{C}_8\text{mim}_2]^{2+}$: 962.8903; found: 962.8941. Analyt. HPLC (analyt. method 1) = 8.5 min.

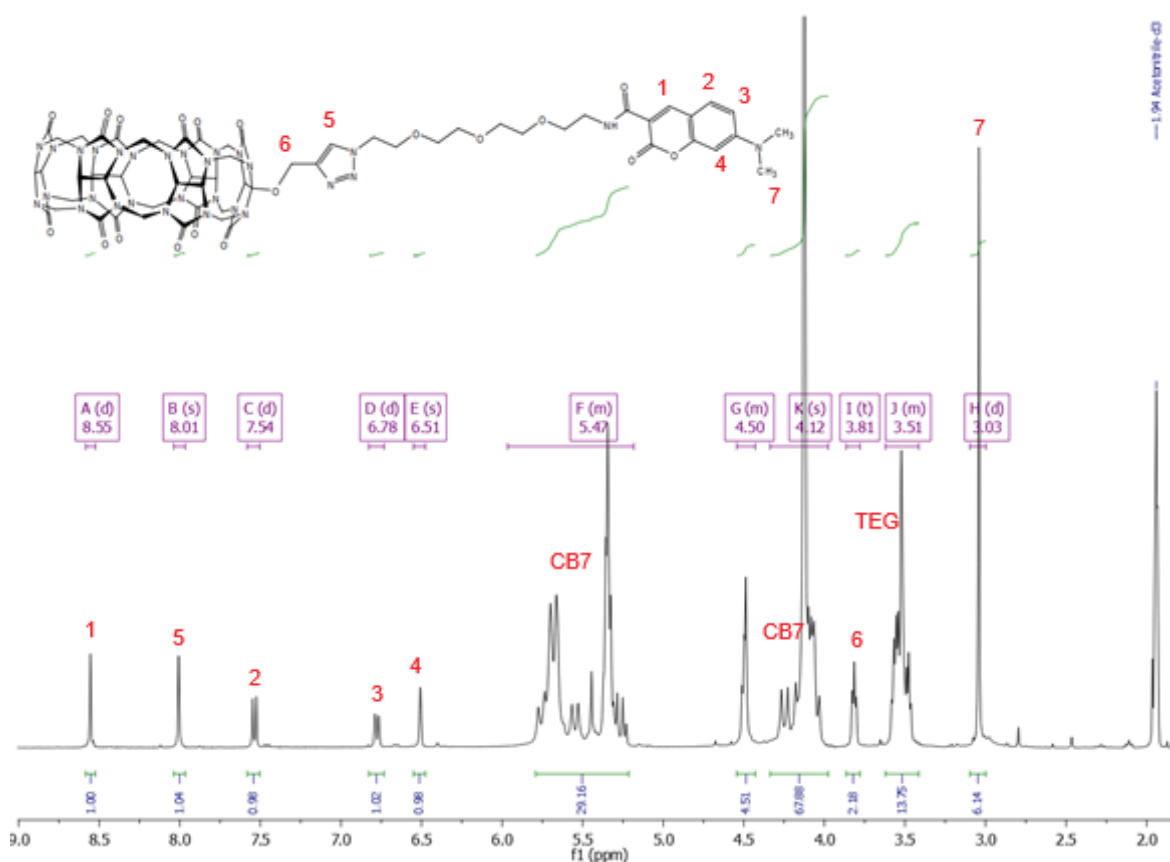


Fig. 6.78. ^1H NMR ($\text{CD}_3\text{CN}/\text{D}_2\text{O}$ 3:2) of CB7-DMC.

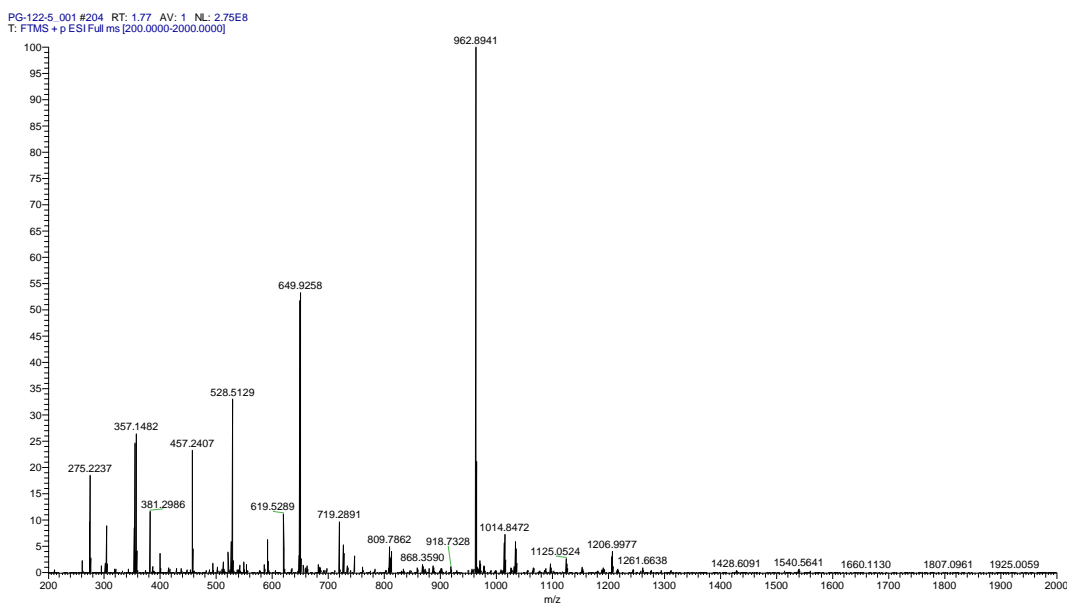


Fig. 6.79. ESI-MS of CB7-DMC measured as $[\text{M}+\text{C}_8\text{mim}_2]^{2+}$ adduct.

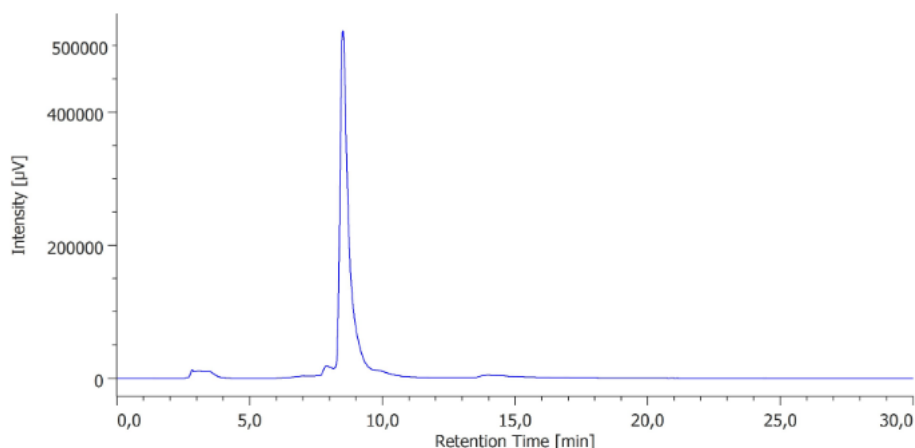
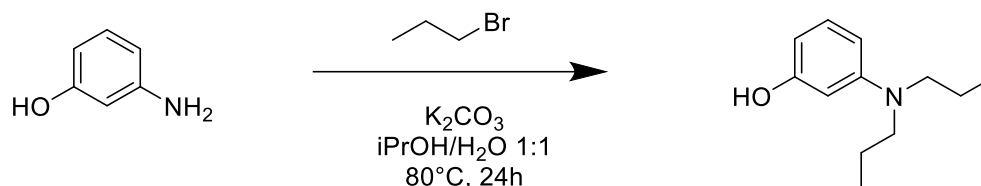


Fig. 6.80. Analytical trace of CB7-DMC (anal. method 1).

6.11.2.13. 3-(dipropylamino)phenol



According to literature procedures³⁹⁸, 3-aminophenol (0.5 g, 4.6 mmol, 1 equiv.) and 1-bromopropane (1.41 g, 11.5 mmol, 2.5 equiv.) were dissolved in *i*-PrOH/H₂O 1:1 (v/v). To this solution potassium carbonate (1.27 g, 9.2 mmol, 2 equiv.) was added and the mixture was stirred at 80°C overnight. The solvent was evaporated in vacuo and the residue diluted with water (10 mL). The mixture was extracted with EtOAc and the organic phase was washed with brine and dried over Na₂SO₄. The crude product is purified by silica column chromatography (*n*-Hex/EtOAc 10:1). The product is obtained as deep red oil. (392.9 mg, 2.0 mmol, 45%) ¹H NMR (400 MHz, CDCl₃) δ 7.05 (dd, *J* = 10.6, 5.7 Hz, 1H), 6.26 (dd, *J* = 16.1, 5.2 Hz, 1H), 6.21 – 6.05 (m, 2H), 4.71 (s, 1H), 3.26 – 3.15 (m, 4H), 1.60 (dq, *J* = 14.9, 7.4 Hz, 4H), 0.91 (t, *J* = 7.4 Hz, 6H). ¹³C NMR (101 MHz, CDCl₃) δ 157.17 (s), 130.51 (s), 105.24 (s), 218.75 – 77.37 (m), 53.49 (s), 20.82 (s), 11.87 (s). ESI-MS: Calc. for [M+H]⁺ 194.1511; found: 194.1523. HPLC-MS: 10.601 min, *m*=194.1⁺

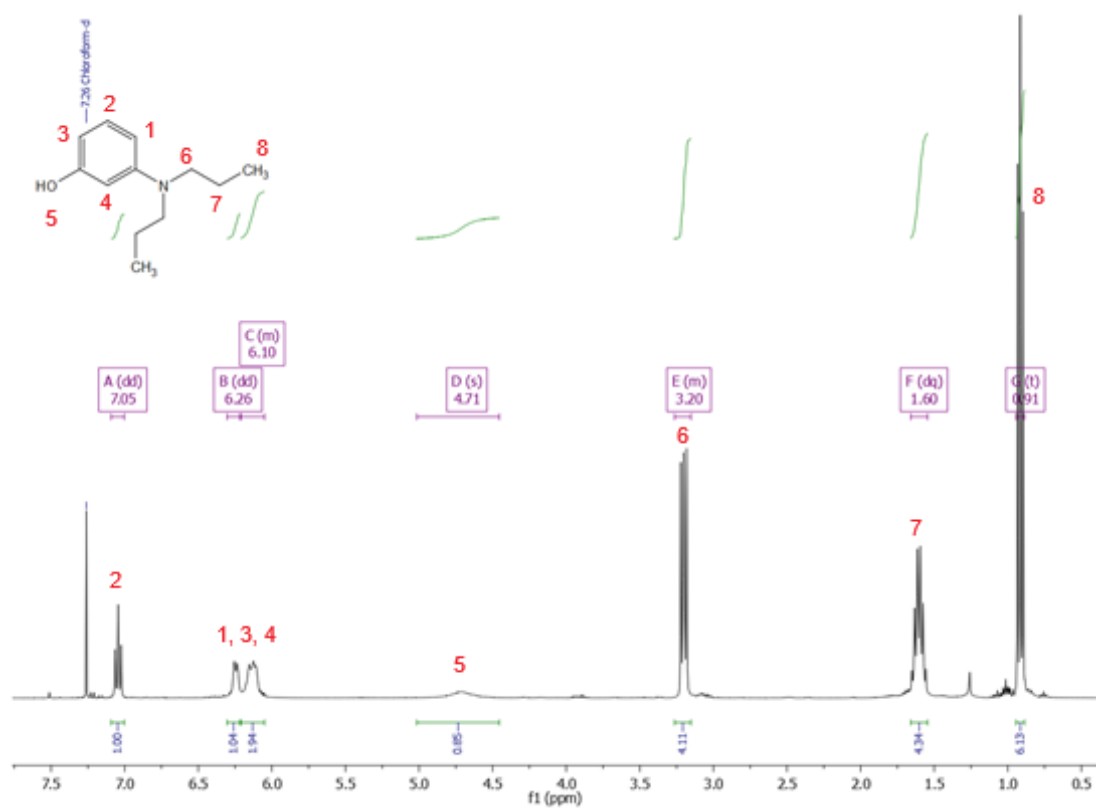


Fig. 6.81. ^1H NMR (CDCl_3) of 3-(dipropylamino)phenol.



Fig. 6.82. ^{13}C NMR (CDCl_3) of 3-(dipropylamino)phenol.

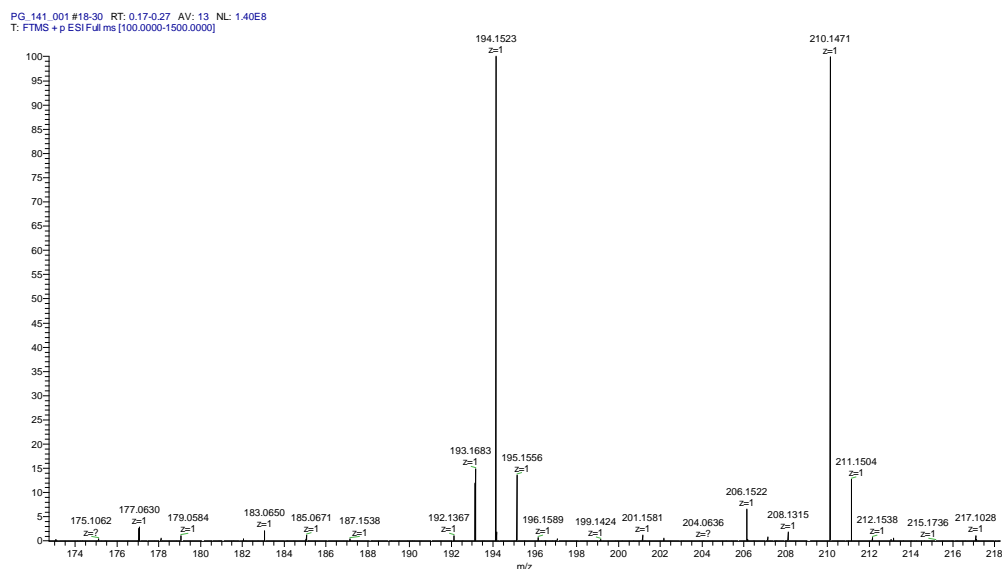


Fig. 6.83. ESI-MS of 3-(dipropylamino)phenol. The peak 194.1523^+ corresponds to $[M+H]^+$.

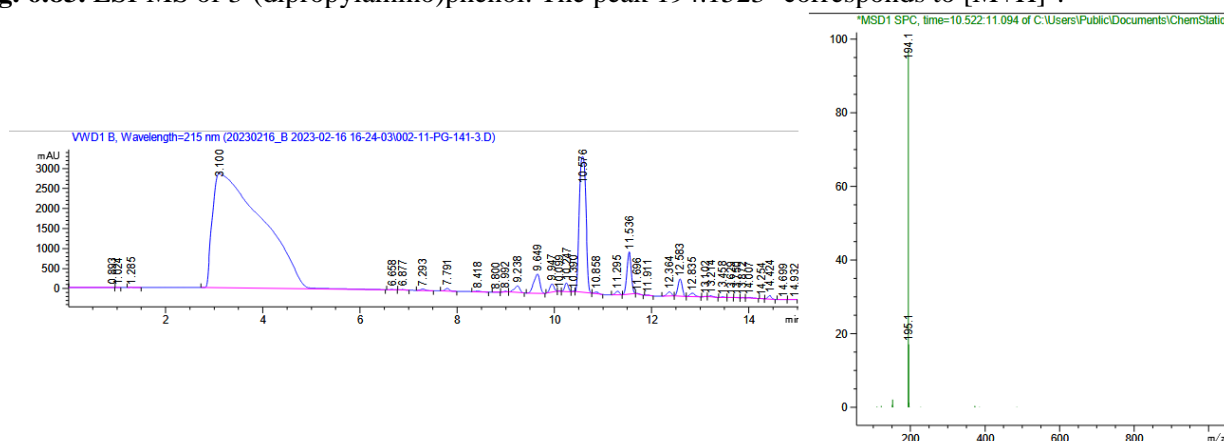
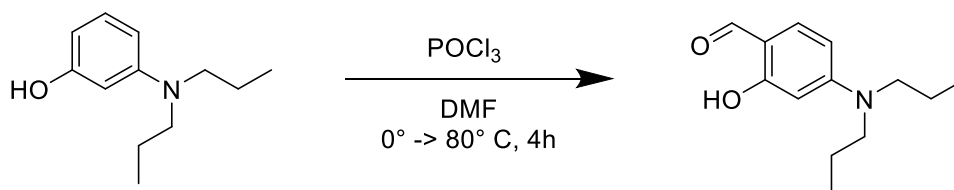


Fig. 6.84. Analytical UV trace (left) and observed mass at 10.6 min (right).

6.11.2.14. 4-(dipropylamino)-2-hydroxybenzaldehyde



According to literature procedures³⁹⁹, POCl_3 (0.79 g, 5.2 mmol, 4 equiv., 481 μl) was added to ice-cold DMF (2.5 mL) and the solution is stirred for 30 min. 3-Dibutylaminophenol (0.25 g, 1.1 mmol, 1 equiv.) in DMF (1 mL) is then added dropwise and the mixture is stirred for 1 h at room temperature, following by heating to 80°C for an additional 1 h. After cooling, the reaction was quenched by pouring on ice-water and neutralized with Na_2CO_3 . The yellow suspension was then extracted with EtOAc. The organic layer was washed with brine and dried over Na_2SO_4 . The crude product is purified by silica column chromatography. (Hex/EtOAc 10:1) The product was obtained as an orange oil. (177.5 mg, 0.8 mmol, 62%) ^1H NMR (400 MHz, CDCl_3) δ 11.63 (s, 1H), 9.48 (s, 1H), 7.26 (s, 1H), 6.24 (dd, $J = 8.9, 2.3$ Hz, 1H), 6.05 (d, $J = 2.2$ Hz, 1H), 3.33 – 3.24 (m, 4H), 1.72 – 1.57 (m, 4H), 0.94 (t, $J = 7.4$ Hz, 6H).

^{13}C NMR (101 MHz, CDCl_3) δ 192.12 (s), 164.42 (s), 154.58 (s), 135.39 (s), 105.00 (s), 97.42 (s), 53.25 (s), 20.60 (s), 11.42 (s).

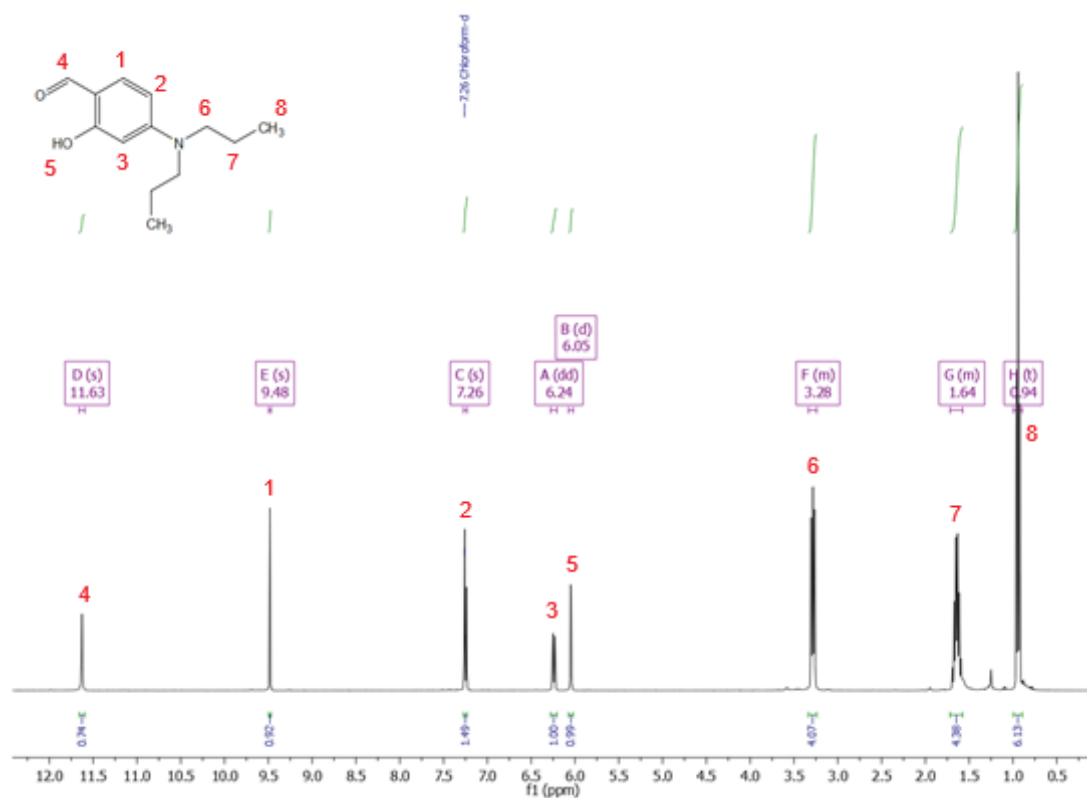


Fig. 6.85. ^1H NMR (CDCl_3) of 4-(dipropylamino)-2-hydroxybenzaldehyde.

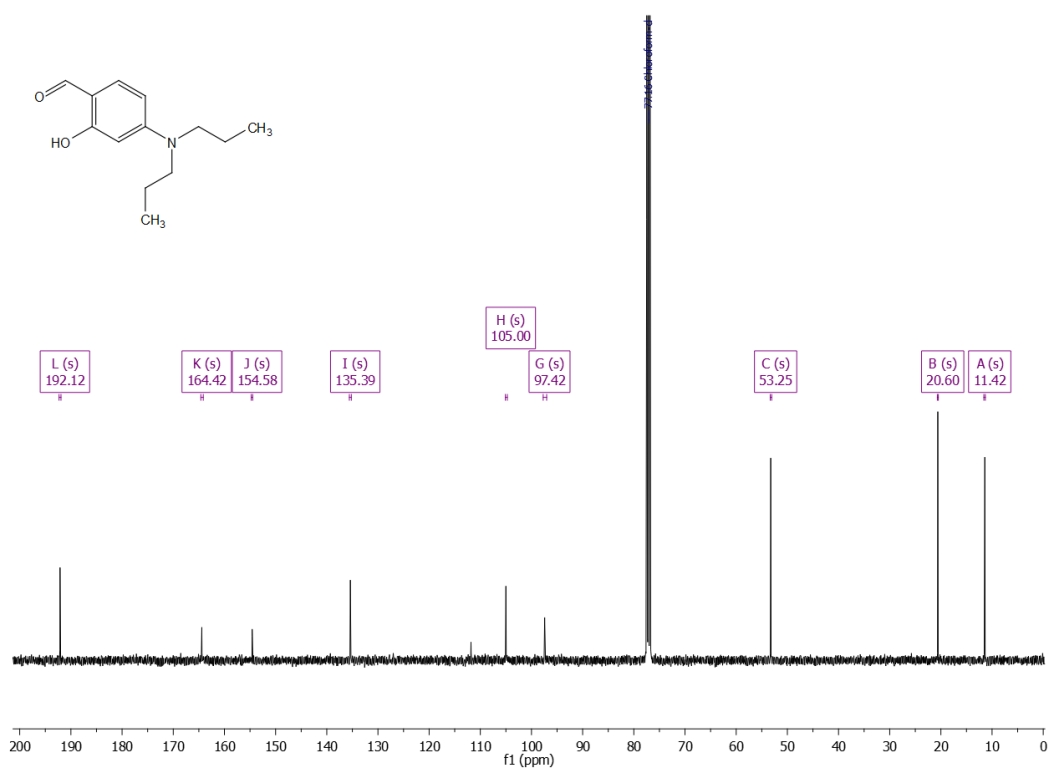
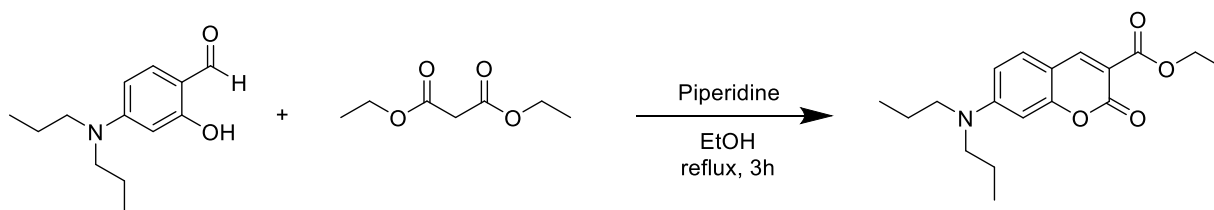


Fig. 6.86. ^{13}C NMR (CDCl_3) of 4-(dipropylamino)-2-hydroxybenzaldehyde.

6.11.2.15. Ethyl 7-(dipropylamino)-2-oxo-2H-chromene-3-carboxylate



According to literature procedures³⁹⁴, a flask was charged with 4-dipropylaminosalicylaldehyde (170 mg, 0.76 mmol, 1 equiv.), diethyl malonate (246.1 mg, 1.5 mmol, 2 equiv.), piperidine (100 μ l) and EtOH (4 mL). The solution was heated to reflux for 3h. After cooling to room temperature, the solvent was evaporated in vacuo and the crude product was purified by silica column chromatography (EtOAc/DCM 1:2). The product was obtained as a very dark yellow oil. (214.4 mg, 0.7 mmol, 88%) Note: the yield is always greter than 100% since redidual diethyl malonate is very hard to remove. This can still be used for the next step. ¹H NMR (400 MHz, CDCl₃) δ 8.42 (s, 1H), 7.34 (d, J = 9.0 Hz, 1H), 6.59 (dd, J = 9.0, 2.4 Hz, 1H), 6.45 (d, J = 2.1 Hz, 1H), 4.37 (q, J = 7.1 Hz, 2H), 3.35 – 3.28 (m, 4H), 1.65 (dq, J = 15.0, 7.4 Hz, 4H), 1.39 (t, J = 7.1 Hz, 3H), 0.96 (t, J = 7.4 Hz, 6H). ¹³C NMR (101 MHz, CDCl₃) δ 166.77 (s), 164.43 (s), 158.52 (s), 153.37 (s), 149.32 (s), 131.02 (s), 109.87 (s), 109.23 (s), 107.91 (s), 97.18 (s), 61.64 (s), 61.32 (s), 53.33 (s), 41.83 (s), 20.50 (s), 14.53 (s), 14.19 (s), 11.40 (s).

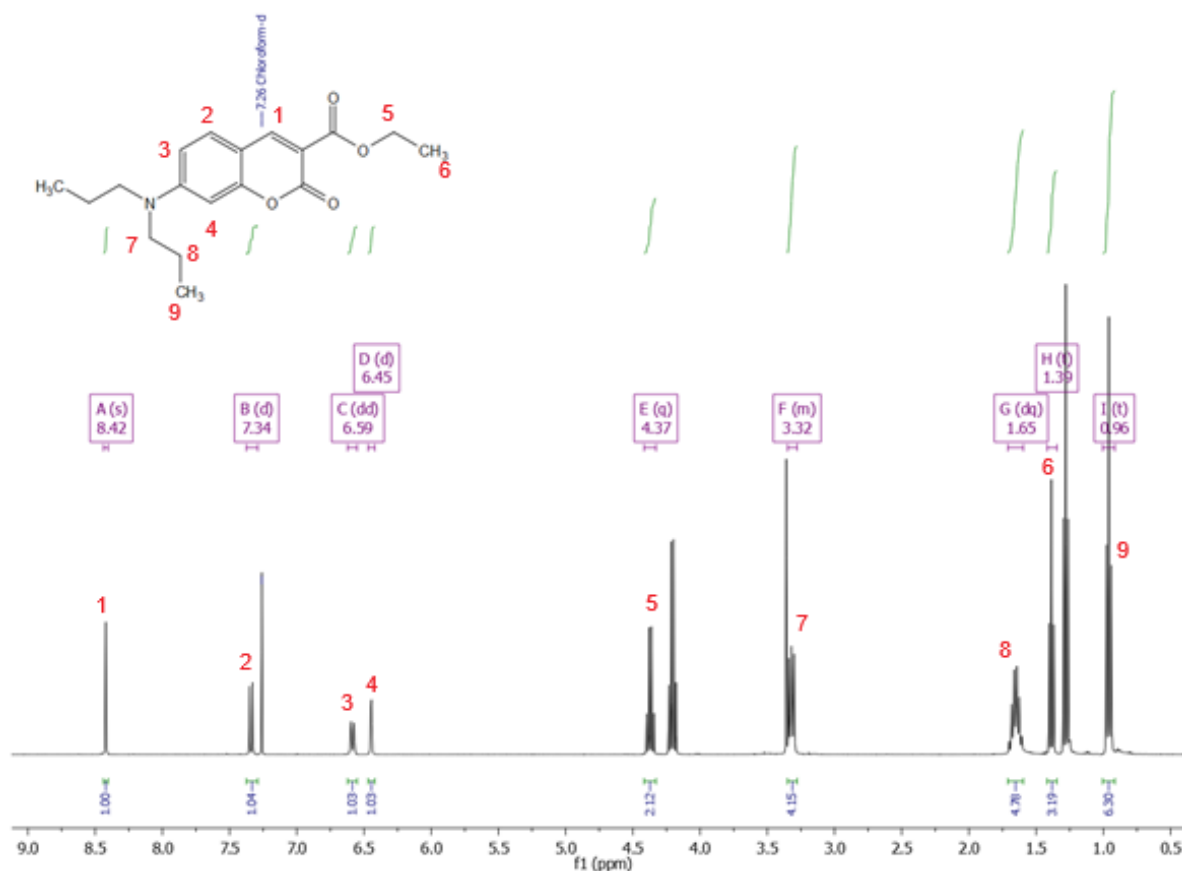


Fig. 6.87. ¹H NMR (CDCl₃) of Ethyl 7-(dipropylamino)-2-oxo-2H-chromene-3-carboxylate.

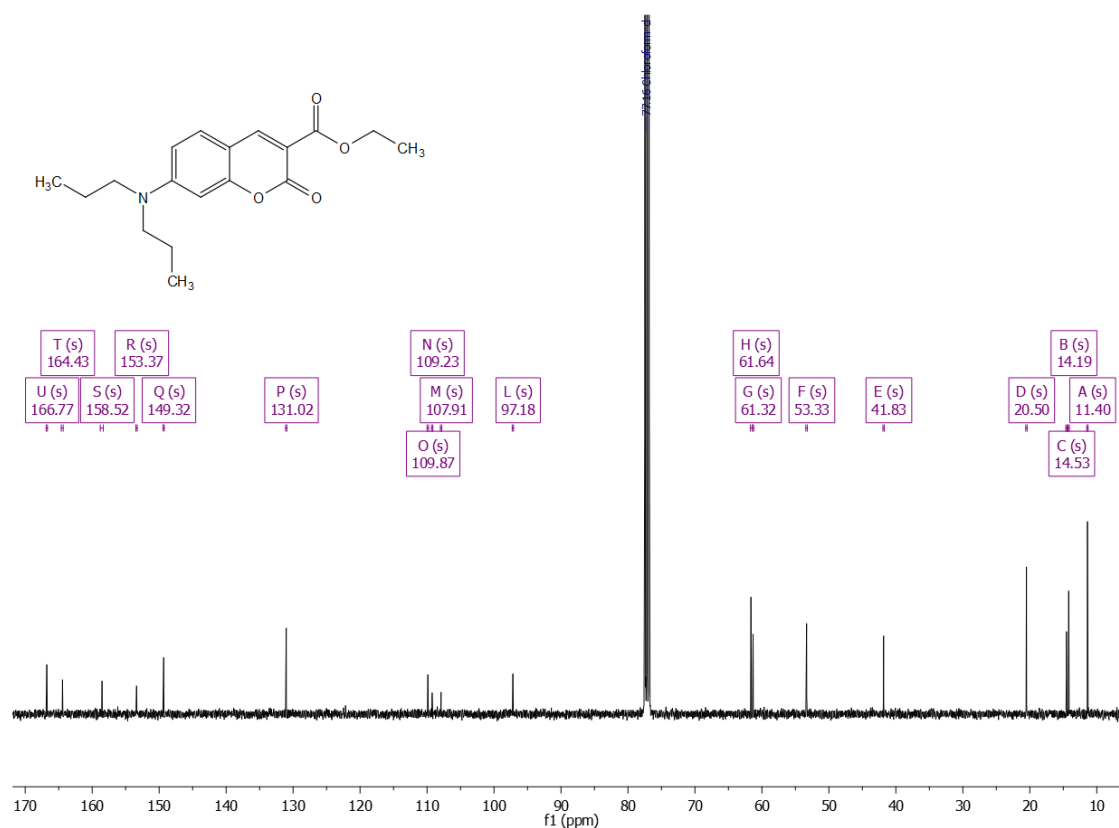
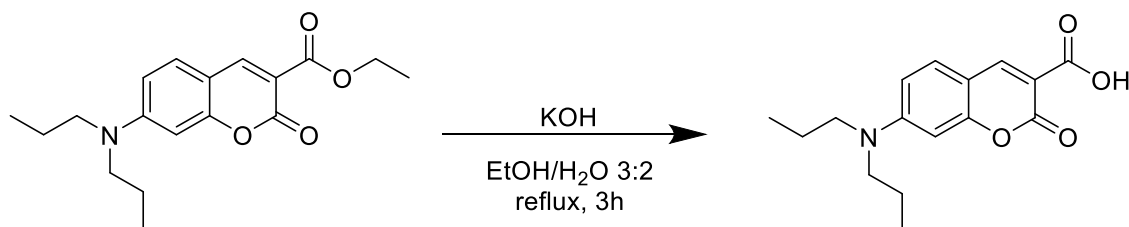


Fig. 6.88. ^{13}C NMR (CDCl_3) of Ethyl 7-(dipropylamino)-2-oxo-2H-chromene-3-carboxylate.

6.11.2.16. 7-(dipropylamino)-2-oxo-2H-chromene-3-carboxylic acid



According to a adapted literature procedure³⁹⁵, a solution of 7-Dipropylaminocoumarin-3-carboxylic acid ethyl ester (220 mg, 0.7 mmol, 1 equiv.), KOH (62.2 mg, 1.1 mmol, 1.6 equiv.) in EtOH/H₂O 3:2 (8 mL) was heated to reflux for 3h. EtOH was evaporated in vacuo and the aqueous phase was acidified with 1M HCl to pH=6. The precipitated solid was removed by filtration and washed with water and hexane. The product was obtained as a dark green powder. (120.9 mg, 0.4 mmol, 61%) ^1H NMR (500 MHz, CDCl_3) δ 12.32 (s, 2H), 8.66 (s, 2H), 7.45 (t, J = 8.1 Hz, 2H), 6.69 (dd, J = 9.1, 2.4 Hz, 2H), 6.51 (d, J = 2.2 Hz, 2H), 3.41 – 3.34 (m, 8H), 1.68 (dq, J = 15.0, 7.5 Hz, 9H), 0.99 (t, J = 7.4 Hz, 12H). ^{13}C NMR (126 MHz, CDCl_3) δ 164.63 (s), 154.32 (s), 150.47 (s), 131.98 (s), 111.21 (s), 108.73 (s), 105.80 (s), 97.22 (s), 53.41 (s), 20.54 (s), 11.41 (s), 0.14 (s), -0.06 (s).

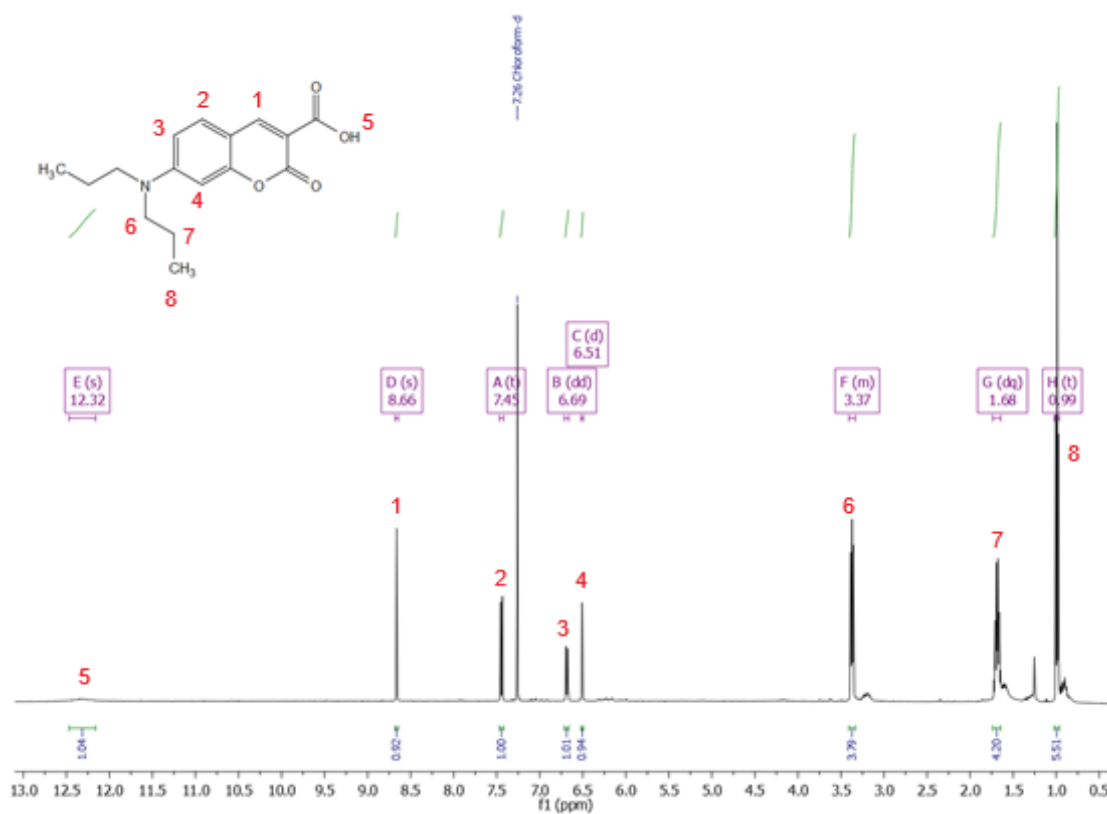


Fig. 6.89. ^1H NMR (CDCl₃) of 7-(dipropylamino)-2-oxo-2H-chromene-3-carboxylic acid

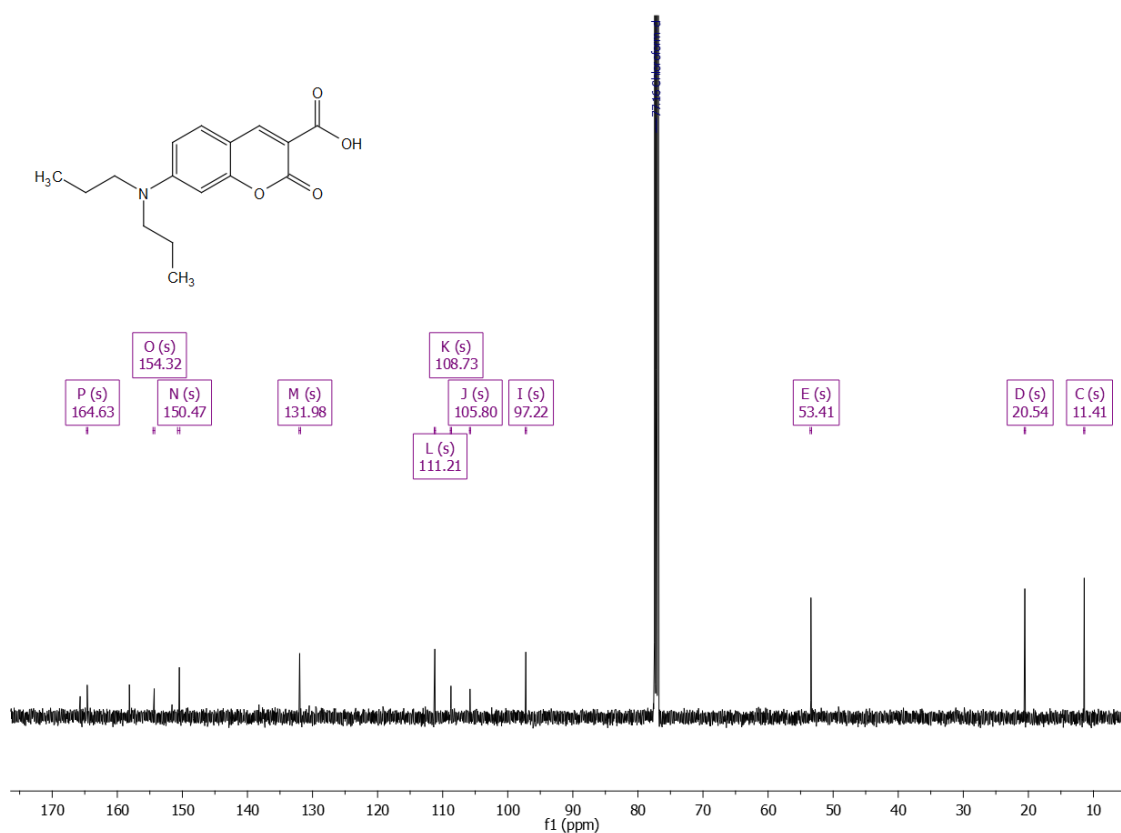
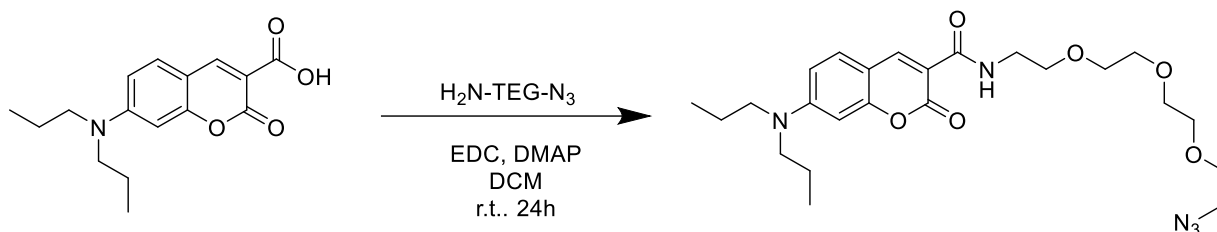


Fig. 6.90. ^{13}C NMR (CDCl₃) of 7-(dipropylamino)-2-oxo-2H-chromene-3-carboxylic acid

6.11.2.17. *N*-(2-(2-(2-(2-azidoethoxy)ethoxy)ethoxy)ethyl)-7-(dipropylamino)-2-oxo-2H-chromene-3-carboxamide (DPC-N₃)



According to a modified literature procedure³⁹⁶, in a glass vial 7-dipropylaminocoumarin-3-carboxylic acid (250 mg, 0.9 mmol, 1 equiv.) was dissolved in dry DCM (5 mL). To this solution was added 11-Azido-TEG-NH₂ (245.2 mg, 223 μ l, 0.2 mmol, 1.3 equiv.), 4-DMAP (126.7 mg, 1.0 mmol, 1.2 equiv.) and EDC HCl (126.7 mg, 1.0 mmol, 1.1 equiv.). The vial was closed and the mixture was stirred overnight under an N₂ atmosphere. The crude product was purified by silica gel column chromatography (CHCl₃/MeOH 10:1). The product was isolated as an intense yellow oil. (79.6 mg, 0.16 mmol, 94%)
¹H NMR (400 MHz, MeOD) δ 9.21 (s, 1H), 8.62 (s, 1H), 7.54 (d, J = 9.0 Hz, 1H), 6.79 (dd, J = 9.0, 2.5 Hz, 1H), 6.53 (d, J = 2.3 Hz, 1H), 3.69 – 3.55 (m, 14H), 3.45 – 3.39 (m, 4H), 3.33 (dd, J = 8.8, 4.0 Hz, 2H), 1.74 – 1.60 (m, 4H), 1.02 – 0.94 (m, 6H). ¹³C NMR (101 MHz, MeOD) δ 166.39 – 164.08 (m), 161.02 – 157.15 (m), 157.37 – 153.49 (m), 149.29 (s), 132.53 (s), 111.85 (s), 110.46 – 109.93 (m), 109.68 – 109.30 (m), 97.49 (s), 71.93 – 71.46 (m), 53.87 (s), 51.76 (s), 40.55 (s), 21.40 (s), 11.43 (s).
 ESI-MS: Calc. for [M+H]⁺ 490.2630; found: 490.2620

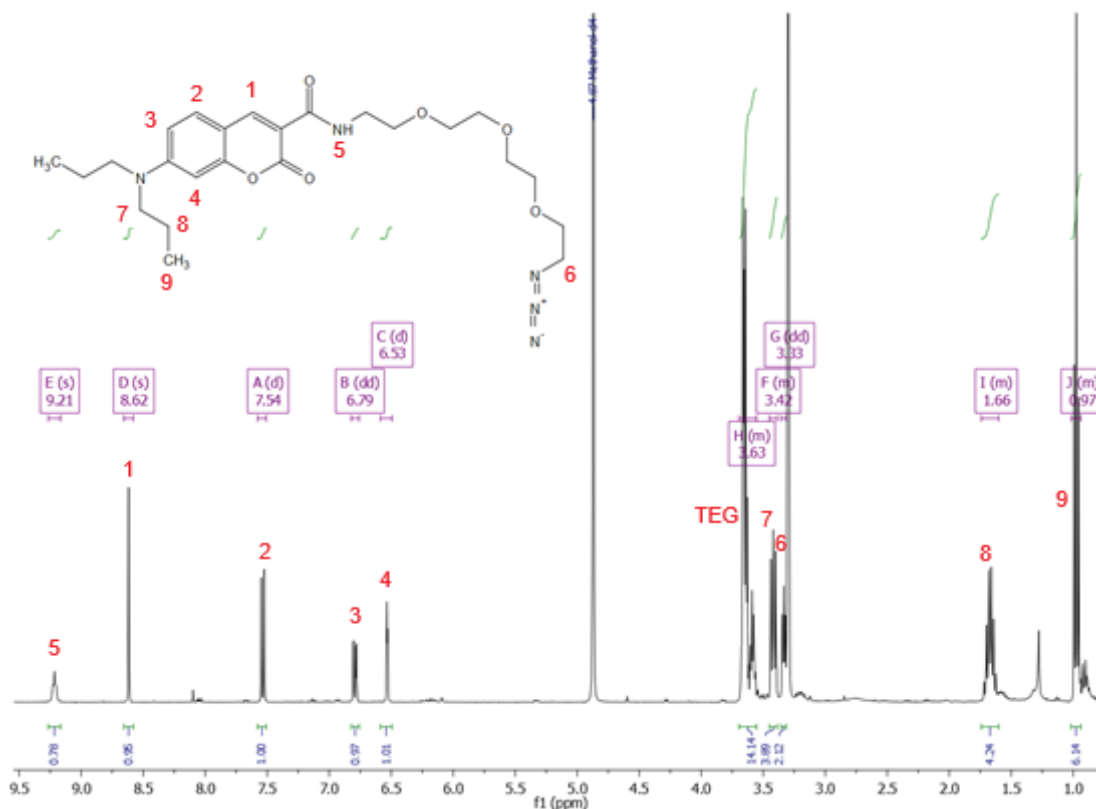


Fig. 6.91. ¹H NMR (MeOD) of DPC-N₃.

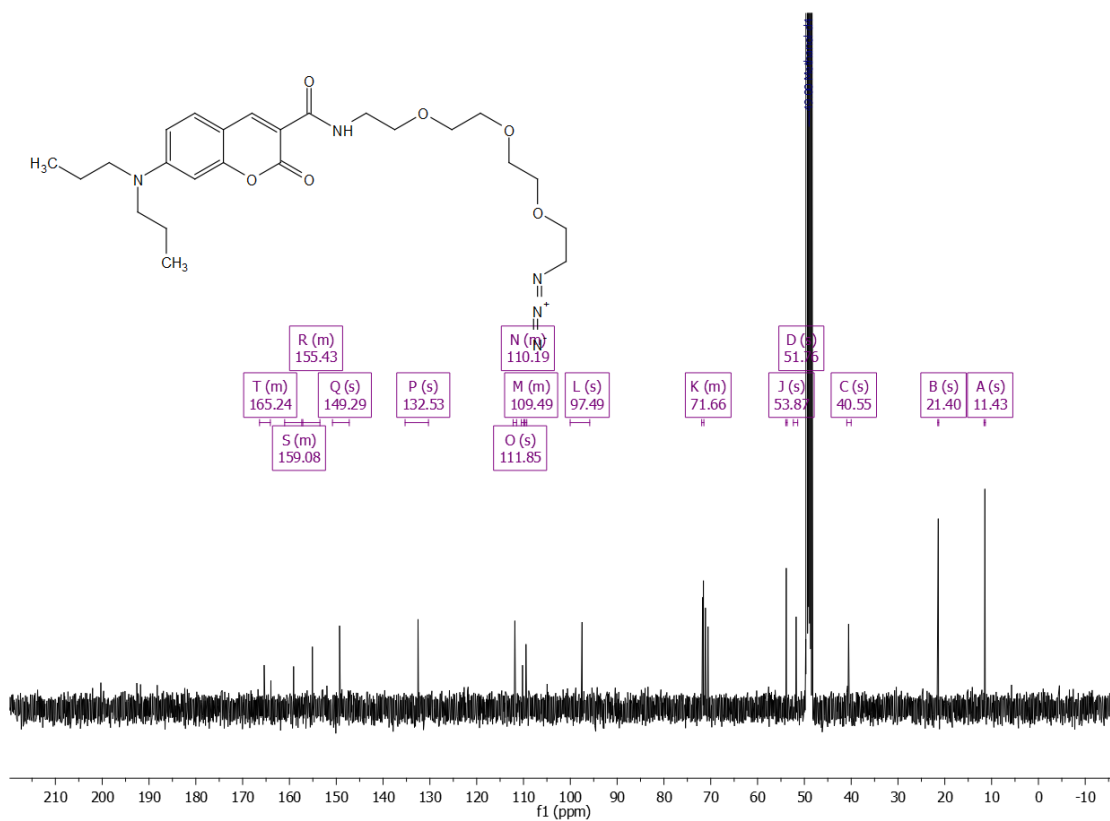


Fig. 6.92. ^{13}C NMR (MeOD) of DPC- N_3 .

PG: 151_001 #32-41 RT: 0.29-0.37 AV: 10 NL: 1.36E8
T: FTMS + p ESI Full ms [100.0000-1500.0000]

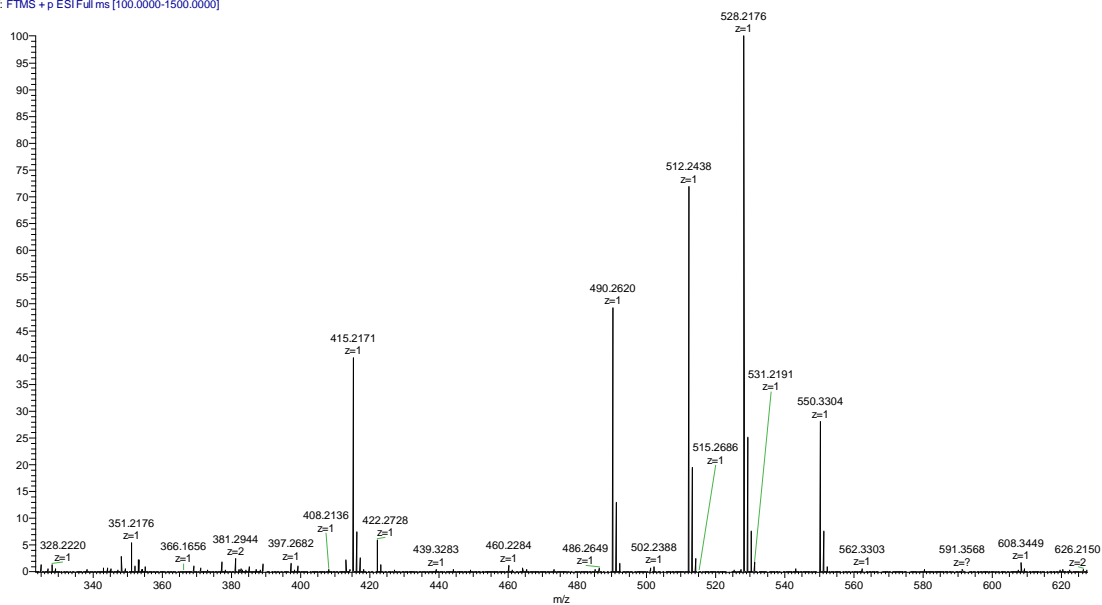
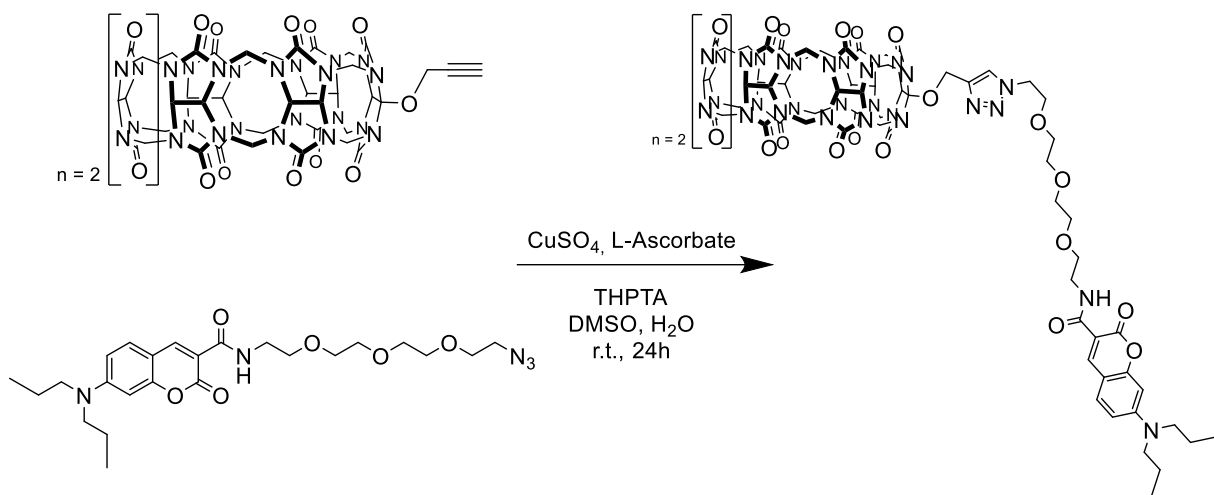


Fig. 6.93. ESI-MS of DPC- N_3 . The peak 490.2620^+ corresponds to $[\text{M}+\text{H}]^+$.

6.11.2.18. CB7-dipropylcoumarin (CB7-DPC)



CB7-(OPr) (17.4 mg, 14.4 μmol , 1 equiv.), DPC-N₃ (12.6 mg, 25.8 μmol , 1.8 equiv.), and THPTA (24.8 mg, 56 μmol , 4 equiv.) were placed in a vial and dissolved in 1400 μL DMSO. After closing of the vial, it was placed in ultrasound then purged with N₂. In a second vial, 5.6 mL 55% DMSO aqueous solution was also purged with N₂, then CuSO₄ (9.1 mg, 56.0 μmol , 4 equiv.) was added to the 55% DMSO followed by sodium L-ascorbate (19.8 mg, 100.0 μmol , 7 equiv.) while it was taken care for least oxygen exposure as possible. The click solution was placed in the ultrasound for approx. 1 min. while a color change to yellow (Cu⁺ forming) was observed. The two solutions were mixed and stirred at room temperature for 24 h under an N₂ atmosphere. Afterwards, the product was precipitated by dropwise addition of the reaction solution in 50 mL MeOH. The solid was then washed with MeOH (3 \times 25 mL). Purification is done by preparative HPLC. The product elutes after 23.0 min (prep. method 3). The product was obtained as a fluffy yellow solid after freeze-dry. (13.6 mg, 7.8 μmol , 55%) ¹H NMR (400 MHz, CD₃CN) δ 8.55 (s, 1H), 8.00 (s, 1H), 7.52 (d, J = 8.9 Hz, 1H), 6.76 (d, J = 8.5 Hz, 1H), 6.49 (s, 1H), 5.81 – 5.24 (m, 28H), 4.51 (d, J = 4.3 Hz, 4H), 3.52 (t, J = 13.0 Hz, 14H), 3.34 (d, J = 7.0 Hz, 4H), 1.58 (d, J = 6.9 Hz, 4H), 1.22 (s, 4H), 0.88 (t, J = 7.0 Hz, 6H). Due to complex structure, precise peak assignment was not possible. It was not possible to measure ¹³C NMR even after multiple attempts. ESI MS: Calc. for [M+C₈mim₂]²⁺: 991.5099; found: 991.4276. Analyt. HPLC (analyt. method 1) = 18.0 min

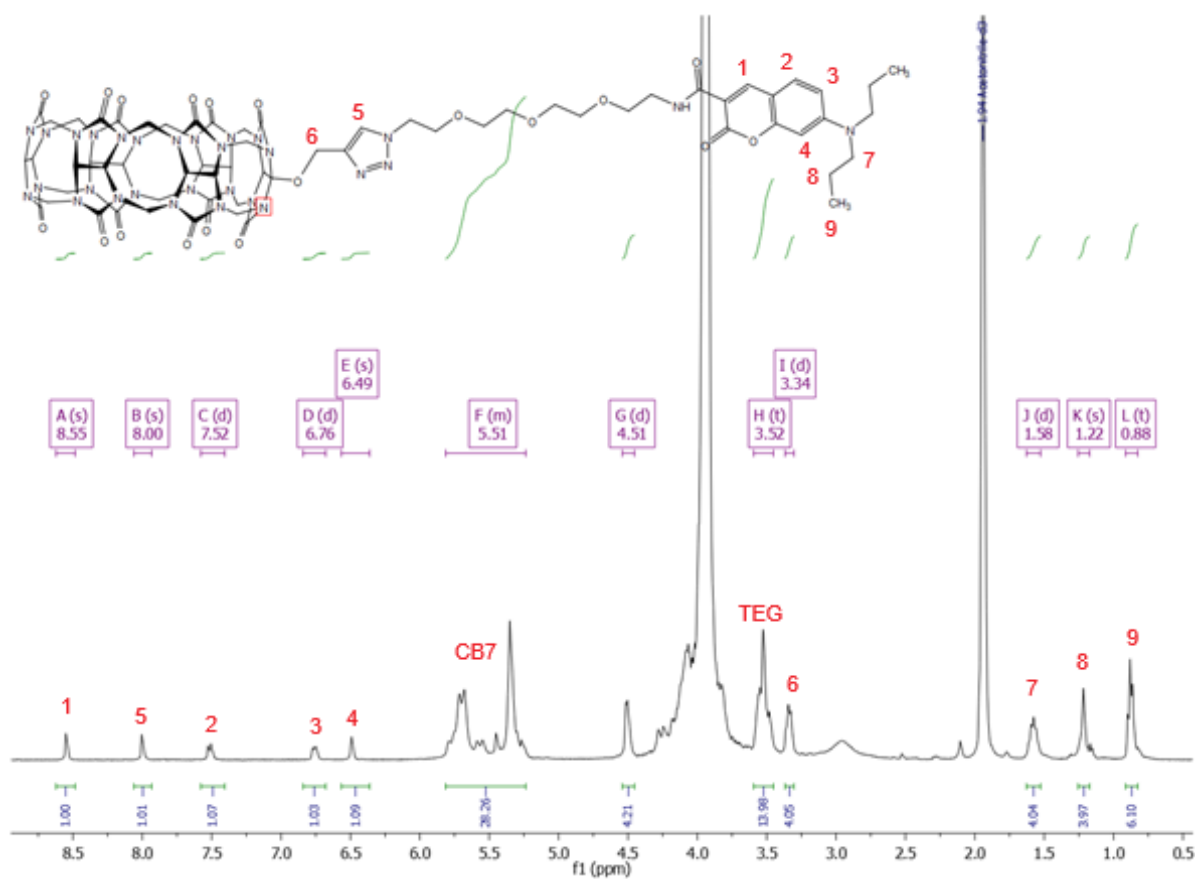


Fig. 6.94. ^1H NMR ($\text{CD}_3\text{CN}/\text{D}_2\text{O}$ 3:2) of CB7-DPC.

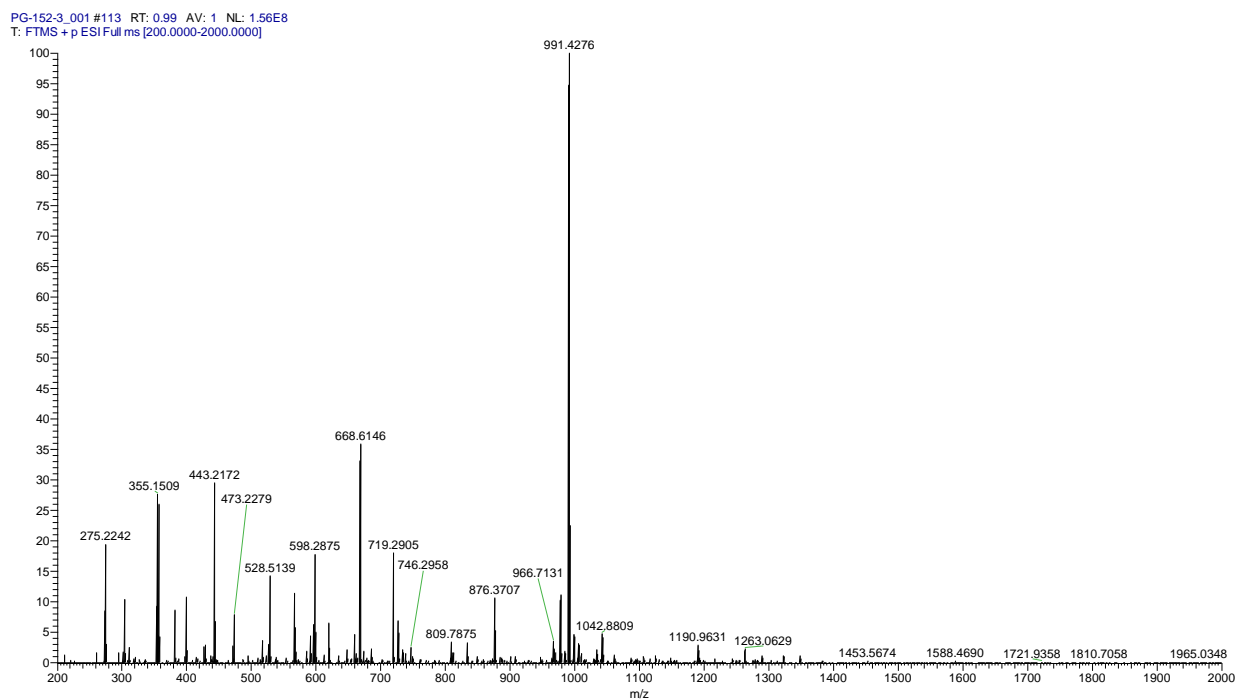


Fig. 6.95. ESI-MS of CB7-DMC measured as $[\text{M}+\text{C}_8\text{mim}_2]^{2+}$ adduct.

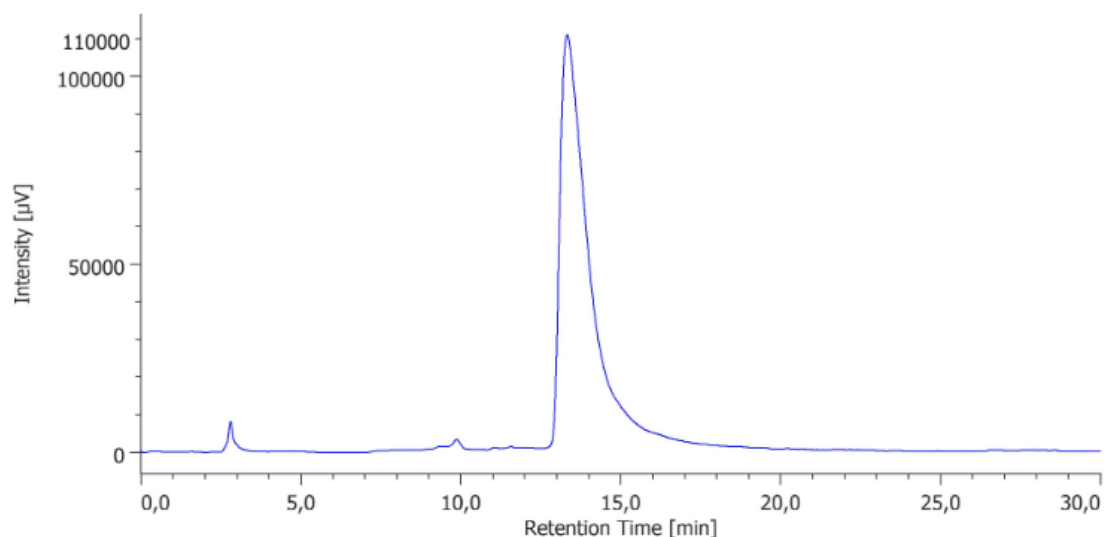
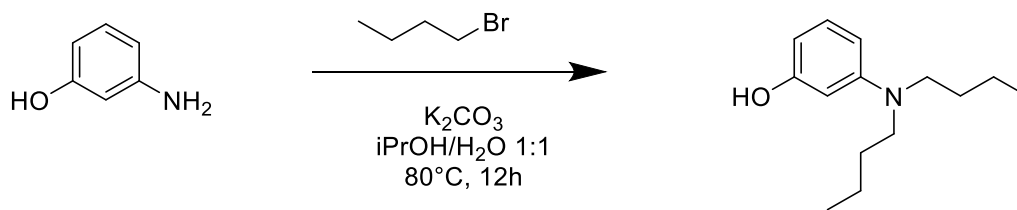


Fig. 6.96. Analytical trace of CB7-DPC (anal. method 1).

6.11.2.19. 3-(dibutylamino)phenol



According to literature procedures³⁸¹, 3-aminophenol (1 g, 9.2 mmol, 1 equiv.) and 1-bromobutane (3.14 g, 22.9 mmol, 2.5 equiv., 2.5 mL) were dissolved in *i*-PrOH/H₂O 1:1 (v/v) (20 mL). To this solution potassium carbonate (2.53 g, 18.3 mmol, 2 equiv.) was added and the mixture was stirred at 80°C overnight. The solvent was evaporated in vacuo and the residue diluted with water (20 mL). The mixture was extracted with EtOAc and the organic phase was washed with brine and dried over Na₂SO₄. The crude product is purified by silica column chromatography (n-Hex/EtOAc 10:1). The product was obtained as a deep-red oil. (1.3228 g, 5.9 mmol, 66%) ¹H NMR (400 MHz, CDCl₃) δ 7.05 (dd, *J* = 14.7, 6.6 Hz, 1H), 6.24 (dd, *J* = 8.4, 2.0 Hz, 1H), 6.13 (d, *J* = 9.8 Hz, 1H), 6.11 (d, *J* = 7.9 Hz, 1H), 4.76 (s, 1H), 3.27 – 3.20 (m, 4H), 1.56 (ddd, *J* = 12.1, 8.6, 6.6 Hz, 4H), 1.41 – 1.29 (m, 4H), 0.95 (t, *J* = 7.3 Hz, 6H). ¹³C NMR (101 MHz, CDCl₃) δ 156.83 (s), 149.93 (s), 130.16 (s), 104.87 (s), 102.26 (s), 98.77 (s), 51.02 (s), 29.53 (s), 20.49 (s), 14.14 (s). ESI-MS: calc. for [M+H]⁺: 222.1824; found: 222.1834. HPLC-MS: 11.9 min, m=222.2⁺

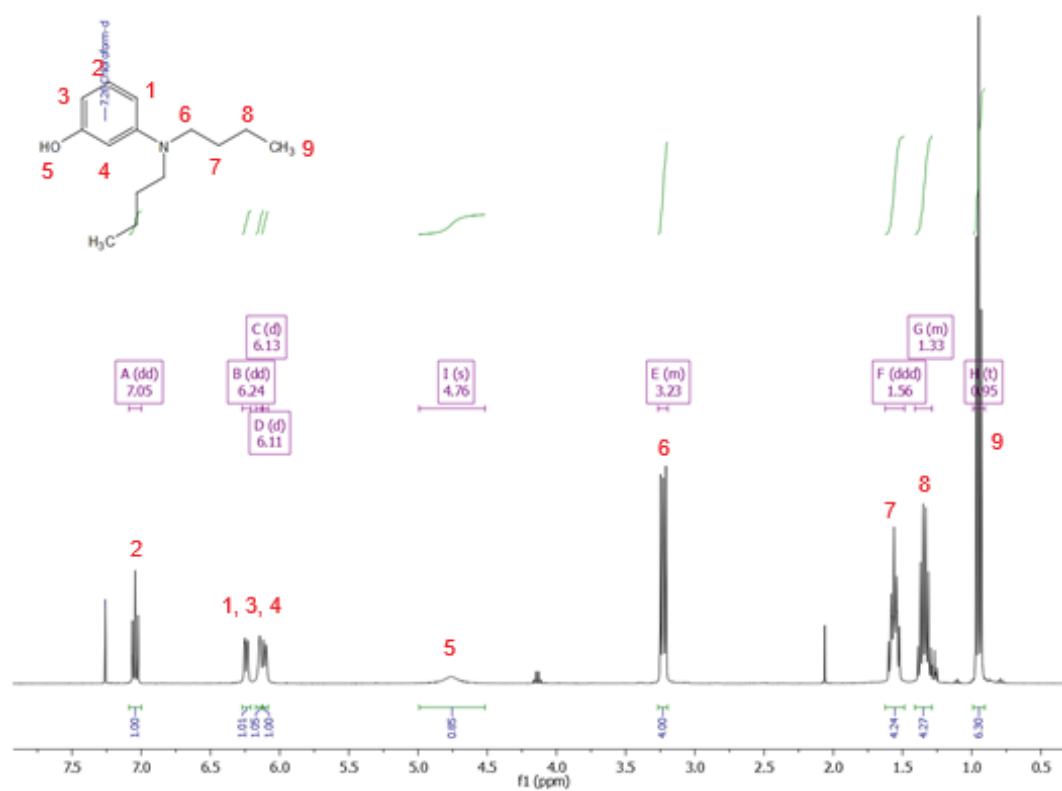


Fig. 6.97. ^1H NMR (CDCl_3) of 3-(dibutylamino)phenol.

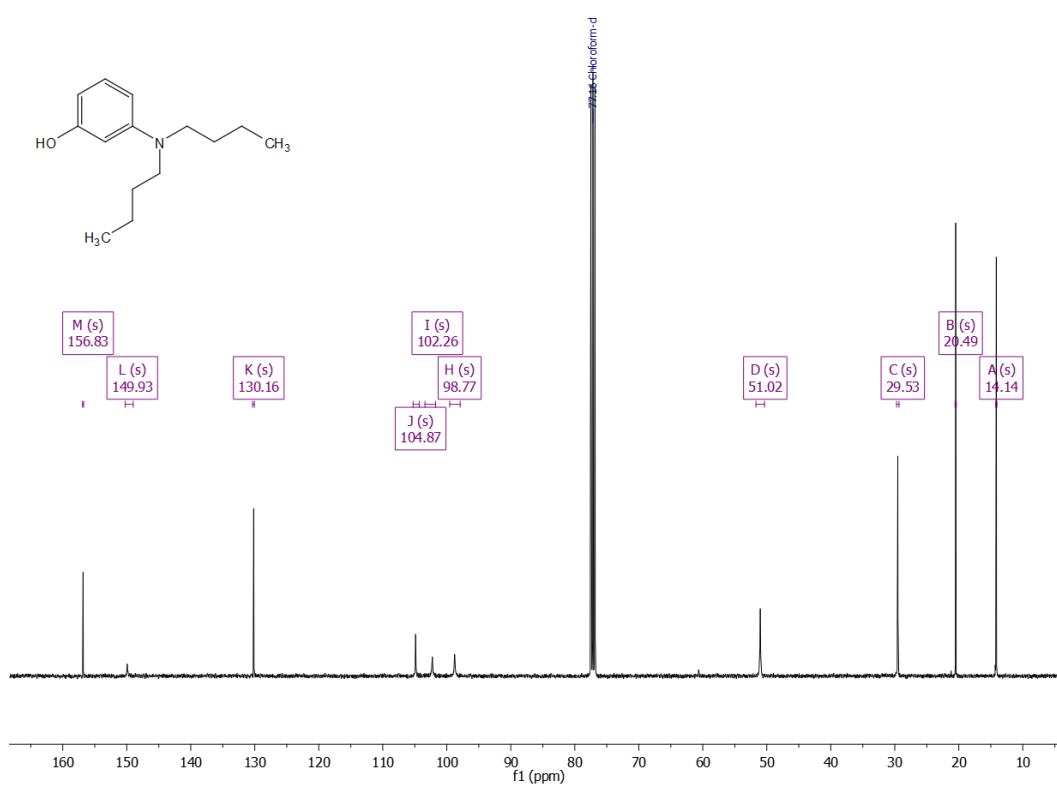


Fig. 6.98. ^{13}C NMR (CDCl_3) of 3-(dibutylamino)phenol.

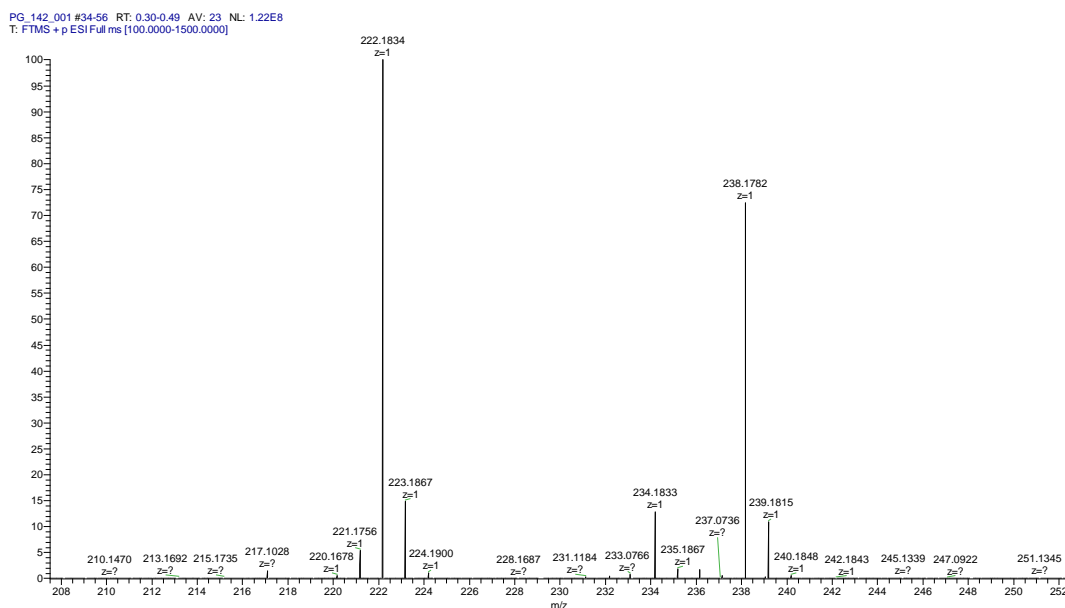
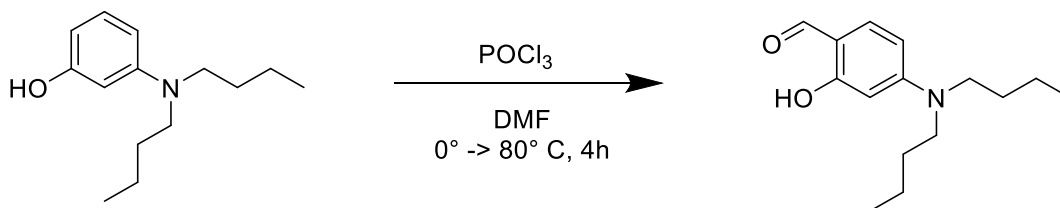


Fig. 6.99. ESI-MS of 3-(dibutylamino)phenol. The peak 222.1834⁺ corresponds to [M+H]⁺.

6.11.2.20. 4-(dibutylamino)-2-hydroxybenzaldehyde



According to literature procedures³⁹⁹, POCl₃ (0.69 g, 4.5 mmol, 4 equiv., 420 μl) was added to ice-cold DMF (2 mL) and the solution is stirred for 5 min. A color change can be observed. 3-dibutylaminophenol (0.25 g, 1.1 mmol, 1 equiv.) in DMF (1 mL) is then added dropwise and the mixture is stirred for 1 h at room temperature, following by heating to 80° C for an additional h. After cooling, the reaction was quenched by pouring on ice-water and the mixture is neutralized with Na₂CO₃. The suspension was extracted with EtOAc. The organic layer was washed with brine and dried over Na₂SO₄. The crude product is purified by silica column chromatography. (Hex/EtOAc 10:1) The product is obtained as a light orange oil. (208.5 mg, 0.8 mmol, 74%) ¹H NMR (400 MHz, CDCl₃) δ 11.67 (s, 1H), 9.50 (s, 1H), 7.28 (d, J = 0.9 Hz, 1H), 6.25 (dd, J = 8.9, 2.4 Hz, 1H), 6.06 (d, J = 2.4 Hz, 1H), 3.37 – 3.30 (m, 4H), 1.62 (tt, J = 7.8, 6.7 Hz, 5H), 1.38 (dq, J = 14.7, 7.4 Hz, 4H), 0.99 (t, J = 7.3 Hz, 6H). ¹³C NMR (101 MHz, CDCl₃) δ 192.01 (s), 164.42 (s), 154.66 (s), 135.39 (s), 111.56 (s), 104.75 (s), 97.06 (s), 51.16 (s), 29.51 (s), 20.36 (s), 14.03 (s). ESI-MS: Calc. for [M+H]⁺: 250.1799; found: 250.1781. HPLC-MS: 12.715 min, m=250.1⁺

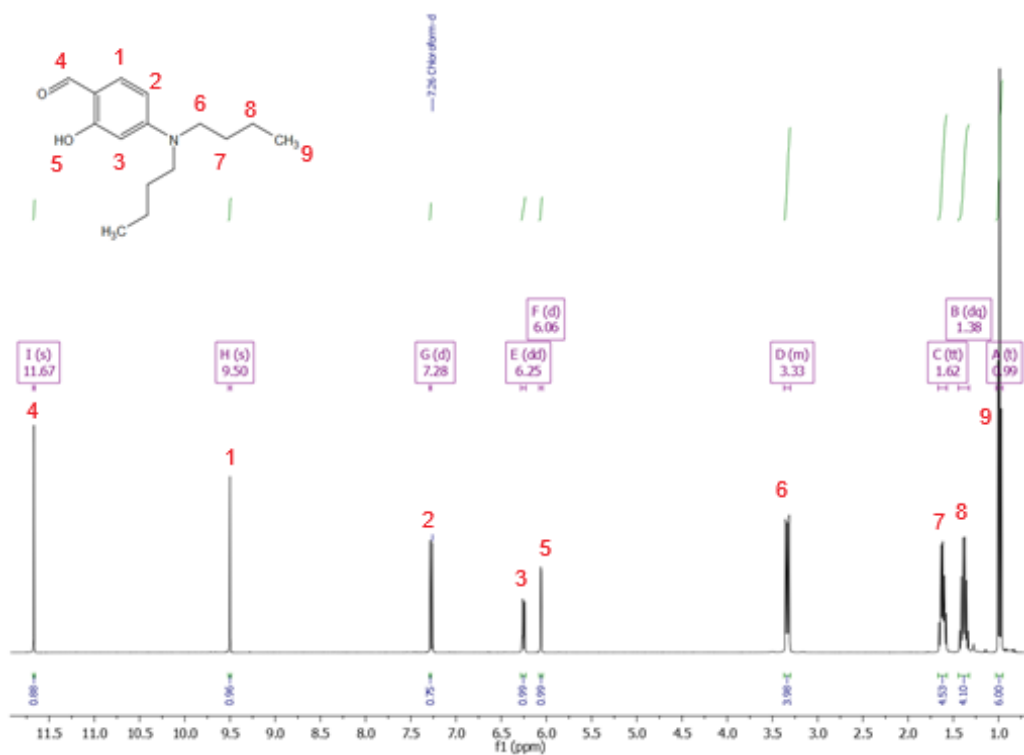


Fig. 6.100. ^1H NMR (CDCl_3) of 4-(dibutylamino)-2-hydroxybenzaldehyde.

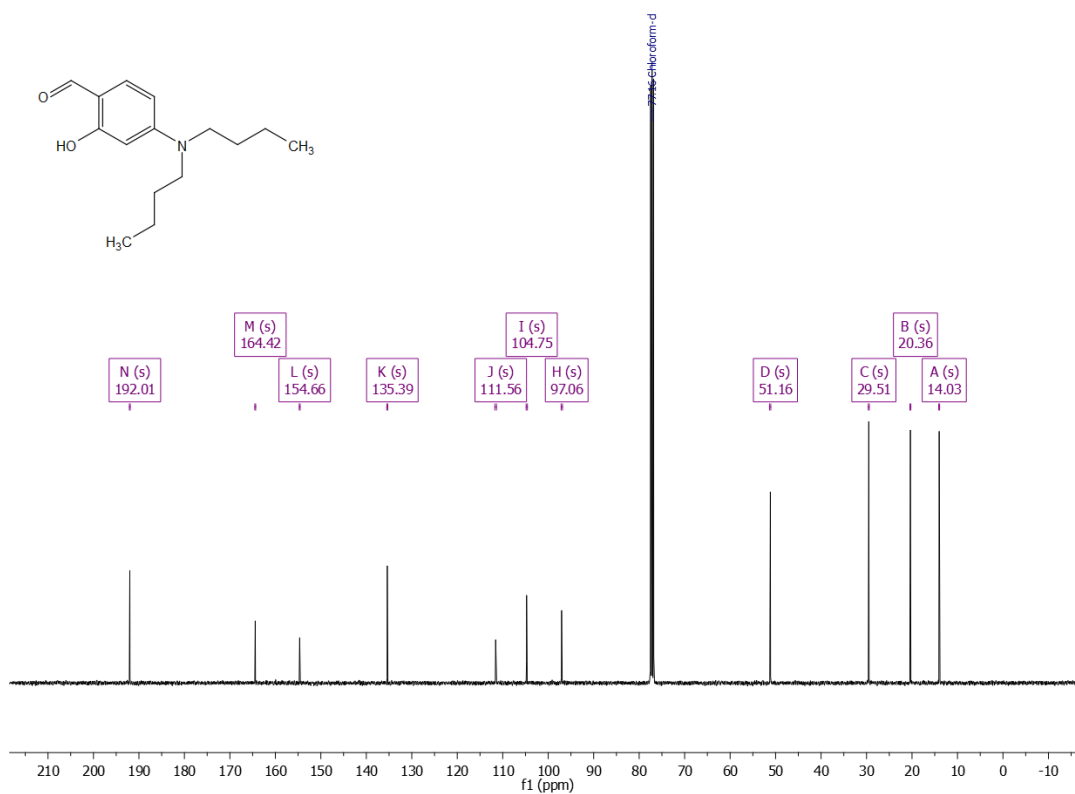


Fig. 6.101. ^{13}C NMR (CDCl_3) of 4-(dibutylamino)-2-hydroxybenzaldehyde.

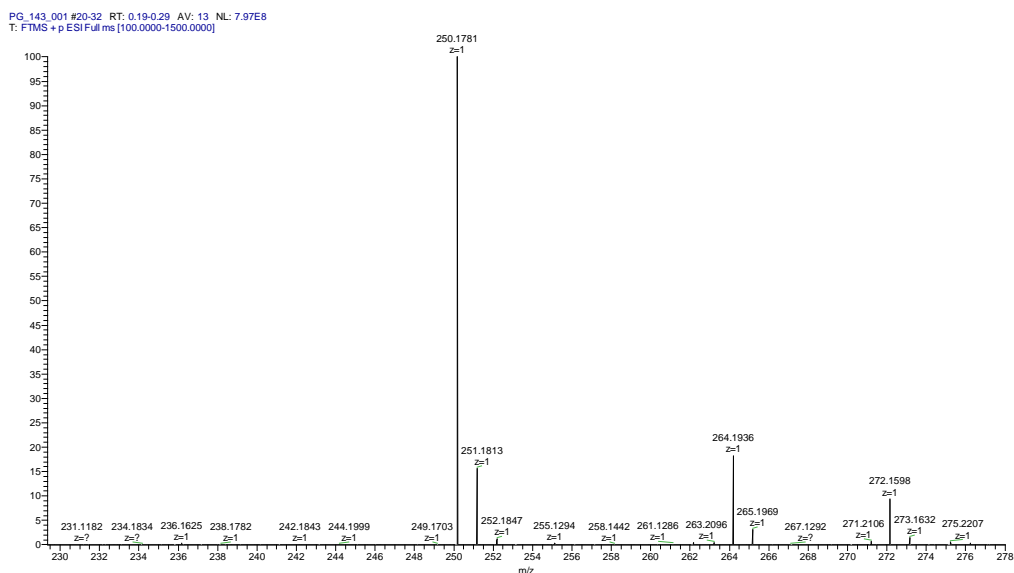


Fig. 6.102. ESI-MS of 4-(dibutylamino)-2-hydroxybenzaldehyde. The peak 250.1781⁺ corresponds to [M+H]⁺.

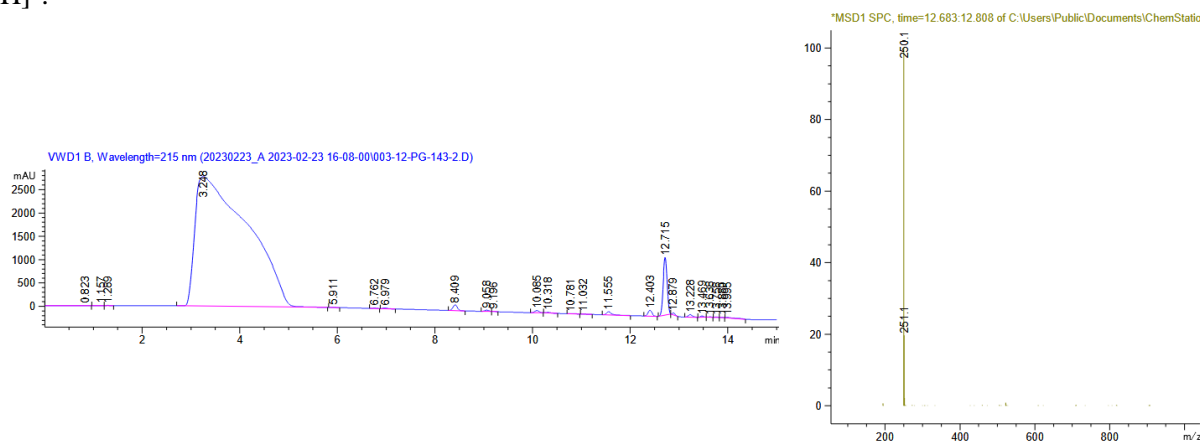
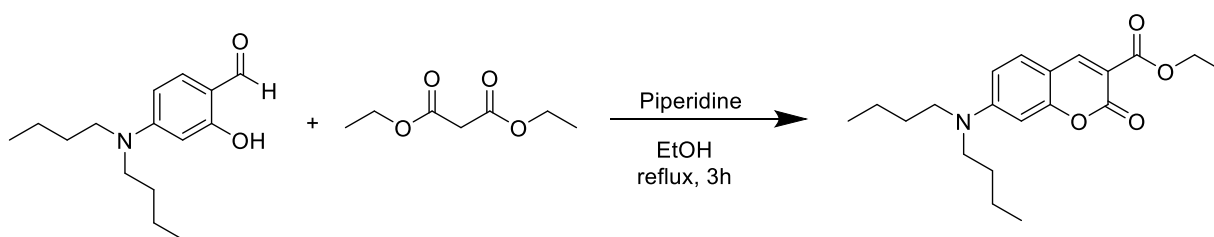


Fig. 6.103. Analytical UV trace at $\lambda=215$ nm (left) and observed mass at 12.7 min (right).

6.11.2.21. Ethyl 7-(dibutylamino)-2-oxo-2H-chromene-3-carboxylate



According to literature procedures³⁹⁴, a flask was charged with 4-diethylaminosalicylaldehyde (500 mg, 0.8 mmol, 1 equiv.), diethyl malonate (642.4 mg, 4.0 mmol, 2 equiv.), piperidine (100 μ l) and EtOH (60 mL). The solution was heated to reflux for 3h. After cooling to room temperature, the solvent was evaporated in vacuo and the crude product was purified by silica column chromatography (EtOAc/DCM 1:2). The product was obtained as a yellow-green oil. (519.5 mg, 1.5 mmol, 75%). ¹H NMR (400 MHz, CDCl₃)

(t, $J = 7.3$ Hz, 6H). ^{13}C NMR (101 MHz, CDCl_3) δ 158.19 (s), 148.99 (s), 130.73 (s), 109.67 (s), 96.98 (s), 61.33 (s), 61.02 (s), 51.20 (s), 41.52 (s), 29.02 (s), 20.04 (s), 14.22 (s), 13.80 (d, $J = 18.1$ Hz). HPLC-MS: 12.6 min, $m=346.1^+$

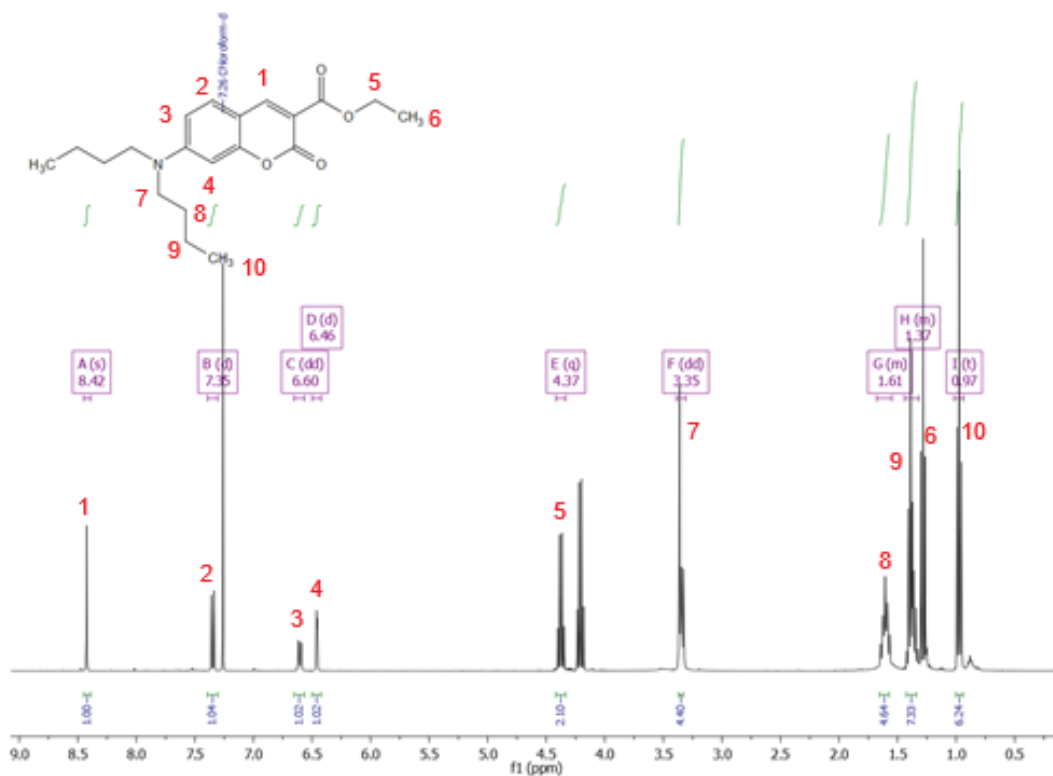


Fig. 6.104. ^1H NMR (CDCl_3) of Ethyl 7-(dibutylamino)-2-oxo-2H-chromene-3-carboxylate.



Fig. 6.105. ^{13}C NMR (CDCl_3) of Ethyl 7-(dibutylamino)-2-oxo-2H-chromene-3-carboxylate.

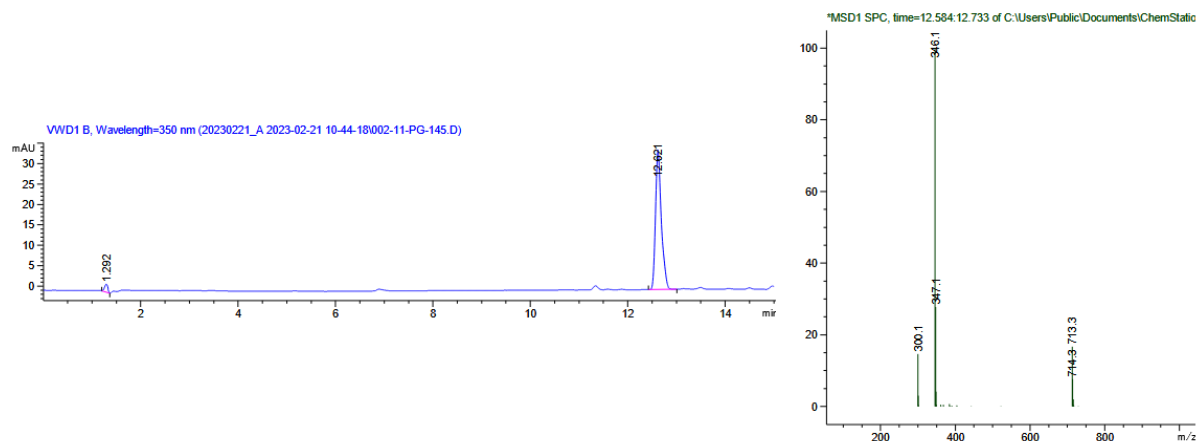
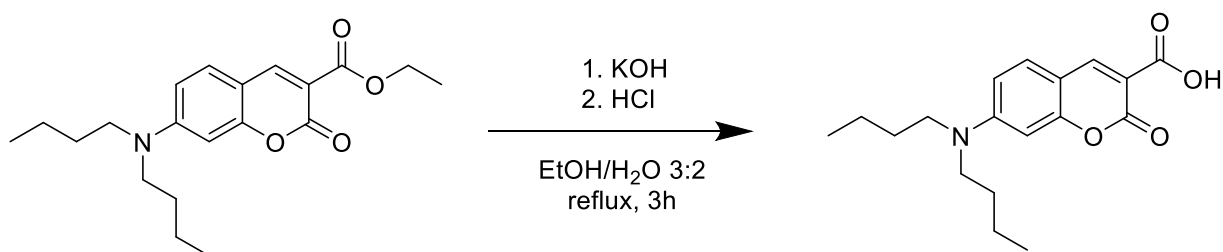


Fig. 6.106. Analytical trace at $\lambda=350$ nm (left) and observed mass at 12.6 min (right).

6.11.2.22. 7-(dibutylamino)-2-oxo-2H-chromene-3-carboxylic acid



According to literature procedures³⁹⁵, a solution of 7-dibutylaminocoumarin-3-carboxylic acid ethyl ester (700 mg, 2.4 mmol, 1 equiv.), KOH (217.2 mg, 3.9 mmol, 1.6 equiv.) in EtOH/H₂O 3:2 (30 mL) was heated to reflux for 3h. EtOH was evaporated in vacuo and the aqueous phase was first diluted with water and acidified with 1M HCl to pH=6. The precipitated solid was removed by filtration and washed with water and hexane. The product was isolated as a dark green solid. (391.5 mg, 1.2 mmol, 61%) ¹H NMR (500 MHz, CDCl₃) δ 12.34 (s, 1H), 8.66 (s, 1H), 7.44 (d, J = 9.0 Hz, 1H), 6.68 (d, J = 7.4 Hz, 1H), 6.50 (s, 1H), 3.44 – 3.36 (m, 4H), 1.63 (dt, J = 15.3, 7.7 Hz, 4H), 1.44 – 1.36 (m, 4H), 0.99 (t, J = 7.3 Hz, 6H). ¹³C NMR (126 MHz, CDCl₃) δ 132.00 (s), 111.18 (s), 97.17 (s), 77.41 (s), 77.16 (s), 76.91 (s), 51.53 (s), 29.36 (s), 20.35 (s), 14.02 (s).

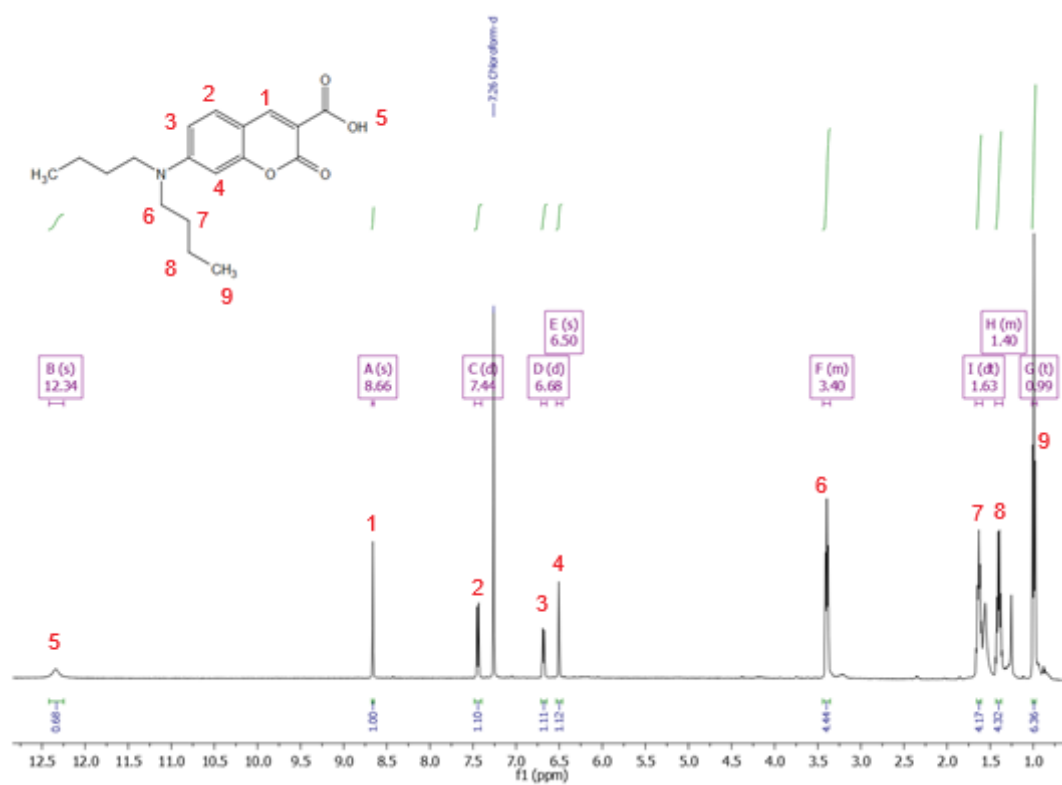


Fig. 6.107. ¹H NMR (CDCl₃) of 7-(dibutylamino)-2-oxo-2H-chromene-3-carboxylic acid.

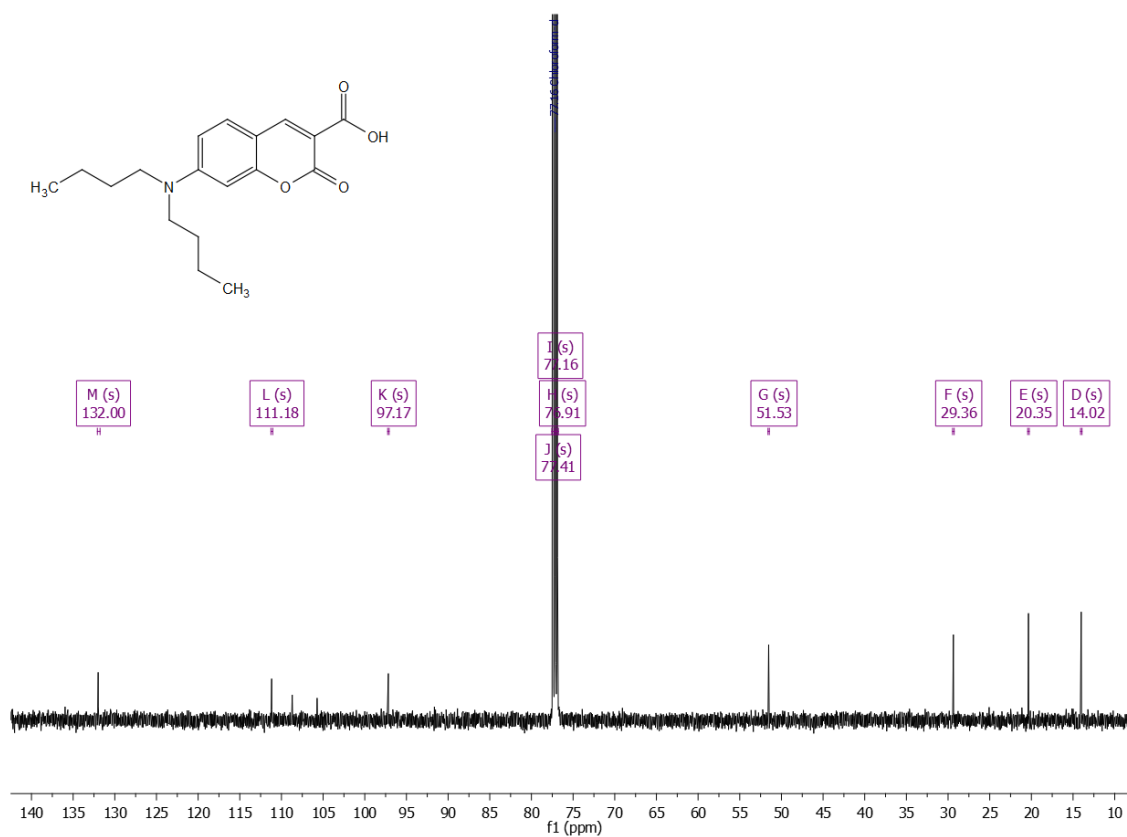
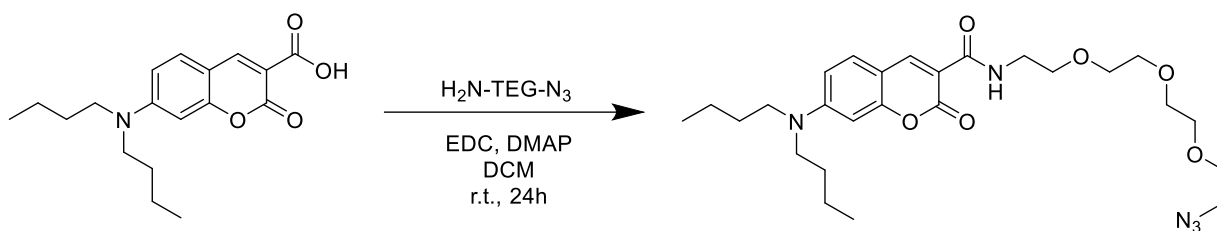


Fig. 6.108. ¹³C NMR (CDCl₃) of 7-(dibutylamino)-2-oxo-2H-chromene-3-carboxylic acid.

6.11.2.23. N-(2-(2-(2-(2-azidoethoxy)ethoxy)ethoxy)ethyl)-7-(dibutylamino)-2-oxo-2H-chromene-3-carboxamide (DBC-N₃)



According to literature procedures³⁹⁶, in a glass vial 7-dibutylaminocoumarin-3-carboxylic acid (300 mg, 0.3 mmol, 1 equiv.) was dissolved in dry DMF (5 mL). To this solution was added 11-Azido-TEG-NH₂ (268.2 mg, 1.2 mmol, 1.3 equiv.), 4-DMAP (138.6 mg, 1.2 mmol, 1.2 equiv.) and EDC HCl (199.3 mg, 1.0 mmol, 1.1 equiv.). The vial was closed and the mixture was stirred overnight under an N₂ atmosphere. The crude product was purified by silica gel column chromatography (CHCl₃/MeOH 20:1). The product was obtained as a dark green oil. ¹H NMR (500 MHz, CDCl₃) δ 9.01 (s, 1H), 8.69 (s, 1H), 7.41 (d, J = 9.0 Hz, 1H), 6.61 (dd, J = 8.9, 2.3 Hz, 1H), 6.46 (d, J = 1.9 Hz, 1H), 3.71 – 3.66 (m, 9H), 3.41 – 3.38 (m, 2H), 3.38 – 3.33 (m, 3H), 1.65 – 1.57 (m, 5H), 1.38 (dq, J = 14.8, 7.3 Hz, 4H), 0.98 (t, J = 7.4 Hz, 5H). ¹³C NMR (126 MHz, CDCl₃) δ 148.16 (s), 131.13 (s), 70.84 (dd, J = 13.3, 8.6 Hz), 70.08 (d, J = 18.0 Hz), 51.34 (s), 50.84 (s), 39.63 (s), 29.37 (s), 20.37 (s), 14.05 (s). ESI-MS: Calc. for [M+H]⁺: 518.2915, found: 518.2927; Calc. for [M+Na]⁺: 540.2733, found: 540.2745. HPLC-MS: 12.5 min, 518.3⁺

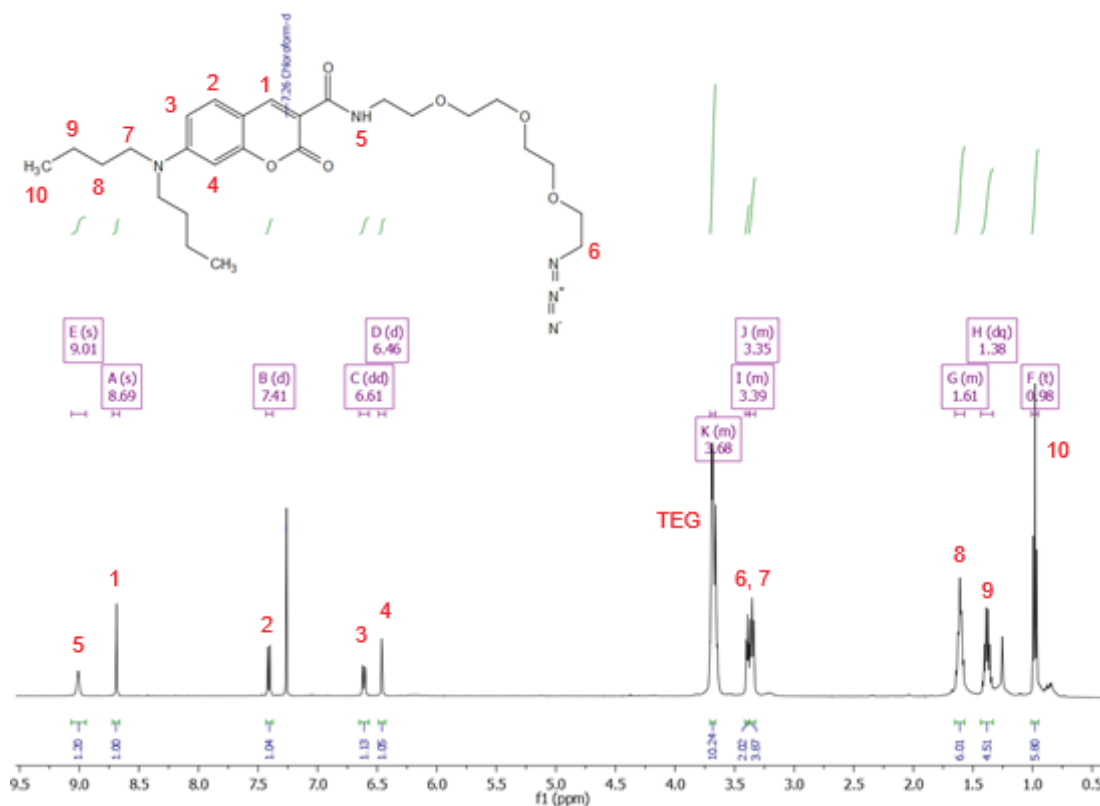


Fig. 6.109. ¹H NMR (CDCl₃) of DBC-N₃.

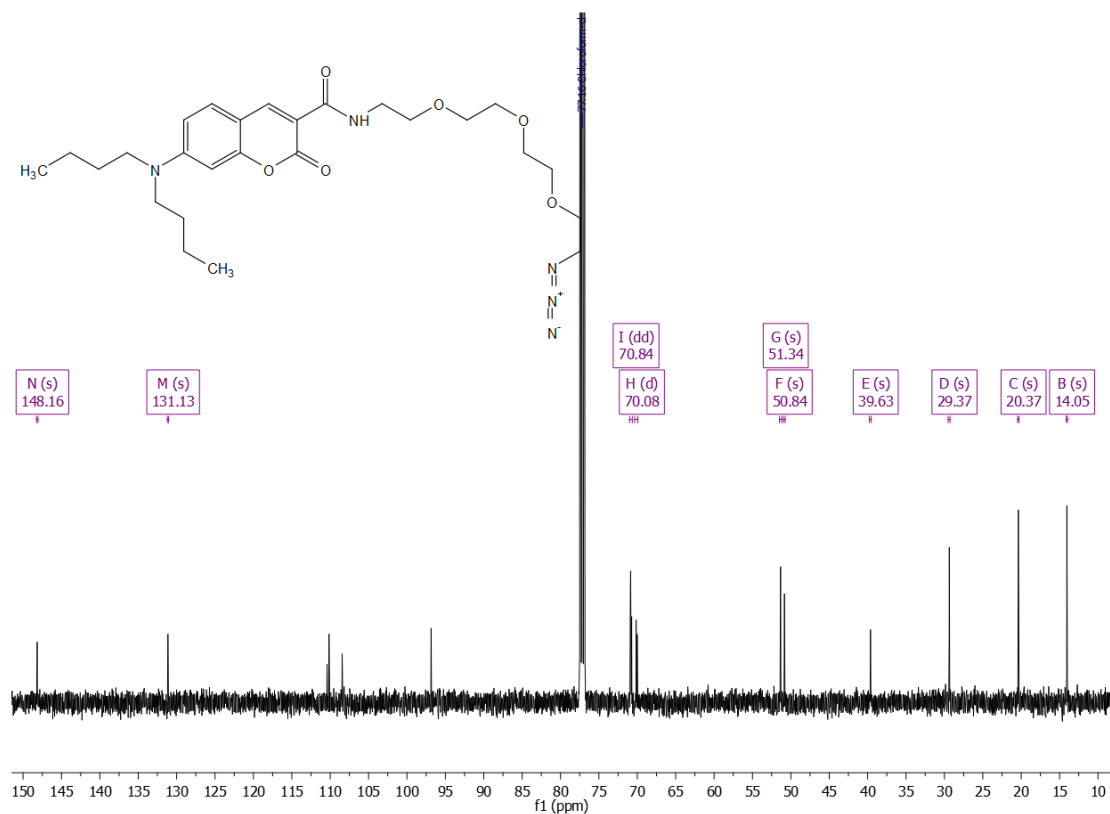


Fig. 6.110. ^{13}C NMR (CDCl_3) of DBC- N_3 .

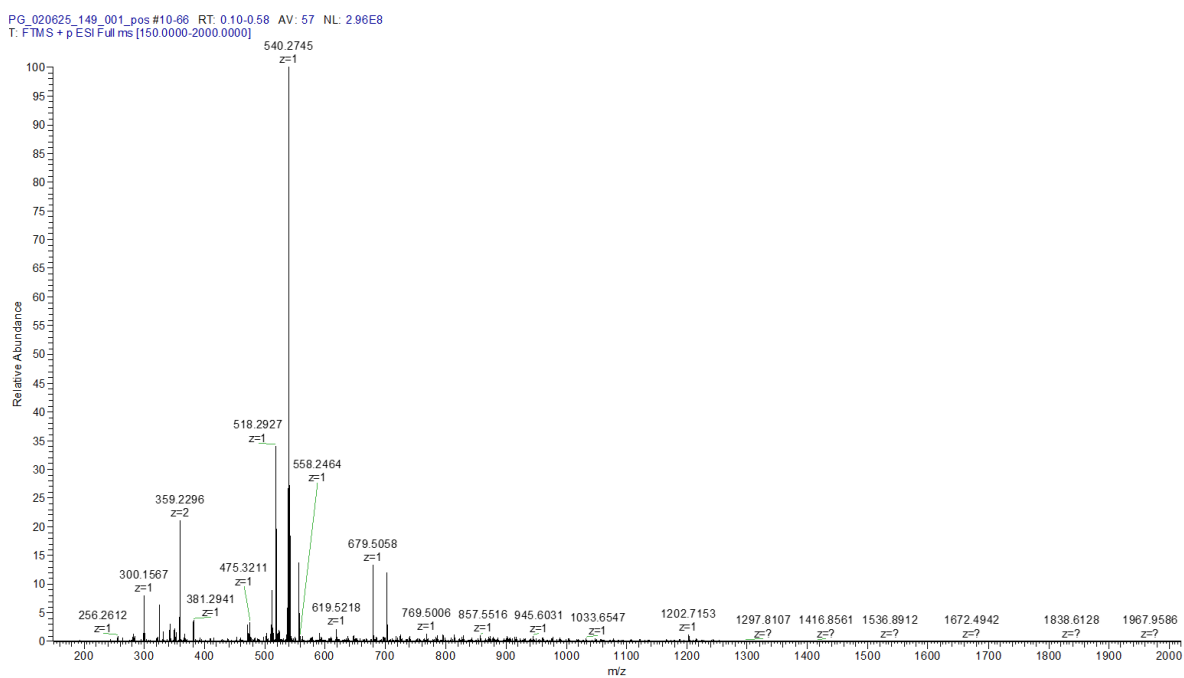


Fig. 6.111. ESI-MS of DBC- N_3 . The peaks 518.2927^+ and 540.2745^+ correspond to $[\text{M}+\text{H}]^+$ and $[\text{M}+\text{Na}]^+$, respectively.

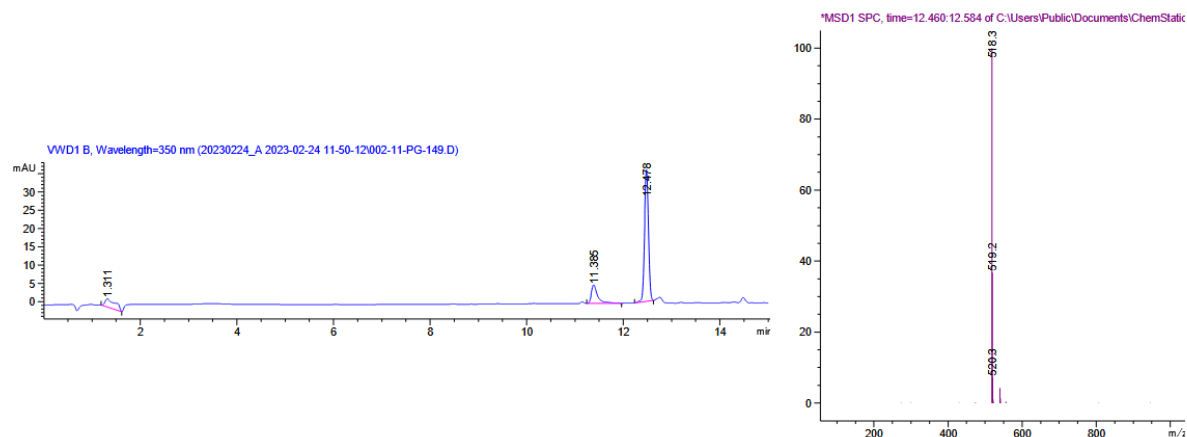
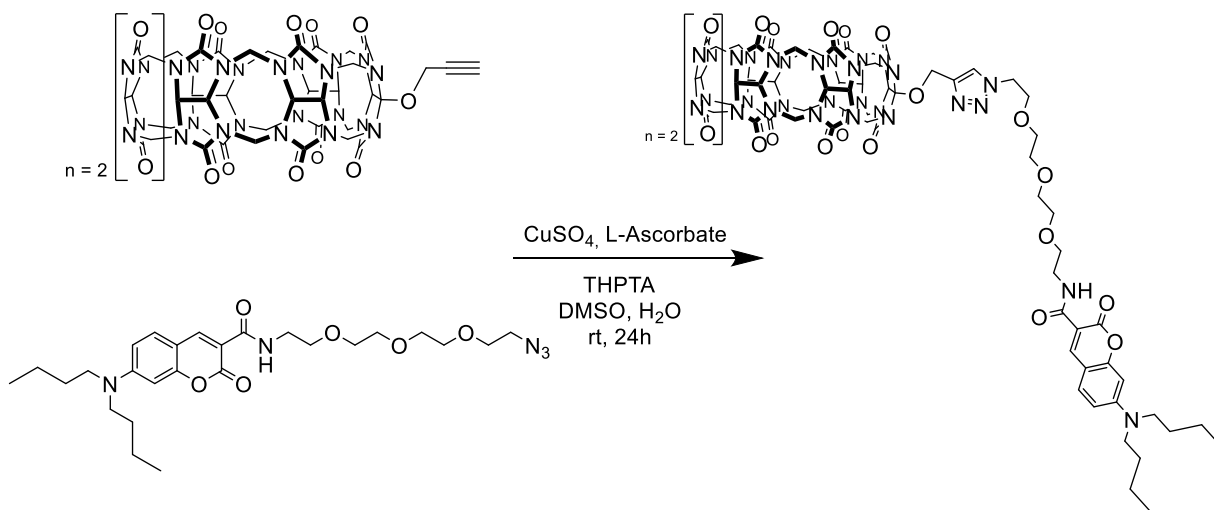


Fig. 6.112. Analytical UV trace at $\lambda=350$ nm (left) and observed mass in positive mode at 12.6 min (right).

6.11.2.24. CB7-dibutylcoumarin (CB7-DBC)



According to a modified literature procedure²³¹, CB7-(OPr) (17.4 mg, 14.4 μmol , 1 equiv.), DBC-N3 (12.6 mg, 25.8 μmol , 1.8 equiv.), and THPTA (24.8 mg, 56 μmol , 4 equiv.) were placed in a vial and dissolved in 1400 μL DMSO. After closing of the vial, it was placed in ultrasound then purged with N_2 . In a second vial, 5.6 mL 55% DMSO aqueous solution was also purged with N_2 , then CuSO_4 (9.1 mg, 56.0 μmol , 4 equiv.) was added to the 55% DMSO followed by sodium L-ascorbate (19.8 mg, 100.0 μmol , 7 equiv.) while it was taken care for least oxygen exposure as possible. The click solution was placed in the ultrasound for approx. 1 min. while a color change to yellow (Cu^+ forming) was observed. The two solutions were mixed and stirred at room temperature for 24 h under an N_2 atmosphere. Afterwards, the product was precipitated by dropwise addition of the reaction solution in 50 mL MeOH. The solid was then washed with MeOH (3×25 mL). Purification is done by preparative HPLC. The product elutes after 28.1 min (prep. method 2). The product was obtained as a fluffy yellow solid after freeze-dry. (11.5 mg, 6.4 μmol , 45%) Due to complex structure, precise peak assignment was not possible. It was not possible to measure ^{13}C NMR even after multiple attempts. ^1H NMR (400 MHz, CD_3CN) δ 8.52 (s, 1H), 8.00 (s, 1H), 7.51 (d, $J = 8.9$ Hz, 1H), 6.77 (d, $J = 8.7$ Hz, 1H), 6.53 (s, 1H), 6.04 – 5.10 (m, 28H), 4.49 (d, $J = 6.2$ Hz, 4H), 4.10 (dd, $J = 24.7, 11.9$ Hz, 14H), 3.81 (s, 2H), 3.61 – 3.42 (m, 12H), 3.34 (t, $J = 7.1$ Hz,

4H), 1.48 (d, J = 6.6 Hz, 4H), 1.36 – 1.22 (m, 4H), 0.84 (t, J = 7.2 Hz, 6H). ESI MS: Calc. for $[M+C_8mim_2]^{2+}$: 1005.4440; found: 1005.4431. Analyt. HPLC (analyt. method 1) = 18.0 min

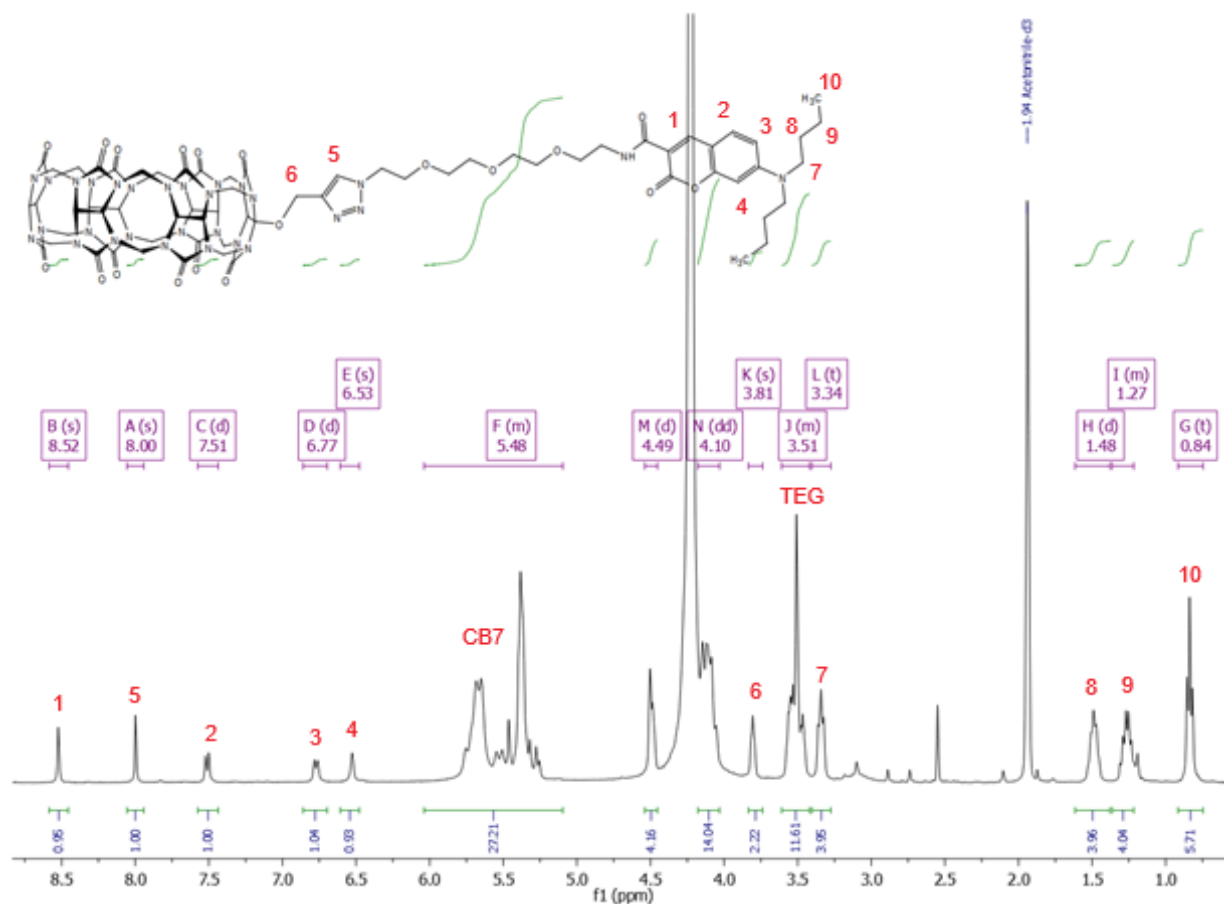


Fig. 6.113. 1H NMR (CD_3CN) of CB7-DBC.

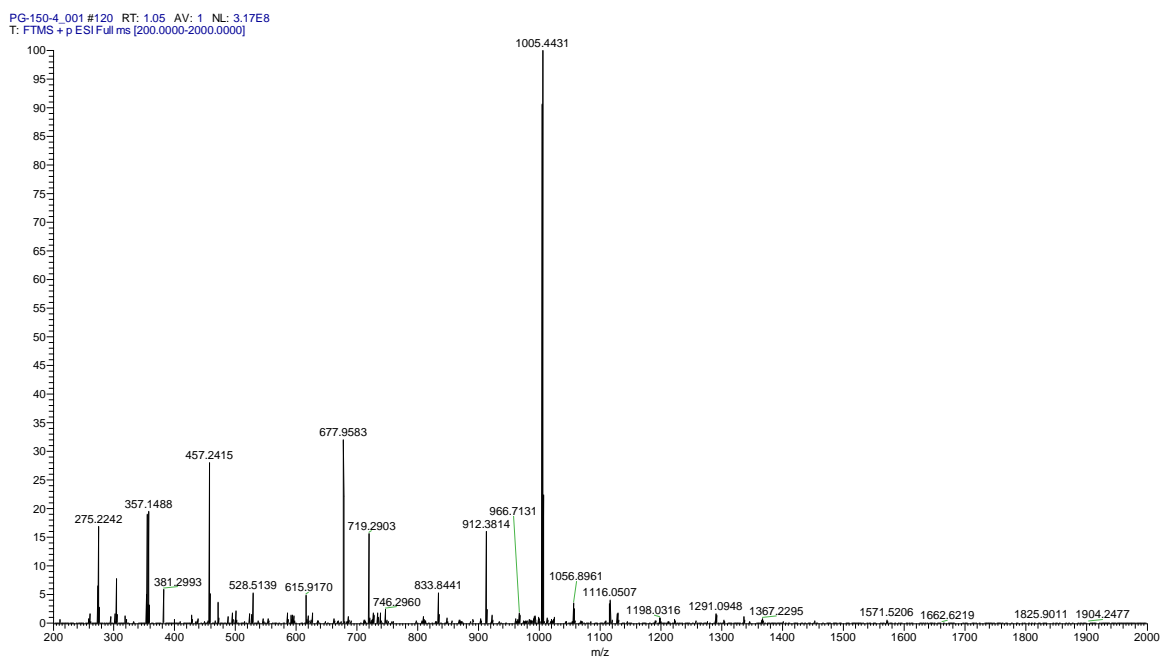


Fig. 6.114. ESI-MS of CB7-DBC measured as $[M+C_8mim_2]^{2+}$ adduct.

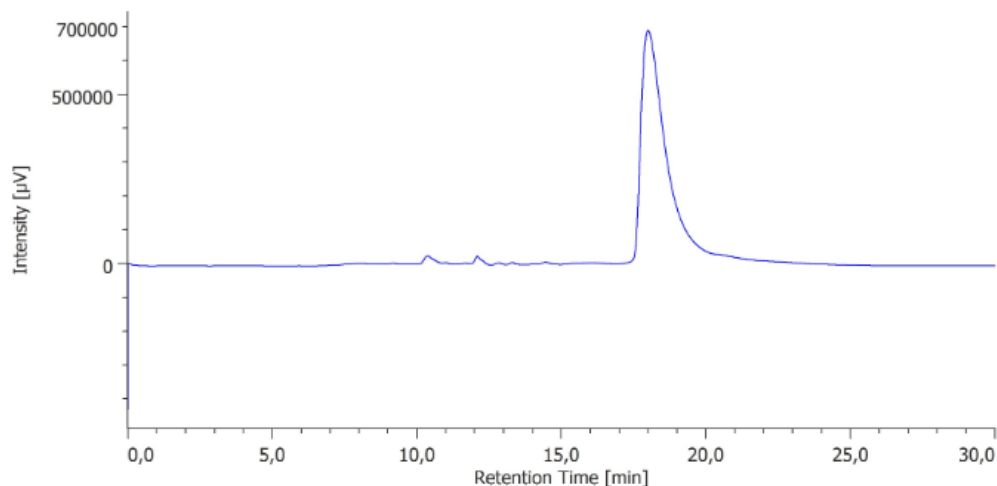
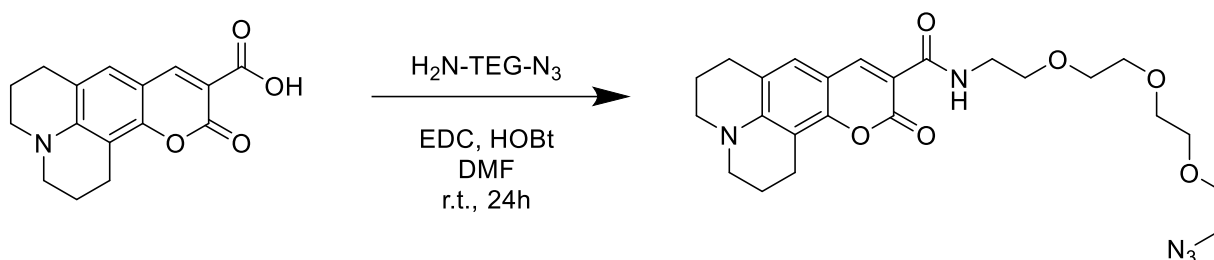


Fig. 6.115. Analytical trace of CB7-DBC (anal. method 1).

6.11.2.25. N-(2-(2-(2-(2-azidoethoxy)ethoxy)ethoxy)ethyl)-11-oxo-2,3,6,7-tetrahydro-1H,5H,11H-pyrano[2,3-f]pyrido[3,2,1-ij]quinoline-10-carboxamide (DCC-N₃)



In a glass vial coumarin 343 (100 mg, 0.4 mmol, 1 equiv.) was dissolved in dry DMF (3 mL). To this solution was added 11-Azido-TEG-NH₂ (99.5 mg, 90.5 µl, 0.5 mmol, 1.3 equiv.), HOBt (64.4 mg, 0.4 mmol, 1.2 equiv.) and EDC HCl (80.6 mg, 0.4 mmol, 1.2 equiv.). The vial was closed and the mixture was stirred overnight under an N₂ atmosphere. The crude product was purified by silica gel column chromatography (DCM/MeOH 15:1). The product was isolated as an orange oil. (139.5 mg, 0.3 mmol, 82%) ¹H NMR (400 MHz, CDCl₃) δ 9.06 (s, 1H), 8.59 (s, 1H), 7.00 (s, 1H), 3.70 – 3.63 (m, 14H), 3.39 (t, J = 5.1 Hz, 2H), 3.32 (dd, J = 11.2, 5.0 Hz, 4H), 2.88 (t, J = 6.4 Hz, 2H), 2.77 (t, J = 6.2 Hz, 2H), 2.02 – 1.93 (m, 4H). ¹³C NMR (101 MHz, CDCl₃) δ 163.81 (s), 148.18 (s), 127.16 (s), 119.71 (s), 108.45 (s), 105.90 (s), 71.03 – 70.68 (m), 70.14 (d, J = 3.6 Hz), 50.90 (s), 50.40 (s), 49.99 (s), 39.64 (s), 27.63 (s), 21.37 (s), 20.36 (d, J = 13.2 Hz). ESI MS: Calc. for [M+Na]⁺: 508.2029; found: 508.2036

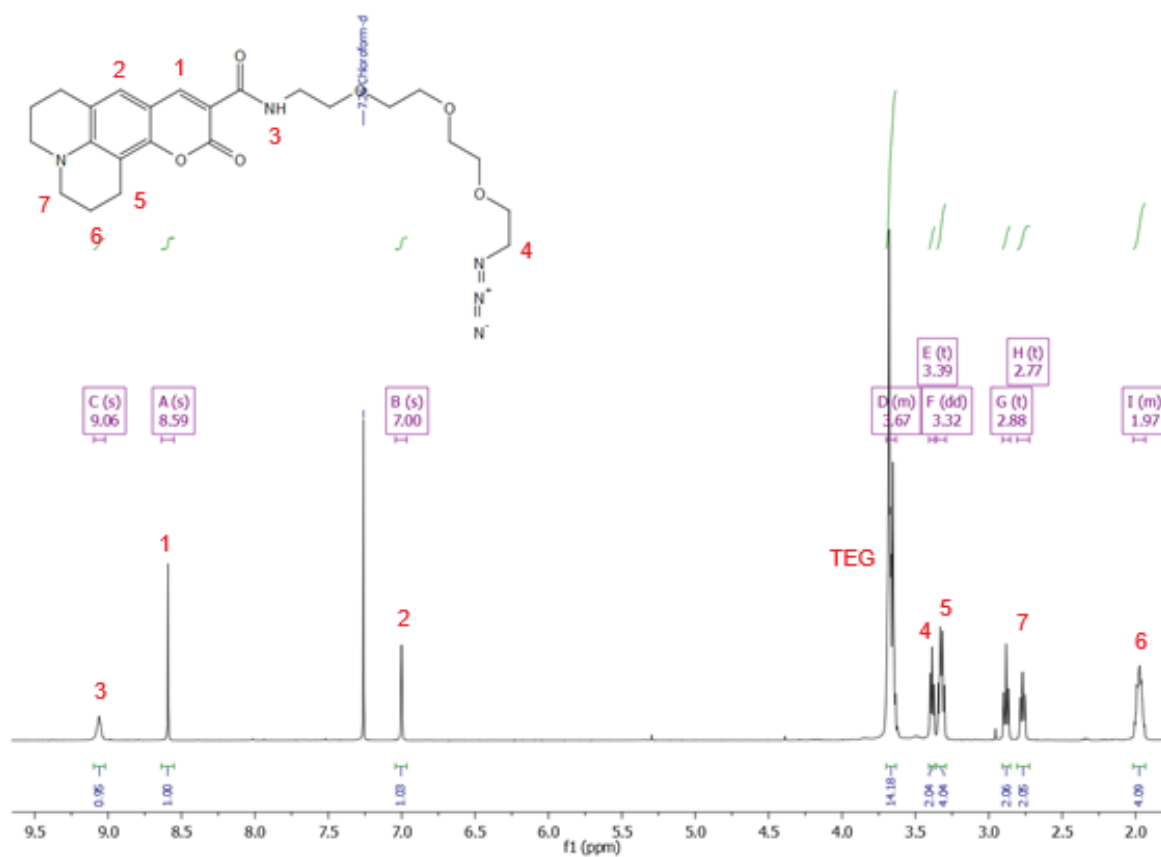


Fig. 6.116. ¹H NMR (CDCl₃) of DCC-N₃.

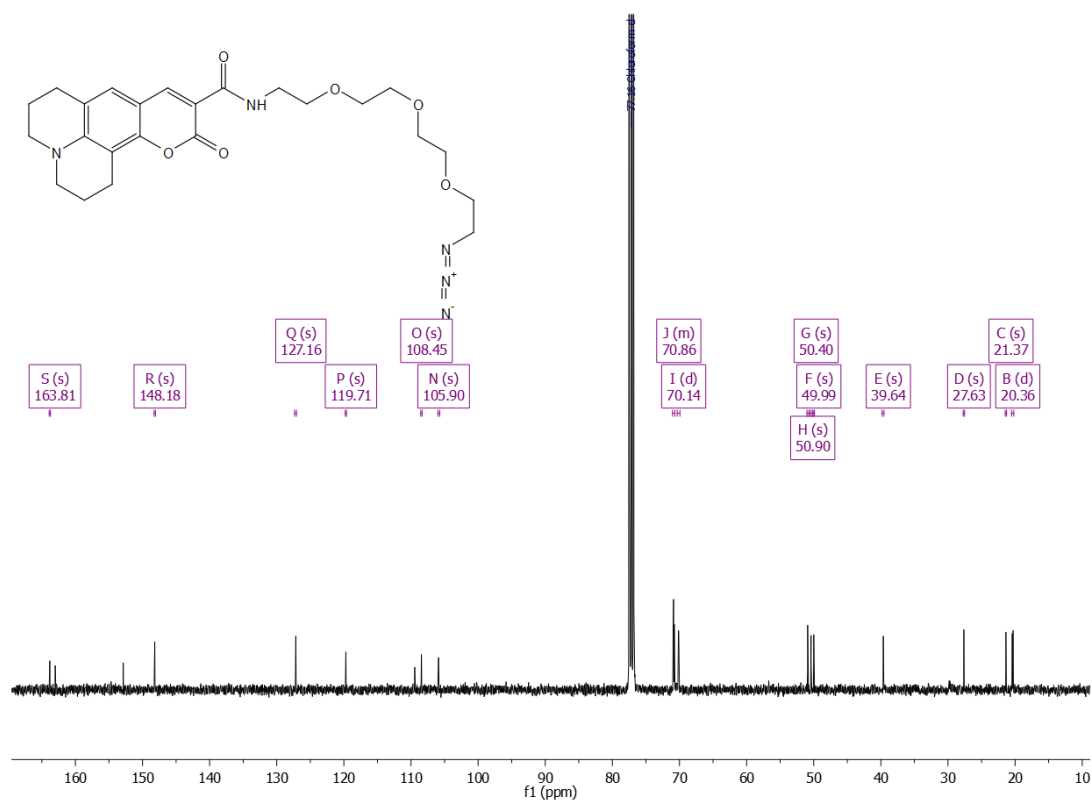


Fig. 6.117. ¹³C NMR (CDCl₃) of DCC-N₃.

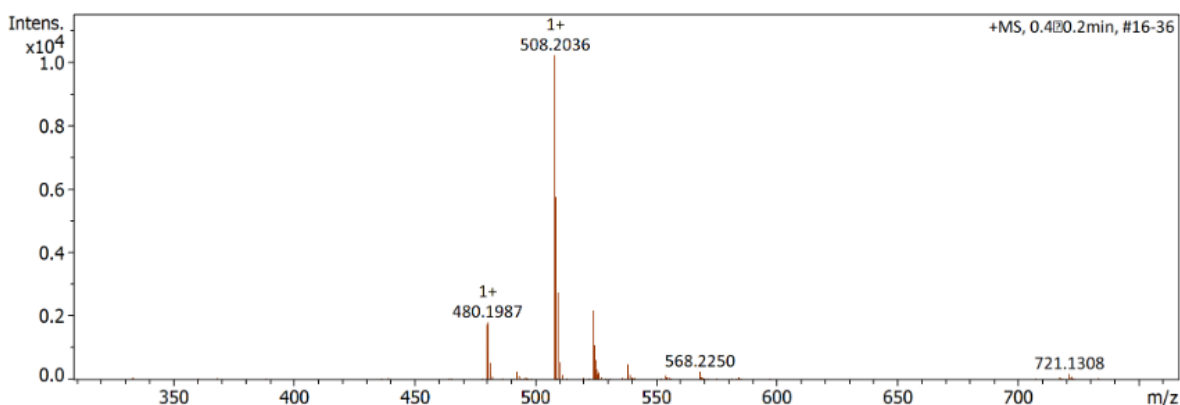
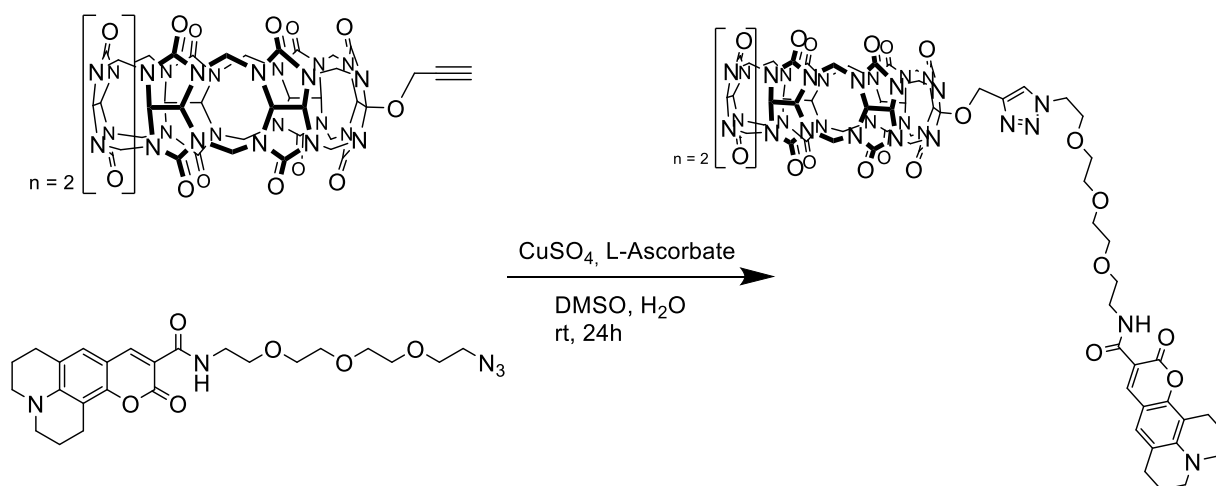


Fig. 6.118. ESI-MS of DCC-N₃. The peak 508.2036⁺ corresponds to [M+Na]⁺.

6.11.2.26. CB7-dicyclohexylcoumarin (CB7-DCC)



CB7-(OPr) (17.4 mg, 14.4 μmol , 1 equiv.), DCC-N₃ (12.5 mg, 25.8 μmol , 1.8 equiv.), and THPTA (24.8 mg, 56 μmol , 4 equiv.) were placed in a vial and dissolved in 1400 μL DMSO. After closing of the vial, it was placed in ultrasound then purged with N₂. In a second vial, 5.6 mL 55% DMSO aqueous solution was also purged with N₂, then CuSO₄ (9.1 mg, 56.0 μmol , 4 equiv.) was added to the 55% DMSO followed by sodium L-ascorbate (19.8 mg, 100.0 μmol , 7 equiv.) while it was taken care for least oxygen exposure as possible. The click solution was placed in the ultrasound for approx. 1 min. while a color change to yellow (Cu⁺ forming) was observed. The two solutions were mixed and stirred at room temperature for 24 h under an N₂ atmosphere. Afterwards, the product was precipitated by dropwise addition of the reaction solution in 50 mL MeOH. The solid was then washed with MeOH (3 \times 25 mL). Purification is done by preparative HPLC. The product elutes after 18.2 min (prep. method 1). The product was obtained as a fluffy orange solid after freeze-dry. (9.4 mg, 5.7 μmol , 40%). Due to complex structure, precise peak assignment was not possible. It was not possible to measure ¹³C NMR even after multiple attempts. Because of aggregation, peak resolution was not good in ¹H NMR. ¹H NMR (400 MHz, CD₃CN) δ 8.38 (d, J = 22.2 Hz, 1H), 8.01 (s, 1H), 7.08 (s, 1H), 5.93 – 5.07 (m, 28H), 4.50 (d, J = 5.0 Hz, 2H), 3.60 – 3.43 (m, 14H), 3.29 (s, 6H), 2.63 (d, J = 41.1 Hz, 4H). ESI MS: Calc. for [M+C₈mim₂]²⁺: 989.4941; found: 989.3734. Analyt. HPLC (analyt. method 1) = 8.0 min

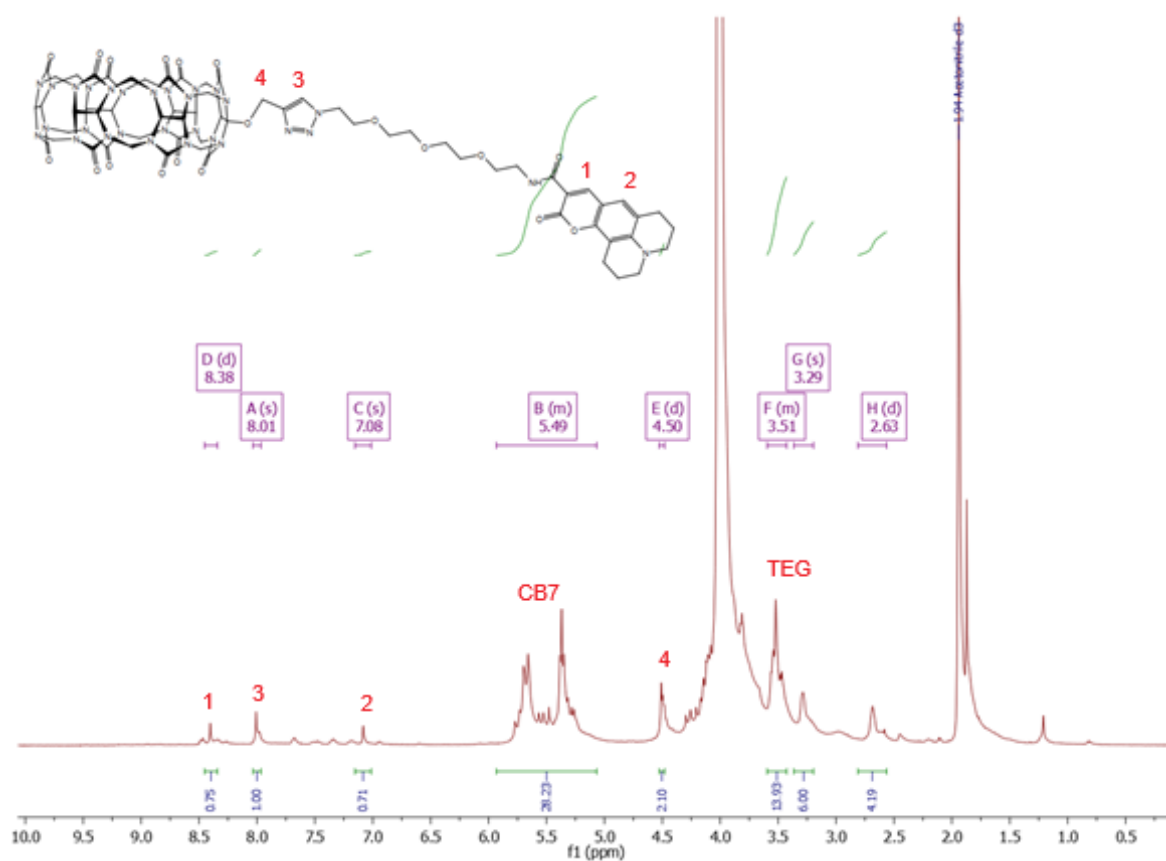


Fig. 6.119. ¹H NMR (CD₃CN) of CB7-DCC.

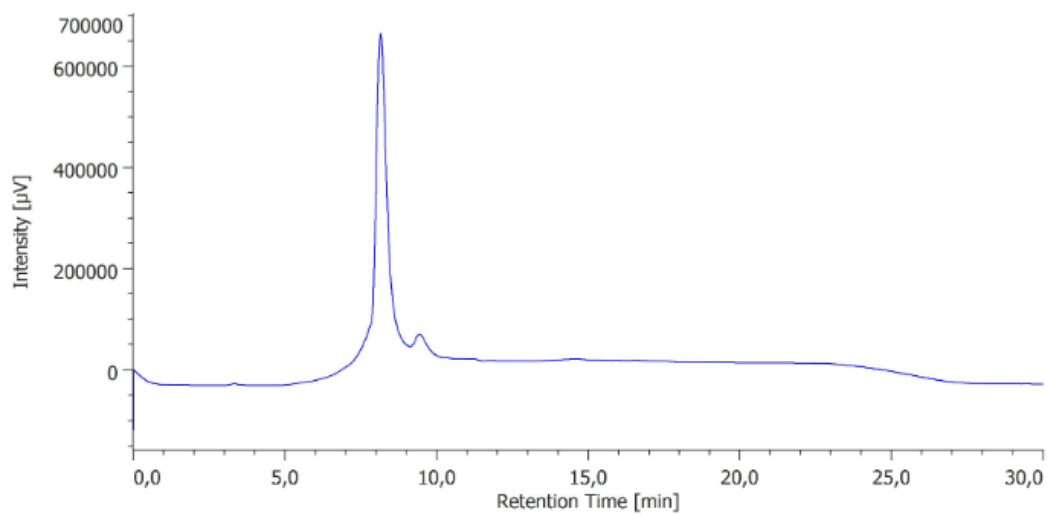


Fig. 6.120. Analytical trace of CB7-DCC (anal. method 1).

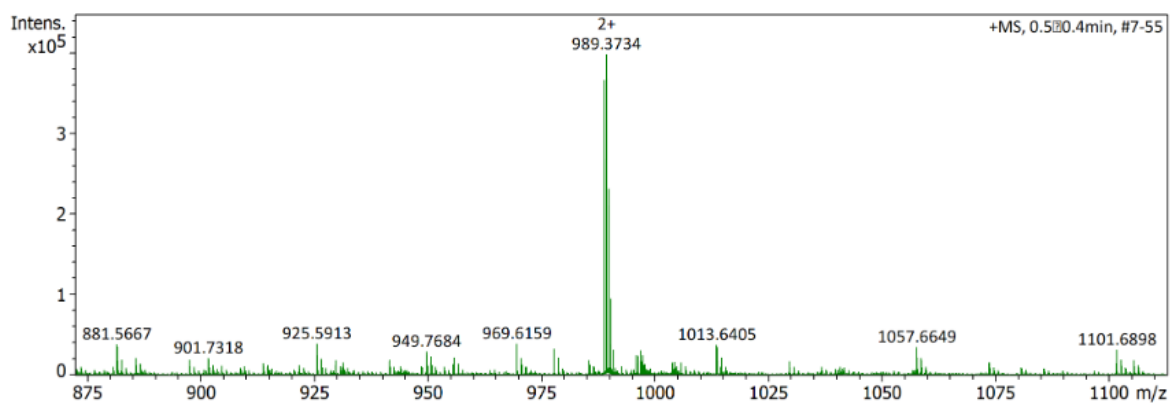


Fig. 6.121. ESI-MS of CB7-DCC measured as $[M+C_8mim_2]^{2+}$ adduct.

7. References

- (1) Waals, J. D. v. d. *Over de Continuïteit van den Gas- en Vloeistoestand (Die Kontinuität des flüssigen und gasförmigen Zustands)*; Universität Leiden 1873.
- (2) Lehn, J. M. *Supramolecular Chemistry Science* **1993** *260*, 1762-1763.
- (3) F. Biedermann, H.-J. S. Experimental Binding Energies in Supramolecular Complexes. *Chem. Rev.* **2016**, *116* (9), 5216-5300.
- (4) Lehn, J. M. Cryptates: Inclusion Complexes of Macropolycyclic Receptor Molecules *Pure & Appl. Chem.* **1978**, *50*, 871-892.
- (5) Lehn, J. M. Supramolecular Chemistry - Scope and Perspectives Molecules, Supermolecules, and Molecular Devices (Nobel Lecture) *Angew. Chem. Int. Ed. Engl.* **1988**, *27* (1), 89-112.
- (6) Cram, D. J. The Design of Molecular Hosts, Guests, and Their Complexes (Nobel Lecture) *Angew. Chem. Int. Ed. Engl.* **1988**, *27* (8), 1009-1112.
- (7) Pedersen, C. J. The Discovery of Crown Ethers (Nobel Lecture) *Angew. Chem. Int. Ed. Engl.* **1988**, *27* (8), 1021-1027.
- (8) J.-P. Sauvage, P. G. *From non-covalent assemblies to molecular machines*; Wiley-VCH Verlag &Co. , 2010.
- (9) C. J. Bruns, J. F. S. *The nature of the mechanical bond: from molecules to machines*; Wiley-VCH Verlag &Co., 2017.
- (10) B. L. Feringa, W. R. B. *Molecular switches*; Wiley-VCH Verlag &Co. , 2011.
- (11) Chem. Rev. 1997, *5*, 1231–1232. Introduction: Molecular Recognition. *Chem. Rev.* **1997**, *97* (5), 1231-1232.
- (12) S. Chang, H. A., Y. Chen., Q. Zhu, H. Luo, Y. Huang. Highly Efficient Supramolecular Catalysts Assembled by Dawson-Type POMs and Metal-Organic Complexes for the Synergistic Catalytic Synthesis of *p*-Benzoquinones. *ACS. Sustainable Chem. Eng.* **2022**, *10* (14), 4728-2740.
- (13) D. B. Amabilino, D. K. S., J. W Steed Supramolecular materials. *Chem. Soc. Rev.* **2017**, *46*, 2404-2420.
- (14) D. A. Uhlenheuer, K. P., L. Brunsveld Combining supramolecular chemistry with biology. *Chem. Soc. Rev.* **2010**, *39*, 2817-2826.
- (15) F. Esteve, R. P., M. Bolte, B. Altava, S. V. Luis, E. Garcia-Verdugo. A bioinspired approach toward efficient supramolecular catalysts for CO₂ conversion. *Chem. Catal.* **2023**, *3* (4).
- (16) Lehn, J. M. Supramolecular chemistry: Where from? Where to? *Chem. Soc. Rev.* **2017**, *46*, 2378-2379.
- (17) F. Teng, T. C., L. Zhou, Q. Gao, Q. Zhou, W. Lei Programmable synthetic receptors: the next-generation of cell and gene therapies. *Signal Transduc. Target. Ther.* **2024**, *9*.
- (18) J. Manhas, H. I. E., J. N. Leonard, L. Morsut. The evolution of synthetic receptor systems *Nat. Chem. Biol.* **2022**, *2022* (18), 244-255.

- (19) J. T. Davis, P. A. G., R. Quesada. Advances in anion transport and supramolecular medicinal chemistry *Chem. Soc. Rev.* **2020**, *49*, 6056-6086.
- (20) P. A. Gale, J. T. D., R. Quesada. Anion transport and supramolecular medicinal chemistry. *Chem. Soc. Rev.* **2017**, *46*, 2497-2519.
- (21) Q. Chen, Y. S., J. Zheng. A review of cystic fibrosis: Basic and clinical aspects. *AMEM* **2021**, *4* (3), 220-232.
- (22) H. Li, H. V., A. G. Thorne, C. M. Dias, J. A. Cooper, M. Kieffer, N. Busschaert, P. A. Gale, D. N. Sheppard, A. P. Davis. Anion carriers as potential treatments for cystic fibrosis: transport in cystic fibrosis cells, and additivity to channel-targeting drugs. *Chem. Sci.* **2019**, *10* (9663-9672).
- (23) E. Hernando, V. C., C. Cossu, M. Fiore, M. Garcia-Valverde, V. Soto-Cerrato, R. Perez-Tomas, O. Zegarra-Moran, R. Quesada. Small molecule anionophores promote transmembrane anion permeation matching CFTR activity. *Sci. Rep.* **2018**, *8*.
- (24) Schneider, H. J. Binding Mechanisms in Supramolecular Complexes. *Angew. Chem. Int. Ed. Engl.* **2009**, *48* (22), 3924-3977.
- (25) Würthner, F. Solvent Effects in Supramolecular Chemistry: Linear Free Energy Relationships for Common Intermolecular Interactions *J. Org. Chem.* **2021**, *87* (3), 1602-1615.
- (26) Satake, A. The Solvent Effect on Weak Interactions in Supramolecular Polymers: Differences between Small Molecular Probes and Supramolecular Polymers *ChemPlusChem* **2020**, *85* (7), 1542-1548.
- (27) K. Haav, S. A. K., L. Toom, P. A. Gale, N. Busschaert, M. Wenzel, J. R. Hiscock, I. L. Kirby, T. Haljasorg, M. Lokov, I. Leito Accurate Method To Quantify Binding in Supramolecular Chemistry *J. Org. Chem.* **2013**, *78* (16), 7796-7808.
- (28) Thordarson, P. Determining association constants from titration experiments in supramolecular chemistry. *Chem. Soc. Rev.* **2010**, *40*, 1305-1323.
- (29) S. Sinn, J. K., F. Biedermann. Teaching old indicators even more tricks: binding affinity measurements with the guest-displacement assay (GDA). *Chem. Commun.* **2020**, *56* (49), 6620-6623.
- (30) S. Sinn, F. B. Chemical Sensors Based on Cucurbit[n]uril Macrocycles. *Isr. J. Chem.* **2018**, *58* (3-4), 357-412.
- (31) J. Krämer, R. K., L. M. Grimm, L. De Cola, P. Picchetti, F. Biedermann. Molecular Probes, Chemosensors, and Nanosensors for Optical Detection of Biorelevant Molecules and Ions in Aqueous Media and Biofluids. *Chem. Rev.* **2022**, *122* (3), 3459-3636.
- (32) A. Prabodh, S. S., L. Grimm, Z. Miskolczy, M. Megyesi, L. Biczok, S. Bräse, F. Biedermann. Teaching indicators to unravel the kinetic features of host-guest inclusion complexes. *Chem. Commun.* **2020**, *56*, 12327-12330.
- (33) B. T. Nguyen, E. V. A. Indicator-displacement assays. **2006**, *250* (23-24), 3118-3127.

- (34) A. C. Sedgwick, J. T. B., II, T. Wu, X. Feng, S. D. Bull, X. Qian, J. L. Sessler, T. D. James, E. V. Anslyn, X. Sun. Indicator displacement assays (IDAs): the past, present and future. *Chem. Soc. Rev.* **2020**, *50*, 9-38.
- (35) J. Wu, B. K., W. Liu, E. V. Anslyn, P. Wang, J. S. Kim Chromogenic/Fluorogenic Ensemble Chemosensing Systems *Chem. Rev.* **2015**, *115* (15), 7893-7943.
- (36) X.-M. Yin, L.-L. G., P. Li, R. Bu, W.-J. Sun, E.-Q. Gao Fluorescence Turn-On Response Amplified by Space Confinement in Metal-Organic Frameworks *ACS Appl. Mater. Interfaces* **2019**, *11* (50), 47112-47120.
- (37) J. Qiao, X. L., L. Zhang, J. F. Eubank, X. Liu, Y. Liu. Unique Fluorescence Turn-On and Turn-Off-On Responses to Acids by a Carbazole-Based Metal-Organic Framework and Theoretical Studies. *J. Am. Chem. Soc.* **2022**, *144* (37), 17054-17063.
- (38) C. Yang, J. Z. A simple 'turn-on' fluorescence chemosensor for Al(III) detection in aqueous solution and solid matrix *RSC Adv.* **2024**, *14*, 1464-1471.
- (39) W.-E. Lee, Y.-J. J., S.-I. Kim, G. Kwak, J. H. Kim, T. Sakaguchi, C.-L. Lee. Fluorescence turn-on response of a conjugated polyelectrolyte with intramolecular stack structure to biomacromolecules. *Chem. Commun.* **2013**, *49*, 9857-9859.
- (40) D. Wu, A. C. S., T. Gunnlaugsson, E. U. Akkaya, J. Yoon, T. D. James. Fluorescent chemosensors: the past, present and future *Chem. Soc. Rev.* **2017**, *46*, 7105-7123.
- (41) H. Li, Y. K., H. Jung, J. Y. Hyun, I. Shin. Near-infrared (NIR) fluorescence-emitting small organic molecules for cancer imaging and therapy. *Chem. Soc. Rev.* **2022**, *51*, 8957-9008.
- (42) J. O. Escobedo, O. R., S. Lim, R. M. Strongin. NIR dyes for bioimaging applications. *Curr. Opin. Chem. Biol.* **2010**, *14* (1), 64-70.
- (43) Q. Duan, R. C., S. Deng, C. Yang, X. Ji, G. Qi, H. Li, X. Li, S. Chen, M. Lou, K. Lu. Cucurbit[*n*]uril-based fluorescent indicator-displacement assays for sensing organic compounds. *Front. Chem.* **2023**, *11*.
- (44) Kubik, S. Anion Recognition in Aqueous Media by Cyclopeptides and Other Synthetic Receptors *Acc. Chem. Res.* **2017**, *21* (50), 2870-2878.
- (45) F. Biedermann, D. H., W. M. Nau Associative chemosensing by fluorescent macrocycle-dye complexes - a versatile enzyme assay platform beyond indicator displacement *Chem. Commun.* **2015**, *51*, 4977-4980.
- (46) F. Biedermann, W. M. N. Noncovalent chirality sensing ensembles for the detection and reaction monitoring of amino acids, peptides, proteins and aromatic drugs. *Angew. Chem. Int. Ed.* **2014**, *53*, 5694-5699.
- (47) F. Biedermann, O. A. S. Cucurbit[8]uril mediated donor-acceptor ternary complexes: A model system for studying charge-transfer interactions. *J. Phys. Chem. B* **2012**, *116*, 2842-2849.
- (48) J. Krämer, L. M. G., C. Zhong, M. Hirtz, F. Biedermann. A supramolecular cucurbit[8]uril-based rotaxane chemosensor for the optical tryptophan detection in human serum and urine *Nat. Commun.* **2023**, *14*.

- (49) L. M. Grimm, S. S., M. Krstic, E. D'Este, I. Sonntag, E. A. Prasetyanto, T. Kuner, W. Wenzel, L. De Cola, F. Biedermann. Fluorescent nanozeolite receptors for the highly selective and sensitive detection of neurotransmitters in water and biofluids *Adv. Mat.* **2021**, *33* (49).
- (50) J. Wankar, N. G. K., S. Gera, S. Rasala, A. Pandit, Y. A. Rochev. Recent advances in Host-Guest self-assembled cyclodextrin carriers: implications for responsive drug delivery and biomedical engineering. *Adv. Func. Mater.* **2020**, *30* (44).
- (51) M. Sayed, F. B., V. D. Uzunova, K. I. Assaf, A. C. Bhasikhuttan, H. Pal, W. M. Nau, J. Mohanty. Triple emission from *p*-dimethylaminobenzonitrile-cucurbit[8]uril triggers the elusive excimer emission. *Chem. Eur. J.* **2014**, *21* (2), 691-696.
- (52) M. Sayed, H. P. pH-assisted control over the binding and relocation of an acridine guest between a macrocyclic nanocarrier and natural DNA *Phys. Chem. Chem. Phys.* **2015**, *17*, 9519-9532.
- (53) M. Sayed, K. S., R. Shah, H. Pal. pH-responsive indicator displacement assay of acetylcholine based on acridine-*p*-sulfonatocalix[4]arine supramolecular system: fluorescence off/on switching and reversible pK_a shift. *Chem. Eur. J.* **2016**, *1* (5), 989-999.
- (54) X. Ma, Y. Z. Biomedical applications of supramolecular systems based on host-guest interactions *Chem. Rev.* **2015**, *115* (15), 7794-7839.
- (55) G. W. Gokel, W. M. L., M. E. Weber. Crown ethers: sensors for ions and molecular scaffolds for materials and biological models. *Chem. Rev.* **2004**, *104* (5), 2723-2750.
- (56) Pedersen, C. J. Cyclic polyethers and their complexes with metal salts *J. Am. Chem. Soc.* **1967**, *89* (26), 7017-7036.
- (57) Z. Qi, P. M. d. M., W. Jiang, Q. Wang, K. Nowosinski, A. Schulz. Systems chemistry: Logic gates based on the stimuli-responsive gel-sol transition of a crown ether-functionalized bis(urea) gelator. *Chem. Sci.* **2012**, *3*, 2073-2082.
- (58) Z. Qi, N. L. T., P. Malo de Molina, C. Schlaich, M. Gradzielski, C. A. Schalley. Self-recovering stimuli-responsive macrocycle-equipped supramolecular ionogels with unusual mechanical properties. *Org. Biomol. Chem.* **2014**, *12*, 503-510.
- (59) M. C. Ali, R. L., J. Chen, T. Cai, H. Zhang, Z. Li. New deep eutectic solvents composed of crown ether, hydroxide and polyethylene glycol for extraction of non-basic N-compounds. *Chin. Chem. Lett* **2019**, *30* (871-874).
- (60) F. Ullah, T. A. K., J. Iltaf, S. ANwar, M. F. A. Khan, M. R. Khan, S. Ullah, M. F. ur Rehman, M. Mustaqueem, K. Kotwica-Mojzych, M. Mojzych. Heterocyclic crown ethers with potential biological and pharmacological properties: From synthesis to applications. *Appl. Sci.* **2022**, *12* (3).
- (61) M. Kralj, L. T.-B., L. Frkanec. Biomedical potentials of crown ethers: prospective antitumor agents. *ChemMedChem.* **2008**, *3* (10), 1478-1492.
- (62) H. E. Simmons, C. H. P. Macrobicyclic amines. I. Out-in isomerism of 1,(*k*+2)-diazabicyclo[*k*.1.*m*]alkanes. *J. Am. Chem. Soc.* **1968**, *90* (9), 2428-2429.

- (63) B. Dietrich, J. M. L., J. P. Sauvage Diaza-polyoxa-macrocycles et macrobicycles. *Tet. Lett.* **1969**, *10* (34), 2885-2888.
- (64) Y. Gholiee, S. S. The solvent effect on selectivity of four well-known cryptands and crown ethers toward Na⁺ and K⁺ cations; A computational study *J. Mol. Liq.* **2020**, *309*.
- (65) Gokel, G. W. Lariat ethers: from simple sidearms to supramolecular systems. *Chem. Soc. Rev.* **1992**, *21* (1), 39-47.
- (66) Gutsche, C. D. *Calixarenes*; Royal Society of Chemistry 1989.
- (67) C. D. Gutsche, B. D., K. H. No, R. Muthikrishnan. Calixarenes. 4. The synthesis, characterization, and properties of the calixarenes from *p-tert*-Butylphenol. *J. Am. Chem. Soc.* **1981**, *103*, 3782-3792.
- (68) F. Biedermann, W. M. N., H.-J. Schneider The hydrophobic effect revisited - Studies with supramolecular complexes imply high-energy water as a noncovalent driving force. *Angew. Chem. Int. Ed.* **2014**, *53* (42), 11158-11171.
- (69) R. Kumar, A. S., H. Singh, P. Suating, H. S. Kim, K. Sunwoo, I. Shim, B. C. Gibb, J. S. Kim. Revisiting fluorescent calixarenes: from molecular sensors to smart materials. *Chem. Rev.* **2019**, *119* (16), 9657-9721.
- (70) J. S. Kim, D. T. Q. Calixarene-derived fluorescent probes *Chem. Rev.* **2007**, *107* (9), 3780-3799.
- (71) J. S. Kim, S. H. Y., J. A. Rim, J. Y. Kim, J. Vicens S. Shinkai. Silver ion oscillation through calix[4]azacrown tube *Tet. Lett.* **2001**, *42* (45), 8047-8050.
- (72) L. Baklouti, J. H., B. Pulpoa, J. Vicens. 1,3-Alternate, the smart conformation of calix[4]arenes. *Mini-Rev. Org. Chem.* **2006**, *3*, 355-384.
- (73) R. Joseph, C. P. R. Ion and molecular recognition by lower rim 1,3-di-conjugates of calix[4]arene as receptors. *Chem. Rev.* **2011**, *111* (8), 4658-4702.
- (74) C. Danila, M. B., V. Böhmer. 1,3-Alternate calix[4]arenes, selectively functionalized by amino groups *Org. Biomol. Chem.* **2005**, *3*, 172-184.
- (75) L. Toma, L. L., F. Compostella, M. Giuliani, F. Faroldi, A. Casnati, F. Sansone. Molecular architecture and symmetry properties of 1,3-alternate calix[4]arenes with orientable groups at the para position of the phenolic rings. *J. Org. Chem.* **2016**, *81* (20), 9718-9727.
- (76) A. P. de Silva, H. Q. N. G., T. Gunnlaugsson, A. J. M. Huxley, C. P. McCoy, J. T. Rademacher, T. E. Rice. Signaling recognition events with fluorescent sensors and switches. *Chem. Rev.* **1997**, *97* (5), 151-1566.
- (77) B. Valeur, I. L. Ion-responsive supramolecular fluorescent systems based on multichomophoric calixarenes: A review. *Inorg. Chim. Acta* **2007**, *360* (3), 765-774.
- (78) B. Valeur, J. B., J. Pouget. Ion recognition detected by changes in photoinduced charge or energy transfer. *ACS Symposium Series* **1993**, *538*, 25-44.
- (79) B. G. Poulsen, Q. A. A., A. Sharfalddin, E. F. El Agammy, F. Mouffouk, A.-H. Emwas, L. Jaremko, M. Jaremko. Cyclodextrins: Structural, chemical, and physical properties, and applications. *Polysaccharides* **2022**, *3* (1), 1-31.

- (80) B. Gidwani, A. V. A comprehensive review on cyclodextrin-based carriers for delivery of chemotherapeutic cytotoxicity anticancer drugs *Biomed Res. Int.* **2015**, *2015* (1).
- (81) Crini, G. Review: A history of cyclodextrins. *Chem. Rev.* **2014**, *114* (21), 10940-10975.
- (82) Szejtli, J. Introduction and general overview of cyclodextrin chemistry *Chem. Rev.* **1998**, *98* (5), 1743-1754.
- (83) French, D. The Schardinger dextrans. *Adv. Carb. Chem.* **1957**, *12*, 189-260.
- (84) E. Gaidamauskas, E. N., E. Butkus, D. C. Crans, G. Grinciene. Deprotonation of β -Cyclodextrin in alkaline solutions. *Carbohydr. Res.* **2009**, *344*, 250-254.
- (85) E. Merisko-Liversidge, G. G. L., E. R. Cooper. Nanosizing: a formulation approach for poorly-water soluble compounds. *Eur. J. Pharm. Sci.* **2003**, *18* (2), 113-120.
- (86) T. Loftsson, P. J., M. Masson, T. Järvinen. Cyclodextrins in drug delivery *Expert Opin. Drug Deliv.* **2005**, *2*, 335-351.
- (87) E. Sabadini, T. C., F. do Carmo Edigio. Solubility of cyclomatoooligosaccharides (cyclodextrins) in H₂O and D₂O. *Carbohydr. Res.* **2006**, *314*, 270-274.
- (88) P. Saokham, C. M., P. Jansook, T. Loftsson. Solubility of cyclodextrins and drug/cyclodextrin complexes. *Molecules* **2018**, *23*.
- (89) A. F. Bell, L. H., L. D Barron. New evidence for conformational flexibility in cyclodextrins from vibrational raman optical activity *Chem. Eur. J.* **1997**, *3*, 1292-1298.
- (90) Dodziuk, H. Rigidity versus flexibility. A review of experimental and theoretical studies pertaining to the cyclodextrin nonrigidity. *J. Mol. Struct.* **2002**, *614*, 33-45.
- (91) N. Sharma, A. B. Exploring versatile applications of cyclodextrins: An overview. *Drug Deliv.* **2016**, *23*, 729-747.
- (92) H. M. Chu, R. X. Z., Q. Huang, C. C. Bai, Z. Z. Wang. Chemical conjugation with cyclodextrins as a versatile tool for drug delivery *J. Incl. Phenom. Macrocycl. Chem.* **2017**, *89*, 29-38.
- (93) B. V. K. J. Schmidt, C. B.-K. Dynamic macromolecular material design - the versatility of cyclodextrin-based host-guest chemistry *Angew. Chem. Int. Ed.* **2017**, *56*, 8350-8369.
- (94) L. Jiang, Y. Y., J. Huang. Versatility of cyclodextrins in self-assembly systems of amphiphiles. *Adv. Colloid Interface Sci.* **2011**, *169*, 13-25.
- (95) L. N. C. Rodrigues, A. C. M. T., B. T. Ferreira, A. K. C. A. Reis, L. M. Katiki. Inclusion complexes and self-assembled cyclodextrin aggregates for increasing the solubility of benzimidazoles. *Braz. J. Pharm. Sci.* **2019**, *55*.
- (96) T. Küster, B. S., D. Aeschbacher, A. Hemphill. Activities of Fenbendazole in comparison with Albendazole against *Echinococcus Multilocularis* metacestodes *in vitro* and in a murine infection model. *Int. J. Antimicrob. Agents* **2014**, *43* (4), 335-342.
- (97) C. Cagliero, B. S., C. Cordero, E. Liberto, P. Rubiolo, C. Bicchi. *Enantioselective Gas Chromatography with Cyclodextrin in Odorant Analysis*. In: A. Büttner, *Springer Handbook of Odor.* ; Springer, 2017.

- (98) A. Harada, H. A., Y. Kawaguchi, M. Kamachi. Recognition of alkyl groups on a polymer chain by cyclodextrins. *Macromolecules* **1997**, *30* (17), 5181-5182.
- (99) W. Cai, Y. Y., X. Shao. Chiral recognition based on bimodal complexation. *J. Mol. Model.* **2005**, *11*, 186-193.
- (100) D. J. DiScenza, M. L. Selective detection of non-aromatic pesticides via cyclodextrin-promoted fluorescence modulation. *New J. Chem.* **2016**, *40* (1), 798-793.
- (101) B. Yang, L.-J. Y., J. Lin, Y. Chen, Y. Liu. Binding behaviours of scutellarin with α -, β -, γ -cyclodextrins and their derivatives. *J. Incl. Phenom. Macrocycl. Chem.* **2009**, *64*, 149-155.
- (102) J. Wojcik, A. E., M. Nowakowski. Shape adaption of quinine in cyclodextrin cavities: NMR studies *Phys. Chem. Chem. Phys.* **2019**, *21*, 6925-6934.
- (103) A. Ryzhakov, T. D. T., J. Stappaerts, L. Bertolotti, K. Kimpe, A. R. Sa Couto, P. Saokham, G. van den Mooter, P. Augustijns, G. W. Somsen. Self-assembly of cyclodextrins and their complexes in aqueous solutions *J. Pharm. Sci.* **2016**, *105* (9), 2556-2569.
- (104) A. Rodrigues Sa Couto, A. R., K. Lambertsen Larsen, T. Loftsson. Interaction of native cyclodextrins and their hydroxypropylated derivatives with carbamazepine in aqueous solution. Evaluation of inclusion complexes and aggregates formation. *ACS Omega* **2019**, *4* (1), 1460-1469.
- (105) T. F. G. G. Cova, S. M. A. C., A. J. M. Valente, P. E. Abreu, J. M. C. Marquez, A. A. C. C. Pais. *Aggregation of cyclodextrins: Fundamental issues and applications. In: Cyclodextrin - a versatile ingredient*; InTech, 2018.
- (106) S. K. S. Al-Burtomani, F. O. S. Inclusion complexs of norepinephrine with β -cyclodextrin, 18-crown-6 and cucurbit[7]uril: experimental and molecular dynamics study *RSC Adv.* **2017**, *7*, 9888-9901.
- (107) L. Cao, M. S., P. Y. Zavalij, D. K. Mlinaric-Majerski, R. Glaser, L. Isaacs. Cucurbit[7]uril guest pair with an attomolar dissociation constant. *Angew. Chem. Int. Ed.* **2014**, *53* (4), 988-993.
- (108) R. Behrend, E. M., F. Rusche. Ueber Condensationsproducte aus Glycoluril und Formaldehyd. *Liebigs Ann. Chem.* **1905**, *339*, 1-37.
- (109) Balaram, P. William L. Mock and cucurbituril: The resurrection of the Behrend paper of 1905. *ACS Omega* **2024**, *9* (4), 4162-4165.
- (110) G. Marx, C. G. History of chemical notations from alchemy to psychochemistry. Special issue: Peptide and protein self-assembly and interactions. *Isr. J. Chem.* **2022**, *62* (9-10).
- (111) Isaacs, L. The mechanism of cucurbituril formation. *Isr. J. Chem.* **2011**, *51* (5-6), 578-591.
- (112) W. A. Freeman, W. L. M., N.-Y. Shih. Cucurbituril. *J. Am. Chem. Soc.* **1981**, *103*, 7367-7368.
- (113) W. L. Mock, N.-Y. S. Host-guest binding capacity of cucurbituril. *J. Org. Chem.* **1983**, *48* (20), 3618-3619.
- (114) L. W. Mock, N.-Y. S. Structure and selectivity in host-guest complexes of cucurbituril. *J. Org. Chem.* **1986**, *51*, 4440-4446.
- (115) W. L. Mock, N.-Y. S. Organic ligand-receptor interactions between cucurbituril and alkylammonium ions. *J. Am. Chem. Soc.* **1988**, *110* (14), 4706-4710.

- (116) W. L. Mock, T. A. W., T. L. Manimaran. Cycloaddition induced by cucurbituril. A case of Pauling principle catalysis. *J. Org. Chem.* **1983**, *48* (20), 3619-3620.
- (117) J. Kim, I.-S. J., S.-Y. Kim, E. Lee, J.-K. Kang, S. Sakamoto, K. Yamaguchi, K. Kim. New cucurbituril homologues: Synthesis, isolation, characterization, and X-ray crystal structures of cucubit[*n*]uril (*n*=5, 7, and 8). *J. Am. Chem. Soc.* **2000**, *122* (3), 540-541.
- (118) J. W. Lee, S. S., N. Selvapalam, H. J. Kim, K. Kim. Cucurbituril homologues and derivatives: New opportunities in supramolecular chemistry *Acc. Chem. Res.* **2003**, *36* (621-630).
- (119) H.-J. Kim, W. S. J., Y. H. Ko, K. Kim. Inclusion of methylviologen in cucurbit[7]uril. *Proc. Natl. Acad. Sci.* **2002**, *99*, 5007-5011.
- (120) W. Ong, M. G.-K., A. E. Kaifer. Cucurbit[7]uril: a very effective host for viologens and their cation radicals. *Org. Lett.* **2002**, *4*, 1791-1794.
- (121) A. Flinn, G. C. H., J. F. Stoddart. Decamethylcucurbit[5]uril. *Angew. Chem. Int. Ed. Engl.* **1992**, *31* (11), 1475-1477.
- (122) A. Day, A. P. A., R. J. Blanch, B. Snushall. Controlling factors in the synthesis of cucurbituril and its homologues. *J. Org. Chem.* **2001**, *66* (24), 8094-8100.
- (123) D. Lucas, T. M., G. Iannuzzi, L. Cao, J. B. Wittenberg, P. Anzenbacher Jr., L. Isaacs. Templated synthesis of glycoluril hexamer and monofunctionalized cucurbit[6]uril derivatives. *J. Am. Chem. Soc.* **2011**, *133* (44), 17966-17976.
- (124) Y. Shen, L. Z., Q. Wang. Template-directed synthesis of cucurbituril analogues using propanediurea as building block. *New J. Chem.* **2017**, *41*.
- (125) C. Marquez, H. F., W. M. Nau. Cucurbiturils: molecular nanocapsules for time-resolves fluorescence-based assays. *IEEE Trans. Nanobiosci.* **2004**, *3* (1), 39-45.
- (126) Y. Yang, X.-L. N., J.-F. Xu, X. Zhang. Fabrication of *nor-seco*-cucurbit[10]uril based supramolecular polymers *via* self-sorting. *Chem. Commun.* **2019**, *55* (92), 13836-13839.
- (127) L. Isaacs, S.-K. P., S. Liu, Y. Ho Ko, N. Selvapalam, Y. Kim, H. Kim, P. Y. Zavalij, G.-H. Kim, H.-S. Lee, K. Kim. The inverted cucurbit[*n*]uril family *J. Am. Chem. Soc.* **2005**, *127* (51), 18000-18001.
- (128) Q. Li, S.-C. Q., J. Zhang, K. Chen, Y. Huang, X. Xiao, Y. Zhang, F. Li, Y.-Q. Zhang, S.-F. Xue, Q.-J. Zhu, Z. Tao, L. F. Lindoy, G. Wei. Twisted cucurbit[*n*]urils. *Org. Lett.* **2016**, *18* (16), 4020-4023.
- (129) S. Liu, P. Y. Z., L. Isaacs. Cucurbit[10]uril. *J. Am. Chem. Soc.* **2005**, *127*, 16798-16799.
- (130) O. Danylyuk, V. S. A three-in-one crystal of mixed sized cucurbit[*n*]uril homologues. *CrystEngComm* **2020**, *22*, 2900-2903.
- (131) S. Lim, H. K., N. Selvapalam, K. J. Kim, S. J. Cho, G. Seo, K. Kim. Cucurbit[6]uril: organic molecular porous material with permanent porosity, exceptional stability, and acetylene sorption properties *Angew. Chem.* **2008**, *120*, 3400-3403.
- (132) D. Jiao, N. Z., O. A. Scherman. A "green" method for isolation of cucurbit[7]uril *via* a solid state metathesis reaction. *Chem. Commun.* **2010**, *46*, 2007-2009.

- (133) W. H. Huang, P. Y. Z., L. Isaacs. Cucurbit[*n*]uril formation proceeds by step-growth cycloligomerization. *J. Am. Chem. Soc.* **2008**, *130*, 8446-8454.
- (134) Q. Li, Y.-Q. Z., Q.-J. Zhu, S.-F. Xue, Z. Tao, X. Xiao. Coordination of alkaline earth metal ions in the inverted cucurbit[7]uril supramolecular assemblies formed in the presence of $[\text{ZnCl}_4]^{2-}$ and $[\text{CdCl}_4]^{2-}$. *Chem. Asian J.* **2015**, *10* (5), 1159-1164.
- (135) Limited, A. <https://aqdot.com/our-technology/> (accessed).
- (136) Kim, K. *Cucurbiturils and related macrocycles* Royal Society of Chemistry, 2019.
- (137) Isaacs, L. Cucurbit[*n*]urils: from mechanism to structure and function. *Chem. Commun.* **2009**, (6), 619-629.
- (138) Isaacs, L. The mechanism of cucurbituril formation *Isr. J. Chem.* **2011**, *51* (5-6), 578-591.
- (139) A. Chakraborty, A. W., D. Witt, J. Lagona, J. C. Fettinger, L. Isaacs. Diastereoselective formation of glycoluril dimers: Isomerization mechanism and implications for cucurbit[*n*]uril synthesis. *J. Am. Chem. Soc.* **2002**, *124* (28), 8297-8306.
- (140) D. Witt, J. L., F. Damkaci, J. C. Fettinger, L. Isaacs. Diastereoselective formation of methylene-bridged glycoluril dimers. *Org. Lett.* **2000**, *2* (6), 755-758.
- (141) L. Gilberg, B. Z., P. Y. Zavalij, V. Sindelar, L. Isaacs. Acyclic cucurbit[*n*]uril-type molecular containers: Influence of glycoluril oligomer length on their function as solubilizing agents. *Org. Biomol. Chem.* **2015**, (13), 4041-4050.
- (142) T. Lizal, L. U., M. Necas, V. Sindelar Propanediurea-based molecular clips bind halide anions: An insight into the mechanism of cucurbituril formation. *J. Org. Chem.* **2016**, *81* (19), 8906-8910.
- (143) R. P. Slijbesma, S. S. W., R. J. M. Nolte. A molecular clip that binds aromatic guests by an induced-fit mechanism. *J. Am. Chem. Soc.* **1992**, *114* (25), 9807-9813.
- (144) S. Zhang, L. G., Z. Miskolczy, L. Biczok, F. Biedermann, W. M. Nau. Binding affinities of cucurbit[*n*]urils with cations. *Chem. Commun.* **2019**, *55*, 14131-14134.
- (145) Y.-M. Jeon, J. K., D. Whang, K. Kim. Molecular container assembly capable of controlling binding and release of its guest molecules: Reversible encapsulation of organic molecules in sodium ion complexed cucurbituril *J. Am. Chem. Soc.* **1996**, *118* (40), 9790-9791.
- (146) D. Whang, J. H., J. H. Park, K. Kim. A molecular bowl with metal ion as bottom: Reversible inclusion of organic molecules in cesium ion complexed cucurbituril. *Angew. Chem. Int. Ed.* **1998**, *37* (1), 78-80.
- (147) J.-X. Liu, L.-S. L., R.-B. Huang, L.-S. Zheng. Molecular capsules based on cucurbit[5]uril encapsulating "naked" anion chlorine *Cryst. Growth Des.* **2006**, *6* (11), 2611-2614.
- (148) O. A. Gerasko, E. A. M., M. I. Naumova, M. Neumaier, M. M. Kappes, S. Lebedkin, D. Fenkse, V. P. Fedin. Sandwich-type tetranuclear lanthanide complexes with cucurbit[6]uril: From molecular compounds to coordination polymers. *Inorg. Chem.* **2008**, *47* (19), 8869-8880.

- (149) K. Jansen, H.-J. B., A. Wego, D. Dopp, C. Mayer, H.-J. Drexler, H.-J. Holdt, E. Schollmeyer. Cucurbit[5]uril, decamethylcucurbit[5]uril and cucurbit[6]uril. Synthesis, solubility and amine complex formation. *J. Incl. Phenom. Macrocycl. Chem.* **2001**, 39 (3-4), 357-363.
- (150) S. J. Barrow, S. K., M. J. Rowland, J. del Barrio, O. A. Scherman. Cucurbituril-based molecular recognition. *Chem. Rev.* **2015**, 115 (22), 12320-12406.
- (151) W. M. Nau, J. M. Taming fluorescent dyes with cucurbituril. *Int. J. Photoenergy* **2005**, 7 (3), 133-141.
- (152) M. A. Rankin, B. D. W. Fluorescence enhancement of curcumin upon inclusion into cucurbituril. *Supramol. Chem.* **2004**, 16 (7), 513-519.
- (153) S. Gupta, Y. Z., R. Varadharajan, V. Ramamurthy. Competitive binding of organic dyes between cucurbiturils and octa acid. *ACS Omega* **2018**, 3 (5), 5083-5091.
- (154) M. F. Czar, R. A. J. Understanding photophysical effects of cucurbituril encapsulation: A model study with acridine orange in the gas phase. *ChemPhysChem* **2013**, 14 (6), 1138-1148.
- (155) J. Ren, X. Z., C. Redshaw, X.-L. Ni Cucurbit[8]uril triggered fluorescence visualization of concentration-dependent interconversion of supramolecular polymer and dimer assemblies *Dyes and Pigments* **2022**, 203.
- (156) R. R. Hudgins, F. H., G. Gramlich, W. M. Nau. A fluorescence-based method for direct measurement of submicrosecond intramolecular contact formation in biopolymers: An explanatory study with polypeptides. *J. Am. Chem. Soc.* **2002**, 124 (4), 556-564.
- (157) J. Mohanty, W. M. N. Refractive index effects on the oscillator strength and radiative decay rate of 2,3-diazabicyclo[2.2.2]oct-2-ene. *Photochem. Photobiol. Sci.* **2004**, 3, 1026-1031.
- (158) K. I. Assaf, W. M. N. Cucurbiturils: from synthesis to high-affinity binding and catalysis. *Chem. Soc. Rev.* **2015**, 44 (2), 394-418.
- (159) W. M. Nau, M. F., K. I. Assaf. Deep inside cucurbiturils: Physical properties and volumes of their inner cavity determine the hydrophobic driving force for host-guest complexation. *Isr. J. Chem.* **2011**, 51 (5-6), 559-577.
- (160) S. Mecozzi, J. R. J. The 55% solution: A formula for molecular recognition in the liquid state *Chem. Eur. J.* **1998**, 4 (6), 1016-1022.
- (161) A. I. Lazar, F. B., K. R. Mustafina, K. I. Assaf, A. Henning, W. M. Nau Nanomolar binding of steroids to cucurbit[*n*]urils: Selectivity and applications *J. Am. Chem. Soc.* **2016**, 138 (39), 13022-13029.
- (162) S. He, B. H., B. Xiao, S. Chang, M. Podalko, W. M. Nau. Stabilization of Guest Molecules inside Cation-Lidded Cucurbiturils Reveals that Hydration of Receptor Sites Can Impede Binding *Angew. Chem. Int. Ed.* **2023**, 62 (49).
- (163) V. Wintges, L. B., Z. Miskolczy. Thermodynamics of inclusion complex formation between 1-alkyl-3-methylimidazolium ionic liquids and cucurbit[7]uril. *Supramol. Chem.* **2010**, 22 (10), 612-618.

- (164) Z. Miskolczy, L. B., M. Megyesi, I. Jablonkai. Inclusion complex formation of ionic liquids and other cationic organic compounds with cucurbit[7]uril studied by 4',6-diamino-2-phenylindole fluorescent probe. *J. Phys. Chem. B* **2009**, *113* (6), 1645-1651.
- (165) Kaifer, A. E. Portal effects on the stability of cucurbituril complexes *Isr. J. Chem.* **2018**, *58* (3-4), 244-249.
- (166) N. Zhao, G. O. L., O. A. Scherman. Monofunctionalized cucurbit[6]uril synthesis using imidazolium host-guest complexation. *Chem. Commun.* **2012**, *48*, 3070-3072.
- (167) Y.-J. Xu, J.-J. L., Z.-J. Feng, X.-L. Wang, M.-Y. Fan, X.-S. Wu, J. Sun, K.-Z. Shao, Z.-M. Su. Coordination environment regulation of cucurbit[6]uril-based metal-organic rotaxane networks for protection conduction. *Cryst. Growth Des.* **2022**, *22* (5), 2793-2798.
- (168) A. Kermagoret, D. B. The diversity of cucurbituril molecular switches and shuttles *Chem. Eur. J.* **2023**, *29* (70).
- (169) O. A. A. Alabraham, S. A. F., H. M. El-Said Azzazy Stimuli-responsive cucurbit[*n*]uril-based supramolecular nanocarriers for delivery of chemotherapeutics. *ACS Appl. Nano Mater.* **2023**, *6* (5), 3139-3158.
- (170) F. Liu, J. Z., Y. Mei. The origin of the cooperativity in the streptavidin-biotin system: A computational investigation thorough molecular dynamics simulations. *Sci. Rep.* **2016**, *6*.
- (171) O. A. Efremova, Y. V. M., N. V. Kuratieva, V. E. Fedorov. Novel supramolecular compounds based on cucurbit[6]uril, 1,8-diaminooctane and octahedral thiohydroxo anions with cluster core [Re₆S₈]. *Inorg. Chim. Acta* **2010**, *363* (15), 4411-4415.
- (172) S. J. C. Lee, J. W. L., H. H. Lee, J. Seo, D. H. Noh, Y. H. Ko, K. Kim, H. I. Kim. Host-guest chemistry from solution to the gas phase: An essential role of direct interaction with water for high-affinity binding of cucurbiturils. *J. Phys. Chem. B* **2013**, *117* (29), 8855-8864.
- (173) F. Bellia, D. L. M., C. Pendone, E. Rizzarelli, M. Saviano, G. Vecchio. Selectively functionalized cyclodextrins and their metal complexes. *Chem. Soc. Rev.* **2009**, *38* (9), 2756-2781.
- (174) S. B. Nimse, T. K. Biological applications of functionalized calixarenes. *Chem. Soc. Rev.* **2013**, *42* (1), 366-386.
- (175) G. Yu, M. X., Z. Zhang, J. Li, C. Han, F. Huang. A water-soluble pillar[6]arene: Synthesis, host-guest chemistry, and its application in dispersion of multiwalled carbon nanotubes in water. *J. Am. Chem. Soc.* **2012**, *134* (32), 13248-13251.
- (176) A. I. Day, A. P. A., R. J. Blanch A method for synthesizing partially substituted cucurbit[*n*]uril *Molecules* **2003**, *8* (1), 74-84.
- (177) C. A. Burnett, J. L., A. Wu, J. A. Shaw, D. Coady, A. I. Day, L. Isaacs. Preparation of glycoluril monomers for expanded cucurbit[*n*]uril synthesis. *Tetrahedron* **2003**, *59* (11), 1961-1970.
- (178) B. D. Wagner, P. G. B., J. Lagona, L. Isaacs. A cucurbit[6]uril analogue: Host properties monitored by fluorescence spectroscopy. *J. Phys. Chem. B* **2005**, *109* (16), 7686-7691.

- (179) B. Vinciguerra, L. C., J. R. Cannon, P. Y. Zavalij, C. Fenselau, L. Isaacs. Synthesis and self-assembly process of monofunctionalized cucurbit[7]uril *J. Am. Chem. Soc.* **2012**, *134* (31), 13133-13140.
- (180) S. Y. Jon, N. S., D. H. Oh, J.-K. Kang, S.-Y. Kim, Y. J. Jeon, J. W. Lee, K. Kim. Facile synthesis of cucurbit[*n*]uril derivatives via direct functionalization: Expanding utilization of cucurbit[*n*]uril. *J. Am. Chem. Soc.* **2003**, *125* (34), 10186-10187.
- (181) J. Lagona, B. D. W., L. Isaacs. Molecular-recognition properties of a water-soluble cucurbit[6]uril analogue. *J. Org. Chem.* **2006**, *71* (3), 1181-1190.
- (182) Y. Ahn, Y. J., N. Selvapalam, G. Yun, K. Kim. Supramolecular velcro for reversible underwater adhesion. *Angew. Chem.* **2013**, *125*, 3222-3226.
- (183) N. Dong, J. H., T. Li, A. Peralta, M. R. Awei, M. Ma, A. E. Kaifer. Synthesis and binding properties of monohydroxycucurbit[7]uril: A key derivative for the functionalization of cucurbituril hosts. *J. Org. Chem.* **2018**, *83* (10), 5467-5473.
- (184) M. Munteanu, S. C., H. Ritter. Cyclodextrin-*click*-cucurbit[6]uril: Combi-receptor for supramolecular polymer systems in water. *Macromolecules* **2009**, *42* (12), 3887-3891.
- (185) A. Koc, R. K., D. Tuncel "Clicked" porphyrin-cucurbituril conjugate: A new multifunctional supramolecular assembly based on triglycosylated porphyrin and monopropargyloxycucurbit[7]uril *Chem. Eur. J.* **2018**, *24* (58), 15550-15555.
- (186) D. A. Doyle, J. M. C., R. A. Pfuetzner, A. Kuo, J. M. Gulbis, S. L. Cohen, B. T. Chait, R. MacKinnon. The structure of the potassium channel: Molecular basis of K⁺ conduction and selectivity. *Science* **1998**, *280* (5360), 69-77.
- (187) Y. J. Jeon, H. K., S. Jon, N. Selvapalam, D. H. Oh, I. Seo, C.-S. Park, S. R. Jung, D.-S. Koh, K. Kim. Artificial ion channel formed by cucurbit[*n*]uril derivatives with a carbonyl group fringed protal reminiscent of the selectivity filter of K⁺ channels. *J. Am. Chem. Soc.* **2004**, *126* (49), 15944-15945.
- (188) P. Zhu, L. K., Y. Zhang, Q. Liu, X. Liao, Y. Song, B. Yang. Synthetic transmembrane channel molecules formed by acyclic cucurbiturils and pillararene: Tuning cation selectivity and generating membrane potential *J. Mol. Liq.* **2023**, 372.
- (189) G. Hettiarachchi, D. N., J. Wu, D. Lucas, D. Ma, L. Isaacs. Toxicology and drug delivery by cucurbit[*n*]type molecular containers. *PLoS ONE* **2010**, *5*, e10514.
- (190) S. Walker, R. O., F. J. McInnes, N. J. Wheate The potential of cucurbit[*n*]urils in drug delivery *Isr. J. Chem.* **2011**, *51* (5-6), 616-624.
- (191) Das, D.; Assaf, K. I.; Nau, W. M. Applications of Cucurbiturils in Medicinal Chemistry and Chemical Biology. *Frontiers in Chemistry* **2019**, *Volume 7 - 2019*, Review. DOI: 10.3389/fchem.2019.00619.
- (192) S. Walker, R. K., F. J. McInnes, N. J. Wheate. Synthesis, processing and solid state excipient interactions of cucurbit[6]uril and its formulation into tablets for oral drug delivery *Mol. Pharmaceutics* **2010**, *7* (6), 2166-2172.

- (193) N. S. Venkatamaranan, S. A., H. Mizuseki, Y. Kawazoe Theoretical prediction of the complexation behaviors of antitumor platinum drugs with cucurbiturils *J. Phys. Chem. B* **2012**, *116* (48), 14029-14039.
- (194) G. Jiang, G. L. Preparation and biological activity of novel cucurbit[8]uril-fullerene complex. *J. Photochem. Photobiol. B* **2006**, *85* (3), 223-227.
- (195) Q. Tang, J. Z., T. Sun, C.-H. Wang, Y. Huang, Q. Zhou. A turn-on supramolecular fluorescent probe for sensing benzimidazole fungicides and its application in living cell imaging. *Spectrochim. Acta Part A* **2018**, *191*, 372-376.
- (196) A. L. Koner, I. G., N. Saleh, W. M. Nau Supramolecular encapsulation of benzimidazol-derived drugs by cucurbit[7]uril *Can. J. Chem.* **2011**, *89*, 139-147.
- (197) Y. Zhao, D. P. B., D. L. Morris, M. H. Pourgholami, A. I. Day, J. G. Collins. Solubilisation and cytotoxicity of albendazole encapsulated in cucurbit[n]uril. *Org. Biomol. Chem.* **2008**, *6*, 4509-4515.
- (198) A. C. Bhasikuttan, J. M., W. M. Nau, H. Pal Efficient fluorescence enhancement and cooperative binding of an organic dye in a supra-biomolecular host-protein assembly *Angew. Chem. Int. Ed.* **2007**, *46*, 4120-4122.
- (199) H. S. El-Sheshtawy, S. C., K. L. Assaf, M. N. Shine, W. M. Nau, J. Mohanty. A supramolecular approach for enhanced antibacterial activity and extended shelf-life of fluoroquinolone drugs with cucurbit[7]uril. *Sci. Rep.* **2018**, *8*.
- (200) S. Adep, S. R. Controlled drug delivery systems: Current status and future directions *Molecules* **2021**, *26* (19).
- (201) J. A. Plumb, B. V., R. Oun, N. Gomez-Raman, Y. Kawazoe, N. S. Venkataramanan Cucurbit[7]uril encapsulated cisplatin overcomes cisplatin resistance via a pharmacokinetic effect *Metallomics* **2012**, *4* (6), 561-567.
- (202) M. J. Pisani, Y. Z., L. Wallace, C. E. Woodward, F. R. Keene, A. I. Day, J. G. Collins. Cucurbit[10]uril binding of dinuclear platinum(II) and ruthenium(II) complexes: association/dissociation rate from seconds to hours *Dalton Trans.* **2010**, *39*, 2078-2086.
- (203) C. Marquez, W. M. N. Two mechanisms of slow host-guest complexation between cucurbit[6]uril and cyclohexylmethylamine: pH-responsive supramolecular kinetics *Angew. Chem. Int. Ed.* **2001**, *40* (17), 3155-3160.
- (204) C. P. Carvalho, V. D. U., J. P. da Silva, W. M. Nau, U. Pischel. A photoinduced pH jump applied to drug release from cucurbit[7]uril *Chem. Commun.* **2011**, *47*, 8793-8795.
- (205) D. Jiao, J. G., X. J. Loh, D. Das, T.-C. Lee, O. A. Scherman Supramolecular peptide amphiphile vesicles through host-guest complexation *Angew. Chem. Int. Ed.* **2012**, *51*, 9633-9637.
- (206) L. Cao, G. H., V. Briken, L. Isaacs. Cucurbit[7]uril containers for targeted drug delivery of oxaliplatin to cancer cells. *Angew. Chem. Int. Ed.* **2013**, *52* (46), 12033-12037.
- (207) R. Sasmal, N. D. S., P. Nilanjana, R. Meenakshi, S. Rao, D. Joshi, I. Divyesh, S. Maneesha, V. Sheeba, S. S. Agasti. Synthetic host-guest assembly in cells and tissues: Fast, stable, and selective bioorthogonal imaging via molecular recognition *Analyt. Chem.* **2018**, *90* (19), 11305-11314.

- (208) X. Yang, K. V., M. Godard, F. Gassiot, R. Sonnette, G. Ferracci, B. Pecqueux, V. Monnier, L. Charles, S. Maria, M. Hardy, O. Ouari, M. Khrestchatisky, P. Lecorche, G. Jacqout, D. Bardelang. Preparation and *in vitro* validation of a cucurbit[7]uril-peptide conjugate targeting the LDL receptor. *J. Med. Chem.* **2023**, *66* (13), 8844-8857.
- (209) K. M. Park, K. S., H. Jung, D. W. Lee, Y. Ahn, J. Kim Cucurbituril-based nanoparticles: A new efficient vehicle for targeted intracellular delivery of hydrophobic drugs. *Chem. Commun.* **2009**, 71-73.
- (210) H. Jung, K. M. P., J. A. Yang, E. J. Oh, D. L. Lee, K. Park Theranostic systems assembled *in situ* on demand by host-guest chemistry. *Biomaterials* **2011**, *32*, 7687-7694.
- (211) A. Henning, H. B., W. M. Nau Label-free continuous enzyme assays with macrocycle fluorescent dye complexes *Nat. Methods* **2007**, *4* (8), 629-632.
- (212) N. Mohamed, S. K., W. M. Nau, A. Henning. Proton-gradient-driven sensitivity enhancement of liposome-encapsulated supramolecular chemosensors. *Angew. Chem. Int. Ed.* **2022**, *61* (35), e202207950.
- (213) K. L. Kim, G. S., J. Sim, J. Murray, M. Li, A. Lee, A. Shrinidhi, K. M. Park, K. Kim. Supramolecular latching system based on ultrastable synthetic binding pairs as versatile tools for protein imaging. *Nat. Commun.* **2018**, *9*.
- (214) B. Gong, B.-K. C., J.-Y. Kim, D. Shetty, Y.-H. Ko, N. Selvapalam, N. K. Lee, K. Kim High affinity host-guest FRET pair for single-vesicle content-mixing assay: Observation of flickering fusion events *J. Am. Chem. Soc.* **2015**, *137* (28), 8908-8911.
- (215) A. T. Bockus, L. C. S., A. G. Grice, O. A. Ali, C. C. Young, W. Mobley, A. Leek, J. L. Roberts, B. Vinciguerra, L. Isaacs, A. R. Urbach. Cucurbit[7]uril-tetramethylrhodamine conjugate for direct sensing and cellular imaging. *J. Am. Chem. Soc.* **2016**, *138*, 16549-16552.
- (216) L. Briant, J. M., A. Fürstenberg. Super-resolution imaging with a cucurbituril-encapsulated fluorophore. *Chem. Commun.* **2024**, *60* (94), 13943-13946.
- (217) G. Ghale, V. R., A. R. Urbach, W. M. Nau Determining protease substrate selectivity and inhibition by label-free supramolecular tandem enzyme assays. *J. Am. Chem. Soc.* **2011**, *133* (19), 7528-7535.
- (218) S. Sankaran, E. C., J. Huskens, P. Jonkheim. Cell adhesion on RGD-displaying knottins with varying numbers of tryptophan amino acids to tune the affinity for assembly on cucurbit[8]uril surfaces. *Langmuir* **2017**, *33* (35), 8813-8820.
- (219) F. Tian, M. C., D. Jiao, K. Wahlström, J. Geng, O. A. Scherman. Peptide separation through a CB[8]-mediated supramolecular trap-and-release process *Langmuir* **2011**, *27* (4), 1387-1390.
- (220) J. Chen, Q. H., Q. Wang, Y. Ding, S. Lu, L.-H. Wang, S. Li, R. Wang. Supramolecular luminol-AIEgen nanoparticles for deep-tissue-inflammation imaging. *ACS Appl. Nano Mater.* **2022**, *5* (5), 5993-6000.
- (221) Y. B. Lim, T. K., J. W. Lee, S. M. Kim, H. J. Kim, K. Kim. Self-assembled ternary complex of cationic dendrimer, cucurbituril, and DNA: Noncovalent strategy in developing a gene delivery carrier. *Bioconjug. Chem.* **2002**, *13* (6), 1181-1185.

- (222) S. Li, N. J., W. Zhao, Y.-F. Ding, Y. Zheng, L.-H. Wang, . An eco-friendly *in situ* activateable antibiotic via cucurbit[8]uril-mediated supramolecular crosslinking of branched polyethyleneimine. *Chem. Commun.* **2017**, 53, 5870-5873.
- (223) Q. Huang, S. L., Y.-F. Ding, H. Yin, L.-H. Wang, R. Wang Macrocyclic-wrapped polyethyleneimine for gene delivery with reduced cytotoxicity *Biometer. Sci.* **2018**, 6, 1031-1039.
- (224) S. Murkli, J. K., A. T. Brockett, M. Shuster, V. Briken, M. R. Roesch, L. Isaacs. In vitro and in vivo sequestration of phencyclidine by Me₄Cucurbit[8]uril *Chem. Eur. J.* **2020**, 27, 3098-3105.
- (225) D. Ma, B. Z., U. Hoffmann, M. G. Sundrup, M. Eikermann, L. Isaacs. Acyclic cucurbit[*n*]uril-type molecular containers bind neuromuscular blocking agents in vitro and reverse neuromuscular block in vivo *Angew. Chem. Int. Ed.* **2012**, 51, 11358-11362.
- (226) D. Das, K. I. A., W. M. Nau Applications of cucurbiturils in medicinal chemistry and chemical biology. *Front. Chem.* **2019**, 7.
- (227) C. Yang, Q. W., W. Ding. Recent progress in the imaging detection of enzyme activities *in vivo*. *RSC Adv.* **2019**, 9, 25285-25302.
- (228) Z. Haida, M. H. A comprehensive review on the determination of enzymatic assay and nonenzymatic antioxidant activities *Food Sci Nutr.* **2019**, 7 (5), 1555-1563.
- (229) S. Zhang, K. I. A., C. Huang, A. Henning, W. M. Nau Ratiomeric DNA sensing with a host-guest FRET pair. *Chem. Commun.* **2019**, 55 (5), 671-674.
- (230) M. Kubista, J. M. A., M. Bengtsson, A. Forootan, J. Jonak, K. Lind, R. Sindelka, R. Sjöback, B. Sjögreen, L. Strömbaum, A. Stahlberg, N. Zoric The real-time polymerase chain reaction *Mol Aspects Med* **2006**, 27 (2-3), 95-125.
- (231) C. Hu, L. G., A. Prabodh, A. Bakshi, A. Siennicka, P. A. Levkin, M. M. Kappes, F. Biedermann Covalent cucurbit[7]uril-dye conjugates for sensing in aqueous saline media and biofluids *Chem. Sci.* **2020**, 11 (41), 11142-11153.
- (232) C. Hu, T. J., P. Chakraborty, M. Neumaier, P. A. Levkin, M. M. Kappes, F. Biedermann. Further dimensions for sensing in biofluids: Distinguishing bioorganic analytes by the salt-induced adaption of a cucurbit[7]uril-based chemosensor. *J. Am. Chem. Soc.* **2022**, 144 (29), 13084-13095.
- (233) W.-I. K. Chio, H. X., Y. Zhang, Y. Lan, T.-C. Lee. SERS biosensors based on cucurbituril-mediated nanoaggregates for wastewater-based epidemiology *Trends Anal. Chem.* **2022**, 146.
- (234) N. M. Kumar, P. P., C. Hu, L. M. Grimm, F. Biedermann. Chemiluminescent cucurbit[*n*]uril-based chemosensor for the detection of drugs in biofluids *ACS Sens.* **2022**, 7 (8), 2312-2319.
- (235) E. Masson, Y. M. S., J.-P. Masson, M. E. Kordesch, C. Yuwono. "Supramolecular circuitry": Three chemiluminescent, cucurbit[7]uril-controlled on/off switches *Org. Lett.* **2011**, 13 (15), 3872-3875.
- (236) Q. Wang, L. L., X. Bing. Bioinspired supramolecular confinement of luminol and heme proteins to enhance the chemiluminescent quantum yield *Chem. Eur. J.* **2009**, 15 (13), 3168-3172.
- (237) A. Roda, M. G. Analytical chemiluminescence and bioluminescence: Lates achievements and new horizons. *Anal. Bioanal. Chem.* **2011**, 402, 69-76.

- (238) S. He, W. S., X. Zhang, J. Li, Y. Huang. β -cyclodextrins-based inclusion complexes of CoFe_2O_4 magnetic nanoparticles as catalyst for the luminol chemiluminescence system and their applications in hydrogen peroxide detection *Talanta* **2010**, 82 (1), 377-383.
- (239) R. J. Dinis-Oliveira, J. A. D., A. Sanchez-Navarro, F. Remiao, M. L. Bastos, F. Carvalho. Paraquat poisonings: mechanisms of lung toxicity, clinical features, and treatment *Crit. Rev. Toxicol.* **2008**, 38 (1), 13-71.
- (240) N. M. Kumar, P. G., A. Casini, F. Biedermann, G. Moreno-Alcantar, P. Picchetti Electrochemical detection of drugs via a supramolecular cucurbit[7]uril-based indicator displacement assay *ACS Sens.* **2023**, 8 (7), 2525-2532.
- (241) M. del Pozo, P. H., L. Hernandez, C. Quinatana. The use of cucurbit[8]uril host-guest interactions in the development of an electrochemical sensor: characterization and application to tryptophan determination *J. Mater. Chem.* **2011**, 21 (35), 13657-13663.
- (242) R. Pinalli, A. P., E. Dalcanale Biochemical sensing with macrocyclic receptors *Chem. Soc. Rev.* **2018**, 47 (18), 7006-7026.
- (243) Bard, A. J. *Electrogenerated Chemiluminescence* CRC Press 2004.
- (244) Z. Liu, W. Q., G. Xu Recent advances in electrochemiluminescence *Chem. Soc. Rev.* **2015**, 44 (10), 3117-3142.
- (245) C. Ma, Y. C., X. Gou, J.-J. Zhu Recent Progress in Electrochemiluminescence Sensing and Imaging. *Anal. Chem.* **2019**, 91 (1), 431-454.
- (246) H. Qi, C. Z. Electrogenerated Chemiluminescence Biosensing *Anal. Chem.* **2019**, 92 (1), 524-534.
- (247) N. E. Tokel, A. J. B. Electrogenerated chemiluminescence. IX. Electrochemistry and emission from systems containing tris(2,2'-bipyridine)ruthenium(II) dichloride. *J. Am. Chem. Soc.* **1972**, 94 (8), 2862-2863.
- (248) E. Terpetschnig, H. S., H. Malak, J. R. Lakowicz. Metal-ligand complexes as a new class of long-lived fluorophores for protein hydrodynamics *Biophys. J.* **1995**, 68 (1), 342-350.
- (249) H. Yang, J. K. L., D. Yost, R. J. Massey. Electrochemiluminescence: a new diagnostic and research tool *Nat. Biotechnol.* **1994**, 12, 193-194.
- (250) L. D'Alton, S. C., G. J. Barbante, D. Hoxley, D. J. Hayne, P. S. Francis, C. F. Hogan A simple, low-cost instrument for electrochemiluminescence immunoassays based on a Raspberry Pi and screen-printed electrodes *Bioelectrochem.* **2022**, 146.
- (251) Magub, S. *How to make your own ECL* 2025. <https://bitesizebio.com/25028/how-to-make-your-own-ecl-2/> (accessed).
- (252) X. Gou, Z. X., C. Ma, J.-J. Zhu. A close look at mechanism, application, and opportunities of electrochemiluminescence microscopy. *Chem. Biomed. Imaging* **2023**, 1 (5), 414-433.
- (253) C. Meng, S. K., F. Du, Y. Guan, F. Kanoufi, N. Sojic, G. Xu Recent advanced in electrochemiluminescence imaging analysis. *eScience* **2022**, 2 (6), 591-605.

- (254) M. Hesari, Z. D. Spooling electrochemiluminescence spectroscopy: development, applications and beyond. *Nat. Protoc.* **2021**, *16*, 2109-2130.
- (255) M. Sornambigai, L. B., N. Sojic, S. S. Kumar Tris(2,2'-bipyridyl)ruthenium (II) complex as a universal reagent for the fabrication of heterogeneous electrochemiluminescence platforms and its recent analytical applications *Crit. Rev.* **2023**, *415*, 5875-5898.
- (256) E. Villani, K. S., Y. Einaga, S. Inagi, A. Fiorani, . Photophysics and electrochemistry of ruthenium complexes for electrogenerated chemiluminescence. *J. Electroanal. Chem.* **2022**, 921.
- (257) C. Stephenson, T. Y., D. W. C. MacMillan. An Overview of the Physical and Photophysical Properties of $[\text{Ru}(\text{bpy})_3]^{2+}$. In *Visible Light Photocatalysis in Organic Chemistry, First* 2018.
- (258) F. E. Beideman, D. M. H. Electrogenerated chemiluminescence from 9,10-diphenylanthracene cations reacting with radical anions *J. Phys. Chem.* **1979**, *83* (17), 2203-2209.
- (259) E. L. Ritchie, P. P., R. M. Wightman Free energy control of reaction pathways in electrogenerated chemiluminescence *J. Am. Chem. Soc.* **1997**, *119* (49), 11920-11925.
- (260) Richter, M. M. Electrochemiluminescence (ECL). *Chem. Rev.* **2004**, *104* (6), 3003-3036.
- (261) L. Hu, G. X. Applications and trends in electrochemiluminescence *Chem. Soc. Rev.* **2010**, *39* (8), 3275-3304.
- (262) Ma, C.; Cao, Y.; Gou, X.; Zhu, J.-J. Recent Progress in Electrochemiluminescence Sensing and Imaging. *Analytical Chemistry* **2020**, *92* (1), 431-454. DOI: 10.1021/acs.analchem.9b04947.
- (263) M.-M. Chang, T. S., A. J. Bard Electrogenerated chemiluminescence. 30. Electrochemical oxidation of oxalate ion in the presence of luminescers in acetonitrile solutions *J. Am. Chem. Soc.* **1977**, *99* (16), 5399-5403.
- (264) Deaver, D. R. A new non-isotopic detection system for immunoassays. *Nature* **1995**, *377*, 758-760.
- (265) Noffsinger, J. B. Generation of chemiluminescence upon reaction of aliphatic amines with tris(2,2'-bipyridine)ruthenium(III). *Anal. Chem.* **1987**, *59* (6), 865-868.
- (266) W. Miao, J.-P. C., A. J. Bard Electrogenerated chemiluminescence 69: The tris(2,2'-bipyridine)ruthenium(II), $(\text{Ru}(\text{bpy})_3^{2+})/\text{tri-}n\text{-propylamine}$ (TPrA) system revisited - a new route involving TPrA⁺ cation radicals. *J. Am. Chem. Soc.* **2002**, *124* (48), 14478-14485.
- (267) S. Workman, M. M. R. The effects of nonionic surfactants on the Tris(2,2'-bipyridyl)ruthenium(II)-tripropylamine electrochemiluminescence system *Anal. Chem.* **2000**, *72* (22), 5556-5561.
- (268) Y. Zu, A. J. B. Electrogenerated chemiluminescence. 67. Dependence of light emission of the Tris(2,2')bipyridylruthenium(II)/tripropylamine system on electrode surface hydrophobicity. *Anal. Chem.* **2001**, *73* (16), 3960-3964.
- (269) F. Li, Y. Z. Effect of nonionic fluorosurfactant on the electrogenerated chemiluminescence of the Tris(2,2'-bipyridine)ruthenium(II)/tri-*n*-propylamine system: Lower oxidation potential and higher emission intensity *Anal. Chem.* **2004**, *76* (6), 1768-1772.
- (270) G. Xu, H.-L. P., B. Xu, S. Dong, K.-Y. Wong Enhancing the electrochemiluminescence of the Tris(2,2'-bipyridyl)ruthenium(II) by ionic surfactants. *Analyst* **2004**, *130* (4), 541-544.

- (271) D. J. Vinyard, M. M. R. Enhanced electrogenerated chemiluminescence in the presence of fluorinated alcohols *Anal. Chem.* **2007**, *79* (16), 6404-6409.
- (272) X. Liu, L. S., W. Niu, H. Li, G. Xu Environmentally friendly and highly sensitive ruthenium(II) tris(2,2'-bipyridyl) electrochemiluminescent system using 2-(dibutylamino)ethanol as co-reactant *Angew. Chem. Int. Ed.* **2007**, *46* (3), 421-424.
- (273) S. Han, W. N., H. Li, L. Hu, Y. Yuan, G. Xu Effect of hydroxyl and amino groups on electrochemiluminescence activity of tertiary amines at low tris(2,2'-bipyridyl)ruthenium(II) concentrations *Talanta* **2010**, *81* (1-2), 44-47.
- (274) G. Xu, S. D. Electrochemiluminescence of the $\text{Ru}(\text{bpy})_3^{2+}/\text{S}_2\text{O}_8^{2-}$ *Electroanalysis* **2000**, *12* (8), 583-587.
- (275) L. Hu, H. L., S. Zhu, L. Fan, L. Shi, X. Liu, G. Xu. Cathodic electrochemiluminescence in aqueous solutions at bismuth electrodes *Chem. Commun.* **2007**, (40), 4146-4148.
- (276) J.-G. Lee, K. Y., G.-S. Lim, S. E. Lee, S. Kim, J.-K. Park DNA biosensor based on the electrochemiluminescence of $\text{Ru}(\text{bpy})_3^{2+}$ with DNA-binding intercalators *Bioelectrochem.* **2007**, *70* (2), 228-234.
- (277) F. Du, Y. C., C. Meng, B. Lou, W. Zhang, G. Xu Recent advances in electrochemiluminescence immunoassay based on multiple-signal strategy *Curr. Opin. Electrochem.* **2021**, 28.
- (278) A. Zanut, A. F., S. Canola. Insights into the mechanism of coreactant electrochemiluminescence facilitating enhanced bioanalytical performance. *Nat. Commun.* **2020**, *11*.
- (279) M. J. Duffy, D. E., E. W. McDermott. CA 15-3: uses and limitation as a biomarker for breast cancer *Clin Chim Acta* **2010**, *411* (23-24), 1869-1874.
- (280) M. Li, M. Z., S. Ge, M. Yuan, J. Yu, J. Huang, S. Liu. Ultrasensitive electrochemiluminescence immunosensor based on nanoporous gold electrode and Ru-AuNPs/graphene as signal labels *Sens Actuators B Chem* **2013**, *181*, 50-56.
- (281) X. Yang, Y. W., Y. Du, H. Qi, Q. Gao, C. Zhang Electrogenerated chemiluminescence immunoassays on nanoelectrode ensembles platform with magnetic microbeads for the determination of carbohydrate antigen *Anal. Chem.* **2020**, *92* (24), 15837-15844.
- (282) W. Miao, A. J. B. Electrogenerated chemiluminescence. 80. C-Reactive protein determination at high amplification with $[\text{Ru}(\text{bpy})_3]^{2+}$ -containing microspheres *Anal. Chem.* **2004**, *76* (23), 7109-7113.
- (283) W. Zhan, A. J. B. Electrogenerated chemiluminescence. 83. Immunoassay of human C-reactive protein by using $\text{Ru}(\text{bpy})_3^{2+}$ -encapsulated liposomes as labels. *Anal. Chem.* **2006**, *79* (2), 459-463.
- (284) N. Egashira, S.-I. M., E. Hifumi, Y. Mitoma, T. Uda Attomole detection of hemagglutinin molecule of influenza virus by combining an electrochemiluminescence sensor with an immunoliposome that encapsulates a Ru complex. *Anal. Chem.* **2008**, *80* (11), 4020-4025.
- (285) T. Kenakin, P. D. Pharmacologists get a bigger and better tool box *Curr. Opin. Pharm.* **2007**, *7* (5), 505-506.

- (286) W. Miao, A. J. B. Electrogenerated chemiluminescence. 77. DNA hybridization detection at high amplification with $[\text{Ru}(\text{bpy})_3]^{2+}$ -containing microspheres. *Anal. Chem.* **2004**, 76 (18), 5379-5386.
- (287) J. Zhang, H. Q., Y. Li, J. Yang, Q. Gao, C. Zhang Electrogenerated chemiluminescence DNA biosensor based on hairpin DNA probe labeled with ruthenium complex *Anal. Chem.* **2008**, 80 (8), 2888-2894.
- (288) W. Cao, J. P. F., J. Demas, J. P. Landers Quenching of the electrochemiluminescence of Tris(2,2'-bipyridine)ruthenium(II) by ferrocene and its potential application to quantitative DNA detection *J. Am. Chem. Soc.* **2006**, 128 (23), 7572-7578.
- (289) X. Wang, W. Y., P. Dong, J. Zhou, P. He, Y. Fang A controllable solid-state $\text{Ru}(\text{bpy})_3^{2+}$ electrochemiluminescence film based on conformation change of ferrocene-labeled DNA molecular beacon *Langmuir* **2008**, 24 (5), 2200-2205.
- (290) J. G. Bruno, J. L. K. In vitro selection of DNA aptamers to anthrax spores with electrochemiluminescence detection *Biosens. Bioelectron.* **1999**, 14 (5), 457-464.
- (291) Y. Li, H. Q., Y. Peng, J. Yang, C. Zhang Electrogenerated chemiluminescence aptamer-based biosensor for the determination of cocaine *Electrochem. Comm.* **2007**, 9 (10), 2571-2575.
- (292) L. Fang, Z. L., H. Wei, E. Wang A electrochemiluminescence aptasensor for detection of thrombin incorporating the capture aptamer labeled with gold nanoparticles immobilized onto thio-silanized ITO electrode *Anal. Chim. Acta* **2008**, 628 (1), 80-86.
- (293) S. Liang, G. J. C. An electrochemiluminescent aptamer switch for a high-throughput assay of an RNA editing reaction *RNA* **2009**, 15, 1929-1938.
- (294) X. Wang, J. Z., W. Yun, S. Xiao, Z. Chang, P. He, Y. Fang. Detection of thrombin using electrogenerated chemiluminescence based on $\text{Ru}(\text{bpy})_3^{2+}$ -doped silica nanoparticle aptasensor via target protein-induced strand displacement. *Anal. Chim. Acta* **2007**, 598 (2), 242-248.
- (295) J. M. Gott, R. B. E. Functions and mechanisms of RNA editing *Annu. Rev. Genet.* **2000**, 34.
- (296) S. Zanarini, M. F., G. Valenti, M. Marcaccio, L. Prodi, S. Bonacchi, P. Contreras-Carballada, R. M. Williams, M. C. Feiters, R. J. M. Nolte, L. De Cola, F. Paolucci Green and blue electrochemically generated chemiluminescence from click chemistry - customizable iridium complexes. *Chem. Eur. J.* **2011**, 17 (16), 4640-4647.
- (297) E. Rampazzo, S. B., D. Genovese, R. Juris, M. Marcaccio, M. Montalti, F. Paolucci, M. Sgarzi, G. Valenti, N. Zaccheroni, L. Prodi Nanoparticles in metal complexes-based electrogenerated chemiluminescence for highly sensitive applications *Coord. Chem. Rev.* **2012**, 256 (15-16), 1664-1681.
- (298) J. Li, S. G., E. Wang Recent advances in new luminescent nanomaterials for electrochemiluminescence sensors *RSC Adv.* **2012**, 2 (9), 3579-3586.
- (299) S. Deng, H. J. Electrogenerated chemiluminescence of nanomaterials for bioanalysis *Analyst* **2013**, 138 (1), 43-61.

- (300) Y. Zhang, H. Y., Y. Dong Electrochemiluminescence of an iridium complex doped with SiO₂ nanoparticles to detect 2-adamantanamine based on the host-guest interaction of cucurbit[7]uril *Analyst* **2024** *149* (4), 1160-1168.
- (301) D. Feng, X. T., Y. Wu, C. Ai, Y. Lao, Q. Chen, H. Han Electrochemiluminescence nanogears aptasensor based in MIL-53(Fe)@CdS for multiplexed detection of kanamycin and neomycin *Biosens. Bioelectron.* **2019**, *129*, 100-106.
- (302) W. Gu, X. W., J. Wen, S. Cao, L. Jiao, Y. Wu, X. Wei, L. Zheng, L. Hu, L. Zhang, C. Zhu Modulating oxygen reduction behaviors on nickel single-atom catalysts to probe the electrochemiluminescence mechanism at the atomic level *Analyt. Chem.* **2021**, *93* (24), 8663-8670.
- (303) M.-H. Jiang, S.-K. L., X. Zhong, W.-B. Liang, Y.-Q. Chai, Y. Zhuo, R. Yuan Electrochemiluminescence enhanced by restriction of intramolecular motions (RIM): tetraphenylethylene microcrystals as a novel emitter for mucin 1 detection *Analyt. Chem.* **2019**, *91* (6), 3710-3716.
- (304) Y. Jiang, C. R., Y. Qiao, S. Zhang, J. Shi, X. Yang, S. Li, Y. Zhou, Y. Li A programmable dynamic range electrochemiluminescence platform with dual-signal output and single luminophore, utilizing polyadenine-anchored triblock DNA *Anal. Chem.* **2025**, *97* (25), 13151-13159.
- (305) S. Qasim, S.-Y. H., E. Rossi, Z. Salahshoor, C.-H. Lin, L. Polo Parada, M. Fidalgo Detection of progesterone in aqueous samples by molecularly imprinted photonic polymers *Microchim. Acta* **2022**, *189*.
- (306) X. Zhang, Y. J., R. Feng, T. Wu, N. Zhang, Y. Du, H. Ju Cucurbituril enhanced electrochemiluminescence of gold nanoclusters via host-guest recognition for sensitive D-dimer sensing *Anal. Chem.* **2023**, *95* (2), 1461-1469.
- (307) X. Zhang, Y. D., R. Feng, X. Ren, T. Wu, Y. Jia, N. Zhang, F. Li, O. Wei, H. Ju An electrochemiluminescence insulin sensing platform based in the molecular recognition properties of cucurbit[7]uril *Biosens. Bioelectron.* **2023**, *227*.
- (308) V. Hong, N. F. S., M. Manchester, M. G. Finn. Labelling live cells by copper-catalyzed alkyne-azide click chemistry *Bioconjug. Chem.* **2010**, *21*, 1912-1916.
- (309) C. Bannwarth, S. E., S. Grimme. GFN2-xTB - An accurate and broadly parametrized self-consistent tight-binding quantum chemical method with multipole electrostatics and density-dependent dispersion contributions. *J. Chem. Theory Comput.* **2019**, *15* (3), 1652-1671.
- (310) P. Pracht, F. B., S. Grimme Automated exploration of the low-energy chemical space with fast quantum chemical methods. *Phys. Chem. Chem. Phys.* **2020**, *22*, 7169-7192.
- (311) C. Larriba, C. J. H. J. Ion mobilities in diatomic gases: Measurement versus prediction with non-specular scattering models. *J. Phys. Chem. A* **2013**, *117* (19), 3887-3901.
- (312) C. Plett, S. G. Automated and efficient generation of general molecular aggregate structures *Angew. Chem. Int. Ed.* **2022**, *62* (4).
- (313) S. Grimme, A. H., S. Ehlert, J.-M. Mewes r2SCAN-3c: A "swiss army knife" composite electronic structure method *J. Chem. Phys.* **2021**, *154*.

- (314) S. Senler, W. L., M. H. Tootoonchi, S. Yi, A. E. Kaifer The cucurbituril 'portal' effect *Supramol. Chem.* **2014**, *26* (9), 677-683.
- (315) V. F. Pais, E. F. A. C., J. P. C. Tome, U. Pischel Supramolecular control of phthalocyanine dye aggregation *Supramol. Chem.* **2014**, *26* (9), 642-647.
- (316) E.-C. Lee, H.-J. K., S. Y. Park Reversible shape-morphing and fluorescence-switching in supramolecular nanomaterials consisting of amphiphilic cyanostilbene and cucurbit[7]uril *Chem. Asian J.* **2019**, *14* (9), 1457-1461.
- (317) L. M. Grimm, J. S., B. Tkachenko, P. R. Schreiner, M. K. Gilson, F. Biedermann The temperature-dependence of host-guest binding thermodynamics: experimental and simulation studies *Chem. Sci.* **2023**, *14* (42), 11818-11829.
- (318) A. D. Stancu, H.-J. B., L. Mutihac. Survey on thermodynamic properties for the complexation behaviour of some calixarene and cucurbituril receptors *J. Incl. Phenom. Macrocycl. Chem.* **2013**, *75*, 1-10.
- (319) N. Zhao, L. L., F. Biedermann, O. A. Scherman. Binding studies on CB[6] with a series of 1-alkyl-3-methylimidazolium ionic liquids in an aqueous system. *Chem. Asian J.* **2010**, *5* (3), 530-537.
- (320) K. Kikuchi, C. S., M. Watabe, H. Ikeda, Y. Takahashi, T. Miyashi. New aspects on fluorescence quenching by molecular oxygen *J. Am. Chem. Soc.* **1993**, *115*, 5180-5184.
- (321) C. J. Adams, N. G. C., N. J. Goodwin, O. D. Hayward, A. G. Orpen, A. J. Wood Metal-metal charge transfer and solvatochromism in cyanomanganese carbonyl complexes of ruthenium and osmium *Dalton Trans.* **2006**, (29), 3584-3596.
- (322) Nakamaru, K. Solvent effect on the nonradiative deactivation of the excited state of Tris(2,2'-bipyridyl)ruthenium(II) ion *Bull. Chem. Soc. Jpn.* **1982**, *55*, 1639-1640.
- (323) S. Chaemchuen, N. A. K., K. Zhou, F. Verpoort Metal-organic frameworks for upgrading biogas via CO₂ adsorption to biogas green energy. *Chem. Soc. Rev.* **2013**, *24* (42), 9304-9332.
- (324) X. Sun, B. L., C. Xia, X. Zhou, H. Zhang "Liquid-like" type (COO⁻)₂(H₂O)₁₀ anion water clusters in three-dimensional supramolecular structure of cucurbit[6]uril *CrystEngComm* **2012**, *14* (24), 8525-8529.
- (325) R. Eelkerna, K. M., B. Odell, H. L. Anderson. Radical cation stabilization in a cucurbituril oligoaniline rotaxane *J. Am. Chem. Soc.* **2007**, *129* (41), 12384-12385.
- (326) E. Mezzina, F. C., G. F. Pedulli, M. Lucarini. Nitroxide radicals as probes for exploring the binding properties of the cucurbit[7]uril host *Chem. Eur. J.* **2007**, *13* (25), 7223-7233.
- (327) D. Luo, K. A. C., D. Miranda, J. F. Lovell Chemophototherapy: an emerging treatment option for solid tumors *Adv. Sci.* **2017**, *4*.
- (328) T. J. Dougherty, C. J. G., B. W. Henderson, G. Jori, D. Kessel, M. Korbelik, J. Moan, Q. Peng Photodynamic therapy *JNCI* **1998**, *90* (12), 889-905.
- (329) R. W. Redmond, J. N. G. A compilation of singlet oxygen yields from biologically relevant molecules. *Photochem. Photobiol.* **1999**, *70*, 391-475.

- (330) E. Gandin, Y. L., A. Van de Vorst Quantum yield of singlet oxygen production by xanthene derivatives *Photochem. Photobiol.* **1983**, *37*, 271-278.
- (331) Ochsner, M. Photophysical and photobiological processes in the photodynamic therapy of tumors. *J. Photochem. Photobiol. B* **1997**, *39*, 1-18.
- (332) A. Gorman, J. K., C. O'Shea, W. M. Gallagher, D. F. O'Shea. In vitro demonstration of the heavy-atom effect for photodynamic therapy. *J. Am. Chem. Soc.* **2004**, *126*, 10619-10631.
- (333) B. Valeur, M. N. B.-S. *Molecular fluorescence. Principles and applications* Wiley-VCH, 2013.
- (334) D. García-Fresnadillo, Y. G., G. Orellana, A. M. Braun and E. Oliveros. Singlet-oxygen ($^1\Delta_g$) production by ruthenium (II) complexes containing polyazaheterocyclic ligands in methanol and in water. *Helv. Chim. Acta* **1996**, *79*, 1222-1238.
- (335) S. Monro, K. L. C., H. Yin, J. Roque, P. Konda, S. Gujar, R. P. Thummel, L. Lilge, C. G. Cameron, S. A. McFarland Transition metal complexes and photodynamic therapy from a tumor-centered approach: Challenges, opportunities, and highlights from the development of TLD1433. *Chem. Rev.* **2019**, *119*, 797-828.
- (336) Hamblin, M. R. Fullerenes as photosensitizers in photodynamic therapy: pros and cons. *Photochem. Photobiol. Sci* **2018**, *17*, 1515-1533.
- (337) W. Zhou, Y. C., Y. Zhang, X. Xin, R. Li, C. Xie, Q. Fan Iodine-rich semiconducting polymer nanoparticles for CT/fluorescence dual-modal imaging-guided enhanced photodynamic therapy *Small* **2020**, *16*.
- (338) L. Guo, J. G., Q. Liu, Q. Jia, H. Zhang, W. Liu, G. Niu, S. Liu, J. Gong, S. Hackbarth, P. Wang Versatile polymer nanoparticles as two-photon-triggered photosensitizers for simultaneous cellular, deep-tissue imaging, and photodynamic therapy *Adv. Healthcare Mater.* **2017**, *6*.
- (339) D. Jiao, F. B., O. A. Scherman. Size selective supramolecular cages from aryl-bisimidazolium derivatives and cucurbit[8]uril *Org. Lett.* **2011**, *12* (12), 3044-3047.
- (340) L. A. Wingard, E. C. J., J. J. Sabatini Efficient method for the cycloaminomethylation of glycoluril *Tet. Lett.* **2016**, *57* (13), 1681-1682.
- (341) S. Zhang, Z. D., K. I. Assaf, M. Nilam, T. Thiele, U. Pischel, U. Schedler, W. M. Nau, A. Henning Precise supramolecular control of surface coverage densities on polymer micro- and nanoparticles *Chem. Sci.* **2018**, *9* (45), 8575-8581.
- (342) B. M. Zeglis, J. K. B. A mismatch-selective bifunctional rhodium-oregon green conjugate: A fluorescent probe for mismatched DNA *J. Am. Chem. Soc.* **2006**, *128* (17), 5654-5655.
- (343) Z. Fan, J. W., W. Liu, J. Ma, J. Sun, P. Wang Thiol-selective sensor based on intramolecular energy transfer between a bichromophoric system *Tet. Lett.* **2013**, *69* (23), 4536-4540.
- (344) F. Annunziata, C. P., S. Dallavalle, L. Tamborini, A. Pinto. An overview of coumarin as a versatile and readily accessible scaffold with broad-ranging biological activities. *Int. J. Mol. Sci.* **2020**, *21* (13).

- (345) Z. D. Nan, Y. S., Y. D. Zhu, H. Zhang, R. R. Sun, J. J. Tian, Z. B. Jiang, X. L. Ma, C. Bai Systematic review of natural coumarins in plants (2019-2024): Chemical structures and pharmacological activities *Phytochemistry* **2025**, 235.
- (346) F. Borges, F. R., N. Milhanes, L. Santana, E. Uriarte. Simple coumarins and analogues in medicinal chemistry: Occurrence, synthesis and biological activity. *Curr. Med. Chem.* **2005**, *12*, 887-916.
- (347) A. E. Kummerle, F. V., D. P. Franco, T. M. Pereira Coumarin compounds in medicinal chemistry: Some important examples from last year *Curr. Top. Med. Chem.* **2018**, *18*, 124-128.
- (348) L. Wu, X. W., W. Xu, F. Farzaneh, R. Xu. The structure and pharmacological functions of coumarins and their derivatives *Curr. Med. Chem.* **2009**, *16* (32), 4236-4260.
- (349) M. I. Hussain, Q. A. S., M. N. K. Khatkhat, B. Hafez, M. J. Reigosa, A. El-Keblawy. Natural product coumarins: Biological and pharmacological perspectives *Biologia* **2019**, *74*, 863-888.
- (350) A. Stefanachi, F. L., L. Pisani, M. Catto, A. Carotti Coumarin: A natural, privileged and versatile scaffold for bioactive compounds *Molecules* **2018**, *23* (2).
- (351) N. Rohman, B. A., T. Wukisari, Z. Judeh Recent trends in the synthesis and bioactivity of coumarin, coumarin-chalcone, and coumarin-triazole molecular hybrids *Molecules* **2024**, *29* (5).
- (352) D. Srikrishna, C. G., P. K. Dubey. A review on pharmacological properties of coumarins *Mini Rev. Med. Chem.* **2016**, *2* (18), 113-141.
- (353) H. K. Santra, D. B. Natural bioactive products in sustainable agriculture. Springer, 2020; pp 131-219.
- (354) D. Gupta, E. G., K. Bajaj. Coumarin - Synthetic methodologies, pharmacology, and application as natural fluorophore *Top. Curr. Chem.* **2024**, 382.
- (355) G. Kaur, I. S., R. Tandon, N. Tandon Recent advancements in coumarin based colorimetric and fluorescent chemosensors *Inorg. Chem. Commun.* **2023**, 158.
- (356) Y. Gao, H. L., P. Li, Q. Liu, W. Wang, B. Zhao. Coumarin-based fluorescent chemosensor for the selective quantification of Zn^{2+} and AcO^- in an aqueous solution and living cells. *Tet. Lett.* **2017**, *58* (23), 2193-2198.
- (357) R. H. Vekariya, H. D. P. Recent advances in the synthesis of coumarin derivatives via Knoevenagel condensation: a review. *Synth. Commun.* **2014**, *44* (19), 2756-2788.
- (358) B. V. Kumar, H. S. B. N., D. Girija, B. V. Kumar ZnO nanoparticle as catalyst for efficient green one-pot synthesis of coumarins through Knoevenagel condensation *J. Chem. Sci.* **2011**, *123*, 615-621.
- (359) J. S. Ghomi, Z. A. Ultrasonic accelerated Knoevenagel condensation by magnetically recoverable $MgFe_2SO_4$ nanocatalyst: a rapid and green synthesis of coumarins under solvent-free conditions *Ultrason. Sonochem.* **2018**, *40*, 78-83.
- (360) Rosen, T. The perkin reaction In *Comprehensive organic synthesis, vol. 1* Press, P. Ed.; 1991; pp 395-408.
- (361) T. J. Rashamuse, R. K., P. T. Kaye Synthesis of Baylis-Hillman-derived phosphonated 3-(benzylaminomethyl) coumarins *Synth. Commun.* **2010**, *40* (24), 3683-3690.

- (362) U. Sharma, T. N., A. Maji, S. Manna, D. Maiti. Palladium-catalyzed synthesis of benzofurans and coumarins from phenols and olefins *Angew. Chem. Int. Ed.* **2013**, *52* (48), 12669-12673.
- (363) J. Ferguson, F. Z., H. Alper Synthesis of coumarins via Pd-catalyzed oxidative cyclocarbonylation of 2-vinylphenols *Org. Lett.* **2012**, *14* (21), 5602-5605.
- (364) S. R. K. Priyanka, D. K. Recent advances in transition-metal-catalyzed synthesis of coumarins *Synthesis* **2016**, *48* (15), 2303-2322.
- (365) F. Ulgheri, M. M., O. Piccolo Enantioselective synthesis of (S)- and (R)-tolterodine by asymmetric hydrogenation of a coumarin derivative obtained by a Heck reaction *J. Org. Chem.* **2007**, *72* (16), 6056-6059.
- (366) B. M. Trost, F. D. T., K. Greenman Atom economy. Palladium-catalyzed formation of coumarins by addition of phenols and alkynoates via a net C-H insertion *J. Am. Chem. Soc.* **2003**, *125* (15), 4518-4526.
- (367) J. Oyamada, T. K. Synthesis of coumarins by Pt-catalyzed hydroarylation of propiolic acids with phenols *Tetrahedron* **2006**, *62* (19), 6918-6925.
- (368) M. M. Heravi, V. Z., M. Malmir, L. Mohammadi Buchwald-Hartwig reaction: an update *Monatsh. Chemie* **2021**, *152* (10), 1127-1171.
- (369) Y. Li, Z. Q., H. Wang, X. Fu, C. Duan Palladium-catalyzed oxidative Heck coupling reaction for direct synthesis of 4-arylcoumarins using coumarins and arylboronic acids. *J. Org. Chem.* **2012**, *77* (4), 2053-2057.
- (370) J.-J. Zhu, J.-G. J. Pharmacological and nutritional effects of natural coumarins and their structure-activity relationships *Mol. Nutr. Food Res.* **2018**, *62*.
- (371) E. J. T. Sierra, C. F. C., L. Diniz, I. S. Caldas, J. A. Hawkes, D. T. Carvalho Coumarins as potential antiprotozoal agents: biological activities and mechanism of action *Rev. Bras. Farmacognosia* **2021**, *31* (5), 592-611.
- (372) Y. Zeng, H. G. M. A., X. Li, L. E. Yang, X. Pu, X. Yang Physiological mechanisms by which the functional ingredients in beer impact human health *Molecules* **2024**, *29*.
- (373) S. S. Ghare, H. D., W.-Y. Chen, D. F. Barker, L. Gobejishvilli, C. J. McClain, S. S. Barve, S. Joshi-Barve Acrolein enhances epigenetic modifications, FasL expression and hepatocyte toxicity induced by anti-HIV drug Zidovudine *Toxicol. In Vitro* **2016**, *35*, 66-76.
- (374) Y. Kashman, K. R. G., R. W. Fuller, J. H. Cardellina II, J. B. McMahon, M. J. Currens, R. W. Buckheit Jr., S. H. Hughes, G. M. Cragg, M. R. Boyd HIV inhibitory natural products. Part 7. The calanolides, a novel HIV-inhibitory class of coumarin derivatives from the tropical rainforest tree, *Calophyllum lanigerum* *J. Med. Chem.* **1992**, *35* (15), 2735-2743.
- (375) G. Z. J. Cesar, M. G. G. A., M. M. Marius, E. M. Elizabeth, C. B. M. Angel, H. R. Maira, C. L. M. Guadalupe, J. E. Manuel, R. C. Ricardo Inhibition of HIV-1 reverse transcriptase, toxicological and chemical profile of *Calophyllum brasiliense* extracts from Chiapas, Mexico *Fitoterapia* **2011**, *82* (7), 1027-1034.

- (376) Kostanova, I. Coumarins as inhibitors of HIV reverse transcriptase *Curr. HIV res.* **2006**, *4* (3), 347-363.
- (377) N. Guo, J. W., J. Fan, P. Yuan, Q. Shi, K. Jin, W. Cheng, X. Zhao, Y. Zhang, W. Li, X. Tang, L. Yu *In vitro* activity of isoimperatorin, alone and in combination, against *Mycobacterium tuberculosis* *Let. Appl. Microbiol.* **2013**, *58* (4), 344-349.
- (378) M. Di Braccio, G. G., G. Roma, M. G. Signorello, G. Leoncini. Synthesis and in vitro inhibitory activity on human platelet aggregation of novel properly substituted 4-(1-piperazinyl)coumarins *Eur. J. Med. Chem.* **2004**, *39* (5), 397-409.
- (379) M. E. Riveiro, R. V., A. Moglioni, N. Gomez, A. Baldi, C. Davio, C. Shayo. Biochemical mechanisms underlying the pro-apoptotic activity of 7,8-dihydroxy-4-methylcoumarin in human leukemic cells *Bio. Pharm.* **2008**, *75* (3), 725-736.
- (380) R. Vazquez, M. E. R., M. Vermeulen, E. Alonso, C. Mondillo, G. Facorro, L. Piehl, N. Gomez, A. Moglioni, N. Fernandez Structure-anti-leukemic activity relationship study of *ortho*-dihydroxycoumarins in U-937 cells: Key role of the δ -lactone ring in determining differentiation-inducing potency and selective pro-apoptotic action *Bioorg. Med. Chem.* **2012**, *20* (18), 5537-5549.
- (381) A. Beillerot, J.-C. R. D., G. Kirsch, D. Bagrel Synthesis and protective effects of coumarin derivatives against oxidative stress induced by doxorubicin *Bioorg. Med. Chem. Lett.* **2008**, *18* (3), 1102-1105.
- (382) T. Smyth, V. N. R., W. F. Smyth A study of the antimicrobial activity of selected naturally occurring and synthetic coumarins *Int. J. Antimicrob. Agents* **2009**, *33* (5), 421-426.
- (383) S. Sardari, Y. M., K. Horita, R. G. Micetich, S. Nishibe, M. Daneshtalab Synthesis and antifungal activity of coumarins and angular furanocoumarins *Bioorg. Med. Chem.* **1999**, *7* (9), 1933-1940.
- (384) B. S. Rauckman, M. Y. T., J. V. Johnson, B. Roth. 2,4-Diamino-5-benzylpyrimidines and analogs as antibacterial agents. 10. 2,4-Diamino-5-(6-quinolylmethyl)- and - [(tetrahydro-6-quinolyl)methyl]pyrimidine derivatives. Further specificity studies *J. Med. Chem.* **1989**, *32* (8).
- (385) N. Barooah, J. M., H. Pal, A. C. Bhasikuttan Non-covalent interactions of coumarin dyes with cucurbit[7]uril macrocycle: modulation of ICT to TICT state conversion *Org. Biomol. Chem.* **2012**, *10*, 5055-5062.
- (386) N. Saleh, Y. A. A.-S., L. Al-Kaabi, I. Ghosh, W. M. Nau A coumarin-based fluorescent PET sensor utilizing supramolecular pK_a shifts *Tet. Lett.* **2011**, *52* (41), 5249-5254.
- (387) R. S. Bojesomo, K. I. A., H. A. Saadeh, L. A. Siddig, N. Saleh Benzimidazole-piperazine-coumarin/cucurbit[7]uril supramolecular photoinduced electron transfer fluorochromes for detection of carnesol by stimuli-responsive dye displacement and pK_a tuning *ACS Omega* **2022**, *7* (2), 2356-2363.
- (388) P. Jana, T. M., R. Khurana, N. Barooah, V. Soppina, J. Mohanty, S. Kanvah Fluorescence enhancement of cationic styrylcoumarin-cucurbit[7]uril complexes: Enhanced stability and cellular membrane localization *J. Photochem. Photobiol. A* **2019**, 384.

- (389) M. E. Aliaga, L. G.-R., M. Pessego, R. Montecinos, D. Fuentealba, I. Uribe, M. Martin-Pastor, O. Garcia-Beltran Host-guest interaction of coumarin-derivative dyes and cucurbit[7]uril: leading to the formation of supramolecular ternary complexes with mercuric ions *New J. Chem.* **2015**, 39 (4), 3084-3092.
- (390) M. O. Park, M. G. M., T. J. Kang Fluorescence enhancement of 7-diethylamino-4-methylcoumarin by noncovalent dipolar interactions with cucurbiturils *Bull. Korean Chem. Soc.* **2013**, 34 (5), 1378-1382.
- (391) B. C. Pemberton, R. K. S., A. C. Johnson, S. Jockusch, J. P. da Silva, A. Ugrinov, N. J. Turro, D. K. Srivastava, J. Sivaguru. Supramolecular catalysis: Insights into cucurbit[8]uril catalyzed photodimerization of 6-methylcoumarin. *Chem. Commun.* **2011**, 47, 6323-6325.
- (392) D. Bardelang, K. A. U., D. M. Leek, J. C. Margeson, G. Chan, C. I. Ratcliffe, J. A. Ripmeester Cucurbit[n]urils ($n = 5-8$): A comprehensive solid state study. *Cryst. Growth Des.* **2011**, 11 (12), 5598-5614.
- (393) M. D. Krasowski, D. D., C. S. Morris, J. Maakestad, J. L. Blau, S. Ekins. Cross-reactivity of steroid hormone immunoassays: clinical significance and two-dimensional molecular similarity prediction *BMC Clin Pathol* **2014**, 14.
- (394) Z. Deng, N. W., Y. Liu, Z. Xu, Z. Wang, T.-C. Lau, G. Zhu A photocaged, water-oxidizing, and nucleolus-targeted Pt(IV) complex with a distinct anticancer mechanism *J. Am. Chem. Soc.* **2020**, 142 (17), 7803-7812.
- (395) C. Muller, P. E., M.-L. Viriot, M.-C. Carre Protection and labelling of thymidine by a fluorescent photolabile group *Helv. Chim. Acta* **2001**, 84 (12), 3735-3741.
- (396) A. Hatano, Y. K., Y. Kondo, Y. Sunaga, H. Umezawa, M. Okada, H. Yamada, R. Iwaki, A. Kato, K. Fukui Synthesis and characterization of novel, conjugated, fluorescent DNJ derivatives for α -glucosidase recognition *Bioorg. Med. Chem.* **2017**, 25 (2), 773-778.
- (397) M. Zhu, L. M., J. Wen, B. Dong, Y. Wang, Z. Wang, J. Zhou, G. Zhang, J. Wang, Y. Guo, C. Liang, S. Cen, Y. Wang Rational design and structure-activity relationship of coumarin derivatives effective on HIV-1 protease and partially on HIV-1 reverse transcriptase *Eur. J. Med. Chem.* **2020**, 186.
- (398) J.-F. Ge, C. A., M. Kaiser, S. Wittlin, R. Brun, M. Ihara Synthesis and in vitro antiprotozoal activities of water-soluble, inexpensive 3,7-bis(dialkylamino)phenoxazin-5-ium derivatives *J. Med. Chem.* **2008**, 51 (12), 3654-3658.
- (399) H. Takakura, K. S., T. Ueno, Y. Urano, T. Terai, K. Hanaoka, T. Tsuboi, T. Nagano. Development of luciferin analogues bearing an amino group and their application as BRET donors *Chem. Asian J.* **2010**, 5 (9), 2053-2061.

8. List of Abbreviations

A549	lung adenocarcinoma
ABA	associative binding assay
ACN	acetonitrile
AMCA	Amino-4-methyl-3-coumarinylacetic acid
Ac ₂ O	acetic anhydride
AcOH	acetic acid
BG	brilliant green
BRET	bioluminescence resonance energy transfer
BSA	bovine serum albumin
C1	coumarin 1
C481	coumarin 481
CA	carbohydrate antigen
CB	cucurbituril
CB7-Ab	CB7-conjugated antibodies
CB7-BC	CB7-berberine conjugate
CB7-BiPy	CB7-bipyridine conjugate
CB7-NBD	CB7-nitrobenzoxadiazole conjugate
CB7-OPr	monopropargyloxy CB7
CB7-Ru	CB7-ruthenium(II) tris(bipyridine) conjugate
CBA	competitive binding assay
CCD	charge coupled device
CD	cyclodextrin
cDNA	complementary DNA
CE	crown ether
CEA	carcinoembryonic antigen
CF	cystic fibrosis
CFTR	cystic fibrosis transmembrane conductance regulator
CRP	c-reactive protein
CSA	cellulosic sulfonic acid
CV	cyclic voltammetry
CuAAC	copper (I)-catalyzed azide-alkyne cycloaddition
DABCO	1,4-diazabicyclo[2.2.2]octane
DBAE	2-(dibutylamino)ethanol
DBO	2,3-diazabicyclo[2.2.2]oct-2-ene
DBU	1,8-diazabicyclo[5.4.0]undec-7-ene
DFT	density functional theory

List of Abbreviations

DHMC	4-methyl-7,8-dihydroxycoumarin
DNA	deoxyribonucleic acid
DPA	9,10-diphenylanthracene
dsDNA	double strand DNA
ECL	electrochemiluminescence
ELISA	enzyme-linked immunosorbent assay
em	emission
ER	endoplasmic reticulum
EYPC	L- α -phosphatidylcholine
exc	excitation
FPRL1	formyl peptide receptor
GDA	guest displacement assay
GMO	genetically modified organism
HIV	human immunodeficiency virus
HP- β CD	2-hydroxypropyl- β -cyclodextrin
HPLC	high-performance liquid chromatography
HT29	colorectal adenocarcinoma
Hsp90	heat shock protein 90
ICT	internal charge transfer
IDA	indicator-displacement-assay
IMS	ion mobility spectrometry
IN	integrase
IR	infrared
ISC	intersystem crossing
ITC	isothermal titration calorimetry
ITO	indium tin oxide
IUPAC	international union of pure and applied chemistry
LC	ligand centered
LDLR	low density lipoprotein receptor
LE	lariat ether
LOD	limit of detection
MB	molecular beacon
MEF	mouse embryonic fibroblast
MLCT	metal-ligand charge transfer
MOF	metal organic framework
NIR	near-infrared
NMBA	neuromuscular blocking agent

List of Abbreviations

NMR	nuclear magnetic resonance
NSCLC	non-small cell lung carcinoma
PC	packing coefficient
PCA	principal component analysis
PCP	phencyclidine
PDDA	poly(diallyldimethylammoniumchloride)
PDT	photodynamic therapy
PET	photoinduced electron transfer
PMT	photomultiplier tube
PR	protease
PSA	prostate-specific antigen
PpIX	protoporphyrin IX
Q7R	CB7-tetramethylrhodamine conjugate
RNA	ribonucleic acid
RPE-1	non-cancerous retinal pigment epithelial cells
RT	reverse transcriptase
Ru-COOH	Bis(2,2'-bipyridine)-[4-(4'-methyl-2,2'-bipyridin-4-yl)butanoic acid]ruthenium (II)
Ru-N ₃	azide-functionalized ruthenium (II) complex
SAR	structure activity relationship
SEC	size exclusion chromatography
SERS	surface-enhanced raman spectroscopy
ssDNA	single strand DNA
TEG	tetraethylene glycol
TFA	trifluoroacetic acid
THPTA	tris(3-hydroxypropyltriazolylmethyl)amine
TICT	twisted intramolecular charge transfer
TMPD	<i>N,N,N,N</i> -tetramethyl- <i>p</i> -phenylenediamine
TPM	triphenylmethane
TPrA	tripropylamine
U87	glioblastoma

9. Appendices

9.1. Curriculum Vitae

Patrick Gruhs

Education

M.Sc. Analytical and bioanalytical chemistry Aalen University/KIT

Title of thesis: Development of Synthetic Strategies for Cyclopropanated Fragrances **10/19 – 09/21**

B. Sc. Biological chemistry Aalen University

Title of thesis: Festphasensynthese eines fluorophormarkierten Kurstakin-Analogons **10/14 – 09/19**

A-levels Hariolf-Gymnasium
Ellwangen
09/2006 – 06/2014

Research experience

Since 11/2021: PhD candidate

Design and synthesis of new chemosensors based on cucurbit[*n*]uril Priv. Doz. Dr. Frank Biedermann

- Multi-level synthesis of dyes, fluorophores and metal complexes
- Click-reaction with CB; synthesis of sensor libraries; advanced organic techniques
- Photophysical, electrochemical, electroluminescent measurements with biorelevant analytes

INT, KIT

03/2021 – 09/2021 Master Thesis

Synthesis and development of new cyclopropanated fragrances Prof. Dr. Stefan Bräse

- Cooperation with Symrise AG
- Synthesis and development of a Ruthenium-based catalyst and application on various alkene educts

IOC, KIT

09/2020 Internship at Aalen university

Synthesis and application of new matrices for MALDI-MS Prof. Dr. Hans Junker

- Synthesis of a library based on 9-aminoacridine
- Evaluation of function in MALDI experiments

Hochschule Aalen

03/2019 – 09/2019 Bachelor Thesis

Synthesis of a coumarin-labelled kurstakin analogue Prof. Dr. Norbert Schaschke

- Solid phase peptide synthesis in a robot-supported system
- Evaluation as a potential new antibiotic compound

Hochschule Aalen

03/2017 – 08/2017 Practical semester

Natural product synthesis (flavonoids) Georg Knobloch, M.Sc.

- Multi-level organic synthesis, retrosynthetic approaches

Dr. Ing. Max Schlötter GmbH

- Improvement of skills in organic chemistry, planning of synthesis

02/2017 Research project

Synthesis of pseudopelletierine

Prof. Dr. Hans-Dieter Junker
Hochschule Aalen

- Biomimetic synthesis of a naturally occurring alkaloid
- Sublimation purification of final product; characterization

Research interest

- Organic chemistry
- Medicinal chemistry and pharmacology
- Supramolecular chemistry

Publications and patents

1. PCT/EP2021/075035 Cyclopropanated fragrance compounds, Symrise AG, **2021**
2. Electrochemical Detection of Drugs via a Supramolecular Cucurbit[7]uril-Based Indicator Displacement Assay, **ACS Sens.** 2023, 8, 7, 2525–2532
3. Unimolecular Cucurbit[7]uril-Based Indicator Displacement Assay with Dual Signal-Readout for the Detection of Drugs, **Analysis & Sensing** 2024, 4, e202400025
4. EP 4 467 974 A1 NOVEL CHEMOSENSORS AND THEIR USE IN ELECTROCHEMICAL DETECTION METHODS, 2024 Bulletin 2024/48

Skills

Practical skills

- Multi-level organic synthesis, advanced organic synthesis
- Purification techniques; chromatography and HPLC
- Solid phase peptide synthesis
- Working with metal-organics
- Characterization: HPLC, NMR (1D and 2D), FT-IR, UV-VIS, Fluorimeter, MALDI-TOF, ESI-TOF, HPLC-MS
- Basic skills in molecular biology and microbiology

Software skills

- ChemDraw, MestreNova, Bruker TopSpin, ChemAxon, Origin, Microsoft office

9.2. Acknowledgements

In this section, I would like to express my great gratitude to all people that were involved in completing this PhD thesis.

First of all, I would like to thank my supervisor Priv. Doz. Dr. Frank Biedermann. I am extremely grateful for giving me this opportunity to grow both as a person and a researcher. During this period of guidance, I learnt countless things. For example, that you should not directly dispose important NMR tubes in case they are needed later. Not only in the lab, also on a few journeys to Italy we had a great time together. I appreciate very much the handling of both family and being a PhD supervisor for several people and I always wonder how it is possible to manage everything. I also am very grateful to Dr. Pierre Picchetti, who basically served as a second supervisor in the beginning of my PhD. We always had some good scientific discussions. Of course, I also want to thank Prof. Dr. Stefan Bräse, who initiated my PhD studies by introducing me to Frank.

Next, I want to thank all of my former and current colleagues. When we shared an office, I really enjoyed the company of Dr. Changming Hu, from whom I learnt a lot about cucurbituril synthesis. Also special thanks to Dr. Joana Krämer and Dr. Laura Grimm. I am truly happy to be a part of the current team. Especially I want to thank Alberto Kraft for sharing the office and countless stupid jokes. Thanks to Panos Bizirtsakis, who became a real good Brudi during my time and thank you for always driving the bus. Of course, not to forget Ahmad Omira, whose courage to flee a war-torn country I deeply admire. You have always been a fantastic Atze. Thanks to Rita Maksimova, who is an amazing person and always looks in the hole, same goes for Guillermo Galceran. Of course, I also thank Vahideh Mahram for helping me with photophysical related measurements. A big thanks to my internship students, Ferdinand Selbinger and especially Hanna Hönle for helping me with the measurements, both of which truly have a special place in my heart. I thank Dr. Nilima Manoj, Dr. Amrutha Prabodh, Wenjing Wang, Seth Baker, Kseniia Weber and Vinh Hao La for sharing a pleasant time in the lab. I am glad I met all of you, and hope to always stay in touch, since we all shared the same destiny after all.

I am grateful for all of the accompanying colleagues, Maria Vittoria Balli with whom I shared the ECLipse project, as well as Dr. Florian Feist, Dr. Marco Neumaier, Dr. Papri Chakraborty, for all of your contributions.

Last but not least I want to express my greatest gratitude for all of my family and friends. Stefan Lämmerer, Silvio Collerone, Manuel Nelke, and Volker Höfer - thank you for being the best mäns and all the great time we spent together in Schönau or beyond. Thanks to my parents, Silke and Sven, who always supported my but also kicked my ass when it was necessary. Thanks to my dear brother Moritz for all the great time we spent together, I could not imagine a better brother. And finally, to my wonderful fiancée Valentina (Stüße) Gruhsovic: thank you for always believing in me. I love you with all my heart and soul, and I look forward to spent the rest of my life with you.

9.3. Artificial Intelligence (AI) Disclaimer

This thesis was prepared with limited assistance from artificial intelligence (AI) tools. The use of AI was restricted to stylistic editing, linguistic refinement, and the generation of section titles. All scientific content, data interpretation, and original writing were conceived, developed, and verified by the author. No fully AI-generated material is included in this thesis.